Stochastic Modeling and Simulation of Near-Fault Ground Motions for Performance-Based Earthquake Engineering

By

Mayssa Nabil Dabaghi

A dissertation submitted in partial satisfaction of the

requirements for the degree of

Doctor of Philosophy

in

Engineering - Civil and Environmental Engineering

in the

Graduate Division

of the

University of California, Berkeley

Committee in charge:

Professor Armen Der Kiureghian, Chair
Professor Yousef Bozorgnia
Professor Douglas Dreger
Professor Jack Moehle

Fall 2014

Stochastic Modeling and Simulation of Near-Fault Ground Motions
for Performance-Based Earthquake Engineering

by

Mayssa Nabil Dabaghi

Abstract

Stochastic Modeling and Simulation of Near-Fault Ground Motions
for Performance-Based Earthquake Engineering

by

Mayssa Nabil Dabaghi

Doctor of Philosophy in Engineering - Civil and Environmental Engineering

University of California, Berkeley

Professor Armen Der Kiureghian, Chair

A comprehensive parameterized stochastic model of near-fault ground motions in two orthogonal horizontal directions is developed. The proposed model uniquely combines several existing and new sub-models to represent major characteristics of recorded near-fault ground motions. These characteristics include near-fault effects of directivity and fling step; temporal and spectral non-stationarity; intensity, duration and frequency content characteristics; directionality of components, as well as the natural variability of motions for a given earthquake and site scenario. By fitting the model to a database of recorded near-fault ground motions with known earthquake source and site characteristics, empirical "observations" of the model parameters are obtained. These observations are used to develop predictive equations for the model parameters in terms of a small number of earthquake source and site characteristics. Functional forms for the predictive equations that are consistent with seismological theory are employed.

A site-based simulation procedure that employs the proposed stochastic model and predictive equations is developed to generate synthetic near-fault ground motions at a site. The procedure is formulated in terms of information about the earthquake design scenario that is normally available to a design engineer. Not all near-fault ground motions contain a forward directivity pulse, even when the conditions for such a pulse are favorable. The proposed procedure produces pulselike and non-pulselike motions in the same proportions as they naturally occur among recorded near-fault ground motions for a given design scenario.

The proposed models and simulation procedure are validated by several means. Synthetic ground motion time series with fitted parameter values are compared with the corresponding recorded motions. The proposed empirical predictive relations are compared to similar rela-tions available in the literature. The overall simulation procedure is validated by comparing suites of synthetic ground motions generated for given earthquake source and site characteristics to the ground motion prediction equations (GMPEs) developed as part of phase 2 of the Next Generation Attenuation (NGA) program, (NGA-West2, see, e.g., Campbell and Bozorgnia, 2014). Comparison is made in terms of the estimated median level and variability of elastic ground motion response spectra.

The use of synthetic motions in addition to or in place of recorded motions is desirable in performance-based earthquake engineering (PBEE) applications, particularly when recorded motions are scarce or when they are unavailable for a specified design scenario. As a demonstrative application, synthetic motions from the proposed simulation procedure are used to perform probabilistic seismic hazard analysis (PSHA) for a near-fault site. The analysis shows that the hazard at a near-fault site is underestimated when the ground motion model used does not properly account for the possibility of pulselike motions due to the directivity effect.

To Teta Zouzou and Tante Najla

To Jeddo, my Parents, Lamia and Mazen

To my extended Family and my Friends

Table of Contents

List of Figures

List of Tables

Acknowledgements

I would like to express my utmost gratitude to my research supervisor Professor Der Kiureghian, for mentoring and supporting me during the course of my PhD. His exceptional teaching and guidance have been fundamental in my academic development and growth as a researcher and a person. I am grateful for his continued support in many aspects, including academic, personal, motivational, and career support. He made it possible for me to develop valuable experience teaching and presenting my research at seminars and conferences. His great availability and the convivial relationships he nurtures with and among his students are extremely appreciated. I am also very grateful for his support of my various extra-curricular activities. I consider myself very fortunate to have been his student.

I am also extremely grateful to Professor Yousef Bozorgnia for his mentorship from the onset of my research work. He often attended my seminar presentations and gave me constructive comments and suggestions for improvements. He was always available to meet, answer my questions, provide me with guidance, and point me to valuable resources. Not only am I grateful for his contribution to my development as a researcher, but also for his advice on post-graduation plans and career paths.

My grateful thanks are extended to Professor Douglas Dreger and Professor Jack Moehle for valuable discussion and for sitting on my dissertation and qualifying exam committees. The participation of Professor Steven Mahin and Professor David Brillinger in my qualifying exam committee and the suggestions they gave me are also greatly appreciated. I am very grateful for the opportunity that Professor Francisco Armero gave me to work as a graduate student instructor and reader for his courses. I am also thankful to all my Professors at UC Berkeley for the valuable knowledge and expertise that I gained in their courses.

I wish to acknowledge the help I received from Dr. Tadahiro Kishida from PEER. Dr. Kishida provided with valuable data, answered the many questions I addressed to him, and performed several processing tasks that were very useful to my research. I would also like to thank Tom Shantz from the California Department of Transportation for his interest in my research and for his relevant questions and comments that led me to undertake improvements. I wish to acknowledge the feedback and suggestions that Dr. Sanaz Rezaeian and Dr. Nico Luco from USGS have provided me in several aspects of my research. I thank Professor Jack Baker and Dr. Shrey Shahi for providing me with their pulse-extraction codes and with the extracted pulses and residuals of the database as well as for their consultation during the course of this study.

I would like to offer my special thanks to Shelley Okimoto and the administration of the Civil and Environmental Engineering department for always being helpful and cheerful. I am also grateful to the many fellow and past SEMM students and friends for their support and the memorable times spent together. I look forward to opportunities to collaborate with some of them in the future. I also am thankful to all the students and scholars who, at some point, were members of Professor Der Kiureghian's research group, for our interactions and collaborations. They include Katerina Konakli, Sanaz Rezaeian, Michelle Bensi, Marco Broccardo, Sara Broglio, Smitha Koduru, Iris Tien, Matteo Pozzi, Wiggo Smeby, James-A. Goulet, Binbin Li, He-Qing (Max) Mu and Ziqi Wang. Among them, I am particularly grateful to Marco Broccardo.

We started and are concluding our PhD journeys together, and I value his presence and all the conversations we have had along the way.

During the course of my studies at UC Berkeley, I was fortunate to cross paths with some amazing people. I would like to acknowledge the invaluable support I received from incredible friends like Edson Severnini, Tarso Madeira, and Amina Al Kandari, only to name a few. They were available to give me advice and motivation when I needed them the most, and their friendship and company greatly contributed to making this journey positive and pleasant.

I am thankful to all my Lebanese Berkeley friends, who often come and go, but always make Berkeley feel a little bit closer to home. I particularly want to thank Narine Bolghourjian, with whom I started the Berkeley journey, as well as Shaghig Kasparian and Marwan Harajli, who were of great support in the final stages of this dissertation. I also want to thank the Balabanians for being my second family, here in the Bay area.

Last but not least, I am profoundly grateful to my parents, my family and my close friends for their endless love, support and encouragements despite the distance and throughout my studies.

This study was sponsored by the Pacific Earthquake Engineering Research Center (PEER) and funded by the California Department of Transportation, the Pacific Gas & Electric Company, and PEER Transportation Systems Research Program. Any opinions, findings, and conclusions or recommendations expressed in this material are those of the author and do not necessarily reflect those of the sponsoring agencies. Additional support was provided by the Taisei Chair in Civil Engineering at the University of California, Berkeley. These sources of financial support are gratefully acknowledged.

1 Introduction

1.1 MOTIVATION, OBJECTIVE AND SCOPE

Near-fault ground motions often possess distinct characteristics that can have strong influence on structural response. These include the rupture directivity effect in the fault-normal direction and a permanent displacement, the "fling step", in the fault-parallel direction. When a site is located in the near-field region of a fault, the characteristics of the ground motion at the site depend, among other factors, on how the rupture propagates relative to the site. One of such ground motion characteristics is termed the rupture directivity effect. A near-fault site may experience forward directivity when the fault rupture propagates towards the site with a velocity almost equal to the shear-wave velocity. The resulting ground motion typically exhibits a large velocity pulse, which may impose extreme demands on a structure. Forward directivity is generally characterized by the presence of a two-sided, long-period, large-amplitude velocity pulse in the fault-normal direction. Backward directivity occurs when the fault rupture propagates away from the site. The resulting ground motion tends to be of low intensity and long duration. The fling step is caused by the permanent displacement of the fault and is usually characterized by a one-sided velocity pulse in the fault-parallel direction. In this dissertation, the characterization of a ground motion as pulselike or non-pulselike refers to the presence or absence of a directivity pulse.

Despite continuous expansion of the database of recorded earthquake ground motions, recorded near-fault ground motions, especially those exhibiting pulse motions, remain scarce. This produces interest in developing synthetic ground motions for near-fault sites, which can be used in performance-based earthquake engineering (PBEE) in addition to recorded motions. Moreover, response history dynamic analysis is necessary when the response of a structural or geotechnical system to the earthquake ground motion excitation is expected to be non-linear. This is often the case at near-fault sites where the ground motion is severe. Recorded ground motions, possibly modified by scaling or spectral matching, can be used. However, the use of synthetic ground motions is of particular interest when recorded motions are scarce or when the modified motions are deemed to be unrealistic.

Obviously, it is crucial that the synthetic motions be realistic and capture the important characteristics and natural variability of recorded near-fault ground motions. For engineering applications, the synthetic ground motion model should properly represent the temporal and spectral non-stationarity of recorded earthquake ground motions and the characteristics that control the response of structural and geotechnical systems, namely the intensity, duration and frequency content characteristics and their evolution in time. For probabilistic seismic hazard analysis (PSHA), the synthetic ground motion model should properly represent the natural variability of recorded ground motions. Furthermore, from a practical standpoint, it is most useful if the synthetic motions are generated in terms of information that is normally available to the design engineer. This information describes the earthquake design scenario, or earthquake source and site characteristics, and typically includes the type of faulting, the earthquake

magnitude, the position of the site relative to the potential fault rupture, and the shear-wave velocity of the soil at the site.

Our objective in this study is to develop a parameterized stochastic model of near-fault ground motions in two orthogonal horizontal directions and use it to generate synthetic motions. We formulate the model, develop prediction equations for the model parameters, and describe and illustrate a site-based (or empirical) simulation method that employs the proposed model and generates synthetic near-fault ground motions at a site. Not all near-fault ground motions contain a forward directivity pulse, even when the conditions for such a pulse are favorable. The model proposed in this study allows consideration of both pulselike and non-pulselike motions in the same proportions as they naturally occur among recorded near-fault ground motions for a given design scenario. The model captures the rupture directivity characteristics, the temporal and spectral non-stationarity, and the intensity, duration and frequency content characteristics of recorded earthquake ground motions. Moreover, it properly represents the natural variability of recorded ground motions and is practically formulated in terms of information about the earthquake design scenario that is normally available to the design engineer.

We validate the proposed near-fault ground motion model by validating its various constituents. Synthetic ground motions are compared to their recorded counterparts. The predictive relations we develop are compared to similar relations available in the literature. Finally, the overall methodology is validated by comparing suites of synthetic ground motions generated for given earthquake source and site characteristics to the ground motion prediction equations (GMPEs) developed as part of phase 2 of the Next Generation Attenuation (NGA) program, (NGA-West2, see, e.g., Bozorgnia et al, 2014; Campbell and Bozorgnia, 2013, 2014). Comparison is made in terms of the estimated median level and variability of the elastic ground motion response spectra.

In addition to developing and validating the proposed stochastic model of near-fault ground motion, we demonstrate the importance of the model in characterizing near-fault ground motions for engineering applications. We emphasize the ground motion characteristics that are represented by our model but are lacking in existing GMPEs. We also illustrate the use of synthetic ground motions to perform PSHA. The seismic hazard is directly characterized in terms of the synthetic ground motion time series, instead of a response spectrum. The analysis shows that the hazard at a near-fault site is underestimated when the ground motion model used does not properly account for the possibility of pulselike motions due to the directivity effect.

The formulation of the model accounts for the two near-fault effects of rupture directivity and the fling step, with focus on the former. The scope of this study is limited to the representation of two horizontal components of ground motion. Moreover, the present dissertation is only focused on modeling the ground motion at a single near-fault site. In its present formulation, the model does not account for the correlation and spatial variability of ground motions from the same event but at different locations.

The major contributions of this study can be summarized as follows:

- Development of a stochastic model for near-fault ground motions that properly accounts for the special characteristics of sites near the earthquake source, including the rupture directivity effect and fling step;
- Development of a method for generation of synthetic ground motions that possess characteristics similar to recorded ground motions, including temporal and frequency

characteristics, near-fault effects, as well as variability of the motions for a given earthquake source and site scenario;

- Novel application of the proposed simulation method for probabilistic seismic hazard analysis at a near-fault site, demonstrating that the seismic hazard at such site could be underestimated when the rupture directivity effect is not properly accounted for.

1.2 ORGANIZATION OF THE DISSERTATION

This dissertation is organized into 8 chapters. Chapter 2 reviews the relevant literature about near-fault ground motions, while Chapter 3 reviews signal processing techniques commonly applied to earthquake ground motion records and extends some of them for application to synthetic ground motions. A parameterized stochastic model of near-fault ground motion is constructed in Chapter 4 and its parameters are fitted to existing data in Chapter 5. The model is then used to generate synthetic near-fault ground motions in Chapter 6, and to illustrate a simulation-based probabilistic seismic hazard analysis (PSHA) in Chapter 7. A more detailed description of each chapter is presented below.

After this introductory chapter, Chapter 2 gives a review of the state-of-the-art on characterization and modeling of near-fault ground motions. It starts with a discussion of the physics of near-fault ground motion. It then reviews different types of models that describe ground motions, namely ground motion prediction equations (GMPEs) and models of ground motion time series. Models that have been proposed to represent the near-fault rupture directivity effect are discussed. The chapter lastly reviews available models to describe the orientation of ground motions relative to fault strike, to compute the probability of occurrence of a forward directivity pulse, and to predict the fling step.

Chapter 3 reviews relevant signal processing techniques applied to ground motion records, including baseline correction, low-cut filtering and resampling. First, models that describe the theoretical shape and scaling of the Fourier amplitude spectrum (FAS) of ground motion are reviewed. The chapter then discusses baseline correction and low-cut filtering, which are techniques employed to correct recorded earthquake signals for distortions and to remove frequencies with unacceptable signal-to-noise ratio. These techniques are extended to synthetic ground motions with the aim of adjusting the scaling of the FAS of synthetic motions to be consistent with the scaling of recorded motions. They also assure that the velocity and displacement at the end of the motion converge to zero upon integration of the synthetic acceleration time series. This desired feature is not directly guaranteed by stochastic models developed for an acceleration process. Finally, methods to modify the time step of an earthquake signal are studied. The ground motion database that is used in later chapters to fit the ground motion model is a collection of worldwide records by a variety of instruments and at different time steps or sampling rates. For consistency, it is essential that the ground motion model be fitted to signals that have the same time step. This requires resampling.

In Chapter 4, a parameterized stochastic model of near-fault ground motion in two orthogonal horizontal directions is developed. The chapter starts with a brief review of different types of ground motion models available in the literature. It describes existing models of the forward directivity pulse and of pulselike near-fault ground motions. It also presents the wavelet-based pulse extraction algorithm developed by Baker (2007). This algorithm is employed in Chapter 5 to classify recorded ground motions as pulselike or non-pulselike and to extract the

largest velocity pulse from the former. The chapter then provides a detailed formulation of the proposed stochastic model of pulselike and non-pulselike near-fault ground motions. The model of pulselike ground motion is formulated in the direction along which the pulse has its largest magnitude and the corresponding orthogonal direction. The model in the direction of the largest pulse consists of two sub-models, one for the velocity pulse and one for the residual motion, which is defined as the total ground acceleration minus the derivative of the velocity pulse. The velocity pulse model is a 5-parameter modified version of the idealized model earlier developed by Mavroeidis and Papageorgiou (2003). The model for the residual motion is the non-stationary, filtered white-noise model formulated by Rezaeian and Der Kiureghian (2008, 2010) with a modified modulating function and a total of 7 parameters. This model is also employed for motion in the horizontal direction orthogonal to the direction of the largest pulse. The model for non-pulselike ground motions is formulated in the "principal" horizontal directions. The modified version of the model by Rezaeian and Der Kiureghian (2008, 2010) is also used to describe these ground motion components. The chapter ends by presenting two additional models that are needed for a complete characterization of near-fault ground motions: A pulse probability model, which is used to combine pulselike and non-pulselike models; a directionality model to describe the orientation of the ground motion components relative to the fault strike.

In Chapter 5, the database of recorded near-fault pulselike and non-pulselike ground motions used in the study is presented. Each pulselike ground motion record is rotated into its component containing the largest horizontal pulse and the corresponding orthogonal component. The component in the direction of the largest pulse is then decomposed into the pulse, extracted using the algorithm developed by Baker (2007), and the residual motion. Each non-pulselike ground motion record is rotated into horizontal components in the major and intermediate "principal directions". For each pulselike ground motion record in the database, the 12 parameters of the pulselike model are identified by fitting the pulse and residual models to the recorded counterparts in the direction of the largest pulse; the 7 parameters of the non-pulselike model are identified by fitting to the corresponding recorded orthogonal component. For each non-pulselike ground motion record in the database, the 7 parameters of the non-pulselike model are identified by fitting to the recorded major and intermediate components. Empirical predictive equations are then developed for the parameters of the pulselike and non-pulselike models in terms of the earthquake source and site characteristics (i.e., type of faulting, the earthquake magnitude, depth to top of rupture, the position of the site relative to the potential fault rupture, and the shear-wave velocity of the soil at the site). Most parameters can be classified into intensity parameters, period or frequency parameters, and time or duration parameters, and predictive equations proposed in literature for similar parameters are reviewed beforehand. They guide our choice of explanatory variables and functional forms. After transforming the samples of identified parameter values to the standard normal space, regression analysis with random effects is used to develop empirical predictive equations in terms of the earthquake source and site characteristics. Estimated correlation coefficients between the regression residuals provide estimates of the correlations between the model parameters in the normal space. The chapter ends with a comparison of the empirical predictive equations that we develop with similar relations proposed in the literature.

Chapter 6 presents the procedure for simulating synthetic pulselike and non-pulselike near-fault ground motions. The inclusion into the simulation procedure of a model to compute the probability of occurrence of a pulselike motion is described. Two types of synthetic ground motions are investigated: synthetic motions generated using model parameters that are obtained

by fitting the model to a recorded motion, and synthetic motions generated using randomly selected values of the model parameters for prescribed earthquake source and site characteristics. The synthetic motions generated using fitted model parameters essentially represent different realizations of near-fault ground motion for the same earthquake. As an example, pulselike and non-pulselike synthetic ground motions are generated using fitted model parameters and the model is validated by comparing the time series as well as the elastic spectra of the recorded and synthetic motions. Synthetic motions generated using randomly selected values of the model parameters for prescribed earthquake source and site characteristics represent realizations of near-fault ground motion from different earthquakes with similar source and site characteristics. The type of motion, i.e. pulselike or non-pulselike, is generated according to the pulse probability model, and the corresponding model parameters are generated according to the empirical predictive equations and estimated correlation coefficients. Example pulselike and non-pulselike synthetic ground motions are generated and examined. For a given earthquake design scenario, sets of model parameters are randomly selected and used to generate an ensemble of synthetic near-fault ground motions. The model captures the variability in the model parameters and accounts for their correlations. The resulting synthetic motions have the same statistical characteristics as the motions in the database, including the record-to-record variability for the given set of earthquake source and site characteristics. The model is validated by comparing the spectra of the synthetic ground motions to spectra from the most recent Next Generation Attenuation (NGA-West2) GMPEs in terms of the median level and period-dependent standard deviation. The chapter ends by describing and illustrating a procedure to incorporate a model of the fling step into our ground motion simulation methodology. Despite being preliminary, this addition permits a more complete characterization of near-fault ground motion, accounting for both the directivity effect and fling step.

In Chapter 7, the use of synthetic ground motions to perform PSHA is illustrated. The chapter starts by outlining the Monte Carlo procedure that is employed to simulate an earthquake ground motion catalog over a selected period of time. The procedure is illustrated by building a realistic but simplified catalog of rupture occurrences on a fault near a site located in Berkeley, CA. The seismic hazard at the site is directly characterized in terms of synthetic ground motion time series from the simulated catalog of earthquake design scenarios, instead of a response spectrum. Finally, the hazard is calculated for a simple structure located at the site and idealized as an inelastic single-degree-of-freedom (SDOF) oscillator. The deaggregation of the hazard demonstrates the important contribution of pulselike ground motions to the seismic hazard at a near-fault site.

Chapter 8 summarizes the major findings and conclusions of the study. It also describes the limitations of the model and lists a number of improvements that can be undertaken.

2 Review of State of the Art on Characterization of Near-Fault Ground Motions

2.1 INTRODUCTION

It has been observed that earthquake ground motion recordings in the near-fault region, here taken as within 30 km from the fault rupture, often significantly differ in their characteristics from recordings of far field ground motions. Some of these differences are usually observed in the velocity and displacement time series and have been attributed to two effects: the rupture directivity effect and the fling step. Rupture directivity denotes the effect of the rupture propagation relative to the site on the ground motion at the site. Near-fault directivity often manifests in the fault-normal (FN) direction, which is the direction perpendicular to the surface of the fault rupture. A near-fault site may experience forward directivity when the fault rupture propagates towards the site with a velocity almost equal to the shear-wave velocity. As illustrated in Figure 2.1 for the recordings at the Lucerne station during 1992 Landers earthquake, this effect appears in the form of a large, long-period velocity pulse. Backward directivity occurs when the fault rupture propagates away from the site. The resulting ground motion tends to be of low intensity and long duration. The fling step is observed in the fault-parallel (FP) direction, i.e., the direction parallel to the fault slip, and appears in the form of a permanent displacement. These effects, especially the rupture directivity effect, result in large spatial variations in the amplitude and duration of near-fault ground motions, as well as in significant differences between the horizontal strike-normal (SN) and strike-parallel (SP) components. Note that when a fault is vertical and of strike slip type, then the FN direction coincides with the SN direction, and the FP direction coincides with the SP direction. Figure 2.2 shows ground motions recorded at two near-fault stations at Lucerne and Joshua Tree during the Landers earthquake. Since the fault is vertical and strike slip, the SN component here is the same as the FN component. It is seen that the Lucerne site, which is located in the direction of propagation of the rupture, records a large amplitude, short duration two-sided velocity pulse, while the Joshua Tree site, which is located near the epicenter and away from the direction of propagation of the rupture, records a small amplitude long duration velocity time series. The differences between the SN and SP components (same as the FN and FP components in this case) can be noticed in Figure 2.1, with two-sided and one-sided velocity pulses in the SN and SP directions, respectively.

Near-fault directivity effects of ground motions are not properly represented in modern codes and their effects have not been properly incorporated into current ground motion prediction equations or probabilistic seismic hazard analysis methods, though efforts in this direction are ongoing (e.g., Spudich et al., 2014; Shahi and Baker, 2013b). The large pulse inherent in these motions can potentially subject structures to one or two cycles of severe inelastic deformation and result in a large amount of damage. The damage potential of near-fault pulses was originally discovered by Bertero et al. (1976, 1978); however, it is only after the 1994 Northridge earthquake that the severe implications of near-fault ground motions on the performance of structures and the importance of incorporating their effects into the design process was recognized (e.g., Somerville and Abrahamson, 1996; Bozorgnia and Mahin, 1998; Mavroeidis and Papageorgiou, 2003). In the near-fault region, the seismic demands on elastic

long period structures, such as base-isolated buildings, tall buildings and long-span bridges, are generally underestimated. However, the damage potential mostly concerns short and medium period structures (e.g., Sasani and Bertero, 2000). Indeed, ductile short and medium period structures can be heavily damaged when their effective period elongates towards the pulse period (e.g., Anderson and Bertero, 1987; Tothong et al., 2007). Unfortunately, near-fault records are scarce, and thus a large effort has been recently focused on trying to understand, model and simulate these ground motions and their effects on the response of structures.

Special attention needs to be given to the design of bridges in the near-fault region. In addition to the large velocity pulse in the FN direction and the large static displacements in the FP direction, near-fault bridges with multiple supports are often subjected to large dynamic differential motions. These may arise from wave passage and incoherence effects, as well as from spatial variations in directivity conditions and from permanent differential displacements, especially when the fault rupture reaches the surface (Somerville, 2002).

In this chapter, we present an overview of the state-of-the-art on characterization and modeling of near-fault ground motion. The chapter starts with a discussion of the physics of near-fault ground motions. It then describes several spectral and time-domain models that are proposed in the literature to account for the forward directivity effect. It lastly describes available models to compute the probability of occurrence of a forward directivity pulse, to predict the orientation of such pulses, and to predict the fling step. A thorough understanding of the underlying phenomena and principles is needed for the developments in the subsequent chapters of this report.

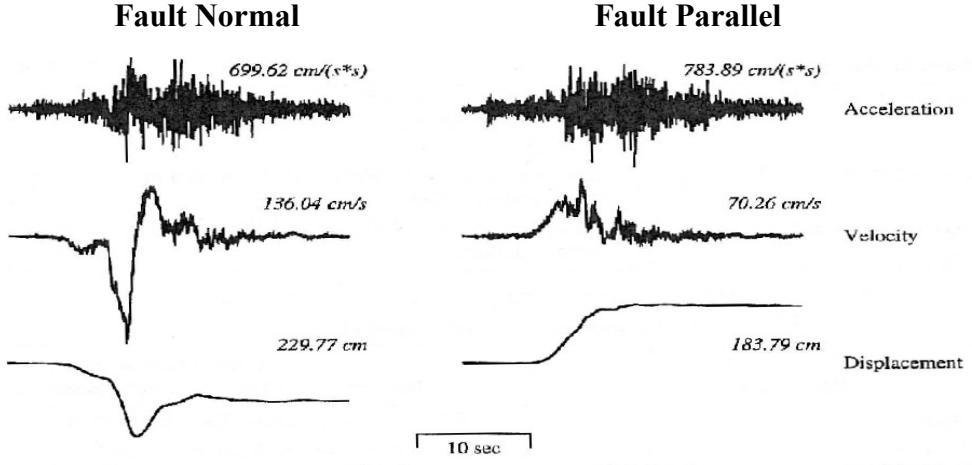

Figure 2.1 FN and FP acceleration, velocity and displacement time histories at the Lucerne near-fault forward directivity station during the 1992 Landers earthquake (after Somerville et al., 1997).

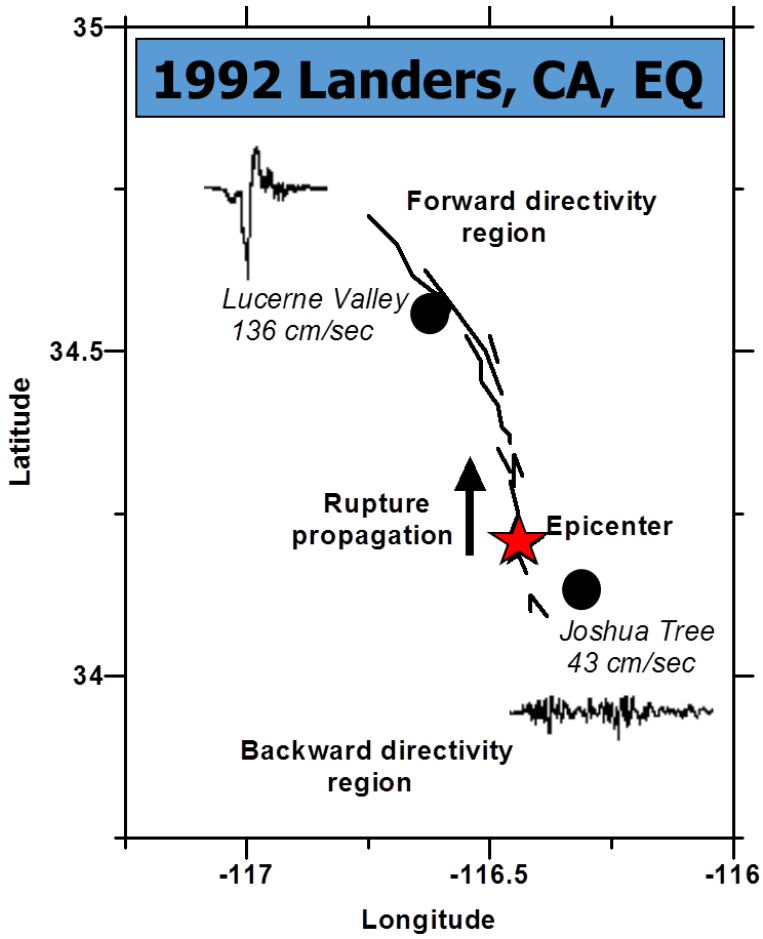

Figure 2.2 SN velocity time series at the near-fault Lucerne (forward directivity) and Joshua Tree (backward directivity) stations (Figure courtesy of Y.Bozorgnia, adopted from Somerville et al., 1997).

2.2 PHYSICS OF NEAR-FAULT GROUND MOTIONS

For sites located sufficiently far from the earthquake source, the size of the rupture is small compared to the distance between the fault and the site. The fault appears as a point source and the radiation of waves effectively comes from a single point and, thus, the distance and the radiation pattern are well defined. Moreover, the arrival times of the P and S waves are quite clear. This is not the case in the near-field region, where, due to the finite nature of the fault, there no longer is a unique definition of distance or radiation angle. As the rupture propagates along the fault, the radiation angle between the fault rupture and the site continuously changes (Archuleta and Hartzell, 1981; Somerville et al. 1997).

As mentioned earlier, the directivity effect and the fling step are two of the important effects that are characteristic of near-fault ground motions and cause them to be different from far-field ground motions. The forward directivity effect results in a large amplitude, long period two-sided pulse in the velocity time series of the FN component of the ground motion. The fling step results in a one-sided velocity pulse and permanent displacement at the end of the ground motion record in the FP direction (along the fault plane, in the direction of the slip). These

effects, which are currently not adequately taken into consideration in the design process, are described in greater detail in this section. They have been observed in a variety of tectonic environments but have been mostly idealized for strike-slip and dip-slip (normal and reverse) faults. Other effects that are typically ignored and that may also influence ground motions are also discussed. Finally, parameters that have been found adequate to describe directivity effects are introduced.

2.2.1 Directivity effect

An earthquake occurs when a rupture and slip suddenly occur along a fault, resulting in the release of the accumulated strain energy in the form of seismic waves. The rupture starts at the hypocenter and propagates in two dimensions along the fault plane. If the rupture propagates towards a site, the site is said to be located in the forward directivity region. Such a site usually experiences a short duration, large amplitude pulse at the beginning of the velocity time series, in the direction perpendicular to the fault plane or the FN direction. If the rupture propagates away from the site, the site is said to be in the backward directivity region and records a small amplitude, long duration ground motion in the FN direction (Somerville et al., 1997). The polarity of the pulse depends on the location of the site relative to the epicenter (Archuleta and Hartzell, 1981).

Two conditions must be met for the forward directivity effect to be observed at a site. First, the rupture front should propagate towards the site and at a velocity almost equal to the shear-wave velocity of the ground, such that all the seismic energy arrives at the site in a single, short duration pulse due to the constructive interference of the radiated waves (primarily shear or S-waves) from the fault rupture between the hypocenter and the site. The S-wave radiation pattern is typically split into SH waves and SV waves, defined below. Second, the direction of wave propagation between the hypocenter and the site should be aligned with the direction of the slip on the fault, which corresponds to the maximum of the SH radiation pattern (waves travelling in the tangential direction, normal to the fault plane), such that large amplitudes are obtained in the FN direction. In other words, the three directions of rupture, of slip, and of wave propagation between the hypocenter and the site should be aligned together to maximize the directivity effect (Somerville and Graves, 1993; Somerville et al., 1997). Note that when the fault plane is not vertical, the FN direction does not coincide with a horizontal direction. Only when the fault plane is vertical or near vertical does the FN direction coincide with the horizontal strike normal (SN) direction. Figure 2.3 illustrates the effect of rupture propagation and wave propagation on the waveforms in the forward and backward directivity regions.

The conditions for the forward directivity effect are more easily met in strike-slip faulting: the maximum in the SH radiation pattern is oriented in the direction along the strike, which is also the slip direction, as can be seen in Figure 2.4. Furthermore, the rupture propagates along the strike, resulting in constructive interference of the SH waves (tangential motion, normal to the direction of wave propagation) in the direction(s) of propagation of the rupture. Indeed, starting from the epicenter, the rupture front may propagate in either one or both directions along the strike of the fault. All locations close to the fault rupture and towards which the rupture propagates will then have large dynamic motions in the FN (tangential) direction, except for locations close to the epicenter. Sites close to the epicenter are too close to the initial rupture point for constructive interference to be significant, and the rupture mainly propagates away from them, resulting in the backward directivity effect. As also illustrated in Figure 2.4, the

SV radiation pattern (radial motion, in the direction of wave propagation) has a minimum in the direction along the strike, so that the dynamic motion in the FP (radial) direction is expected to be small, even though there may still be a large static FP displacement (Somerville and Graves, 1993; Somerville et al., 1997).

Directivity conditions can also be met in dip-slip faulting, for both normal and reverse cases. However directivity effects occur less often and are less severe. This is reflected in empirical models that predict the probability of occurrence of a pulselike motion, as described later in this chapter. This happens because the maximum of the SH radiation pattern in the slip direction (along the dip of the fault) coincides with the rupture direction only in the updip direction. Therefore, for a site to experience the forward directivity effect, it must be located directly updip from the hypocenter, around the surface exposure of the fault (or its updip projection if it is a buried fault). Stations located along the strike don't experience directivity effects because the horizontal rupture direction coincides with a minimum in the total S radiation pattern. Moreover, even a favorably located station will generally have a less pronounced directivity effect than in the strike-slip case, because the length of the rupture towards the station is limited by the downdip depth of the fault (e.g., about 25 km for an 18 km deep hypocenter and a dip angle of 45°), while for strike-slip earthquakes the limit is the rupture length along the strike, which can reach hundreds of kilometers (Somerville and Graves, 1993; Somerville et al., 1997). Dip-slip faults are usually far from vertical, in which case the FN direction has components in both the horizontal SN direction and the vertical direction. The larger the dip angle, the better is the FN direction approximated by the SN direction. The smaller the dip angle, the better is the FN direction approximated by the vertical direction of the ground motion (Mavroeidis and Papageorgiou, 2002).

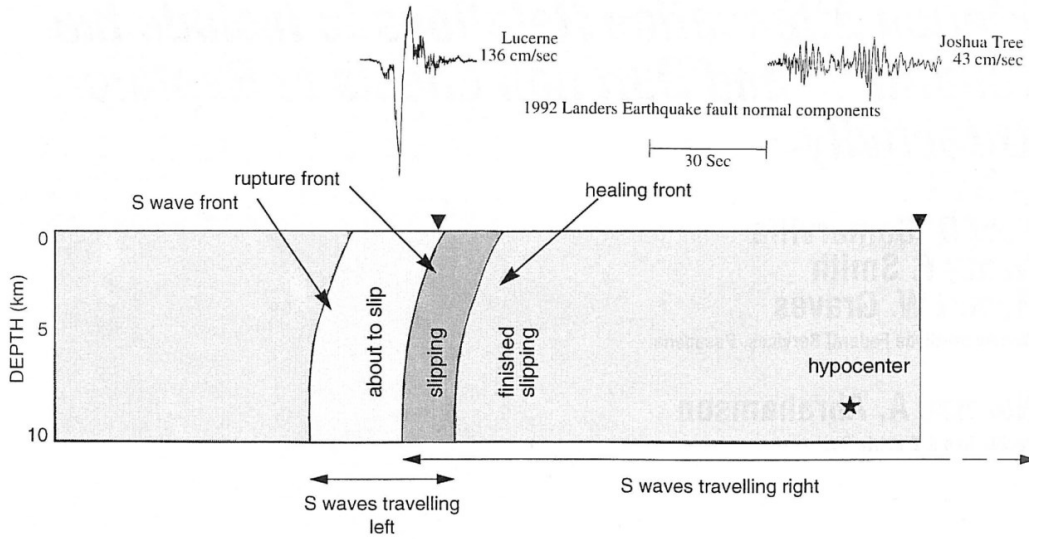

Figure 2.3 Rupture propagation and directivity effects (after Somerville et al., 1997).

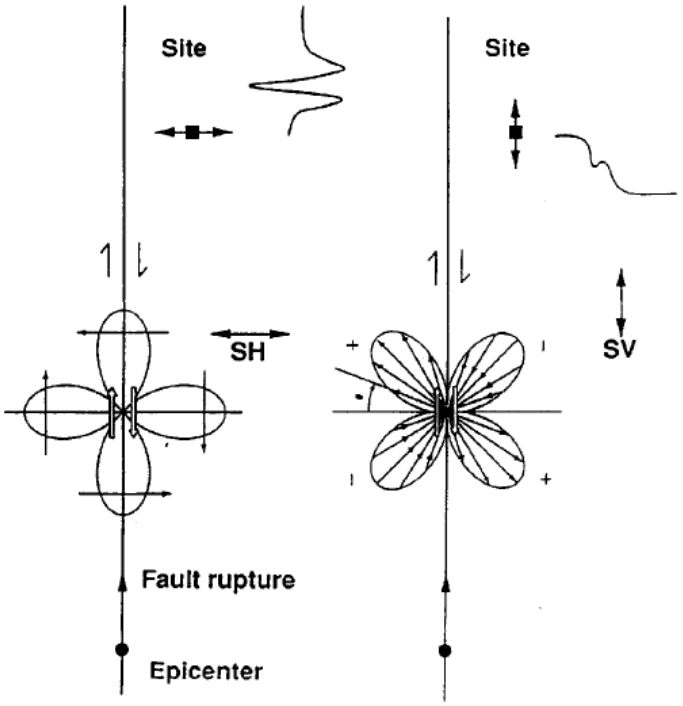

Figure 2.4 SH and SV radiation patterns for a vertical strike-slip fault (after Somerville et al., 1997).

2.2.2 Fling step

The so called fling step is another effect that results in a pulse in the velocity time series. While the forward directivity velocity pulse is two-sided, the fling step velocity pulse is usually one-sided. When an earthquake occurs along a fault, the two sides of the rupturing fault move relative to one another, resulting in the permanent tectonic deformation of the ground. This deformation, known as the fling step, does not depend on the details of the source rupture process nor on the velocity structure of the Earth. If the fault has a surface rupture, the ground displacement across the fault will be discontinuous, thus subjecting a bridge crossing the fault to large differential displacements. Static deformations occur even in the absence of surface faulting, as illustrated in Figure 2.5 for a strike-slip fault. These deformations are maximum at some distance away from the fault and they gradually decrease as one moves away from either side of the fault (Somerville, 2002). This static ground displacement is typically observed in the FP direction along the slip; it appears as a step function in the displacement time series and as a one-sided pulse in the velocity time series. For strike-slip faults, the fling step is visible in the SP direction and for dip-slip faults it appears in the SN and vertical directions (Mavroeidis and Papageorgiou, 2002; Bray and Rodriguez-Marek, 2004). Thus, in the case of a dip-slip fault, directivity and fling both appear in the SN direction; whereas they appear separately on orthogonal horizontal SN and SP directions in the case of a strike-slip fault (Mavroeidis and Papageorgiou, 2002). It has been observed that the fling-step pulse usually has a shorter period than the directivity pulse, but occurs at about the same time. The two effects, thus, can be modeled separately and then treated as coincident events (Bray and Rodriguez-Marek, 2004; Somerville, 2002). It should be noted that standard filtering and baseline correction procedures applied to raw ground motion

records remove the static displacement, which constitutes the zero-frequency part of the seismic signal. Thus, special processing should be used to preserve this information (Mavroeidis and Papageorgiou, 2002). Information about the size of permanent displacement after a large earthquake can be obtained from GPS measurements and geodetic surveys. To recover the fling step, Zhu (2003) proposed a method consisting of time-domain deconvolution followed by least-square inversion. This method gives an optimal estimate of the permanent deformation.

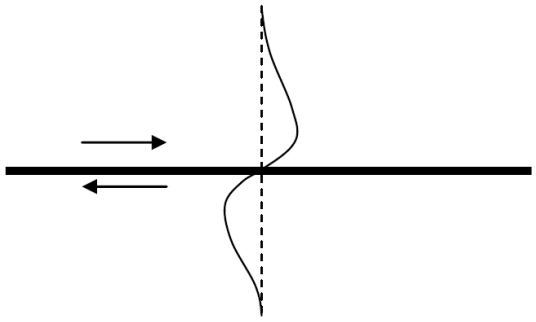

Figure 2.5 FP displacements for a strike-slip fault with buried rupture (plan view).

2.2.3 Other effects

Several effects besides the rupture directivity and fling step are present in earthquake ground motions. For example, hanging-wall effects, which are typically observed at short periods, are another near-fault ground motion characteristic. On the other hand, crustal waveguide effects (path effects) and basin effects (site effects) may produce large, long period pulses (Mavroeidis and Papageorgiou, 2002; Somerville, 2000). Such other effects were previously treated as randomness but some are gradually being incorporated into more recent ground motion prediction equations (GMPEs), such as the GMPEs for shallow crustal earthquakes in active tectonic regions developed as part of phase 2 of the Next Generation Attenuation (NGA) program (NGA-West2, see, e.g., Bozorgnia et al, 2014; Campbell and Bozorgnia, 2013, 2014), to reduce model uncertainty.

Hanging-wall effects arise from geometrical conditions in the near-fault region. For two sites located at the same closest distance to a dip-slip fault, but with one being on the hanging wall and the other being on the footwall, the former site will experience ground motions with larger amplitudes. This is because stations on the hanging wall are closer to a larger surface area of the fault rupture (Abrahamson and Somerville, 1996; Donahue and Abrahamson, 2014). This may also be due to the trapping of seismic energy in the hanging-wall wedge (Chang et. al, 2004). These differences in amplitudes are most pronounced at short periods. Therefore, while directivity effects result in spatial variation of near-fault ground motions at longer periods, hanging-wall effects result in spatial variations at shorter periods (Mavroeidis and Papageorgiou, 2002; Somerville, 2000; Dreger et al., 2011). The NGA-West2 project used finite fault simulations to model hanging-wall effects (Donahue and Abrahamson, 2014). For example, Abrahamson et al. (2014) and Campbell and Bozorgnia (2014) calibrated the simulation-based hanging-wall model to empirical data and used it in their GMPEs. Mavroeidis and Papageorgiou (2002) also mention other special effects resulting in large ground motions in the near-fault region. Special geometric conditions, such as a circular barrier on the fault plane, can result in the coherent addition of seismic waves and thus in extreme accelerations. Also, supershear

rupture velocity, which is an unusual but possible situation, results in large velocity pulses in the SP direction. This effect has been modeled by Mendez and Luco (1988) as a steady-state dislocation embedded in a layered half-space.

Somerville (2000) discusses crustal waveguide effects, which highlight other differences between near-field and far-field ground motions. At close distances, say within 50 km of the fault, the largest ground motion amplitudes are usually caused by direct body waves travelling upward from the source to the site. As the distance increases, these direct waves become weaker and the largest amplitudes are caused by reflected and refracted waves. These waves initially travel downward from the source until they reach interfaces below the source, where they undergo critical reflections. They arrive at the surface at distances between 50 km and 100 km and result in a reduction of the rate of attenuation. At this distance range, amplitudes are actually not large by themselves, but may produce damage if amplified by local soils.

Basin effects can be of two types, basin-edge effects and focusing effects, and may result in large, long period ground motions that can cause significant damage (e.g., Somerville, 2000; Choi et al., 2005). Such damaging effects were observed, for example, during the 1971 San Fernando and the 1989 Loma Prieta earthquakes. Compared to rock sites, much more complex waveforms were recorded at basin sites, with relatively weak direct S-waves and peak ground velocities controlled by surface waves generated within the basin (Somerville and Graves, 1993). The response of sedimentary basins, composed of alluvial deposits and sedimentary rocks with relatively small shear-wave velocity, is usually computed using 1D models in which the site is represented by horizontal layers and is characterized by the time-averaged shear wave velocity in the top 30m of soil (V_{s30}) (e.g., Boatwright et al., 1991). In such a representation, waves can resonate but they cannot be trapped within a layer. Thus, amplifications due to impedance contrast are reproduced, but not the trapping and focusing of seismic waves, which usually result in large amplitude surface waves and long durations of shaking. When body waves enter a basin (even a small and shallow basin) through its thickening edge, internal reflection of energy can occur and the waves can become trapped as surface waves in the basin and propagate across the basin until they reach the thinning edge, from where they escape as body waves. The amplitudes can become quite large due to constructive interference of direct waves with laterally propagating surface waves. This is known as the basin-edge effect (Graves, 1993; Somerville and Graves, 1993). Moreover, at periods longer than 1 s, seismic waves have wavelengths much longer than 30m and their amplitudes are controlled by deeper geologic (sedimentary and/or topographic) structures, which might not be horizontally layered and which may focus energy in spatially restricted areas on the surface, resulting in localized zones of high ground motion levels. These are known as focusing effects (Gao et al., 1996; Somerville, 2000; Baher and Davis, 2003). To represent these basin effects, 2D or 3D basin models are needed. For example, Day et al. (2008) use a 3D seismic velocity model and 3D numerical simulations to model the trapping and amplification of seismic waves by deep sedimentary basins and the resulting effect on long period response spectra. Their model guided the development of the NGA-East and West GMPEs (e.g., Campbell and Bozorgnia, 2008). Basin effects are also being incorporated in the more recent NGA-West2 GMPEs (e.g., Gregor et al., 2014; Campbell and Bozorgnia, 2014).

2.3 REVIEW OF GROUND MOTION MODELS

Before discussing models that have been proposed to represent the near-fault rupture directivity effect, we start by reviewing the different types of ground motion models that are generally

available in the literature. These models can be classified into two groups, (1) ground motion prediction equations (GMPEs) for specific ground motion characteristics, including measures of intensity, duration and frequency content, and (2) models of ground motion time series. Both GMPEs and models of ground motion time series can be used to perform dynamic analysis. GMPEs for spectral accelerations are used in response-spectrum dynamic analysis, while models of ground motion time-series are used in response-history dynamic analysis.

2.3.1 Models of specific ground motion measures (GMPEs)

Most commonly, GMPEs refer to models of intensity measures such as the peak ground acceleration (PGA) and velocity (PGV) and response spectral values such as pseudo-spectral acceleration (PSA) at multiple oscillator periods. The PEER NGA ground motion relations predict peak ground motion and response spectral pseudo-accelerations for shallow crustal earthquakes and are among the most well known GMPEs. More generally, GMPEs refer to empirical relationships that are developed for various ground motion characteristics, including measures of intensity (e.g., Arias intensity), ground motion duration (e.g., effective duration D_{5-95}), frequency content (e.g., mean period T_m and smoothed spectral predominant period T_o, Rathje et. al 2004), and other special features (e.g., rupture directivity pulse period T_p). These predictive equations represent the scaling of the specific ground motion measure in terms of variables that describe the earthquake source, the path of the seismic waves, and the effects of the site where the ground motion is observed. For a given earthquake design scenario, these relationships provide estimates of the median and standard deviation of the measure of interest. The design scenario is defined in terms of predictor variables as described below.

2.3.1.1 Ground motion predictor variables

We focus our discussion on the GMPEs developed as part of the NGA-West2 project. As detailed in Bozorgnia et al. (2014), the latest version of the NGA-West2 database includes 21,332 three-component ground motion recordings. These records are from events with moment magnitudes **M** ranging from 3.0 to 7.9 and at sites with closest distance to the rupture plane ranging from 0.05 to 1533 km. Later in this study, we use a subset of this database recorded at distances less than 30 km from the rupture plane to fit the near-fault ground motion model that we develop.

The NGA-West2 GMPEs represent the scaling of the ground motion intensity measures of peak ground acceleration (PGA), peak ground velocity (PGV), and the 5% damped linear-elastic pseudo-absolute response spectral acceleration (PSA) at oscillator periods between 0.01 s and 10 s (Bozorgnia et al. 2013, 2014). Five researcher teams developed five different GMPE models, which are compared by Gregor et al. (2014). Regarding source scaling, all five GMPEs are in terms of the moment magnitude **M** and account for the effect of magnitude saturation at short distances, which affects short periods. The five GMPEs have different models for faulting mechanism, which determines the definition of their respective style of faulting factors. Some explicitly include hanging wall and rupture depth terms, others do not. To model the path effect, the five GMPEs use diverse combinations of distance metrics. For the site effect, all five GMPEs model the linear soil amplification in terms of V_{s30}. Four GMPEs also have a nonlinear site amplification term that depends on some measure of the ground motion intensity and on the depth to the 1.0 km/sec ($Z_{1.0}$) or to the 2.5 km/sec ($Z_{2.5}$) shear-wave velocity boundary. These

additional factors allow some representation of basin effects. The nonlinear amplification factors are based on empirical data and/or numerical simulations (Gregor et. al, 2014).

The GMPE of Campbell and Bozorgnia (2013, 2014) is used here as an example to illustrate some of the predictor variables and scaling laws in greater details. Predictor variables in their model include, but are not limited to:

- **M**, the earthquake moment magnitude
- F_{RV}, an indicator variable that is equal to 1 for reverse and reverse-oblique faulting and equal to 0 otherwise
- F_{NM}, an indicator variable that is equal to 1 for normal and normal-oblique faulting and equal to 0 otherwise
- Z_{TOR} (km), the depth to the top of the coseismic rupture plane
- W (km), the down-dip width of the fault rupture plane;
- R_{RUP} (km), the closest distance to the coseismic rupture plane (or rupture distance)
- R_{JB} (km), the closest distance to the surface projection of the coseismic fault rupture plane (or Joyner-Boore distance)
- V_{s30} (m/sec), the time-averaged shear wave velocity in the top 30m of soil at the site
- A_{1100}(g), the median estimated value of PGA on rock with $V_{s30} = 1100$ m/s
- $Z_{2.5}$ (km), the depth to the 2.5 km/s shear-wave velocity boundary beneath the site (or sediment depth)

Since intensity measures (PGA, PGV or PSA) can be reasonably assumed to follow a lognormal distribution (see, e.g., Abrahamson 1998, Jayaram and Baker, 2008), the NGA-West2 GMPEs predict the natural logarithm of the intensity measure of interest and have the form

$$\ln IM = \mu_{IM}(\mathbf{M}, R_{RUP}, V_{s30}, \dots) + \eta + \epsilon \tag{2.1}$$

where $\mu_{IM}(\mathbf{M}, R_{RUP}, V_{s30}, \dots)$ is the expected value of $\ln IM$ and η and ϵ are the inter- and intra-event error terms. Random-effects regression is used to estimate the model parameters (Brillinger and Preisler, 1985; Abrahamson and Youngs, 1992). The Campbell and Bozorgnia (2013, 2014) model predicts μ_{IM} as the sum of nine terms. The source is represented by a magnitude term, which omitting the case $\mathbf{M} < 4.5$ is given by

$$\begin{aligned} f_{mag} &= c_0 + c_1 M_w + c_2(\mathbf{M} - 4.5) && 4.5 < \mathbf{M} \leq 5.5 \\ &= c_0 + c_1 M_w + c_2(\mathbf{M} - 4.5) + c_3(\mathbf{M} - 5.5) && 5.5 < \mathbf{M} \leq 6.5, \\ &= c_0 + c_1 M_w + c_2(\mathbf{M} - 4.5) + c_3(\mathbf{M} - 5.5) + c_4(\mathbf{M} - 6.5) && 6.5 < \mathbf{M} \end{aligned} \tag{2.2}$$

a style-of-faulting term

$$f_{flt} = f_{flt,F} f_{flt,M}, \tag{2.3}$$

where

$$f_{flt,F} = c_8 F_{RV} + c_9 F_{NM}, \tag{2.4}$$

$$f_{flt,M} = \begin{cases} 0 & \mathbf{M} \leq 4.5 \\ \mathbf{M} - 4.5 & 4.5 < \mathbf{M} \leq 5.5, \\ 1 & 5.5 < \mathbf{M} \end{cases} \tag{2.5}$$

a hypocentral depth term f_{hyp}, and a fault dip term f_{dip}. The path is represented by a geometric attenuation term

$$f_{dis} = (c_5 + c_6\mathbf{M}) \ln\left(\sqrt{R_{RUP}^2 + c_7^2}\right), \tag{2.6}$$

a hanging-wall term f_{hng}, and an anelastic attenuation term f_{atn}. Lastly, the site is represented by a shallow site response term

$$f_{site} = f_{site}(V_{s30}, A_{1100}) \tag{2.7}$$

and a basin response term

$$f_{sed} = f_{sed}(Z_{2.5}). \tag{2.8}$$

For more details, the reader is referred to the original sources.

2.3.1.2 Geometrical directivity parameters

In the near-fault region, ground motions are more complex and more variable. As described earlier, they depend on the spatial distribution of the slip along the fault rupture, on the spatially varying radiation pattern between the fault rupture and the site, on the velocity and direction of propagation of the rupture relative to the site (Archuleta and Hartzell, 1981). Consequently, additional parameters are needed to represent near-fault effects. For the reasons described in earlier sections, the presence and characteristics of a forward directivity pulse mainly depend on the geometric configuration of the site relative to the rupture surface and the direction of propagation of the rupture. Thus, several geometrical parameters have been proposed to model the forward directivity effect.

Somerville et al. (1997) used two parameters to characterize the forward directivity effect: (1) the fraction of the fault rupturing between the hypocenter and the site in the direction of slip, and (2) the angle between the rupture plane and the direction between the hypocenter and the site, which represents the path of the travelling waves. For strike-slip faulting, they define X as the ratio of the length of the fault rupturing between the epicenter and the site to that of the total rupture length. Similarly, for dip-slip faulting, they define Y as the ratio of the width of the fault rupturing between the hypocenter and the site to that of the total width of the rupture plane. Thus, letting s and d be the length and width of the rupture between the hypocenter and the site, respectively, and L and W be the total length and width of the rupture, respectively, we have $X = s/L$ and $Y = d/W$. Somerville et al. (1997) define θ as the angle in the horizontal plane between the fault rupture plane and the direction between the epicenter and the site for strike-slip earthquakes. Similarly, they define ϕ as the angle in a vertical plane between the fault rupture plane and the direction between the hypocenter and the site for dip-slip earthquakes. In reality, for near-fault sites, the radiation angle between the fault rupture and the site varies as the rupture propagates along the fault, because the dimension of the fault is large relative to the distance

between the source and the site. For simplicity, however, only the radiation angle between the hypocenter and the site has been used in directivity models. All the geometric parameters described above are illustrated in Figure 2.6, where it can be seen that X and θ are measured in the horizontal plane, while Y and ϕ are measured in the vertical plane oriented normal to the fault strike. Somerville et al. (1997) explain that they expect the ground motion amplitude to increase and the duration to decrease when the geometric conditions increasingly favor directivity effects, i.e., as the angle θ or ϕ decreases and the fraction X or Y of the rupture increases. They, thus, expect an inverse relationship between the amplitude and duration. Somerville et al. (1997) investigated simple functional forms of the directivity parameters for use in their model. They ended up selecting $Xcos\theta$ and $Ycos\phi$ for strike-slip and dip-slip earthquakes, respectively, because the cosine function gives a smooth decay when the angle increases.

Iervolino and Cornell (2008) and later Abrahamson and Watson-Lamprey (2010) and Shahi and Baker (2011) suggested using the length and width of the portion of the rupture that propagates towards the site, s and d, rather than the fractions X and Y to characterize strike-slip and dip-slip near-fault ground motions, respectively. This modification makes sense, since the constructive interference should be correlated with the length or width of the rupture between the source and the site, rather than the fraction of the rupture. In particular, a large s or d is likely to result in a directivity pulse, independently of the total length of the rupture. Note that the rupture dimensions are typically related to the earthquake magnitude (Iervolino and Cornell, 2008). In addition to the geometric parameters, Archuleta and Hartzell (1981) show that the rupture velocity also affects rupture directivity. This is confirmed by Dreger et al. (2006). However, to our knowledge, this effect has not been included in any existing prediction model. For oblique-slip earthquakes, which have components of both strike-slip and dip-slip faulting, typically the parameters for dip-slip faults have been used, though this is an incomplete representation. In Chapter 5, where we develop predictive equations for the model parameters, we represent the directivity parameter as the larger of s and d (we denote it $s_{or}d$), and the corresponding angle θ or ϕ (we denote it $\theta_{or}\phi$). We find this parameterization to provide a better representation for reverse-oblique faults.

It is important to note that the closest distance between the site and the fault rupture is not independent of the other geometric parameters. For strike-slip faults, R_{RUP}, s and θ are related by $R_{RUP} = s\tan\theta$, if the rupture can be represented by a straight line and if the site is located alongside the rupture. If the rupture cannot be represented by a straight line, which is sometimes the case, or if the site is not located alongside the fault rupture, this relationship does not hold. Taking the example of a vertical strike-slip fault with surface rupture, such as the one depicted in Figure 2.7, it is clear that $R_1 = s_1\tan\theta_1$ but that $R_2 > s_2\tan\theta_2$. Similarly, for dip-slip faults, R_{RUP}, d and ϕ are related by $R_{RUP} = d\tan\phi$, if the rupture width can be represented by a straight line and the site is located alongside the rupture width. Otherwise, this relationship does not hold.

As part of the NGA-West2 efforts, and based on data from the NGA-West2 database and from numerical simulations of large earthquakes, five directivity models were developed. Spudich et al. (2013, 2014) compare these directivity models, which strongly depend on the individual assumptions, and conclude that these models need further development.

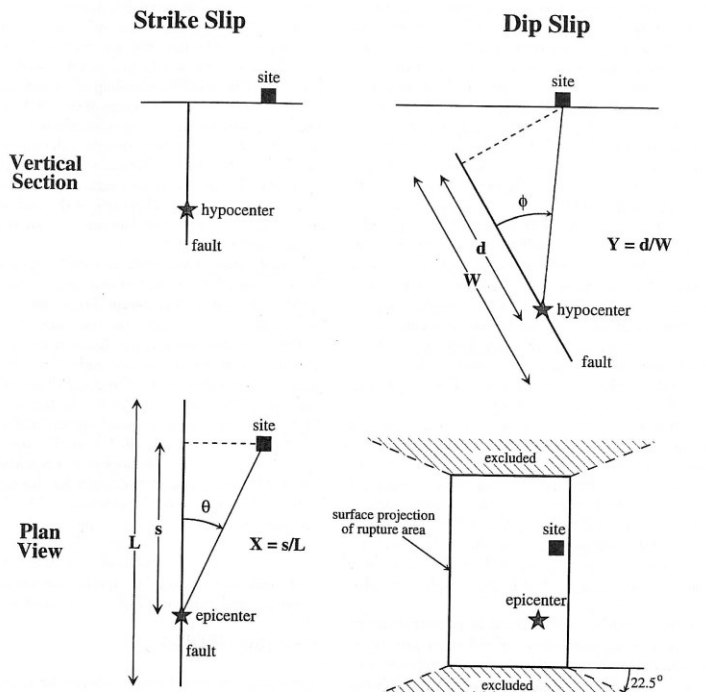

Figure 2.6 Directivity parameters (after Somerville et al. 1997).

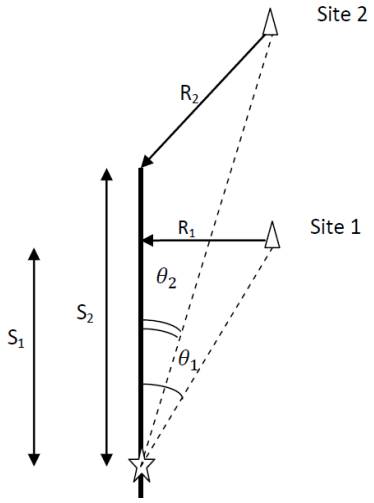

Figure 2.7 Geometric relationship between the directivity parameters for a strike-slip fault (plan view).

2.3.2 Models of ground motion time series

While GMPEs are restricted to modeling a single ground motion characteristic at a time, models of ground motion time series, also known as synthetic ground motion models or numerical ground motion models, represent the whole ground motion acceleration time series. These more comprehensive models allow generation of synthetic ground motions that represent a specific earthquake design scenario.

To be useful, models of ground motion time series and the resulting synthetics must properly represent the main characteristics and the natural variability of recorded earthquake ground motions. In addition to capturing the intensity, duration and frequency content characteristics, a good model must represent the temporal and spectral non-stationarities of real ground motions. Temporal non-stationarity denotes the variation of intensity with time, while spectral non-stationarity denotes the variation of frequency content with time. Because of the moving resonance effect in inelastic structures, capturing the intensity, duration, and frequency content characteristics and their non-stationarity is essential when models of ground motion time series are used in nonlinear dynamic analysis. Moreover, these models should account for the natural variability of real earthquake ground motions. This condition can be achieved by modeling the variability of the model parameters and their correlations (Rezaeian, 2008). The challenge in time series generation is the validation of the methods to make sure they capture realistic median and standard deviation response spectra as observed in empirical data.

Models of ground motion time series fall in one of two classes, source-based models, and site-based models. Source-based models describe the fault rupture process and the propagation of the resulting seismic waves from the source to the site. Site-based models directly describe the ground motion as observed at a specific site, having some knowledge of the earthquake and site characteristics.

2.3.2.1 Source-based models

Source-based models are also referred to as "physics-based" or seismological models and have been reviewed by Zerva (1988). They model the source mechanism and the wave travel path to the site of interest and include fewer idealizations than site-based models. There are three classes of source-based models: deterministic models, which use a dynamic or kinematic rupture model and Green's functions, stochastic models, which use a model of the ground motion spectrum and random vibration theory, and hybrid models that combine the two.

Deterministic models combine a dynamic or kinematic rupture model with Green's functions of the ground medium to yield synthetic ground motion time series. Rupture models typically represent the earthquake source as a shear dislocation on an extended fault plane and account for spatial and temporal variations of the slip on the rupture surface (the slip distribution is usually highly variable with asperities surrounded by regions of low slip). The difference between dynamic and kinematic rupture models is in the way they model the slip. While dynamic rupture models simulate the earthquake rupture as frictional sliding and use material models and constitutive stress-strain relations to dynamically determine the slip at each point on the rupture surface, kinematic models directly assume the slip functions without imposing the physical principles of rock fracturing and slip (Aki and Richard, 2002). No matter how the rupture is modeled, theoretical or empirical Green's functions are used to represent wave propagation in the ground medium to the site of interest. Ideally, these functions must be complete, i.e., contain near, intermediate and far field terms (Somerville, 2000). Based on the elasto-dynamic representation theorem, the convolution at each point on the rupture surface of the slip-velocity time history with the Green's functions for the appropriate distance and depth of the medium, integrated over the fault rupture surface, gives the synthetic motion (Somerville, 2002). Deterministic simulations can be randomized by randomizing the slip distribution. They produce realistic synthetic ground motions at low frequencies (<1 Hz).

Similar to deterministic models, stochastic source-based models are physics-based models that represent the source process, the wave propagation and the site response. However, these models do not model the slip along the fault. They directly represent the theoretical shape and scaling of the Fourier amplitude spectrum (FAS) of the ground motion at a particular site as the product of shape and scaling functions that describe the earthquake source (E), path (P) and site (G) (Boore, 2003b). These functions are calibrated empirically and are given in terms of seismological parameters describing the source (e.g., the seismic moment M_0 and stress drop $\Delta\sigma$), the path (e.g. the rate of geometrical spreading and the anelastic attenuation operator $Q(f)$), and the site (e.g. shallow rock damping κ_0). The source spectrum can be based on point-source modeling, finite-fault modeling, or equivalent finite-fault modeling. Point-source models, such as Aki's ω^2-model (1967) and its later developments by Brune (1970, 1971), are based on a kinematic representation of the source rupture and assume that seismic waves originate from a single point. They tend to over-predict ground motion amplitudes at low-to-intermediate frequencies (≤1 Hz), in particular for moderate-to-large earthquakes, which are richer in long periods (Atkinson and Silva, 2000). Point-source models are described in greater detail in Chapter 3. Finite-fault models subdivide the fault into several sub-faults each modeled as a point source (e.g., Atkinson and Silva 1997; Atkinson et al. 2009; Boore 2009). Equivalent finite-fault models use a more complex point-source spectrum with two corner frequencies to capture the finite-fault effect (Joyner 1984; Atkinson and Silva 2000). Models of ground motion spectra constitute the basis of the stochastic method, which is extensively reviewed by Boore (2003b) and in which models are combined with random vibration theory to simulate ground motions by modulating and filtering white noise. These stochastic models can suitably represent the high-frequency content (>1 Hz) of ground motions.

Lastly, hybrid models result from combining deterministic models, which can capture the low-frequency content portion of ground motion, with stochastic models, which capture the high-frequency content portion. The stochastic component that supplements a deterministic model with high-frequency content may be source-based or site-based. Site-based stochastic models are described in the following section.

Source-based simulations have been used as a sound physical basis to extend GMPEs for PGA, PGV, and Sa(T) to ranges that are not well represented by recorded motions (e.g., Atkinson and Silva 2000) or to regions where earthquakes and ground motion records are rare, such as the Central Eastern U.S. (e.g., Somerville et al. 2001). Because source-based models are computationally demanding, heavily rely on seismological principles, and require the identification of region-specific physical parameters describing the source, path, and site characteristics, they are seldom used in engineering practice.

2.3.2.2 Site-based models

Site-based models, also referred to as empirical models, were developed more recently. They fit a parameterized stochastic model to recorded motions at different sites. Design engineers prefer using site-based models because these models are more time-efficient, have simpler formulations, and only require readily available knowledge of the earthquake source and site characteristics such as magnitude, distance and shear-wave velocity of the site (Rezaeian and Der Kiureghian 2010).

Several classes of site-based stochastic ground motion models exist and are reviewed in some detail by Rezaeian and Der Kiureghian (2008, 2010, and 2012). These classes include

modulated and filtered white-noise processes, modulated and filtered Poisson processes, auto-regressive moving average (ARMA) models, as well as models based on various forms of spectral representation. Site-based stochastic models have different abilities in representing temporal and spectral non-stationarity, with their advantages and disadvantages. As previously mentioned, a good stochastic ground motion model must represent both the temporal and spectral non-stationary characteristics of earthquake ground motions. One such model is the non-stationary filtered white-noise model of far-field ground motion by Rezaeian and Der Kiureghian (2008, 2010, and 2012). This model is reviewed in Chapter 4 and a modified form is employed in our parameterized stochastic model of near-fault ground motion. More recently, Yamamoto and Baker (2011, 2013) developed a site-based stochastic model using wavelets. They used an approach similar to that of Rezaeian and Der Kiureghian (2010) to assess the parameters of their model by fitting to a database of recorded motions. This model is briefly reviewed in Chapter 4.

In the present study, we develop a site-based model of near-fault ground motion by improving on our earlier versions (see Dabaghi et al. 2011; Dabaghi and Der Kiureghian 2014). Site-based models of near-fault ground motion were earlier developed by Menun and Fu (2002, 2004) and by Mavroeidis and Papageorgiou (2003). These are reviewed in Chapter 4. As described there, these earlier models lack some important features, such as variability consistent with actual recordings and correlations between the model parameters for a given earthquake design scenario.

2.4 MODELS OF THE DIRECTIVITY EFFECT

In this section, we discuss the models that have been proposed and used to account for the near-fault rupture directivity effect. The fling step is modeled separately, but the two effects should be ultimately combined in developing ground motions. The rupture directivity models are generally of two types: (1) those that account for the directivity effect by modifying the currently used response spectra, and (2) those that attempt to directly model the near-fault ground motion time series. Note that most authors use the terms FN and FP to actually signify SN and SP. In this report, we make a distinction between the two notations: FN and FP are used when discussing the physics of near-fault ground motions, as the directions in which the directivity effect and fling step occur, respectively, while SN and SP are the horizontal directions for which the near-fault models are typically formulated.

2.4.1 Spectral methods for forward directivity

As already described, near-fault ground motions tend to exhibit a large pulse in the velocity time series in the FN direction, when forward directivity conditions are met. This is reflected by a peak in the corresponding response spectrum near the period of the pulse, and by a large ratio of the SN to SP spectral accelerations at intermediate to long periods (Somerville and Graves, 1993). These characteristics do not appear in far-field ground motions. Methods to modify response spectra developed for far-field ground motions to account for the directivity effect have been proposed by various authors. Broadband directivity models were initially formulated, before narrowband models were found to be more accurate. These are described in the following sections (Spudich et al., 2014).

2.4.1.1 Broadband directivity model

A broadband directivity model was first developed by Somerville et al. (1997). It was later modified by Abrahamson (2000) to incorporate saturation effects and tapering for small magnitudes and large distances (Bozorgnia and Campbell, 2004a). Both models amplify spectral amplitudes of the SN component of the ground motion at all periods in order to account for the forward directivity effect. The amplification factor is a function of the geometrical parameters of the site relative to the fault, specifically$X\cos\theta$ for strike-slip faults and $Y\cos\phi$ for dip-slip faults (Somerville, 2003). Somerville et al. (2003) also developed modifications to the average duration predicted by ground motion prediction models as a function of the same geometrical parameters, and they found negative correlation between the amplitude and duration (Somerville et al. 1997). This is consistent with the finding that the forward directivity effect favors the constructive interference of waves into a pulse motion with a large amplitude and a short duration. The more recent directivity models by Spudich and Chiou (2008) and by Bayless and Somerville (2013) also are broadband.

2.4.1.2 Narrowband directivity model

As we have seen, near-fault ground motions with forward directivity typically contain a long period pulse in the FN velocity time series, which is also observed in the SN horizontal component. This pulse is narrowband and its period, or duration, tends to increase with the earthquake magnitude. For this reason, modification of the response spectrum for the forward directivity effect should scale with the earthquake magnitude instead of being uniform at all periods, such that the peak in the response spectrum occurs at a period that increases with the magnitude. This feature has been observed in response spectra of recorded near-fault ground motions. Because of this phenomenon, it is possible that spectral amplitudes in the intermediate period range from a small earthquake at a near-fault site exceed spectral amplitudes from a larger earthquake (Somerville, 2002). This observation led to the development of narrowband directivity models, which amplify the response spectrum only in a narrowband region around the period of the velocity pulse.

Somerville (2003) suggested developing the acceleration response spectrum of the SN component of a ground motion with a forward directivity pulse of period T_p by using a conventional response spectrum and scaling it by a cosine shaped function that is centered at $0.75T_p$, has a peak amplitude of 2 and a width of $1.5T_p$. Shahi and Baker (2011) computed the amplification factor A_f in the spectral accelerations of recorded near-fault ground motions containing directivity pulses. On average, the amplification is bell-shaped and centered near the pulse period T_p, as can be observed in Figure 2.8. They fitted the following function to the mean of the logarithm of the amplification factor:

$$\begin{aligned}\mu_{lnA_f} &= 1.131\exp\left\{-3.11\left[ln\left(\frac{T}{T_p}\right)+0.127\right]^2+0.058\right\} \quad \text{if } T\le 0.88T_p \\ &= 0.896\exp\left\{-2.11\left[ln\left(\frac{T}{T_p}\right)+0.127\right]^2+0.255\right\} \quad \text{if } T> 0.88T_p\end{aligned} \tag{2.9}$$

The above function takes a maximum value of 1.19 at $T = 0.88T_p$, which corresponds to a peak median value of 3.29 of the amplification factor A_f. The NGA-West2 directivity models, apart

from the Bayless and Somerville (2013) model, also are narrowband (e.g., Shahi and Baker, 2013b; Spudich and Chiou, 2013; Spudich et al., 2013, 2014).

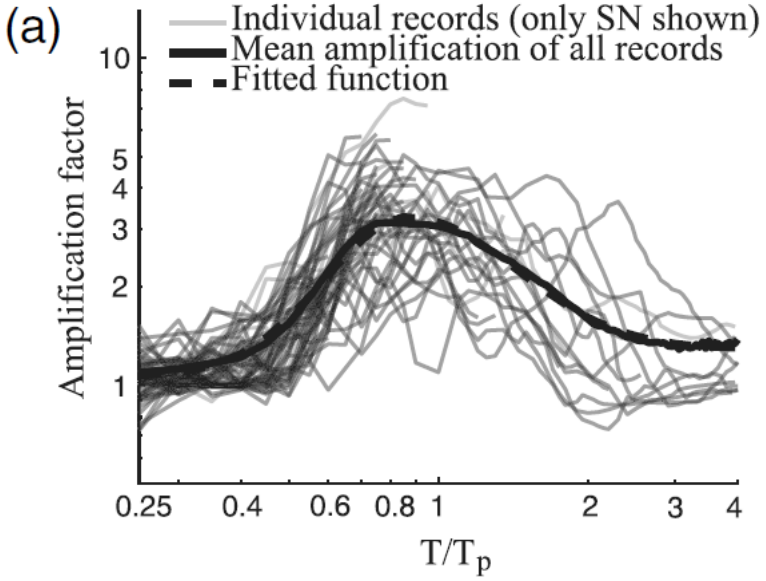

Figure 2.8 Narrowband spectral amplification factor for SN component of pulse-like ground motions (after Shahi and Baker, 2011).

2.4.2 Time series methods for forward directivity

Response spectra can be appropriate to characterize the demands of far-field ground motions, which tend to be long duration processes with relatively uniform distribution of energy over the duration of strong shaking (Bray and Rodriguez-Marek, 2004). However, they are not adequate to characterize the demands resulting from shorter duration, impulsive near-fault ground motions (Somerville, 1998; Somerville, 2000). One reason is that they do not adequately represent the demand of the velocity pulse for a high rate of energy absorption. Another reason is that most near-fault pulses drive structures into the inelastic range, while response spectra assume linear elastic behavior (Somerville, 2002). For such cases, nonlinear dynamic response history analysis is required, thus the need to represent near-fault ground motions by suites of time series, or at least by time domain parameters such as the pulse amplitude, period and number of half-cycles, to supplement the response spectrum (Somerville, 1998).

Time series to be used in the design and analysis of structures located near faults should be carefully selected. It is not sufficient to select time series that have response spectra matching a design spectrum, because spectral matching cannot create a pulse in a record that does not initially contain a pulse, even if the design spectrum includes the contribution of a directivity pulse (Somerville et al., 1997; Somerville, 2000; Mavroeidis and Papageorgiou, 2002). Since near-fault recordings that contain directivity pulses are relatively scarce, there exists a need to model and simulate near-fault ground motions that include the rupture directivity effect. As previously mentioned, a good model must capture the intensity, duration and frequency content characteristics and represent the temporal and spectral non-stationarities of real ground motions. Below, we describe existing work on this topic. In the subsequent chapters of this study, we develop new models and simulation methods to generate pulselike, i.e. containing a forward directivity pulse, and non-pulselike, i.e. lacking a forward directivity pulse, synthetic near-fault

ground motions. These synthetic motions possess the statistical characteristics of recorded near-fault ground motions.

2.4.2.1 Velocity pulse models

Bertero et al. (1976) were the first to develop simplified near-fault directivity pulses and examined their effects on structural response. Alavi and Krawinkler (2000) observed that the response of structures to near-fault ground motions had similarities with the response of structures to pulse-type motions. On this basis, they suggested that pulselike near-fault ground motions (or, more appropriately, the velocity pulses they contain) can be represented by simple time domain waveforms, formulated in terms of a few physically meaningful parameters, the most important of which are the pulse amplitude, the pulse period and the number of half-cycles of the pulse. However, there is no unique definition of the pulse amplitude and period. Mavroeidis and Papageorgiou (2002) and Bray and Rodriguez-Marek (2004) review several definitions proposed in the literature, which involve varying levels of subjectivity. Alavi and Krawinkler (2000) defined the equivalent pulse amplitude by minimizing the difference between the maximum story ductility demands estimated for the pulse-type record and the equivalent pulse. They observed that the equivalent pulse amplitude lies within 20% of the peak ground velocity (PGV) in most cases. Mavroeidis and Papageorgiou (2003), on the other hand, determined the pulse amplitude such that both the pulse waveform and its peak pseudo-spectral velocity closely match the corresponding quantities of the actual record. As for the pulse period, Alavi and Krawinkler (2000) defined it as the period at which the pseudo-velocity response spectrum has its peak value. Mavroeidis and Papageorgiou (2003) determined the pulse period by matching the periods at which the pseudo-velocity spectra of the pulse waveform and of the recorded ground motion assume their peak values. Finally, Bray and Rodriguez-Marek (2004) defined the directivity pulse period as the period of the pulse having the largest amplitude in the recorded motion, where the pulse period is defined as twice the interval between two successive zero-level crossing times.

2.4.2.1.1 Simple pulse models

Somerville (1998) developed an improved parametrization of pulselike near-fault ground motions by including time-domain parameters to complement the response spectrum representation. Parameters of the preliminary model are the amplitude and duration of the largest velocity cycle, which consists of a peak, a trough and three zero crossings. With this defintion, the pulse amplitude equals the PGV and the pulse period equals the duration of the full velocity cycle. Using recorded data, these parameters were regressed against the earthquake magnitude, **M**, and the closest distance, R_{RUP}. The pulse period was found to be related to the magnitude through

$$\log_{10} T_p = -2.5 + 0.425\mathbf{M} \tag{2.10}$$

With the constraint of self-similarity between the pulse period and magnitude, i.e., the constraint that the pulse period and magnitude grow in proportion with the fault dimensions, Somerville (1998) obtained

$$\log_{10} T_p = -3 + 0.5\mathbf{M} \tag{2.11}$$

Finally, assuming a linear relation between the PGV and R_{RUP}, which is not realistic at close distances, Somerville (1998) obtained

$$\log_{10} PGV = -1.0 + 0.5\mathbf{M} - 0.5 \log_{10} R_{RUP} \tag{2.12}$$

Krawinkler and Alavi, (1998) investigated three idealized pulse shapes, denoted P1, P2 and P3 and shown in Figure 2.9, which are defined in terms of two parameters: the pulse period T_p and pulse amplitude $v_{g,max}$. They then related a set of near-fault records to these parameters. They found that these idealized pulse shapes are capable of representing near-fault ground motions within some limitations. Pulse P2 was capable of representing many records. Alavi and Krawinkler (2000) regressed the parameters of the equivalent idealized pulses against the earthquake magnitude and closest distance to the fault rupture, arriving at the following predictive relations:

$$\log_{10} T_p = -1.76 + 0.31\mathbf{M} \tag{2.13}$$

$$\log_{10} v_{g,max} = -2.22 + 0.69\mathbf{M} - 0.58 \log_{10} R_{RUP} \tag{2.14}$$

Alavi and Krawinkler (2000) warn that caution should be exercised in interpreting these results, because a small number of records was used to derive them, and they came from events with different faulting mechanisms and geologic environments, resulting in large scatters.

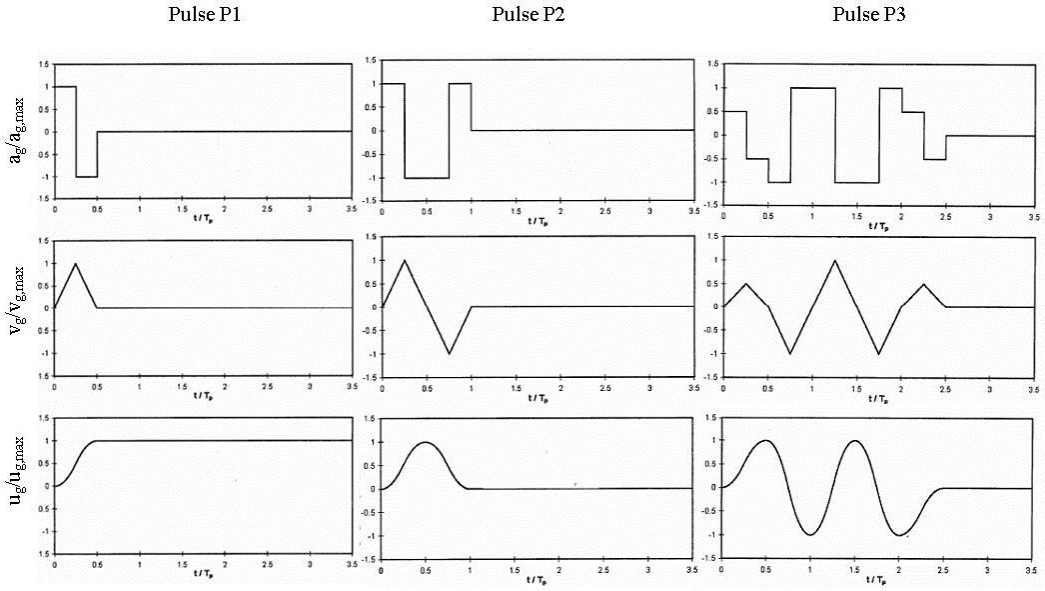

Figure 2.9 Acceleration, velocity and displacement time series of idealized pulses P1, P2 and P3 (after Krawinkler and Alavi, 1998).

Somerville (2003) used simple triangular velocity pulses to incorporate the effect of the directivity pulse on response spectra. The pulse period was obtained from the database of

recorded near-fault SN pulselike velocity time series as the period of the largest cycle of motion. He assumed the period to be independent of distance from the fault and developed separate relations for rock and soil sites. For rock sites, assuming self-similarity, he obtained the relation

$$\log_{10} T_p = -3.17 + 0.5\mathbf{M} \tag{2.15}$$

The relation for soil sites was allowed to depart from self-similarity in order to accommodate non-linear effects, since the soil layer tends to increase both the peak velocity and the period by amounts that depend on the level of the input ground motion and on the thickness and physical properties of the soil layer. The regression for soil sites resulted in the relation

$$\log_{10} T_p = -2.02 + 0.346\mathbf{M} \tag{2.16}$$

Bray and Rodriguez-Marek (2004) chose to represent both directivity and fling velocity pulses by half-sine waves. To fully define the bi-directional motion, the pulses are represented in terms of the number, N, of equivalent half-cycles in each direction, the period, T_{vi}, and amplitude, A_i, of each half cycle, and the lag time, t_{off}, between the beginnings of the SN and SP pulses. However, for the purpose of developing a model of the SN forward directivity pulse, they chose to limit the model parameters to the PGV, the approximate period of the dominant pulse, T_p, and the number N of significant half-cycles, which are defined as half-cycles with amplitude equal to or greater than $0.5PGV$. In developing predictive equations for the parameters of near-fault pulses, Bray and Rodriguez-Marek (2004) noted that simplified functional forms can be used because distances are relatively short, eliminating the need for a complex model form that can account for a wide range of distances. They noted that the PGV of the SN component of pulselike motions varies significantly with $\mathbf{M}$ and R_{RUP}, that it is larger for soil than for rock sites, and that it has a nearly zero slope at close distances and linearly decreases with the logarithm of distance at larger distances. Their recommended relations are

$$\begin{aligned} \ln PGV &= 4.51 + 0.34\mathbf{M} - 0.57\ln(R_{RUP}^2 + 7^2) && \text{for all sites} \\ &= 4.46 + 0.34\mathbf{M} - 0.58\ln(R_{RUP}^2 + 7^2) && \text{for rock sites} \\ &= 4.58 + 0.34\mathbf{M} - 0.58\ln(R_{RUP}^2 + 7^2) && \text{for soil sites} \end{aligned} \tag{2.17}$$

where R_{RUP} is measured in kilometers. As with previous investigators, they used a linear dependence of $\ln T_p$ on $\mathbf{M}$, but they constrained the predicted pulse periods to be equal on rock and soil sites at $\mathbf{M} = 7.6$ in order to avoid larger periods on rock than on soil for $7 < \mathbf{M}$. The resulting relations are

$$\begin{aligned} \ln T_v &= -6.37 + 1.03\mathbf{M} && \text{for all sites} \\ &= -8.60 + 1.32\mathbf{M} && \text{for rock sites} \\ &= -5.60 + 0.93\mathbf{M} && \text{for soil sites} \end{aligned} \tag{2.18}$$

Thus, for small magnitudes, longer periods are predicted at soil sites than at rock sites, but the differences decrease and disappear for larger magnitudes.

2.4.2.1.2 The Menun and Fu model

Menun and Fu (2002) proposed a model of the velocity pulse time series in terms of five parameters: amplitude V_p of the pulse, period T_p of the pulse, the start time t_0 of the pulse, and shape parameters n_1 and n_2. The analytical expression of their model is

$$\begin{aligned} v(t) &= V_p \exp\left[-n_1\left(\frac{3}{4}T_p - t + t_0\right)\right]\sin\left[\frac{2\pi}{T_p}(t-t_0)\right] && t_0 < t \le t_0 + \frac{3}{4}T_p \\ &= V_p \exp\left[-n_2\left(t - t_0 - \frac{3}{4}T_p\right)\right]\sin\left[\frac{2\pi}{T_p}(t-t_0)\right] && t_0 + \frac{3}{4}T_p < t \le t_0 + 2T_p \\ &= 0 && \text{elsewhere} \end{aligned} \tag{2.19}$$

Figure 2.10 shows plots of the above pulse model for several selections of the model parameters.

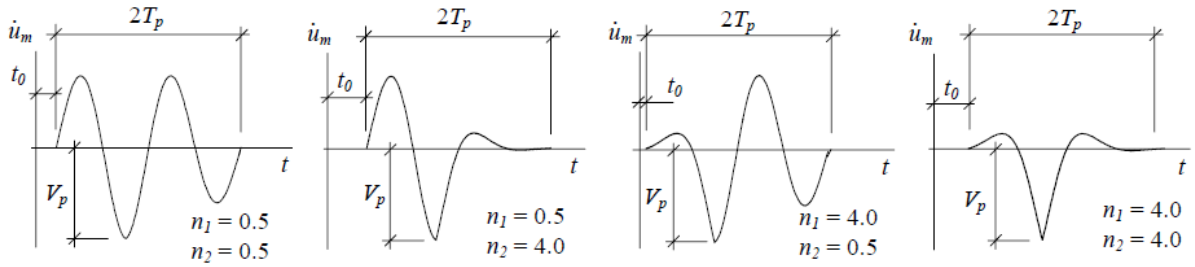

Figure 2.10 Sample velocity pulses generated by the Menun and Fu model (after Menun and Fu, 2002).

Fu and Menun (2004) later proposed a different formulation of the velocity pulse, based on idealizing the velocity pulses appearing in synthetic time series generated according to the Haskell seismological source model (Aki and Richards 1980) with forward directivity site conditions. This formulation is in terms of four parameters: amplitude V_p of the pulse, period T_p of the pulse, the start time t_0, and a shape parameter α. The model is defined by

$$\begin{aligned} v(t) &= V_p \exp\{1 - \alpha(t - t_p) - \exp[-\alpha(t - t_p)]\}\sin\left[\frac{2\pi}{T_p}(t-t_0)\right] && t_0 < t \le t_0 + 2T_t \\ &= 0 && \text{elsewhere} \end{aligned} \tag{2.20}$$

where $t_p = t_0 + 0.75T_p$ is the time at which the peak velocity occurs. Fu and Menun (2004) developed predictive relations for V_p, T_p and α by using a sample of recorded motions. They first developed a predictive relation for PGV in terms of **M** and R_{RUP}, and found V_p to be strongly correlated with PGV so that approximately $V_p = 0.8PGV$. The resulting predictive equations are

$$\log_{10} PGV = 0.49 + 0.21\mathbf{M} - 0.16\log_{10} R_{RUP} \tag{2.21}$$

$$\log_{10} V_p = 0.39 + 0.21\mathbf{M} - 0.16\log_{10} R_{RUP} \tag{2.22}$$

$$\log_{10} T_p = -3.38 + 0.54\mathbf{M} \quad \text{(for both rock and soil)} \tag{2.23}$$

They noted that the relation for T_p is different for rock and soil conditions at small magnitudes, but the difference disappears as **M** increases. Finally, for parameter α, which influences the waveform of the velocity pulse in time domain and the width and location of the spectral peak in the frequency domain, they noted that as α increases in absolute value, the length of the signal in time domain increases, but the bandwidth in frequency domain decreases. On this basis, they proposed the predictive relation

$$|\alpha| = \frac{2.5}{T_p} \tag{2.24}$$

2.4.2.1.3 The Mavroeidis and Papageorgiou pulse model

Mavroeidis and Papageorgiou (2003) warned that the use of simplified waveforms (square, triangular or sinusoidal) may be misleading. Instead, they proposed a velocity pulse model in terms of five parameters: amplitude V_p of the pulse, period T_p of the pulse, parameter γ describing the oscillatory character of the pulse, the phase angle ν of the pulse, and the time t_0 at which the pulse envelope assumes it peak value. The model consists of the product of a harmonic function and a bell-shaped envelope function (a shifted haversed sine function):

$$\begin{aligned} v(t) &= \frac{1}{2} V_p \left\{ 1 + \cos\left[\frac{2\pi}{\gamma} \left(\frac{t - t_0}{T_p} \right) \right] \right\} \cos\left[2\pi \left(\frac{t - t_0}{T_p} \right) + \nu \right] \quad t_0 - \frac{\gamma}{2} T_p < t \le t_0 + \frac{\gamma}{2} T_p \\ &= 0 \qquad \text{elsewhere} \end{aligned} \tag{2.25}$$

The advantages of this model are that it has a relatively simple mathematical expression, the parameters are physically meaningful, and it is sufficiently flexible to accommodate a wide range of pulse shapes.

Mavroeidis and Papageorgiou (2003) also developed predictive equations for their model parameters using regression analysis with a dataset of near-fault pulselike records. They noted that the pulse period and amplitude are directly related to the rise time and slip velocity of faulting, respectively, and that the pulse period is strongly correlated with magnitude. They also observed trends with the faulting mechanism: for the same earthquake magnitude, on average, the pulse period is largest for strike-slip faults, smallest for dip-slip faults, with oblique faults, which are a combination of strike-slip and dip-slip faults, being in between. Assuming the pulse period is independent of R_{RUP} for $R_{RUP} < 10$ km, they obtained

$$\log_{10} T_p = -2.2 + 0.4\mathbf{M} \tag{2.26}$$

To satisfy the self-similarity condition, the above was modified to read

$$\log_{10} T_p = -2.9 + 0.5\mathbf{M} \tag{2.27}$$

Although PGV and V_p appear to vary with **M** and R_{RUP}, Mavroeidis and Papageorgiou suggest using $V_p = 100$ cm/s because PGV mostly varies between 70 and 130 cm/s for the entire range of magnitudes. They found no systematic relation for γ with **M** or R_{RUP}.

As pointed out later in this study, one shortcoming of the Mavroeidis and Papageorgiou (2003) model is that the algebraic area underneath the velocity pulse is not zero. This results in a non-zero residual displacement, which is not physically compliant. A modified version of this model introduced in Chapter 3 addresses this shortcoming.

2.4.2.1.4 Extraction of velocity pulse by wavelet processing

Baker (2007) proposed an automated method to extract pulses from velocity time series of near-fault ground motions by use of wavelet-based signal processing. The extracted pulse consists of the ten Daubechies wavelets of order 4 having the largest wavelet coefficients, as computed by the wavelet transform. Baker defines the pulse period as the pseudo-period of the largest wavelet, i.e. the period associated with the maximum Fourier amplitude of the wavelet having the largest wavelet coefficient. From linear regression analysis with a database of near-fault recordings, Baker obtained a relation between the expected value of the pulse period and the earthquake magnitude, which is given by

$$\mathrm{E}\left[\ln T_p\right] = -5.78 + 1.02\mathbf{M} \tag{2.28}$$

This predictive model has an error standard deviation of $\sigma_{\ln T_p} = 0.55$, which is less than what he obtained when he used the pulse period corresponding to the peak spectral velocity, indicating that the proposed wavelet pseudo-period is better correlated with the earthquake magnitude than the pulse period defined in terms of the spectral shape.

2.4.2.2 Seismological or source-based models of near-fault ground motion

Deterministic models based on a dynamic or kinematic rupture model and Green's functions have typically been developed to simulate near-fault ground motions. Such models have been validated against recorded data, and they can be used to improve near- and far-field ground motion models by adding to the database of recorded ground motions (Somerville, 2000). Complete Green's functions containing near, intermediate and far field terms should be used to capture the directivity and fling effects (Somerville, 2002).

For example, Archuleta and Hartzell (1981) used a kinematic source model to simulate and study near-fault ground motions. They modeled the earthquake as a propagating stress drop over a finite area. For simplicity, they assumed a buried circular strike-slip fault in a half-space. They used a slip function consistent with a constant propagating stress drop, as derived by Kostrov in 1964, and assumed a constant rupture velocity equal to 0.9 times the shear-wave velocity. They modeled the wave propagation based on the Green's function for semi-infinite linear elastic isotopic homogeneous medium. In place of a Green's functions method, Dreger et al. (2011) used a 3D finite-difference method that accounts for far-, intermediate-, and near-field information, and they combined it with several distributed slip kinematic models to simulate and study near-fault ground motions in a simple elastic half-space.

However, such deterministic models tend to lack the high-frequency contents of recorded ground motions. For example, Archuleta and Hartzell (1981) noted that real earthquakes have a much more complex stress and geologic environments, which were not incorporated into their model, and which tend to complicate the ground motions. For that reason, hybrid models involving stochastic correction for high frequencies have also been studied (Douglas and Aochi, 2008).

2.4.3 Comparison of predictive equations for pulse parameters

As described above, several investigators have developed predictive equations for the directivity pulse period and pulse amplitude in terms of the earthquake magnitude and the closest distance to the fault. In some cases, local site conditions have also been taken into account. All investigators have obtained similar trends, but the predictive equations are different. This is due to the fact that the investigators have used different definitions of the pulse amplitude and pulse period, they have selected different definitions of what constitutes "near fault" (maximum distances considered range from 10 km to 30 km), and they have used different databases of recorded (and sometimes simulated) near-fault ground motions. It should be noted that all these relations are predictions of the mean pulse amplitude and the mean pulse period. A large scatter or even outliers exist in the data due to the complex nature of the earthquake phenomenon and the fact that the models exclude many other relevant variables. For example, for a given magnitude and distance, a larger than average stress drop will result in a shorter rise time and a shorter pulse period and vice versa (Mavroeidis and Papageorgiou, 2003); yet, most existing predictive equations do not include the stress drop or the rise time as explanatory variables.

Somerville (1998) has shown that the pulse period is related to certain source parameters, namely the rise time (duration of the slip at a single point on the fault) and the fault dimensions, which tend to increase with magnitude. He regressed the rise time T_R against the earthquake magnitude with the self-similarity constraint between the two and obtained

$$\log_{10} T_R = -3.34 + 0.5\mathbf{M} \tag{2.29}$$

Comparing with the predictive equation for the pulse period given in (2.11), one has

$$T_p = 2.2T_R \tag{2.30}$$

This result is consistent with the fact that the rise time is a lower bound on the period of the pulse in the case of a point-source, when ignoring wave propagation effects. It is also confirmed by a simple analytical fault-rupture model. Moreover, Somerville (1998) indicates a correlation between the rise time and the style of faulting, with the rise time for dip-slip earthquakes being on average about half the rise time for strike-slip earthquakes. The pulse period in a dip-slip earthquake is, thus, expected to be shorter than that in a strike-slip earthquake. Moreover, a smaller rise time results in a larger amplitude, a trend which is present in the current ground motion models.

Although many authors have noted the importance of the number of impulsive half-cycles as it may significantly affect the structural response in the inelastic range (Mavroeidis and Papageorgiou, 2002; Somerville, 1998), no predictive equations have been developed. There is a need to identify the conditions that give rise to multiple cycles or pulses. One such reason could be the existence of multiple asperities on the fault rupture plane, in which case the number of pulses depends on the slip distribution, which is difficult to predict, and on the relative locations of the hypocenter, the asperities and the site (Somerville, 1998). Conversely, a uniform slip distribution, or a slip concentrated in a single zone, would result in a well defined pulse sequence (unless local site effects introduce complexities), since all nearby stations will be at more or less equal distances from the region of high slip (Bray and Rodriguez-Marek, 2004).

2.5 NEAR-FAULT GROUND MOTION DIRECTIONALITY AND PROBABILITY OF OCCURRENCE OF A PULSE

2.5.1 Ground motion directionality

Earthquake ground motions are multi-dimensional, with three translational and three rotational components. However, seismic design considerations are generally limited to translational ground motion components in the horizontal plane. Recently, efforts have been made to characterize the two-dimensional horizontal ground motion and to develop models for ground motion directionality, i.e., to determine how the ground motion varies with orientation. Knowledge about both the characteristics of ground motion (intensity, duration and frequency content) and its directionality or lack thereof is important in the seismic design of structures.

Several definitions have been proposed and empirical models developed for spectral acceleration values that are representative of ground motions in two horizontal directions. The geometric mean of spectral accelerations in two orthogonal directions, denoted $S_{a_{GM}}$, was initially used. Boore et al. (2006) introduced orientation independent measures of horizontal ground motion, $S_{a_{GMRotD}}$ and $S_{a_{GMRotI}}$. These measures are both based on the sets of geometric means computed from the as-recorded orthogonal horizontal motions after rotation through all possible angles. More recently, Boore (2010) proposed new orientation-independent spectra, $S_{a_{RotDnn}}$ and $S_{a_{RotInn}}$. $S_{a_{RotDnn}}$ is the nn^{th} percentile of the spectral acceleration over all horizontal orientations at each period and may arise from different orientations at different periods. $S_{a_{RotInn}}$ is the spectrum in the specific orientation that is the closest and most representative of $S_{a_{RotDnn}}$. The NGA-West2 ground motion models were developed for the median spectrum over all orientations, i.e., $S_{a_{RotD50}}$. Shahi and Baker (2013a, 2014) proposed a model for the maximum spectral acceleration over all orientations $S_{a_{RotD100}}$, or more precisely for the ratio of $S_{a_{RotD100}}$ to $S_{a_{RotD50}}$. Their model is to be used in conjunction with the NGA-West2 models of $S_{a_{RotD50}}$.

Using a single response spectrum to represent a bi-directional motion, as described above, does not capture the directionality of the ground motion. It is important to characterize whether the ground motion is polarized, and how it is polarized relative to the geometry of the fault rupture. A ground motion is unpolarized, or lacks directionality, when it is similar in all directions. The ground motion is polarized when motion is concentrated in one direction and varies significantly from one direction to another. Shahi and Baker (2013a, 2014) investigated the directionality of ground motion by examining $S_{a_{RotD100}}$ to determine whether it is observed in random or in specific orientations. They modeled the probability distribution of the orientation, relative to the strike of the fault, from which the value of $S_{a_{RotD100}}$ arises. They found the orientation to be uniformly distributed for short period ($T < 0.5$ sec) spectral values or for closest distance between the site and the fault greater than 5 km, i.e., $R_{RUP} > 5$ km.

When the near-fault effects of forward rupture directivity or fling step are present, ground motions tend to be polarized (or exhibit directionality). Somerville et al. (1997) noted that the fling step occurs in the fault-parallel direction while the rupture directivity velocity pulse usually occurs in the fault-normal (FN) direction. Since, in the horizontal plane, the fault-normal (FN) direction corresponds to the strike-normal (SN) direction, this last observation agrees with Shahi

and Baker's (2013a, 2014) finding that for long period motion ($T > 0.5$ sec) at very near-fault sites ($R_{RUP} \leq 5$ km) the orientation of $S_{a_{RotD100}}$ has a higher probability of being close to the strike-normal direction and a lower probability of being close to the strike-parallel direction.

2.5.2 Probability of occurrence of a pulse

Not all near-fault ground motions contain a forward directivity pulse, and when they do, the pulselike features from the directivity effect are not restricted to a single orientation. Some near-fault sites experience the backward directivity effect. Other near-fault sites record a forward directivity pulse even when they are not in a geometric configuration that is favorable for such an event. For example, in a strike-slip earthquake, if the hypocenter is located at some depth, the rupture will also propagate updip, and sites located updip but close to the epicenter will experience some forward directivity effect. Other sites do not experience a velocity pulse even though they may have a source to site geometry that is favorable to the forward directivity effect. One such case is when the site is located at the end of the fault rupture, where most of the slip is concentrated (Bray and Rodriguez-Marek, 2004). Additionally, the largest velocity pulse might occur in a direction other than the SN direction. Pulselike features from the directivity effect are not restricted to a single orientation. They are observed in a range of orientations, which often but not always includes the SN orientation. Several explanations for this phenomenon can be given. For example, the strike direction, which is usually defined based on an idealized fault plane, may not locally coincide with the actual fault orientation, or the anisotropy of the medium in which the waves propagate might result in a modification of the orientation of the largest pulse (Mavroeidis and Papageorgiou, 2002). Shahi and Baker (2011) rotated recorded pairs of horizontal ground motion components and classified them as pulselike or non-pulselike in each orientation. They used the wavelet-based method developed by Baker (2007) to identify and extract the velocity pulse and they classified a ground motion at a site as pulselike if it was pulselike in at least one horizontal direction. Shahi and Baker (2011) identified 243 recordings as pulselike based on the NGA West2 database (later published as June 2012 version). They omitted from their database ground motions in which a pulse is present in a vertical plane, but not in the horizontal plane, a situation that can occur in non-strike-slip faulting (Shahi and Baker, 2011).

In the context of probabilistic seismic hazard analysis, prediction equations are needed for both pulselike and non-pulselike ground motions. The former are expected to yield ground motion levels that are higher than what the current models predict, while the latter are expected to yield lower intensity ground motions. Pulse occurrence probability models are needed to combine the two cases into a single hazard estimate. Pulse occurrence probability models are also needed to simulate pulselike and non-pulselike near-fault ground motions in appropriate proportions.

Iervolino and Cornell (2008) and later Shahi and Baker (2011) used logistic regression to develop models of the pulse occurrence probability. In these regression models, the log of the ratio of the odds is assumed to be a linear function of selected explanatory variables. Iervolino and Cornell (2008) developed a model to predict the probability of occurrence of the pulse in the SN direction. They used a database of SN near-fault records within 30 km of the fault rupture, which they divided into pulselike and non-pulselike records based on the classification method developed by Baker (2007). For strike-slip earthquakes, they found the model with geometric

parameters R_{RUP} and θ to perform best, but they elected to use a model that includes all three geometric parameters R_{RUP}, s and θ. In a slightly modified form, their model reads

$$\Pr[\text{pulse}|R_{RUP}, s, \theta] = \frac{1}{1+\exp(-0.85925 + 0.11137R_{RUP} - 0.018704s + 0.04441\theta)} \tag{2.31}$$

where R_{RUP} and s are in kilometers and θ is in degrees. The model for non strike-slip earthquakes was selected to be of the same form, even though it was not the best performing model. This was done because the non-strike-slip models were found to be less robust, probably because of the heterogeneity of the data, as it comes from different fault mechanisms, and due to the fact that the explanatory variables used are actually calibrated for dip-slip earthquakes. Their model has the form

$$\Pr[\text{pulse}|R_{RUP}, d, \phi] = \frac{1}{1+\exp(-0.55278 + 0.0551R_{RUP} - 0.002669d + 0.0271\theta)} \tag{2.32}$$

where R_{RUP} and d are in kilometers and ϕ is in degrees. In general, the predicted probabilities of occurrence of a pulse are smaller for non-strike-slip faults than for strike-slip faults. This is reasonable, since directivity conditions are more difficult to realize in the case of non-strike-slip earthquakes. Figure 2.11 shows plots of the probability of pulse occurrence for selected values of R_{RUP}, s or d, and θ or ϕ, where $R_{RUP} = s\tan\theta$ and $R_{RUP} = d\tan\phi$ are assumed for strike-slip and non-strike-slip faults, respectively. As expected, the pulse probability decreases with increasing distance $R_{RUP}$from the fault rupture (except for the case of a strike-slip fault with $\theta = 5^{\text{o}}$, probably because for this small angle a large R_{RUP} corresponds to a large s, which has the opposite effect) and with increasing angle θ or ϕ between the direction of propagation of the rupture and the direction of wave propagation between the hypocenter and the site. It should be noted from the sign of the coefficient of d in (2.32) and from Figure 2.11 that, for the case of a non-strike-slip fault, the probability of occurrence of a pulse decreases as d increases. This seems counterintuitive, since a large rupture width d between the hypocenter and the site should favor the directivity effect. The reason might be that the information provided by R_{RUP} and ϕ is sufficient to describe the geometry, making d superfluous and, thus, resulting in this unexpected trend. A similar trend is observed for the variation with s in the case of a strike-slip fault with $\theta = 30^{\text{o}}$. For these reasons, this model is somewhat questionable.

Shahi and Baker (2011) adopted a different approach. They looked for pulses in all directions and classified a site as "pulselike" if it experienced a pulse in at least one direction. Using the obtained pulselike and non-pulselike databases, they first developed a model to predict the occurrence of a pulse at a site in at least one direction. They used the same explanatory variables as Iervolino and Cornell (2008). For the case of a strike-slip fault, they found that only R_{RUP} and s are significant, resulting in the relation:

$$\Pr[\text{pulselike}|R_{RUP}, s] = \frac{1}{1+\exp(0.642 + 0.167R_{RUP} - 0.075s)} \tag{2.33}$$

For the case of a non-strike-slip fault, their model is

$$\Pr[\text{pulselike}|R_{RUP}, d, \phi] = \frac{1}{1+\exp(0.128 + 0.055R_{RUP} - 0.061d + 0.036\phi)} \tag{2.34}$$

Letting α be the smaller angle between the orientation being considered and the strike of the fault, the fraction of pulselike ground motions that exhibit a pulse in direction α was fitted a capped linear model by minimizing the squared error. Thus, the probability of having a pulse in direction α for strike-slip faults is given by

$$\Pr[\text{pulse in direction } \alpha|\text{pulselike}] = \min[0.67, 0.67 - 0.0041(77.5 - \alpha)] \tag{2.35}$$

and for non-strike-slip faults, it is given by

$$\Pr[\text{pulse in direction } \alpha|\text{pulselike}] = \min[0.53, 0.53 - 0.0041(70.2 - \alpha)] \tag{2.36}$$

According to the above models, orientations close to the SN direction are more likely to experience a pulse. The least likely orientation to observe a pulse is the SP direction. The unconditional probability of observing a pulse in direction α is obtained as

$$\Pr[\text{pulse in direction } \alpha] = \Pr[\text{pulse in direction } \alpha|\text{pulselike}]\,\Pr[\text{pulselike}] \tag{2.37}$$

Figure 2.12 shows the probability of occurrence of a pulse at $\alpha = 90^{\circ}$, i.e. in the SN direction, for selected values of R_{RUP}, s or d, and θ or ϕ, where, for the sake of simplicity, $R_{RUP} = s\tan\theta$ and $R_{RUP} = d\tan\phi$ are assumed for strike-slip and non-strike-slip faults, respectively. As expected, the probability decreases with increasing distance R_{RUP} from the fault rupture, when s is fixed, and with increasing angle θ or ϕ between the direction of rupture propagation and the direction of wave propagation between the hypocenter and the site. The probability increases with increasing s or d, except for the case of a strike-slip fault with $\theta = 30^{\circ}$, possibly because at this large angle an increase in s results in a large increase in R_{RUP}, which has the opposite effect. When the angle θ or ϕ is fixed, the trend with R_{RUP} is generally increasing or constant, due to the fact that, for given θ or ϕ, as R_{RUP} increases s or d increases, which has the opposite effect. The trends with R_{RUP}, s or d, and θ or ϕ of the model by Shahi and Baker are more reasonable than those of the model by Iervolino and Cornell (2008). In later chapters of this study, the model by Shahi and Baker (2011) is used to compute the probability of occurrence of a pulse in the SN direction at a site, given its geometric configuration relative to the fault.

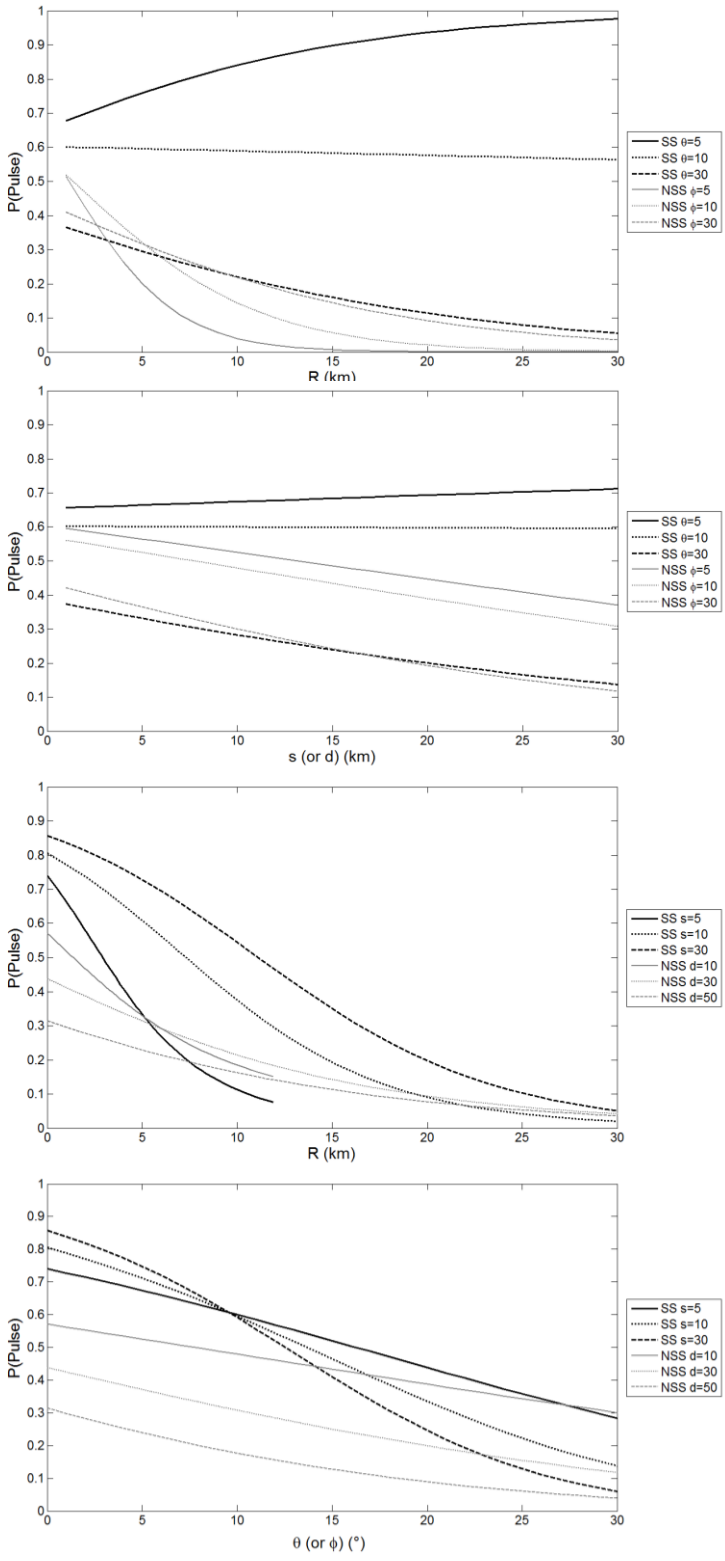

Figure 2.11 Probability of occurrence of a pulse in the SN direction versus directivity parameters for strike-slip (SS) and non-strike-slip (NSS) faults according to the model by Iervolino and Cornell (2008).

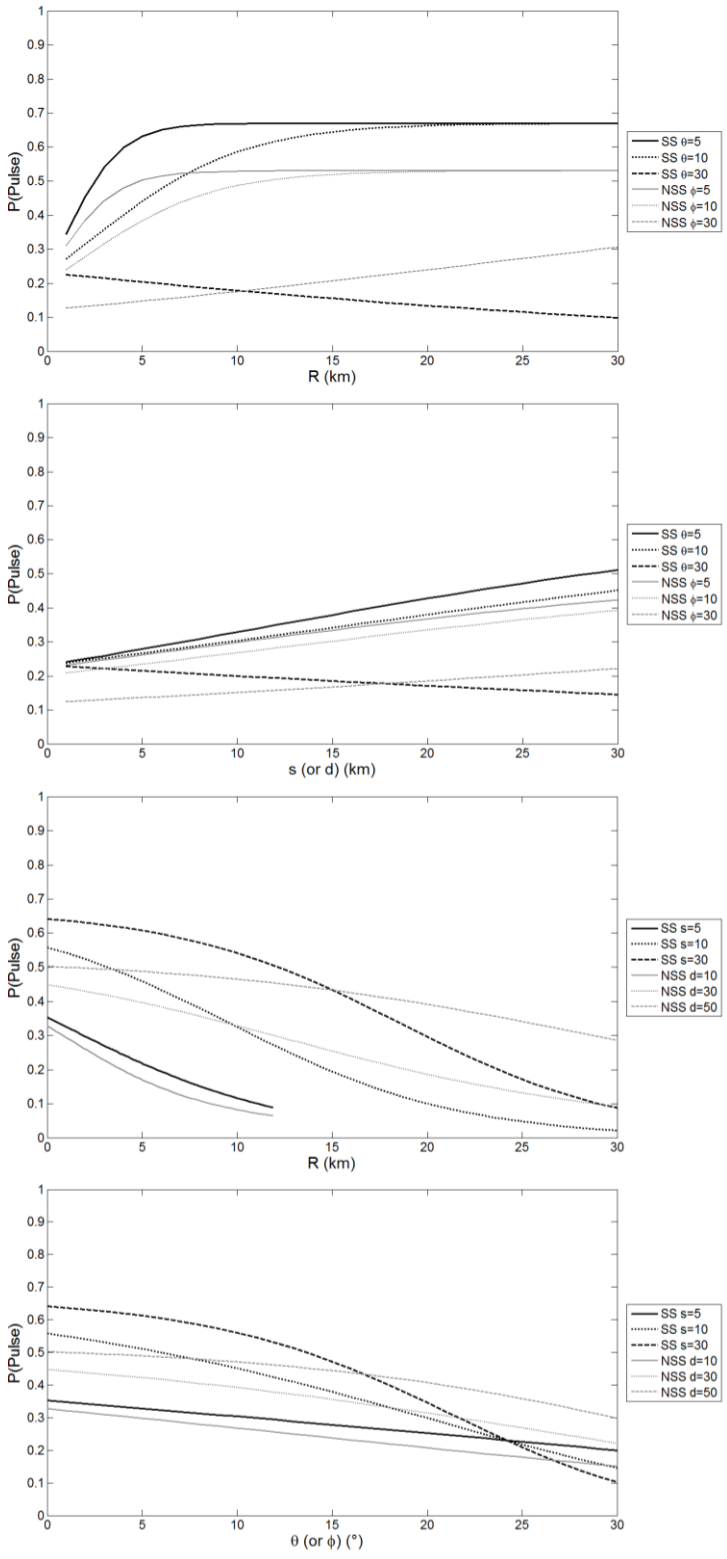

Figure 2.12 Probability of occurrence of a pulse in the SN direction versus directivity parameters for strike-slip (SS) and non-strike-slip (NSS) faults according to the model by Shahi and Baker (2011).

In Chapter 4, we develop a parameterized stochastic model of near-fault ground motion in two orthogonal horizontal directions, accounting for the pulselike and non-pulselike cases as defined by Shahi and Baker (2011). The model can later be extended to include the vertical component. We formulate the pulselike model in the direction of the largest pulse and the corresponding orthogonal direction. Following Rezaeian and Der Kiureghian (2012), we formulate the non-pulselike model in the "principal" horizontal directions, i.e. the orthogonal directions along which the components are statistically uncorrelated.

2.6 MODEL OF THE FLING STEP

The fling step is the permanent tectonic deformation of the ground. It appears in near-fault ground motion components parallel to the direction of slip. Dislocation theory can be used to develop models of the fling step.

Dislocation theory is the area of seismology that describes fault displacements and the associated elastic stresses and strains (Stacey and Davis, 2008). Simple dislocation models that assume a fault of infinite length have been developed and can be used to represent faults having one dimension that is much longer than the other. The assumption of infinite length is generally reasonable for strike-slip faults and at sites located at close proximity to these faults. For a vertical strike slip fault that ruptures the surface, i.e., the depth to top of rupture $Z_{TOR} = 0$, a simple expression can be derived for the strain across a vertical plane at a distance R_x from the fault rupture plane. Integrating the strain at the free surface along the SN direction, the permanent displacement (or the static offset) of the ground in the SP direction at a point on the surface located at a horizontal distance R_x from the vertical strike-slip fault rupture is given by

$$D_{site} = \frac{D_{fault}}{2}\left[1 - \frac{2}{\pi}\tan^{-1}\left(\frac{R_x}{W}\right)\right], \tag{2.38}$$

where W is the width of the fault and D_{fault} is the average total slip along the fault. At the location of the surface rupture of the fault, i.e., for $R_x = 0$, this expression assumes the amplitude of the fling displacement to be equal to half the average total slip on the fault. The amplitude of the fling decreases with distance R_x from the fault, while being equal and in opposite directions on the two sides of the fault. The reader is referred to Roechester (1956), Chinnery (1961) and Stacey and Davis (2008) for more details on the mathematical derivations. For a buried infinite fault also having width W but extending from depth to top of rupture Z_{TOR} to depth to bottom of rupture $(Z_{TOR} + W)$, Dreger et al. (2011) suggest calculating the SP displacement by subtracting from (2.38) the contribution of a shallow infinite fault extending from the surface to depth Z_{TOR},

$$D_{site} = \frac{D_{fault}}{\pi}\left[\tan^{-1}\left(\frac{R_x}{Z_{TOR}}\right) - \tan^{-1}\left(\frac{R_x}{Z_{TOR} + W}\right)\right]. \tag{2.39}$$

The variation of the fling displacement with distance from the fault described by (2.38) and (2.39) is illustrated in Figure 2.13. These simplified procedures were adopted by, e.g., Abrahamson (2001) and Dreger et al. (2011) to compute the static offset in the SP direction for vertical strike-slip faults. The SP ground displacement time series can then be obtained by combining equation 2.37 or 2.38 with an estimate of the rise time (e.g., Somerville et al., 1999) and a model of the functional form of the slip function (e.g., Brune, 1970).

To represent the fling step at a site, Abrahamson (2001) proposed a simple time-domain model, which is to be added to baseline-corrected FP ground motion time series. The fling is modeled in the acceleration domain as a single cycle of a sine wave. The model is formulated in terms of three parameters: the amplitude of the fling displacement at the site D_{site}, the period of the fling T_{fling}, and the arrival time of the fling t_{fling}.. Abrahamson (2001) proposed a model to predict the average slip D_{fault} (in units of centimeter) on a fault as a function of the earthquake magnitude given by

$$\mathrm{E}\left[\ln D_{fault}\right] = 1.15\mathbf{M} - 2.83. \tag{2.40}$$

This model can in turn be used in (2.38) or (2.39) to predict the fling displacement at the site D_{site} as a function of the earthquake magnitude. For an earthquake with $\mathbf{M} = 7$, Figure 2.13 shows plots of the fling displacement predicted at a site as a function of the horizontal distance R_x from a vertical strike-slip fault for a surface and a buried rupture, respectively. Despite having the same rupture width, $W = 10$ km, the surface rupture unsurprisingly results in larger displacements. Abrahamson (2001) also developed a model to predict the average fling period as a function of the earthquake magnitude,

$$\mathrm{E}\left[\ln T_{fling}\right] = -6.96 + 1.15\mathbf{M}. \tag{2.41}$$

The acceleration amplitude in units of g can then be determined as

$$A_{fling} = \frac{D_{site} 2\pi}{981 T_{fling}^2}. \tag{2.42}$$

It is conservatively assumed that the fling pulse arrives at the time of arrival of S-waves and that its polarity is such that constructive interference occurs between the fling and the S waves in the velocity time series.

Figure 2.14 shows the example of a fling step acceleration time series computed according to the model by Abrahamson (2001) for $= 7$, $R_x = 10$ km, $Z_{TOR} = 2$ km and $W = 10$ km. Figure 2.14 also shows the corresponding velocity and displacement time series that are obtained by integration of the acceleration.

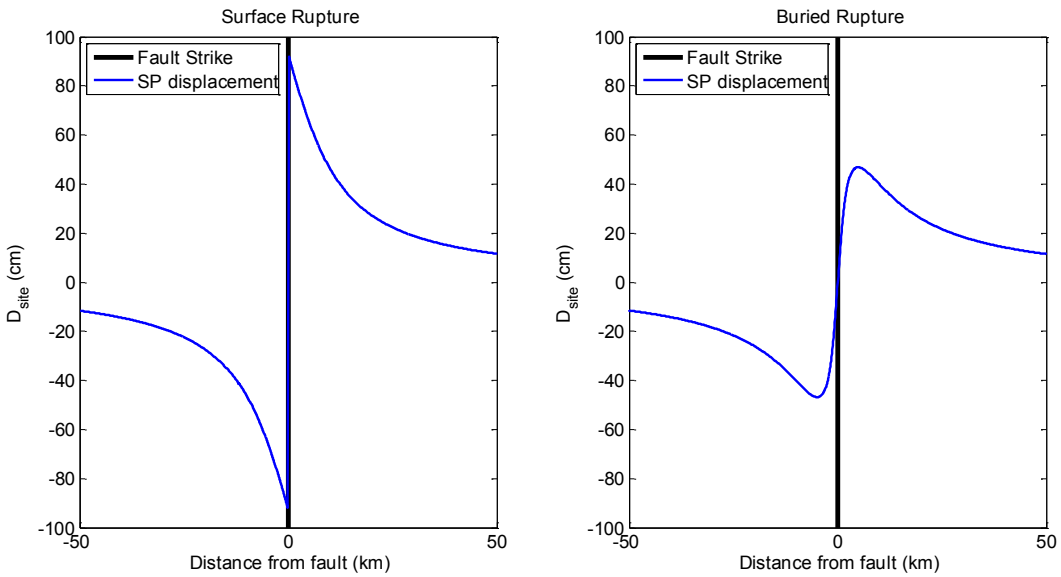

Figure 2.13 Modeled SP permanent displacement of the ground from a M $= 7$ earthquake as a function of distance R_x from a vertical strike-slip fault, for surface rupture with $Z_{TOR} = 0$ km $W = 10$ km (left) and buried rupture with $Z_{TOR} = 2$ km and $W = 10$ km (right).

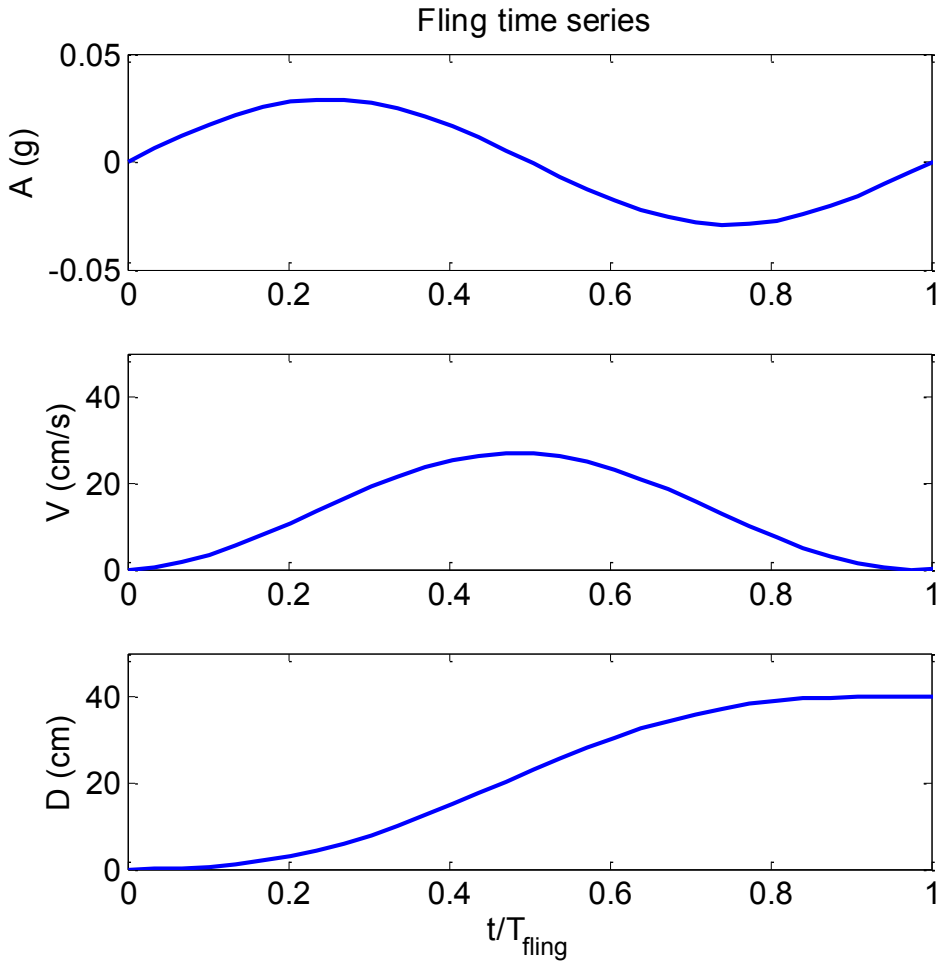

Figure 2.14 Time domain fling step model by Abrahamson (2001) for M $= 7$, $R_x = 10$ km, $Z_{TOR} = 2$ km and $W = 10$ km.

2.7 SUMMARY

In this chapter, we present the state-of-the-art on characterization and modeling of near-fault ground motions. The chapter starts with a discussion of the physics of near-fault ground motion. Different types of ground motion models are then presented followed by some of the spectral and time series models that are proposed in the literature to account for the forward directivity effect. Lastly, the chapter reviews available models to describe the orientation of ground motions relative to fault strike, to compute the probability of occurrence of a forward directivity pulse, and to predict the fling step. A thorough understanding of these underlying phenomena and principles is needed for the developments in the subsequent chapters of this dissertation.

3 Review of Signal Processing Techniques and their Application to Earthquake Ground Motions

3.1 MOTIVATION AND CONTEXT

In this chapter we review and investigate relevant signal processing techniques, which are often employed when processing recorded ground motion data. These include baseline correction, low-cut filtering and resampling. Baseline correction and low-cut (i.e., high-pass, but the former term is used in this dissertation) filtering are commonly applied to recorded ground acceleration time series to correct for distortions and remove frequencies (or periods) with unacceptable signal-to-noise ratio. The extension of these techniques to synthetic ground motions is investigated with the aim of forcing the velocity and displacement time series to achieve zero values at the end of the motion upon integration of the synthetic acceleration. This desired feature is not directly guaranteed by stochastic models developed for an acceleration process. Next, methods to modify the time step of a ground motion signal are studied. Ground motion signals used later in this dissertation to fit the stochastic ground motion model are recorded worldwide by a variety of instruments and at different time steps. For consistency, the model should be fitted to signals that have the same time step. Hence, resampling is necessary.

3.2 PROCESSING OF RECORDED ACCELERATION TIME SERIES

3.2.1 Introduction

When an earthquake occurs, the motion of the ground is often recorded by multiple analog or digital strong-motion instruments that are deployed at various locations. These records are invaluable in characterizing the seismic hazard at a site and the seismic demand on structures. However, these recorded signals invariably contain noise, which distorts the earthquake ground motion signal at high and low frequencies and limits the amount of information that can be retrieved (Boore and Bommer, 2005). Before the record is used to estimate its parameters and characteristics of interest, signal processing techniques should be applied to improve the signal-to-noise ratio. Boore and Bommer (2005) provide a detailed overview of such techniques. The details of the methodology used by PEER to process the records in the NGA-West2 database are described in Ancheta et al. (2013).

The seismic signal recorded by an instrument differs from the signal radiated by the earthquake source. When a fault ruptures, seismic waves are released from the source during a finite duration. The amplitude and frequency characteristics of this radiated seismic signal are normally described by the Fourier source spectra. As seismic waves travel through the ground medium and undergo path effects, e.g., attenuation, geometric spreading, reflections, refractions, superposition, the source signal is modified. This modification can be described by a filter that represents the propagation path of the waves. Lastly, a filter that represents the characteristics of the instrument affects the modified motion to produce the signal that is recorded by the instrument. Thus, the recorded signal contains the characteristics of the seismic source, the path followed by the seismic waves, and the characteristics of the recording instrument.

Seismologists and engineers are interested not in the response of the instrument but in the motion of the ground. The ground motion can be obtained by correcting the recorded signal for the instrument response. The resulting signal, typically a record of the ground acceleration time series, is often distorted by noise arising from many possible sources. The major source of noise in digitized records is the digitization procedure for analog instruments and the ambient seismic noise for digital instruments.

The effect of noise is most apparent when integration of the acceleration signal gives physically unrealistic velocity and displacement time series. Shifts and trends in the baseline of the velocity and displacement time series, residual velocity and displacement values that do not return to zero at the end of the shaking, and large asymmetrical displacement values are typical results of distortion due to noise (e.g., Converse and Brady, 1992; Boore and Akkar, 2003; Boore and Bommer, 2005).

The major source of noise in analog records is the digitization procedure (Boore, 2003a). This noise is difficult to identify and remove. Therefore, the processing procedure generally consists of identifying and removing from the record frequency components that have a low signal-to-noise ratio (SNR). In digital records, the need for the digitization process is eliminated, but noise and the need for processing are not. Microseisms, natural sources (e.g., wind and water), and human sources (e.g., traffic, vibrating machines) cause ambient noise, which can be modeled based on the pre- and post-event portions of digital records (e.g., Douglas and Boore, 2011). Digital records also contain signal-generated noise, i.e., local waves that are generated from seismic waves of the main event arriving at a low angle of incidence (Key, 1968). These noises and the uncertainty in the true baseline of the record require signal processing (e.g., Converse and Brady, 1992; Boore and Bommer, 2005; Ancheta et al. 2013). For this purpose, filtering and/or baseline correction procedures are generally used.

3.2.2 Theoretical acceleration FAS of earthquake ground motions

Before discussing signal processing techniques that correct for distortions introduced by noise in the earthquake signal, we start by reviewing the theoretical shape and scaling of the Fourier amplitude spectrum (FAS) of the ground motion. Seismological models of ground motion spectra constitute the basis of the stochastic method, which is extensively reviewed by Boore (2003b) and in which seismological models are combined with random vibration theory to simulate ground motions.

Several models based on the physics of the fault rupture and wave propagation have been proposed to represent the ground motion spectrum at a particular site. Following the notation used by Boore (2003b), the total ground acceleration Fourier amplitude spectrum (Y_{acc}) at a site is broken down into contributions from the earthquake source (E), path (P), and site (G),

$$Y_{acc}(M_0, R, f) = E(M_0, f)P(R, f)G(f), \tag{3.1}$$

where M_0 is the seismic moment and R is a measure of distance. M_0 is a measure of the total energy released by the earthquake and is related to the moment magnitude **M** through

$$M_0 = \exp(1.5\mathbf{M} + 16.05). \tag{3.2}$$

R is usually taken as the closest distance to the fault rupture surface R_{RUP}.

3.2.2.1 The source effect

The source spectrum $E(M_0, f)$ is a seismological model of the spectrum of the waves radiated from a seismic source and is based on the physics of the fault rupture. It is given by (Boore, 2003)

$$E(M_0, f) = CM_0S(M_0, f)(2\pi f)^2, \tag{3.3}$$

where C is a constant that depends on the radiation pattern and on certain source characteristics, $S(M_0, f)$ is the displacement source spectrum, and $(2\pi f)^2$ is a factor that is applied to convert to the acceleration source spectrum. The displacement source spectrum is generally described by a simple single-corner-frequency model or by a slightly more complicated two-corner frequency model. Aki's ω^2-model (1967), one of the earliest to be proposed, is the most commonly used source model. It is a single-corner frequency model given by

$$S(M_0, f) = \frac{1}{1 + \left(\frac{f}{f_0}\right)^2}, \tag{3.4}$$

where the corner frequency f_0 is inversely proportional to the duration of the source rupture, which depends on the size of the earthquake, and is given by the expression (Brune 1970,1971)

$$f_0 = 4.9 \times 10^6 \, \beta_s \left(\frac{\Delta\sigma}{M_0}\right)^{\frac{1}{3}}, \tag{3.5}$$

where β_s is the shear-wave velocity in the vicinity of the source and $\Delta\sigma$ is the stress drop, which is a measure of the compactness of energy release in space and/or time and is assumed to be constant over the fault rupture. Here, our focus is on S-waves, which are the main source of seismic hazard for structures – hence the use of the shear-wave velocity β_s.

3.2.2.2 The path effect

The path term $P(R, f)$ accounts for geometrical spreading, intrinsic attenuation, and attenuation due to scattering. It is defined in terms of simple functions (Boore, 2003b)

$$P(R, f) = Z(R) \exp\left(-\frac{\pi f R}{Q(f)\beta_s}\right), \tag{3.6}$$

where $Z(R)$ is the geometrical spreading function and $Q(f)$ is the anelastic attenuation operator. For example in Atkinson and Boore (1995), $Z(R)$ is given by,

$$\begin{aligned} Z(R) &= R^{-1}; && R \le 70 \\ &= 1/70; && 70 \le R \le 130 \\ &= \sqrt{130}/70 \; R^{-0.5}; && 130 \le R, \end{aligned} \tag{3.7}$$

where R is measured in kilometers.

Duration is another ground motion characteristic that depends on the path effect and it is not captured by the FAS. The total duration is the sum of the source duration, which is related to

the inverse of the corner frequency ($1/f_0$ for single-corner frequency models), and the path-dependent duration, which increases with distance due to wave propagation and scattering.

3.2.2.3 The site effect

In absence of nonlinear behavior, the site effect does not depend on the path and distance. Simplified functions can then be used to represent the site term as (Boore, 2003b)

$$G(f) = A(f)D(f), \tag{3.8}$$

where $A(f)$ is an amplification function that accounts for the impedance contrast in the crust and $D(f)$ is a diminution or attenuation function that models the path independent damping or loss of high-frequency energy due to source and/or site effects. Two filters are commonly used to represent the diminution effect. One is the $f_{\max}$ filter (e.g., Boore, 1983)

$$D(f) = [1 + (f/f_{\max})^8]^{-1/2}, \tag{3.9}$$

and the other is the κ_0 filter (Anderson and Hough,1984)

$$D(f) = \exp(-\pi\kappa_0 f), \tag{3.10}$$

where parameter κ_0 denotes the shallow rock damping.

All of the above terms are combined to describe the scaling of the acceleration FAS with frequency. At low frequencies, the scaling is controlled by the source term. Due to finiteness of the fault, amplitudes decay in proportion to f^2 with decreasing frequencies below the corner frequency. At high frequencies, if the κ_0 filter is used in the site term, the amplitudes decay exponentially with frequency. This decay is controlled by the anelastic attenuation $Q(f)$ and the shallow rock damping parameter κ_0.

Some attributes of a good model of ground motion times series were listed in Chapter 2. In addition, the resulting simulated time series should be physically sound. While source-based models explicitly account for the physics of the earthquake rupture and wave propagation, site-based models do not. For example in the filtered and modulated white noise model of Rezaeian and Der Kiureghian (2010), the physical properties and scaling of the ground motion are not directly accounted for in the formulation. However these desirable features can be incorporated by (1) selection of a proper functional form for the equations used to predict the model parameters (see Chapter 5), and (2) applying an additional filter to the simulated motions.

The theoretical form of the Fourier amplitude spectrum of total ground acceleration, as described by (3.1)-(3.10), has been increasingly used to guide the selection of the functional form of ground motion prediction equations. We follow this rationale in Chapter 5 to select the functional form of the equations used to predict the parameters of our model.

Even when we use physically consistent relations to predict the parameters of our model, the resulting raw synthetic acceleration time series do not scale like recorded times series at the low frequencies. Below a certain frequency, the acceleration FAS of a simulated modulated and filtered white-noise process does not decay as rapidly as that of an equivalent recorded motion. This results in physically unrealistic synthetic velocity and displacement time series. To increase

resemblance with recorded ground motions, the low frequency (i.e., long period) content of simulated motions can be reduced by use of filtering and/or baseline correction procedures that are similar to the ones used to reduce the long-period noise in recorded acceleration time series. In the following sections, we review how these procedures are applied in the context of recorded ground motions.

3.2.3 Baseline correction

Unrealistic offsets and distortions in the baseline of the velocity and displacement time series can be corrected by baseline adjustments (e.g., Trifunac, 1971; Converse and Brady, 1992). In this procedure, straight line or low-order polynomial baselines are fitted to and removed from the acceleration or velocity time series. This can be done for the whole record or sequentially on multiple segments of the record. In digitized analog records, the distortion of the baseline is often caused by long period noise. Thus, applying baseline adjustments effectively acts as a low-cut filter of unknown frequency characteristics and removes the long period noise and signal from the record.

The baseline adjustment is usually designed so that the ground velocity and displacement return to zero at the end of the shaking. In some situations near the fault, however, the ground undergoes a permanent deformation or fling step and the displacement does not return to zero.One of the advantages of baseline correction over low-cut filtering is that the baseline parameters can be adjusted to preserve the permanent displacement at the end of the motion (e.g., Iwan et al., 1985; Graizer, 1979; Darragh et al., 2004). This can prove useful if measurements (e.g., GPS) of the permanent displacement are available. The disadvantage of baseline correction is its subjectivity.

3.2.4 Filtering

The purpose of a filter is to remove from a signal frequency components that are contaminated by noise. Filtering is more commonly used and is less subjective than baseline correction. It can correct the velocity and displacement time series with minimal effect on the acceleration time series (Bommer and Boore, 2005). In the frequency domain, a filter is represented by a function that has a value close to 1 in the range of frequencies to retain and close to 0 in the range of frequencies to remove. As its name indicates, a low-cut filter filters out low frequencies, a high-cut filter filters out high frequencies, and a band-pass filter cuts out both low and high frequencies.

As reviewed by Bommer and Boore (2005), a filter is defined by its family, its cutoff frequency, and its order. Many filter families exist, such as the Chebyshev filter, which makes use of the Chebyshev (1854) approximation (e.g., Cauer, 1931; Darlington, 1939) and the Butterworth (1930) filter. In application to seismic signals, the choice of the filter family is minor relative the choice of the filter frequency and order. The filter cutoff frequency is the frequency beyond which the signal is attenuated. The filter order characterizes the rate at which the filter function transitions from 1 to 0; the higher the order, the more rapid the transition.

Filtering can be applied in the time domain by convolving the input signal with the impulse-response function of the filter. Alternatively, filtering can be done in the frequency domain by multiplying the Fourier amplitude spectrum of the input signal by the filter function.

Two types of filters exist: causal and acausal. The output of a causal filter depends on only the past and present values of the input and has a phase shift relative to the input signal. An acausal filter does not introduce phase distortions in the output signal. However its output signal can depend on past, present and future values of the input signal.

Causal filtering can be performed only in the time domain. It does not require pre-event zero-padding and does not produce precursory motion in the filtered signal. However, it is typically not used because inelastic response spectra are sensitive to phase shifts and because the shape of the resulting displacement time series is highly dependent on the choice of the cutoff frequency (Boore and Akkar, 2003).

Acausal filtering is preferred because it does not introduce phase shifts and the shape of the resulting displacement time series is not as dependent on the choice of the cutoff frequency (e.g., Boore and Akkar, 2003). However, it requires pre- and post-event zero-padding to allow for the filter response to develop fully (Converse and Brady, 1992; Boore, 2005). The necessary amount of zero-padding depends on the filter frequency and order. When padding causes sudden jumps in the signal, tapering should be used to smoothen the transition and prevent ringing in the filtered signal. Acausal filtering is most easily performed in the frequency domain by multiplying the Fourier amplitude spectrum of the input signal by the filter function while keeping the Fourier phase spectrum unchanged. Acausal filtering can also be performed in the time domain by applying a causal filter twice, forward and backward. This double application ensures that no phase shift is introduced.

When a record contains a significant amount of noise at high frequencies, a high-cut (or low-pass) filter should be applied to remove these high frequencies (Boore, 2005). To have an effect, the frequency of the filter should be smaller than the Nyquist frequency f_N, which is the largest frequency that can be represented by a digitized record. For a record sampled at an interval Δt, $f_N = 1/(2\Delta t)$. However, processing is seldom applied to seismic signals at high frequencies so we hereafter limit our discussion to low-cut filters.

As described above, low-cut filters remove from a signal the low-frequencies (or long periods) that are contaminated by noise. The filter frequency and order should be selected carefully because they strongly influence the resulting filtered times series. The displacement time series and the peak displacement are particularly sensitive to the cutoff frequency. Moreover, when causal filtering is used, the elastic and inelastic response spectra of the filtered signal at short periods are strongly dependent on the choice of the cutoff frequency. The filter frequency generally is taken as the frequency below which the signal-to-noise ratio is unacceptably low.

We illustrate the differences between causal and acausal filters and between time- and frequency-domain applications using the Butterworth filter, which is the filter used for processing the ground motion records of the NGA West2 Database. The low-cut Butterworth filter of order n is defined by (Kanasewich, 1981)

$$Y_{Butter}(f) = \sqrt{\frac{\left(\frac{f}{f_c}\right)^{2n}}{1+\left(\frac{f}{f_c}\right)^{2n}}}, \tag{3.11}$$

where f_c is the cutoff frequency. Applying this filter once in the time domain gives the causal Butterworth filter of order n

$$Y_{causal}(f) = Y_{Butter}(f) = \sqrt{\frac{\left(\frac{f}{f_c}\right)^{2n}}{1+\left(\frac{f}{f_c}\right)^{2n}}}. \tag{3.12}$$

Applying the filter forward and backward in the time domain, gives the time-domain acausal Butterworth filter of order n, which is defined by (Converse and Brady, 1992)

$$Y_{acausal-time}(f) = Y^2_{Butter}(f) = \frac{\left(\frac{f}{f_c}\right)^{2n}}{1+\left(\frac{f}{f_c}\right)^{2n}}. \tag{3.13}$$

Thus, in the time domain, a causal and an acausal filter with identical parameters will have different filter functions. For example, at $f = f_c$, the causal filter has the value $1/\sqrt{2}$ whereas the acausal filter has the value $1/2$, so that the acausal filter transitions more rapidly from 1 to 0. As a result, the two filters will produce different filtered time series. When the Butterworth filter is applied in the frequency domain, it acts as an acausal filter of order n so that

$$Y_{acausal-frequency}(f) = Y_{Butter}(f) = \sqrt{\frac{\left(\frac{f}{f_c}\right)^{2n}}{1+\left(\frac{f}{f_c}\right)^{2n}}}. \tag{3.14}$$

A 5th order acausal Butterworth filter applied in the frequency domain is used to process most of the recorded ground motions in the NGA West2 database (Ancheta et al., 2013).

3.2.5 Selection of filter parameters for recorded ground motions

The most important filter parameter to be selected is the cutoff frequency, the frequency below which the signal is distorted by noise and the data is unreliable. This frequency can be determined in several different ways, but it is best to use them in combination as described in Bommer and Boore (2005).

First, the FAS of the record is compared with the FAS of the noise, which is obtained from the pre-event memory, to estimate the frequency around which the amplitude of the record (signal + noise) becomes comparable to the amplitude of the noise alone. From seismological theory and as previously discussed, the FAS of an earthquake acceleration time series decays with f^2 at low frequencies. The frequency at which the FAS of the record starts to deviate from this trend is another indicator of the cutoff frequency. Finally, for any selected cutoff frequency, the resulting velocity and displacement time series should be plotted to ensure that they look realistic. This check permits to reject filters but does not allow identifying the optimal filter parameters (Bommer and Boore, 2005).

At frequencies below the cutoff, the FAS of the low-cut filtered time series should decay faster than the theoretical FAS, which decays with f^2 when a single-corner frequency model is

assumed. Since it is not possible to distinguish the signal from the noise in the record, the function of the filter is to remove all the frequency content below the cutoff frequency and not to achieve an f^2 decay. Preferably, the selected cutoff frequency f_c should be smaller than the theoretical corner frequency f_0, which is inversely related to the earthquake magnitude as shown in (3.5). A more severe filter would remove an essential part of the signal and the resulting filtered signal would lose its physical significance (Bommer and Boore, 2005).

During an earthquake event, normally three horizontal ground motion components are recorded at each station. A question that often arises is whether to apply the same filter to all components or to optimize the processing for each component at a time. For consistency, a single cut-off frequency is often chosen for all three components (e.g., Ambraseys et al., 2005). However, since the optimal filter for a component with low signal-to-noise ratio may be too severe a filter for the stronger components, processing of the records of the NGA-West2 database was performed one component at a time (Ancheta et al., 2013, 2014). Bommer and Boore (2005) advise using uniform processing of all components only in special applications that require preserving the ground motion phase information. Moreover in these cases acausal filtering should be used and all components should be padded identically.

Similarly, when multiple nearby stations record the same event, records from each station are processed independently. However, coherence is expected in the low frequency content of nearby stations, so agreement in the low-cut filter parameters among stations should be checked (Bommer and Boore, 2005).

3.2.6 Usable range of periods

Using the techniques presented above, ground motion records are processed before computing any ground motion characteristic of interest. A key element is to identify and emphasize the usable range of periods, i.e., the range of periods over which the processed signal is reliable. In fact, computed responses may be sensitive to the processing applied. For example, response spectral values at long periods can be sensitive to the parameters of the low-cut filter. This limits the range of periods over which response spectral values can be reliably computed. Analog records require more severe filters than digital records and often are not reliable at periods greater than 3 or 4 s. GMPE developers have taken this limitation into account by using computed spectral values only up to a fraction of the cutoff period of the low-cut filter that is used. Digital records and seismological models constrain the spectral values at longer periods.

3.3 EXTENSION TO SIMULATED ACCELERATION TIME SERIES

The discussion so far was limited to signal processing techniques that are applied to recorded ground motions. As mentioned earlier, raw synthetic acceleration time series that are generated from a modulated and filtered white noise process do not scale like recorded times series at the low frequencies (i.e., long periods). Signal processing techniques can be used for synthetic ground motions to increase resemblance with recorded ground motions and force the velocity and displacement at the end of the motion to approach zero upon integration of the synthetic acceleration. The latter desired feature is not directly guaranteed by stochastic models developed for an acceleration process.

3.3.1 Low-cut filtering of simulated acceleration time series

Due to the subjectivity of baseline correction, low-cut filtering is preferred to process synthetic acceleration time series. The purpose of the filter is not to improve the signal-to-noise ratio or to remove the frequency components contaminated by noise. Here, the low-cut filter serves two functions: (1) as for recorded time series, it forces the resulting velocity and displacement time series to go to zero at the end of the shaking, and (2) it controls the low-frequency content of the synthetics in a manner consistent with the physics of real earthquake events.

In this study, a 4th order acausal Butterworth filter is selected and applied to simulated ground motions in the frequency domain. Apart from the order, this filter is similar to the one used to process most of the recorded ground motions in the NGA West2 database. A 5th order filter is used to process the NGA-West2 records (Ancheta et al., 2013, 2014).

Due to the finiteness of fault rupture, the amplitude of a real earthquake ground motion decays gradually at frequencies below the corner frequency, which depends on the size of the earthquake. To reproduce this scaling in simulated motions, we relate the cutoff frequency of the filter to earthquake magnitude. A study is performed to identify a suitable relation. This study uses recorded ground motions and synthetic ground motions that are simulated using parameters fitted to the recorded motions (More details about our model and simulation procedure are provided in Chapters 4-6). For each recorded ground motion, we vary the cutoff frequency of the filter that is applied to the raw synthetic acceleration time series until the amplitudes of the resulting velocity and displacement time series are similar to their recorded counter-parts. Using linear regression analysis and ignoring the error term, we find that

$$\log_{10} f_c = 1.41 - 0.345\mathbf{M}. \tag{3.15}$$

We use this relation to determine the cutoff frequency of the low-cut filter that we apply to simulated time series. The same filter is applied to all the components of the same simulated ground motion. The above relation is consistent with similar relations found in the literature as described below.

Boore (2003b) compares several source spectral models found in the literature, including how their corner frequencies relate to earthquake magnitude. For example, they refer to Frankel et al. (1996), who found that the corner frequency of their single-corner-frequency model is well predicted by the relation

$$\log_{10} f_a = 2.623 - 0.5\mathbf{M}. \tag{3.16}$$

In their two-corner-frequency model, Atkinson and Silva (2000) found that for $\mathbf{M} \geq 2.4$

$$\log_{10} f_a = 2.181 - 0.496\mathbf{M}, \tag{3.17}$$

and

$$\log_{10} f_b = 2.41 - 0.408\mathbf{M}, \tag{3.18}$$

where f_a and f_b are the lower and the higher corner frequencies, respectively. The lower corner frequency is determined by the source duration, which is related to the size of the finite fault rupture. The higher corner frequency is related to the size of the subfaults and is the frequency at which the FAS acceleration spectrum reaches a value equal to half the high-frequency acceleration amplitude. Similarly, Boatwright and Choy (1992) found that for $\mathbf{M} \geq 5.3$

$$\log_{10} f_a = 3.409 - 0.681\mathbf{M}, \tag{3.19}$$

and

$$\log_{10} f_b = 1.495 - 0.319\mathbf{M}. \tag{3.20}$$

The relations in (3.15)-(3.20) are plotted in Figure 3.1. This figure shows that the relation we developed (black dashed line) falls within the range predicted by the relations proposed by Frankel et al. (1996) (blue), Boatwright and Choy (1992) (green) and Atkinson and Silva (2000) (red). Moreover, our relation is almost parallel but falling below the higher corner frequency relation of Boatwright and Choy (1992).

Converse and Brady (1992) recommend adding pre- and post-event pads before filtering a ground motion signal. The pads should be sufficiently long to avoid steps in the filter response and to allow the filer transient response to develop and subside. They recommend a pad having a total length

$$T_{pad} = 1.5\frac{n}{f_c}, \tag{3.21}$$

where n is the order of the Butterworth filter and f_c is the filter cutoff frequency. We use (3.21) with $n = 4$ and f_c from (3.15) to compute the number of zero-pads. Half the pads are added to the beginning and the other half at the end of the simulated motion. After processing an acceleration time series, we do not remove the zero-pads prior to computing other measures of ground motion, such as the resulting velocity and displacement time series and response spectra. This is done to ensure compatibility of the various computed measures (see, e.g., Boore, 2005; Boore et al., 2012).

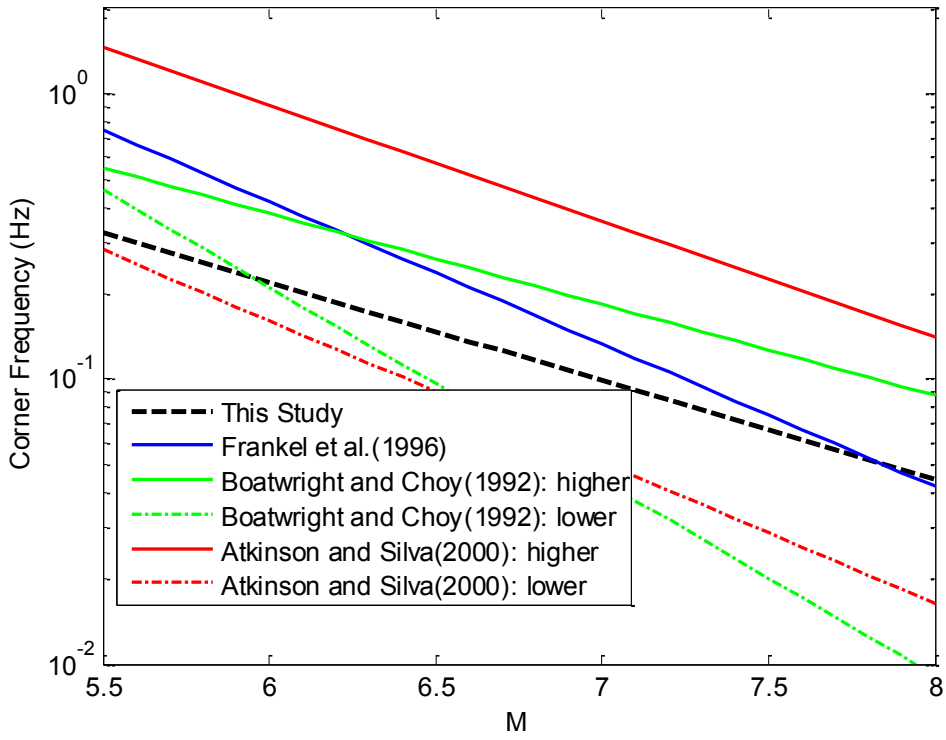

Figure 3.1 Comparison of relations between corner frequency and earthquake magnitude.

3.4 RESAMPLING OF DIGITAL ACCELERATION TIME SERIES

Ground motion records used to fit the stochastic ground motion model developed in this study are recorded worldwide by a variety of instruments and at different time steps Δt. Most records in the NGA database have time steps of $\Delta t = 0.005$ s, 0.01 s or 0.02 s, but a few records have unusual time steps such as $\Delta t = 0.002$ s, 0.00244 s, 0.004 s or 0.0125 s. For consistency, it is desirable that all records are processed to a common Δt before computing their characteristics of interest and fitting a ground motion model. This requires selecting a common time step and resampling ground motion records that have a different time step. Resampling at a smaller time step requires interpolation of the ground motion signal, while a longer time step requires decimation, i.e., low-pass filtering and downsampling. Interpolation and decimation modify the Nyquist frequency $f_N = 1/(2\Delta t)$ of a signal and may introduce distortions. These distortions should be minimized.

3.4.1 Decreasing the time step: interpolation

Using interpolation, a digital signal with an initial time step Δt_0 can be resampled to a time step $\Delta t_f < \Delta t_0$. The original signal can represent frequencies up to f_{N_0} and the resampled signal up to $f_{N_f} > f_{N_0}$, but resampling should not introduce any energy at frequencies beyond those of the original signal, i.e., between f_{N_0} and f_{N_f}.

Ground motion records are often resampled at a higher rate (or shorter time step) to avoid introducing numerical errors in the response spectral values computed at short periods. Linear time interpolation, which assumes that the data points of the original signal are connected by straight lines, is often used in the earthquake engineering practice. However, this practice leads to errors in the response spectral values because it introduces spurious energy between f_{N_0} and f_{N_f}. The effect usually is underestimation of the true peak motions and of the response spectral values at short periods (frequencies near f_{N_0}).

Phillips et al. (2012) have shown that *sinc* interpolation is a preferred alternative that does not introduce noise at high frequencies. In the time domain, it consists of convolving the original signal with the *sinc* function. This is equivalent to padding the FAS of the original signal with zeros at frequencies between f_{N_0} and f_{N_f} then transforming back to the time domain.

Whether the *sinc*-interpolated signal provides a good representation of the true continuous signal depends on the Fourier amplitudes of the signal at frequencies near f_{N_0}. In turn, these amplitudes depend on the physical phenomena that control the decay of ground motion amplitudes at high frequencies, namely anelastic attenuation and damping. The *sinc*-interpolated signal adequately represents the true ground motion signal if the high corner frequency of the ground motion is smaller than f_{N_0}, i.e., if the amplitudes of the true ground motion signal start to decay before $f_{N_0}$and approach zero at f_{N_0}.

Boore and Goulet (2014) used simulations to demonstrate the advantages of the *sinc* interpolation over linear interpolation: *sinc* interpolation better estimates the peak motions, more accurately reproduces the true time series, and does not underestimate response spectral values at short periods (frequencies near f_{N_0}). The resampling algorithm that they use requires that the resampled time step Δt_f be a power of 2 smaller than the original time step Δt_0, i.e., $\Delta t_f = \Delta t_0/2^n$, where n is an integer. The procedure can be summarized as follows.

1. Pre- or post-pad the acceleration time series with zeros to achieve a total number of points that is a power of 2.
2. Apply the fast Fourier transform (FFT) to compute the Fourier spectra of the zero-padded time series.
3. Add zeros to the Fourier spectra from the Nyquist frequency of the original time series, $f_{N_0} = 1/(2\Delta t_0)$, up to the Nyquist frequency of the resampled time series, $f_{N_f} = 1/(2\Delta t_f)$.
4. Apply inverse FFT to the zero-padded Fourier spectra to obtain the *sinc*-interpolated time series

3.4.2 Increasing the time step: decimation

Downsampling is a signal processing procedure that increases the initial sampling time step Δt_0 of a signal to $\Delta t_f = n\Delta t_0$, where n is usually an integer. Every n points are selected and the points in between are discarded. Increasing the sampling time step from Δt_0 to Δt_f reduces the Nyquist frequency from f_{N_0} to f_{N_f}. Let $f_{max} \leq f_{N_0}$ be the largest frequency that the original signal contains. If $f_{max} \leq f_{N_f}$, no information is lost in the downsampling procedure and the downsampled signal represents the original signal. However, if $f_{N_f} < f_{max}$ and no other

processing is applied, downsampling results in aliasing, which is an undesirable effect that causes frequencies to overlap and become indistinguishable. The resulting signal no longer represents the original signal adequately. Aliasing can be avoided by applying to the original signal, before downsampling, an anti-aliasing high-cut filter that removes frequencies between f_{N_f} and f_{max}. Anti-aliasing filters are also applied to analog records before digitizing them. The procedure of high-cut filtering followed by downsampling is known as decimation.

When the attenuation of the high-frequency content is slow and the true ground motion signal has significant frequency content above f_{N_f}, the anti-aliasing filter removes a substantial portion of the signal. The resulting signal does not adequately represent the high-frequency content of the true ground motion and errors are potentially introduced in the computation of ground motion characteristics that depend on the high-frequency content, such as response spectral values at short periods.

Boore and Goulet (2014) used simulations to investigate the effect of anti-aliasing filters on response spectra. They used a causal high-cut filter given by a raised half-cosine function, which starts with a value of 1 at the cutoff frequency f_{saa} (slightly below f_{N_f}) and goes to 0 at f_{N_f}. They found that the key parameter that determines potential errors in the computation of response spectral values at short periods is the ratio of the maximum value of the acceleration FAS to its value at f_{saa}. If this ratio is greater than about 10, response spectral values at short periods are controlled by the ground motion frequencies below f_{N_f} and are practically unaffected by the anti-aliasing filter. However, if this ratio is lower than about 10, response spectral values at short periods can be influenced by ground motion frequencies that are removed by the anti-aliasing filter (above f_{N_f}) and these short period spectral values might thus be significantly underestimated.

3.4.3 Implementation for near-fault ground motion records

The parameterized model of near-fault ground motion that is developed in this dissertation is fitted to a selected set of recorded near-fault ground motions obtained from the NGA West2 database. In order to ensure consistency in the fitting of the model parameters, and especially those parameters that are related to the frequency content, all the recorded motions should have the same time step. Most near-fault records have an original time step $\Delta t_0 = 0.005$ s, 0.01 s or 0.02 s, which are factors of 2 from one another, so they can be easily resampled to any of these time steps using the methods described above.

A common time step $\Delta t_f = 0.005$ s corresponding to a Nyquist frequency $f_{N_f} = 100$ Hz is selected for the following reasons:

1. Most near-fault records have $\Delta t_0 = 0.005$ s.
2. Records having $\Delta t_0 = 0.01$ s and $\Delta t_0 = 0.02$ s (corresponding to Nyquist frequencies $f_{N_0} = 50$ Hz and $f_{N_0} = 25$ Hz, respectively) can be resampled using *sinc* interpolation because they are powers of 2 larger than 0.005 s.
3. While decimation involves loss of information from the application of an anti-aliasing filter, *sinc* interpolation maintains all the information from the original record and only involves padding the FAS with zeros at frequencies between f_{N_0} and f_{N_f}.

4. Most of the original recorded motions in the selected database have extremely small Fourier amplitudes near f_{N_0}. Padding their FAS with zeros at frequencies above f_{N_0} is expected to be a good approximation of the true signal, were it recorded at a higher sampling rate (see Tables A.1 and A.6 in Appendix A).

Following the above procedure, the database that is used later in this study to fit the stochastic ground motion model consists of near-fault ground motion time series sampled at a time step $\Delta t = 0.005$ s. Records having $\Delta t_0 = 0.005$ s are used as they are, while records having $\Delta t_0 = 0.01$ s or $\Delta t_0 = 0.02$ s are resampled to $\Delta t_f = 0.005$ s using the *sinc* interpolation. A few records with sampling steps that are not multiples of 0.005 s are discarded.

3.5 SUMMARY

In this chapter, first the shape and scaling of the theoretical Fourier amplitude spectrum of earthquake ground motions is described. Following a discussion of the sources and consequences of noise, the processing techniques of baseline correction and filtering are described. These are used to correct for the noise in ground motion records. Low-cut filtering is reviewed in some detail before being applied to synthetic ground motions. Finally, interpolation and decimation methods, which are techniques used to resample an earthquake signal at a different time step, are described. Among them, *sinc* interpolation is chosen to resample near-fault ground motion records of the selected database to a common time step $\Delta t_f = 0.005$ s.

4 Stochastic Model of Near-Fault Ground Motion

4.1 INTRODUCTION

As we have seen in Chapter 2, near-fault ground motions possess distinct characteristics that can have strong influence on the response of structures, particularly in the inelastic range. These characteristics include the rupture directivity effect in the FN or SN (fault-normal or strike-normal) direction and the fling step in the FP or SP (fault-parallel or strike-parallel) direction. A site in the near-field region of the fault may experience forward directivity when the fault rupture propagates towards the site with a velocity more or less equal to the shear-wave velocity of the ground medium. The resulting ground motion typically exhibits a large velocity pulse in the FN or SN direction, which may impose extreme demands on a structure. The fling step arises from the fault slip and manifests as a residual displacement at the end of the ground motion, in opposite directions on the two sides of the fault. Not all near-fault ground motions contain a forward directivity pulse or a fling step. When a ground motion does contain pulselike features from the directivity effect, these features are not restricted to a single orientation. Shahi and Baker (2011) have investigated the probability of occurrence of directivity pulses and their orientation. Due to scarcity of recorded near-fault ground motions, there is interest in developing synthetic ground motions for near-fault sites, which can be used in performance-based earthquake engineering in addition to or in place of recorded motions. Obviously, it is crucial that such synthetic motions be realistic and have characteristics that are consistent with those of recorded near-fault ground motions.

In this chapter we develop a parameterized stochastic model of near-fault ground motion in two orthogonal horizontal directions, accounting for the pulselike and non-pulselike cases, as defined by Shahi and Baker (2011). The model can later be extended to include the vertical component. Following Shahi and Baker (2011), the ground motion at a site is said to be pulselike if it contains a velocity pulse in at least one direction. We formulate the pulselike model in the direction along which the pulse has its largest magnitude and the corresponding orthogonal direction. These directions may not coincide with the SN and SP directions. This formulation permits the use of a larger database of recorded pulselike motions than if we used records with a pulse in the SN direction. We employ the method developed by Rezaeian and Der Kiureghian (2012) to formulate the model for non-pulselike ground motions in the "principal" horizontal directions, i.e., the orthogonal directions along which the two components are statistically uncorrelated. Lastly, to complete the characterization of near-fault ground motions, the pulse probability model by Shahi and Baker (2011) is used and new models of the directionality of pulselike and non-pulselike near-fault ground motions are developed.

In the case of a pulselike ground motion, the stochastic model of ground motion in the direction of the largest pulse consists of two sub-models, one for the directivity pulse and one for the residual motion, i.e., the total motion minus the directivity pulse. An existing wavelet-based method by Baker (2007) is used to characterize the directivity pulse and extract it from the total motion of each recorded accelerogram. A modified version of the idealized pulse model by Mavroeidis and Papageorgiou (2003) is employed and fitted to the extracted pulse, thereby generating a sample of data for the five parameters of the model. For the residual, a modified version of the non-stationary filtered white-noise model by Rezaeian and Der Kiureghian (2008, 2010) is employed and its seven parameters are identified by fitting to the database of residual

motions. The modified version of the model by Rezaeian and Der Kiureghian (2008, 2010) is also used to describe near-fault ground motion components that do not contain a pulse, namely the motion in the horizontal direction orthogonal to the direction of the largest pulse, and the major and intermediate components of non-pulselike ground motions. The seven parameters of this model are directly fitted to the databases of (1) the orthogonal components of pulselike motions, (2) the major components of non-pulselike motions, and (3) the intermediate components of non-pulselike motions.

In the following, we first review and discuss stochastic near-fault ground motion models that have been proposed in the literature. This is followed by a brief description of the pulse extraction algorithm developed by Baker (2007). In the subsequent sections, we introduce the pulse model by Mavroeidis and Papageorgiou (2003) and the non-stationary filtered white-noise model by Rezaeian and Der Kiureghian (2008, 2010) and their parameterization. The model developed in this chapter accounts only for the rupture directivity effect and does not consider the fling step in the FP or SP component of the near-fault ground motion. A preliminary model of the fling step is considered at the end of Chapter 6 to provide a complete bi-directional model of the near-fault ground motion.

We remind the reader that we distinguish between the FN direction, which is perpendicular to the fault plane, and the SN direction, which is the horizontal direction perpendicular to the strike of the fault. Similarly, we make a distinction between the FP direction, which is in the plane of the fault in the direction of the slip, and the SP direction, which is the horizontal direction parallel to the strike of the fault. For a vertical strike-slip fault, the two pairs of directions naturally coincide.

4.2 EXISTING MODELS

Menun and Fu (2002, 2004), whose velocity pulse models were presented in Chapter 2, proposed a method for simulating near-fault pulselike ground motions at a site with specified seismic environment. They first noted that models developed to represent the velocity pulse, such as their 2002 and 2004 models, when fitted to recorded ground motions, did well at predicting the displacement demands caused by the recorded motion within a range of periods centered around the period of the pulse. However, this model underestimated demands outside of this range, especially at shorter periods. This is because the fitted pulse cannot replicate the frequency content beyond that associated with the pulse itself, namely it lacks the high frequency content (Fu and Menun, 2004; Menun and Fu, 2002). They thus proposed to separately model the velocity pulse and the non-stationary high-frequency content and to superimpose them. They opted for a stochastic process with a deterministic modulating function and randomly generated phase angles and frequency coefficients to model the high frequency content. They noted that, contrary to far-field ground motions that are typically characterized by an initial build up of energy followed by a relatively long quasi-stationary phase and a gradually decaying tail, the high frequency content of near-fault ground motions does not have a long, stationary strong motion phase. They fitted their model to a database of recorded ground motions in the SN direction and developed empirical relations to predict the model parameters, given the earthquake and site characteristics. They later used these predictive equations to generate synthetic pulselike ground motions for arbitrary sites. They evaluated the suitability of their model by comparing linear and nonlinear displacement demands imposed by recorded and simulated ground motions (Fu and Menun, 2004).

Mavroeidis and Papageorgiou (2003) also proposed a mathematical model of the velocity pulse (presented in Chapter 2) and noted that their model can accurately replicate the intermediate to long period features of near-fault pulselike ground motions, but not the high frequency content. They thus proposed a methodology to model and simulate realistic near-fault pulselike ground motions: they used their velocity pulse model to describe the coherent, long period velocity pulse, and they suggested using a stochastic approach based on a seismological source model (because of the small distance to the source) to describe the incoherent high frequency content. They fitted the parameters of the pulse model to a database of recorded pulselike ground motions in the SN direction, and developed empirical relations to predict the pulse model parameters, given the earthquake and site characteristics. They then used these predictive equations to generate a synthetic velocity pulse and the corresponding acceleration, to which they added a synthetic acceleration time series generated from a source model, such as the specific barrier model (Papageorgiou and Aki, 1983). More details can be found in their paper (Mavroeidis and Papageorgiou, 2003).

The procedure for modeling pulselike ground motions that we present in this study is similar in concept to that of Fu and Menun (2004). There are, however, several important differences. Firstly, we select different models to represent the velocity pulse and the high frequency content (or residual), while Fu and Menun (2004) do not make such a distinction. Secondly, we fit the pulselike model to recorded pulselike ground motions that are rotated to the direction of the largest pulse and not to the SN direction. Thirdly, Fu and Menun (2004) ignore the uncertainty inherent in the predictive equations and the correlations between the model parameters; they simply use the predicted mean values of the parameters as input to their model in order to simulate ground motions. We fully account for the parameter uncertainties and correlations; as a result our simulated models have the same level of variability as recorded near-fault ground motions with similar earthquake and site characteristics. Finally, we develop and fit our model to account for both pulselike and non-pulselike near-fault ground motions, while Fu and Menun only fit their model to pulselike ground motions.

More recently, as mentioned in Chapter 2, Yamamoto and Baker (2011, 2013) developed a site-based stochastic model to simulate ground motions. Their model has features similar to the model by Rezaeian and Der Kiureghian (2008, 2010) but uses wavelets and the wavelet packet transform instead of a filtered white-noise process to represent temporal and spectral non-stationarities. Yamamoto and Baker (2013) formulate their model in the SN direction for sites located at distance $1 \leq R_{RUP} \leq 100$ km and they fit it to a set of 1408 ground motions, some of which are pulselike near-fault ground motions. However, they do not explicitly account for the directivity effect nor does the database that they use explicitly reflect the proportion of pulselike and non-pulselike motions. Therefore, the resulting synthetic motions may exhibit a velocity pulse, but we do not expect an appropriate proportion of pulselike and non-pulselike motions to be guaranteed in their simulations. Furthermore, with their model, it is not possible to specifically simulate pulselike or non-pulselike motions. Moreover, the wavelet transform, on which their model relies, has limited period resolution of at longer periods. This limitation may justify the large logarithmic standard deviations at periods greater than 1 s of the response spectra from their simulations, compared to those from corresponding GMPEs (Yamamoto and Baker, 2013). This limitation becomes problematic in a PSHA or PBEE framework, if their model is used for the analysis and design of long-period structures and of ductile short- and medium-period structures that are expected to respond inelastically.

4.3 EXTRACTION OF THE VELOCITY PULSE

Having a database of recorded near-fault ground motions, the first step is to determine whether or not each recorded motion contains a velocity pulse, typically observed in the FN direction. In the case of strike-slip faults, the FN direction is identical to the horizontal SN direction. For dip-slip faults, the FN direction has components in both the horizontal SN direction and the vertical direction. In a recent work Shahi and Baker (2011) performed classification at several orientations to determine the range of orientations over which the motion is pulselike. Indeed, a pulse might be present in a large range of directions, including or excluding the SN direction (Shahi and Baker, 2011). Following their classification, the ground motion at a site is said to be pulselike if it contains a velocity pulse in at least one direction. Moreover, the direction along which the pulse has the largest magnitude is identified.

We use a quantitative method proposed by Baker (2007) to identify and extract pulses from the velocity time series of recorded ground motions. Prior to Baker's work, classification of near-fault records as pulselike or non-pulselike was based on visual identification of pulses and, thus, depended a lot on the analyst's judgment. Baker (2007) proposed an automated method for detecting pulses and classifying near-fault ground motions, which uses wavelet-based signal processing. The method identifies and extracts the largest velocity pulse from a ground motion and classifies it as an actual pulse or a non-pulse based on the value of a Pulse Indicator (PI). The approach only depends on signal-processing and cannot distinguish between the causal mechanisms of the pulse, i.e., whether the pulse is caused by forward directivity or some other phenomenon, such as an asperity in the fault rupture, basin effects, etc. Furthermore, the method cannot detect the fling step.

Similar to the way Fourier analysis decomposes a signal into the summation of sine waves of different amplitudes, periods and phase angles, wavelet analysis decomposes a signal into wavelets that are localized in time and represent a narrow range of frequencies. Since earthquake records are non-stationary signals, they are more easily represented by wavelets than by stationary sine waves. Wavelets are basis functions satisfying a set of mathematical requirements. There are many wavelet prototypes that can be used to decompose a signal. A Daubechies wavelet of order 4 (Figure 4.1) was selected by Baker because it approximates the shape of many velocity pulses. This mother wavelet is then scaled and translated in time to form a set of basis functions. Any signal can then be represented as a linear combination of these basis functions. The corresponding coefficients are determined from a convolution integral (or summation for digital signals) computed by the continuous wavelet transform. The presence of a pulse is indicated by a significant portion of the original record being described by one or a few wavelets with large coefficients (Baker, 2007).

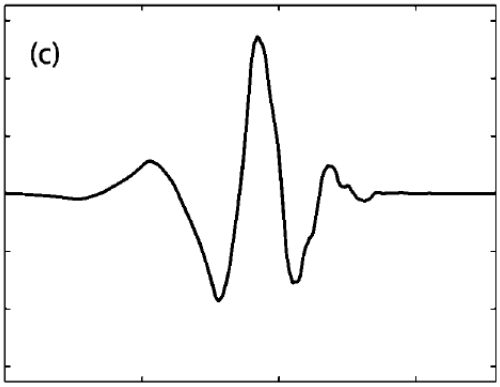

Figure 4.1 Daubechies wavelet of order 4 (after Baker, 2007).

The largest velocity pulse is identified and extracted as follows: Using the wavelet transform, the wavelet coefficients, which are also measures of the energy in each wavelet, are computed for the velocity time series. The wavelet having the largest coefficient, thus the largest energy, is subtracted from the original ground motion. This wavelet determines the period and location of the velocity pulse. The procedure is repeated on the time series from which the largest wavelet was subtracted, to extract the next largest wavelet having the same period and located in nearby times. This is repeated until the 10 largest wavelets are extracted. The sum of the 10 largest wavelets constitutes the extracted velocity pulse. The extracted pulse does not contain high frequency components; it captures the velocity and displacement time series well, but not the acceleration time series. The residual velocity time series is defined as the original time series minus the extracted pulse (Baker, 2007).

According to Baker's method, ground motions are classified as pulselike or non-pulselike based on the significance of the extracted pulse relative to the original ground motion. This is measured by a Pulse Indicator (PI) defined by Baker (2007) and computed for each velocity time series. First, Baker rotated records from the NGA database (with $5.5 < M_w$ and $R < 30$ km) to the SN direction and manually classified the rotated records as pulselike, non-pulselike and ambiguous by visual inspection. He then built a statistical predictive model to reproduce the manual classifications as closely as possible. He found two intuitive and easy-to-compute variables to have good predictive ability: The PGV ratio (ratio of the PGV of the residual to the PGV of the original ground motion) and the energy ratio (ratio of the energy of the residual to the energy of the original ground motion, where energy is computed as the cumulative squared velocity of the record). The predictive equation for the pulse indicator, obtained using logistic regression, is given by

$$PI = \frac{1}{1 + \exp[-23.3 + 14.6(\text{PGV ratio}) + 20.5(\text{Energy ratio})]} \tag{4.1}$$

The PI takes values between 0 and 1; the higher the value, the stronger the indication that the motion is pulselike. Baker selected thresholds for the automated classification procedure based on the value of the PI computed for each record. Thus, records with PI greater than 0.85 are classified as pulselike, records with PI less than 0.15 are classified as non-pulselike, and the remaining records are classified as ambiguous (Baker, 2007).

Up to this point, the extraction and classification procedure only depends on processing of the ground motion record and conveys no information about whether the pulse is caused by forward directivity or not. Baker thus includes two additional criteria that should be satisfied for the record to be classified as pulselike: (1) the pulse should arrive early in the ground motion record, as is the case with forward directivity pulses, and (2) the PGV of the record should be greater than 30 cm/s to exclude lower intensity ground motions that may appear pulselike only because their time series is simple. With this classification procedure, Baker (2007) identified 91 records from the NGA database to be pulselike in the SN direction. In a follow up study, Shahi and Baker (2011) extended the classification procedure to any direction, not only SN. Based on the NGA West2 database (http://ngawest2.berkeley.edu/, June 2012 version) and their 2011 classification scheme, Shahi and Baker (2011) identified 243 recordings as pulselike. A database of 130 pulselike ground motions, out of the 243 identified by Shahi and Baker (2011), is used in this study, as described in greater details in Chapter 5.

Having identified and extracted the velocity pulse from a pulselike record, it is important to identify the period of the pulse in order to compare it with the fundamental period of a structure, as it can strongly influence the response. Contrary to sine waves, there is no well-defined concept of period for wavelets. Baker defines the pulse period as the pseudo-period of the largest wavelet, i.e., the period associated with the maximum Fourier amplitude of the wavelet having the largest wavelet coefficient. It is worth noting that the wavelet pseudo-period is generally slightly larger than the period associated with the peak velocity response spectrum of the original record (Baker, 2007).

In this study, we use Baker's algorithm to identify near-fault ground motions that are pulselike in at least one direction and to extract the pulse from their velocity time series. The derivative of the extracted velocity pulse is then subtracted from the total acceleration time series to obtain the residual acceleration time series. In the following sections, the pulselike and non-pulselike models are formulated in details.

4.4 MODEL OF PULSELIKE NEAR-FAULT GROUND MOTIONS

The pulselike ground motion model is formulated for ground acceleration in the direction of the largest pulse, $a_{PP}(t)$, and in the corresponding orthogonal direction, $a_{PO}(t)$. The model for $a_{PP}(t)$ is further broken down into two sub-models, one for the directivity pulse, $a_{pul}(t)$, and one for the residual motion, $a_{res}(t)$, i.e., the total motion minus the pulse. A modified version of the idealized pulse model by Mavroeidis and Papageorgiou (2003) is employed for the directivity pulse. The non-stationary filtered white-noise model by Rezaeian and Der Kiureghian (2010) is employed for the residual motion and for the motion in the orthogonal direction.

4.4.1 Model of the ground motion in the direction of the largest pulse

4.4.1.1 Model of the velocity pulse

For the purpose of developing a stochastic model of the near-fault ground motion, we need a simple mathematical model of the directivity pulse in terms of a few, preferably physically meaningful, parameters. After examining several models proposed in the literature and reviewed in Chapter 2, we selected the analytical forward directivity pulse model proposed by Mavroeidis and Papageorgiou (2003). In its original formulation, the model for the velocity pulse consists of

the product of a harmonic function and a bell-shaped envelope function (a shifted haversed sine function). Although the expression is given in Chapter 2, we repeat it here for convenience:

$$v_{pul}(t) = \frac{1}{2}V_p\left\{1+\cos\left[\frac{2\pi}{\gamma}\left(\frac{t-t_0}{T_p}\right)\right]\right\}\cos\left[2\pi\left(\frac{t-t_0}{T_p}\right)+\nu\right] \quad t_0-\frac{\gamma}{2}T_p < t \le t_0+\frac{\gamma}{2}T_p \qquad (4.2)$$
$$= 0 \quad \text{elsewhere}$$

The five model parameters are: the pulse amplitude V_p, the pulse period T_p, parameter γ characterizing the number of oscillations in the pulse, the phase angle ν, and the time of the peak of the envelope t_0. Closed-form expressions for the corresponding acceleration and displacement time series are given in Mavroeidis and Papageorgiou (2003).

The formulation in (4.2) results in a non-zero displacement at the end of the pulse given by

$$D_r = V_p T_p \frac{\sin(\nu+\gamma\pi)-\sin(\nu-\gamma\pi)}{4\pi(1-\gamma^2)}. \qquad (4.3)$$

This is problematic, since the ground motion normally does not have residual displacement in directions normal or nearly normal to the fault. We address this problem by slightly modifying the pulse model to achieve zero residual displacement at the end of the pulse. Specifically, we add to the expression in (3.2) a shifted haversed sine function of the same form as in the original formulation and set its amplitude so as to achieve zero displacement at the conclusion of the pulse. Replacing t_0 by $t_{max,p}$ for notational purposes and rearranging terms, the resulting expression of the velocity pulse is

$$v_{pul}(t) = \left\{\frac{1}{2}V_p\cos\left[2\pi\left(\frac{t-t_{max,p}}{T_p}\right)+\nu\right]-\frac{D_r}{\gamma T_p}\right\}\left\{1+\cos\left[\frac{2\pi}{\gamma}\left(\frac{t-t_{max,p}}{T_p}\right)\right]\right\} \quad t_{i,p} < t \le t_{f,p} \qquad (4.4)$$
$$= 0 \quad \text{elsewhere}$$

where the pulse starts at time

$$t_{i,p} = t_{max,p} - \frac{\gamma}{2}T_p, \qquad (4.5)$$

and ends at time

$$t_{f,p} = t_{max,p} + \frac{\gamma}{2}T_p. \qquad (4.6)$$

Note that the modified pulse is still defined by the five parameters described earlier. Hereafter, we call the model defined by (3.3) and (3.4) as the modified Mavroeidis-Papageorgiou (mMP) pulse model. In this study, we fit this model to extracted velocity pulses and later use it to simulate velocity pulses. The derivative of $v_{pul}(t)$ gives the pulse acceleration, $a_{pul}(t)$.

4.4.1.2 Model of broadband near-fault ground motion

Residuals of pulselike near-fault ground motions after removal of the pulse as well as near-fault ground motion components that do not contain a pulse are generally broadband time series. We expect these motions to have characteristics that are similar to each other and to characteristics of far-field ground motions. Hence, we use the filtered white-noise model of Rezaeian and Der Kiureghian (2008, 2010) to describe these broadband motions. We start by introducing a general formulation of the Rezaeian and Der Kiureghian (2008, 2010) model. In subsequent sections, we

use this model for the residual motion, motion in the direction orthogonal to the largest pulse, and for non-pulselike motions in the major and intermediate "principal directions".

Following Rezaeian and Der Kiureghian (2008, 2010), we model the broadband near-fault ground motion as a modulated, filtered white-noise (MFW) process with the filter having time varying parameters. The model for the acceleration process is described by

$$a_{MFW}(t) = q(t)\left\{\frac{1}{\sigma_h(t)}\int_{-\infty}^{t} h[t-\tau, \boldsymbol{\lambda}(\tau)]w(\tau)d\tau\right\} \tag{4.7}$$

where $w(t)$ is a white-noise process, $h[t-\tau, \boldsymbol{\lambda}(\tau)]$ is the unit-impulse response function (IRF) of a linear filter with time-varying parameters $\boldsymbol{\lambda}(\tau) = [\omega_f(\tau), \zeta_f(\tau)]$, $\sigma_h(t)$ is the standard deviation of the process defined by the integral (so that the process inside the curled brackets has unit variance), and $q(t)$ is a time-modulating function that characterizes the root-mean-square of the acceleration process. For the IRF, the following form selected in Rezaeian and Der Kiureghian (2008) is adopted:

$$\begin{aligned} h[t-\tau, \boldsymbol{\lambda}(\tau)] &= \frac{\omega_f(\tau)}{\sqrt{1-\zeta_f^2(\tau)}}\exp\left[-\zeta_f(\tau)\omega_f(\tau)(t-\tau)\right]\sin\left[\omega_f(\tau)\sqrt{1-\zeta_f^2(\tau)}(t-\tau)\right] \quad \tau \le t \\ &= 0 \qquad\qquad \text{elsewhere} \end{aligned} \cdot \tag{4.8}$$

For the modulating function $q(t)$, Rezaeian and Der Kiureghian (2008) used a 3-parameter model that is proportional to the gamma probability density function. That model was found to be appropriate for far-field ground motions. However, as also noted by Fu and Menun (2004), while far-field ground motions are typically characterized by an initial build-up of energy followed by a relatively long quasi-stationary phase and a gradually decaying tail, near-fault ground motions do not have a long quasi-stationary strong-motion phase. Thus, we replace the gamma modulating function by a 4-parameter piecewise function that exhibits sharper build-up and decay segments with no quasi-stationary phase in between. Starting at $t_{0,q}$, the modulating function peaks at time $t_{max,q}$ and consists of a build-up phase in the form of a polynomial of order α up to $t_{max,q}$, followed by a decay phase in the form of an exponential function decaying at a rate of β. Parameter c controls the amplitude of the modulating function, which is given by

$$q(t) = \begin{cases} 0 & t \le t_{0,q} \\ c\left(\dfrac{t-t_{0,q}}{t_{max,q}-t_{0,q}}\right)^{\alpha} & t_{0,q} < t \le t_{max,q}. \\ c\exp\left[-\beta(t-t_{max,q})\right] & t_{max,q} < t \end{cases} \tag{4.9}$$

Following Rezaeian and Der Kiureghian (2010), parameters (c,α,β,$t_{max,q}$) are mapped onto the physical quantities of the expected Arias intensity of the motion, I_a, the effective duration, D_{5-95} (corresponding to the interval between 5% and 95% of Arias intensity values), the time from $t_{0,q}$ to the 5% Arias intensity value, D_{0-5}, and the time from $t_{0,q}$ to the 30% Arias intensity value, D_{0-30}, as described in greater detail in Chapter 5. Figure 4.2 shows plots of the modulating function for selected typical values of the model parameters. The initial part of the modulating function is convex when $\alpha < 1$, linear when $\alpha = 1$ and concave when $\alpha > 1$. Parameter β controls the shape of the tail of the modulating function; as β increases energy decays more rapidly.

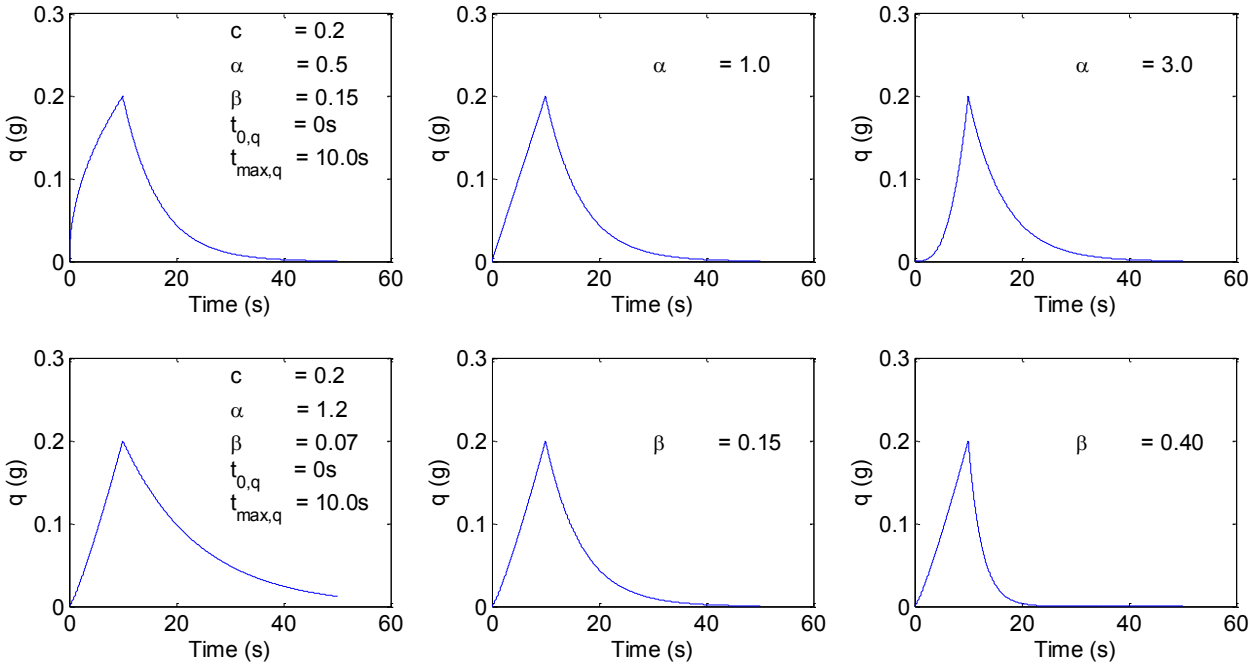

Figure 4.2 Plots of the modulating function for selected model parameter values; varying α parameter (top) and varying β parameter (bottom).

For the filter frequency, which represents the predominant frequency of the motion, the linear form

$$\omega_f(\tau) = \omega_{mid} + \omega'(\tau - t_{mid}) \tag{4.10}$$

used by Rezaeian and Der Kiureghian (2008, 2010) is adopted, where ω_{mid} is the filter frequency at the middle of the ground shaking t_{mid}, taken here as the time t_{30} of the 30% Arias intensity value of the motion, and ω' is the rate of change of the frequency with time. To overcome the arbitrariness in the start time of recorded motions, when fitting to a recorded ground motion, we usually set the start time $t_{0,q}$ to a value that is different from zero. Hence, t_{mid} is given by

$$t_{mid} = t_{30} = t_{0,q} + D_{0-30}. \tag{4.11}$$

When simulating a synthetic ground motion, we set $t_{0,q} = 0$ and obtain $t_{30} = D_{0-30}$. Finally, the filter damping, representing the bandwidth of the acceleration process, is taken to be a constant,

$$\zeta_f(\tau) = \zeta_f \tag{4.12}$$

as was also done in Rezaeian and Der Kiureghian (2010) when fitting to a database or ground motions. Thus, the seven physically relevant parameters (I_a, D_{5-95}, D_{0-5}, D_{0-30}, ω_{mid}, ω', ζ_f) completely define the process representing the broadband near-fault ground acceleration.

One of the advantages of using the model by Rezaeian and Der Kiureghian (2008, 2010) is that it separates the temporal and spectral non-stationarities of the process, so that the selection and fitting of the modulating function is independent of the selection and fitting of the IRF. This

advantage will be exploited in Chapter 5 when identifying the model parameters from recorded motions.

4.4.1.3 Model of the residual motion

The residual motion $a_{res}(t)$ is defined as the remainder of the acceleration time series after subtracting the derivative of the velocity pulse. The residual motion is typically a broadband process with slowly evolving temporal and spectral characteristics. Thus, the modulated, filtered white-noise model of Rezaeian and Der Kiureghian (2008, 2010) with the characteristics described in equations (4.7)-(4.12) is appropriate and is used to describe the residual acceleration motion. For clarity, the seven parameters of the model for the residual motion are denoted by ($I_{a,res}$, $D_{5-95,res}$, $D_{0-5,res}$, $D_{0-30,res}$, $\omega_{mid,res}$, ω'_{res}, $\zeta_{f,res}$).

4.4.2 Model of the ground motion in the direction orthogonal to the largest pulse

To complete the bidirectional characterization of pulselike near-fault ground motion, we model the motion in the horizontal direction orthogonal to the direction of the largest pulse. We assume the orthogonal motion $a_{PO}(t)$ does not contain a directivity pulse and use the model by Rezaeian and Der Kiureghian (2008, 2010) and equations (4.7)-(4.12) to define this motion. For clarity, the seven parameters of the model for the orthogonal component are denoted as ($I_{a,PO}$, $D_{5-95,PO}$, $D_{0-5,PO}$, $D_{0-30,PO}$, $\omega_{mid,PO}$, ω'_{PO}, $\zeta_{f,PO}$).

The complete set of parameters of the pulselike model, denoted $\alpha_{P,i}, i = 1, \dots, 19$, are summarized in Table 4.1. In the following chapter, we describe a method for estimating these parameters.

Table 4.1 Complete list of the parameters $\alpha_{P,i}$ of the pulselike model, $i = 1, \dots, 19$.

Pulse Parameters	$\boldsymbol{\alpha_{P,1}}$	$\boldsymbol{\alpha_{P,2}}$	$\boldsymbol{\alpha_{P,3}}$	$\boldsymbol{\alpha_{P,4}}$	$\boldsymbol{\alpha_{P,5}}$		
	V_p	T_p	γ	ν/π	$t_{max,p}$		
	[cm/s]	[s]	[-]	[rad]	[s]		
Residual Parameters	$\boldsymbol{\alpha_{P,6}}$	$\boldsymbol{\alpha_{P,7}}$	$\boldsymbol{\alpha_{P,8}}$	$\boldsymbol{\alpha_{P,9}}$	$\boldsymbol{\alpha_{P,10}}$	$\boldsymbol{\alpha_{P,11}}$	$\boldsymbol{\alpha_{P,12}}$
	$I_{a,res}$	$D_{5-95,res}$	$D_{0-5,res}$	$D_{0-30,res}$	$\frac{\omega_{mid,res}}{\pi}$	$\frac{\omega'_{res}}{\pi}$	$\zeta_{f,res}$
	[cm/s]	[s]	[s]	[s]	[rad/s]	[rad/s^2]	[-]
Orthogonal Component Parameters	$\boldsymbol{\alpha_{P,13}}$	$\boldsymbol{\alpha_{P,14}}$	$\boldsymbol{\alpha_{P,15}}$	$\boldsymbol{\alpha_{P,16}}$	$\boldsymbol{\alpha_{P,17}}$	$\boldsymbol{\alpha_{P,18}}$	$\boldsymbol{\alpha_{P,19}}$
	$I_{a,PO}$	$D_{5-95,PO}$	$D_{0-5,PO}$	$D_{0-30,PO}$	$\frac{\omega_{mid,PO}}{\pi}$	$\frac{\omega'_{PO}}{\pi}$	$\zeta_{f,PO}$
	[cm/s]	[s]	[s]	[s]	[rad/s]	[rad/s^2]	[-]

4.5 MODEL OF NON-PULSELIKE NEAR-FAULT GROUND MOTIONS

We employ the method developed by Rezaeian and Der Kiureghian (2012) to formulate the model for non-pulselike ground motions in the "principal" horizontal directions, i.e., the

orthogonal directions along which the horizontal components are statistically uncorrelated. Their method is based on the definition of the "principal directions" proposed by Penzien and Watabe (1975).

Generally, three translational components of ground acceleration are recorded at a site, the vertical and two orthogonal horizontal directions. Let $a_i(t)$, $i = 1,2,3$, denote the three recorded components of ground acceleration time series. The correlation coefficient between any pair of components $i, j = 1,2,$ or 3, over the duration t_n of the record is defined by

$$\rho_{a_i a_j} = \frac{\int_0^{t_n} a_i(t) a_j(t) dt}{\sigma_{a_i} \sigma_{a_j}}, \tag{4.13}$$

where

$$\sigma_{a_i}^2 = \int_0^{t_n} a_i^2(t) dt \tag{4.14}$$

is the temporal variance of the i^{th} component of acceleration. The correlation coefficient depends on the directions along which the motions are recorded. Penzien and Watabe (1975) defined the "principal directions" of ground motion as the rotated orthogonal directions along which the three components of ground acceleration are uncorrelated. They adopted an additional simplifying assumption that the ground motion components along these "principal directions" are statistically independent. Following Rezaeian and Der Kiureghian (2012), the three "principal directions" are categorized into major, intermediate and minor "principal directions" based on Arias intensity, where the major direction is the direction with the largest Arias intensity and the minor direction is the direction with the smallest Arias intensity. The Arias intensity of an acceleration time series $a_i(t)$ is a measure of the total energy in the motion at the end of the record and is defined by

$$I_{a_i} = \frac{\pi}{2g} \int_0^{t_n} {a_i}^2(t) dt \tag{4.15}$$

where g is the gravitational acceleration (Arias, 1970). It is seen that the Arias intensity of an acceleration time series $a_i(t)$ is nothing but a scaled version of its temporal variance $\sigma_{a_i}^2$.

As Rezaeian and Der Kiureghian (2012) do for far-field ground motions, we assume, for non-pulselike near-fault ground motions, that the minor "principal direction" coincides with the vertical direction and that the major and intermediate "principal directions" lie in the horizontal plane. The non-pulselike horizontal ground motion model is thus formulated for ground acceleration in the major, $a_{NP1}(t)$, and intermediate, $a_{NP2}(t)$, "principal directions". Moreover, these two components are assumed to be statistically independent. The Rezaeian and Der Kiureghian (2008, 2010) model and equations (4.7)-(4.12) are employed for the motions in both directions. The seven parameters of the model for the motion in the major direction are denoted ($I_{a,NP1}$, $D_{5-95,NP1}$, $D_{0-5,NP1}$, $D_{0-30,NP1}$, $\omega_{mid,NP1}$, ω'_{NP1}, $\zeta_{f,NP1}$) and those for the motion in the intermediate direction are denoted ($I_{a,NP2}$, $D_{5-95,NP2}$, $D_{0-5,NP2}$, $D_{0-30,NP2}$, $\omega_{mid,NP2}$, ω'_{NP2}, $\zeta_{f,NP2}$). The complete set of parameters of the non-pulselike model, denoted $\alpha_{NP,i}, i = 1, \ldots, 14$, are summarized in Table 4.2. In the following chapter, we describe a method for estimating these parameters.

Table 4.2 Complete list of the parameters $\alpha_{NP,i}$ of the non-pulselike model, $i = 1, \ldots, 14$.

	$\boldsymbol{\alpha_{NP,1}}$	$\boldsymbol{\alpha_{NP,2}}$	$\boldsymbol{\alpha_{NP,3}}$	$\boldsymbol{\alpha_{NP,4}}$	$\boldsymbol{\alpha_{NP,5}}$	$\boldsymbol{\alpha_{NP,6}}$	$\boldsymbol{\alpha_{NP,7}}$
Major Parameters	$I_{a,NP1}$	$D_{5-95,NP1}$	$D_{0-5,NP1}$	$D_{0-30,NP1}$	$\frac{\omega_{mid,NP1}}{\pi}$	$\frac{\omega'_{NP1}}{\pi}$	$\zeta_{f,NP1}$
	[cm/s]	[s]	[s]	[s]	[rad/s]	[rad/s^2]	[-]
	$\boldsymbol{\alpha_{NP,8}}$	$\boldsymbol{\alpha_{NP,9}}$	$\boldsymbol{\alpha_{NP,10}}$	$\boldsymbol{\alpha_{NP,11}}$	$\boldsymbol{\alpha_{NP,12}}$	$\boldsymbol{\alpha_{NP,13}}$	$\boldsymbol{\alpha_{NP,14}}$
Intermediate Parameters	$I_{a,NP2}$	$D_{5-95,NP2}$	$D_{0-5,NP2}$	$D_{0-30,NP2}$	$\frac{\omega_{mid,NP2}}{\pi}$	$\frac{\omega'_{NP2}}{\pi}$	$\zeta_{f,NP2}$
	[cm/s]	[s]	[s]	[s]	[rad/s]	[rad/s^2]	[-]

4.6 ADDITIONAL MODELS

4.6.1 Pulse probability model

For a complete representation of the near-fault ground motion at a specified site, two additional pieces of information are needed. The first piece is the probability of the ground motion being pulselike at the site, and should be reflected in the proportion of pulselike and non-pulselike synthetic motions generated for the site. As previously discussed in Chapter 2, Shahi and Baker (2011) developed a model to predict the occurrence of a pulse at a site in at least one direction. We choose to use this model to simulate pulselike and non-pulselike ground motions in appropriate proportions and we repeat the model formulas here for the sake of convenience. For a strike-slip fault, Shahi and Baker (2011) found that

$$\Pr[\text{pulselike}|R_{RUP}, s] = \frac{1}{1 + \exp(0.642 + 0.167R_{RUP} - 0.075s)}, \tag{4.16}$$

and for a non-strike-slip fault,

$$\Pr[\text{pulselike}|R_{RUP}, d, \phi] = \frac{1}{1 + \exp(0.128 + 0.055R_{RUP} - 0.061d + 0.036\phi)}. \tag{4.17}$$

4.6.2 Directionality models

In addition to a pulse probability model, a model of the directionality of the motion is needed to provide, for pulselike motions, the orientation of the direction of the largest pulse relative to the fault strike and, for non-pulselike motions, the direction of the major horizontal "principal direction".

In addition to identifying the 243 pulselike ground motions in the NGA West2 database, Shahi and Baker (2011, 2013b) also document for these motions the angle between the strike of the fault and the direction of the largest pulse. This data for the 130 records of the pulselike database of this study is used to model the probability distribution of the largest pulse being at an angle α_p in degrees from the strike of the fault. Figure 4.3 shows the normalized frequency diagram of the data together with a simple trapezoidal fitted probability density function (PDF). The fitted PDF is described by

$$f_{\alpha_p}(\alpha_p) = c_0 + c_1\alpha_p, \quad 0^o \le \alpha_p \le 90^o. \tag{4.18}$$

The corresponding cumulative distribution function (CDF) is given by

$$F_{\alpha_p}(\alpha_p) = c_0\alpha_p + \frac{c_1}{2}\alpha_p^2. \tag{4.19}$$

Constants c_0 and c_1 are obtained by least-squares fitting of $F_{\alpha_p}(\alpha_p)$ to the empirical CDF of α_p. With linear constraints to impose $F_{\alpha_p}(\alpha_p = 0) = 0$ and $F_{\alpha_p}(\alpha_p = 90) = 1$, we obtain

$$f_{\alpha_p}(\alpha_p) = 0.0014 + 2.155.10^{-4}\alpha_p. \tag{4.20}$$

A Kolmogorov-Smirnoff test indicates that this distribution cannot be rejected at a 5% significance level. Figure 4.4 shows the empirical and fitted CDFs.

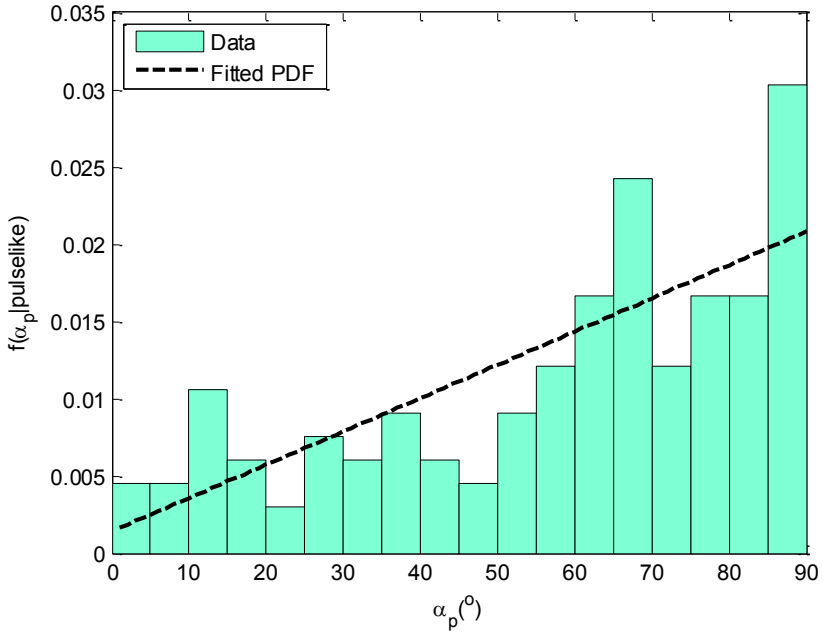

Figure 4.3 Normalized frequency diagram and fitted PDF of the direction of the largest pulse relative to the strike of the fault for pulselike motions.

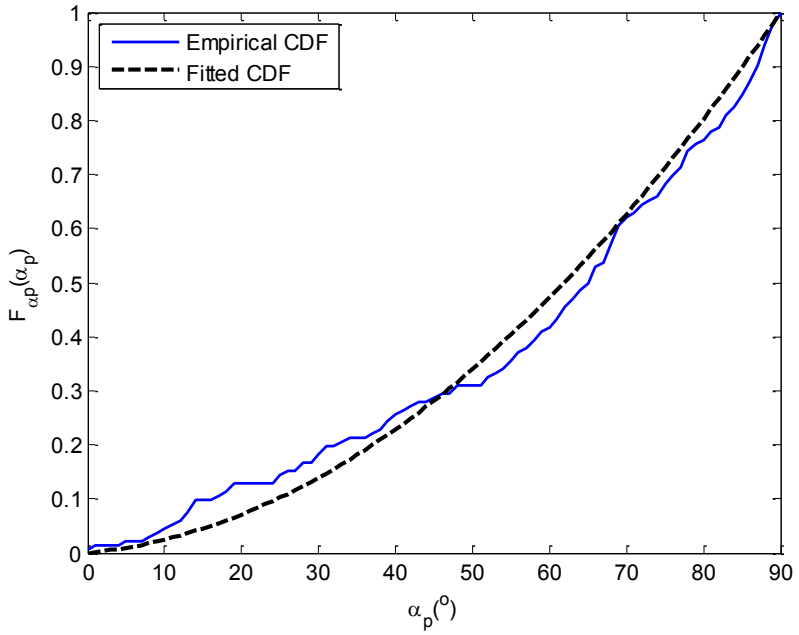

Figure 4.4 Empirical (blue, solid) and fitted (black, dashed) CDF of the direction, relative to the strike of the fault, of the largest pulse in a pulselike ground motion.

For each non-pulselike ground motion record, following the procedure described in Rezaeian and Der Kiureghian (2012), we compute the angle of the rotation from the as-recorded orientations to the major and intermediate "principal directions". We use this rotation angle along with data about the as-recorded orientations and the strike of the fault to compute, for each record in the database, the angle between the major "principal direction" and the strike of the fault. Figure 4.5 shows the normalized frequency diagram of the computed angles for 311 non-pulselike, near-fault ground motions. The distribution appears to be nearly uniform. Hence, we use a uniform distribution for α_{NP1} over the interval $0° \leq \alpha_{NP1} \leq 90°$. This fitted PDF is also shown in Figure 4.5.

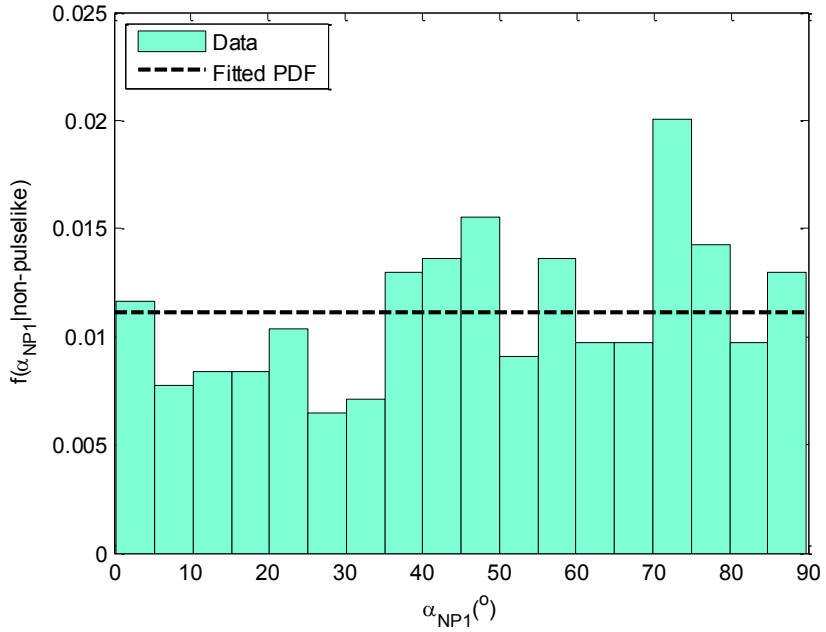

Figure 4.5 Normalized frequency diagram and fitted uninform distribution of the angle of the major direction relative to the strike of the fault for non-pulselike ground motions.

4.7 SUMMARY

In this chapter, we develop a parameterized stochastic model of near-fault ground motion in two orthogonal horizontal directions. The chapter starts with a brief review of some existing models of the forward directivity pulse and of pulselike near-fault ground motions. It then presents the wavelet-based pulse extraction algorithm developed by Baker (2007). A detailed formulation of the proposed stochastic model of pulselike and non-pulselike near-fault ground motions is provided next. The model of pulselike ground motion is formulated in the direction along which the pulse has its largest magnitude and the corresponding orthogonal direction. The model in the direction of the largest pulse consists of two sub-models, one for the velocity pulse and one for the residual motion, which is defined as the total ground acceleration minus the derivative of the velocity pulse. The velocity pulse model is described in (4.4)-(4.6). It is a 5-parameter modified version of the idealized model earlier developed by Mavroeidis and Papageorgiou (2003). The modification is implemented to achieve zero residual displacement at the end of the pulse. The model for the residual motion is described in (4.7)-(4.12). It is the non-stationary, filtered white-noise model formulated by Rezaeian and Der Kiureghian (2008, 2010) with a modified modulating function and a total of 7 parameters. The modification is implemented to better represent the evolution of the amplitudes of near-fault ground motions. This modified model is also employed for motion in the horizontal direction orthogonal to the direction of the largest pulse. The complete set of parameters of the pulselike model, denoted $\alpha_{P,i}, i = 1, \dots, 19$, are summarized in Table 4.1. The model for non-pulselike ground motions is formulated in the "principal" horizontal directions. The modified version of the model by Rezaeian and Der Kiureghian (2008, 2010) is also used to describe these ground motion components. The complete set of parameters of the non-pulselike model, denoted $\alpha_{NP,i}, i = 1, \dots, 14$, are summarized in Table 4.2. Finally, additional models that are needed for a complete characterization of near-fault

ground motions are introduced. The pulse probability of Shahi and Baker is repeated as it will be used to combine the pulselike and non-pulselike models. Additionally, directionality models that describe the probability distributions of the angle between the fault strike and the component with the largest pulse amplitude in pulselike motions and the major “principal” component in non-pulse motions are developed.

5 Estimation of Model Parameters

5.1 INTRODUCTION

Having formulated the model for both pulselike and non-pulselike near-fault ground motions in Chapter 4, we next estimate the model parameters by fitting to recorded near-fault ground motions. The 19 parameters of the pulselike model are fitted to recorded pulselike motions that are rotated into the direction of the largest pulse and the corresponding orthogonal direction. These 19 parameters consist of the 5 parameters (V_p, T_p, γ, ν, $t_{max,p}$) of the pulse, and the 7 parameters (α, β, c, $t_{max,q}$, ω_{mid}, ω', ζ_f) of the filtered white-noise model for both the residual and orthogonal motions. Conversely, the 14 parameters of the non-pulselike model are fitted to recorded non-pulselike motions that are rotated into their major and intermediate "principal directions". These 14 parameters consist of the 7 parameters (α, β, c, $t_{max,q}$, ω_{mid}, ω', ζ_f) of the filtered white-noise model for motions in the major and intermediate directions.

For each pulselike record, the parameters of the pulse model are determined by first extracting the velocity pulse from the recorded motion by use of Baker's wavelet method (Baker 2007) and then fitting to it the modified Mavroeidis-Papageorgiou (mMP) model defined in (4.4)-(4.6). The parameter values are determined by minimizing the squared difference between the extracted pulse and the idealized mMP pulse. For the residual motion and the motion in the orthogonal direction, the parameters of the filtered white-noise model, as defined in (4.8)-(4.12), are fitted to the corresponding recorded motions in accordance to the methods initially described in Rezaeian and Der Kiureghian (2010). The same approach is used to determine the parameters of the filtered white-noise model for the major and intermediate "principal" components of non-pulse recorded motions. The statistical characteristics used are the cumulative mean square (Arias intensity), the cumulative number of zero-level crossings, and the cumulative number of negative peaks and positive minima. Details are presented below. Once the model parameters for the available database of recorded near-fault ground motions are determined, the samples of identified parameter values are transformed to the normal space and regression analysis with random effects is used to develop empirical predictive equations in terms of the earthquake source and site characteristics (e.g., the earthquake magnitude, the type of faulting, the position of the site relative to the potential fault rupture, and the shear-wave velocity of the site). Estimated correlation coefficients between the regression residuals provide estimates of the correlations between the model parameters in the normal space. In Chapter 6, these predictive equations and correlations are used to generate sets of model parameters, which are in turn used in the stochastic models developed in Chapter 4 to generate suites of synthetic ground motions for given earthquake and site characteristics.

In this chapter, we first present the database of pulselike and non-pulselike near-fault ground motions used in the study. Each pulselike ground motion record is rotated into its component containing the largest horizontal pulse and the corresponding orthogonal component. The component in the direction of the largest pulse is then decomposed into the pulse, extracted using Baker's algorithm (2007), and the residual motion. Each non-pulselike ground motion record is rotated into horizontal components in the major and intermediate "principal directions". Next, we describe the methods of fitting and parameter identification of (1) the pulselike ground motion model, for the pulse, residual and orthogonal motions, and (2) the non-pulselike ground

motion model, for motions in the major and intermediate directions. Empirical predictive equations of the pulselike and non-pulselike model parameters are then developed by regression analysis of the data after transformation to the normal space. Next, the correlations between the model parameters in the normal space are estimated. Finally, the empirical predictive equations that we develop are compared to several similar relations proposed in the literature.

5.2 DATABASE OF NEAR-FAULT GROUND MOTIONS

A subset of the Pacific Earthquake Engineering Research (PEER)'s NGA-West2 database (http://peer.berkeley.edu/ngawest2/) is used to fit the models. It consists of pairs of horizontal near-fault ground motion components from moderate to large earthquakes recorded at sites located at a closest distance to the fault rupture less than 31 km, i.e., $R_{RUP} < 31$ km. In order to have a reasonable sample size, no limit is set for the shear-wave velocity, V_{s30}, at the recording site; the effect of the local site is partially accounted for by including V_{s30} as an explanatory variable in the regressions. Only records from shallow crustal strike-slip, reverse, or reverse-oblique earthquakes in active tectonic regions are considered. Infrequent normal earthquakes are disregarded in the current study. The ground motion records in the NGA-West2 database are recorded worldwide by a variety of instruments and at different time steps Δt. For consistency, and as discussed in Chapter 3, only records having time steps of $\Delta t = 0.005$ s, 0.01 s or 0.02 s are included. Moreover, records with $\Delta t = 0.01$ s or 0.02 s are resampled to $\Delta t = 0.005$ s using *sinc* interpolation (see Section 3.4.1). The resampling was kindly performed by Dr. T. Kishida. The ground motion data was provided to us by PEER and by Prof. J. Baker with permission from PEER.

5.2.1 Pulselike database

As mentioned in Chapter 4, we formulate the model for pulselike ground motions in the direction of the largest pulse and the corresponding orthogonal horizontal direction. This model is fitted to a pulselike database that consists of a subset of the ground motions identified as pulselike by Shahi and Baker (2011). As mentioned earlier (in Chapter 2), they identified 243 recorded ground motions as pulselike, i.e., displaying a pulse in at least one horizontal direction, in the June 2012 version of the NGA-West2 database. We exclude aftershocks, records at sites located far from the fault rupture ($R_{RUP} > 31$ km), records from normal and normal-oblique faulting, and records with time step $\Delta t \neq 0.005$ s, 0.01 s or 0.02 s. The resulting pulselike database consists of 130 pairs of records from 27 earthquakes, each contributing 1 or more records with the highest being 32 records for the Chi-Chi earthquake. The pulselike database is summarized in Tables A.1 and A.2 in Appendix A. In order to fit the pulselike ground motion model, each record in the pulselike database is rotated into the direction containing the largest pulse amplitude and the corresponding orthogonal horizontal direction.

For all records in the pulselike dataset, Shahi and Baker provided us with the velocity time series of the ground motion component in the direction of the largest pulse, already decomposed into the pulse $v_{pul}(t)$, extracted using Baker's algorithm (2007), and the residual motion $v_{res}(t)$ (total ground motion minus the extracted pulse motion). These time series have a time step identical to the original time step in the NGA database, which varies from record to record.

Additionally, the two as-recorded horizontal acceleration time series of the records in the pulselike database were obtained from PEER, after being resampled to $\Delta t = 0.005$ s. Using the notation adopted by Rezaeian and Der Kiureghian (2012), let $a_1(t)$ and $a_2(t)$ be the ground acceleration components in their two as-recorded orthogonal horizontal directions. The counter-clockwise rotation by angle θ of $a_1(t)$ and $a_2(t)$ are denoted $a_{1,\theta}(t)$ and $a_{2,\theta}(t)$ and are obtained from

$$\begin{bmatrix} a_{1,\theta}(t) \\ a_{2,\theta}(t) \end{bmatrix} = \begin{bmatrix} \cos\theta & \sin\theta \\ -\sin\theta & \cos\theta \end{bmatrix} \begin{bmatrix} a_1(t) \\ a_2(t) \end{bmatrix}. \tag{5.1}$$

Using (5.1), each pair of resampled as-recorded pulselike ground motion horizontal acceleration components is rotated counter-clockwise by angle $\hat{\theta}$ into the component containing the largest horizontal pulse $a_{PP}(t)$, and the corresponding orthogonal horizontal component $a_{PO}(t)$. The rotation angle $\hat{\theta}$ is computed from knowledge of the as-recorded directions (documented in the NGA-West2 database) and the direction of the largest pulse (identified and documented by Shahi and Baker).

5.2.2 Non-pulselike database

As mentioned earlier, we formulate the model for non-pulselike ground motions in the "principal" horizontal directions, i.e., the orthogonal directions along which the horizontal components are statistically uncorrelated. In particular, the model is formulated for ground acceleration in the major, $a_{NP1}(t)$, and intermediate, $a_{NP2}(t)$, "principal directions". The major direction is the direction with the largest ground motion intensity, here measured in terms of the Arias intensity following Rezaeian and Der Kiureghian (2012). The non-pulselike model is fitted to a non-pulselike database that consists of a subset of the recorded near-fault ground motions in the NGA-West2 database identified as non-pulselike by Shahi and Baker (2011). We exclude aftershocks, records at sites located far from the fault rupture ($R_{RUP} > 31$ km), records from normal and normal-oblique faulting, and records with time step $\Delta t \neq 0.005$ s, 0.01 s or 0.02 s. Since non-pulselike records are more numerous, we also exclude records at very soft sites ($V_{s30} < 360$ m/s). The resulting non-pulselike database consists of 311 pairs of records from 44 earthquakes, each contributing 1 or more records with the highest being 37 records for the Chi-Chi earthquake. The non-pulselike database is summarized in Tables A.6 and A.7 in Appendix A.

The two as-recorded horizontal ground acceleration time series of the records in the non-pulselike database were obtained from PEER, after being resampled to $\Delta t = 0.005$ s. These ground motions are rotated using (5.1), following the procedure described in Rezaeian and Der Kiureghian (2012). By setting to zero the correlation computed according to (4.13) between $a_{1,\theta}(t)$ and $a_{2,\theta}(t)$, Rezaeian and Der Kiureghian (2012) derived the angle between the as-recorded and "principal directions" to be

$$\hat{\theta} = \frac{1}{2}\tan^{-1}\left(\frac{2\rho_{a_1 a_2}\sigma_{a_1}\sigma_{a_2}}{\sigma_{a_1}^2 - \sigma_{a_2}^2}\right) + \frac{k\pi}{2},\ k = \text{integer}, \tag{5.2}$$

where $\rho_{a_1 a_2}$ is given by (4.13) and $\sigma_{a_1}^2$ and $\sigma_{a_2}^2$ are described by (4.14). For each non-pulselike record, (5.2) is used to compute $\hat{\theta}$ and (5.1) to rotate the pair of as-recorded components counter-clockwise by $\hat{\theta}$ to the "principal" horizontal components $a_{1,\hat{\theta}}(t)$ and $a_{2,\hat{\theta}}(t)$. Then, the Arias

intensities of $a_{1,\hat{\theta}}(t)$ and $a_{2,\hat{\theta}}(t)$ are computed using (4.15). The rotated component that has the larger Arias intensity is the major "principal" component, $a_{NP1}(t)$, and the other is the intermediate "principal" component, $a_{NP2}(t)$.

Later in this chapter we develop predictive equations for the model parameters in terms of earthquake source and site characteristics; namely, the type of faulting F ($= 0$ strike-slip faults, $= 1$ reverse and reverse-oblique faults), the depth Z_{TOR} in kilometers to the top of the rupture plane, the moment magnitude **M**, the closest distance R_{RUP} in kilometers from the site to the fault rupture, the shear-wave velocity V_{s30} of the top 30m of soil at the site, and directivity parameters s (or d) in kilometers and θ (or ϕ) in degrees. The ranges of these parameters in the pulselike and non-pulselike databases are listed in Tables 5.1 and 5.2, respectively. They represent the ranges of earthquake source and site characteristics to which simulations ought to be restricted.

Table 5.1 Ranges of earthquake source and site characteristics for records in the pulselike database used.

	M	Z_{TOR}(km)	R_{RUP}(km)	V_{s30}(m/s)	s or d(km)	θ or ϕ(°)
min	5.74	0	0.07	139	4.97	0.1
max	7.90	5.92	30.49	2016	101.51	67.4

Table 5.2 Ranges of earthquake source and site characteristics for records in the non-pulselike database used.

	M	Z_{TOR}(km)	R_{RUP}(km)	V_{s30}(m/s)	s or d(km)	θ or ϕ(°)
min	5.50	0	0.21	361	1.20	0.15
max	7.90	14.50	30.9	1428	135	84.4

5.3 IDENTIFICATION OF MODEL PARAMETERS

For each pulselike ground motion record in the database, the 19 parameters of the pulselike model are identified by fitting the pulse, residual and orthogonal motion models to the recorded counterparts. For each non-pulselike ground motion record in the database, the 14 parameters of the non-pulselike model are identified by fitting the major and intermediate motion models to the recorded counterparts.

To overcome the arbitrariness in the time at which an instrument starts recording a motion, we set up a consistent procedure to define the start time $t_{0,rec}$ of a target recorded ground motion. In the fitting procedure, the start time of the motion $t_{0,q}$ in the filtered white-noise model described in (4.7) is set equal to $t_{0,rec}$. For each recorded pulselike motion, we identify the times at which 0.01% of the total Arias intensity of the residual and orthogonal motions are reached. The smaller of the two values is used as the start time $t_{0,rec}$ of the pulselike record. For each recorded non-pulselike motion, the times at which 0.01% of the total Arias

intensity of the motions in the major and intermediate direction are identified. The smaller of the two values is used as the start time $t_{0,rec}$ of the non-pulselike record. In a few exceptional cases, where a beginning segment of the recorded motion has been truncated, we have set the value of $t_{0,rec}$ subjectively by trial and error such that it improves the fitting of the modulating function.

5.3.1 Identification of the parameters of the mMP pulse model

The 5 parameters (V_p, T_p, γ, ν, $t_{max,p}$) of the idealized mMP velocity pulse model in (4.4) are identified by fitting the model to the largest velocity pulse $v_{pul}(t)$ extracted from a pulselike record. After constraining V_p to the maximum absolute amplitude of the extracted velocity pulse, the fitting of the remaining parameters is done by use of an optimization algorithm that minimizes the squared difference between the two velocity pulse waveforms. Since the fitting is insensitive to the time step Δt, which is much smaller than the period T_p of the pulse, it is not necessary to resample the time series of the velocity pulse motion to a common Δt. Parameter $t_{max,p}$ of the velocity pulse in (4.4) denotes the time of the peak of the pulse envelope and is measured from $t_{0,q}$.

5.3.2 Identification of the parameters of the filtered white-noise model

We start by describing the general procedure used to fit the seven parameters (α, β, c, $t_{max,q}$, ω_{mid}, ω', ζ_f) of the filtered white-noise model to a target recorded acceleration time series. This procedure is used to fit the residual and orthogonal motions of pulselike records, and the major and intermediate ground motion components of non-pulselike records. One of the advantages of the non-stationary filtered white-noise model by Rezaeian and Der Kiureghian (2008) is that it separates the temporal and spectral non-stationarities of the process, thus allowing the selection and fitting of the modulating function to be independent of the selection and fitting of the filter model. The details are described below. In some cases, the target recorded accelerations contain a small amplitude aftershock several seconds after the mainshock. In such cases, we clipped the recorded time series to remove the aftershock and restrict the fitting procedure to the portion containing the mainshock.

5.3.2.1 Fitting the modulating function parameters

We follow a procedure similar to that of Rezaeian and Der Kiureghian (2008, 2010) to perform the fitting of the parameters (α, β, c, $t_{max,q}$) of the modulating function in (4.9) to a target recorded acceleration $a_{rec}(t)$. The recorded residual acceleration in the direction of the largest pulse and the recorded orthogonal motion are the target accelerations for pulselike ground motion. Recorded motions in the major and intermediate "principal directions" are the target accelerations for non-pulselike ground motion.

First, it is preferable to relate (α, β, c, $t_{max,q}$) to physically meaningful characteristics of the ground motion. In this study, we select physical quantities associated with the Arias intensity (I_a) of the ground motion. We start by reviewing and introducing some terminology. The Arias intensity (or total Arias intensity) I_a of an acceleration time series $a(t)$ is a measure of the total energy in the motion. It was defined in (4.15) and is repeated here for convenience,

$$I_a = \frac{\pi}{2g}\int_0^{t_n} a^2(t)dt, \tag{5.3}$$

where g is the gravitational acceleration and t_n is the total duration of the ground motion. The cumulative Arias intensity of $a(t)$ at time t is a function describing a measure of the total energy in the motion up till time t and is defined by

$$I_a(t) = \frac{\pi}{2g}\int_0^t a^2(\tau)d\tau. \tag{5.4}$$

The normalized cumulative Arias intensity function is defined as

$$NI_a(t) = \frac{I_a(t)}{I_a} = \frac{\int_0^t a^2(\tau)d\tau}{\int_0^{t_n} a^2(\tau)d\tau}; \quad t \le t_n. \tag{5.5}$$

A Husid plot is a plot of the cumulative Arias intensity or normalized (in %) cumulative Arias intensity function showing the buildup of the energy of the ground motion over time. Following Trifunac and Brady (1975), the significant duration $D_{z_1-z_2}$ of a ground motion is defined as the time interval between the z_1% and the z_2% time points of the normalized cumulative Arias intensity function. The most commonly used significant duration is D_{5-95}, the time between the 5% and 95% time points of the normalized Arias intensity time series. D_{5-75} is another effective duration that is sometimes used. In this work, we use D_{5-95} and add the subscript I_a to denote that the significant duration D_{5-95,I_a} is related to Arias intensity.

For recorded ground accelerations, let $I_{a,rec}$ and $I_{a,rec}(t)$ denote the total Arias intensity and the cumulative Arias intensity function, respectively. Similar quantities can be defined for the model of the acceleration process $a_{MFW}(t)$, which was defined in (4.7). The expected value of the total Arias intensity of $a_{MFW}(t)$ is

$$E\left[I_{a,MFW}\right] = E\left[\frac{\pi}{2g}\int_0^{t_n} {a_{MFW}}^2(t)dt\right] = \frac{\pi}{2g}\int_0^{t_n} q^2\left(t;\alpha,\beta,c,t_{max,q}\right)dt = I_{a,q}, \tag{5.6}$$

where $I_{a,q}$ is the Arias intensity of the modulating function. The second equality is obtained by switching the orders of the expectation and integration operations and noting that the modulating function is identical to the mean-square function of the process. Similarly, the expected value of the cumulative Arias intensity of the process a_{MFW} at time t is equal to the cumulative Arias intensity of the modulating function at time t

$$E\left[I_{a,MFW}(t)\right] = \frac{\pi}{2g}\int_0^{t} q^2\left(\tau;\alpha,\beta,c,t_{max,q}\right)d\tau = I_{a,q}(t). \tag{5.7}$$

Following Rezaeian and Der Kiureghian (2008, 2010) and making use of the above relations, we perform fitting of parameters (α, β, c, $t_{max,q}$) of the selected modulating function by matching as closely as possible the cumulative Arias intensity of the modulating function, $I_{a,q}(t)$, to that of the target recorded acceleration, $I_{a,rec}(t)$, i.e., by matching as closely as possible their respective Husid plots.

In earlier reports of this study (see Dabaghi et al., 2011), we first set $t_{max,q}$, i.e., the time at which the modulating function takes its maximum value, equal to the time at which the smoothed root-mean-square function of the residual acceleration time series took its maximum value. The remaining parameters α, β and c were then related to the Arias intensity I_a, effective duration D_{5-95,I_a}, and the time of the 30% of Arias intensity, t_{30,I_a}, of the target accelerogram.

This initial procedure provided an adequate fit in most cases that have a clear peak in the smoothed root-mean-square acceleration. In some cases, however, two or more large peaks were observed and $t_{max,q}$ had to be selected subjectively to obtain an acceptable fit. To eliminate this subjectivity, the fitting procedure is slightly modified, as described below.

We no longer constrain $t_{max,q}$. Instead, we fit the modulating function to a target acceleration time series by matching their total Arias intensities, I_a, and three selected points on their respective Husid plots, namely the times t_{5,I_a}, t_{30,I_a} and t_{95,I_a} of the 5%, 30% and 95% of their respective normalized cumulative Arias intensity functions. This is equivalent to matching t_{5,I_a} and t_{30,I_a} and the effective duration D_{5-95,I_a}. First, the starting time of the modulating function is set to the starting time of the target recorded acceleration,

$$t_{0,q} = t_{0,rec}. \tag{5.8}$$

As described earlier, $t_{0,rec}$ is defined by

$$t_{0,rec} = \min\left(t_{0.01,I_a,res}, t_{0.01,I_a,PO}\right) \tag{5.9}$$

for pulselike motions and by

$$t_{0,rec} = \min\left(t_{0.01,I_a,NP1}, t_{0.01,I_a,NP2}\right) \tag{5.10}$$

for non-pulselike motions, where $t_{0.01,I_a,comp}$ is the time at which 0.01% of the total Arias intensity of the component in question is reached. Then, parameters α, β and $t_{max,q}$ of the modulating function are identified by solving the set of nonlinear simultaneous equations

$$t_{5,I_a}\left(\alpha, \beta, t_{max,q}\right) = t_{5,I_a,rec}, \tag{5.11}$$

$$t_{30,I_a}\left(\alpha, \beta, t_{max,q}\right) = t_{30,I_a,rec}, \tag{5.12}$$

$$t_{95,I_a}\left(\alpha, \beta, t_{max,q}\right) = t_{95,I_a,rec}, \tag{5.13}$$

or equivalently, after subtracting $t_{0,q}$ from both sides of equations (5.11)-(5.13) and making use of (5.8),

$$D_{0-5,I_a}\left(\alpha, \beta, t_{max,q}\right) = D_{0-5,I_a rec}, \tag{5.14}$$

$$D_{0-30,I_a}\left(\alpha, \beta, t_{max,q}\right) = D_{0-30,I_a rec}, \tag{5.15}$$

$$D_{0-95,I_a}\left(\alpha, \beta, t_{max,q}\right) = D_{0-95,I_a \mathrm{rec}}, \tag{5.16}$$

where

$$D_{0-z,I_a,rec} = t_{z,I_a,rec} - t_{0,rec} = t_{z,I_a,rec} - t_{0,q}, \tag{5.17}$$

and

$$D_{0-z,I_a}(\alpha,\beta,t_{max,q}) = t_{z,I_a}(\alpha,\beta,t_{max,q}) - t_{0,q}. \tag{5.18}$$

In the above equations, t_{z,I_a} is the time of the z% point on the normalized cumulative Arias intensity function and D_{0-z,I_a} is the same quantity measured from the start time t_0. Quantities $t_{z,I_a,rec}$, for $z = 5, 30$ and 95 are the values for the target recorded acceleration. For the selected form of the modulating function and given $t_{0,q}$, we can easily show that

$$\begin{aligned} t_{z,I_a}(\alpha,\beta,t_{max,q}) &= t_{0,q} + \left\{\frac{z}{100}\left(t_{max,q}-t_{0,q}\right)^{2\alpha}\left[\left(t_{max,q}-t_{0,q}\right)+\frac{(2\alpha+1)}{2\beta}\right]\right\}^{\frac{1}{(2\alpha+1)}} && t_z \le t_{max,q} \\ &= t_{max,q} - \frac{1}{2\beta}\ln\left\{\frac{100-z}{100}\left[1+\frac{2\beta}{2\alpha+1}\left(t_{max,q}-t_{0,q}\right)\right]\right\} && t_{max,q} < t_z. \end{aligned} \tag{5.19}$$

The formulation of the fitting procedure in terms of (5.14)-(5.16) is preferred over (5.11)-(5.13) because it allows to overcome the arbitrariness in the starting time $t_{0,rec}$ when later developing empirical predictive relations. The matching of the parameters ($D_{0-5,I_a,q}$, $D_{0-95,I_a,q}$, $D_{0-95,I_a,q}$) of the modulating function to parameters ($D_{0-5,I_a,rec}$, $D_{0-95,I_a,rec}$, $D_{0-95,I_a,rec}$) of a target recorded ground motion is a non-linear optimization problem. The simultaneous equations are solved numerically for (α, β, $t_{max,q}$) by minimizing the sum of the squared differences between the two sides of the three equations (5.14)-(5.16). Since the converged solution often depends on the selected starting point, we consistently use a set of six starting points that converge to one or more local solutions. Local solutions that yield negative values of α are discarded. Then, among the remaining solutions, the one that minimizes the sum of the squared differences the most is selected. With α, β and $t_{max,q}$ identified, parameter c is determined by setting the total Arias intensity $I_{a,q}$ of the modulating function equal to the total Arias intensity $I_{a,rec}$ of the target recorded acceleration. Starting with the second part of (5.6) and for the modulating function in (4.9), it can be shown that for large t_n

$$I_{a,q} = \frac{\pi}{2g}\int_0^{t_n} q^2(t;\alpha,\beta,c,t_{max,q})dt = \frac{\pi}{2g}c^2\left(\frac{t_{max,q}-t_{0,q}}{2\alpha+1}+\frac{1}{2\beta}\right). \tag{5.20}$$

Thus,

$$c = \sqrt{\frac{I_{a,rec}}{\frac{\pi}{2g}\left(\frac{t_{max,q}-t_{0,q}}{2\alpha+1}+\frac{1}{2\beta}\right)}}, \tag{5.21}$$

where $I_{a,rec}$ is the total Arias intensity of the target recorded acceleration. We visually check that the resulting modulating function adequately describes the evolution of amplitudes of the ground motion.

In summary, and using

$$D_{5-95,I_a} = D_{0-95,I_a} - D_{0-5,I_a}, \tag{5.22}$$

parameters (α, β, c, $t_{max,q}$) of the modulating function are mapped onto the physical quantities of (I_a, D_{5-95,I_a}, D_{0-5,I_a}, D_{0-30,I_a}) of a target recorded acceleration. Later, for the purpose of

simulating an acceleration time series, the values of (I_a, D_{5-95,I_a}, D_{0-5,I_a}, D_{0-30,I_a}) are first simulated. These are used along with (5.14)-(5.16), (5.21) and (5.22) to back-calculate (α, β, c, $t_{max,q}$), which are then used together with $t_{0,q} = 0$ to compute the simulated modulating function.

Without going into the details of the fitting procedure, which we postpone to the following sections, we now briefly discuss the adequacy and limitations of the model and fitting procedure in representing recorded motions. Figure 5.1 shows examples of two recorded motions and the corresponding fitted modulating functions. The example on the left illustrates an excellent fit of the recorded time series and the Husid plot, while the example on the right illustrates a poor fit. For the selected form of the modulating function $q(t)$, the Husid plot $I_{a,q}(t)$ is smooth and increases monotonically with time. The slope of $I_{a,q}(t)$ is proportional to $q^2(t)$; it is zero at $t_{0,q}$, gradually increases up to time $t_{max,q}$, then gradually decreases until the end of the record. This idealized shape represents the evolution of the Husid plot of a recorded near-fault ground motion in an average sense. In cases where energy in the recorded motion arrives in a single event, such as for the record on the left side of Figure 5.1, this idealized shape generally describes the recorded motion well. However in some cases, such as the record shown on the right side of Figure 5.1, energy arrives in multiple sub-events and the Husid plot consists of sections with large slopes separated by sections with near zero slopes. In such cases, the fit is not as close. Even when the energy arrives in one main event, the selected modulating functional form does not necessarily guarantee a perfect match of the evolution of the Husid plot, but only a general match of the overall evolution.

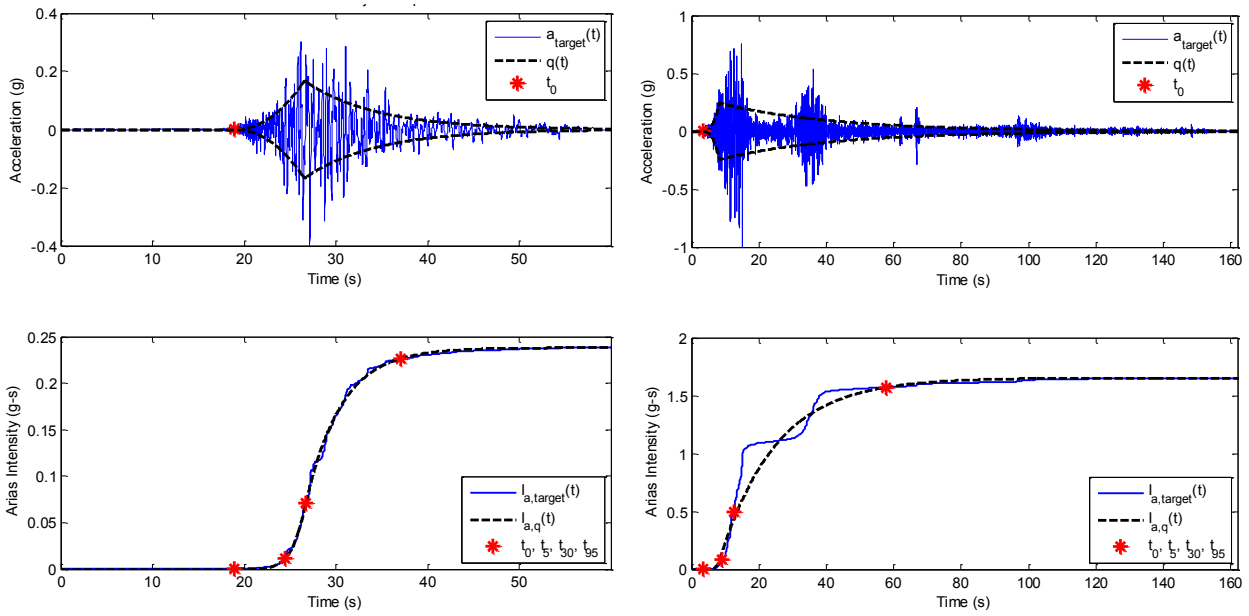

Figure 5.1 Example modulating functions fitted to recorded accelerograms; top: target acceleration time series (blue line) and fitted modulating function (black dashed line); bottom: Husid plots of target acceleration (blue line) and fitted modulating function (black dashed line).

An analogous fitting procedure that uses cumulative absolute velocity (CAV) in place of Arias intensity was briefly investigated. CAV is another measure of ground motion intensity that has been found to be more strongly correlated with damage than Arias intensity (EPRI, 1988; Campbell and Bozorgnia, 2010) and is defined as the integral of the absolute acceleration time series

$$CAV = \int_0^{t_n} |a(t)| dt. \tag{5.23}$$

In this alternate procedure, the time and duration parameters are defined in relation to CAV, e.g., $D_{5-75,CAV}$. Since this method is not pursued in the present study, to simplify the notation, hereafter we drop the subscript I_a. Models based on CAV will be developed in a subsequent study.

5.3.2.2 Fitting the filter parameters

The three parameters (ω_{mid}, ω', ζ_f) of the filter control the evolving predominant frequency and the bandwidth of the broadband acceleration process. Specifically, ω_{mid} defines the predominant frequency in the middle of the ground shaking, ω' defines the rate of change of the predominant frequency with time, assuming the change is linear in time, see (4.10), and ζ_f controls the bandwidth of the process. Following Rezaeian and Der Kiureghian (2010), parameters ω_{mid} and ω' are identified by fitting a second-order polynomial to the cumulative number of zero-level up-crossings of the target recorded acceleration time series. Parameter ω_{mid} is taken as the slope of the fitted polynomial at the middle of the strong shaking, which is defined as the time t_{30} of the 30% cumulative Arias intensity value of the record. Parameter ω' is determined as the second derivative of the fitted polynomial. Following Rezaeian and Der Kiureghian (2010), the bandwidth of the process is measured in terms of the rate of positive minima and negative maxima. With the identified filter frequency parameters ω_{mid} and ω', a set of motions are simulated with varying filter damping ζ_f. The expected cumulative number of positive minima and negative maxima of these simulated motions are compared with the corresponding cumulative curve of the target recorded motion. The filter damping value that has a similar rate (slope of the cumulative curve) is selected as the value of parameter ζ_f. More details about these fitting procedures can be found in Rezaeian and Der Kiureghian (2010).

5.3.3 Pulselike motions: identification of model parameters

In this and the following sections, the fitting procedures described in Sections 5.3.1 and 5.3.2 are illustrated using records from the NGA-West2 database. Throughout this dissertation, records NGA#171 and NGA#351 are used to illustrate the fitting and simulation procedures for pulselike and non-pulselike near-fault ground motions, respectively.

NGA#171 was recorded at the El Centro-Meloland Geotechnical Array station during the 1979 Imperial Valley-06 Earthquake in California. This record was identified as pulselike by Shahi and Baker (2011). The as-recorded components of this record are rotated to the direction of the largest pulse and the corresponding orthogonal direction according to the procedure described in Section 5.2.1. The acceleration, velocity and displacement time series of these rotated components are plotted in Figure 5.2. Figure 5.3 focuses on the component of record NGA#171 containing the largest pulse. In particular, it illustrates how the total motion is decomposed into the pulse and residual motions in the acceleration and velocity domains. In this

figure, $v_{pul}(t)$ is the largest velocity pulse extracted by use of Baker's wavelet method (Baker 2007) and $a_{pul}(t)$ is its derivative. The residual motions $v_{res}(t)$ and $a_{res}(t)$ are obtained by subtracting the extracted pulse motion from the total motion.

5.3.3.1 Identification of parameters of the directivity pulse

For each pulselike ground motion record, the procedure described in Section 5.3.1 is employed to fit (V_p, T_p, γ, ν, $t_{max,p}$) to the largest velocity pulse $v_{pul}(t)$ extracted from the record. Figure 5.4 shows the directivity pulse extracted from record NGA#171 and the fitted idealized mMP pulse. The identified parameters (V_p, T_p, γ, ν, $t_{max,p}$) of the fitted mMP velocity pulse model are listed in Table 5.3. In particular, the period of the fitted mMP pulse is $T_p = 2.8$ s. It can be seen in Figure 5.4 that the fit to the extracted velocity pulse is excellent, and that the fit to the corresponding acceleration and displacement waveforms is also quite good. Note that the fitted displacement waveform has zero displacement at the end of the motion. This would not have been the case had we used the original Mavroeidis and Papageorgiou (2003) pulse model. The adequacy of the fit is also confirmed by comparing the pseudo-acceleration response spectra at 5% damping of the extracted and fitted pulses together with the spectrum of the total recorded motion, see Figure 5.5. The response spectrum of the extracted pulse matches the shape of the response spectrum of the total acceleration at periods longer than about 3 s, which corresponds to the period of the fitted mMP pulse. Furthermore, the response spectrum of the fitted pulse closely matches that of the extracted pulse, especially at periods longer than about 2 s.

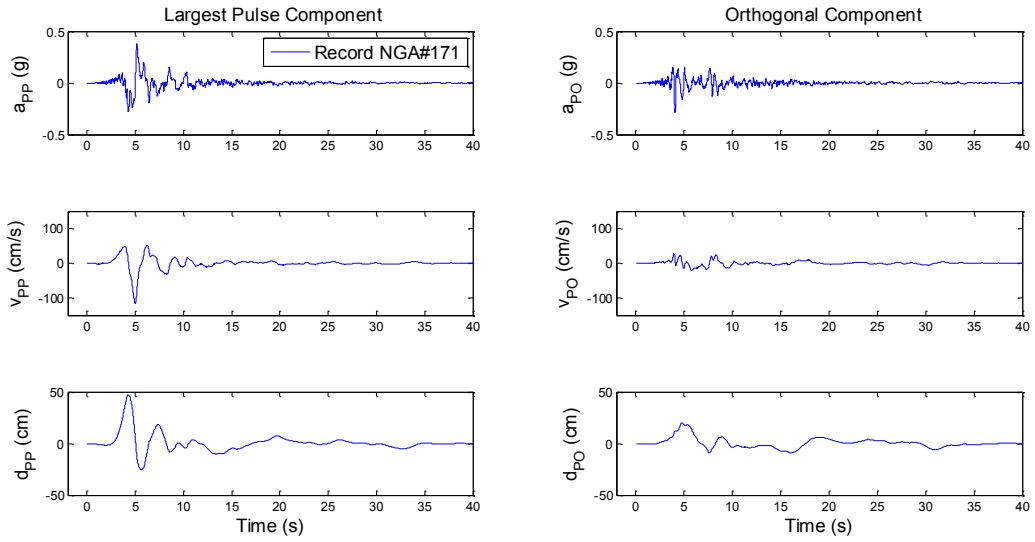

Figure 5.2 Acceleration, velocity and displacement time series of record NGA#171 in the direction of the largest pulse and the corresponding orthogonal direction.

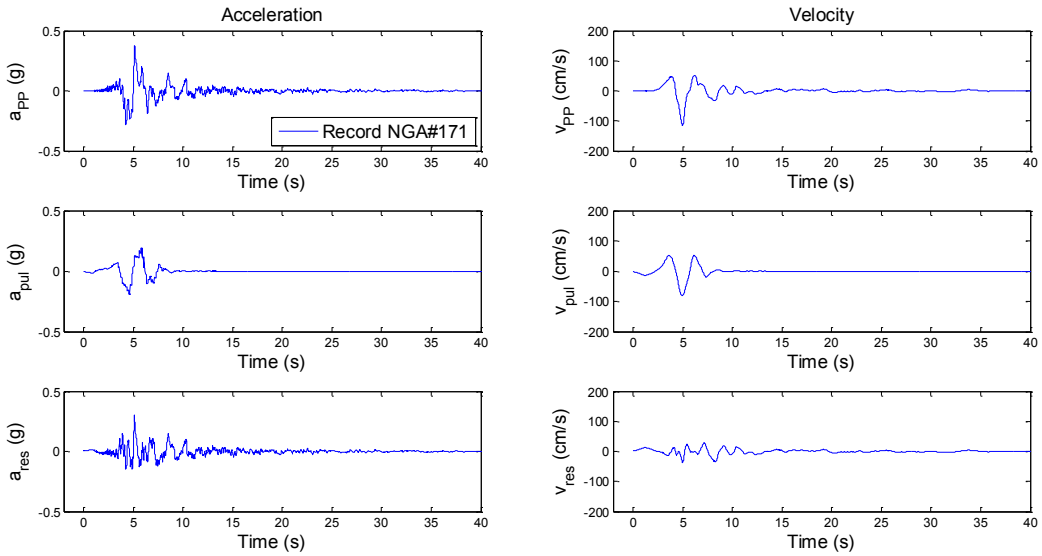

Figure 5.3 Acceleration (left) and velocity (right) time series of total (top), pulse (middle) and residual (bottom) motions in the direction of the largest pulse for record NGA #171.

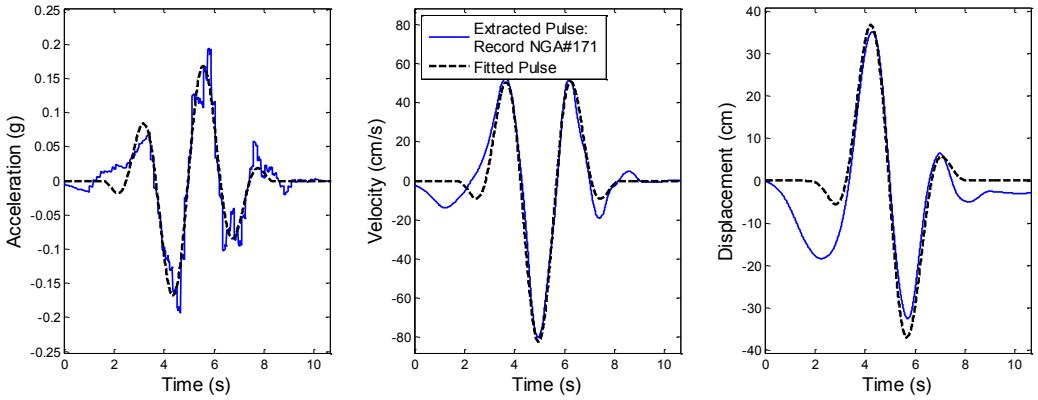

Figure 5.4 Directivity pulse waveforms extracted (blue line) from record NGA#171 in the direction of the largest pulse and fitted mMP pulse (black dashed line): acceleration (left), velocity (center), and displacement (right) time series.

Table 5.3 Identified pulse model parameters for record NGA #171.

	V_p	T_p	γ	ν/π	$t_{max,p}$*	$t_{0,q}$
	cm/s	s		rad	s	s
NGA#171	80.3	2.8	2.4	1.0	3.7	1.3

*$t_{max,p}$ is measured from $t_{0,q}$

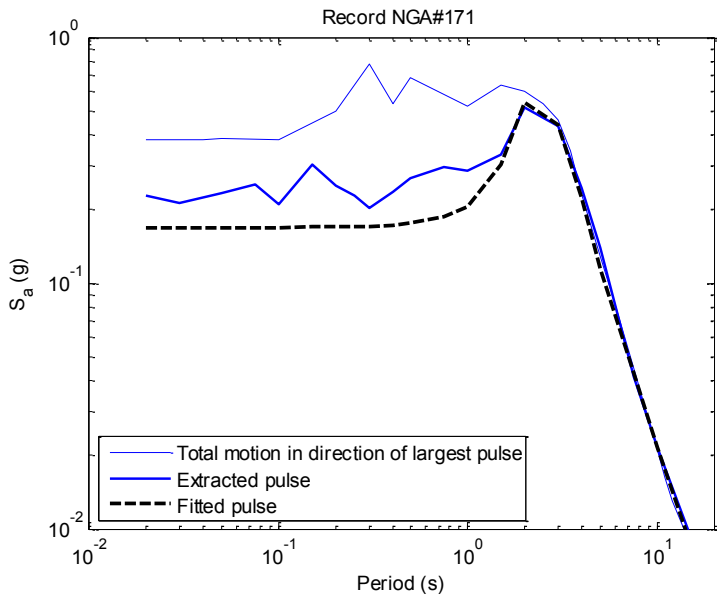

Figure 5.5 Pseudo-acceleration response spectra at 5% damping of recorded motion (thin blue line), extracted pulse (thick blue line) and fitted pulse (black dashed line) for record NGA#171.

5.3.3.2 Identification of modulating function parameters: residual and orthogonal motions

The procedure described in Section 5.3.2 is used to fit the parameters of the modulated and filtered white-noise model of equations (4.7)-(4.12) to the recorded broadband acceleration time series of each pulselike record. We start by illustrating the fitting of the modulating function parameters (α, β, c, $t_{max,q}$) to the residual and orthogonal motions of record NGA#171 by back-calculating them from (I_a, D_{5-95}, D_{0-5}, D_{0-30}). Fitting of the filter parameters is described in the next section. The residual motions that were provided by Shahi and Baker consist of the total ground motions minus the extracted pulse motions. In order to minimize the loss of information from misfits of the pulse, we redefine the residual motion as the total ground motion in the direction of the largest pulse (with $\Delta t = 0.005$ s) minus the fitted mMP pulse motion (defined at discrete time steps of 0.005 s). These redefined residuals then constitute the motions to which the model of the residual motion is fitted.

As described earlier, the selected modulating function is fitted to a target acceleration time series by matching their total Arias intensity I_a, and three selected points on their Arias intensity Husid plots, namely the times $t_{5,}$, t_{30}, and t_{95} of the 5%, 30% and 95% of their normalized cumulative Arias intensity functions. As an example, the acceleration time series of the residual and orthogonal motions of record NGA#171 are shown in the top portion of Figure 5.6 (blue line). First, the cumulative Arias intensity functions $I_{a,res}(t)$ and $I_{a,PO}(t)$ of these motions are computed. They are shown, also with a blue line, in the bottom portion of Figure 5.6. The corresponding total Arias intensity values $I_{a,res}$ and $I_{a,PO}$ are listed in Tables 5.4 and 5.5, respectively. The cumulative Arias intensity functions are then used to identify ($t_{5,res}$, $t_{30,res}$, $t_{95,res}$) and ($t_{5,PO}$, $t_{30,PO}$, $t_{95,PO}$) and to obtain $t_{0,q}$ from (5.9). These time points are indicated by red stars in Figure 5.6. Next, (5.17) and (5.22) are used to calculate ($D_{0-5,res}$, $D_{0-30,res}$, $D_{0-95,res}$, $D_{5-95,res}$) and ($D_{0-5,PO}$, $D_{0-30,PO}$, $D_{0-95,PO}$, $D_{5-95,PO}$), which are listed in

Tables 5.4 and 5.5, respectively. In turn, these values are used in (5.14)-(5.16) and (5.21) to back-calculate (α_{res}, β_{res}, c_{res}, $t_{max,q,res}$) and (α_{PO}, β_{PO}, c_{PO}, $t_{max,q,PO}$), which are listed in Tables 5.6 and 5.7, respectively. The modulating functions calculated using these fitted parameter values are shown in dashed black lines in the top portion of Figure 5.6. Their corresponding cumulative Arias intensity functions are shown in dashed black lines in the bottom portion of Figure 5.6. It can be noted from Figure 5.6 that the residual motion in this example is adequately described by the assumed functional form of the modulating function and that the Husid plot of the fitted modulating function intersects that of the recorded residual acceleration at t_0, t_5, t_{30} and t_{95}. However, it is not always possible to achieve such a good match, as illustrated by the fit to the orthogonal motion, which seems to contain two closely spaced arrivals.

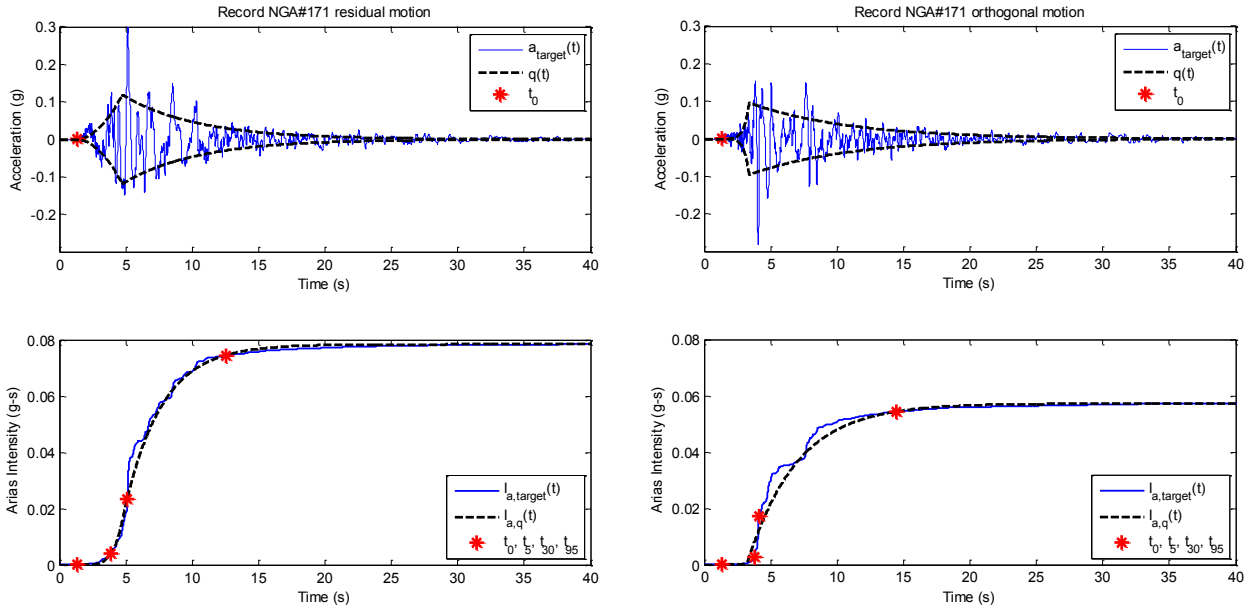

Figure 5.6 Fitting parameters of the modulating function to the recorded residual (left) and orthogonal (right) motions for pulselike record NGA#171: (top) target acceleration time series and fitted modulating function, (bottom) Husid plots of target acceleration and fitted modulating function.

Table 5.4 Identified Arias intensity related parameters for residual motion of record NGA#171.

	$t_{0,q}$	$I_{a,res}$	$D_{5-95,res}$	$D_{0-5,res}$	$D_{0-30,res}$
	s	cm/s	s	s	s
NGA#171	1.3	77	8.6	2.6	3.8

Table 5.5 Identified Arias intensity related parameters for orthogonal motion of record NGA#171.

	$t_{0,q}$	$I_{a,PO}$	$D_{5-95,PO}$	$D_{0-5,PO}$	$D_{0-30,PO}$
	s	cm/s	s	s	s
NGA#171	1.3	56	10.7	2.5	2.8

Table 5.6 Back-calculated modulating function parameters for residual motion of record NGA#171.

	α_{res}	β_{res}	c_{res}	$t_{max,q,res}$
			g	s
NGA#171	1.9	0.18	0.12	4.7

Table 5.7 Back-calculated modulating function parameters for orthogonal motion of record NGA#171.

	α_{PO}	β_{PO}	c_{PO}	$t_{max,q,PO}$
			g	s
NGA#171	5.9	0.13	0.10	3.4

5.3.3.3 Identification of filter parameters: residual and orthogonal motions

The three parameters (ω_{mid}, ω', ζ_f) of the filter are fitted to the residual and orthogonal motions of record NGA#171 using the procedure described in Section 5.3.2.2. The left portion of Figure 5.7 illustrates how parameters ω_{mid} and ω' are obtained by fitting a second-order polynomial to the cumulative number of zero-level up-crossings of the target recorded acceleration time series of the residual (top) and orthogonal (bottom) motions. Note that the lack of fit beyond 25 s is unimportant, because this is the far tail of the record with small intensity. The right portion of Figure 5.7 shows the process of fitting ζ_f by matching the expected cumulative number of positive minima and negative maxima. The identified parameter values for the residual motion are listed in Table 5.14 and those for the orthogonal motion are listed in Table 5.15.

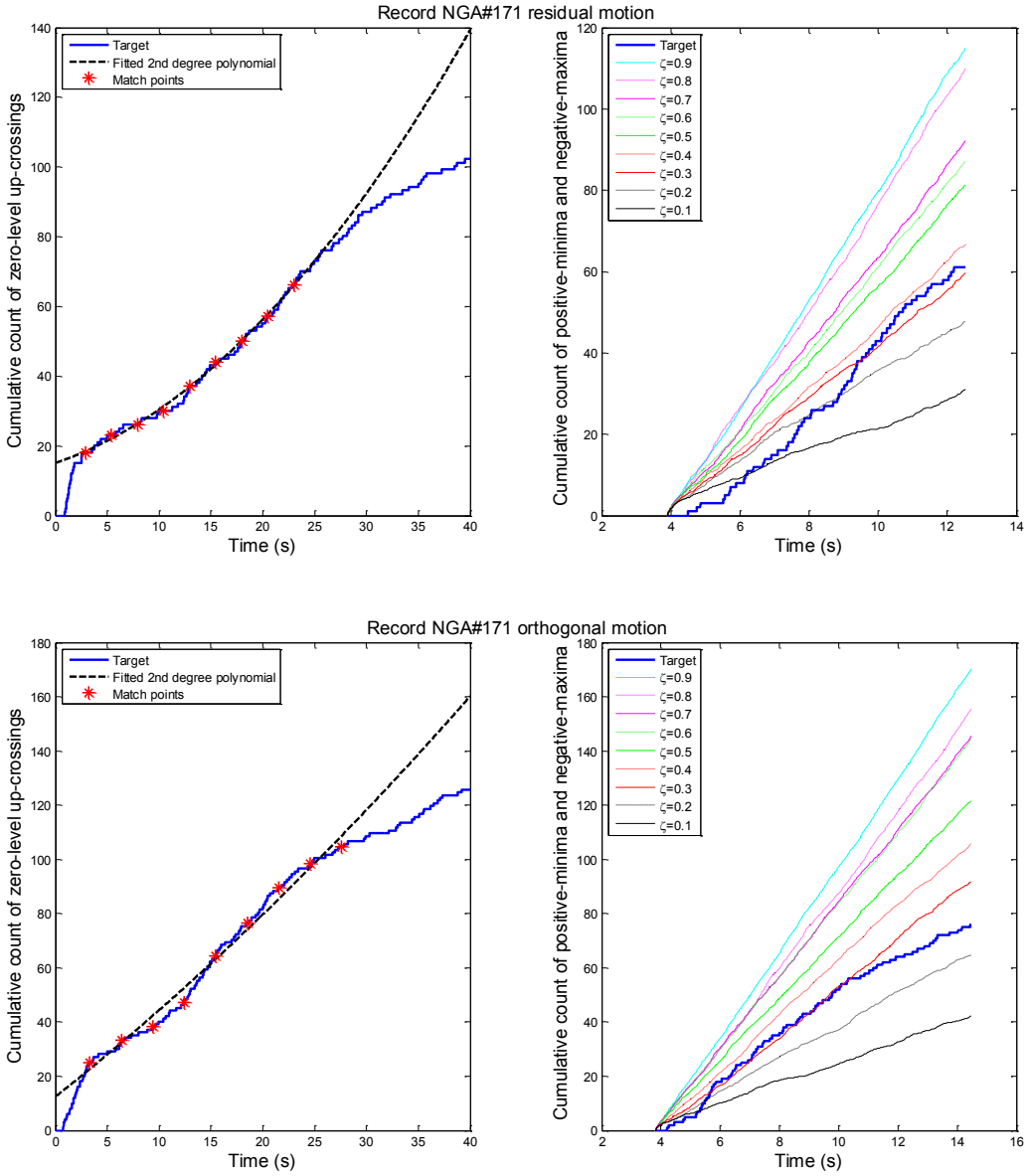

Figure 5.7 Fitting filter parameters to the recorded residual (top) and orthogonal (bottom) motions of record NGA#171: target and fitted cumulative counts of zero-level up-crossings (left) and target and fitted cumulative counts of positive minima and negative maxima (right).

Table 5.8 Identified filter parameters for residual motion of record NGA #171.

	$t_{0,q}$	$D_{0-30,res}$	$\omega_{mid,res}/\pi$	ω'_{res}/π	$\zeta_{f,res}$
	s	s	rad/s	rad/s^2	
NGA#171	1.3	3.8	3.1	0.21	0.27

Table 5.9 Identified filter parameters for orthogonal motion of record NGA #171.

	$t_{0,q}$	$D_{0-30,PO}$	$\omega_{mid,PO}/\pi$	ω'_{PO}/π	$\zeta_{f,PO}$
	s	s	rad	rad/s^2	
NGA#171	1.3	2.8	6.3	0.07	0.27

5.3.4 Non-pulselike motions: identification of model parameters

For each non-pulselike near-fault ground motion record, the procedure described in Section 5.3.2 is used to fit the parameters of the modulated and filtered white-noise model of equations (4.7)-(4.12) to the two horizontal "principal" components. Here, we use record NGA #351 to illustrate the procedure of fitting the parameters ($I_{a,NP1}$, $D_{5-95,NP1}$, $D_{0-5,NP1}$, $D_{0-30,NP1}$, $\omega_{mid,NP1}$, ω'_{NP1}, $\zeta_{f,NP1}$) and ($I_{a,NP2}$, $D_{5-95,NP2}$, $D_{0-5,NP2}$, $D_{0-30,NP2}$, $\omega_{mid,NP2}$, ω'_{NP2}, $\zeta_{f,NP2}$) to the recorded motions.

NGA #351 was recorded at the Parkfield-Gold Hill 3E Station during the 1983 Coalinga-01 earthquake in California and was identified as non-pulselike by Shahi and Baker (2011). The as-recorded ground motion components of this record are rotated to the major and intermediate "principal directions" according to the procedure described in Section 5.2.2. The acceleration, velocity and displacement time series of the major and intermediate ground motion components are plotted in Figure 5.8. Procedures identical to those described in Sections 5.3.3.2 and 5.3.3.3 are employed to fit the modulating function and filter parameters. We do not repeat the details of the discussion and only report the results in a similar fashion in Figures 5.9 and 5.10 and in Tables 5.10-5.15.

The acceleration time series of the major and intermediate components of record NGA#351 are shown in the top portion of Figure 5.9 (blue line). Their cumulative Arias intensity time series $I_{a,NP1}(t)$ and $I_{a,NP2}(t)$ are shown, also with a blue line, in the bottom portion of Figure 5.9. As per our definition, it can be observed in Figure 5.9 that the total Arias intensity of the major component is larger than that of the intermediate component. The values of ($I_{a,NP1}$, $D_{5-95,NP1}$, $D_{0-5,NP1}$, $D_{0-30,NP1}$) and ($I_{a,NP2}$, $D_{5-95,NP2}$, $D_{0-5,NP2}$, $D_{0-30,NP2}$) are listed in Tables 5.10 and 5.11, respectively, and the back-calculated modulating function parameters (α_{NP1}, β_{NP1}, c_{NP1}, $t_{max,q,NP1}$) and (α_{NP2}, β_{NP2}, c_{NP2}, $t_{max,q,NP2}$) are listed in Tables 5.12 and 5.13, respectively. The modulating functions calculated using these fitted parameter values are shown as dashed black lines in the top portion of Figure 5.9. Their corresponding cumulative Arias intensity time series are shown in dashed black lines in the bottom portion of Figure 5.9. The left portion of Figure 5.10 illustrates how parameters ω_{mid} and ω' are obtained by fitting a second-order polynomial to the cumulative number of zero-level up-crossings of the target recorded acceleration time series of the major (top) and intermediate (bottom) ground motion components. The right portion of Figure 5.10 shows the process of fitting ζ_f by matching the expected cumulative number of positive minima and negative maxima. The identified parameter values for the major component are listed in Table 5.14 and those for the intermediate component are listed in Table 5.15.

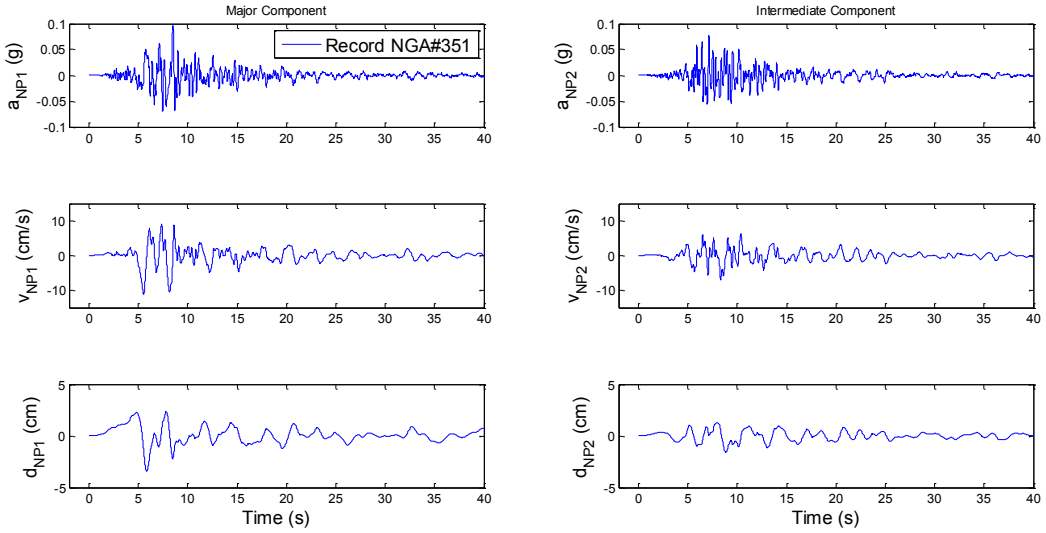

Figure 5.8 Acceleration, velocity and displacement time series of record NGA#351 in the major and intermediate "principal directions".

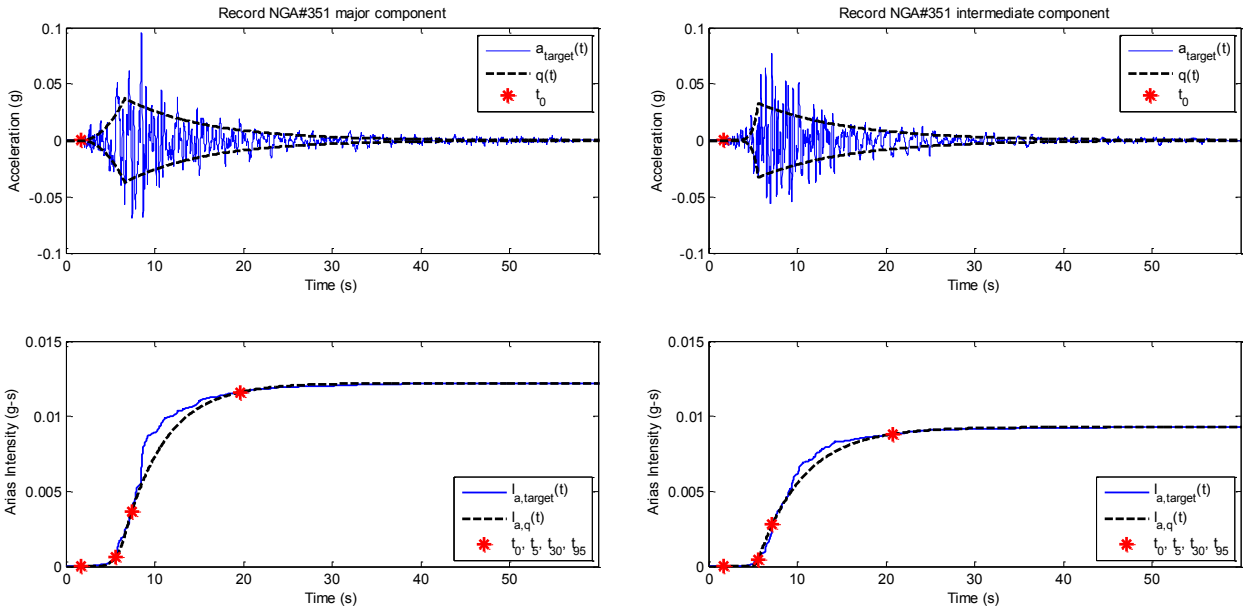

Figure 5.9 Fitting parameters of the modulating function to the recorded major and intermediate ground motion components of non-pulselike record NGA#351: (a) target acceleration time series and fitted modulating function, (b) Husid plots of target acceleration and fitted modulating function.

Table 5.10 Identified Arias intensity related parameters for major component of record NGA#351.

	$t_{0,q}$	$I_{a,NP1}$	$D_{5-95,NP1}$	$D_{0-5,NP1}$	$D_{0-30,NP1}$
	s	cm/s	s	s	s
NGA#351	1.7	12	14.0	3.9	5.7

Table 5.11 Identified Arias intensity related parameters for intermediate component of record NGA#351.

	$t_{0,q}$	$I_{a,NP2}$	$D_{5-95,NP2}$	$D_{0-5,NP2}$	$D_{0-30,NP2}$
	s	cm/s	S	s	s
NGA#351	1.7	9	15.2	3.9	5.5

Table 5.12 Back-calculated modulating function parameters for major component of record NGA#351.

	α_{NP1}	β_{NP1}	c_{NP1}	$t_{max,q,NP1}$
			g	s
NGA#351	2.1	0.11	0.037	6.6

Table 5.13 Back-calculated modulating function parameters for intermediate component of record NGA#351.

	α_{NP2}	β_{NP2}	c_{NP2}	$t_{max,q,NP2}$
			g	s
NGA#351	6.8	0.10	0.033	5.6

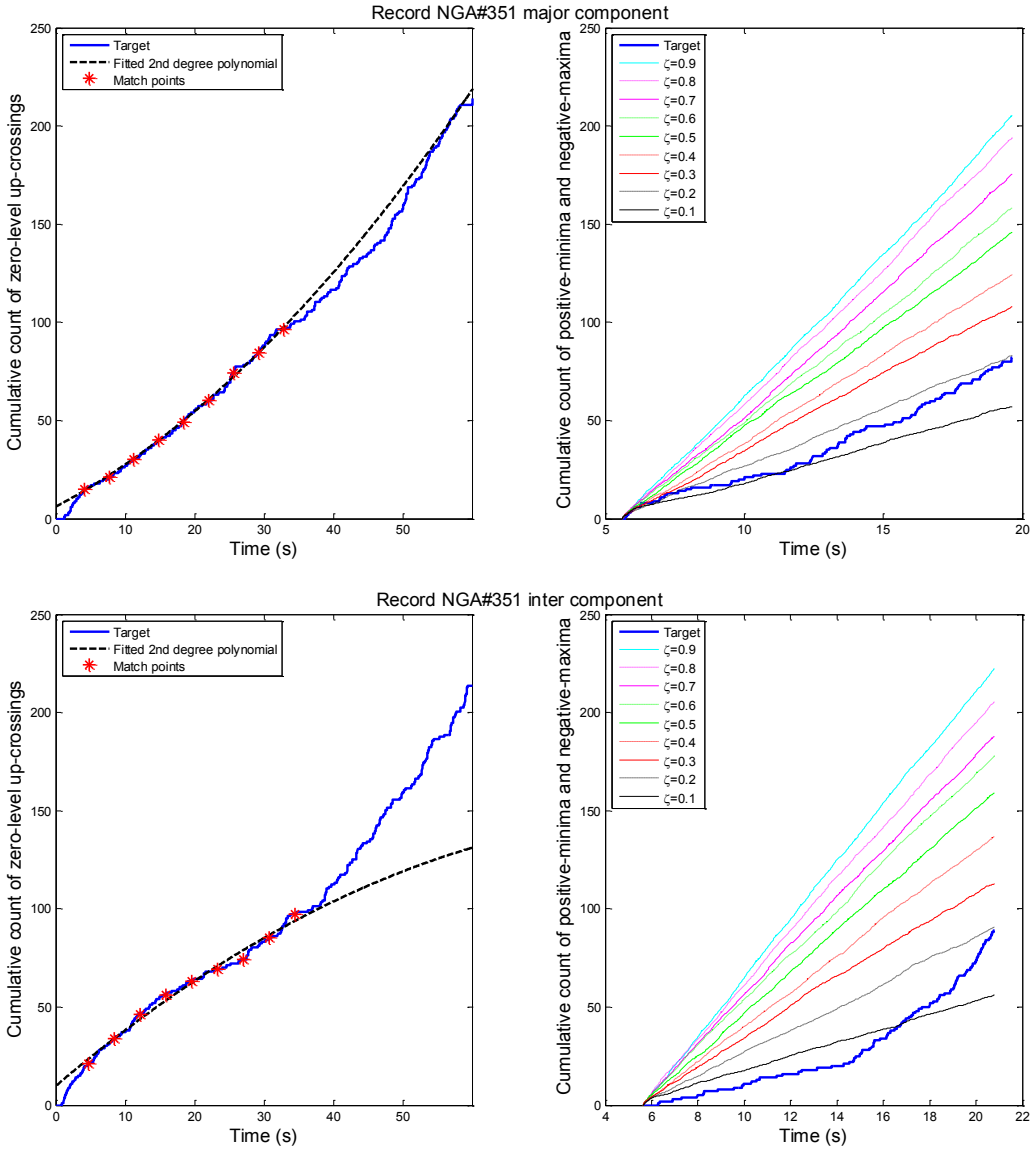

Figure 5.10 Fitting filter parameters to the major (top) and intermediate (bottom) ground motion components of record NGA#351: target and fitted cumulative counts of zero-level up-crossings (left) and target and fitted cumulative counts of positive minima and negative maxima (right).

Table 5.14 Identified filter parameters for major component of record NGA#351.

	$t_{0,q}$	$D_{0-30,NP1}$	$\omega_{mid,NP1}/\pi$	ω'_{NP1}/π	$\zeta_{f,NP1}$
	s	s	rad/s	rad/s^2	
NGA#351	1.7	5.7	4.6	0.11	0.17

Table 5.15 Identified filter parameters for intermediate component of record NGA#351.

	$t_{0,q}$	$D_{0-30,NP2}$	$\omega_{mid,NP2}/\pi$	ω'_{NP2}/π	$\zeta_{f,NP2}$
	s	s	rad/s	rad/s^2	
NGA#351	1.7	5.5	5.5	-0.07	0.09

5.4 EMPIRICAL PREDICTIVE EQUATIONS FOR MODEL PARAMETERS

5.4.1 Introduction

Our aim is to generate synthetic ground motions for a specified earthquake design scenario. For this purpose, it is necessary to develop predictive equations for the model parameters in terms of earthquake and site characteristics that are normally available to the design engineer. We accomplish this by regressing the sample of fitted parameters against the explanatory variables (F, $\mathbf{M}$, Z_{TOR}, R_{RUP}, V_{s30}, $s_{or}d$) describing the earthquake source and site characteristics.

5.4.2 Selected explanatory variables

Ground motion characteristics are generally modeled and predicted in terms of variables that describe the earthquake and site characteristics, specifically the source, the path and the site. In Chapter 2, some of the explanatory variables used in GMPEs to model intensity, frequency and duration parameters were introduced. In the current study, to avoid overfitting of the limited dataset, we only include a subset of these explanatory variables.

The earthquake source and site characteristics that are considered as explanatory variables in this study are the type of faulting F ($= 0$ strike-slip faults, $= 1$ reverse and reverse-oblique faults), the moment magnitude $\mathbf{M}$, the depth Z_{TOR} in kilometers to the top of the rupture plane, the closest distance R_{RUP} in kilometers from the site to the fault rupture, the shear-wave velocity V_{s30} of the top 30m of soil at the site, and directivity parameters s (or d) in kilometers and θ (or ϕ) in degrees. The ranges of these parameters were listed in Tables 5.1 and 5.2 for the pulselike and non-pulselike databases, respectively. Variables F, $\mathbf{M}$ and Z_{TOR} represent the source, R_{RUP} the path, and V_{s30} the local site conditions. Moreover, since ground motions are more variable and complex in the near-fault region, the additional parameters s (or d) and θ (or ϕ) are needed to represent near-fault directivity effects by describing the source-to-site geometry. These directivity parameters were defined in Chapter 2.

Generally, parameters s and θ are used to represent directivity for strike-slip faulting, while d and ϕ are used for reverse, normal and oblique faulting (Somerville et al., 1997). Here, we represent the directivity parameters as the larger of s and d (we denote it $s_{or}d$) and the corresponding angle θ or ϕ (we denote it $\theta_{or}\phi$). This parameterization provides a better representation for reverse-oblique faults, which are a combination of reverse and strike-slip faulting. As expected, $s_{or}d = s$ and $\theta_{or}\phi = \theta$ for most but not all strike-slip cases in our database. Similarly, $s_{or}d = d$ and $\theta_{or}\phi = \phi$ for most but not all reverse cases.

In our analysis, we found the directivity parameter $\theta_{or}\phi$ not to be a good predictor of the model parameters. Somerville et al. (1997) explored terms of the form $X\cos\theta$ and $Y\cos\phi$ in

their models. These forms, by using the normalized versions X and Y of the rupture length s and width d from the hypocenter to the site, problematically overlook the scaling of directivity with magnitude or size of rupture (see, e.g., Spudich et al., 2013, 2014). We overcome this problem by replacing X and Y by the actual rupture length s and width d and investigate using the term $(s_{or}d)\cos(\theta_{or}\phi)$ as an explanatory variable. However, we find this form not to be a good predictor of the model parameters either. Thus in the end, only $s_{or}d$ is used to represent the directivity effect in the regression analysis. However, both parameters $s_{or}d$ and $\theta_{or}\phi$ are required in predicting the probability of a ground motion containing a pulse.

In summary, the selected explanatory variables used are F, $\mathbf{M}$, Z_{TOR}, R_{RUP}, V_{s30}, and directivity parameter $s_{or}d$. The directivity explanatory variable $s_{or}d$ is only considered in the predictive relations for the pulse parameters. Generally, only variables having significant explanatory power are retained in the predictive equations. These are identified as those having regression coefficients with only positive or only negative 95% confidence intervals, and those with confidence intervals strongly skewed to either the positive or negative direction.

5.4.3 Regression analysis and empirical predictive equations

The model parameters are classified into four categories: (1) intensity parameters (V_p and I_a), (2) period and frequency parameters (T_p and ω_{mid}), (3) time and duration parameters ($t_{max,p}$, D_{0-5}, D_{0-30}, and D_{5-95}) and (4) "other" parameters (γ, ν, ω', and ζ_f). We start by transforming all the model parameters to the normal space to satisfy the normality assumption in the subsequent development of regression models. The transformed pulselike and non-pulselike model parameters are denoted $z_{P,i}$, $i = 1, \ldots, 19$, and $z_{NP,i}$, $i = 1, \ldots, 14$, respectively. The transformed data are regressed against the variables (F, $\mathbf{M}$, Z_{TOR}, R_{RUP}, V_{s30}, $s_{or}d$) defining the earthquake source and site characteristics. We use linear predictive (or regression) equations to avoid the more difficult task of non-linear regression analysis. Moreover, due to the limited size of the databases, we employ rather simple equations that are defined in terms of a limited number of explanatory variables. As previously mentioned, the pulselike database consists of 130 records from 27 earthquakes, each contributing 1 or more records, with the highest being 32 records for the Chi-Chi earthquake. The non-pulselike database consists of 311 records from 44 earthquakes, each contributing 1 or more records, with the highest being 37 records for the Chi-Chi earthquake. Random effects regression is used to properly account for the statistical dependence of multiple observations from the same earthquake and to prevent earthquakes with large numbers of records from biasing the results. The total regression error is subdivided into an inter-event term (or residual) η_i and an intra-event term (residual) ϵ_i, where subscript i denotes the model parameter of interest. These error terms are assumed to be independent, normally distributed random variables with zero means and variances τ_i^2 and ϕ_i^2, respectively (Brillinger and Preisler, 1985; Abrahamson and Youngs, 1992). The variance of the total regression error $(\eta_i + \epsilon_i)$ is then given by

$$\sigma_{T,i}{}^2 = \tau_i^2 + \phi_i^2. \tag{5.24}$$

The regression formula for each transformed pulselike model parameter has the form

$$z_{P,i} = g_{P,i}(F, \mathbf{M}, Z_{TOR}, R_{RUP}, V_{s30}, s_{or}d) + \eta_{P,i} + \epsilon_{P,i} \quad i = 1, \ldots, 19, \tag{5.25}$$

where

$$g_{P,i}(\cdot) = \mathrm{E}[z_{P,i}] = \sum_j \beta_{P,ij} X_{P,j}(\cdot) \tag{5.26}$$

are the linear predictive equations for the pulselike model parameters. In these equations, $X_{P,j}(\cdot)$ are the selected explanatory terms and $\beta_{P,ij}$ are the corresponding regression coefficients to be estimated. Similarly, for the transformed non-pulselike model parameters,

$$z_{NP,i} = g_{NP,i}(F, \mathbf{M}, Z_{TOR}, R_{RUP}, V_{s30}, s_{or}d) + \eta_{NP,i} + \epsilon_{NP,i} \quad i = 1, \ldots, 14, \tag{5.27}$$

where

$$g_{NP,i}(\cdot) = \mathrm{E}[z_{NP,i}] = \sum_j \beta_{NP,ij} X_{NP,j}(\cdot) \tag{5.28}$$

are the linear predictive equations for the non-pulselike model parameters. In these equations, $X_{NP,j}(\cdot)$ are the selected explanatory terms and $\beta_{NP,ij}$ are the corresponding regression coefficients to be estimated. The regression coefficients $\beta_{P,ij}$ and $\beta_{NP,ij}$ are solved for numerically following the method used in Rezaeian and Der Kiureghian (2010).

As mentioned earlier, the directivity variables are only considered in the predictive relations for the pulse parameters; the parameters of the non-pulselike model are not regressed against the directivity variable $s_{or}d$. However, to unify the notation of the predictive equations of pulselike and non-pulselike parameters, we include $s_{or}d$ in (5.27) and use the same regression terms X_j in (5.26) and (5.28) but set $\beta_{NP,ij} = 0$ when $X_j = X_j(s_{or}d)$.

To the greatest extent possible, we want the functional forms of the predictive equations (i.e., regression terms X_j) to be consistent with seismological theory, particularly in terms of scaling with magnitude and distance. For each model parameter, this is achieved by adopting and adapting the functional form of an existing GMPE that was derived, for a similar ground motion parameter, based on seismological principles (see Chapter 3). However, the regression coefficients $\beta_{P,ij}$ and $\beta_{NP,ij}$ are determined empirically from the data of this study using regression analysis with random effects. In some cases, the data does not support the use of the random effects regression model. In these cases, regular regression analysis is used. We use the statistical F-test to evaluate whether τ_i is statistically different from zero, i.e., whether the random effect should be included or not. If the F-test is passed with at least 82% confidence, we include the random effect. In most cases where the random effect is included, the F-test is passed with greater than 95% confidence.

Not all terms that are considered at the initial stage (based on existing GMPEs) are included in our final versions of the predictive equations. Simplified forms are used whenever the added complexity is not justified by the data. In fact, the simplest model that also minimizes the variability of the error terms is preferred over more complex models. Only terms having at least some explanatory power are ultimately retained in the predictive equations. Generally, a regression term is eliminated if the estimated value of its coefficient is negligible, if the 95% confidence interval of the estimated value includes zero, or if including the term does not decrease the total standard deviation of the resulting error terms.

In a few cases, we do not strictly adhere to these guidelines. For example, it is sometimes desirable to include a term for comparison with existing GMPEs or with the predictive equation of another model parameter. Also, if the 95% confidence interval of the estimated regression coefficient is strongly skewed towards positive or negative values, we may opt to keep the corresponding regression term. Similarly, despite confidence levels below 10% in the random effect for some of the model parameters (namely, $I_{a,PO}$, $\omega_{mid,res}$, $\omega_{mid,PO}$, $D_{5-95,NP1}$ and $D_{5-95,NP2}$), the random effect is included because it is found to be significant in similar parameters (e.g., $I_{a,res}$, $\omega_{mid,NP1}$, and $D_{5-95,PO}$).

As mentioned earlier, we follow the method used in Rezaeian and Der Kiureghian (2010) to estimate the regression coefficients $\beta_{P,ij}$ and $\beta_{NP,ij}$ and their 95% confidence intervals. In addition, we are interested in ranking the relative importance of the contribution of each explanatory term to the overall prediction. For this purpose, we define the importance factor,

$$IF_{ij} = \frac{\hat{\beta}_{ij}\bar{X}_j}{\sqrt{\sum_j \left(\hat{\beta}_{ij}\bar{X}_j\right)^2}} \tag{5.29}$$

where $\hat{\beta}_{ij}$ are the estimated regression coefficients and $\bar{X}_j$ is the mean value of regression term X_j in the data. For a given model parameter z_i, if the importance factor IF_{ij} of term X_j is small relative to other terms, we can neglect X_j to simplify the predictive equation of z_i and then re-run the regression analysis. After selecting the final regression equation, the normality assumption is checked by examining the regression residuals. We also use a variant of cross-validation (see, e.g., Camstra and Boomsma, 1992) to ensure that the selected models do not over-fit the data; we randomly remove 10% of the data points for each model parameter and we re-run the regressions. Robustness of our regression formula is confirmed if our estimated parameter values change only slightly.

In the following four sections, one for each category of model parameters, we discuss the transformation of the model parameters to the normal space, the selection of the form of the regression equations (i.e., of regression terms X_j), and the final results of the regression analysis.

5.4.3.1 Intensity parameters

Intensity measures can be reasonably assumed to follow a lognormal distribution (see, e.g., Abrahamson 1998, Jayaram and Baker, 2008). Thus, we normalize model parameters V_p and I_a by taking their natural logarithms,

$$z_{P,i} = \ln \alpha_{P,i} \quad i = 1,6,13 \tag{5.30}$$

and

$$z_{NP,i} = \ln \alpha_{NP,i} \quad i = 1,8. \tag{5.31}$$

where $\alpha_{P,1} = V_p$, $\alpha_{P,6} = I_{a,res}$, $\alpha_{P,13} = I_{a,PO}$, $\alpha_{NP,1} = I_{a,NP1}$ and $\alpha_{NP,8} = I_{a,NP2}$. The initial and general predictive equation that we adopt for these intensity parameters is motivated by the functional form of the GMPE developed by Campbell and Bozorgnia (2007, 2008, 2010, and 2012) to predict PGA, PGV, PSA, Arias intensity, and CAV as part of the NGA-West project. This GMPE is an earlier and simpler version of the NGA-West2 GMPE presented in Chapter 2

(Campbell and Bozorgnia, 2013, 2014). The NGA-West version of the Campbell and Bozorgnia GMPE (2007, 2008) predicts the mean $\mu_{ln\,IM}$ of the natural logarithm of an intensity measure of interest as the sum of six terms representing the source, path and site effects:

$$\mu_{\ln IM}(\mathbf{M}, R_{RUP}, V_{s30}, \dots) = f_{mag} + f_{flt} + f_{dis} + f_{hng} + f_{site} + f_{dir} + f_{sed}. \tag{5.32}$$

Because of the limited size of our dataset, we simplify the model by neglecting the hanging-wall term, f_{hng}, and the basin response term, f_{sed}, and, for the pulselike model parameters, we add a directivity term, f_{dir}. Thus, we model the expected value of a transformed intensity parameter, z_{IM}, as

$$\mathrm{E}[z_{IM}] = f_{mag} + f_{flt} + f_{dis} + f_{site} + f_{dir}. \tag{5.33}$$

where each term is described below.

The source is represented by the magnitude term, which includes a break in the magnitude scaling at $\mathbf{M} = 6.5$ and is given by

$$\begin{aligned} f_{mag} &= \beta_0 + \beta_1\mathbf{M} && 5.5 < \mathbf{M} \leq 6.5 \\ &= \beta_0 + \beta_1\mathbf{M} + \beta_2(\mathbf{M} - 6.5) && 6.5 < \mathbf{M}. \end{aligned} \tag{5.34}$$

We rewrite this as

$$f_{mag} = \beta_0 + \beta_1\mathbf{M} + \beta_2(\mathbf{M} - 6.5)\mathbb{I}(\mathbf{M} > 6.5), \tag{5.35}$$

where $\mathbb{I}(\cdot)$ is the indicator function. The other source term is the style-of-faulting given by

$$f_{flt} = \beta_3 F f_{flt,Z}, \tag{5.36}$$

where

$$\begin{aligned} f_{flt,Z} &= Z_{TOR} && Z_{TOR} < 1 \\ &= 1 && Z_{TOR} \geq 1 \end{aligned} \tag{5.37}$$

The path is represented by the geometric attenuation term

$$f_{dis} = (\beta_4 + \beta_5\mathbf{M}) \ln\left(\sqrt{R_{RUP}^2 + h^2}\right), \tag{5.38}$$

where h is the effective focal depth. In order to avoid nonlinearity in the regression equation, we constrain h to 6 km before performing regression analysis. The site is represented by the shallow site response term

$$f_{site} = \beta_6 \ln \hat{V}_{s30}, \tag{5.39}$$

where

$$\hat{V}_{s30} = \min(V_{s30}, 1100 \text{ m/s}). \tag{5.40}$$

Lastly, the directivity term, which describes the source and path, is given by

$$f_{dir} = \beta_7 s_{or} d \tag{5.41}$$

In summary, we get

$$\mathrm{E}[z_{P,i}] = \sum_{j=0}^{7} \beta_{P,ij} X_j, \tag{5.42}$$

and

$$\mathrm{E}[z_{NP,i}] = \sum_{j=0}^{7} \beta_{NP,ij} X_j, \tag{5.43}$$

where the regression terms X_j are defined in Table 5.16. In the regressions for non-pulselike model parameters, we set $\beta_{NP,i7} = 0$.

Table 5.16 Definition of the regression terms X_j for the predictive equations ($h = 6$ is used throughout).

j	X_j
0	1
1	$\mathbf{M}$
2	$(\mathbf{M} - 6.5)\mathbb{I}(\mathbf{M} > 6.5)$
3	$F.f_{flt,Z}$
4	$\ln\left(\sqrt{R_{RUP}^2 + h^2}\right)$
5	$\mathbf{M}\ln\left(\sqrt{R_{RUP}^2 + h^2}\right)$
6	$\ln \hat{V}_{s30}$
7	$s_{or} d$

After exploring with multiple combinations of the regression terms, the forms listed in Tables 5.17 and 5.18 are finally selected. We use a dash to indicate that a regression term is not included in the final regression form. Table 5.17 lists the estimates of the regression coefficients and the standard deviations of the regression errors for the intensity parameters of the pulselike model. The estimated standard deviations τ_i and ϕ_i of the inter- and intra-event error terms are listed in Table 5.17, along with standard deviation $\sigma_{T,i}$ of the total error. The initial sample

standard deviation $\sigma_{0,i}$ of the data is also given for reference. Table 5.18 lists these same estimates for parameters of the non-pulselike model. A large decrease in standard deviation from $\sigma_{0,i}$ to $\sigma_{T,i}$ indicates that the selected regression equation has a significant explanatory power. As mentioned earlier, we set τ_i to zero and neglect the random effect whenever it is statistically insignificant.

For the intensity parameters of the pulselike model, Table 5.19 lists the lower (LB) and upper (UB) bounds of the 95% confidence intervals of the estimates of the regression coefficients as well as the importance factor IF of each predictive term. Table 5.20 lists the same for parameters of the non-pulselike model.

The trends observed in Tables 5.17 and 5.18 between the measures of the ground motion intensity (i.e., V_p, $I_{a,res}$, $I_{a,PO}$, $I_{a,NP1}$ and $I_{a,NP2}$) and the earthquake source and site characteristics make sense overall. They are generally as expected based on seismological principles and existing GMPEs. The results show that intensity measures are positively related to **M** ($\beta_1 > 0$), inversely related to R_{RUP} ($\beta_4 < 0$), and tend to be larger for buried reverse fault ruptures ($\beta_3 > 0$). A relation with site stiffness is not found for $I_{a,res}$ nor $I_{a,PO}$. The other intensity measures increase with increasing site stiffness ($\beta_6 > 0$). In accordance with the directivity effect, V_p is also positively related to $s_{or}d$, the length or width of the rupture ($\beta_7 > 0$).

In the predictive relation for the amplitude V_p of the forward directivity pulse, the constraint $\beta_2 = -\beta_1$ is imposed to prevent oversaturation, i.e., decrease in velocity pulse amplitude with increasing magnitude. Moreover, the random effect is not found to be statistically significant and is ignored. This finding indicates that the amplitudes of velocity pulses arising from the same event but observed at different sites are not strongly correlated and only depend on the individual source and site characteristics.

By examining the importance factors IF in Tables 5.19 and 5.20 (and similar results in the following sections), we observe that coefficient β_3, which relates to the type of faulting, makes little contribution to the overall predictive equation. However, it is retained here for comparison with existing GMPEs. Similarly, coefficient β_2 makes relatively little contribution to predictive equations of Arias intensity, but is retained to ensure the break in magnitude scaling and for comparison with existing GMPEs. Terms related to magnitude and distance scaling tend to be the most important for many of the parameters of our model.

Table 5.17 Estimates of regression coefficients and error standard deviations for intensity parameters of pulselike model ($z_{P,i}$).

i	$\alpha_{P,i}$	$\hat{\beta}_{P,i0}$	$\hat{\beta}_{P,i1}$	$\hat{\beta}_{P,i2}$	$\hat{\beta}_{P,i3}$	$\hat{\beta}_{P,i4}$	$\hat{\beta}_{P,i5}$	$\hat{\beta}_{P,i6}$	$\hat{\beta}_{P,i7}$	$\hat{\sigma}_{0,i}$	$\hat{\phi}_i$	$\hat{\tau}_i$	$\hat{\sigma}_{T,i}$
1	V_p	1.699	0.608	−0.608	0.183	−0.576	–	−0.094	0.007	0.463	0.385	0	0.385
6	$I_{a,res}$	−2.116	1.474	−1.378	0.337	−1.073	–	–	–	0.904	0.592	0.510	0.781
13	$I_{a,PO}$	−0.263	1.131	−1.170	0.404	−1.652	0.105	–	–	0.884	0.669	0.331	0.747

Table 5.18 Estimates of regression coefficients and error standard deviations for intensity parameters of non-pulselike model ($z_{NP,i}$).

i	$\alpha_{NP,i}$	$\hat{\beta}_{NP,i0}$	$\hat{\beta}_{NP,i1}$	$\hat{\beta}_{NP,i2}$	$\hat{\beta}_{NP,i3}$	$\hat{\beta}_{NP,i4}$	$\hat{\beta}_{NP,i5}$	$\hat{\beta}_{NP,i6}$	$\hat{\beta}_{NP,i7}$	$\hat{\sigma}_{0,i}$	$\hat{\phi}_i$	$\hat{\tau}_i$	$\hat{\sigma}_{T,i}$
1	$I_{a,NP1}$	8.097	1.006	−1.393	0.435	−4.859	0.473	−0.863	–	1.432	0.903	0.541	1.053
8	$I_{a,NP2}$	7.307	0.999	−1.331	0.443	−4.953	0.491	−0.835	–	1.418	0.819	0.622	1.028

Table 5.19 95% confidence intervals and relative contribution of regression coefficients for intensity parameters of pulselike model ($z_{P,i}$).

i	$\alpha_{P,i}$	$\beta_{P,ij}$	$\hat{\beta}_{P,i0}$	$\hat{\beta}_{P,i1}$	$\hat{\beta}_{P,i2}$	$\hat{\beta}_{P,i3}$	$\hat{\beta}_{P,i4}$	$\hat{\beta}_{P,i5}$	$\hat{\beta}_{P,i6}$	$\hat{\beta}_{P,i7}$
		LB	−1.003	0.223	−0.223	−0.005	−0.748	–	−0.251	0.001
1	V_p	UB	4.400	0.993	−0.993	0.371	−0.404	–	0.063	0.012
		IF	0.286	0.655	−0.655	0.007	−0.223	–	−0.093	0.029
		LB	−6.988	0.684	−2.419	−0.021	−1.397	–	–	–
6	$I_{a,res}$	UB	2.537	2.264	−0.337	0.694	−0.749	–	–	–
		IF	−0.197	0.951	−0.066	0.007	−0.231		–	–
		LB	−12.803	−0.327	−2.204	0.050	−6.083	−0.510	–	–
13	$I_{a,PO}$	UB	7.213	2.588	−0.135	0.758	2.779	0.720	–	–
		IF	−0.030	0.880	−0.067	0.010	−0.429	0.189	–	–

Table 5.20 95% confidence intervals and relative contribution of regression coefficients for intensity parameters of non-pulselike model ($z_{NP,i}$).

i	$\alpha_{NP,i}$	$\beta_{NP,ij}$	$\hat{\beta}_{NP,i0}$	$\hat{\beta}_{NP,i1}$	$\hat{\beta}_{NP,i2}$	$\hat{\beta}_{NP,i3}$	$\hat{\beta}_{NP,i4}$	$\hat{\beta}_{NP,i5}$	$\hat{\beta}_{NP,i6}$	$\hat{\beta}_{NP,i7}$
		LB	−0.250	−0.288	−2.277	0.157	−7.677	0.054	−1.338	–
1	$I_{a,NP1}$	UB	17.153	2.300	−0.510	0.712	−2.040	0.892	−0.387	–
		IF	0.401	0.332	−0.023	0.010	−0.681	0.441	−0.265	–
		LB	0.998	−0.241	−2.177	0.176	−7.655	0.089	−1.291	–
8	$I_{a,NP2}$	UB	17.550	2.239	−0.485	0.709	−2.252	0.892	−0.380	–
		IF	0.362	0.330	−0.022	0.010	−0.695	0.458	−0.257	–

5.4.3.2 Period and frequency parameters

Parameters T_p and ω_{mid} describe the period of the pulse and the predominant frequency of the motion at the middle of shaking, respectively. They are assumed to follow a lognormal distribution (see, e.g., Bray and Rodriguez-Marek, 2004; Rathje et al., 2004) and thus are transformed to the normal space by taking their natural logarithms,

$$z_{P,i} = \ln \alpha_{P,i} \quad i = 2,10,17 \tag{5.44}$$

and

$$z_{NP,i} = \ln \alpha_{NP,i} \quad i = 5,12, \tag{5.45}$$

where $\alpha_{P,2} = T_p$, $\alpha_{P,10} = \omega_{mid,res}$, $\alpha_{P,17} = \omega_{mid,PO}$, $\alpha_{NP,5} = \omega_{mid,NP1}$ and $\alpha_{NP,12} = \omega_{mid,NP2}$.

We start with the same regression equations (5.42) and (5.43) that were used for the intensity parameters. Regression terms X_j in these equations were defined in Table 5.16. Many of these terms turn out not to have explanatory power and are removed from the regression equations. Specifically, we end up setting $\beta_2 = \beta_4 = \beta_5 = 0$ for the parameters of the pulselike and non-pulselike models, as well as $\beta_{NP,i7} = 0$ for the non-pulselike model. Thus,

$$\mathrm{E}[z_{P,i}] = \beta_{P,i0} + \beta_{P,i1}\mathbf{M} + \beta_{P,i3}Ff_{flt,Z} + \beta_{P,i6}\ln(\hat{V}_{s30}) + \beta_{P,i7}s_{or}d \quad i = 2,10,17, \tag{5.46}$$

and

$$\mathrm{E}[z_{NP,i}] = \beta_{NP,i0} + \beta_{NP,i1}\mathbf{M} + \beta_{NP,i3}Ff_{flt,Z} + \beta_{NP,i6}\ln(\hat{V}_{s30}) \quad i = 5,12. \tag{5.47}$$

Table 5.21 lists the estimates of the regression coefficients and the standard deviations of the regression errors for the period and frequency parameters of the pulselike model. The estimated standard deviations τ_i and ϕ_i of the inter- and intra-event error terms are also listed along with the standard deviation $\sigma_{T,i}$ of the total error. The initial sample standard deviation $\sigma_{0,i}$ of the data is also given for reference. Table 5.22 lists these same estimates for parameters of the non-pulselike model. Table 5.23 lists the lower (LB) and upper (UB) bounds of the 95% confidence intervals of the estimates of the regression coefficients as well as the importance factor IF of each predictive term. Table 5.24 lists the same for parameters of the non-pulselike model.

From the results of the regression analysis listed in Tables 5.21 and 5.22, the trends we observe between the period and frequency parameters (i.e., T_p, $\omega_{mid,res}$, $\omega_{mid,PO}$, $\omega_{mid,NP1}$, and $\omega_{mid,NP2}$) and the earthquake source and site characteristics make sense overall. They are generally as expected based on seismological principles and existing GMPEs.

The results show that the pulse period T_p tends to increase with the magnitude ($\beta_1 > 0$) and decrease with site stiffness ($\beta_6 < 0$), which is as expected and agrees with previous observations, even though T_p is not uniquely defined in the literature (Sommerville, 1998; Mavroieidis and Papageorgiou, 2003, Bray and Rodriguez-Marek, 2004; Fu and Menun, 2004; Baker, 2007). It appears that strike-slip earthquakes result in pulses with periods longer than reverse earthquakes ($\beta_3 < 0$). Moreover, as $s_{or}d$ increases, T_p tends to increase ($\beta_7 > 0$), which is as expected since wave periods tend to lengthen with increasing rupture length and duration.

For the two horizontal components of both pulselike and non-pulselike ground motions, the predominant frequency at the middle of ground shaking ($\omega_{mid,res}$, $\omega_{mid,PO}$, $\omega_{mid,NP1}$, and $\omega_{mid,NP2}$) decreases with magnitude ($\beta_1 < 0$) and increases with site stiffness ($\beta_6 > 0$). Distance was not found to be an important predictor. Note that pulse period and frequency at the middle of ground shaking are measures that are inverse of one another. This inverse relationship translates

into a negation relationship when their natural logarithms are taken, as borne out in the corresponding signs of the regression coefficients.

Table 5.21 Estimates of regression coefficients and error standard deviations for period and frequency parameters of pulselike model ($z_{P,i}$).

i	$\alpha_{P,i}$	$\hat{\beta}_{P,i0}$	$\hat{\beta}_{P,i1}$	$\hat{\beta}_{P,i2}$	$\hat{\beta}_{P,i3}$	$\hat{\beta}_{P,i4}$	$\hat{\beta}_{P,i5}$	$\hat{\beta}_{P,i6}$	$\hat{\beta}_{P,i7}$	$\hat{\sigma}_{0,i}$	$\hat{\phi}_i$	$\hat{\tau}_i$	$\hat{\sigma}_{T,i}$
2	T_p	−2.479	0.670	–	−0.264	–	–	−0.233	0.008	0.869	0.359	0.457	0.581
10	$\omega_{mid,res}$	0.967	−0.111	–	–	–	–	0.183	–	0.422	0.385	0.142	0.410
17	$\omega_{mid,PO}$	0.434	−0.125	–	–	–	–	0.302	–	0.459	0.405	0.171	0.440

Table 5.22 Estimates of regression coefficients and error standard deviations for period and frequency parameters of non-pulselike model ($z_{NP,i}$).

i	$\alpha_{NP,i}$	$\hat{\beta}_{NP,i0}$	$\hat{\beta}_{NP,i1}$	$\hat{\beta}_{NP,i2}$	$\hat{\beta}_{NP,i3}$	$\hat{\beta}_{NP,i4}$	$\hat{\beta}_{NP,i5}$	$\hat{\beta}_{NP,i6}$	$\hat{\beta}_{NP,i7}$	$\hat{\sigma}_{0,i}$	$\hat{\phi}_i$	$\hat{\tau}_i$	$\hat{\sigma}_{T,i}$
5	$\omega_{mid,NP1}$	0.247	−0.149	–	–	–	–	0.377	–	0.480	0.397	0.207	0.448
12	$\omega_{mid,NP2}$	0.425	−0.181	–	–	–	–	0.402	–	0.441	0.353	0.189	0.400

Table 5.23 95% confidence intervals and relative contribution of regression coefficients for period and frequency parameters of pulselike model ($z_{P,i}$).

i	$\alpha_{P,i}$	$\beta_{P,ij}$	$\hat{\beta}_{P,i0}$	$\hat{\beta}_{P,i1}$	$\hat{\beta}_{P,i2}$	$\hat{\beta}_{P,i3}$	$\hat{\beta}_{P,i4}$	$\hat{\beta}_{P,i5}$	$\hat{\beta}_{P,i6}$	$\hat{\beta}_{P,i7}$
		LB	−5.581	0.424	–	−0.528	–	–	−0.473	−0.001
2	T_p	*UB*	−2.257	0.917	–	0.000	–	–	0.008	0.016
		IF	−0.456	0.853	–	−0.011	–	–	−0.252	0.039
		LB	0.727	−0.242	–	–	–	–	0.014	–
10	$\omega_{mid,res}$	*UB*	2.989	0.020	–	–	–	–	0.353	–
		IF	0.590	−0.468	–	–	–	–	0.658	–
		LB	0.385	−0.267	–	–	–	–	0.122	–
17	$\omega_{mid,PO}$	*UB*	2.780	0.017	–	–	–	–	0.481	–
		IF	0.215	−0.428	–	–	–	–	0.878	–

Table 5.24 95% confidence intervals and relative contribution of regression coefficients for period and frequency parameters of non-pulselike model ($z_{NP,i}$).

i	$\alpha_{NP,i}$	$\beta_{NP,ij}$	$\hat{\beta}_{NP,i0}$	$\hat{\beta}_{NP,i1}$	$\hat{\beta}_{NP,i2}$	$\hat{\beta}_{NP,i3}$	$\hat{\beta}_{NP,i4}$	$\hat{\beta}_{NP,i5}$	$\hat{\beta}_{NP,i6}$	$\hat{\beta}_{NP,i7}$
		LB	−0.435	−0.237	–	–	–	–	0.170	–
5	$\omega_{mid,NP1}$	*UB*	2.211	−0.061	–	–	–	–	0.585	–
		IF	0.097	−0.388	–	–	–	–	0.916	–
		LB	−0.199	−0.260	–	–	–	–	0.215	–
12	$\omega_{mid,NP2}$	*UB*	2.181	−0.102	–	–	–	–	0.588	–
		IF	0.152	−0.430	–	–	–	–	0.890	–

5.4.3.3 Time and duration parameters

Several predictive models have been developed for the significant duration of ground motions (e.g., Abrahamson and Silva, 1996; Kempton and Stewart, 2006; and Bommer et al., 2009). These models guide our choice of equations to predict the parameters of our model that describe the significant duration or specific time points of a ground motion. To predict the significant duration D_{5-95} of a ground motion, Abrahamson and Silva (1996) developed a model based on seismological theory. Kempton and Stewart (2006) later adapted this model. In this formulation, the significant duration at the source is equated to the rupture duration, which is inversely proportional to the corner frequency of the earthquake source. The corner frequency is itself related to the size and stress drop of the earthquake. The significant duration at the source is then modified to account for the effects of wave propagation and local site conditions. More recently, Bommer et al. (2009) investigated several duration parameters and developed empirical predictive equations to model them. They predicted the Arias-intensity-based significant duration D_{5-95} using the functional form

$$\mathrm{E}[\ln D_{5-95}] = c_0 + c_1\mathbf{M} + c_3 Z_{TOR} + (c_4 + c_5\mathbf{M}) \ln\left(\sqrt{R_{RUP}^2 + h^2}\right) + \mathrm{c}_6 \ln V_{s30}, \tag{5.48}$$

where the notation and ordering of the terms are slightly modified to resemble the notation used here. All three developers assumed that ground motion duration follows a lognormal distribution. We adopt this assumption and extend it to all parameters that are measures of time or duration in our near-fault ground motion model, namely $t_{max,p}$, D_{5-95}, D_{0-5} and D_{0-30}. Note that $t_{max,p}$, D_{0-5} and D_{0-30} are all measured from t_0, which was defined earlier as the time at 0.01% cumulative Arias intensity. The time and duration parameters are then transformed to the normal space by taking their natural logarithms, i.e.,

$$z_{P,i} = \ln \alpha_{P,i} \quad i = 5,7,8,9,14,15,16 \tag{5.49}$$

and

$$z_{NP,i} = \ln \alpha_{NP,i} \quad i = 2,3,4,9,10,11, \tag{5.50}$$

where $\alpha_{P,5} = t_{max,p}$, $\alpha_{P,7} = D_{5-95,res}$, $\alpha_{P,8} = D_{0-5,res}$, $\alpha_{P,9} = D_{0-30,res}$, $\alpha_{P,14} = D_{5-95,PO}$, $\alpha_{P,15} = D_{0-5,PO}$, $\alpha_{P,16} = D_{0-30,PO}$, $\alpha_{NP,2} = D_{5-95,NP1}$, $\alpha_{NP,3} = D_{0-5,NP1}$, $\alpha_{NP,4} = D_{0-30,NP1}$, , $\alpha_{NP,9} = D_{5-95,NP2}$, $\alpha_{NP,10} = D_{0-5,NP2}$ and $\alpha_{NP,11} = D_{0-30,NP2}$.

Aside from excluding the directivity term (i.e., $\beta_7 = 0$) and setting $\beta_2 = 0$, the predictive equation of Bommer et al. (2009) in (5.48) is almost identical in form to our equations (5.42) and (5.43) that were used to predict intensity measures. We thus use (5.42) and (5.43) with $\beta_2 = \beta_7 = 0$ as the starting point of our regression analysis. We find that the regression term X_5 (see Table 5.16) has no explanatory power and also remove it from the regression equations by setting $\beta_5 = 0$. Thus, the forms we adopt for pulselike and non-pulselike motions are

$$\mathrm{E}[z_{P,i}] = \beta_{P,i0} + \beta_{P,i1}\mathbf{M} + \beta_{P,i3}Ff_{flt,Z} + \beta_{P,i4}\ln\left(\sqrt{R_{RUP}^2 + h^2}\right) + \beta_{P,i6}\ln(\hat{V}_{s30}) \qquad (5.51)$$

$$i = 5,7,8,9,14,15,16,$$

and

$$\mathrm{E}[z_{NP,i}] = \beta_{NP,i0} + \beta_{NP,i1}\mathbf{M} + \beta_{NP,i3}Ff_{flt,Z} + \beta_{NP,i4}\ln\left(\sqrt{R_{RUP}^2 + h^2}\right) + \beta_{NP,i6}\ln(\hat{V}_{s30}) \qquad (5.52)$$

$$i = 2,3,4,9,10,11,$$

where we set $h = 6$ km while Bommer et al. (2009) used $h = 2.5$ km.

Table 5.25 lists the estimates of the regression coefficients and the standard deviations of the regression errors for the time and duration parameters of the pulselike model. The initial sample standard deviation $\sigma_{0,i}$ of the data is also given for reference. Table 5.26 lists these same estimates for parameters of the non-pulselike model. Table 5.27 lists the lower (LB) and upper (UB) bounds of the 95% confidence intervals of the estimates of the regression coefficients as well as the importance factor IF of each predictive term for the pulselike model. Table 5.28 lists the same for parameters of the non-pulselike model.

From the results of the regression analysis listed in Tables 5.25 and 5.26, the trends we observe between the time and duration parameters (i.e., $t_{max,p}$, $D_{5-95,res}$, $D_{0-5,res}$, $D_{0-30,res}$, $D_{5-95,PO}$, $D_{0-5,PO}$, $D_{0-30,PO}$, $D_{5-95,NP1}$, $D_{0-5,NP1}$, $D_{0-30,NP1}$, $D_{5-95,NP2}$, $D_{0-5,NP2}$, $D_{0-30,NP2}$) and the earthquake source and site characteristics make sense overall. They are generally as expected based on seismological principles and existing GMPEs. The results show that the time and duration parameters all follow similar trends. They tend to increase with magnitude ($\beta_1 > 0$) and distance ($\beta_4 > 0$), and to be smaller for buried reverse fault ruptures ($\beta_3 < 0$). Soil stiffness has a statistically significant effect on $t_{max,p}$, which defines the time position of the pulse within the record, and on the duration parameters $D_{5-95,res}$, $D_{5-95,PO}$, $D_{5-95,NP1}$, and $D_{5-95,NP2}$, but not on the remaining time parameters. The time position of the pulse and measures of duration tend to decrease with soil stiffness ($\beta_6 < 0$). These trends are as expected.

Table 5.25 Estimates of regression coefficients and error standard deviations for time and duration parameters of pulselike model ($z_{P,i}$).

i	$\alpha_{P,i}$	$\hat{\beta}_{P,i0}$	$\hat{\beta}_{P,i1}$	$\hat{\beta}_{P,i2}$	$\hat{\beta}_{P,i3}$	$\hat{\beta}_{P,i4}$	$\hat{\beta}_{P,i5}$	$\hat{\beta}_{P,i6}$	$\hat{\beta}_{P,i7}$	$\hat{\sigma}_{0,i}$	$\hat{\phi}_i$	$\hat{\tau}_i$	$\hat{\sigma}_{T,i}$
5	$t_{max,p}$	−4.249	0.852	–	−0.380	0.390	–	−0.088	–	0.842	0.272	0.382	0.469
7	$D_{5-95,res}$	−0.381	0.733	–	−0.163	0.217	–	−0.427	–	0.589	0.279	0.247	0.372
8	$D_{0-5,res}$	−5.563	0.905	–	−0.282	0.385	–	–	–	0.779	0.307	0.318	0.442
9	$D_{0-30,res}$	−4.777	0.880	–	−0.339	0.311	–	–	–	0.764	0.241	0.311	0.394
14	$D_{5-95,PO}$	−0.516	0.754	–	−0.122	0.192	–	−0.424	–	0.630	0.292	0.277	0.402
15	$D_{0-5,PO}$	−5.772	0.923	–	−0.238	0.403	–	–	–	0.772	0.325	0.328	0.461
16	$D_{0-30,PO}$	−5.016	0.905	–	−0.328	0.327	–	–	–	0.764	0.233	0.334	0.408

Table 5.26 Estimates of regression coefficients and error standard deviations for time and duration parameters of non-pulselike model ($z_{NP,i}$).

i	$\alpha_{NP,i}$	$\hat{\beta}_{NP,i0}$	$\hat{\beta}_{NP,i1}$	$\hat{\beta}_{NP,i2}$	$\hat{\beta}_{NP,i3}$	$\hat{\beta}_{NP,i4}$	$\hat{\beta}_{NP,i5}$	$\hat{\beta}_{NP,i6}$	$\hat{\beta}_{NP,i7}$	$\hat{\sigma}_{0,i}$	$\hat{\phi}_i$	$\hat{\tau}_i$	$\hat{\sigma}_{T,i}$
2	$D_{5-95,NP1}$	−1.035	0.769	–	−0.378	0.412	–	−0.424	–	0.656	0.378	0.125	0.398
3	$D_{0-5,NP1}$	−4.727	0.710	–	−0.124	0.471	–	–	–	0.663	0.355	0.287	0.457
4	$D_{0-30,NP1}$	−4.444	0.798	–	−0.231	0.345	–	–	–	0.635	0.288	0.104	0.306
9	$D_{5-95,NP2}$	−0.404	0.672	–	−0.330	0.335	–	−0.367	–	0.590	0.334	0.172	0.376
10	$D_{0-5,NP2}$	−4.798	0.709	–	−0.076	0.473	–	–	–	0.662	0.356	0.289	0.458
11	$D_{0-30,NP2}$	−4.350	0.785	–	−0.222	0.325	–	–	–	0.610	0.278	0.096	0.294

Table 5.27 95% confidence intervals and relative contribution of regression coefficients for time and duration parameters of pulselike model ($z_{P,i}$).

i	$\alpha_{P,i}$	$\beta_{P,ij}$	$\hat{\beta}_{P,i0}$	$\hat{\beta}_{P,i1}$	$\hat{\beta}_{P,i2}$	$\hat{\beta}_{P,i3}$	$\hat{\beta}_{P,i4}$	$\hat{\beta}_{P,i5}$	$\hat{\beta}_{P,i6}$	$\hat{\beta}_{P,i7}$
		LB	−5.627	0.706	–	−0.567	0.205	–	−0.265	–
5	$t_{max,p}$	UB	−3.446	0.999	–	−0.194	0.574	–	0.089	–
		IF	−0.579	0.803	–	−0.012	0.122	–	−0.071	–
		LB	−1.749	0.617	–	−0.310	0.071	–	−0.567	–
7	$D_{5-95,res}$	UB	0.083	0.849	–	−0.015	0.362	–	−0.286	–
		IF	−0.067	0.890	–	−0.007	0.088	–	−0.441	–
		LB	−6.408	0.773	–	−0.457	0.210	–	–	–
8	$D_{0-5,res}$	UB	−4.698	1.037	–	−0.108	0.561	–	–	–
		IF	−0.660	0.744	–	−0.008	0.105	–	–	–
		LB	−5.973	0.764	–	−0.493	0.157	–	–	–
9	$D_{0-30,res}$	UB	−4.491	0.996	–	−0.186	0.465	–	–	–
		IF	−0.615	0.783	–	−0.010	0.092	–	–	–
		LB	−2.173	0.626	–	−0.285	0.031	–	−0.579	–
14	$D_{5-95,PO}$	UB	−0.194	0.882	–	0.041	0.353	–	−0.269	–
		IF	−0.089	0.896	–	−0.005	0.076	–	−0.429	–
		LB	−6.367	0.787	–	−0.418	0.222	–	–	–
15	$D_{0-5,PO}$	UB	−4.604	1.059	–	−0.058	0.584	–	–	–
		IF	−0.667	0.738	–	−0.006	0.107	–	–	–
		LB	−6.066	0.789	–	−0.482	0.173	–	–	–
16	$D_{0-30,PO}$	UB	−4.567	1.021	–	−0.175	0.481	–	–	–
		IF	−0.622	0.777	–	−0.009	0.094	–	–	–

Table 5.28 95% confidence intervals and relative contribution of regression coefficients for time and duration parameters of non-pulselike model ($z_{NP,i}$).

i	$\alpha_{NP,i}$	$\beta_{NP,ij}$	$\hat{\beta}_{NP,i0}$	$\hat{\beta}_{NP,i1}$	$\hat{\beta}_{NP,i2}$	$\hat{\beta}_{NP,i3}$	$\hat{\beta}_{NP,i4}$	$\hat{\beta}_{NP,i5}$	$\hat{\beta}_{NP,i6}$	$\hat{\beta}_{NP,i7}$
		LB	-1.787	0.691	–	-0.478	0.311	–	-0.607	–
2	$D_{5-95,NP1}$	UB	0.596	0.847	–	-0.277	0.513	–	-0.242	–
		IF	-0.173	0.858	–	-0.029	0.195	–	-0.442	–
		LB	-5.166	0.619	–	-0.240	0.353	–	–	–
3	$D_{0-5,NP1}$	UB	-3.872	0.800	–	-0.007	0.589	–	–	–
		IF	-0.694	0.693	–	-0.008	0.196	–	–	–
		LB	-4.908	0.727	–	-0.323	0.252	–	–	–
4	$D_{0-30,NP1}$	UB	-3.868	0.870	–	-0.138	0.439	–	–	–
		IF	-0.635	0.759	–	-0.015	0.140	–	–	–
		LB	-1.027	0.600	–	-0.423	0.242	–	-0.535	–
9	$D_{5-95,NP2}$	UB	1.162	0.745	–	-0.238	0.429	–	-0.198	–
		IF	-0.079	0.873	–	-0.030	0.185	–	-0.444	–
		LB	-5.200	0.618	–	-0.194	0.353	–	–	–
10	$D_{0-5,NP2}$	UB	-3.892	0.800	–	0.042	0.592	–	–	–
		IF	-0.699	0.688	–	-0.005	0.195	–	–	–
		LB	-4.756	0.718	–	-0.309	0.237	–	–	–
11	$D_{0-30,NP2}$	UB	-3.811	0.853	–	-0.134	0.414	–	–	–
		IF	-0.634	0.762	–	-0.015	0.134	–	–	–

5.4.3.4 Other parameters

The remaining model parameters, i.e., γ, ν, ω' and ζ_f, do not follow a lognormal distribution. The procedure explained by Rezaeian and Der Kiureghian (2010) is used to transform these parameters to the standard normal space, thereby satisfying the normality assumption in the subsequent development of regression models. First, a distribution for each parameter is selected by visual inspection of the histogram of the corresponding data, and the distribution parameters are estimated by use of the maximum likelihood method. When applicable, the bounds of the distribution are selected based on the range of the observed data, also taking into consideration physical restrictions. For parameters $\alpha_{P,i}$ $i = 3,4$ (i.e., γ, ν) of the pulselike model, we visually select and fit a marginal probability distribution $F_{\alpha_{P,i}}(\alpha_{P,i})$ to the sample data of each parameter. For filter parameters ω' and ζ_f, sample data obtained from (1) residuals of pulselike motions, (2) ground motion components in the direction orthogonal to the largest pulse, (3) major components of non-pulselike motions, and (4) intermediate components of non-pulselike motions are all combined to select and fit a single marginal distribution. That is, we assume

$$F_{\alpha_{P,11}}(\alpha_{P,11}) = F_{\alpha_{P,18}}(\alpha_{P,18}) = F_{\alpha_{NP,6}}(\alpha_{NP,6}) = F_{\alpha_{NP,13}}(\alpha_{NP,13}), \tag{5.53}$$

and

$$F_{\alpha_{P,12}}(\alpha_{P,12}) = F_{\alpha_{P,19}}(\alpha_{P,19}) = F_{\alpha_{NP,7}}(\alpha_{NP,7}) = F_{\alpha_{NP,14}}(\alpha_{NP,14}). \tag{5.54}$$

We then use the fitted marginal distributions to transform the sample parameter values to the standard normal space by use of the rules

$$z_{P,i} = \Phi^{-1}\left[F_{\alpha_{P,i}}(\alpha_{P,i})\right],\ i = 3,4,11,12,18,19, \tag{5.55}$$

and

$$z_{NP,i} = \Phi^{-1}\left[F_{\alpha_{NP,i}}(\alpha_{NP,i})\right],\ i = 6,7,13,14, \tag{5.56}$$

where $\Phi^{-1}[.]$ denotes the inverse of the standard normal cumulative probability distribution function. Table 5.29 lists the bounds, the mean and the standard deviation of the sample data for the parameters γ, ν, ω' and ζ_f. Table 5.30 lists the fitted marginal distributions, their selected bounds and fitted parameter values. The adopted distributions include the Beta distribution defined by the PDF

$$f_{beta}(x) = \frac{\hat{x}^{\alpha-1}(1-\hat{x})^{\beta-1}}{B(\alpha,\beta)} \quad x_{min} < x < x_{max}, \tag{5.57}$$

where $\mathrm{B}(\alpha,\beta)$ is the beta function and

$$\hat{x} = \frac{x - x_{min}}{x_{max} - x_{min}}, \tag{5.58}$$

and the two-sided exponential distribution defined by the PDF

$$\begin{aligned} f_{exp2}(x) &= c\exp(\alpha x) && x_{min} < x \le 0 \\ &= c\exp(-\beta x) && 0 < x < x_{max}. \\ &= 0 && \text{otherwise} \end{aligned} \tag{5.59}$$

The data histograms of model parameters γ, ν, ω' and ζ_f are plotted in Figure 5.11 along with the fitted marginal distributions. Adequacy of the fitted distributions is evaluated using visual tests and statistical hypothesis tests of goodness of fit, such as the Kolmogorov-Smirnov test. As an example, the beta distribution fitted to the sample values of parameter γ is found to be not rejected at the 5% significance level by the Kolmogorov-Smirnov test. The sample data of the fitted values of parameter ν, which denotes the phase angle of the pulse, range from 0 to 2π rad. As can be observed in Figure 5.11(b), and despite the more limited number of pulses with $\nu < \pi/2$ rad, we select a uniform distribution to describe the sample data of ν. This choice of uniform distribution is rejected at the 5% significance level by the Kolmogorov-Smirnov test, but we do not find a justification for any other distribution. The distributions fitted to parameters ω' and ζ_f are also rejected at the 5% significance level by the Kolmogorov-Smirnov test due to large sample size. Indeed, as the sample size becomes larger, goodness of fit tests require smaller deviations from the assumed distribution and reject the null hypothesis even though the deviations may not be practically significant. Instead, we resort to visual evaluation using histograms or QQ-plots to test the normality of the transformed sample data of filter parameters ω' and ζ_f. Figure 5.12 shows the QQ-plots of the transformed data of parameters γ, ν, ω' and ζ_f versus the standard normal quantiles. It is observed that the normality assumption is generally

satisfied between the mean plus and minus two standard deviations of the distribution (the data follow a linear trend within the range -2 to $+2$).

Table 5.29 Sample statistics of parameters γ, ν, ω' and ζ_f.

Parameter	Unit	Sample lower bound	Sample upper bound	Sample mean	Sample standard deviation
γ	-	2.00	3.19	2.28	0.19
ν/π	π rad	0.02	1.99	1.08	0.54
$\omega'/(2\pi)$	Hz/s	-3.10	1.25	-0.09	0.21
ζ_f	-	0.009	0.9	0.18	0.14

Table 5.30 Marginal distributions fitted to parameters γ, ν, ω' and ζ_f.

Parameter	Unit	Fitted Distribution	Selected lower bound	Selected upper bound	Fitted distribution parameters
γ	-	beta	2.0	3.2	$\alpha = 1.30, \beta = 3.97$
ν/π	π rad	uniform	0	2	
$\omega'/(2\pi)$	Hz/s	two-sided exponential	-3.5	1.5	$\alpha = 6.4, \beta = 14.3, c = 4.42$
$\ln \zeta_f$	-	beta	$\ln 0.009$	$\ln 1$	$\alpha = 5.34, \beta = 3.83$

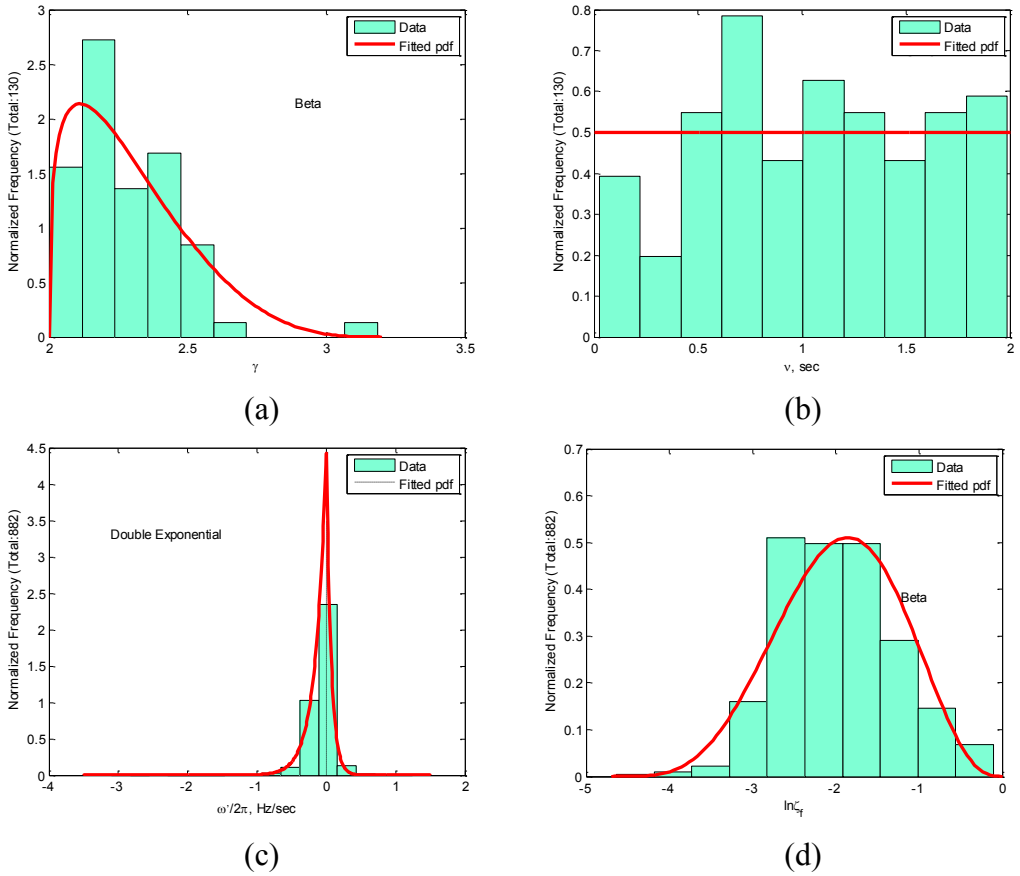

Figure 5.11 Histograms of model parameters with fitted marginal distributions: (a) γ, (b) ν, (c) ω' and (d) $\ln \zeta_f$.

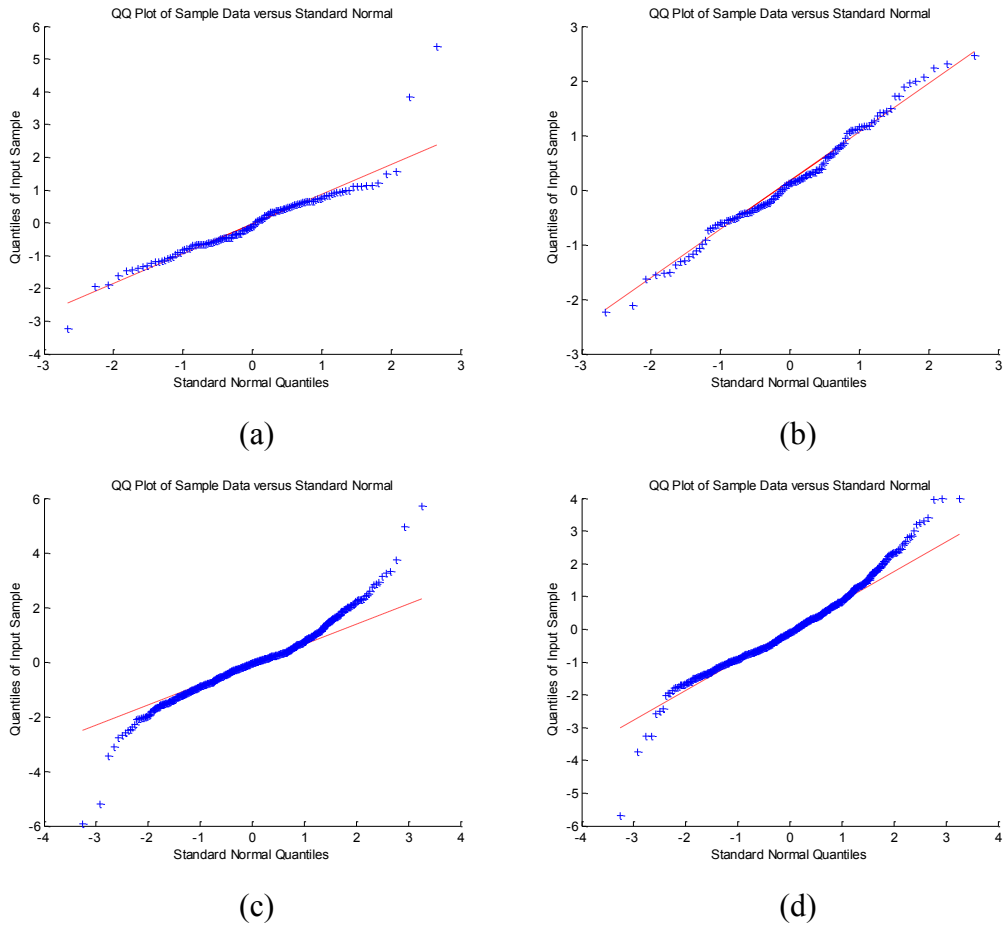

Figure 5.12 QQ-plots of transformed model parameters data: (a) γ, (b) ν, (c) ω' and (d) $\ln\zeta_f$.

Next, we perform regression analysis to fit predictive models to the transformed parameters in terms of the earthquake source and site characteristics. This group of parameters is difficult to relate to physical ground motion characteristics. They are also likely to be least important for structural response. We start our analysis with the same regression terms that were used for the intensity parameters and find that only the magnitude and distance terms provide some explanatory power. Therefore, we set $\beta_2 = \beta_3 = \beta_5 = \beta_6 = \beta_7 = 0$ for both the pulselike and non-pulselike model parameters. This simplifies the regression models to

$$\mathrm{E}[z_{P,i}] = \beta_{P,i0} + \beta_{P,i1}\mathbf{M} + \beta_{P,i4}\ln\left(\sqrt{R_{RUP}^2 + h^2}\right) \quad i = 3,4,11,12,18,19, \tag{5.60}$$

and

$$\mathrm{E}[z_{NP,i}] = \beta_{NP,i0} + \beta_{NP,i1}\mathbf{M} + \beta_{NP,i4}\ln\left(\sqrt{R_{RUP}^2 + h^2}\right) \quad i = 6,7,13,14. \tag{5.61}$$

Table 5.31 lists the estimates of the regression coefficients and the standard deviations of the regression errors for this group of parameters of the pulselike model. No viable predictive

relations were found for $z_{P,3}$ or $z_{P,4}$ (corresponding to γ and ν). For the remaining parameters, the random effect is found not to be significant and is not included. Therefore, only the standard deviation $\sigma_{T,i}$ of the total error is listed in Table 5.31. The initial sample standard deviation $\sigma_{0,i}$ of the data is also given for reference. Table 5.32 lists the estimates for parameters of the non-pulselike model. Table 5.33 lists the lower (LB) and upper (UB) bounds of the 95% confidence intervals of the estimates of the regression coefficients as well as the importance factor IF of each predictive term for the pulselike model (excluding those for γ and ν), and Table 5.34 lists the same for the parameters of the non-pulselike model.

Since no viable predictive models were found for γ and ν, consistent with their marginal distributions, $z_{P,3}$ and $z_{P,4}$ are simply assumed to come from a standard normal distribution with 0 mean and unit standard deviation. The values of $\sigma_{T,i}$ ($= \sigma_{0,i}$) for these parameters, which are listed in Table 5.31, are slightly different from 1 since they are the sample standard deviations. The predictive relations for the other parameters are only able to explain a small portion of the observed variability, as illustrated by the little decrease in variances from $\sigma_{0,i}^2$ to $\sigma_{T,i}^2$.

From the results of the regression analysis listed in Tables 5.31 and 5.32, the trends we observe between filter parameters ω' and ζ (more precisely ω'_{res}, ζ_{res}, ω'_{PO}, ζ_{PO}, ω'_{NP1}, ζ_{NP1}, ω'_{NP2}, and ζ_{NP1}) and the earthquake source and site characteristics are generally similar to those documented in Rezaeian and Der Kiureghian (2010) for far-field motions. The results show that the rate of change of predominant frequency increases with magnitude ($\beta_1 > 0$). They also show that the filter damping, which is a measure of the bandwidth of the ground motion, increases (the ground motion becomes broader band) with magnitude ($\beta_1 > 0$) and decreases (the ground motion becomes narrow band) with distance ($\beta_4 < 0$).

Table 5.31 Estimates of regression coefficients and error standard deviations for "other" parameters of pulselike model ($z_{P,i}$).

i	$\alpha_{P,i}$	$\hat{\beta}_{P,i0}$	$\hat{\beta}_{P,i1}$	$\hat{\beta}_{P,i2}$	$\hat{\beta}_{P,i3}$	$\hat{\beta}_{P,i4}$	$\hat{\beta}_{P,i5}$	$\hat{\beta}_{P,i6}$	$\hat{\beta}_{P,i7}$	$\hat{\sigma}_{0,i}$	$\hat{\sigma}_{T,i}$
3	γ	–	–	–	–	–	–	–	–	1.002	1.002
4	ν	–	–	–	–	–	–	–	–	0.928	0.928
11	ω'_{res}	−2.166	0.322	–	–	–	–	–	–	0.838	0.820
12	ζ_{res}	−1.707	0.433	–	–	−0.413	–	–	–	1.118	1.096
18	ω'_{PO}	−2.875	0.416	–	–	–	–	–	–	0.857	0.825
19	ζ_{PO}	−1.868	0.457	–	–	−0.501	–	–	–	0.996	0.962

Table 5.32 Estimates of regression coefficients and error standard deviations for "other" parameters of non-pulselike model ($z_{NP,i}$).

i	$\alpha_{NP,i}$	$\hat{\beta}_{NP,i1}$	$\hat{\beta}_{NP,i2}$	$\hat{\beta}_{NP,i3}$	$\hat{\beta}_{NP,i4}$	$\hat{\beta}_{NP,i5}$	$\hat{\beta}_{NP,i6}$	$\hat{\beta}_{NP,i7}$	$\hat{\beta}_{NP,i1}$	$\hat{\sigma}_{0,i}$	$\hat{\sigma}_{T,i}$
6	ω'_{NP1}	−1.443	0.223	–	–	–	–	–	–	0.949	0.941
7	ζ_{NP1}	−0.380	0.159	–	–	−0.298	–	–	–	1.018	1.008
13	ω'_{NP2}	−2.979	0.420	–	–	–	–	–	–	0.866	0.832
14	ζ_{NP2}	−0.704	0.161	–	–	−0.146	–	–	–	0.892	0.888

Table 5.33 95% confidence intervals and relative contribution of regression coefficients for "other" parameters of pulselike model ($z_{P,i}$).

i	$\alpha_{P,i}$	$\beta_{P,ij}$	$\hat{\beta}_{P,i0}$	$\hat{\beta}_{P,i1}$	$\hat{\beta}_{P,i2}$	$\hat{\beta}_{P,i3}$	$\hat{\beta}_{P,i4}$	$\hat{\beta}_{P,i5}$	$\hat{\beta}_{P,i6}$	$\hat{\beta}_{P,i7}$
		LB	−3.864	0.077	–	–	–	–	–	–
11	ω'_{res}	UB	−0.468	0.566	–	–	–	–	–	–
		IF	−0.697	0.717	–	–	–	–	–	–
		LB	−3.976	0.088	–	–	−0.874	–	–	–
12	ζ_{res}	UB	0.562	0.778	–	–	0.049	–	–	–
		IF	−0.477	0.838	–	–	−0.266	–	–	–
		LB	−4.583	0.170	–	–	–	–	–	–
18	ω'_{PO}	UB	−1.168	0.661	–	–	–	–	–	–
		IF	−0.707	0.708	–	–	–	–	–	–
		LB	−3.858	0.154	–	–	−0.906	–	–	–
19	ζ_{PO}	UB	0.123	0.760	–	–	−0.096	–	–	–
		IF	−0.485	0.822	–	–	−0.300	–	–	–

Table 5.34 95% confidence intervals and relative contribution of regression coefficients for "other" parameters of non-pulselike model ($z_{NP,i}$).

i	$\alpha_{NP,i}$	$\beta_{NP,ij}$	$\hat{\beta}_{NP,i0}$	$\hat{\beta}_{NP,i1}$	$\hat{\beta}_{NP,i2}$	$\hat{\beta}_{NP,i3}$	$\hat{\beta}_{NP,i4}$	$\hat{\beta}_{NP,i5}$	$\hat{\beta}_{NP,i6}$	$\hat{\beta}_{NP,i7}$
		LB	-2.652	0.042	–	–	–	–	–	–
6	ω'_{NP1}	UB	-0.234	0.404	–	–	–	–	–	–
		IF	-0.697	0.718	–	–	–	–	–	–
		LB	-1.797	-0.032	–	–	-0.539	–	–	–
7	ζ_{NP1}	UB	1.037	0.351	–	–	-0.058	–	–	–
		IF	-0.270	0.753	–	–	-0.600	–	–	–
		LB	-4.042	0.261	–	–	–	–	–	–
13	ω'_{NP2}	UB	-1.917	0.579	–	–	–	–	–	–
		IF	-0.729	0.685	–	–	–	–	–	–
		LB	-1.952	-0.008	–	–	-0.358	–	–	–
14	ζ_{NP2}	UB	0.545	0.329	–	–	0.066	–	–	–
		IF	-0.523	0.795	–	–	-0.307	–	–	–

As can be seen in the above results, due to the limited size of the databases, we are able to achieve only a small to moderate reduction in the total standard deviations. As more data becomes available, the functional forms and coefficients of the regression equations can be updated to reflect the new data and error standard deviations will likely decrease.

5.4.4 Correlation analysis

Having developed the predictive relations for the parameters of the pulselike and non-pulselike models, we next estimate the correlations between the parameters. These correlations describe the relations and dependencies among the model parameters. The correlation coefficients $\rho_{P,ij}$ between pairs of the parameters $z_{P,i}$, $i = 1, \ldots, 19$, of the model of pulselike ground motion are estimated as the correlations between the corresponding total regression residuals $(\eta_i + \epsilon_i)$, $i = 1, \ldots, 19$.

Table 5.35 lists the estimated correlation coefficients. Correlation values larger than 0.3 in absolute value are highlighted. We examine the results again focusing on the different categories of model parameters. As expected, larger positive correlations are generally observed for the same parameters of the residual and orthogonal motions (0.4 to 0.9) and for parameters of the same category.

We find mild negative correlation (-0.2) between $z_{P,1}$ and $z_{P,2}$, which correspond to the velocity pulse amplitude V_p and period T_p. This is consistent with the inverse relation found by Somerville et al. (1997). We also find positive correlation (0.4) between the velocity pulse amplitude V_p and the Arias intensity parameters, I_a. Thus, a pulselike motion with large pulse amplitude tends to have high intensity residual and orthogonal motions. We also find positive correlations between the pulse period T_p and the time of the peak of the velocity pulse envelope $t_{max,p}$ (0.4) and with time parameters D_{0-5} and D_{0-30} of the residual and orthogonal motions (0.3 to 0.4, respectively). Additionally, the time parameters $t_{max,p}$, D_{5-95}, D_{0-5} and D_{0-30} are

all strongly positively correlated with each other (0.7 to 0.9), as expected. Concerning the filter parameters, mild negative correlations (-0.2 and -0.4) are found between the frequency at the middle of ground shaking, ω_{mid}, and the rate of change of frequency, ω', of the residual and orthogonal motions, respectively. Practically no correlation is found between the frequency contents of the pulse, residual and orthogonal motions, namely T_p and ω_{mid}.

Table 5.35 Estimated correlation matrix of regression residuals $\rho_{P,ij}$ for the parameters of the pulselike model $z_{P,i}$ (for legibility, subscript P is dropped in the table and moderate to large correlations are highlighted).

$z_{P,i}$	z_1	z_2	z_3	z_4	z_5	z_6	z_7	z_8	z_9	z_{10}	z_{11}	z_{12}	z_{13}	z_{14}	z_{15}	z_{16}	z_{17}	z_{18}	z_{19}
z_1	1	-0.2	0.0	0.2	0.2	**0.4**	0.0	0.0	0.1	**-0.4**	0.1	0.2	**0.4**	0.0	0.0	0.0	-0.3	0.1	0.0
z_2		1	0.2	0.0	**0.4**	-0.1	0.1	**0.3**	**0.4**	0.1	0.0	0.2	-0.1	0.1	0.3	**0.4**	0.0	-0.1	0.2
z_3			1	-0.2	0.2	0.2	0.1	0.2	0.2	-0.1	0.1	0.1	0.1	0.1	0.1	0.2	-0.1	0.0	0.1
z_4				1	0.1	-0.1	0.1	0.1	0.1	-0.1	-0.1	0.0	0.0	0.0	0.1	0.1	-0.1	0.1	0.0
z_5					1	0.1	0.2	**0.7**	**0.8**	0.0	-0.2	0.1	0.0	0.2	**0.7**	**0.7**	0.0	-0.2	0.2
z_6						1	0.0	0.1	0.1	0.1	0.1	0.0	**0.8**	0.0	0.0	0.1	0.1	0.1	0.0
z_7							1	0.1	0.2	0.0	-0.2	0.0	0.0	**0.8**	0.0	0.2	-0.1	0.0	0.0
z_8								1	**0.9**	0.0	0.0	0.2	0.0	0.1	**0.9**	**0.9**	0.0	0.0	0.2
z_9									1	0.0	-0.1	0.2	0.1	0.3	**0.8**	**0.9**	0.0	0.0	0.2
z_{10}										1	-0.2	0.1	0.2	0.0	0.0	0.1	**0.9**	-0.3	0.2
z_{11}											1	0.1	0.0	0.0	-0.1	-0.1	-0.1	**0.4**	0.2
z_{12}												1	0.0	0.1	0.2	0.3	0.3	-0.2	**0.8**
z_{13}													1	-0.2	0.0	0.1	0.1	0.2	0.0
z_{14}														1	0.1	0.2	0.0	-0.1	0.1
z_{15}															1	**0.8**	0.0	0.0	0.2
z_{16}																1	0.1	-0.1	0.3
z_{17}																	1	**-0.4**	0.3
z_{18}																		1	-0.2
z_{19}																			1

Symmetric

The correlation coefficients $\rho_{NP,ij}$ between pairs of the parameters $z_{NP,i}$, $i = 1, \ldots, 12$, of the model of non-pulselike ground motion are estimated as the correlations between the corresponding total regression residuals $(\eta_i + \epsilon_i)$, $i = 1, \ldots, 12$. Table 5.36 lists the estimated correlation coefficients. Correlation values larger than 0.3 in absolute value are highlighted. The correlation results for the parameters of the non-pulselike model, i.e., the parameters describing the major and intermediate "principal" components, are almost identical to the results for the pulselike model parameters that describe the residual and orthogonal motions.

The predictive equations and the estimated correlations between the parameters of the pulselike and non-pulselike models are used to generate random realizations of pulselike and non-pulselike model parameters. These are in turn used in the stochastic models for the two types

of ground motions to generate random realizations of suites of synthetic ground motions for given earthquake source and site characteristics. The procedure is illustrated in the next chapter.

Table 5.36 Estimated correlation matrix of regression residuals $\rho_{NP,ij}$ for the parameters of the non-pulselike model $z_{NP,i}$ (for legibility, subscript NP is dropped in the table and moderate to large correlations are highlighted).

$z_{NP,i}$	z_1	z_2	z_3	z_4	z_5	z_6	z_7	z_8	z_9	z_{10}	z_{11}	z_{12}	z_{13}	z_{14}
z_1	**1**	-0.2	0.1	0.1	0.0	0.2	-0.2	**0.9**	-0.1	0.0	0.1	0.1	0.1	-0.1
z_2		**1**	0.1	**0.3**	0.0	-0.1	0.1	-0.1	**0.8**	0.1	0.3	-0.1	0.0	0.1
z_3			**1**	**0.8**	-0.2	0.0	-0.1	0.1	0.1	**0.9**	**0.8**	-0.2	0.0	-0.1
z_4				**1**	-0.2	-0.1	0.0	0.1	0.3	**0.8**	**0.9**	-0.2	-0.1	0.0
z_5					**1**	-0.2	-0.2	0.1	-0.1	-0.2	-0.2	**0.9**	-0.1	0.0
z_6						**1**	-0.1	0.2	0.0	0.0	-0.1	-0.1	**0.6**	-0.2
z_7							**1**	-0.1	0.1	-0.1	0.0	-0.1	-0.1	**0.8**
z_8								**1**	-0.1	0.0	0.1	0.1	0.1	-0.1
z_9									**1**	0.1	0.3	-0.1	-0.1	0.1
z_{10}										**1**	**0.8**	-0.2	0.0	-0.1
z_{11}											**1**	-0.2	-0.1	0.0
z_{12}												**1**	-0.2	0.0
z_{13}													**1**	-0.1
z_{14}														**1**

5.5 COMPARISON OF OUR EMPIRICAL PREDICTIVE EQUATIONS WITH THOSE PROPOSED IN THE LITERATURE

5.5.1 Intensity parameters

Next, we compare our results to several predictive relations proposed in the literature. Bray and Rodriguez-Marek (2004) developed a relation to estimate the peak ground velocity PGV of pulselike ground motions (closely related to V_p) as a function of magnitude, distance and soil type. Their relation, with the added assumption that $V_p = PGV$, is given by

$$\begin{aligned} \mathrm{E}\left[\ln V_p\right] &= 4.46 + 0.34\mathbf{M} - 0.57\ln(R_{RUP}^2 + 7), \\ \sigma_{\ln V_p} &= 0.39, \end{aligned} \tag{5.62}$$

for rock sites and by

$$\begin{aligned} \mathrm{E}\left[\ln V_p\right] &= 4.58 + 0.34\mathbf{M} - 0.57\ln(R_{RUP}^2 + 7), \\ \sigma_{\ln V_p} &= 0.49, \end{aligned} \tag{5.63}$$

for soil sites. In comparison, the predictive equation developed in this study for the velocity pulse amplitude is

$$\mathrm{E}\left[\ln V_p\right] = 1.699 + 0.608\mathbf{M} - 0.608(M - 6.5)\mathbb{I}(\mathbf{M} > 6.5) + 0.183 F f_{flt,Z} - 0.576 \ln\left(\sqrt{R_{RUP}^2 + 6^2}\right) - 0.094 \ln\left(\hat{V}_{s30}\right) + 0.007 s_{or} d, \quad (5.64)$$

$$\sigma_{\ln V_p} = 0.385.$$

The median and median plus and minus one standard deviation levels from these two relations are plotted as a function of magnitude in Figure 5.13. These plots are for a strike-slip earthquake ($F = 0$) and a site located at $R_{RUP} = 20$ km, having $V_{s30} = 500$ m/s (i.e., a soil site), and experiencing forward directivity. For $\mathbf{M} = 5.5$, we assume $Z_{TOR} = 6$ km and $s_{or}d = 5$ km; for $\mathbf{M} = 6$, $Z_{TOR} = 3$ km and $s_{or}d = 12$ km; for $\mathbf{M} = 6.5$, $Z_{TOR} = 0$ km and $s_{or}d = 25$ km; for $\mathbf{M} = 7$, $Z_{TOR} = 0$ km and $s_{or}d = 50$ km; and for $\mathbf{M} = 7.5$, $Z_{TOR} = 0$ km and $s_{or}d = 100$ km. Figure 5.13 shows that our results fall within the median plus and minus one standard deviation levels predicted by Bray and Rodriguez-Marek (2004). Similar trends are observed for rock sites.

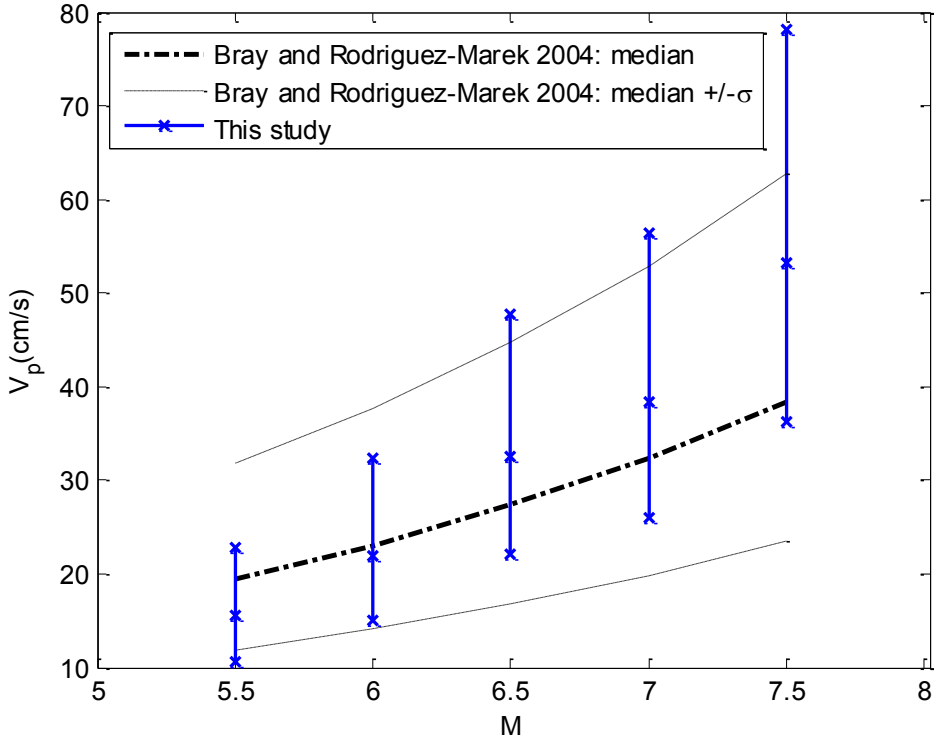

Figure 5.13 Comparison of predictive equations for velocity pulse amplitude V_p for $R_{RUP} = 20$ km and $V_{s30} = 500$ m/s.

For the Arias intensity parameters, we compare our results to the predictive relation proposed by Campbell and Bozorgnia (2010) for the Arias intensity of the geometric mean component. For consistency, we combine our predicted Arias intensity values for the two horizontal components of motion by taking the geometric mean of the two predictions. It is noted that for pulselike motions, we calculate the geometric mean of the Arias intensities of the residual and orthogonal motions, and not of the largest pulse component and orthogonal motion.

The former calculation is a lower bound of the latter, which is not possible because the Arias intensity of the largest pulse component is not a parameter of our model. The standard deviation of the geometric mean of the two Arias intensity predictions is given by

$$\sigma_{\ln I_{a,GM,P}} = \frac{1}{2}\sqrt{\sigma_{z_{P,6}}^2 + 2\rho_{P_{6,13}}\sigma_{z_{P,6}}\sigma_{z_{P,13}} + \sigma_{z_{P,13}}^2} = 0.732 \tag{5.65}$$

for pulselike motions, and

$$\sigma_{\ln I_{a,GM,NP}} = \frac{1}{2}\sqrt{\sigma_{z_{NP,1}}^2 + 2\rho_{NP_{1,8}}\sigma_{z_{NP,1}}\sigma_{z_{NP,8}} + \sigma_{z_{NP,8}}^2} = 1.026 \tag{5.66}$$

for non-pulselike motions, where the subscript GM denotes the geometric mean. The median and median plus and minus one standard deviation levels from these relations are plotted as a function of magnitude in Figures 5.14-5.19. These plots are for the same ($\mathbf{M}$, Z_{TOR}) scenarios used in Figure 5.13, but different combinations of R_{RUP} and V_{s30}. The directivity parameter $s_{or}d$ is not a predictor of the Arias intensity parameters in our model, but it defines the respective probabilities of pulselike and non-pulselike ground motions. For each earthquake scenario, we show our results for pulselike and non-pulselike near-fault ground motions. Several observations can be made from Figures 5.14-5.19 and are discussed next. In general, the two models seem to be in best agreement around $\mathbf{M} = 6$.

First, in a few cases particularly at large magnitude, the median Arias intensity predicted by our model for pulselike ground motions lies below the median Arias intensity predicted for non-pulselike ground motions. This is likely due to the fact that the Arias intensity of the residual motion is used in place of the Arias intensity of the total ground motion in the direction of the largest pulse, i.e., the pulse plus residual motion.

Second, the median Arias intensity predicted by our model for both pulselike and non-pulselike near-fault ground motions generally lies above the median Arias intensity predicted by Campbell and Bozorgnia (2010). Since the model by Campbell and Bozorgnia (2010) is developed for a wide range of distances, ranging from 0 to 200 km, this observation may be an indication that their model at short distances is controlled by scaling at the larger distances and is possibly not well constrained.

Third, the median Arias intensity level predicted by our model for non-pulselike motions is in generally good agreement with the Campbell and Bozorgnia (2010) ground motion model; our prediction falls within the median plus and minus one standard deviation levels predicted by Campbell and Bozorgnia (2010). This may be an indication that the Campbell and Bozorgnia (2010) model does not adequately capture near-fault directivity effects.

Fourth, in the present study, the soil stiffness was not found to be a good predictor of the Arias intensity of pulselike ground motions. While Arias intensity levels decrease for increasing V_{s30} for non-pulselike motions and in the model proposed by Campbell and Bozorgnia (2010), the Arias intensity of pulselike motions does not vary with V_{s30}. For $V_{s30} = 760$ m/s, the median Arias intensity of pulselike motions falls near or above the median plus one standard deviation level predicted by Campbell and Bozorgnia (2010). As more data becomes available, we may be able to find a relation between V_{s30} and the Arias intensity of pulselike ground motions.

Finally, due to the limited size of our database and the limited number of events and recordings per event, the initial standard deviation of the Arias intensity parameters, in particular

for non-pulselike ground motions, is large (see Tables 5.17 and 5.18). Fitting the regression model reduces the standard deviation but it remains large compared to the error standard deviation obtained by Campbell and Bozorgnia (2010). This is true to a lesser extent for pulselike ground motions, possibly because they share more similar rupture characteristics. This discrepancy in the amount of variability may be resolved as more data become available.

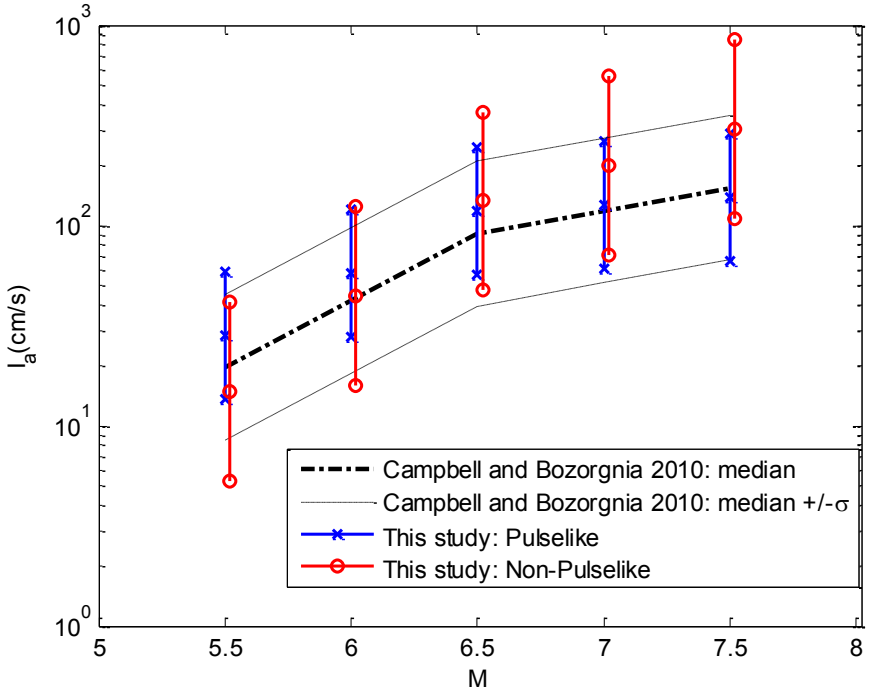

Figure 5.14 Comparison of predictive equations for Arias intensity I_a for $R_{RUP} = 10$ km and $V_{s30} = 350$ m/s.

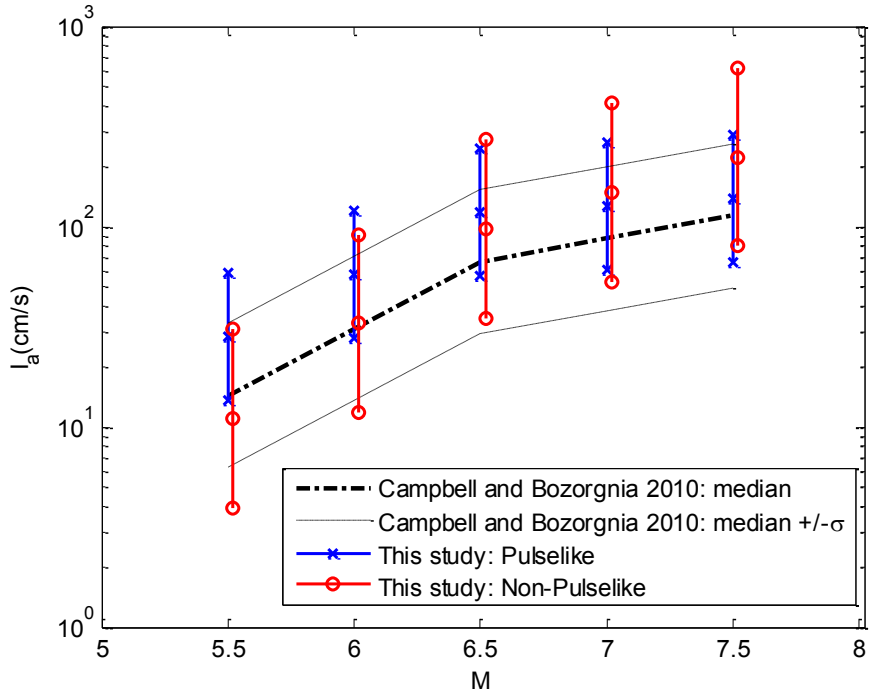

Figure 5.15 Comparison of predictive equations for Arias intensity I_a for $R_{RUP} = 10$ km and $V_{s30} = 500$ m/s.

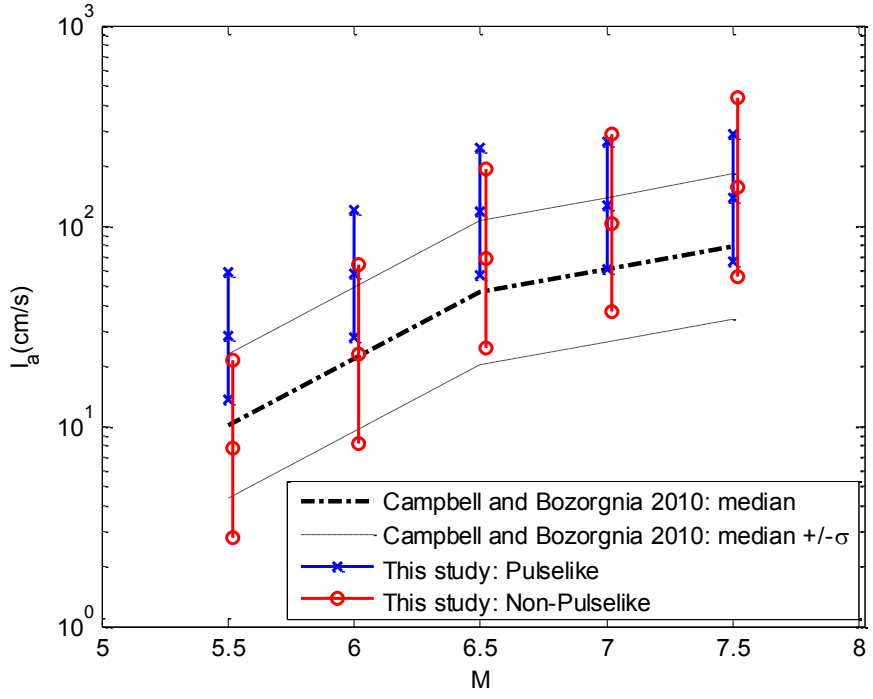

Figure 5.16 Comparison of predictive equations for Arias intensity I_a for $R_{RUP} = 10$ km and $V_{s30} = 760$ m/s.

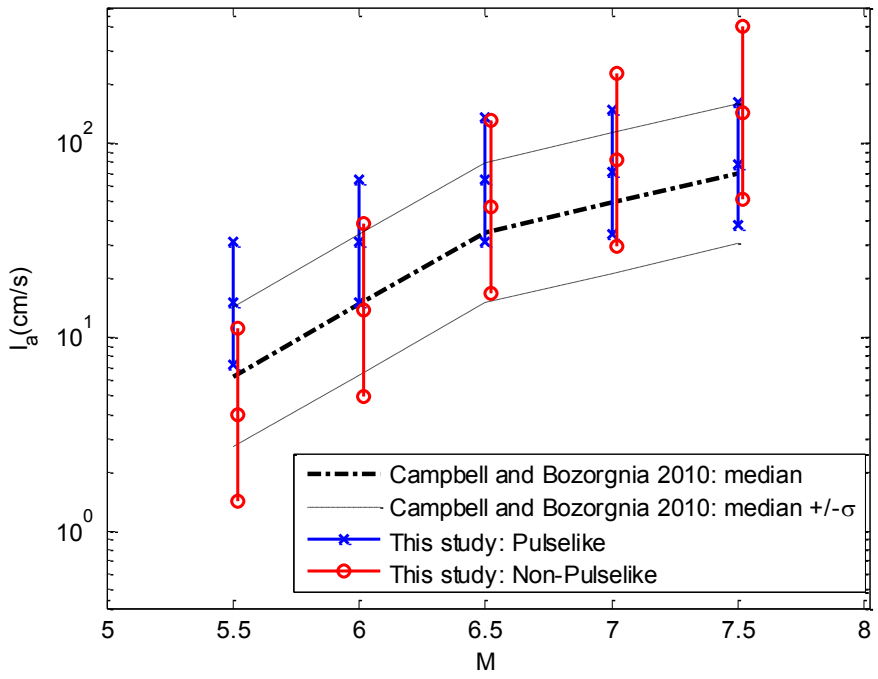

Figure 5.17 Comparison of predictive equations for Arias intensity I_a for $R_{RUP} = 20$ km and $V_{s30} = 350$ m/s.

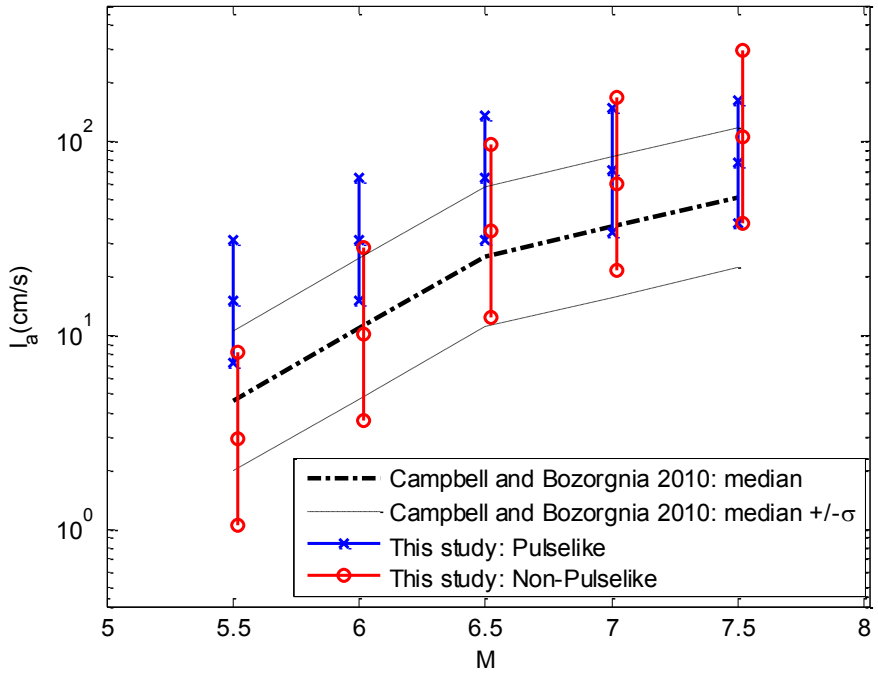

Figure 5.18 Comparison of predictive equations for Arias intensity I_a for $R_{RUP} = 20$ km and $V_{s30} = 500$ m/s.

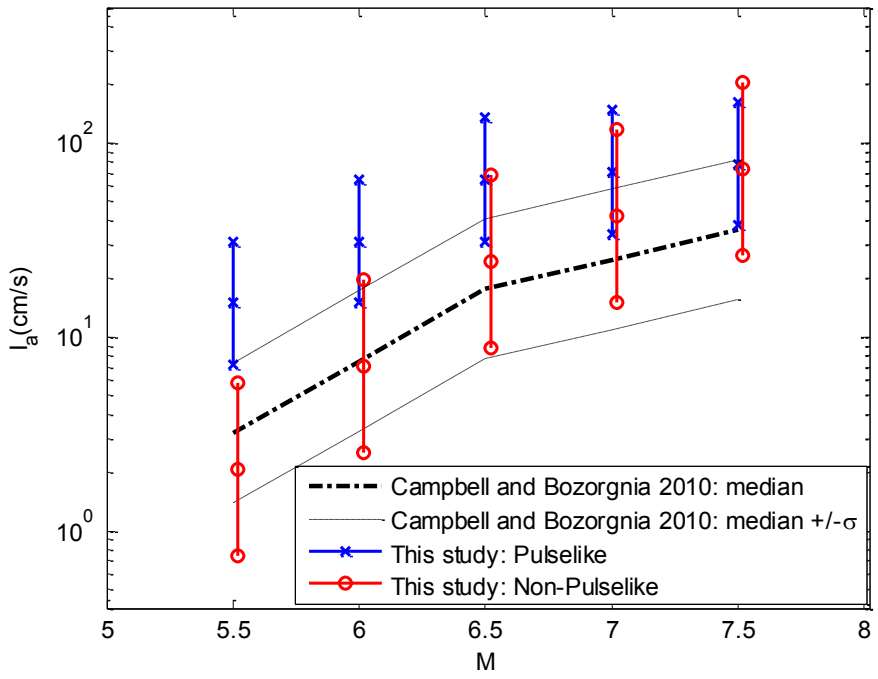

Figure 5.19 Comparison of predictive equations for Arias intensity I_a for $R_{RUP} = 20$ km and $V_{s30} = 760$ m/s.

After examining how the various predictive relations scale with magnitude, we turn our attention to scaling with distance. The median and median plus and minus one standard deviation levels of Arias intensity are plotted as a function of distance in Figures 5.20-5.25. These plots are for different combinations of (**M**, Z_{TOR}) and V_{s30}. As already mentioned, the directivity parameter $s_{or}d$ is not a predictor of the Arias intensity parameters in our model, but it defines the respective probabilities of pulselike and non-pulselike ground motions. We use $\mathbf{M} = 6$, $\mathbf{M} = 6.5$, and $\mathbf{M} = 7$ since our model seems in closest agreement with the model of Campbell and Bozorgnia (2010) near these values. For each earthquake scenario, we show our results for pulselike and non-pulselike near-fault ground motions. From Figures 5.20-5.25, we can make some additional observations. For instance, apart from the larger variability, the scaling of the Arias intensity of non-pulselike ground motions in our model is in good agreement with that of Campbell and Bozorgnia (2010), especially for $\mathbf{M} = 6$ and $\mathbf{M} = 6.5$. On the other hand, the Arias intensity of pulselike motions decays more slowly with distance, even when $V_{s30} = 350$ m/s, which is where our pulselike model is in closest agreement with the model of Campbell and Bozorgnia (2010) (e.g., see Figures 5.20 and 5.23).

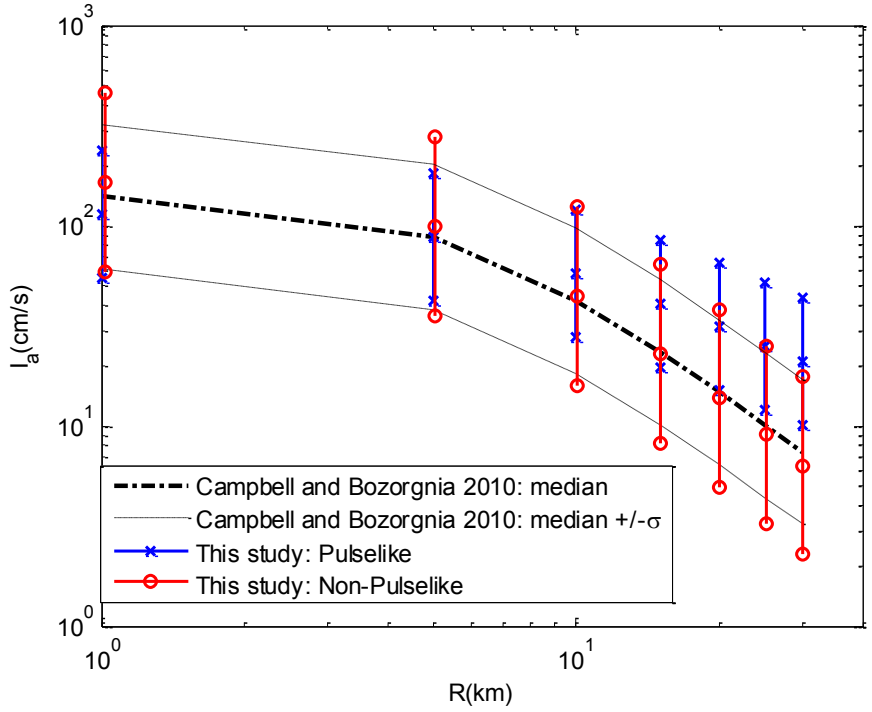

Figure 5.20 Comparison of predictive equations for Arias intensity I_a for M $= 6$, $Z_{TOR} = 3$ km, and $V_{s30} = 350$ m/s.

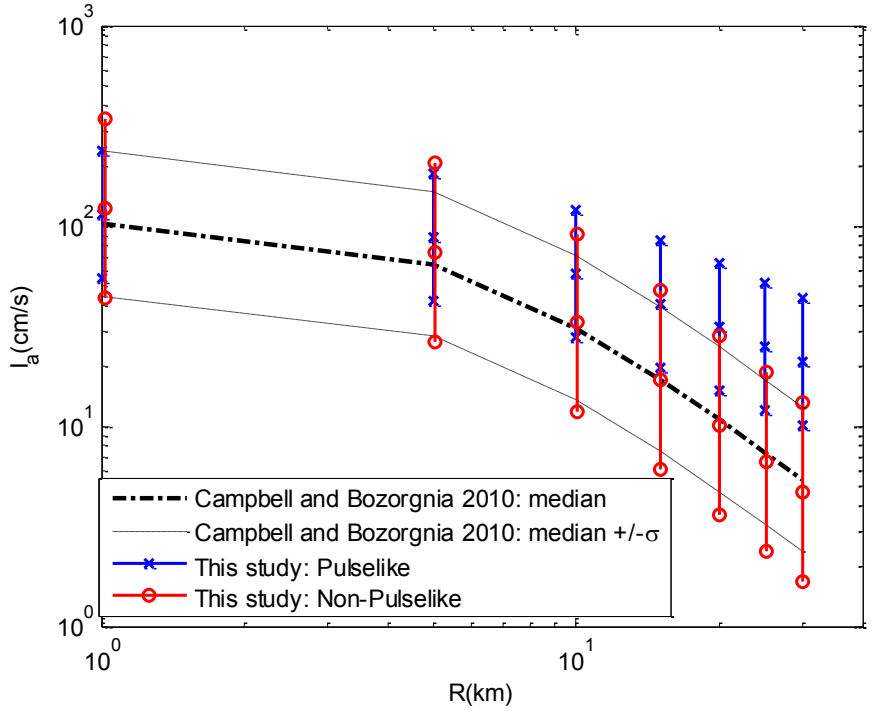

Figure 5.21 Comparison of predictive equations for Arias intensity I_a for M $= 6$, $Z_{TOR} = 3$ km, and $V_{s30} = 500$ m/s.

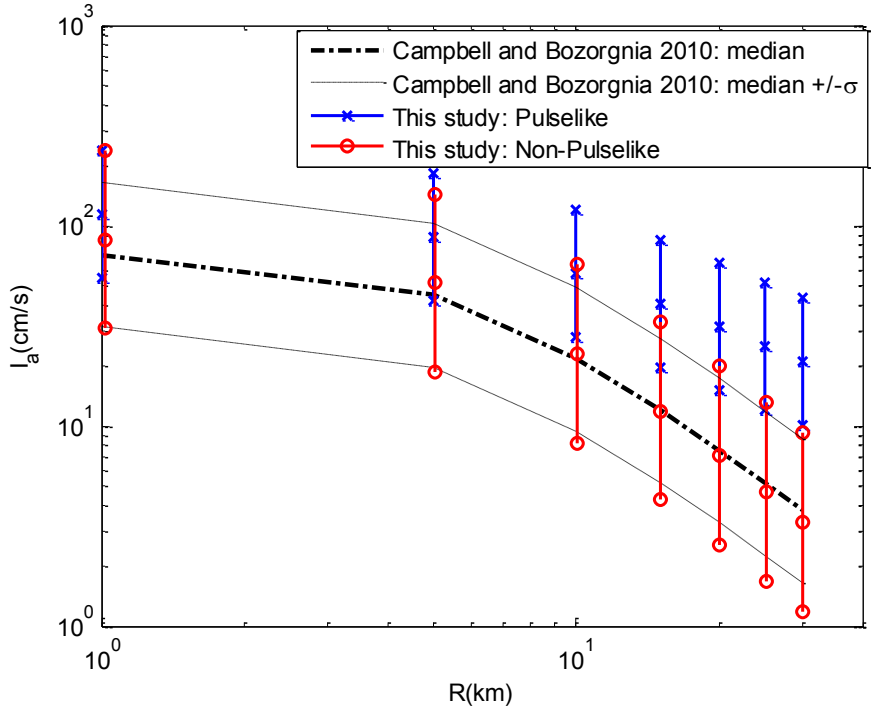

Figure 5.22 Comparison of predictive equations for Arias intensity I_a for M $= 6$, $Z_{TOR} = 3$ km, and $V_{s30} = 760$ m/s.

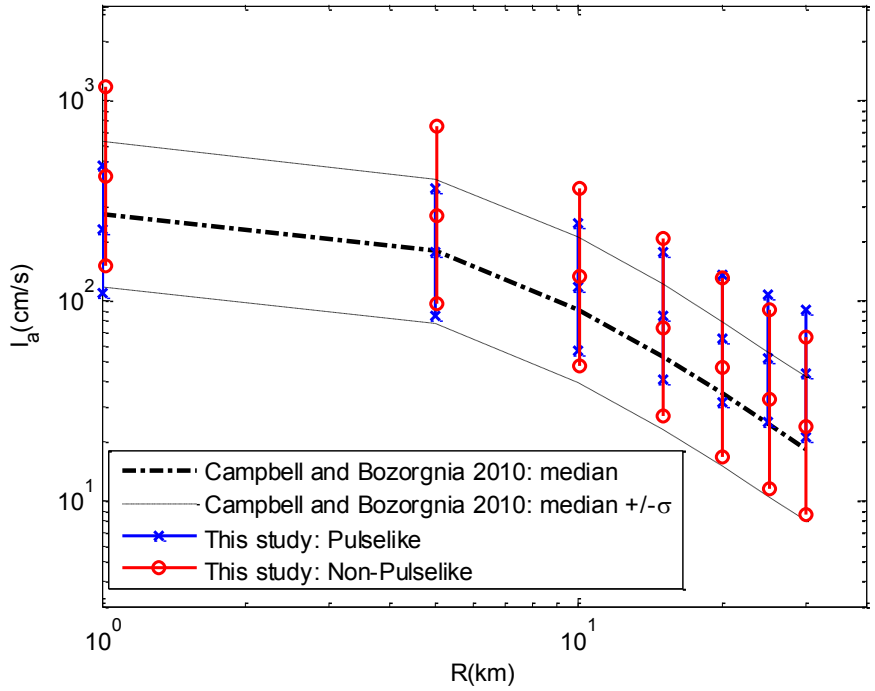

Figure 5.23 Comparison of predictive equations for Arias intensity I_a for M $= 6.5$, $Z_{TOR} = 0$ km, and $V_{s30} = 350$ m/s.

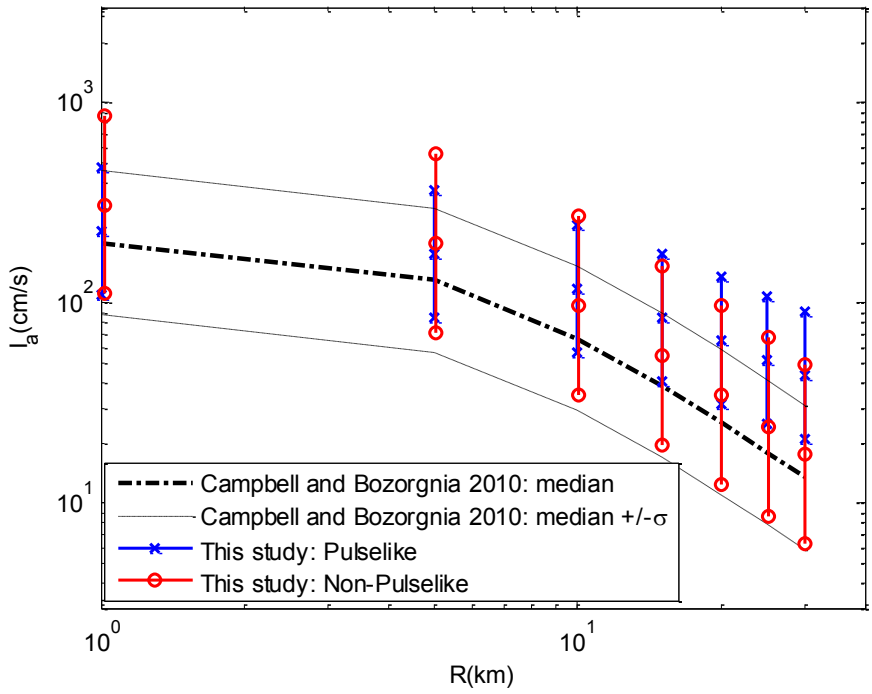

Figure 5.24 Comparison of predictive equations for Arias intensity I_a for M $= 6.5$, $Z_{TOR} = 0$ km, and $V_{s30} = 500$ m/s.

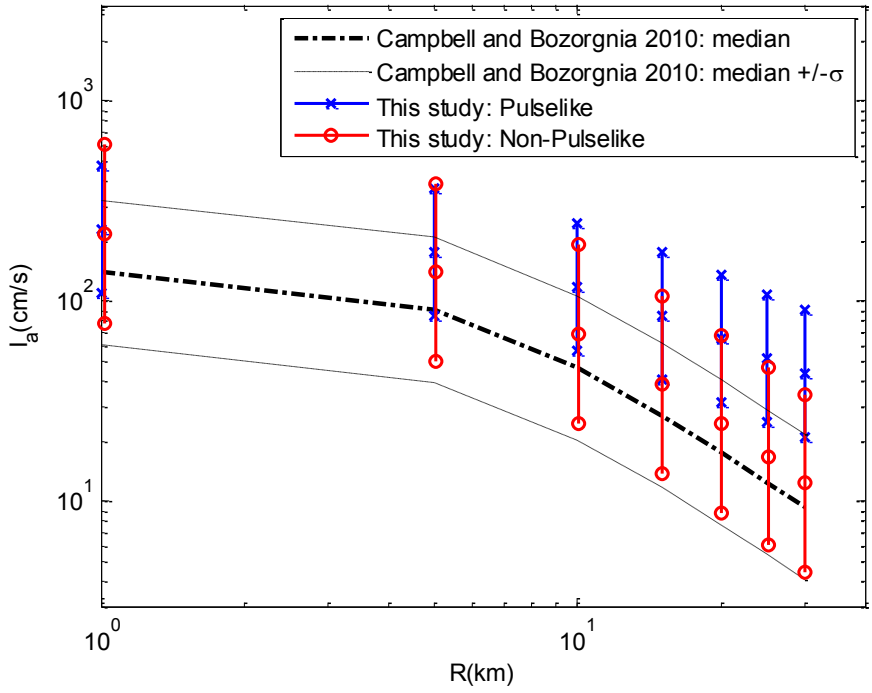

Figure 5.25 Comparison of predictive equations for Arias intensity I_a for M $= 6.5$, $Z_{TOR} = 0$ km, and $V_{s30} = 760$ m/s.

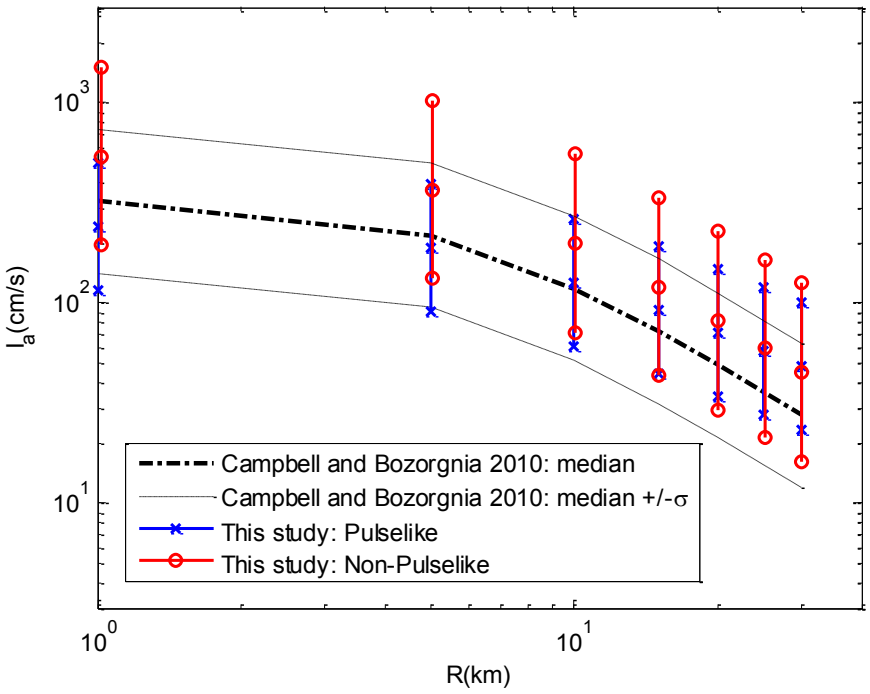

Figure 5.26 Comparison of predictive equations for Arias intensity I_a for M $= 7$, $Z_{TOR} = 0$ km, and $V_{s30} = 350$ m/s.

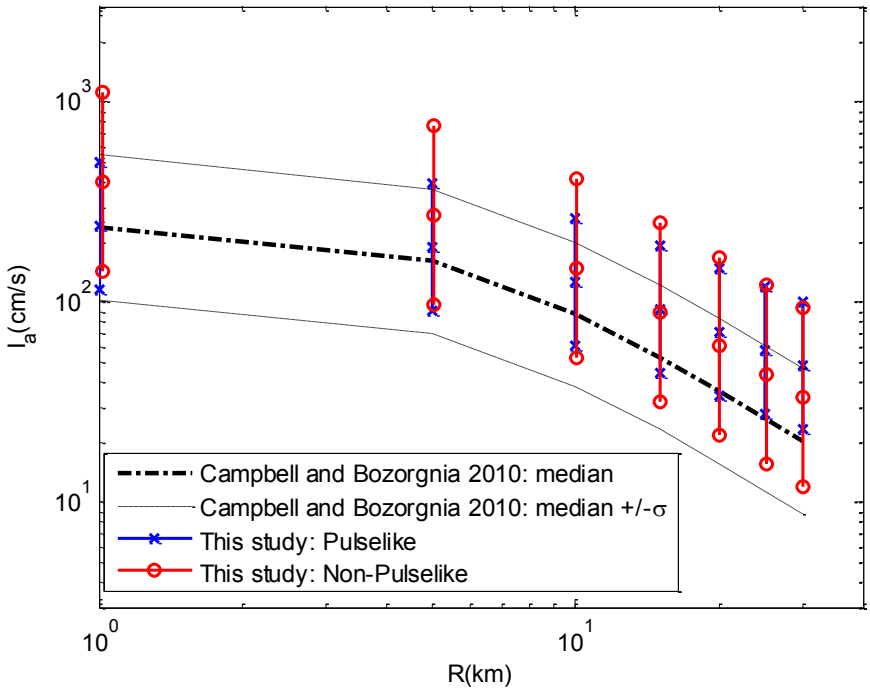

Figure 5.27 Comparison of predictive equations for Arias intensity I_a for M $= 7$, $Z_{TOR} = 0$ km, and $V_{s30} = 500$ m/s.

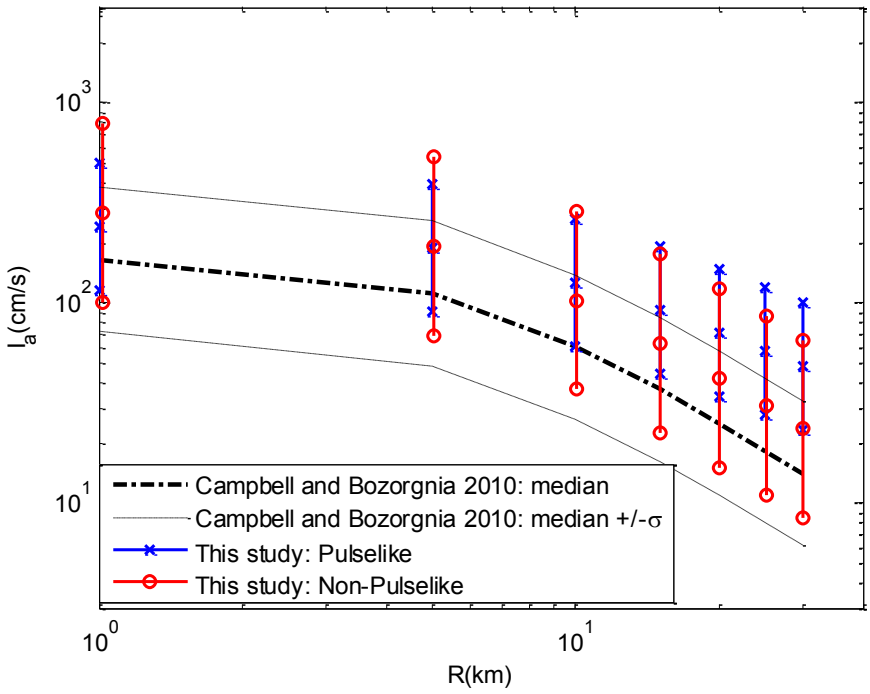

Figure 5.28 Comparison of predictive equations for Arias intensity I_a for $\mathbf{M} = 7$, $Z_{TOR} = 0$ km, and $V_{s30} = 760$ m/s.

5.5.2 Period and frequency parameters

Shahi and Baker (2011) updated the relation that was initially developed by Baker (2007) between the expected value of the pulse period and the earthquake magnitude (see Chapter 2). The new relation is given by

$$\mathrm{E}[\ln T_p] = -5.73 + 0.99\mathbf{M}, \qquad \sigma_{\ln T_p} = 0.56. \tag{5.67}$$

The predictive equation developed for the pulse period in this study is

$$\mathrm{E}[\ln T_p] = -2.479 + 0.670\mathbf{M} - 0.264Ff_{flt,Z} - 0.233\ln(\hat{V}_{s30}) + 0.008s_{or}d, \qquad \sigma_{\ln T_p} = 0.581. \tag{5.68}$$

The median and median plus and minus one standard deviation levels from these two relations are plotted as a function of magnitude and compared in Figure 5.29. Our predictive equation is plotted for the same scenarios used in Figure 5.13 (see Section 5.5.1 for more details). Figure 5.29 shows good agreement between the two relations both in terms of expected values and variability.

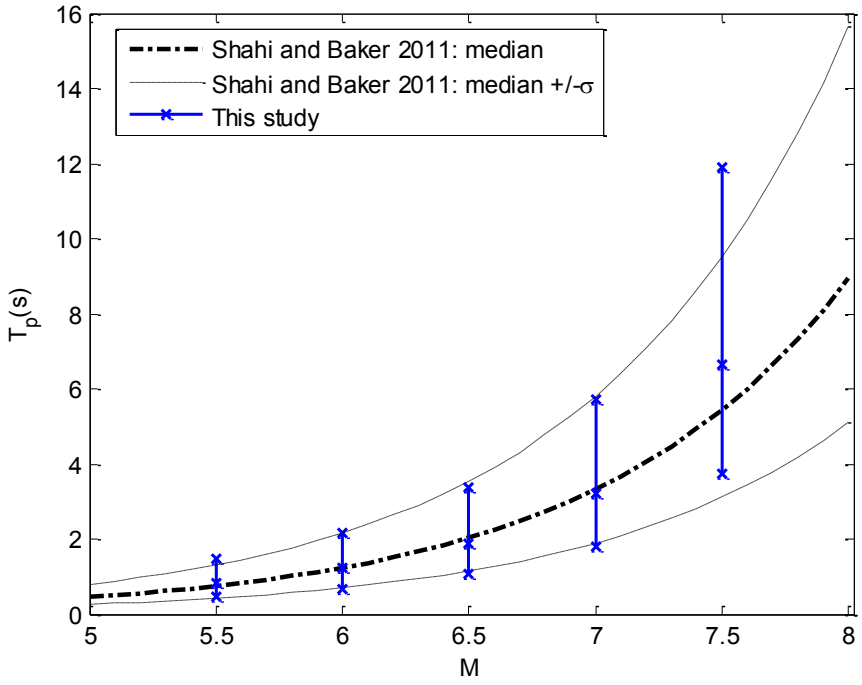

Figure 5.29 Comparison of predictive equations for pulse period T_p.

5.5.3 Time and duration parameters

For the significant duration parameter D_{5-95}, we compare our results to the predictive relations proposed by Kempton and Stewart (2006) and by Bommer et al. (2009). The median and median plus and minus one standard deviation levels from these relations are plotted as a function of magnitude in Figure 5.30. These plots are for the same scenarios used in Figure 5.13 (see Section 5.5.1 for more details). For each earthquake scenario, we show our results for pulselike and non-pulselike near-fault ground motions. The predictions for the two horizontal components of motion are combined using the geometric mean of the two predictions. Figure 5.30 shows good agreement between the relations both in terms of expected values and variability. In our regression analysis, directivity parameter $s_{or}d$ is not found to be a good predictor of time and duration parameters. However, as can be observed in Figure 5.30, the duration of pulselike ground motions does tend to be smaller than that of non-pulselike ground motions. This observation is consistent with the forward directivity effect, which results in shorter but more intense ground motions compared to motions at backward directivity sites.

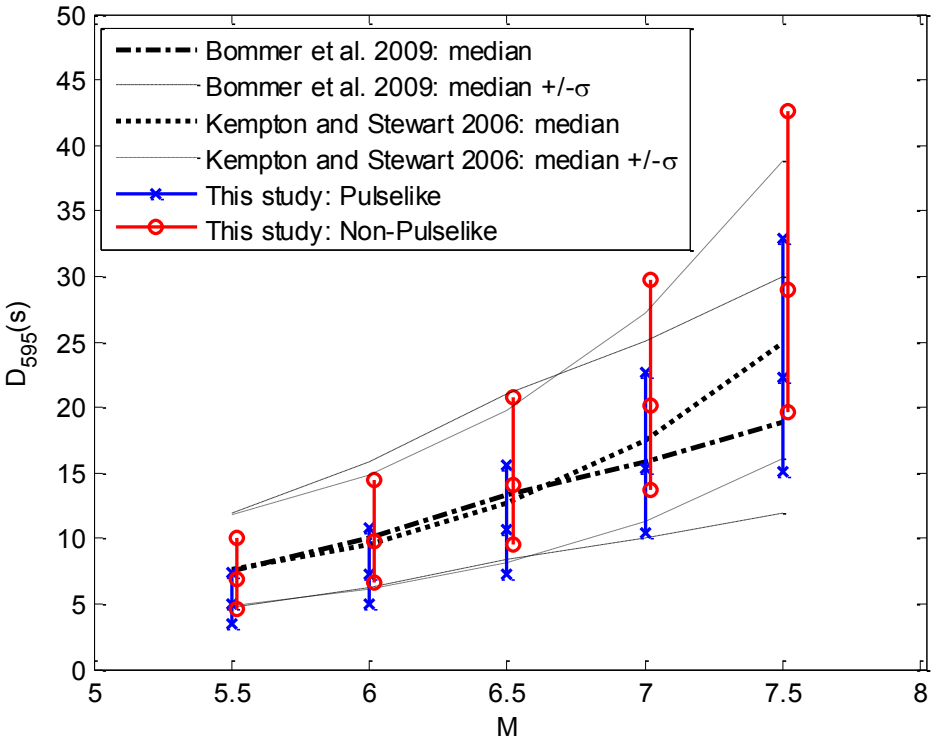

Figure 5.30 Comparison of predictive equations for significant duration D_{5-95}.

5.6 SUMMARY

In this chapter, we estimate the parameters of our stochastic models of pulselike and non-pulselike near-fault ground motions by fitting these models to recorded ground motions in two databases, one for pulselike motions and another for non-pulselike motions. Using the data generated by these fittings, we develop predictive equations for the model parameters in terms of earthquake and source characteristics. The databases used in this study are subsets of PEER's NGA-West2 database. They consist of pulselike and non-pulselike ground motions from large earthquakes ($\mathbf{M} \geq 5.5$), recorded at sites located within 30 km from the fault rupture. To correspond with the model formulation, each pulselike ground motion record is rotated into its component containing the largest horizontal pulse and the corresponding orthogonal component. Each non-pulselike ground motion record is rotated into horizontal components in the major and intermediate "principal directions".

In Section 5.3, we describe the methods of fitting and parameter identification of the pulselike and non-pulselike ground motion models to target recorded ground motions. Most model parameters are related to physically meaningful characteristics of the ground motion. The fitting procedure generally consists of matching these characteristics to those of recorded ground motions, either directly or by matching certain evolutionary statistical characteristics. By fitting to the selected pulselike and non-pulselike databases, samples of model parameters are obtained.

Section 5.4 describes the development of empirical predictive relations for the parameters of the pulselike and non-pulselike ground motion models in terms of earthquake source and site explanatory variables. The model parameters are classified into four categories: (1) intensity parameters (V_p and I_a), (2) period and frequency parameters (T_p and ω_{mid}), (3) time and duration parameters ($t_{max,p}$, D_{0-5}, D_{0-30}, and D_{5-95}) and (4) "other" parameters (γ, ν, ω', and ζ_f). The samples of fitted parameter values are transformed to the normal space, where they are regressed against the explanatory variables (F, $\mathbf{M}$, Z_{TOR}, R_{RUP}, V_{s30}, $s_{or}d$). A random-effects model is used to account for multiple records from certain earthquakes. To the greatest extent possible, the functional forms of the predictive equations are chosen to be consistent with seismological theory. Moreover, the directivity explanatory variable $s_{or}d$ is considered only in the predictive relations for the pulse parameters. Next, the correlations between the model parameters in the normal space are estimated. These correlations reflect the dependencies among the model parameters. In summary of the results, the predictive equations are presented in (5.42), (5.46), (5.51) and (5.60), the estimated regression coefficients and standard deviations are listed in Tables 5.17, 5.18, 5.21, 5.22, 5.25, 5.26, 5.31 and 5.32, and the estimated correlation coefficients are listed in Tables 5.35 and 5.36. This information allows generating sets of the parameters of the pulselike and non-pulselike models for any given set of specified earthquake source and site characteristics (F, $\mathbf{M}$, Z_{TOR}, R_{RUP}, V_{s30}, $s_{or}d$).

Finally, in Section 5.5, we compare our empirical predictive equations with several similar relations proposed in the literature. The comparison shows that our relations provide estimates that are consistent with those provided by other GMPEs. The advantage of our relations is that they distinguish between pulselike and non-pulselike ground motions. Indeed, because of the rupture directivity effect, the characteristics of pulselike and non-pulselike ground motions differ. These differences are borne out by the predictive relations that we develop.

6 Simulation of Near-Fault Ground Motions

6.1 INTRODUCTION

With the stochastic model of near-fault ground motion in two orthogonal horizontal directions formulated (Chapter 4) and predictive equations for its parameters developed (Chapter 5), it is now possible to simulate artificial pulselike and non-pulselike near-fault ground motions that possess the physical and statistical characteristics of real near-fault ground motions, including the characteristics of the velocity pulse arising due to the directivity effect in pulselike motions. In this chapter we consider two simulation approaches: (a) simulating near-fault ground motions that have the same model parameters as those identified for a recorded near-fault ground motion, and (b) simulating near-fault ground motions for specified earthquake source and site characteristics. The former are useful to examine how other realizations of the same event may have appeared. This approach is also useful for validating the simulation method by way of comparing various characteristics of the simulated motions with those of the recorded motion. The second approach is useful for design situations, where the specification is in terms of the characteristics of an earthquake source (type of faulting, location of hypocenter, magnitude, and rupture dimensions) and a site (position relative to the fault rupture, shear-wave velocity). This approach produces near-fault ground motions that have the same natural variability that is present in a collection of recorded ground motions with the specified earthquake source and site characteristics.

In this chapter we simulate samples of two horizontal orthogonal components of pulselike and non-pulselike near-fault ground motions using both methods. By comparing various characteristics of the simulated motions with those of recorded motions, and the spectra of the synthetic ground motions to spectra from the most recent Next Generation Attenuation (NGA-West2) GMPEs, we provide validation for the proposed models and the predictive equations of the model parameters. The chapter ends by describing and illustrating a procedure to incorporate a model of the fling step into our ground motion simulation methodology. Despite being preliminary, this addition permits a more complete characterization of near-fault ground motion, accounting for both the directivity effect and fling step.

6.2 SIMULATION OF NEAR-FAULT GROUND MOTIONS

The parameterized stochastic model of pulselike near-fault ground motion is used to simulate pulselike ground motions in the direction of the largest pulse and the corresponding orthogonal direction. The parameterized stochastic model of non-pulselike near-fault ground motion is used to simulate non-pulselike ground motions in the major and intermediate horizontal "principal directions". As described in Chapter 4, the stochastic model of pulselike ground motion in the direction of the largest pulse consists of two sub-models, one for the directivity pulse and one for the residual motion. As also described in Chapter 4, a modified version of the idealized pulse model by Mavroeidis and Papageorgiou (2003) is employed to model the pulse and a modified version of the non-stationary filtered white-noise model by Rezaeian and Der Kiureghian (2008, 2010) is employed to model the residual. The latter model is also used to describe near-fault ground motion components that do not contain a pulse, namely the motion in the horizontal

direction orthogonal to the direction of the largest pulse, and the major and intermediate components of non-pulselike ground motions.

6.2.1 Simulation of a pulse motion

For a given set of the five parameters (V_p, T_p, γ, ν, $t_{max,p}$) of the mMP pulse model defined in Section 4.4.1.1, the pulse velocity waveform $v_{pul}(t)$ is computed according to (4.4-4.6). This pulse waveform is deterministic for a given set of parameters.

6.2.2 Simulation of a realization of the filtered white-noise process

In this section, we describe the procedure for simulating the residual and orthogonal motions of pulselike records, and the major and intermediate ground motion components of non-pulselike records. These synthetic motions are generated for a given set of the seven parameters (α, β, c, $t_{max,q}$, ω_{mid}, ω', ζ_f), which were defined in Section 4.4.1.2.

First, we generate a band-limited white-noise process at a time step $\Delta t = 0.005$ s, which is the time step used for all the original and resampled records. This time step determines the upper frequency limit, i.e., the Nyquist frequency $f_N = 1/(2\Delta t)$, for the simulated motions (see Chapter 3). Next, parameters (α, β, c, $t_{max,q}$) are used in (4.9) to compute the modulating function $q(t)$, while parameters (ω_{mid}, ω', ζ_f) are used to define the filter as given in (4.8) and (4-10-4.12). The modulating function and the filter are then used in (4.7), together with the simulated band-limited white-noise process, to generate a synthetic acceleration time series. This synthetic motion is low-cut filtered to assure zero velocity and displacement at the end of the simulated time series. As described in Section 3.3, a 4th order acausal Butterworth filter having a magnitude dependent cutoff frequency given by (3.15) and applied in the frequency domain is used. The processed time series constitutes one sample of the simulated acceleration process $a_{MFW}(t)$. Note that our low-cut filtering approach differs from the one employed by Rezaeian and Der Kiureghian (2010b), who used a critically damped, second-order oscillator with a constant filter frequency of 0.1 Hz.

In Chapter 5, we described the procedure for fitting the modulating function $q(t)$ to a target recorded acceleration $a_{rec}(t)$. The aim of that procedure is to match as closely as possible the cumulative Arias intensity of a resulting synthetic acceleration, $I_{a,MFW}(t)$, to that of the target recorded acceleration, $I_{a,rec}(t)$. To attain this goal, we fit parameters (α, β, c, $t_{max,q}$) of the modulating function in (4.9) by matching as closely as possible the cumulative Arias intensity of the modulating function, $I_{a,q}(t)$, to that of the target recorded acceleration, $I_{a,rec}(t)$. This is achieved by equating the parameters ($I_{a,q}$, $D_{0-5,q}$, $D_{0-30,q}$, $D_{0-95,q}$) of the modulating function to parameters ($I_{a,rec}$, $D_{0-5,rec}$, $D_{0-30,rec}$, $D_{0-95,rec}$) of the target. However, due to the stochastic nature of the underlying white-noise process, this procedure does not guarantee that the parameters ($I_{a,MFW}$, $D_{0-5,MFW}$, $D_{0-30,MFW}$, $D_{0-95,MFW}$) of a synthetic acceleration will match the corresponding parameters of the modulating function and consequently of the target recorded motion. Indeed, from the definition of the modulated and filtered white-noise acceleration process, we only have that

$$E\left[I_{a,MFW}(t)\right] = I_{a,q}(t). \tag{6.1}$$

Therefore, to eliminate variability in the total Arias intensity arising from the underlying white-noise, each simulated and low-cut filtered motion $a_{MFW}(t)$ is uniformly scaled,

$$a^*_{MFW}(t) = SF \cdot a_{MFW}(t), \tag{6.2}$$

where the scale factor SF is given by

$$SF = \sqrt{\frac{I_{a,q}}{I_{a,MFW}}}. \tag{6.3}$$

Hence, the scaled synthetic acceleration $a^*_{MFW}(t)$ has total Arias intensity $I^*_{a,MFW} = I_{a,q} = I_{a,rec}$. Note that $I_{a,rec}$ can be the value computed for a fitted target record, or simulated for a given set of earthquake source and site characteristics, as we illustrate later in this Chapter. Simulations requiring a scale factor $SF < 1/2$ or $SF > 2$ are discarded. The matching of the remaining target values of ($D_{0-5,rec}$, $D_{0-30,rec}$, $D_{0-95,rec}$) can only be guaranteed in an average sense.

6.2.3 Simulation of ground motion components containing a pulse

Having simulated a velocity pulse $v_{pul}(t)$ with parameters (V_p, T_p, γ, ν, $t_{max,p}$) and a residual acceleration motion $a_{res}(t) = a^*_{MFW}(t)$ with parameters (α_{res}, β_{res}, c_{res}, $t_{max,q,res}$, $\omega_{mid,res}$, ω'_{res}, $\zeta_{f,res}$), we combine the two to obtain a realization of the horizontal component of the pulselike accelerogram that contains the largest pulse. To do this, the derivative $a_{pul}(t)$ of $v_{pul}(t)$ is added to $a_{res}(t)$ to obtain a sample of the total acceleration waveform $a_{PP}(t)$. The resulting acceleration time series naturally has zero velocity and displacement values at the end of the record. This is because both the pulse and residual models possess these characteristics. It is noted that applying the low-cut filter to the sum of the simulated pulse and the simulated residual motion would have resulted in the undesirable loss of the characteristic large period pulse. Integrations of the total acceleration motion yield the velocity and displacements time series of the artificial ground motion.

6.2.4 Simulation of ground motion components not containing a pulse

The procedure of Section 6.2.2 is used to simulate near-fault ground motion components that do not contain a pulse. In the context of this study, these components consist of, for pulselike ground motion, the component in the horizontal direction orthogonal to the direction of the largest pulse (marked by subscript PO) and, for non-pulselike ground motion, the major and intermediate components (marked by subscripts $NP1$ and $NP2$). Parameters (α_{PO}, β_{PO}, c_{PO}, $t_{max,q,PO}$, $\omega_{mid,PO}$, ω'_{PO}, $\zeta_{f,PO}$), (α_{NP1}, β_{NP1}, c_{NP1}, $t_{max,q,NP1}$, $\omega_{mid,NP1}$, ω'_{NP1}, $\zeta_{f,NP1}$), and (α_{NP2}, β_{NP2}, c_{NP2}, $t_{max,q,NP2}$, $\omega_{mid,NP2}$, ω'_{NP2}, $\zeta_{f,NP2}$) are used to simulate ground acceleration components $a_{PO}(t)$, $a_{NP1}(t)$ and $a_{NP2}(t)$, respectively. As a result of application of the low-cut filter, the resulting acceleration time series all have zero velocity and displacement values at their end. As a result of scaling, these time series all match their target total Arias intensity values.

6.2.5 Additional considerations

When simulating the two horizontal components $a_{PP}(t)$ and $a_{PO}(t)$ of a pulselike ground motion for a given set of model parameters, we assume that the residual and orthogonal ground

motion components are statistically independent. We thus generate their underlying white noises as statistically independent processes. Similarly, when simulating the two horizontal components $a_{NP1}(t)$ and $a_{NP2}(t)$ of a non-pulselike motion for a given set of model parameters, we assume that these two "principal" ground motion components are statistically independent. We thus generate their underlying white noises as statistically independent processes.

For fixed pulselike model parameters, the directivity pulse in each of the simulated pulselike ground motion components is the same, as are the two filter IRFs and two modulating functions of the residual and orthogonal motions. However, the residual and orthogonal motions randomly vary from sample to sample due to the randomness in the underlying white-noise processes. Similarly, for a given set of non-pulselike model parameters, the two filter IRFs and two modulating functions of the major and intermediate components remain the same. However, the simulated major and intermediate ground motion components randomly vary from sample to sample due to the randomness in the underlying white-noise processes. This is reasonable, since we are considering random realizations of the same event; the variations due to the underlying white noise can be thought of as variations in the sequence of ruptures in the fault. However, the overall rupture size and slip direction remain the same for all realizations of a single event. Therefore, while the residual of pulselike motions varies, the waveform of the directivity pulse, which depends on the overall rupture geometry and propagation, is unique. The constraint of a deterministic pulse waveform for a given set of pulse parameters can be eliminated by modeling the pulse as a stochastic process. Broccardo and Der Kiureghian (2014) developed a model that uses frequency-domain discretization to describe the pulse as a narrowband stochastic process. The model by Broccardo and Der Kiureghian (2014) can be used in place of the mMP pulse model, but this development is not pursued in this study.

In the subsequent sections, we illustrate the simulation of motions using model parameters fitted to a recorded motion and model parameters simulated using the predictive equations for a given set of earthquake source and site characteristics.

6.3 SIMULATION BY USE OF FITTED MODEL PARAMETERS

We start by simulating near-fault ground motions using model parameters that were identified by fitting to recorded near-fault ground motions as described in Chapter 5. The model parameters are kept constant. The variability in the simulated motions results from variability in the underlying white-noise process. This approach is useful for validating the model and simulation method by way of comparing various characteristics of the simulated motions with those of the recorded motion. We illustrate this approach for one pulselike and one non-pulselike recorded motion from our databases.

6.3.1 Example application 1: pulselike ground motion

We consider NGA record #171, which was identified as pulselike by Shahi and Baker (2011) and was introduced in Section 5.3.3. The acceleration, velocity and displacement time series of the component containing the largest pulse and of the corresponding orthogonal component of this record were plotted in Figure 5.2. Furthermore, the acceleration and velocity time series of the largest pulse extracted from this record, as well as those of the resulting residual motion and total motion were plotted in Figure 5.3. These times series are repeated in Figure 6.1 for comparison with simulated time series. The fitted mMP pulse and the modulating functions fitted to the

residual and orthogonal motions of this record were shown in Figures 5.4 and 5.6, respectively. The identified pulse parameters and parameters of the fitted residual motion and orthogonal motion models for this record were listed in Tables 5.3-5.9. In particular, the pulse period is $T_p = 2.8$ s. These identified parameters are used as input parameters to the stochastic model of pulselike motion, which is used to generate 300 artificial pairs of acceleration time series, as described above.

Figure 6.1 shows the details in the direction of the largest pulse of one of these simulated motions (right) alongside the recorded counterparts (left). In particular, it shows the acceleration and velocity time series of the simulated mMP pulse, as well as those of the simulated residual motion and total motion (sum of the simulated pulse and residual motions). We observe clear similarities between the features of the recorded and simulated motions.

Figure 6.2 shows the acceleration times series of the two components of record NGA#171 and a sample of five of the motions simulated using the fitted model parameters. Again similarities can be observed in the waveforms of the simulated and recorded motions in terms of amplitude, duration and frequency content. Figure 6.3 shows the velocity time series that are obtained by integration of the acceleration time series in Figure 6.2. The simulated ground motion components are similar to those of the recorded motion, including the presence, shape and time of the large velocity pulse in the largest pulse component. Finally, Figure 6.4 shows the displacement time series that are obtained by integration of the velocity time series in Figure 6.3. Similarities are observed between the recorded and simulated motions, but they are not as marked as those in the acceleration and velocity domains. This is because there are no constraints on displacements in the fitting procedure (the pulse is fitted in the velocity domain and the residual and orthogonal motions are fitted in the acceleration domain), and because the displacement time series is highly dependent on the long period content of the motion and is thus highly sensitive to the choice of the parameters of the low-cut filter. Here, we have used the magnitude $\mathbf{M} = 6.53$ of record NGA#171 in (3.15) to compute $f_c = 0.142$ Hz, which corresponds to a long-period cutoff at 7.03 s (see Chapter 3).

Figure 6.5 shows the Husid plots of the two horizontal components of record NGA#171, of the modulating functions fitted to these components, and of the five simulated motions plotted in Figures 6.2-6.4. It can be seen that the Husid plot of the orthogonal component of the simulated motions generally matches the Husid plots of the corresponding recorded motion and fitted modulating function, including the value of the total Arias intensity. This feature is guaranteed by scaling the simulated motions using (6.2) and (6.3). This observation does not apply to the total component in the direction of the largest pulse, but only to the residual motion. Even if the Husid plot of a simulated residual motion generally matches that of the recorded residual motion, the addition of the fitted pulse does not guarantee that the Husid plot of the total simulated motion matches that of the total recorded motion. This mismatch is due to the non-linearity of the Arias intensity function relative to the intensities of the residual and pulse motions and is illustrated in the left portion of Figure 6.5. Figure 6.6 shows the recorded ground motion and the 300 simulated motions, in the direction of the largest pulse and in the corresponding orthogonal direction. The figure displays an overlay of the 300 simulated motions as thin grey lines together with the recorded motion in blue line. The thin lines illustrate the range of possible realizations of acceleration time series using the fitted model parameters. It can be seen that the general features of the simulated and recorded acceleration time series are similar. Furthermore, the recorded motion is well within the range of the 300 simulated motions.

Elastic pseudo-acceleration response spectra at 5% damping are computed for the recorded and simulated ground motions at periods ranging from 0.02 s to 15 s. Figure 6.7 shows the spectra for the recorded ground motion components by thick blue dashed lines and the spectra of the simulated motions with thin grey lines. The median levels of the spectra of the simulated motions are shown by thick black lines. The median plus and minus one standard deviation levels are shown by thick black dotted lines. One can observe that the response spectra of the recorded ground motion components fall within the ranges spanned by the spectra of the simulated ground motion components at all periods. The recorded motion can be regarded as one sample realization of the stochastic model for the given parameters.

We focus our attention on the ground motion component containing the largest pulse. In Figure 6.7 (left), a peak in the response spectra of both the recorded and simulated motions can be seen at periods around 2 s. This is due to the directivity pulse. Indeed, in the recorded and simulated motions, the extracted and simulated velocity pulses have period $T_p = 2.8$ s. The lower period of the peak is consistent with observations made by Somerville (2003) and Shahi and Baker (2011) regarding the characteristics of the pseudo-acceleration response spectra of pulselike near-fault acceleration time series. For example, Somerville (2003) suggested scaling up conventional response spectra by a cosine shaped function centered at $0.75T_p$ to account for a forward directivity velocity pulse of period T_p. For the present case, this would correspond to a peak in the response spectrum at a period of 2.1 s. Shahi and Baker (2011) computed the mean amplification in the pseudo-acceleration spectrum due to the presence of a pulse in the ground motion and found that it takes a maximum value at $0.88T_p$. For the present case, this would correspond to a peak in the response spectrum at a period of 2.5 s. It is evident that the simulated pulselike motions are consistent with these findings.

Moreover for the ground motion component containing the largest pulse, and in accordance with the period of the pulse, the median spectrum of the simulated motions is comparable to the spectrum of the recorded motion at periods larger than about 2 s. However, at periods below 2 s, where the spectra are primarily influenced by the residual motion, the recorded and median simulated spectra show significant differences. This is due to the idealized nature of our model for the residual. Obviously, with smooth models of the modulating function and the filter IRF, and with a small number of model parameters, it is not possible to capture all the details of the recorded ground motion. What is important is to describe the essential characteristics. In this case, given the pulselike nature of the motion, the long-period segment of the response spectrum is the important feature, and that is well described by the model.

In the orthogonal direction, Figure 6.7 (right), due to the non-pulselike nature of the ground motion, we do not expect the median spectrum of the simulated motions to match the spectrum of the recorded motion at the longer periods. Indeed, the recorded and median simulated spectra show significant differences at most periods. Again, this is due to the idealized nature of our ground motion model, which cannot reproduce all the details of the recorded ground motion. Nevertheless, the spectrum of the recorded motion is within the ensemble of spectra of the simulated motions.

At each period of interest, the geometric mean spectrum of two ground motion components is computed as the square root of the product of the two corresponding spectral values. Figure 6.8 shows in a dashed blue line the geometric mean pseudo-acceleration response spectrum at 5% damping of the largest pulse and orthogonal components of record NGA#171.

The figure also shows in thin grey lines the geometric mean spectra of the 300 simulated ground motions, as well as their median (black line) and median plus and minus one standard deviation levels (dotted black lines). The right portion of Figure 6.8 shows the standard deviation of the natural logarithm of the geometric mean spectra at 5% damping of the 300 simulated ground motions. (This is approximately equal to the coefficient of variation of the spectral ordinates.) For the fixed model parameter values, it illustrates the variability arising from randomness in the underlying white-noise processes. This variability tends to increase with oscillator period from a value of about 0.1 at short periods to reach a value of about 0.3 at a period of 8.5 s, after which the variability decreases slightly with period, to a value of about 0.2 at a period of 15 s.

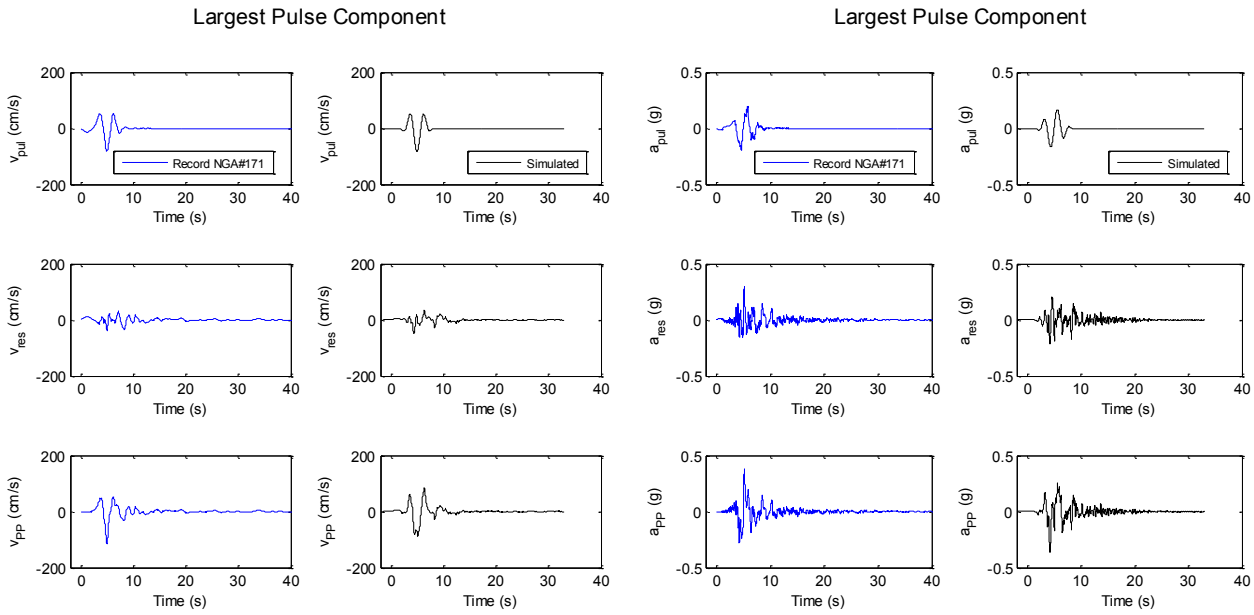

Figure 6.1 Pulselike ground motion in the direction of the largest pulse for record NGA#171 (blue) and sample simulated motion with parameters identified for record NGA#171 (black): velocity times series (left), acceleration time series (right), pulse motion (top), residual motion (middle), and total motion (bottom).

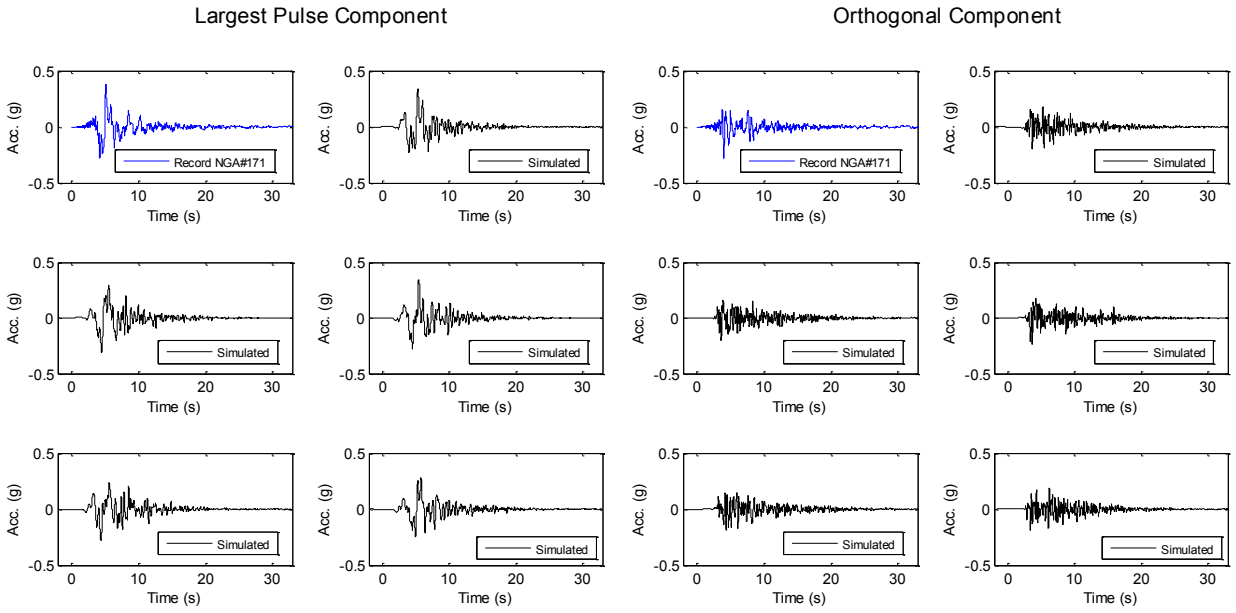

Figure 6.2 Acceleration time series of record NGA#171 (blue) and five simulated motion with parameters identified for record NGA#171 (black): ground motion component in the direction of the largest pulse (left) and corresponding orthogonal direction (right).

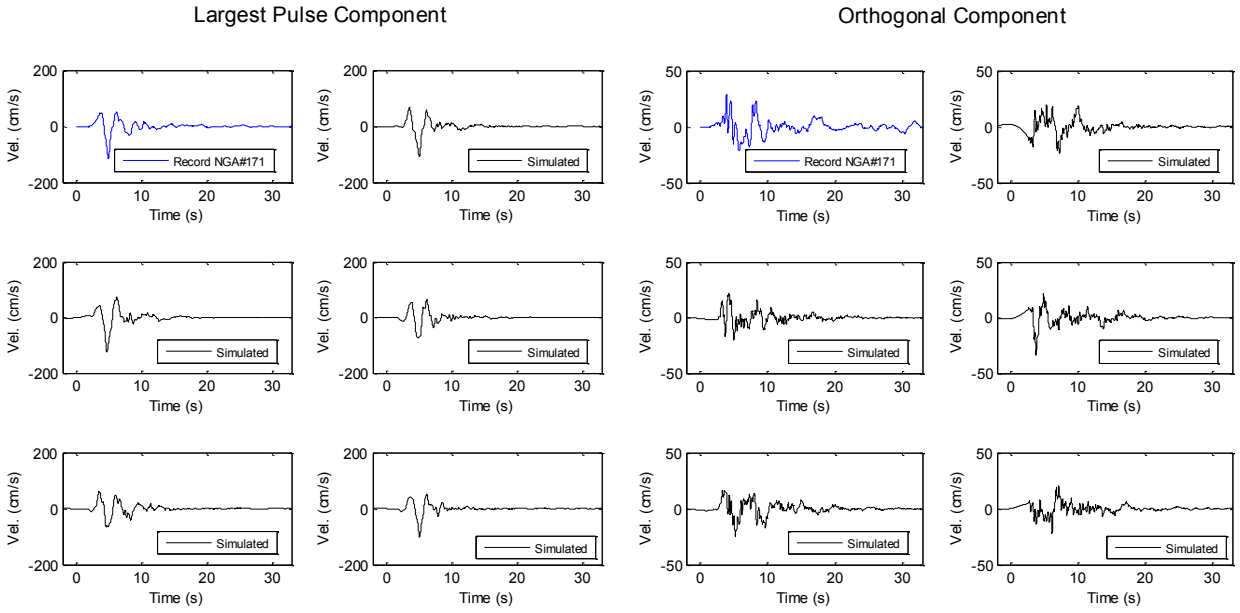

Figure 6.3 Velocity time series of record NGA#171 (blue) and five simulated motion with parameters identified for record NGA#171 (black): ground motion component in the direction of the largest pulse (left) and corresponding orthogonal direction (right).

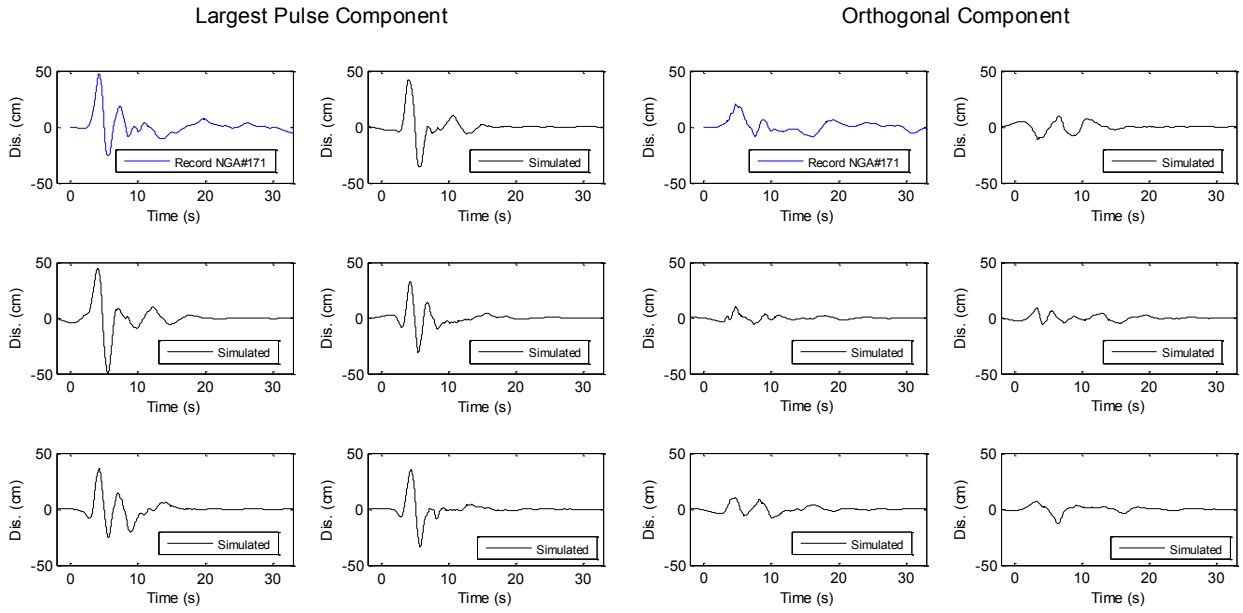

Figure 6.4 Displacement time series of record NGA#171 (blue) and five simulated motion with parameters identified for record NGA#171 (black): ground motion component in the direction of the largest pulse (left) and corresponding orthogonal direction (right).

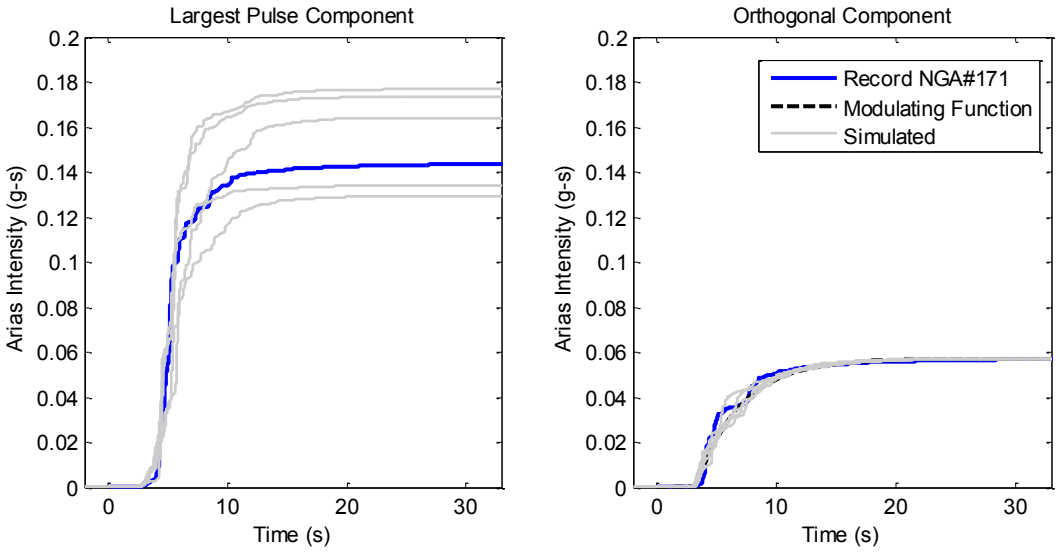

Figure 6.5 Husid plots of record NGA#171 (blue), modulating functions fitted to the recorded motions (black dashed), and five simulated motion with parameters identified for record NGA#171 (black): ground motion component in the direction of the largest pulse (left) and corresponding orthogonal direction (right).

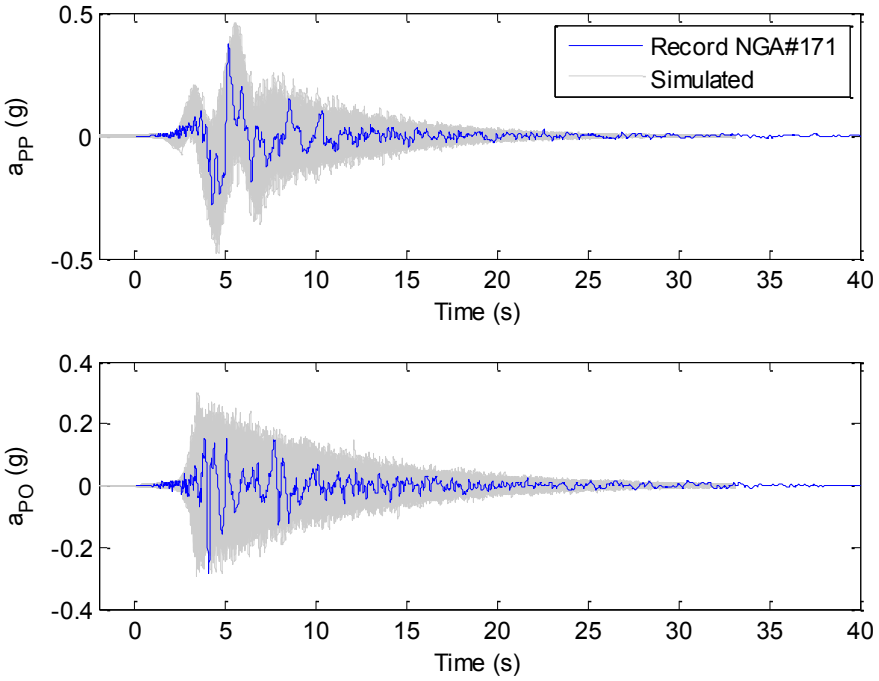

Figure 6.6 Acceleration time series of record NGA #171 (blue line) and 300 simulated acceleration time series using the fitted parameters: horizontal component containing the largest pulse (top) and corresponding orthogonal component (bottom).

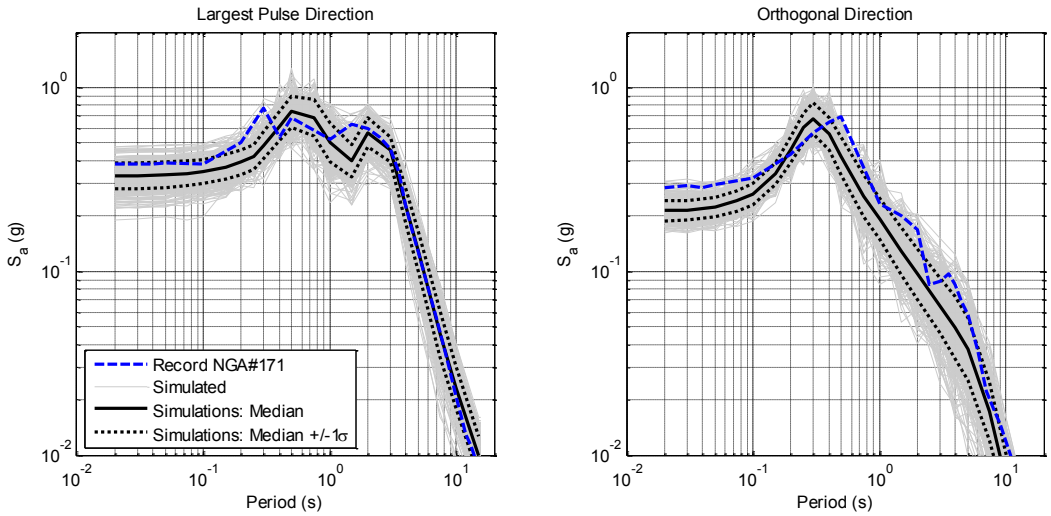

Figure 6.7 Pseudo-acceleration response spectra at 5% damping of the record NGA#171 (dashed blue line), of 300 simulated ground motions using the fitted parameters (thin grey lines), and of their median (black line) and median plus and minus one standard deviation levels (dotted black lines).

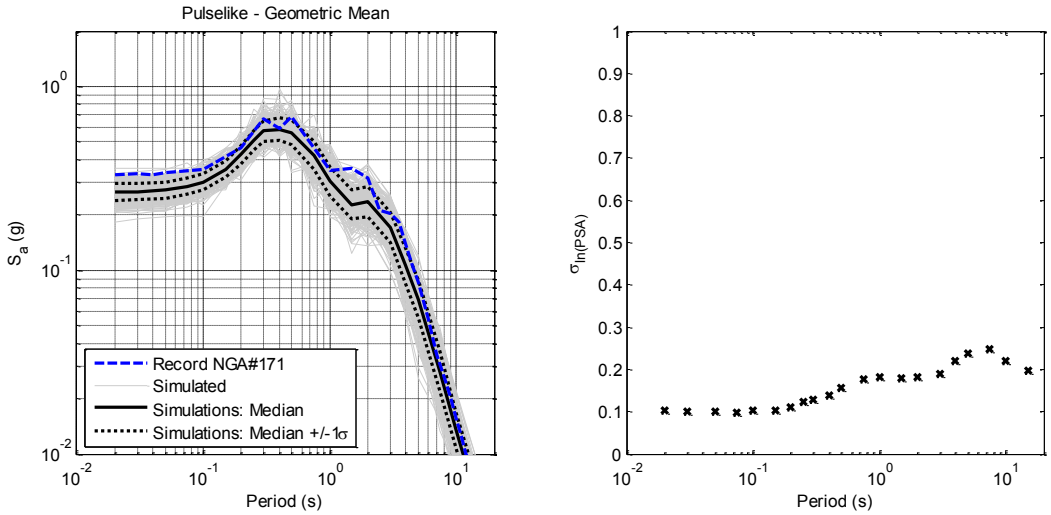

Figure 6.8 (Left) Geometric mean pseudo-acceleration response spectra at 5% damping of the largest pulse and orthogonal components of record NGA#171 (dashed blue line), of 300 simulated ground motions using the fitted parameters (thin grey lines), and of their median (black line) and median plus and minus one standard deviation levels (dotted black lines), (Right) Standard deviation of log of the geometric mean spectra at 5% damping of the 300 simulated ground motions.

6.3.2 Example application 2: non-pulselike ground motion

As a second example, consider NGA record #351, which was identified as non-pulselike by Shahi and Baker (2011) and was introduced in Section 5.3.4. The acceleration, velocity and displacement time series of the major and intermediate "principal" components of this record were plotted in Figure 5.8.

Figure 6.9 shows the acceleration times series of the two "principal" components of record NGA#351 and a sample of five of the motions simulated using the fitted model parameters. It is evident that the simulated motions are visually similar to the recorded motion in terms of amplitude, duration and frequency content. Figure 6.10 shows the velocity time series that are obtained by integration of the acceleration time series in Figure 6.9. The simulated ground motion components are similar to those of the recorded motion. Figure 6.11 shows the displacement time series that are obtained by integration of the velocity time series in Figure 6.10. Similarities are observed between the recorded and simulated motions, but they are not as marked as those in the acceleration and velocity domains. Again, this is because there are no constraints on displacements in the fitting procedure (the major and intermediate ground motion components are fitted in the acceleration domain), and because the displacement time series is highly dependent on the long period content of the motion and is thus highly sensitive to the choice of the parameters of the low-cut filter. Here, we have used the magnitude $\mathbf{M} = 6.36$ of record NGA#351 in (3.15) to compute $f_c = 0.163$ Hz, which corresponds to a long-period cutoff at 6.14 s (see Chapter 3).

Figure 6.12 shows the Husid plots of the two horizontal components of record NGA#351, of the modulating functions fitted to these components, and of the five simulated motions plotted in Figures 6.9-6.11. It can be seen that the Husid plots of the major and intermediate components of the simulated motions generally match the Husid plots of the corresponding recorded components and fitted modulating functions, including the values of the total Arias intensities. As mentioned earlier, this feature is guaranteed by scaling the simulated motions using (6.2) and (6.3).

Figure 6.13 shows the recorded ground motion and the 300 simulated motions, in the major and intermediate "principal directions". The figure displays an overlay of the 300 simulated motions as thin grey lines together with the recorded motions in blue line. The thin lines illustrate the range of possible realizations of acceleration time series using the fitted model parameters. It can be seen that the general features of the simulated and recorded acceleration time series are similar. Furthermore, the recorded motion is well within the range of the 300 simulated motions.

Elastic pseudo-acceleration response spectra at 5% damping are computed for the recorded and simulated ground motions at periods ranging from 0.02 s to 15 s. Figure 6.14 shows the spectra for the recorded ground motion components by thick blue dashed lines and the spectra of the simulated motions with thin grey lines. The median levels of the spectra of the simulated motions are shown by thick black lines. The median plus and minus one standard deviation levels are shown by thick black dotted lines. One can observe that the response spectra of the recorded ground motion components fall within the ranges spanned by the spectra of the simulated ground motion components at all periods. The recorded motion is regarded as one sample realization of the modulated and filtered white-noise process for the given parameters. In this example and due to the non-pulselike nature of the ground motion, we do not expect the

median spectrum of the simulated motions to match the spectrum of the recorded motion at the longer periods. Indeed, the recorded and median simulated spectra show significant differences at most periods. Again, this is due to the idealized nature of our ground motion model, which cannot reproduce all the details of the recorded ground motion.

Figure 6.15 (left) shows in a dashed blue line the geometric mean pseudo-acceleration response spectrum at 5% damping of the major and intermediate components of record NGA#351. The figure also shows in thin grey lines the geometric mean spectra of the 300 simulated ground motions, as well as their median (black line) and median plus and minus one standard deviation levels (dotted black lines). The right portion of Figure 6.15 shows the standard deviation of the natural logarithm of the geometric mean spectra at 5% damping of the 300 simulated ground motions. It illustrates, for the fixed model parameter values, the variability arising from randomness in the underlying white-noise processes. This variability tends to increase with oscillator period from a value of about 0.1 at short periods to a value of about 0.3 at a period of 6 s, after which variability decreases slightly with period, to a value of about 0.2 at a period of 15 s.

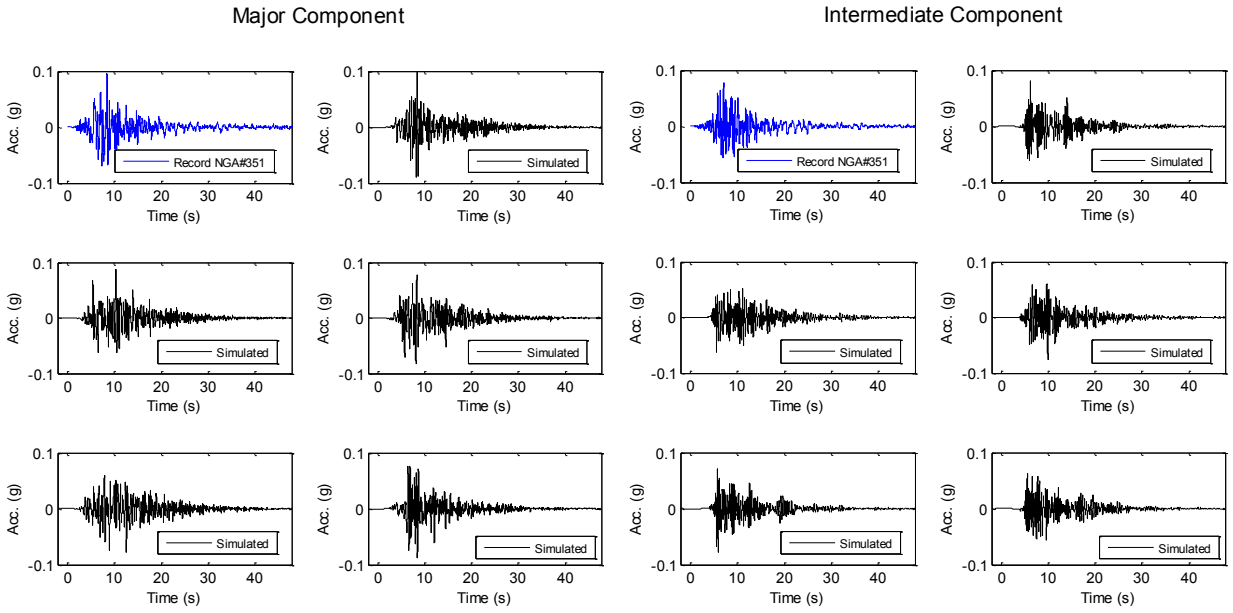

Figure 6.9 Acceleration time series of record NGA#351 (blue) and five simulated motion with parameters identified for record NGA#351 (black): major (left) and intermediate (right) "principal" components of ground motion.

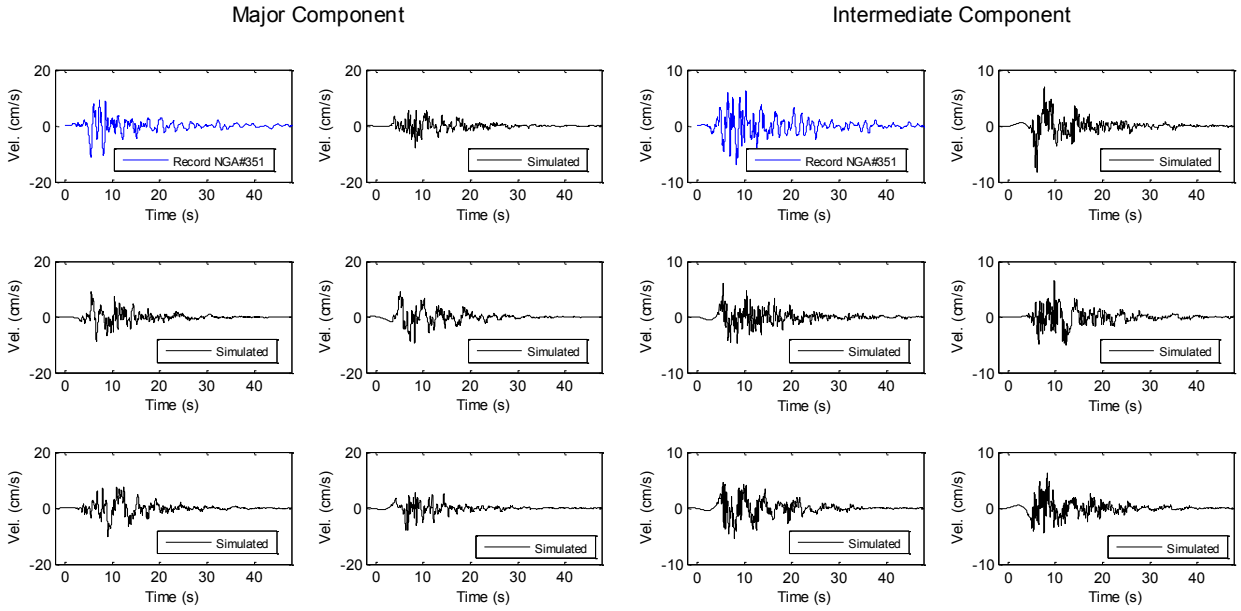

Figure 6.10 Velocity time series of record NGA#351 (blue) and five simulated motion with parameters identified for record NGA#351 (black): major (left) and intermediate (right) "principal" components of ground motion.

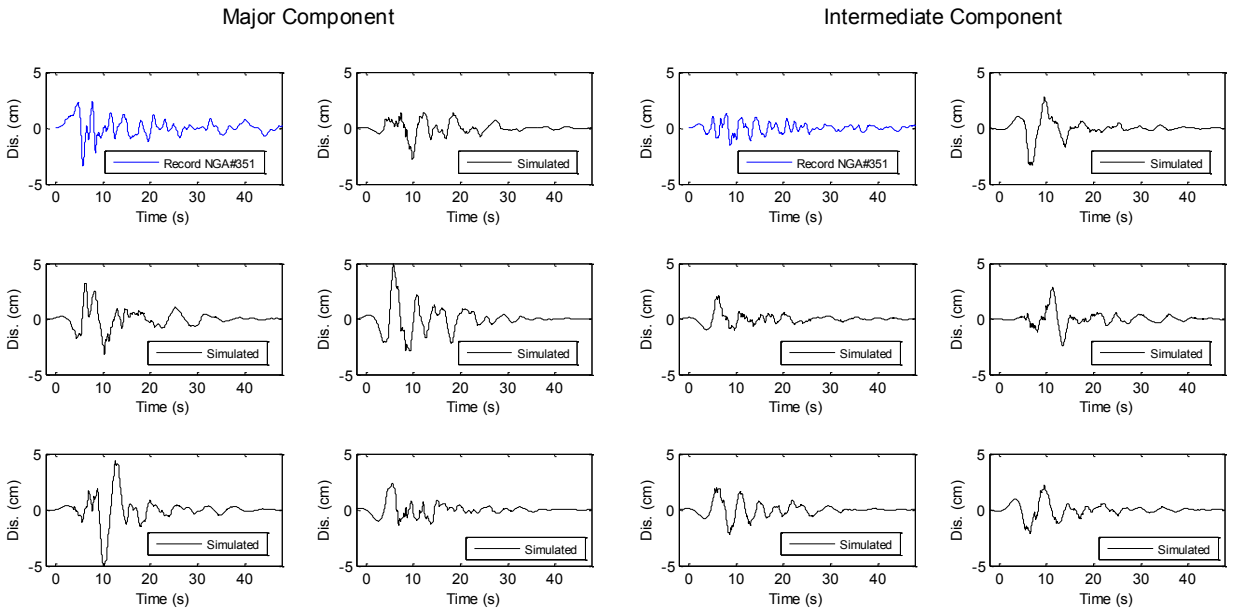

Figure 6.11 Displacement time series of record NGA#351 (blue) and five simulated motion with parameters identified for record NGA#351 (black): major (left) and intermediate (right) "principal" components of ground motion.

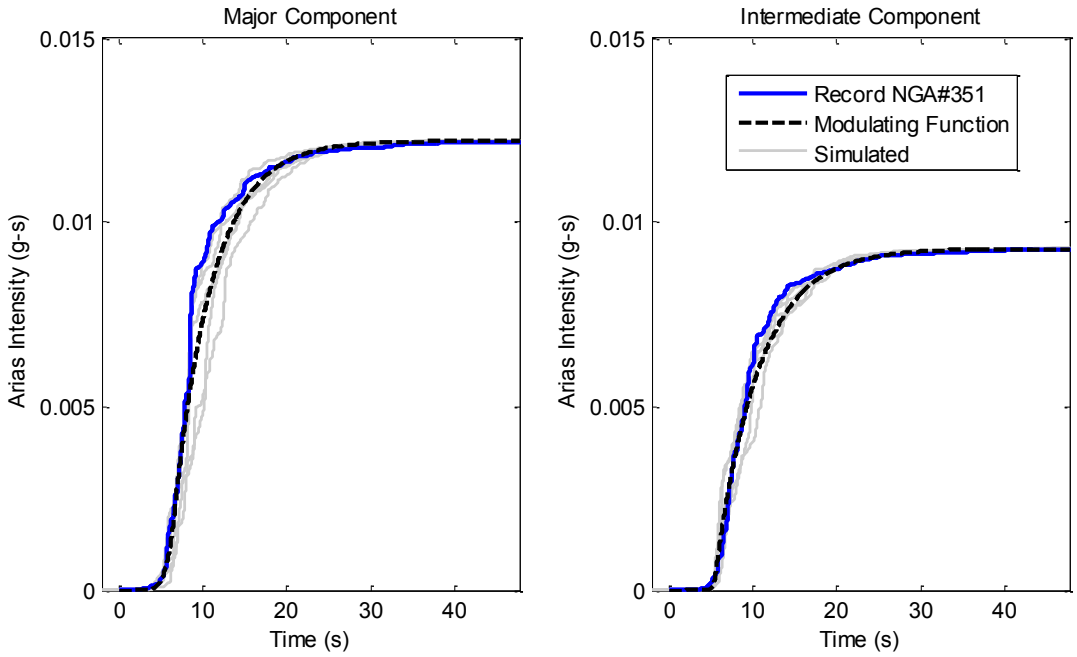

Figure 6.12 Husid plots of record NGA#351 (blue), modulating functions fitted to the recorded motions (black dashed), and five simulated motion with parameters identified for record NGA#351 (black): major (left) and intermediate (right) "principal" components.

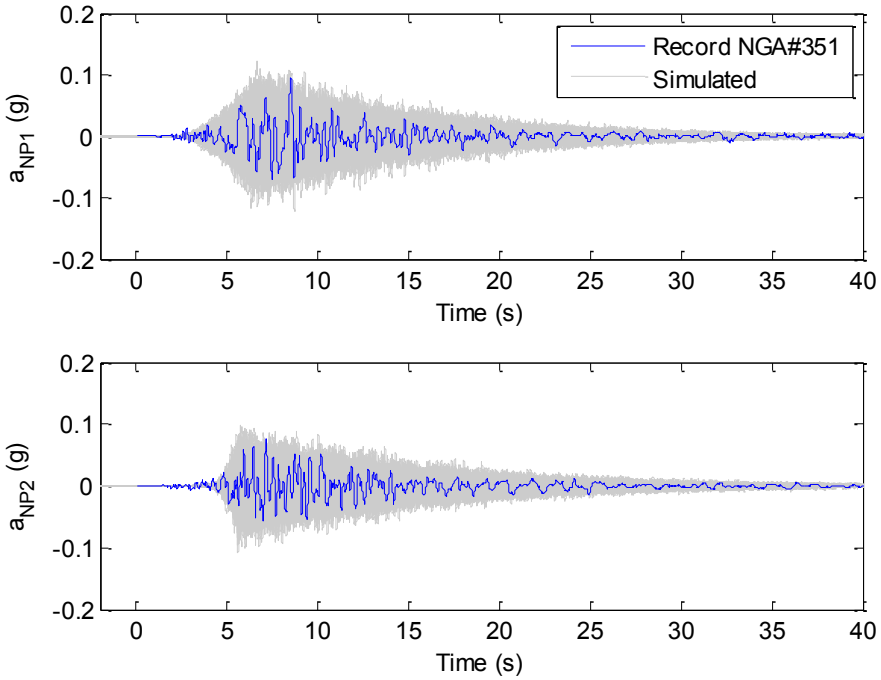

Figure 6.13 Acceleration time series of record NGA #351 (blue line) and 300 simulated acceleration time series using the fitted parameters: major (top) and intermediate (bottom) "principal" horizontal components.

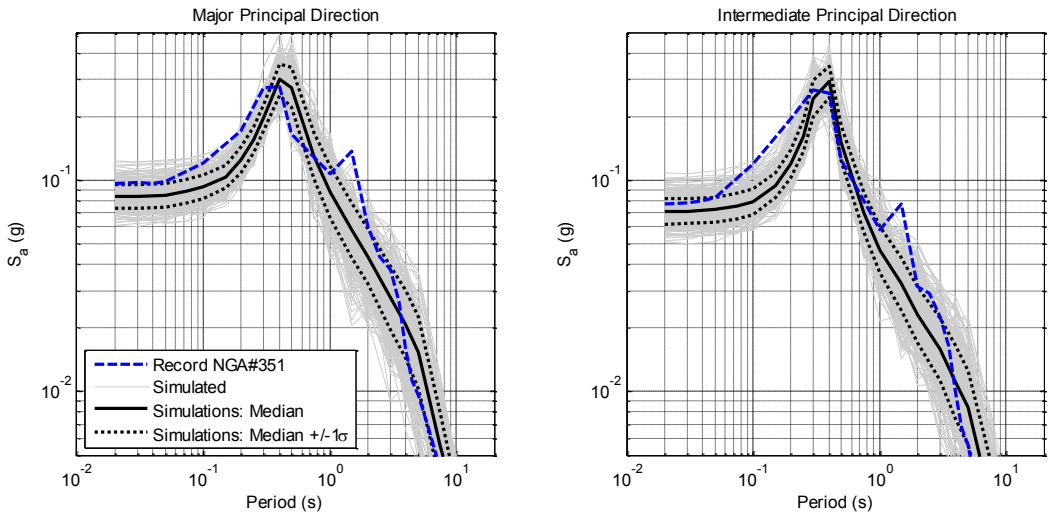

Figure 6.14 Pseudo-acceleration response spectra at 5% damping of the record NGA #351 (dashed blue line), of 300 simulated ground motions using the fitted parameters (thin grey lines), and of their median (black line) and median plus and minus one standard deviation levels (dotted black lines).

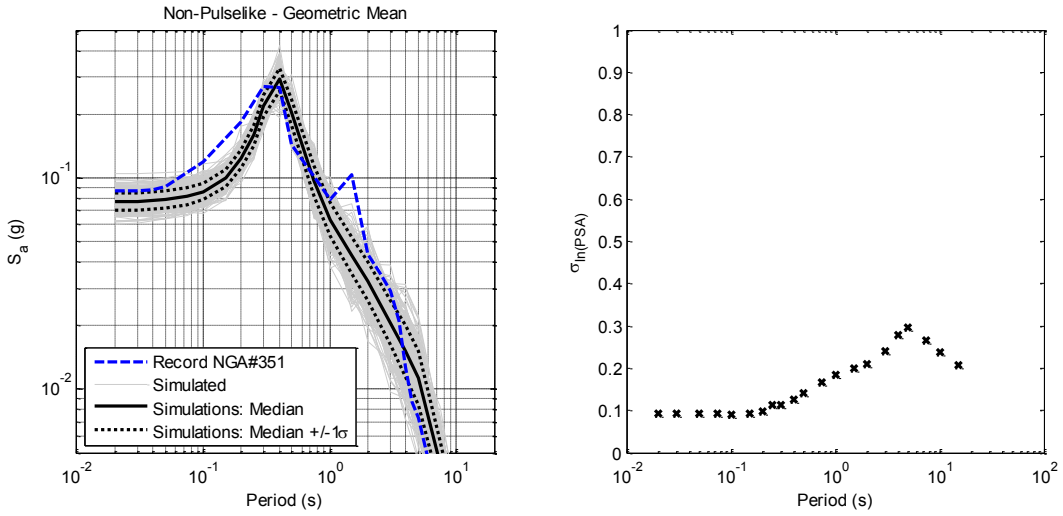

Figure 6.15 (Left) Geometric mean pseudo-acceleration response spectra at 5% damping of the major and intermediate components of record NGA#351 (dashed blue line), of 300 simulated ground motions using the fitted parameters (thin grey lines), and of their median (black line) and median plus and minus one standard deviation levels (dotted black lines), (Right) Standard deviation of log of the geometric mean spectra at 5% damping of the 300 simulated ground motions.

6.4 SIMULATION FOR SPECIFIED EARTHQUAKE SOURCE AND SITE CHARACTERISTICS

In this section, we describe and illustrate the procedure for simulating near-fault ground motions for specified earthquake source and site characteristics. This application is the main goal of the study and is useful for design situations, where the necessary input specification is in terms of the characteristics of an earthquake source (F, $\mathbf{M}$, Z_{TOR}), a site (V_{s30}), and the position of the site relative to the fault rupture (R_{RUP}, $s_{or}d$, $\theta_{or}\phi$). In this case, the earthquake source and site characteristics are kept constant and the model parameters vary from simulation to simulation. Sets of model parameters are randomly simulated using the predictive equations and the estimated correlation matrix between model parameters. The variability in the simulated motions results from variability in the model parameters and in the underlying white noise process.

The procedure employs the stochastic models of pulselike and non-pulselike near-fault ground motions formulated in Chapter 4, the models for predicting the model parameters resulting from the regression and correlation analyses of Chapter 5, as well as the pulse probability model by Shahi and Baker (2011) and the pulselike and non-pulselike directionality models developed in Chapter 4. This approach produces near-fault ground motions that have the same natural variability that is present in a collection of recorded near-fault ground motions with the specified earthquake source and site characteristics. It is also possible to generate only pulselike or only non-pulselike synthetic near-fault ground motions for given source and site characteristics, eliminating the need for the pulse probability model.

6.4.1 Step 1: Simulation of the number of pulselike versus non-pulselike motions

For a complete representation of near-fault ground motion, the probability of the ground motion being pulselike at a specified site is required, and should be reflected in the proportion of pulselike and non-pulselike synthetic motions generated for the site. We use the model developed by Shahi and Baker (2011) to predict the occurrence of a pulse in at least one direction at a specified site.

To simulate two orthogonal horizontal components of a near-fault ground motion, we proceed as follows: Given the set of earthquake source and site characteristic variables (F, $\mathbf{M}$, Z_{TOR}, R_{RUP}, V_{s30}, $s_{or}d$, $\theta_{or}\phi$), we first compute the probability of observing a pulse in at least one direction, according to the model of Shahi and Baker (2011). Combining (4.16) and (4.17), we compute

$$\begin{aligned}\Pr[\text{pulselike}|F, R_{RUP}, s_{or}d, \theta_{or}\phi] &= \frac{1}{1+\exp(0.642+0.167R_{RUP}-0.075s_{or}d)}, && if\ F=0\\ &= \frac{1}{1+\exp(0.128+0.055R_{RUP}-0.061s_{or}d+0.036\theta_{or}\phi)}, && if\ F=1\end{aligned}, \tag{6.4}$$

where R_{RUP} and $s_{or}d$ are in kilometers and $\theta_{or}\phi$ is in degrees. For each simulation, we first use a random number generator to uniformly sample a number between 0 and 1. If the sampled number is less than or equal to $\Pr[\text{pulselike}|F, R_{RUP}, s_{or}d, \theta_{or}\phi]$, a pulselike ground motion is generated as described in Section 6.4.2. If the generated number is greater than $\Pr[\text{pulselike}|F, R_{RUP}, s_{or}d, \theta_{or}\phi]$, a non-pulselike ground motion is generated as described in Section 6.4.3. This process can be repeated to generate as many near-fault synthetic ground motions as necessary for the given design scenario. The suite of synthetic ground motions generated at a given site will have proportions of pulselike and non-pulselike motions that more or less match the proportions observed among recorded near-fault ground motions.

6.4.2 Step 2: Simulation of pulselike near-fault ground motions

Given that a near-fault ground motion is pulselike for a given set of earthquake source and site characteristics, the stochastic model of pulselike near-fault ground motion is used, together with the predictive equations and correlation matrix of the 19 parameters of the pulselike model, to simulate two orthogonal horizontal ground motion components.

6.4.2.1 Simulation of orientation of the largest pulse relative to fault strike

For each pulselike ground motion simulation, we first use a random number generator to obtain the orientation α_P of the largest pulse relative to the strike of the fault. We do so by sampling a number between 0° and 90° according to the probability distribution given in (4.20) of the direction of the largest pulse relative to the strike of the fault.

6.4.2.2 Simulation of model parameters

To simulate two orthogonal horizontal components of a pulselike near-fault ground motion for a given set of earthquake source and site characteristics (F, $\mathbf{M}$, Z_{TOR}, R_{RUP}, V_{s30}, $s_{or}d$) and the angle α_P, we proceed as follows:

1. Given (F, $\mathbf{M}$, Z_{TOR}, R_{RUP}, V_{s30}, $s_{or}d$), we compute the conditional mean values of the transformed pulselike model parameters $z_{P,1}, \dots, z_{P,19}$, by use of the predictive equations

presented in (5.42), (5.46), (5.51) and (5.60) with the regression coefficients listed in Tables 5.17, 5.21, 5.25, and 5.31, respectively.

2. We add to these mean values simulated values of the corresponding error terms $\epsilon_{P,i}$, $i = 1, \ldots, 19$, generated as correlated normal random variables with zero means and variances and correlation coefficients as listed in Tables 5.17, 5.21, 5.25, 5.31 and 5.35.
3. The generated $z_{P,i}$ values are transformed back to the original space according to the inverse of the relations in (5.30), (5.44), (5.49) and (5.55).
4. Generated residual parameters ($I_{a,res}$, $D_{5-95,res}$, $D_{0-5,res}$, $D_{0-30,res}$) and orthogonal motion parameters ($I_{a,PO}$, $D_{5-95,PO}$, $D_{0-5,PO}$, $D_{0-30,PO}$) are used in (5.14-5.16) and (5.21) to back-calculate the modulating function parameters (α_{res}, β_{res}, c_{res}, $t_{max,q,res}$) and (α_{PO}, β_{PO}, c_{PO}, $t_{max,q,PO}$) respectively.
5. The simulated set of correlated model parameters is used with two simulated statistically independent white-noise processes to generate synthetic pairs of orthogonal horizontal pulselike near-fault ground motion components. The procedure of Section 6.2.3 is used to simulate the ground motion in the direction α_p of the largest pulse while the procedure of Section 6.2.4 is used to simulate the ground motion in the orthogonal direction.

This procedure, beginning with the generation of new parameter values, is repeated to generate as many synthetic pulselike near-fault ground motions for the specified earthquake source and site characteristics as is necessary for the given design scenario. The resulting synthetic motions have the same statistical characteristics as the pulselike motions in the database, including the inherent variability for the given set of earthquake and site characteristics. This is because the model is fitted to the database of recorded pulselike ground motions from different earthquakes. Thus, for the same earthquake source and site characteristics, we will have simulated motions that will have large, medium or small velocity pulses with a range of periods, and residual and orthogonal motions that will have a variety of intensities, frequency contents and durations. Moreover, the observed correlation between the model parameters is preserved. For example, the negative correlation between pulse amplitude and pulse period, or the positive correlations between all the time and duration parameters are accounted for, see Chapter 5.

6.4.3 Step 3: Simulation of non-pulselike near-fault ground motions

Given that a near-fault ground motion is non-pulselike for a given set of earthquake source and site characteristics, the stochastic model of non-pulselike near-fault ground motion is used, together with the predictive equations and correlation matrix of the non-pulselike model parameters, to simulate two orthogonal horizontal ground motion components.

6.4.3.1 Simulated orientation of the major "principal" component relative to fault strike

For each non-pulselike ground motion simulation, we first use a random number generator to obtain the orientation α_{NP1} of the major "principal" component relative to the strike of the fault. We do so by uniformly sampling a number between 0˚ and 90˚, i.e., according to the uniform probability distribution of the angle of the major direction relative to the strike of the fault, as described in Section 4.6.2 and shown in Figure 4.5.

6.4.3.2 Simulated model parameters

To simulate two orthogonal horizontal components of a non-pulselike near-fault ground motion for a given set of earthquake source and site characteristics (F, $\mathbf{M}$, Z_{TOR}, R_{RUP}, V_{s30}, $s_{or}d$) and angle α_{NP1}, we proceed as follows:

1. Given (F, $\mathbf{M}$, Z_{TOR}, R_{RUP}, V_{s30}, $s_{or}d$), we compute the conditional mean values of the transformed non-pulselike model parameters $z_{NP,1}, \dots, z_{NP,14}$, by use of the predictive equations presented in (5.43), (5.47), (5.52) and (5.61) with the regression coefficients listed in Tables 5.18, 5.22, 5.26, and 5.32, respectively.
2. We add to these mean values simulated values of the corresponding error terms $\epsilon_{NP,i}$, $i = 1, \dots, 14$, generated as correlated normal random variables with zero means and variances and correlation coefficients as listed in Tables 5.18, 5.22, 5.26, 5.32 and 5.36..
3. The generated $z_{NP,i}$ values are transformed back to the original space according to the inverse of the relations in (5.31), (5.45), (5.50) and (5.56).
4. Generated parameters ($I_{a,NP1}$, $D_{5-95,NP1}$, $D_{0-5,NP1}$, $D_{0-30,NP1}$) and ($I_{a,NP2}$, $D_{5-95,NP2}$, $D_{0-5,NP2}$, $D_{0-30,NP2}$) of the major and intermediate "principal" components are used in (5.14-5.16) and (5.21) to back-calculate the modulating function parameters (α_{NP1}, β_{NP1}, c_{NP1}, $t_{max,q,NP1}$) and (α_{NP2}, β_{NP2}, c_{NP2}, $t_{max,q,NP2}$) respectively.
5. The simulated set of correlated model parameters is used with two simulated statistically independent white-noise processes to generate synthetic pairs of orthogonal horizontal non-pulselike near-fault ground motion components. The procedure of Section 6.2.4 is used to simulate the ground motion in the major and intermediate "principal directions" α_{NP1} and $\alpha_{NP2} = \alpha_{NP1} + 90°$, respectively.

This procedure, beginning with the generation of new parameter values, is repeated to generate as many synthetic non-pulselike near-fault ground motions for the specified earthquake source and site characteristics as is necessary for the given design scenario. The resulting synthetic motions have the same statistical characteristics as the non-pulselike motions in the database, including the variability for the given set of earthquake and site characteristics. Again, this is because the model is fitted to the database of recorded non-pulselike ground motions from different earthquakes. Thus, for the same earthquake source and site characteristics, we will have simulated major and intermediate components of ground motion that will have a variety of intensities, frequency contents, and durations. Moreover, the observed correlation between model parameters is preserved. For example, the positive correlation between all the time and duration parameters is accounted for, see Chapter 5.

In summary, for a given set of earthquake source and site characteristics (F, $\mathbf{M}$, Z_{TOR}, R_{RUP}, V_{s30}, $s_{or}d$, $\theta_{or}\phi$), and following the procedure described in 6.4.1-6.4.3, we are able to generate as many near-fault ground motions, pulselike and non-pulselike, as necessary. These simulated motions should be viewed as ground motions resulting from different earthquakes that happen to have common source and site characteristics. If we select the earthquake source and site characteristics of a particular record to generate synthetic ground motions, the recorded motion can then be seen as one realization arising from that design scenario. Since in the design or risk assessment stage one only has information about the general characteristics of the

earthquake source and the site, the simulated near-fault ground motions obtained by this approach would be an appropriate set for design or risk assessment considerations.

6.4.4 Example application 1: pulselike ground motion

For illustrative purposes, we simulate five pairs of horizontal components of pulselike motions for the following scenario: $F = 0$, $\mathbf{M} = 6.53$, $Z_{TOR} = 0$ km, $R_{RUP} = 0.1$ km, $V_{s30} = 265$ m/s, $s_{or}d = 19.5$ km and $\theta_{or}\phi = 5.4°$. For this scenario, which is similar to the scenario for record NGA#171 in the NGA West2 database, the predicted probability of observing a pulse in any direction is calculated in (6.4) to be 0.69. Record NGA#171 is a pulselike record and was used in prior examples in Chapter 5 and Section 6.3.1. The recorded and five simulated ground motions should be regarded as random realizations of pulselike ground motions resulting from an earthquake with source and site characteristics as prescribed above. Non-pulselike ground motions may also occur at the site, but we do not consider them in this example.

Tables 6.1, 6.2 and 6.3 list the median, fitted and simulated parameters of the models of the pulse, residual and orthogonal motions for the selected design scenario, respectively. The first rows show the predicted median values that are obtained by back transforming the predicted mean values of the normalized variables $z_{P,1}, \ldots, z_{P,19}$. The second rows list the identified parameters of the recorded motion. The remaining rows show the parameter values generated for the five synthetic motions. Figures 6.16, 6.17 and 6.18 show the times series of the recorded (blue) and synthetic (black) motions that correspond to the model parameters in Tables 6.1-6.3. In particular, these figures show the acceleration, velocity and displacement time series of the component of pulselike ground motion containing the largest pulse (left) and the orthogonal component (right), respectively. Note that all simulated motions end with zero velocity and displacement values.

As can be noted from Tables 6.1-6.3, the simulated values of the model parameters show significant variability around their respective predicted median values. They reflect the expected range of variability in the intensity, duration and frequency content parameters, and the randomness that is inherent in pulselike near-fault ground motions having common earthquake source and site characteristics. This variability is also seen in the plots of the time series in Figures 6.16-6.18. The recorded and simulated motions all represent possible realizations of pulselike ground motions for the specified design scenario.

We now focus our discussion around the directivity pulses found in the pulselike ground motions. Table 6.1 lists the parameters of the mMP pulse model fitted to the velocity pulse extracted from the recorded ground motion (see Figure 4.1 for a plot of this pulse) along with those of the simulated mMP pulses.

In this example, the recorded velocity pulse has an amplitude and a period that are larger than the corresponding median values computed using the predictive equations (peak velocity of 80.3 cm/s versus 68.2 cm/s and period of 2.8 s versus 2.1 s, respectively). Thus, based on the available data set of recorded pulselike near-fault ground motions, this particular recorded motion has a larger pulse amplitude and a larger pulse period than would be expected, on the average, from such an earthquake. The simulated velocity pulses have amplitudes ranging from 52.7 cm/s to 94.1 cm/s, thus bracketing the predicted median value of 68.2 cm/s. Their periods range from 1.7 s to 8.3 s, bracketing the predicted median value of 2.1 s. Simulated values for the other parameters, γ, ν and $t_{max,p}$, also show significant variabilities around their respective

predicted median values. As mentioned earlier, these variabilities reflect the randomness that is inherent in the directivity pulses of near-fault ground motions for a given set of earthquake source and site characteristics.

Table 6.2 lists the parameters of the residual parts of the recorded and simulated motions. As can be observed, the recorded residual motion has an Arias intensity of $I_a = 77$ cm/s, an effective duration of 8.6 s, and a predominant frequency of 3.1π rad/s at the middle of the strong shaking. These are respectively smaller, shorter and smaller than the corresponding median values (256 cm/s, 11.2 s and 7.1π rad/s) computed using the predictive equations. Thus, the residual motion of this particular record has a lower intensity and a shorter effective duration than would be expected, on the average, from a ground motion generated by an earthquake of the given source and site characteristics, and its predominant frequency is also below average. The simulated residuals have Arias intensity values ranging from 281 cm/s to 696 cm/s, effective durations ranging from 8.5 s to 23.0 s, and predominant frequencies ranging from 4.3π rad/s to 11.6π rad/s. Except for Arias intensity, these all bracket the predicted median values. Simulated values of the other parameters, D_{0-5}, D_{0-30}, ω' and ζ_f, also show significant variabilities around their respective predicted median values. As mentioned earlier, these variabilities reflect the randomness that is inherent in the residuals of near-fault ground motions for a given set of earthquake source and site characteristics.

Table 6.3 lists the parameters of the orthogonal component of the recorded and simulated motions. As can be observed, the recorded orthogonal motion has an Arias intensity of $I_a = 56$ cm/s, an effective duration of 10.7 s, and a predominant frequency of 6.3π rad/s at the middle of the strong shaking. These are respectively smaller, almost equal and smaller than the corresponding median values (211 cm/s, 10.9 s and 7.3π rad/s) computed using the predictive equations. Thus, the orthogonal motion of this particular record has a lower intensity and a similar effective duration than would be expected, on the average, from a ground motion generated by an earthquake of the given source and site characteristics, and its predominant frequency is below average. The simulated orthogonal components have Arias intensity values ranging from 156 cm/s to 360 cm/s, effective durations ranging from 10.2 s to 25.3 s, and predominant frequencies ranging from 3.1π rad/s to 10.7π rad/s. These all bracket the predicted median values. Simulated values of the other parameters, D_{0-5}, D_{0-30}, ω' and ζ_f, also show significant variabilities around their respective predicted median values. As mentioned earlier, these variabilities reflect the randomness that is inherent in the orthogonal components of near-fault ground motions for a given set of earthquake source and site characteristics.

Figure 6.19 shows the elastic pseudo-acceleration response spectra at 5% damping of the recorded (blue line) and simulated (black lines) ground motions. For each case, a peak is observed at periods longer than 1 s in the response spectra of the largest pulse component. These peaks generally occur at or slightly below the period of the corresponding mMP velocity pulse. The variability in the spectral shapes reflects the variability in the ground motion properties (intensity and frequency content) that can be realized for a prescribed set of earthquake source and site characteristics. It is also observed that the recorded motion has much smaller spectral amplitudes than most of the simulated motions. This is because the recorded motion has residual and orthogonal motion Arias intensities that are much smaller than expected, on the average, from a pulselike near-fault ground motion of the given earthquake source and site characteristics.

Table 6.1 Median, fitted and simulated parameters of the mMP pulse model for the prescribed earthquake source and site characteristics.

	V_p	T_p	γ	ν/π	$t_{max,p}$*	$t_{0,q}$
	cm/s	s		rad	s	s
median	68.2	2.1	2.3	1.0	4.6	0
NGA#171	80.3	2.8	2.4	1.0	3.7	1.3
Sim#1	94.1	2.5	2.1	1.0	4.0	0
Sim#2	77.6	1.7	2.1	1.6	6.9	0
Sim#3	52.7	8.3	2.6	1.1	18.6	0
Sim#4	62.1	3.5	2.5	0.4	6.2	0
Sim#5	84.1	5.2	2.4	0.2	7.7	0

Table 6.2 Median, fitted and simulated parameters of the residual motion for the prescribed earthquake source and site characteristics.

	$t_{0,q}$	$I_{a,res}$	$D_{5-95,res}$	$D_{0-5,res}$	$D_{0-30,res}$	$\omega_{mid,res}/\pi$	ω'_{res}/π	$\zeta_{f,res}$
	s	cm/s	s	S	s	rad/s	rad/s^2	
median	0	256	11.2	2.8	4.6	7.1	−0.12	0.19
NGA#171	1.3	77	8.6	2.6	3.8	3.1	0.21	0.27
Sim#1	0	502	9.5	3.5	4.3	4.3	0.09	0.32
Sim#2	0	297	23.0	2.7	4.9	6.8	−0.59	0.35
Sim#3	0	281	8.5	6.7	7.2	11.6	−0.37	0.49
Sim#4	0	408	9.6	3.3	4.2	9.3	−0.37	0.16
Sim#5	0	696	10.7	3.0	5.6	5.8	−0.16	0.27

Table 6.3 Median, fitted and simulated parameters of the orthogonal motion for the prescribed earthquake source and site characteristics.

	$t_{0,q}$ s	$I_{a,PO}$ cm/s	$D_{5-95,PO}$ s	$D_{0-5,PO}$ s	$D_{0-30,PO}$ s	$\omega_{mid,PO}/\pi$ rad/s	ω'_{PO}/π rad/s^2	$\zeta_{f,PO}$
median	0	211	10.9	2.7	4.4	7.3	−0.14	0.17
NGA#171	1.3	56	10.7	2.5	2.8	6.3	0.07	0.27
Sim#1	0	320	13.3	3.0	3.5	3.1	0.31	0.31
Sim#2	0	190	25.3	2.8	4.1	6.9	−0.41	0.31
Sim#3	0	156	11.0	6.1	9.2	10.1	−0.53	0.48
Sim#4	0	208	10.2	3.0	4.7	10.7	−0.50	0.09
Sim#5	0	360	13.4	2.7	5.5	7.8	−0.55	0.29

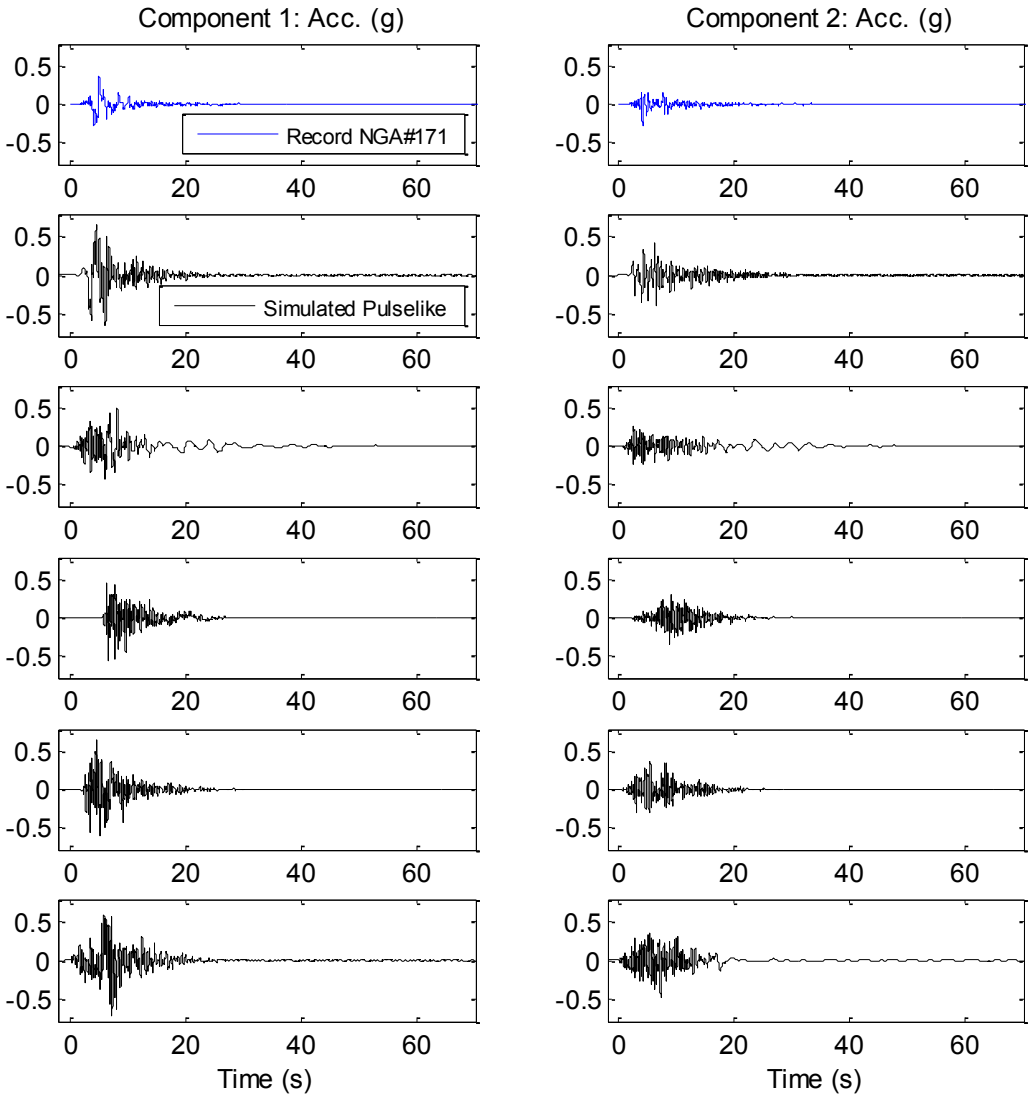

Figure 6.16 Recorded (blue) and synthetic (black) horizontal components of pulselike near-fault ground motion for model parameters in Tables 6.1, 6.2 and 6.3; acceleration time series.

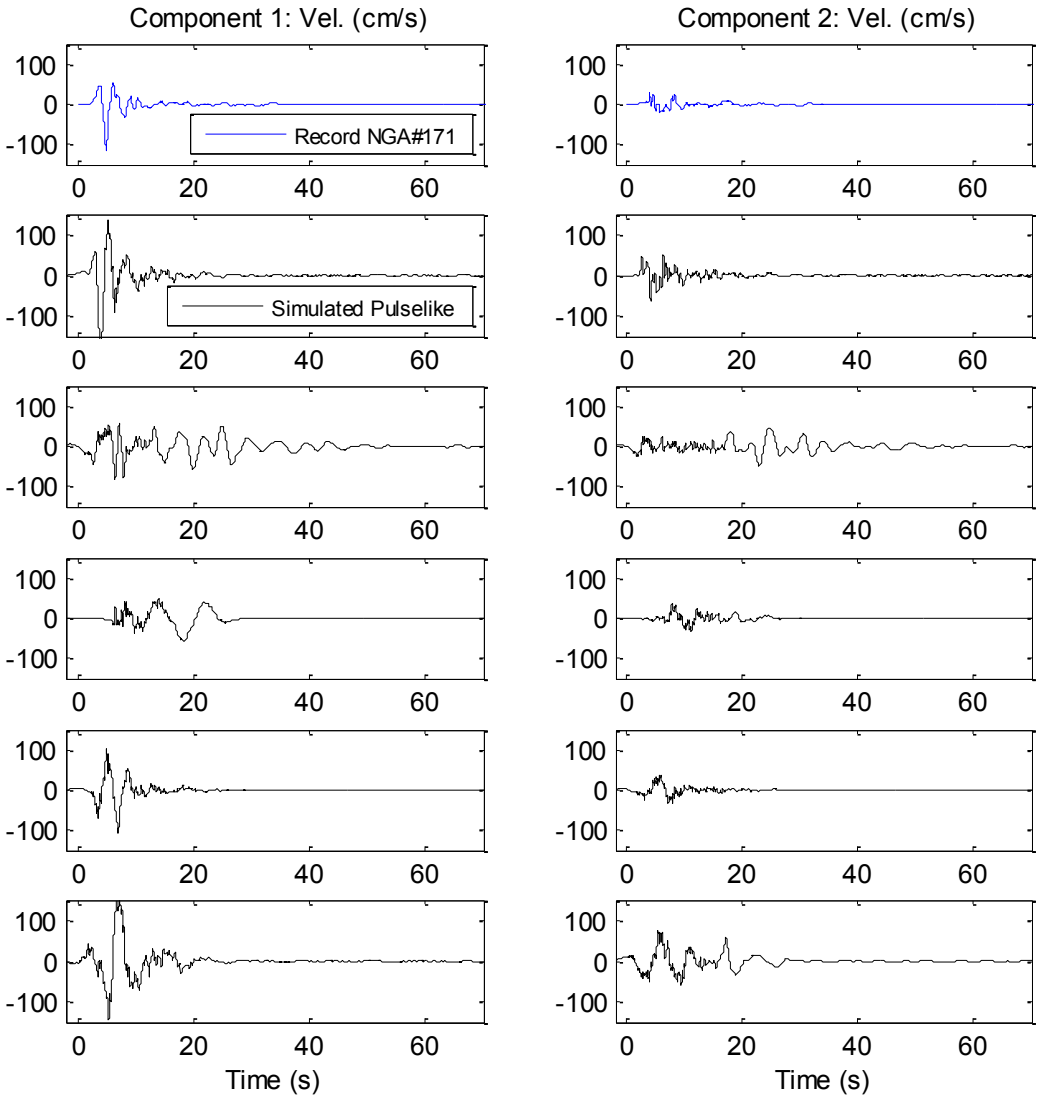

Figure 6.17 Recorded (blue) and synthetic (black) horizontal components of pulselike near-fault ground motion for model parameters in Tables 6.1, 6.2 and 6.3; velocity time series.

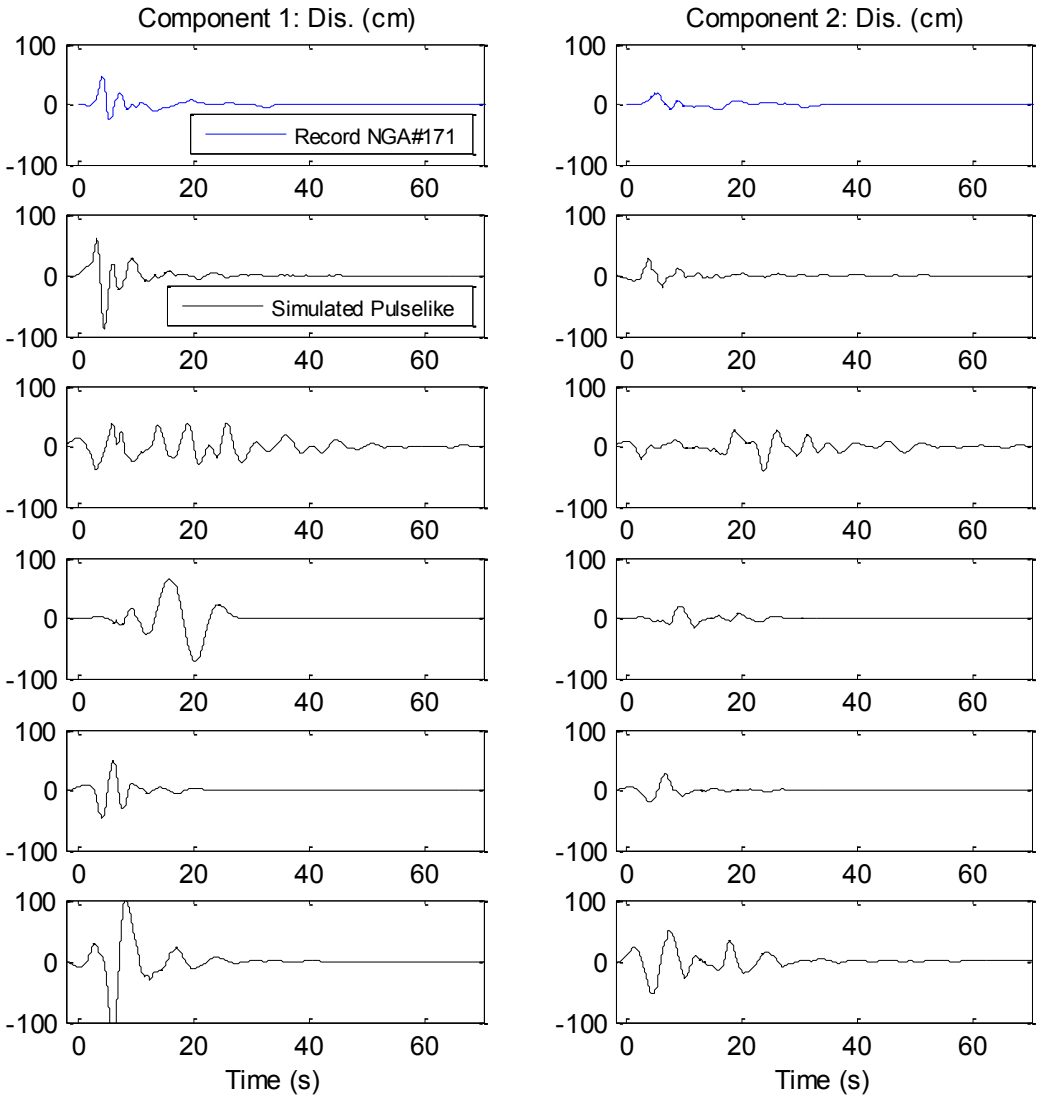

Figure 6.18 Recorded (blue) and synthetic (black) horizontal components of pulselike near-fault ground motion for model parameters in Tables 6.1, 6.2 and 6.3; displacement time series.

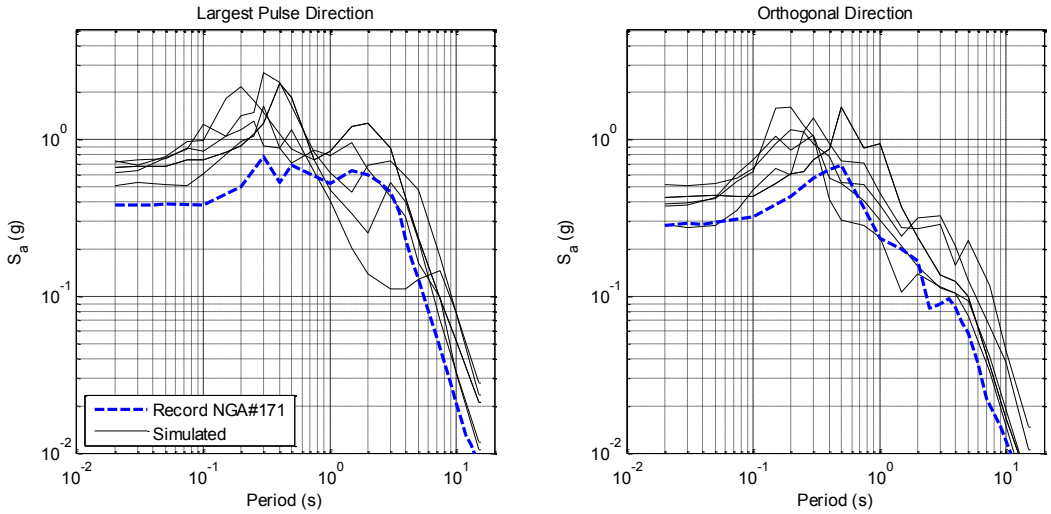

Figure 6.19 Pseudo-acceleration response spectra at 5% damping of the pulselike record NGA #171 (dashed blue line) and of the 5 synthetic pulselike ground motions. Simulations are for the earthquake source and site characteristics of record NGA#171 (black lines). The peaks at long period in the response spectra of the ground motion in the direction of the largest pulse are due to the velocity pulse.

6.4.5 Example application 2: non-pulselike ground motion

Next, we simulate five pairs of horizontal components of non-pulselike motion for the following scenario: $F = 1$, $\mathbf{M} = 6.36$, $Z_{TOR} = 3.4$ km, $R_{RUP} = 30$ km, $V_{s30} = 451$ m/s, $s_{or}d = 9.15$ km and $\theta_{or}\phi = 46.1°$. For this scenario, which is similar to the scenario for record NGA#351 in the NGA West2 database, the predicted probability of observing a pulse in any direction is calculated in (6.4) to be 0.05. Record NGA#351 is a non-pulselike record and was used in prior examples in Chapter 5 and Section 6.3.2. The recorded and five simulated ground motions are sample realizations from the pool of non-pulselike ground motions that could occur at the given site. Pulselike ground motions may also occur at the site, but we do not consider them in this example.

Tables 6.4 and 6.5 list the median, fitted and simulated parameters of the model of ground motion in the major and intermediate "principal directions" for the selected design scenario, respectively. The first rows show the median values that are obtained by back transforming the predicted mean values of the normalized variables $z_{NP,1}, \ldots, z_{NP,14}$. The second rows list the identified parameters of the recorded motion. The remaining rows show the parameter values generated for the five synthetic motions. Figures 6.20, 6.21 and 6.22 show the acceleration, velocity and displacement time series of the two horizontal components of the corresponding recorded (blue) and synthetic (black) motions, respectively. The simulated values of the model parameters show significant variability around their respective predicted median values. They reflect the expected range of variability in the intensity, duration and frequency content parameters, and the randomness that is inherent in non-pulselike near-fault ground motions for a given set of earthquake source and site characteristics. This variability is also seen in the plots of the time series in Figures 6.20-6.22.

In this example, as illustrated in Tables 6.4 and 6.5 as well as in Figures 6.20-6.22, the recorded motion has Arias intensity values that are smaller than the corresponding median predicted values. Simulations 1 and 2 have amplitudes that are close to those of the recorded motion. Simulation 4 is a shorter but more intense ground motion. They all represent possible realizations of non-pulselike ground motions for the specified design scenario.

Figure 6.23 shows the elastic pseudo-acceleration response spectra at 5% damping of the recorded (blue line) and simulated (black lines) ground motions. The variability in the spectral shapes reflects the variability in the ground motion properties (intensity and frequency content) that can be realized for a prescribed set of earthquake source and site characteristics.

Table 6.4 Median, fitted and simulated parameters of the ground motion in the major "principal direction" for the prescribed earthquake source and site characteristics.

	$t_{0,q}$ s	$I_{a,NP1}$ cm/s	$D_{5-95,NP1}$ s	$D_{0-5,NP1}$ s	$D_{0-30,NP1}$ s	$\omega_{mid,NP1}/\pi$ rad/s	ω'_{NP1}/π rad/s^2	$\zeta_{f,NP1}$
median	0	27.6	10.0	3.6	4.9	9.9	−0.11	0.11
NGA#351	1.7	12	14.0	3.9	5.7	4.6	0.11	0.17
Sim#1	0	11.2	13.2	3.0	4.5	16.0	−0.07	0.11
Sim#2	0	14.7	5.3	3.2	4.4	10.0	0.26	0.06
Sim#3	0	41.7	7.2	2.9	5.4	11.3	−0.21	0.18
Sim#4	0	76.1	4.7	2.5	4.5	10.9	0.02	0.03
Sim#5	0	39.6	10.0	5.3	6.1	9.5	−0.09	0.16

Table 6.5 Median, fitted and simulated parameters of the ground motion in the intermediate "principal direction" for the prescribed earthquake source and site characteristics.

	$t_{0,q}$ s	$I_{a,NP2}$ cm/s	$D_{5-95,NP2}$ s	$D_{0-5,NP2}$ s	$D_{0-30,NP2}$ s	$\omega_{mid,NP2}/\pi$ rad/s	ω'_{NP2}/π rad/s^2	$\zeta_{f,NP2}$
median	0	15.3	11.6	3.5	4.6	11.2	−0.19	0.13
NGA#351	1.7	9	15.2	3.9	5.5	5.5	−0.07	0.09
Sim#1	0	7.1	16.1	3.9	4.1	18.6	−0.23	0.14
Sim#2	0	8.2	7.0	3.7	4.8	11.5	0.05	0.08
Sim#3	0	27.3	7.0	3.5	5.8	9.6	−0.13	0.42
Sim#4	0	35.0	7.8	1.6	3.4	13.5	0.00	0.03
Sim#5	0	26.3	11.2	5.9	6.5	12.7	−0.35	0.11

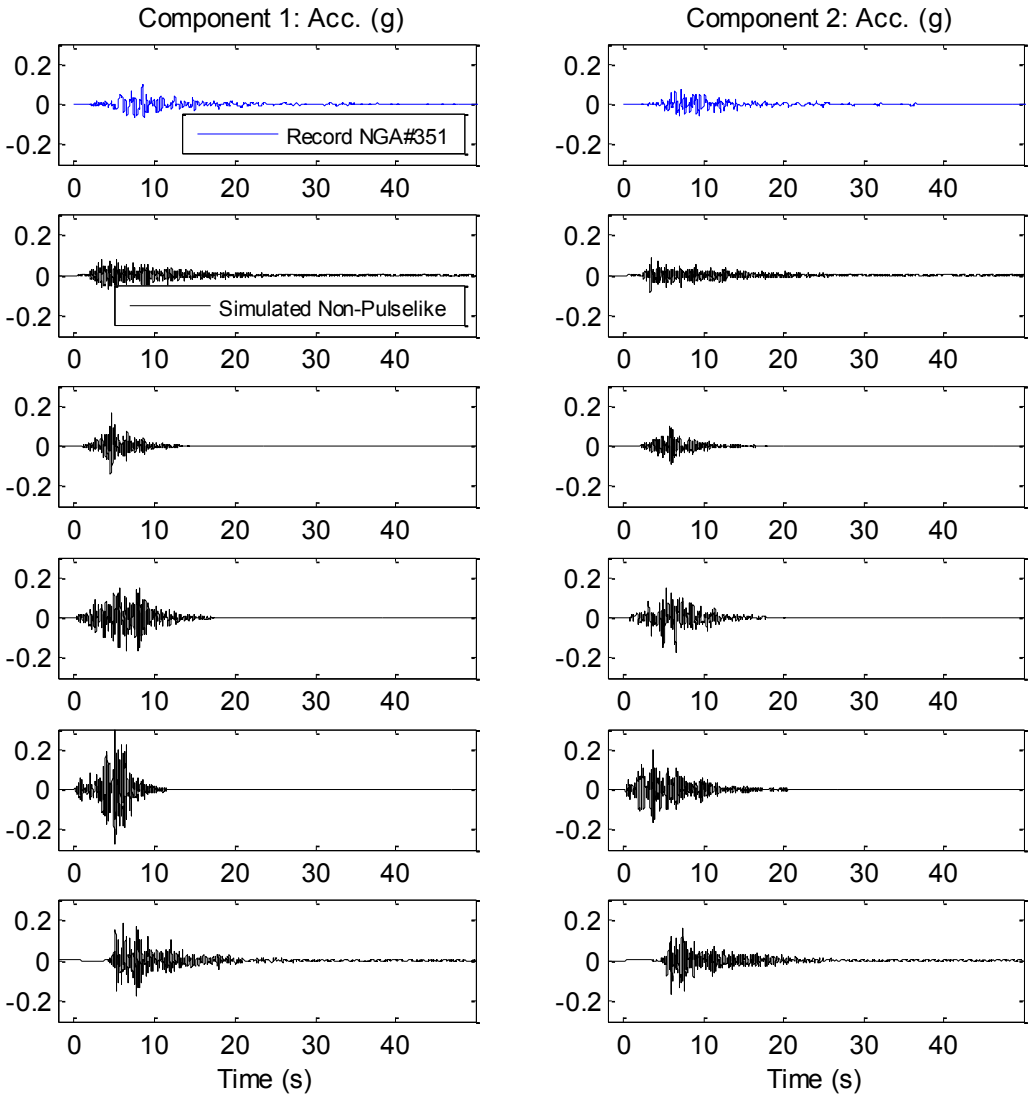

Figure 6.20 Recorded (blue) and synthetic (black) horizontal components of pulselike near-fault ground motion for model parameters in Tables 6.4 and 6.5; acceleration time series.

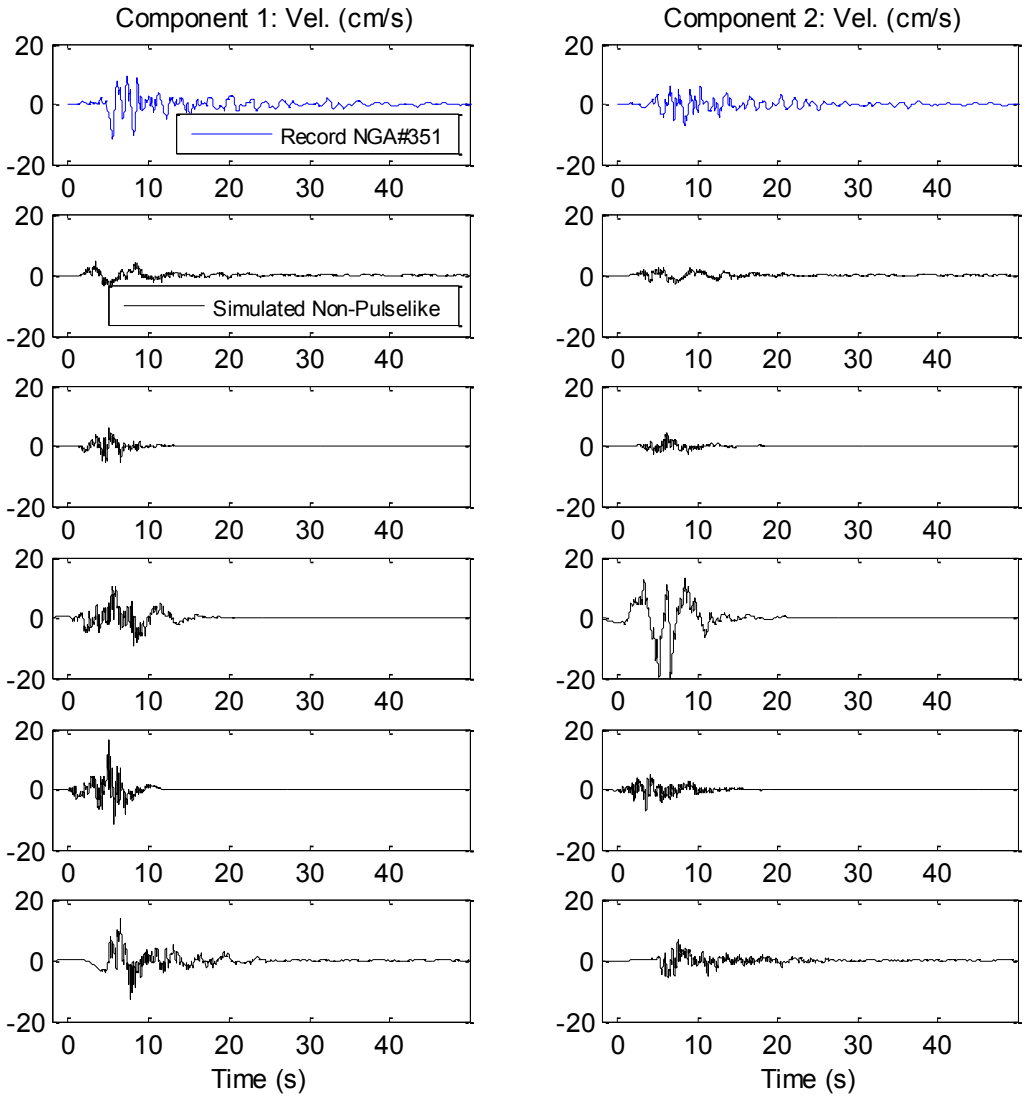

Figure 6.21 Recorded (blue) and synthetic (black) horizontal components of pulselike near-fault ground motion for model parameters in Tables 6.4 and 6.5; velocity time series.

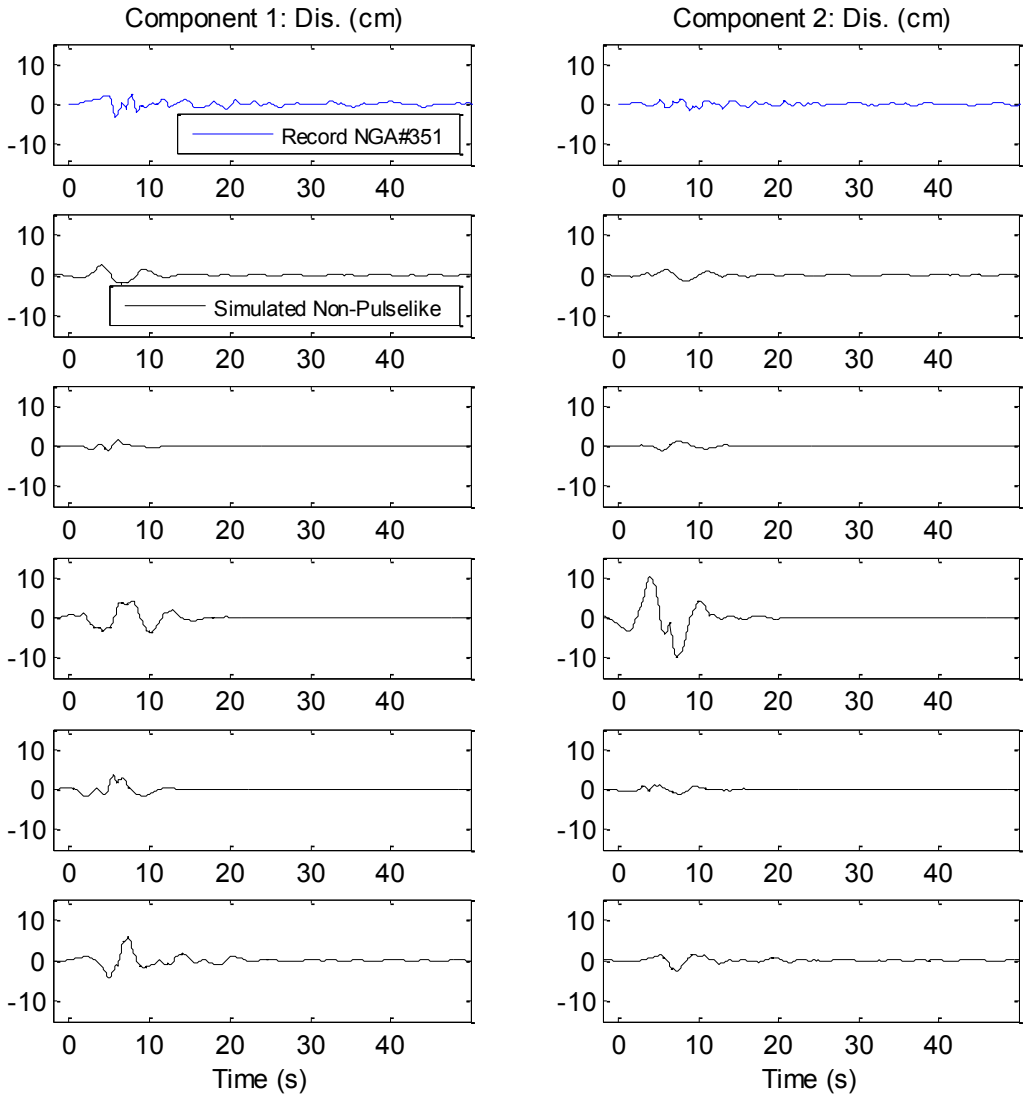

Figure 6.22 Recorded (blue) and synthetic (black) horizontal components of pulselike near-fault ground motion for model parameters in Tables 6.4 and 6.5; displacement time series.

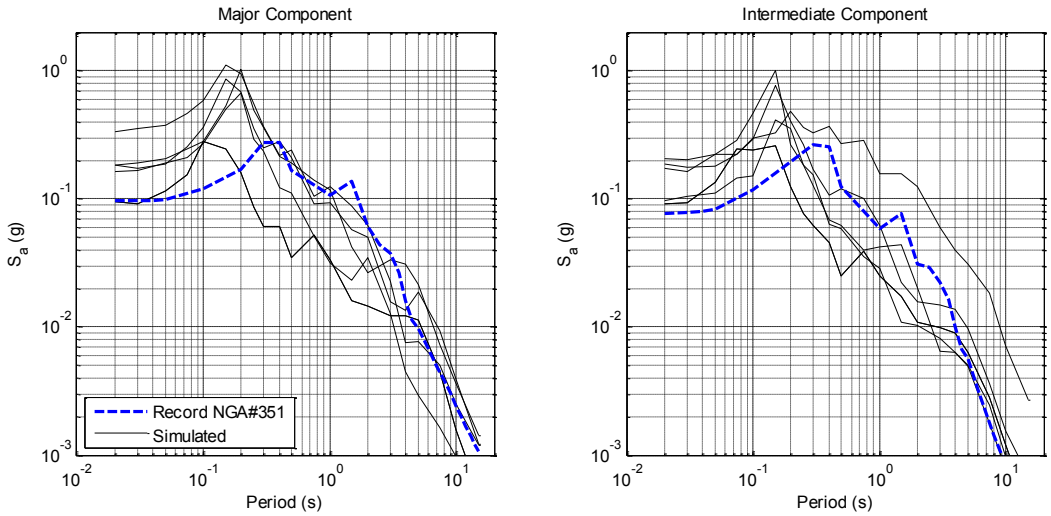

Figure 6.23 Pseudo-acceleration response spectra at 5% damping of the non-pulselike record NGA#351 (dashed blue line) and of the 5 synthetic non-pulselike ground motions. Simulations are for the earthquake source and site characteristics of record NGA#351 (black lines).

6.4.6 Example application 3: comparison with NGA-West2 GMPEs (model validation)

As part of the NGA-West2 project, five teams developed GMPEs for the average (RotD50) horizontal component of PGA, PGV and the pseudo-acceleration response spectrum at 5% damping at 21 periods ranging from 0.01 to 10 s (Bozorgnia et al., 2014). The five developers are (1) Abrahamson, Silva, and Kamai (ASK14), (2) Boore, Stewart, Seyhan, and Atkinson (BSSA14), (3) Campbell and Bozorgnia (CB14), (4) Chiou and Youngs (CY14), and (5) Idriss (I14). These five GMPEs, as well as our stochastic ground motion model, are all based on the PEER NGA-West2 database.

As a final validation of our model in this study, we compare the statistics of the elastic response spectra of synthetic ground motions with those of recorded ground motions as described by the NGA-West2 GMPEs. We use a weighted average of the five models listed above. Following the recommendation for the 2014 National Seismic Hazard Maps (Rezaeian et al., in press), ASK14, BSSA14, CB14 and CY14 are all assigned a weight of 2/9 while I14 is assigned a weight of 1/9. The weighted average of the GMPEs provides an estimate of the median and median plus and minus one standard deviation levels for the RotD50 horizontal component of recorded ground motions. The RotD50 spectrum is an orientation-independent spectrum that was defined in Section 2.5.1. We compare these median and median plus and minus one standard deviation levels to the corresponding levels of our synthetic ground motions.

As was done by Rezaeian and Der Kiureghian (2010b), we first perform a study to identify the number of simulations required to properly characterize the median ground motion level and variability of the synthetic motions for a given design scenario. We find that 300 simulations provide a relatively stable estimate of the statistics of the response spectra of synthetic near-fault ground motions, namely the median ground motion level and the logarithmic

standard deviation, $\sigma_{\ln S_a}$. Figure 6.24 shows the median (black) and median plus and minus one logarithmic standard deviation (grey) levels of the geometric mean spectra of 10 samples of 30 (left) and 300 (right) simulations for a given design scenario. It can be observed that 300 simulations provide much more stable estimates.

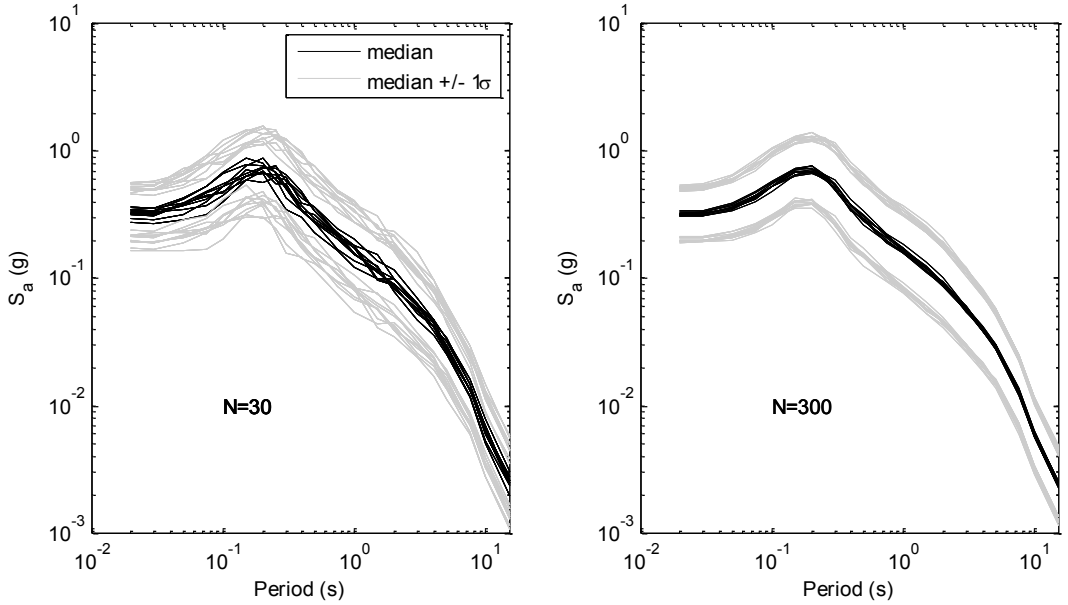

Figure 6.24 Examining the stability of statistical measures of synthetic ground motions for N=30 (left) and N=300 (right) simulations for a given design scenario: Geometric mean pseudo-acceleration response spectra at 5% damping of 10 samples of N simulated ground motions; median (black line) and median plus and minus one logarithmic standard deviation (grey lines) levels.

Simulated ground motions are compared to the GMPEs for several hypothetical design scenarios of interest. These scenarios are described in detail later on. For each design scenario, we simulate 300 pairs of synthetic horizontal ground motion components. For each simulated pair, the RotD50 horizontal component is obtained and its acceleration response spectrum at 5% damping is computed at periods between 0.01 s and 100 s. These computations were kindly performed by Dr. T. Kishida.

As discussed in Chapter 2, the NGA-West2 GMPEs do not explicitly include a directivity model and thus do not explicitly account for forward versus backward directivity conditions or for pulselike versus non-pulselike near-fault ground motions. For a given design scenario (F, **M**, Z_{TOR}, R_{RUP}, V_{s30}, etc…), these GMPEs merely represent some average of forward and backward directivity conditions and of pulselike and non-pulselike near-fault ground motions. In contrast, our stochastic model of near-fault ground motion holds the advantage of explicitly representing forward and backward directivity conditions, through directivity parameters $s_{or}d$ and $\theta_{or}\phi$, as well as pulselike and non-pulselike ground motion characteristics. To compare our model with GMPEs, we consider for each (F, **M**, Z_{TOR}, R_{RUP}, V_{s30}) scenario two distinct cases of ($s_{or}d$, $\theta_{or}\phi$) representing the two extremes of rupture directivity, namely maximum forward directivity and backward directivity.

In any design scenario, the value of $s_{or}d$ should be constrained by the subsurface length L_R of the fault rupture, an upper bound. In fact, in the case of a strike-slip fault and for a given site and rupture geometry, $s_{or}d = L_R$ only when the rupture propagates uni-directionally towards the site and the site is located at or beyond the end of the fault rupture. In all other cases, $s_{or}d < L_R$. We use the mean relation developed by Wells and Coppersmith (1994) to predict the subsurface rupture length in kilometers of a strike-slip fault as a function of magnitude,

$$\mathrm{E}[\log_{10} L_R] = -2.57 + 0.62\mathbf{M}. \tag{6.5}$$

In this section, we restrict our attention to simulations for vertical strike-slip faults ($F = 0$). We assume $Z_{TOR} = 0$ for $\mathbf{M} \geq 6.5$. Even though our model is fitted to and can be used to simulate ground motions from earthquakes with $5.5 \leq \mathbf{M} \leq 7.9$ recorded at sites located at $0 < R_{RUP} \leq 30$ km and having $139 \leq V_{s30} \leq 2016$ m/s, we expect the model to perform best in the mid-ranges, i.e., for $6 \leq \mathbf{M} \leq 7.5$, $5 < R_{RUP} \leq 25$ km and $400 < V_{S30} < 1000$ m/s. Therefore, we investigate scenarios with (1) $\mathbf{M} = 6.5$, $\mathbf{M} = 7$ and $\mathbf{M} = 7.5$, (2) $R_{RUP} = 10$ km, and (3) $V_{s30} = 525$ m/s and $V_{s30} = 760$ m/s. Sites with $V_{s30} = 525$ m/s represent the median of NEHRP site class C (very dense soil and soft rock), while sites with $V_{s30} = 760$ m/s represent the boundary between NEHRP site classes B (rock) and C (Building Seismic Safety Council, 2009). Other distance values, e.g., $R_{RUP} = 5$ km and $R_{RUP} = 30$ km will be examined in the future course of this study. For scenarios with the maximum forward directivity (FD) effect, we pick a value of $s_{or}d$ almost equal to L_R, when $\mathbf{M} = 6.5$ and $\mathbf{M} = 7$, and slightly smaller than L_R, when $\mathbf{M} = 7.5$. For the other extreme, i.e., backward directivity (BD) scenarios, we use $s_{or}d = 0$, i.e., the site is located by the epicenter at a distance of R_{RUP}. We also assume the site to be located alongside the fault rupture, thus allowing us, as discussed in Section 2.3.1.2, to obtain $\theta_{or}\phi$ by

$$\theta_{or}\phi = \tan^{-1}\frac{R_{RUP}}{s_{or}d}. \tag{6.6}$$

Values for the scenario parameters ($\mathbf{M}$, Z_{TOR}, R_{RUP}, V_{s30}, $s_{or}d$ and $\theta_{or}\phi$) that we consider in the current study are summarized in Table 6.6. The earthquake scenarios used in the NGA-West2 GMPEs do not include the directivity parameters $s_{or}d$ and $\theta_{or}\phi$, nor do they differentiate between FD and BD sites. We assume that these NGA-West2 GMPE predictions represent an average or random forward directivity condition. For the input parameters that remain unspecified in the various GMPEs, default values are assigned. For each of these scenarios, the median and median plus and minus one logarithmic standard deviation response spectra of the RotD50 component are calculated for the selected weighted average of the five NGA-West2 GMPEs at periods between 0.01 s and 10 s. To calculate the desired weighted average, we use a spreadsheet developed by PEER researchers (PEER, 2014), which assigns the proper default input parameter values where necessary.

Next, we associate forward (FD) and backward (BD) directivity conditions with each of the six scenarios by specifying the values of $s_{or}d$ and $\theta_{or}\phi$, and denote them by a and b, respectively (see Table 6.6). For each of these twelve scenarios, the probability of observing a pulse in the ground motion in at least one direction is calculated from (6.4) and listed in the last column of Table 6.6. At backward directivity sites, the probability of observing a pulselike ground motion is greater than 0 but does not exceed 0.1. For each scenario, the median and

median plus and minus one logarithmic standard deviation response spectra of the corresponding RotD50 components of 300 simulated ground motions are computed from the individual spectra at periods between 0.01 s and 100 s.

Table 6.6 Description of design scenarios used for comparison of our stochastic model with NGA-West2 GMPEs.

	M	Z_{TOR} (km)	R_{RUP} (km)	V_{s30} (m/s)	Directivity	s or d (km)	θ or ϕ (°)	P_{pulse}
1.a	6.5	0	10	760	FD	30	18.4	0.48
1.b					BD	0	90	0.09
2.a	7.0	0	10	760	FD	60	9.5	0.90
2.b					BD	0	90	0.09
3.a	7.5	0	10	760	FD	100	5.7	0.99
3.b					BD	0	90	0.09
4.a	6.5	0	10	525	FD	30	18.4	0.48
4.b					BD	0	90	0.09
5.a	7.0	0	10	525	FD	60	9.5	0.90
5.b					BD	0	90	0.09
6.a	7.5	0	10	525	FD	100	5.7	0.99
6.b					BD	0	90	0.09

The results for scenario 1 ($\mathbf{M} = 6.5$ and $V_{s30} = 760$ m/s) are plotted in Figures 6.25-6.28. Figure 6.25 shows the median and median plus and minus one logarithmic standard deviation levels of the 5% damped pseudo-acceleration response spectra of the RotD50 component for 300 synthetic motions at a forward directivity (FD) site (in red) and for 300 synthetic motions at a backward directivity (BD) site (in blue), as well as the corresponding values predicted by the weighted average of the five NGA-West2 GMPEs (in black). Although GMPEs predict spectral values only between 0.01 s and 10 s, we plot the spectra of simulated motions in this and subsequent figures up to a period of 20 s. The range is extended to illustrate the effect on response spectra of the directivity pulses in simulated pulselike motions, since a few of these pulses may have periods longer than 10 s. Figure 6.26 shows the histogram of the period of the pulse in the pulselike synthetic motions at the forward (blue) and backward (red) directivity sites.

In Figure 6.27, the synthetic motions from scenarios 1.a (forward directivity) and 1.b (backward directivity) are combined. We assume that the combined 600 synthetic motions represent motions resulting from an average or random directivity condition. A more accurate representation of the average condition would require taking into account, when simulating ground motions, the entire range of possible values of the directivity parameters $s_{or}d$ and $\theta_{or}\phi$

with their corresponding likelihoods, for the given earthquake scenario 1. The median and median plus and minus one logarithmic standard deviation levels of the 5% damped pseudo-acceleration response spectra of the RotD50 component for the combined 600 synthetic motions are plotted in green. The corresponding values from the NGA-West2 GMPEs are shown in black and are identical to those in Figure 6.25. Finally, Figure 6.28 shows estimates of the logarithmic standard deviation of the 5% damped pseudo-acceleration response spectra of the RotD50 component for the combined 600 synthetic motions (in green) and from the NGA-West2 GMPEs (in black). Similar results for scenarios 2,3,4,5 and 6 are plotted in Figures 6.29-6.32, Figures 6.33-6.36, Figures 6.37-6.40, Figures 6.38-6.44, and Figures 6.45-6.48, respectively.

Several observations can be made about earthquake scenario 1 from Figure 6.25. First, and consistent with our expectation, the forward directivity scenario 1.a results in larger median spectral values than the backward directivity scenario 1.b at periods between about 0.2 s and 5 s. The two spectra are generally similar at other periods. Indeed, from Figure 6.26 and consistent with the last column of Table 6.6, we observe that scenario 1.a results in more pulselike ground motions than scenario 1.b. The numerous pulses from scenario 1.a have periods between 0.4 s and 5 s and produce peaks in the corresponding response spectra near their pulse periods (see Section 2.4.1). These pulses explain the spectral differences in Figure 6.25 at periods of 0.2 s to 5 s between the forward and backward directivity sites for an otherwise identical earthquake scenario. Also from Figure 6.25, we observe that the median spectrum from simulated motions at the backward directivity site is in good agreement with the median spectrum predicted by the NGA-West2 GMPEs, apart from periods between 2 s and 10 s. At these longer periods, the spectrum from the backward directivity simulations lies above the median level, but below the median plus one standard deviation level from the GMPEs.

Next for earthquake scenario 1, we compare in Figure 6.27 the median ground motion levels from the simulated motions and from the GMPEs, under the assumption that both represent average or random directivity conditions. Good agreement is observed in general. The median level from the simulations lies above the median level from the GMPEs at periods of about 0.01 s to 0.05 s, 0.1 s to 0.3 s, and 1 s to 10 s. The difference at the longer periods is an indication that the NGA-West2 GMPEs probably do not represent the near-fault rupture directivity effect adequately. The difference at the shorter periods possibly indicates a limitation of our model in representing the high-frequency content.

Finally in Figure 6.28, we compare the logarithmic standard deviations of the RotD50 spectra from the simulated motions and from the GMPEs for earthquake scenario 1 and average or random directivity conditions. Figure 6.28 shows that the variability obtained from simulated motions is generally comparable to that predicted by GMPEs between periods of 0.1 s and 10 s. The variability of the simulated motions is smaller than that predicted by GMPEs at periods below 0.1 s, indicating that our ground motion model underestimates variability at high frequencies. However, these frequencies generally do not influence the response of typical structural systems of interest.

Similar observations as for earthquake scenario 1 are also made for earthquake scenarios 2 to 6. The forward directivity scenarios (a) result in larger median spectral values than the backward directivity scenario (b) at the longer periods, namely at periods greater than 0.2 s for scenario 2 ($\mathbf{M} = 7.0$, $V_{s30} = 760$ m/s) and scenario 3 ($\mathbf{M} = 7.5$, $V_{s30} = 760$ m/s) (see Figures 6.29 and 6.33, respectively), between about 0.4 s and 5 s for scenario 4 **(**$\mathbf{M} = 6.5$, and $V_{s30} = 525$ m/s) (see Figure 6.37), greater than 0.2 s for scenario 5 **(**$\mathbf{M} = 7.0$ and $V_{s30} = 525$ m/s) (see

Figure 6.41), and greater than 1 s for scenario 6 (**M** = 7.5 and V_{s30} = 525 m/s) (see Figure 6.45). These observations are consistent with the large number of pulselike motions among the simulations for the forward directivity scenarios. These pulselike motions contain directivity pulses that have periods between 0.5 s and 10 s for scenario 2.a (see Figure 6.30), between 1.3 s and 15 s for scenario 3.a (see Figure 6.34), between 0.5 s and 5 s for scenario 4.a (see Figure 6.38), between 0.6 s and 10 s for scenario 5.a (see Figure 6.42), and between 1.7 s and 20 s for scenario 6.a (see Figure 6.46).

From Figures 6.29, 6.33, 6.37, 6.41 and 6.45, we also observe that the median spectra from simulated motions at the backward directivity sites are in overall good agreement with the median spectra predicted by the NGA-West2 GMPEs. At the lower and intermediate periods, the median spectra from the backward directivity simulations sometimes lie below the median level, but above the median minus one standard deviation level from the GMPEs. At the longer periods, the median spectra from the backward directivity simulations sometimes lie above the median level, but below the median plus one standard deviation level from the GMPEs.

In Figures 6.31, 6.35, 6.39, 6.43 and 6.47, the median ground motion levels from the simulated motions and from the GMPEs are compared, under the assumption that both represent average or random directivity conditions. In general, these figures show that the simulations and the GMPEs are in overall good agreement. However, the median levels from the simulations generally lie above the median levels from the GMPEs at the longer periods, greater than 1 s or 2 s. As discussed for scenario 1, these differences indicate that the NGA-West2 GMPEs do not adequately represent the near-fault rupture directivity effect.

Finally, Figures 6.32, 6.36, 6.40, 6.44 and 6.48 show that the variability obtained from simulated motions is consistent with or slightly underestimates the variability predicted by GMPEs between periods of 0.1 s and 10 s.

We summarize the observations from all scenarios. First, the forward directivity scenarios result in larger median spectral values than the backward directivity scenarios at longer periods. These differences occur because pulselike motions are more frequent and have longer periods at forward compared to backward directivity sites. The long period pulses in these pulselike motions produce peaks in the corresponding response spectra near their pulse periods (see Section 2.4.1). Second, we observe that the median spectra from ground motions simulated for the backward directivity scenarios are in overall good agreement with the corresponding median spectra predicted by the NGA-West2 GMPEs. If they deviate at some periods, they still lie within the median plus and median minus one standard deviation levels. Next, the difference observed between the simulations and the GMPEs for the average or random directivity condition indicate that the NGA-West2 GMPEs do not adequately represent the near-fault rupture directivity effect. Finally, our ground motion model adequately predicts the variability in elastic response spectral amplitudes at periods between 0.1 s and 10 s but it underestimates variability at lower periods.

The final comment is in regards to the comparison of the right portion of Figures 6.8 and 6.15 to Figures 6.28, 6.32, 6.36, 6.40, 6.44 and 6.48. As expected, we observe that the variability of synthetic ground motions is larger when the simulations are for specified earthquake source and site characteristics (the latter figures) compared to when the simulations are for fitted model parameter values (Figures 6.8 and 6.15). Variability in ground motions simulated for fitted model parameters arises only from the white-noise process. Variability in ground motions simulated for

specified earthquake source and site characteristics arises from the white-noise process and from uncertainty in the model parameter values for the given earthquake source and site characteristics. This latter variability represents the natural variability that we observe among ground motion records obtained for different earthquakes but similar source and site characteristics.

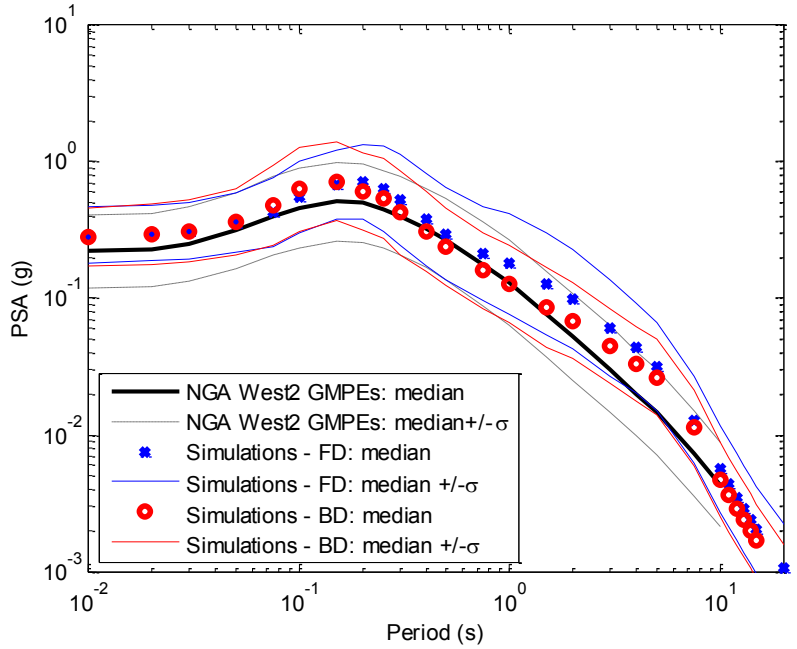

Figure 6.25 Median and median plus and minus one logarithmic standard deviation of 5% damped pseudo-acceleration response spectra of RotD50 component for 300 synthetic motions at a forward directivity site (blue), 300 synthetic motions at a backward directivity site (red), and corresponding values predicted by the NGA-West2 GMPEs (black), for earthquake design scenario 1.

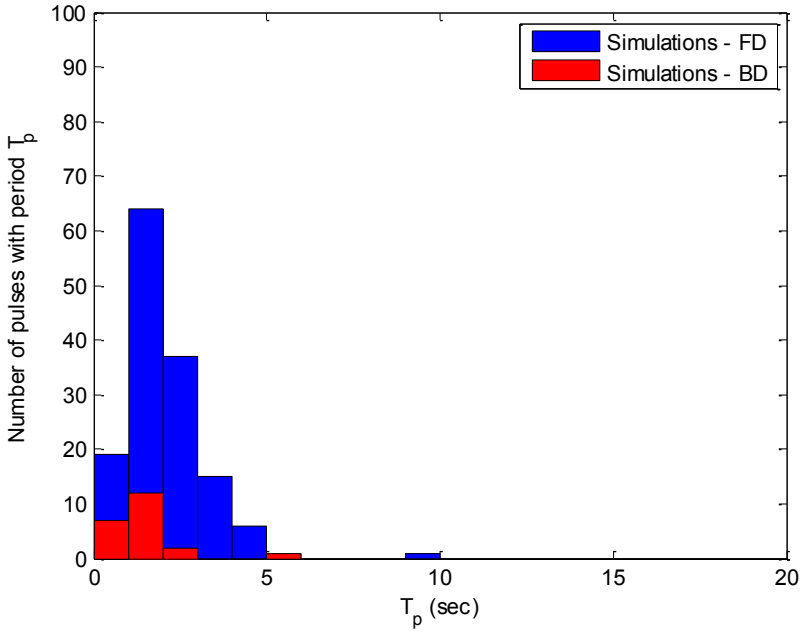

Figure 6.26 Histogram of the period of the pulse in the pulselike synthetic motions at forward directivity (blue) and backward directivity (red) sites, for earthquake design scenario 1.

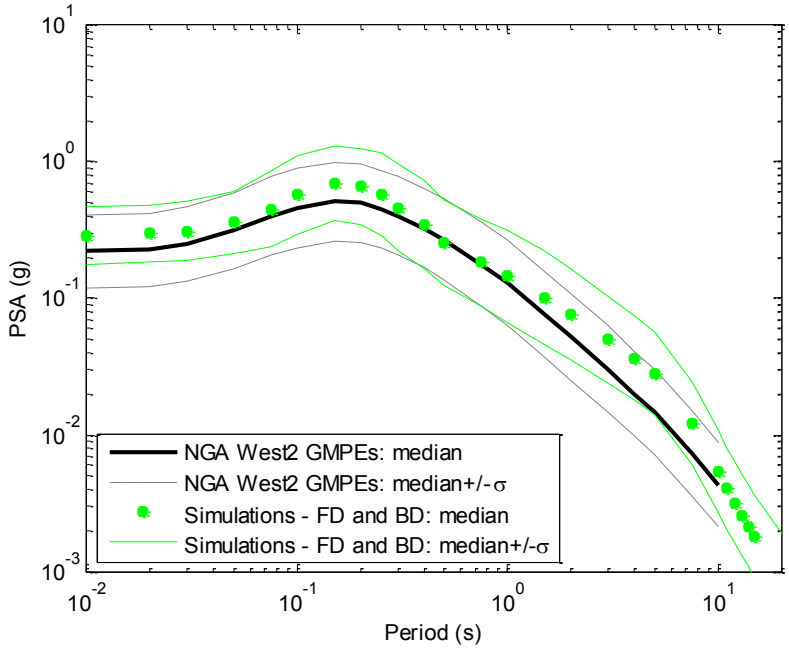

Figure 6.27 Median and median plus and minus one logarithmic standard deviation of 5% damped pseudo-acceleration response spectra of RotD50 component for the 600 combined FD and BD synthetic motions (green) and corresponding values predicted by the NGA-West2 GMPEs (black), for earthquake design scenario 1.

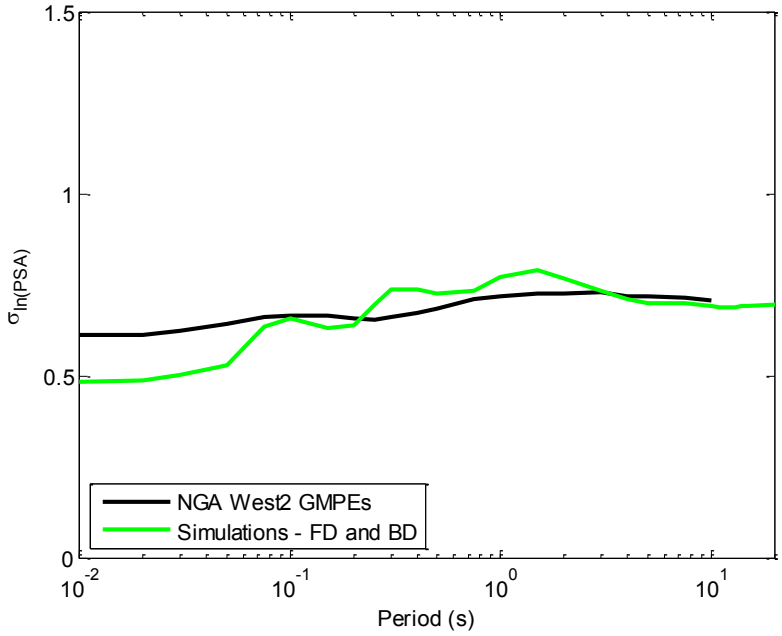

Figure 6.28 Logarithmic standard deviation of 5% damped pseudo-acceleration response spectra of RotD50 component for the 600 combined FD and BD synthetic motions (green) and corresponding values predicted by the NGA-West2 GMPEs (black), for earthquake design scenario 1.

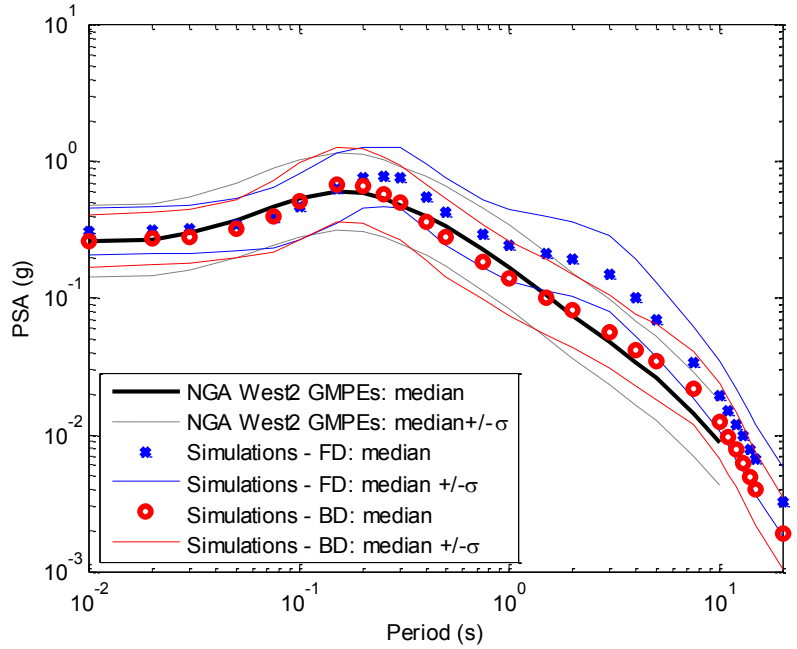

Figure 6.29 Median and median plus and minus one logarithmic standard deviation of 5% damped pseudo-acceleration response spectra of RotD50 component for 300 synthetic motions at a forward directivity site (blue), 300 synthetic motions at a backward directivity site (red), and corresponding values predicted by the NGA-West2 GMPEs (black), for earthquake design scenario 2.

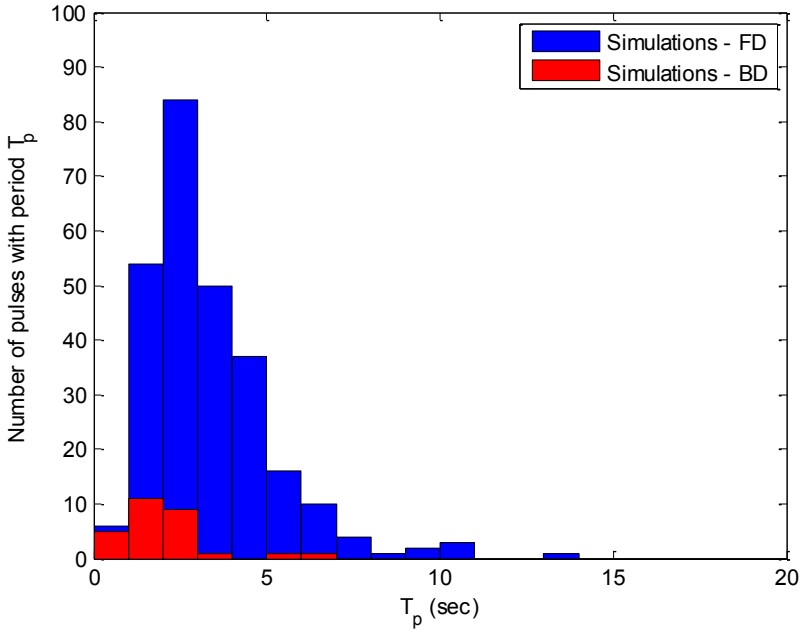

Figure 6.30 Histogram of the period of the pulse in the pulselike synthetic motions at forward directivity (blue) and backward directivity (red) sites, for earthquake design scenario 2.

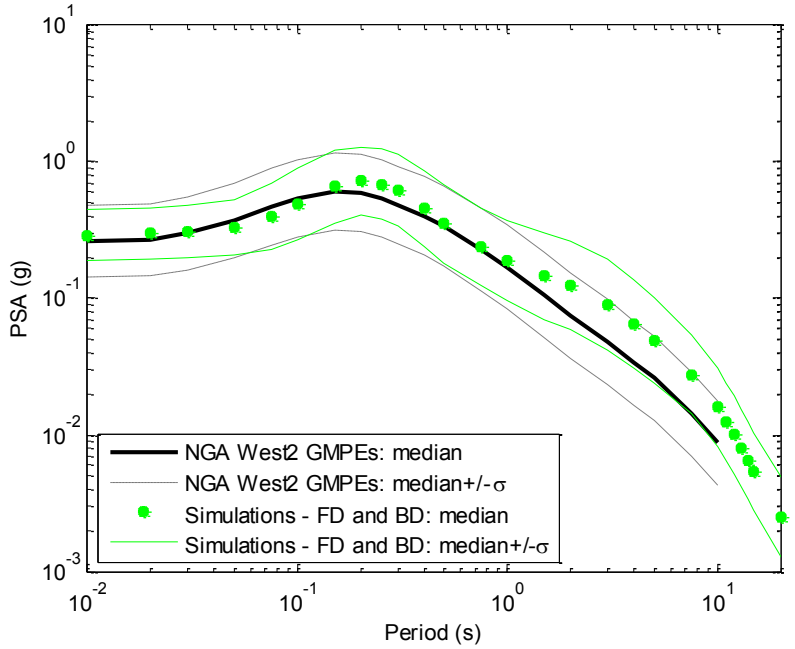

Figure 6.31 Median and median plus and minus one logarithmic standard deviation of 5% damped pseudo-acceleration response spectra of RotD50 component for the 600 combined FD and BD synthetic motions (green) and corresponding values predicted by the NGA-West2 GMPEs (black), for earthquake design scenario 2.

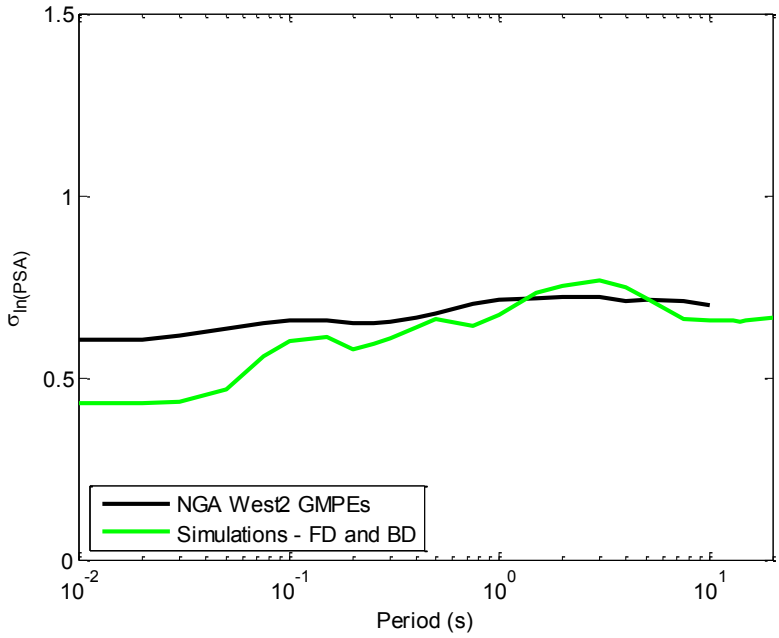

Figure 6.32 Logarithmic standard deviation of 5% damped pseudo-acceleration response spectra of RotD50 component for the 600 combined FD and BD synthetic motions (green) and corresponding values predicted by the NGA-West2 GMPEs (black), for earthquake design scenario 2.

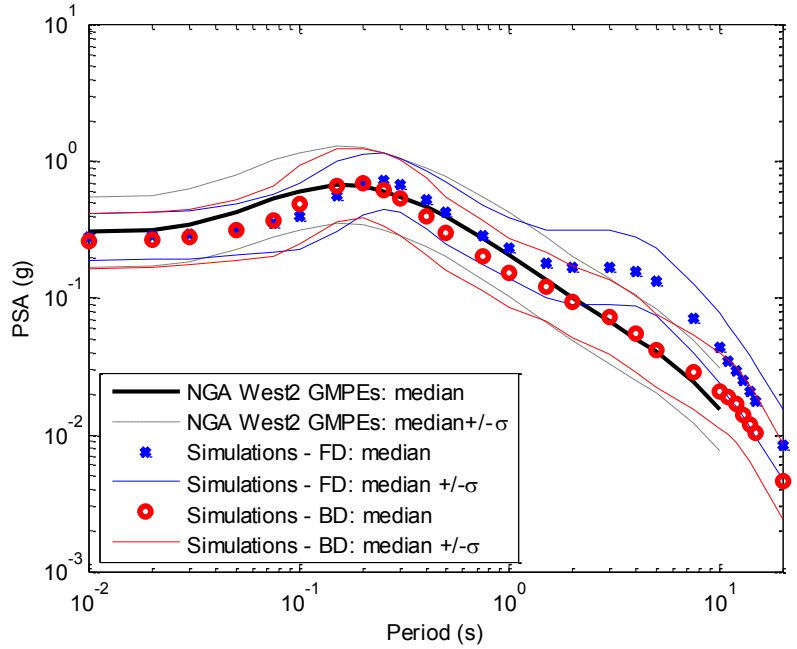

Figure 6.33 Median and median plus and minus one logarithmic standard deviation of 5% damped pseudo-acceleration response spectra of RotD50 component for 300 synthetic motions at a forward directivity site (blue), 300 synthetic motions at a backward directivity site (red), and corresponding values predicted by the NGA-West2 GMPEs (black), for earthquake design scenario 3.

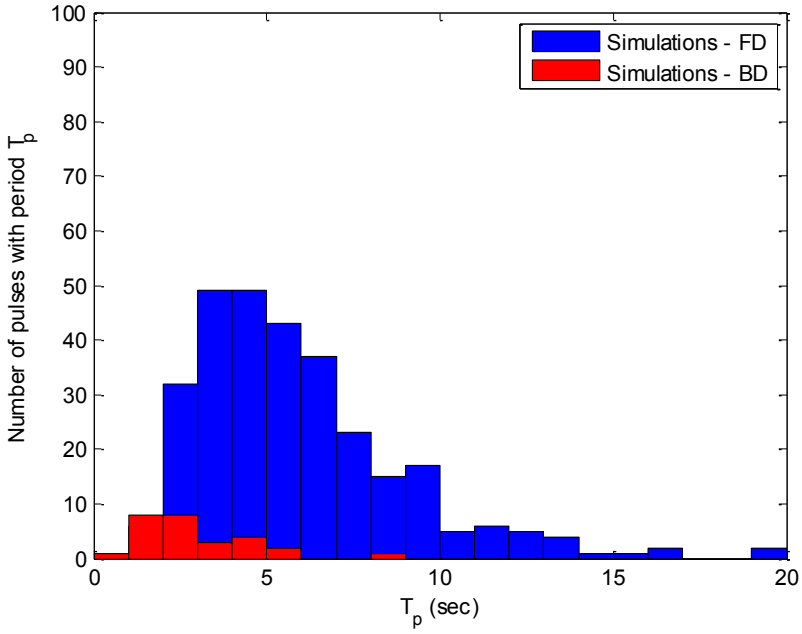

Figure 6.34 Histogram of the period of the pulse in the pulselike synthetic motions at forward directivity (blue) and backward directivity (red) sites, for earthquake design scenario 3.

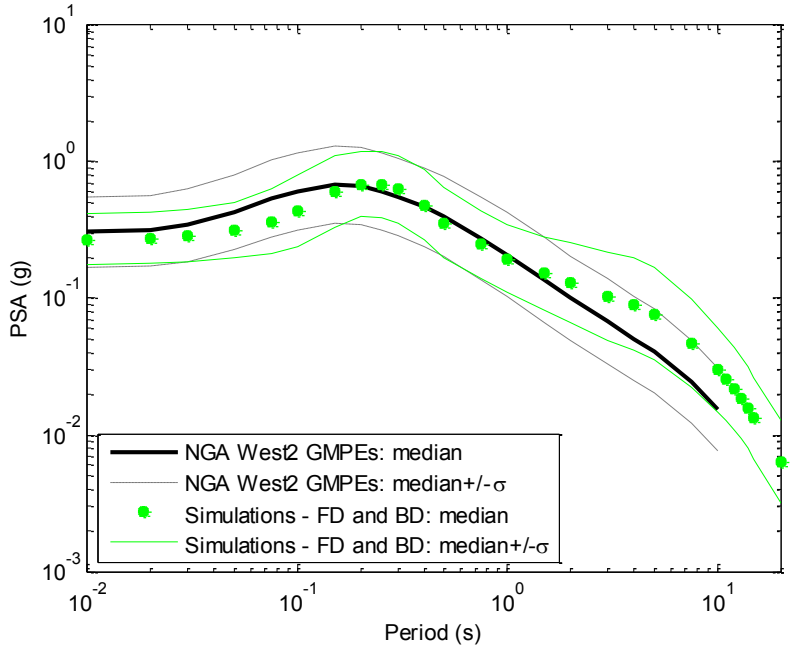

Figure 6.35 Median and median plus and minus one logarithmic standard deviation of 5% damped pseudo-acceleration response spectra of RotD50 component for the 600 combined FD and BD synthetic motions (green) and corresponding values predicted by the NGA-West2 GMPEs (black), for earthquake design scenario 3.

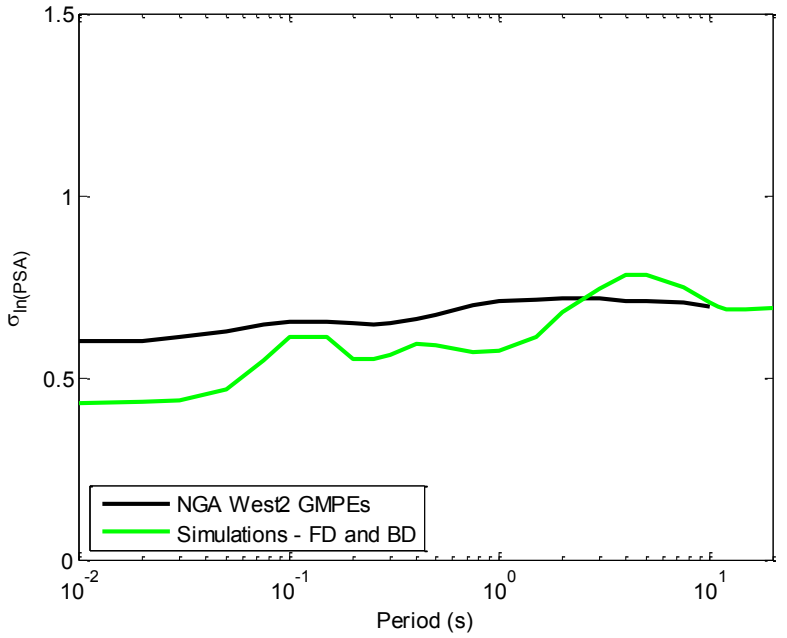

Figure 6.36 Logarithmic standard deviation of 5% damped pseudo-acceleration response spectra of RotD50 component for the 600 combined FD and BD synthetic motions (green) and corresponding values predicted by the NGA-West2 GMPEs (black), for earthquake design scenario 3.

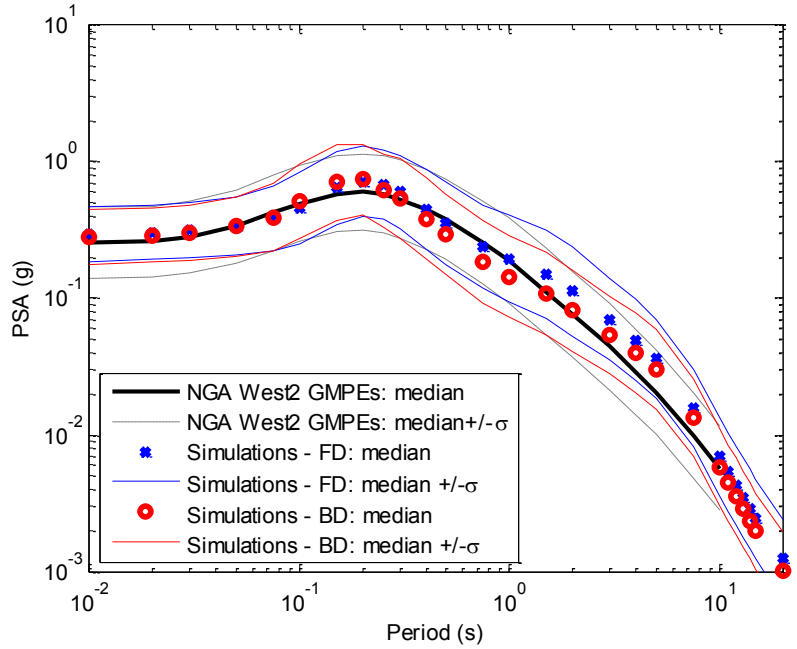

Figure 6.37 Median and median plus and minus one logarithmic standard deviation of 5% damped pseudo-acceleration response spectra of RotD50 component for 300 synthetic motions at a forward directivity site (blue), 300 synthetic motions at a backward directivity site (red), and corresponding values predicted by the NGA-West2 GMPEs (black), for earthquake design scenario 4.

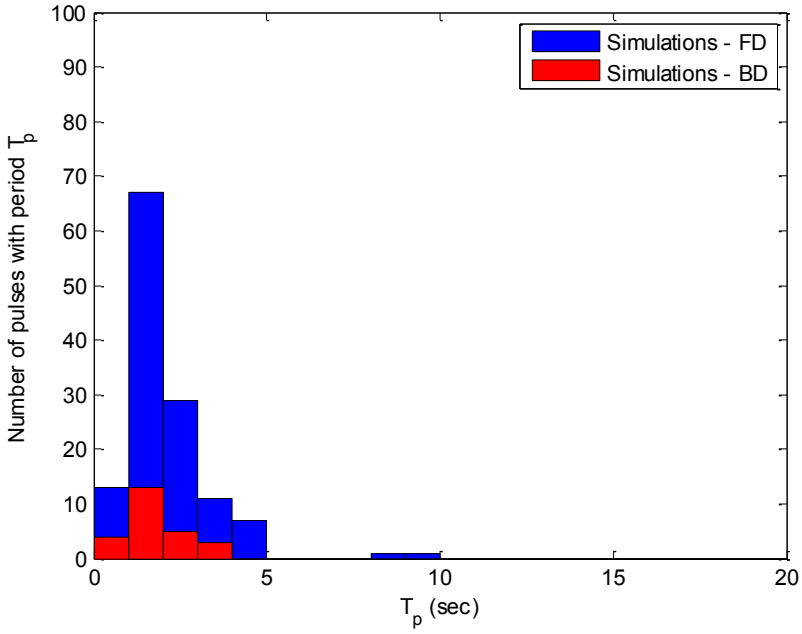

Figure 6.38 Histogram of the period of the pulse in the pulselike synthetic motions at forward directivity (blue) and backward directivity (red) sites, for earthquake design scenario 4.

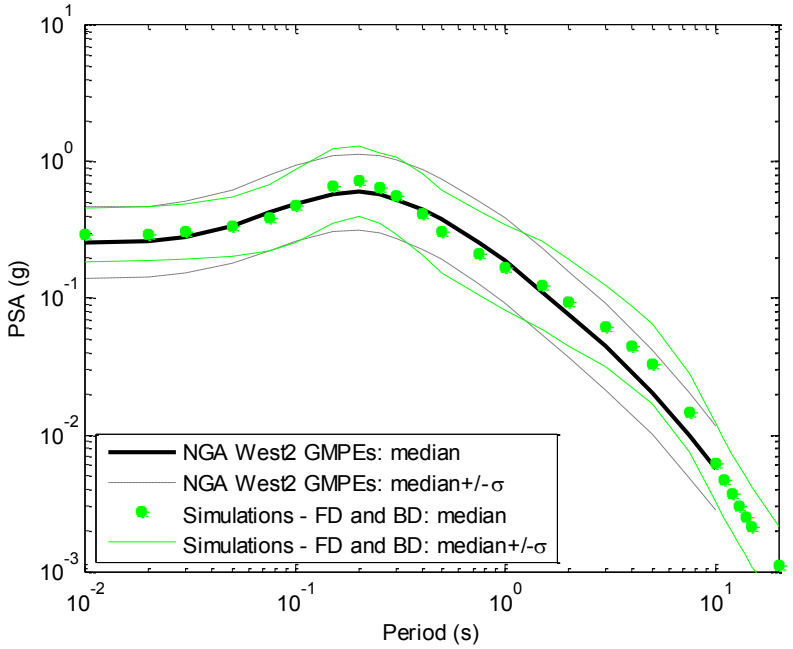

Figure 6.39 Median and median plus and minus one logarithmic standard deviation of 5% damped pseudo-acceleration response spectra of RotD50 component for the 600 combined FD and BD synthetic motions (green) and corresponding values predicted by the NGA-West2 GMPEs (black), for earthquake design scenario 4.

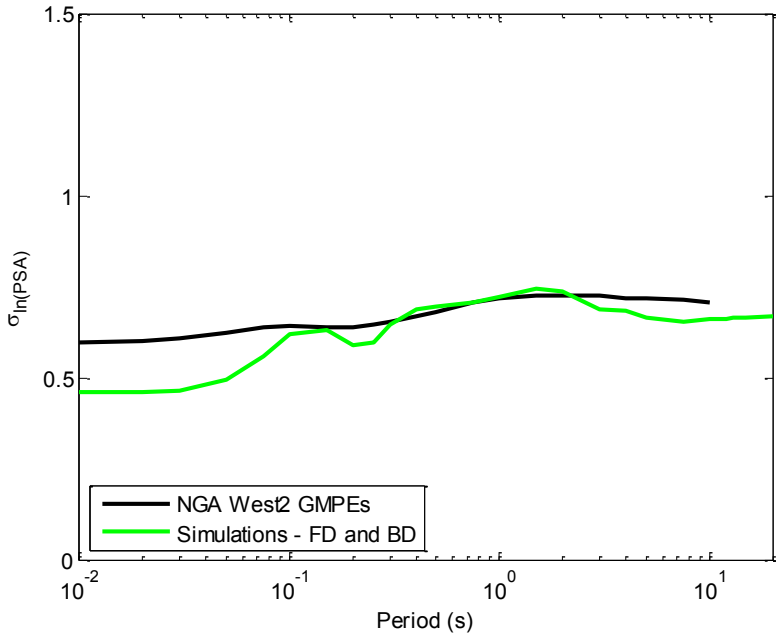

Figure 6.40 Logarithmic standard deviation of 5% damped pseudo-acceleration response spectra of RotD50 component for the 600 combined FD and BD synthetic motions (green) and corresponding values predicted by the NGA-West2 GMPEs (black), for earthquake design scenario 4.

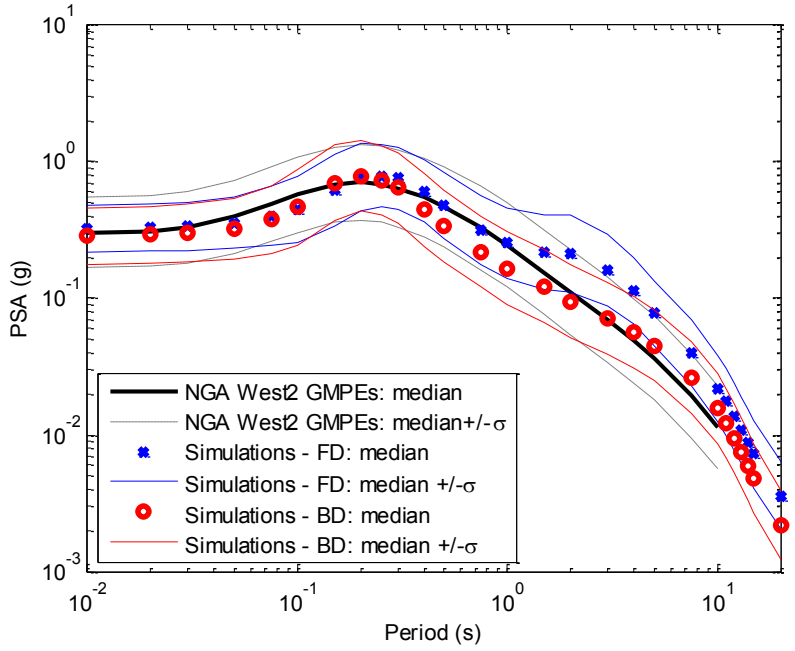

Figure 6.41 Median and median plus and minus one logarithmic standard deviation of 5% damped pseudo-acceleration response spectra of RotD50 component for 300 synthetic motions at a forward directivity site (blue), 300 synthetic motions at a backward directivity site (red), and corresponding values predicted by the NGA-West2 GMPEs (black), for earthquake design scenario 5.

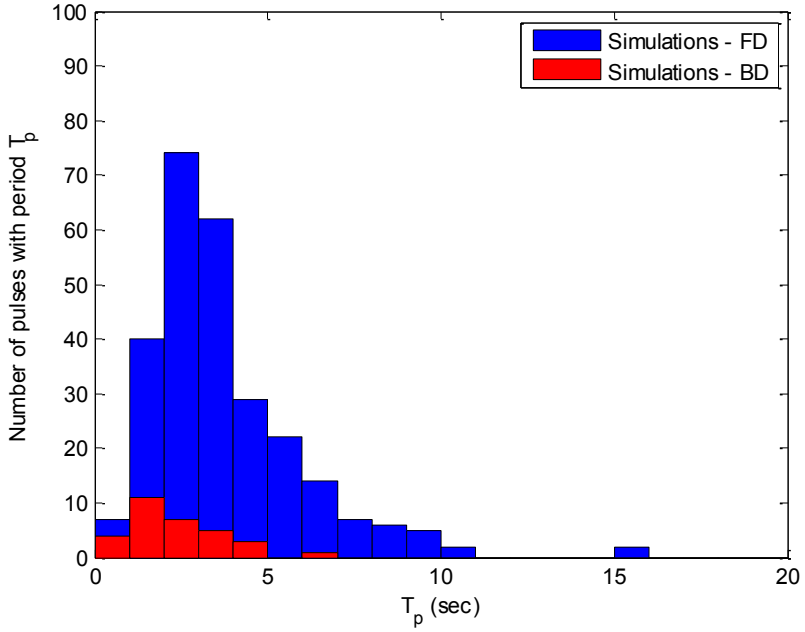

Figure 6.42 Histogram of the period of the pulse in the pulselike synthetic motions at forward directivity (blue) and backward directivity (red) sites, for earthquake design scenario 5.

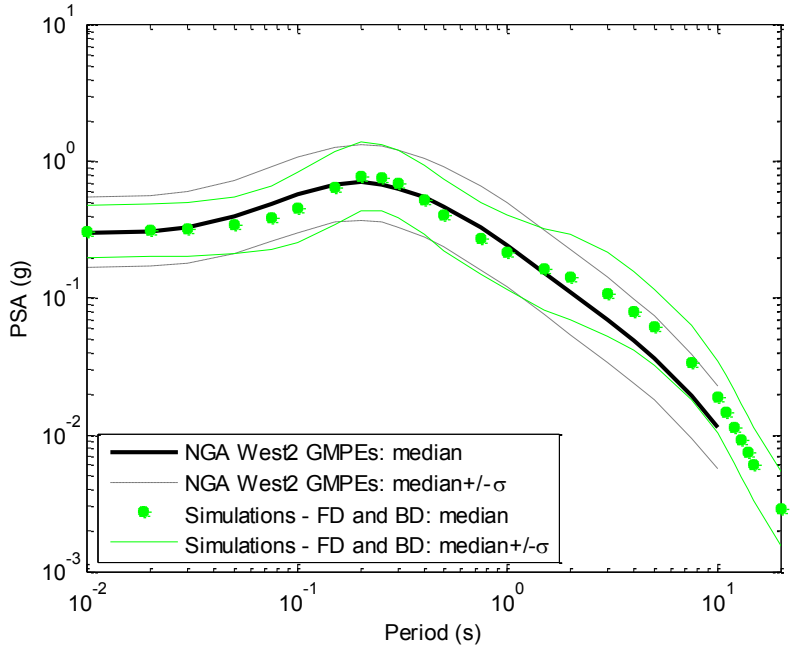

Figure 6.43 Median and median plus and minus one logarithmic standard deviation of 5% damped pseudo-acceleration response spectra of RotD50 component for the 600 combined FD and BD synthetic motions (green) and corresponding values predicted by the NGA-West2 GMPEs (black), for earthquake design scenario 5.

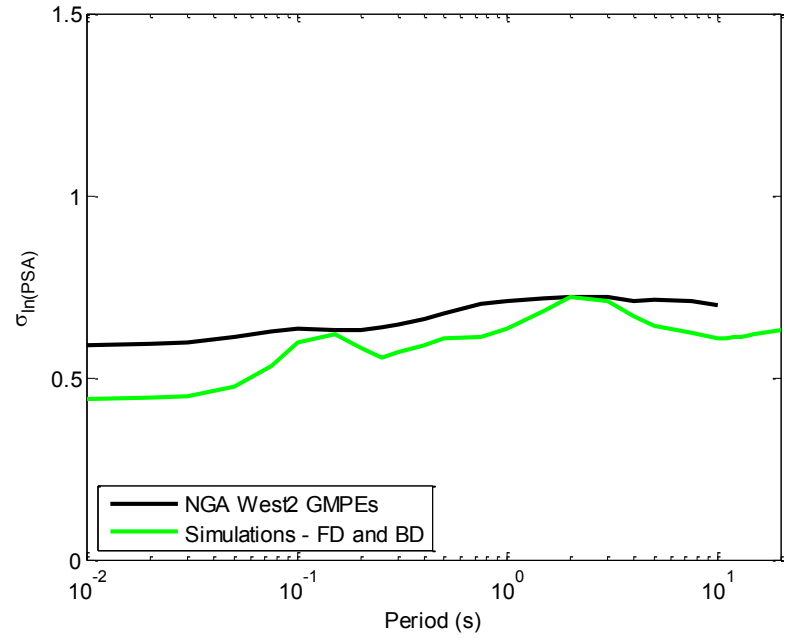

Figure 6.44 Logarithmic standard deviation of 5% damped pseudo-acceleration response spectra of RotD50 component for the 600 combined FD and BD synthetic motions (green) and corresponding values predicted by the NGA-West2 GMPEs (black), for earthquake design scenario 5.

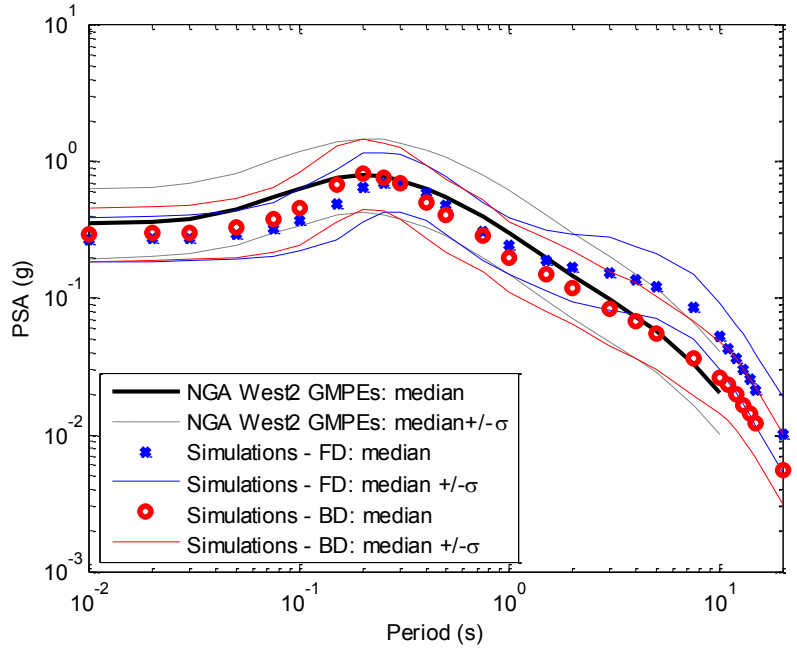

Figure 6.45 Median and median plus and minus one logarithmic standard deviation of 5% damped pseudo-acceleration response spectra of RotD50 component for 300 synthetic motions at a forward directivity site (blue), 300 synthetic motions at a backward directivity site (red), and corresponding values predicted by the NGA-West2 GMPEs (black), for earthquake design scenario 6.

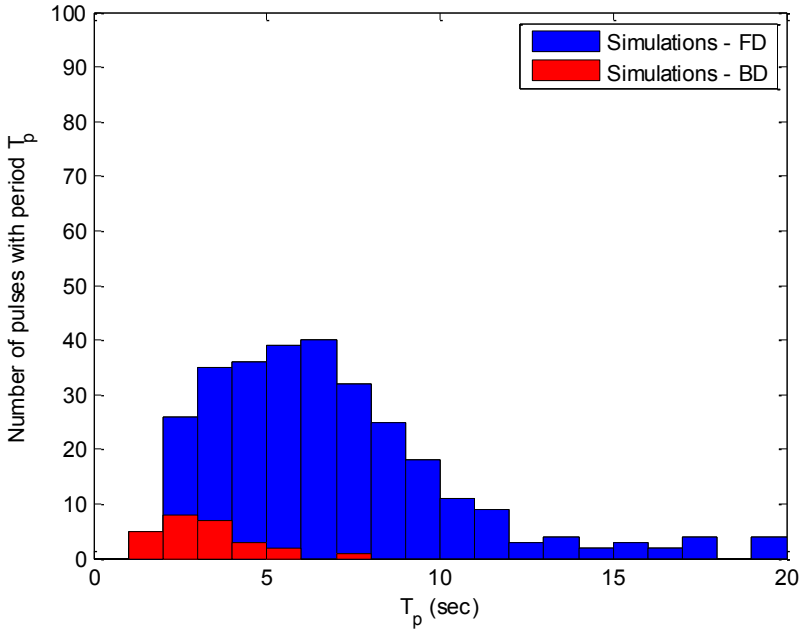

Figure 6.46 Histogram of the period of the pulse in the pulselike synthetic motions at forward directivity (blue) and backward directivity (red) sites, for earthquake design scenario 6.

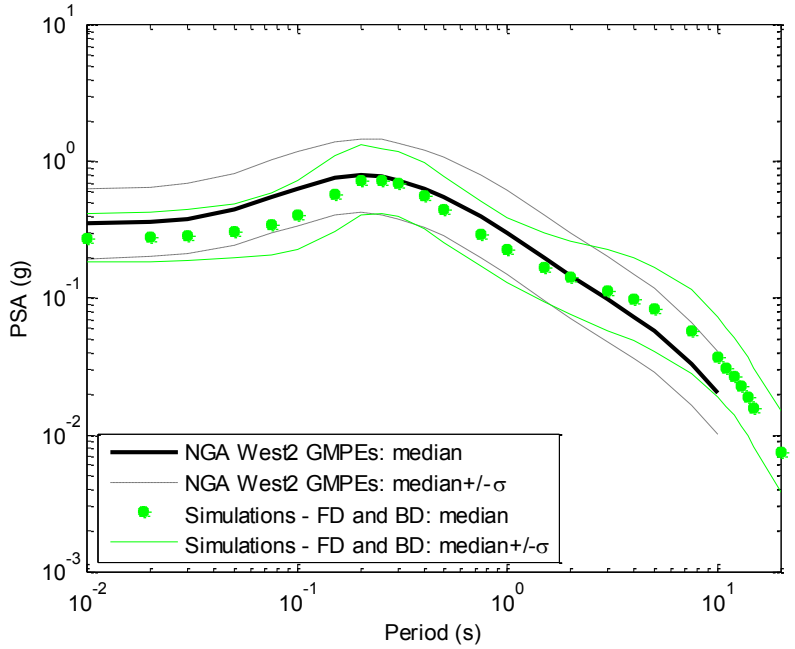

Figure 6.47 Median and median plus and minus one logarithmic standard deviation of 5% damped pseudo-acceleration response spectra of RotD50 component for the 600 combined FD and BD synthetic motions (green) and corresponding values predicted by the NGA-West2 GMPEs (black), for earthquake design scenario 6.

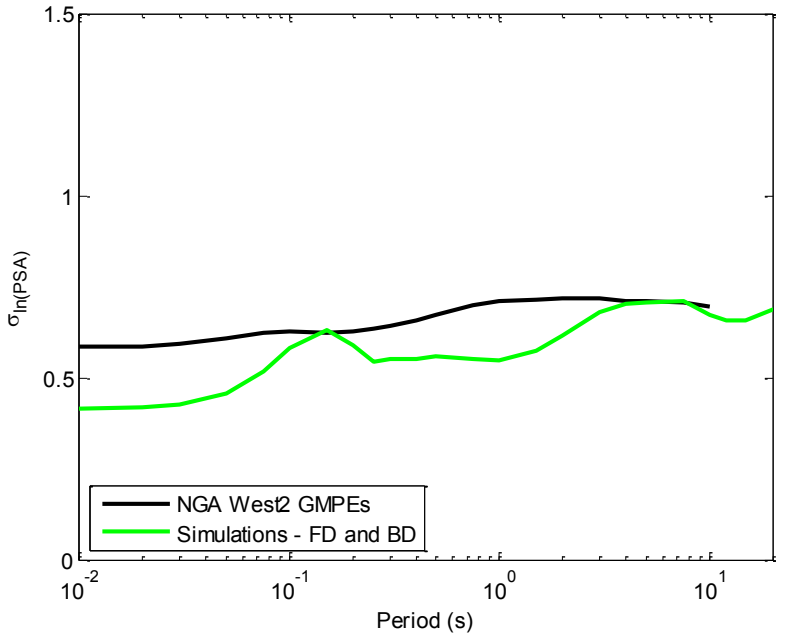

Figure 6.48 Logarithmic standard deviation of 5% damped pseudo-acceleration response spectra of RotD50 component for the 600 combined FD and BD synthetic motions (green) and corresponding values predicted by the NGA-West2 GMPEs (black), for earthquake design scenario 6.

6.5 SIMULATION OF GROUND MOTION WITH FLING STEP

For the near-fault ground motion model and simulation procedure to be complete, they should also include the possibility of a fling step. The fling step can be described using a few parameters and incorporated into the model in a fashion similar to the directivity pulse model. While the directivity pulse appears as a two-sided pulse in the velocity time series, the fling velocity appears as a one-sided pulse. In this dissertation, a ground motion is denoted as pulselike or non-pulselike solely relative to the existence or non-existence of a directivity pulse and regardless of the fling effect.

Methods similar to the ones presented earlier are applicable to fit the model of the fling step to observations, and to use it in the generation of synthetic near-fault ground motions. However, standard filtering and baseline correction procedures remove the static displacement from recorded ground motions. As a result, empirical observations of the fling step are extremely rare and this lack of data prevents us from directly fitting the model. Instead, we resort to using the simple model that was proposed by Abrahamson (2001) and was described in Section 2.6.

Occurrence of the fling step depends on the geometry of the fault rupture and on the location of the site relative to the rupture plane. It is assumed to be independent of the rupture directivity effect, i.e., of the pulselike or non-pulselike nature of the near fault ground motion. Hereafter, the discussion and simulations are limited to vertical strike-slip faulting. In these cases, the fault slips along the strike of the fault. A permanent displacement or fling step is observed only at sites located adjacent to the fault rupture and within a specified distance that depends on whether or not the fault ruptures to the surface (see Figure 2.13). A site is said to be adjacent to the vertical strike-slip fault rupture if the perpendicular distance R_x, in the horizontal plane, between the site and the fault trace *direction*, is equal to the closest distance in the horizontal plane between the site and the fault trace, i.e., if

$$R_x = \sqrt{R_{RUP}^2 - Z_{TOR}^2}. \tag{6.7}$$

The amplitude of the fling depends on the magnitude of the earthquake. For vertical strike-slip faulting, the fling step occurs and is modeled in the strike-parallel component of ground motion, even though it may be observed in a range of orientations. Therefore, to include a fling step in the two orthogonal horizontal components of a synthetic ground motion, the ground motion is first rotated to the strike-normal and strike-parallel directions then the fling is added to the strike-parallel component.

The fling model by Abrahamson (2001) is for vertical strike-slip faulting in the strike-parallel direction. It has three parameters and its acceleration time series is defined by

$$\begin{aligned} a_{fling}(t) &= A_{fling} \sin\left[\frac{2\pi\left(t - t_{fling}\right)}{T_{fling}}\right] \quad t_{fling} \le t < t_{fling} + T_{fling}, \\ &= 0 \qquad\qquad\qquad\qquad\qquad\qquad\qquad\qquad \text{otherwise} \end{aligned} \tag{6.8}$$

where A_{fling} is the acceleration amplitude, T_{fling} is the period, and t_{fling} is the arrival time of the fling. These parameters are predicted as functions of the earthquake source and site characteristics, as described in Section 2.6. The relations in (2.40) and (2.41) are repeated here

for the sake of convenience. Given $\mathbf{M}$, the average slip D_{fault} (in units of centimeter) on the fault is predicted by

$$\mathrm{E}\left[\ln D_{fault}\right] = 1.15\mathbf{M} - 2.83, \tag{6.9}$$

and the period T_{fling} in seconds is predicted by

$$\mathrm{E}\left[\ln T_{fling}\right] = -6.96 + 1.15\mathbf{M}. \tag{6.10}$$

We use the relation developed by Wells and Coppersmith (1994) to predict the rupture width W (in kilometers) of a strike-slip fault as a function of the magnitude,

$$\mathrm{E}[\log_{10} W] = -0.76 + 0.27\mathbf{M}. \tag{6.11}$$

Having computed D_{fault}, the average slip in centimeters at the site, D_{site}, is computed using (2.38) and (2.39), which are repeated here for convenience. If $Z_{TOR} = 0$, i.e., the fault ruptures to the surface,

$$D_{site} = \frac{D_{fault}}{2}\left[1 - \frac{2}{\pi}\tan^{-1}\left(\frac{R_x}{W}\right)\right], \tag{6.12}$$

else,

$$D_{site} = \frac{D_{fault}}{\pi}\left[\tan^{-1}\left(\frac{R_x}{Z_{TOR}}\right) - \tan^{-1}\left(\frac{R_x}{Z_{TOR} + W}\right)\right]. \tag{6.13}$$

Abrahamson (2001) assumes that the arrival time t_{fling} of the fling coincides with the time of arrival of S-waves. We further assume that S-waves arrive at the time of the 5% of Arias intensity of ground motion in the fault-parallel direction, i.e.,

$$t_{fling} = t_{5,FP}. \tag{6.14}$$

Finally, the acceleration amplitude A_{fling} in units of g is computed according to (2.42) which is repeated here,

$$A_{fling} = \frac{D_{site} 2\pi}{981 T_{fling}^2}. \tag{6.15}$$

This formulation does not account for variability in the model parameters, given the earthquake source and site characteristics. Neither does it account for correlation between the three fling model parameters, nor between the fling model parameters and the other parameters of the near-fault ground motion model (i.e., the parameters of the directivity pulse and of the modulated and filtered white-noise model). These limitations arise from lack of data and our ensuing inability to fit the fling model ourselves. In due time, when sufficient numbers of recorded motions with fling step are available, predictive equations for the model parameters in terms of earthquake and site characteristics can be developed.

Thus, to simulate two orthogonal horizontal components of a near-fault ground motion for a strike-slip earthquake ($F = 0$) and a given set of earthquake source and site characteristics ($\mathbf{M}$, Z_{TOR}, R_{RUP}, V_{s30}, $s_{or}d$, $\theta_{or}\phi$), we proceed as follows:

1. Given (F, $\mathbf{M}$, Z_{TOR}, R_{RUP}, V_{s30}, $s_{or}d$, $\theta_{or}\phi$), two horizontal components of near-fault ground motion are simulated, as is done in Section 6.4. The simulated motion may be pulselike or non-pulselike, and its components are associated with an orientation relative to the strike of the fault, given by α_P and α_{NP1}, respectively.
2. The simulated pair of orthogonal components is rotated to the SN and SP orientations $a_{SN}(t)$ and $a_{SP}(t)$, using angle α_P or α_{NP1}in place of θ in (5.1).
3. If the site is not located adjacent to the fault rupture, i.e., if $R_x < \sqrt{R_{RUP}^2 - Z_{TOR}^2}$, the fling step is zero, and the simulated ground motion in the SN and SP directions is as obtained in Step 2.
4. If the site is located adjacent to the fault rupture, the fling acceleration time series $a_{fling}(t)$ is calculated according to (6.8)-(6.15) for the given set of earthquake source and site characteristics.
5. Finally, the fling acceleration time series $a_{fling}(t)$ is added to the strike-parallel rotated component $a_{SP}(t)$ of the simulated motion.

Next, we illustrate the above procedure by simulating two orthogonal horizontal components of ground motion at sites that undergo a fling step. We select earthquake scenario ($F = 0$, $\mathbf{M} = 7$, $Z_{TOR} = 0$ km, $R_{RUP} = R_x = 10$ km, $V_{s30} = 525$ m/s, $s_{or}d = 30$ km and $\theta_{or}\phi = 18.4°$) and we consider three cases.

First, for the selected earthquake scenario, we simulate a ground motion that is pulselike, i.e., that contains both a directivity pulse and a fling step. We also assume that the angle α_P of the largest pulse from the strike of the fault is $\alpha_P = 90°$, i.e., the largest pulse direction and orthogonal direction coincide with the strike-normal and strike-parallel directions, respectively. Figure 6.49 shows the acceleration, velocity and displacement time series of the simulated ground motion in the strike-normal (left) and strike-parallel directions. We show the strike parallel motion before (middle) and after (right) adding the simulated fling step. Here, the two-sided directivity velocity pulse is polarized in the strike-normal direction, while the one-sided fling velocity pulse is polarized in the strike-parallel direction.

Second, and for the same earthquake scenario, we also simulate a ground motion that is pulselike but this time, we randomize α_P. The value of α_P is sampled from the fitted probability distribution in (4.20). Figure 6.50 shows the acceleration, velocity and displacement time series of this simulated ground motion in the strike-normal direction (left), and in the strike-parallel direction before (middle) and after (right) adding the simulated fling step. In this specific example, a value $\alpha_P = 66.9°$ is sampled. After rotation of the simulated ground motion components by angle α_P, the two-sided directivity velocity pulse appears in both the strike-normal and strike-parallel directions, but is larger in the strike-normal direction. The one-sided fling velocity pulse remains polarized in the SP direction.

Finally, also for the same earthquake scenario, we simulate a non-pulselike ground motion that contains a fling step. We randomize the angle α_{NP1} between the major "principal direction" and the strike of the fault by sampling from a uniform distribution (see Section 4.6.2).

Figure 6.51 shows the acceleration, velocity and displacement time series of this simulated ground motion in the strike-normal direction (left), and in the strike-parallel direction before (middle) and after (right) adding the simulated fling step. In this specific example, a value $\alpha_{NP1} = 21.7°$ was sampled. Here, the directivity velocity pulse is absent from both strike-normal and strike-parallel directions but the strike-parallel direction displays a fling step. This ground motion can be regarded as the motion experienced at a backward directivity site located close to the epicenter.

Note that the fling time series is identical in the three cases, because we do not model its variability. The model predicts a permanent displacement $D_{site} = 55$ cm for the given earthquake scenario, as can be observed in the lower right portions of Figures 6.49-6.51.

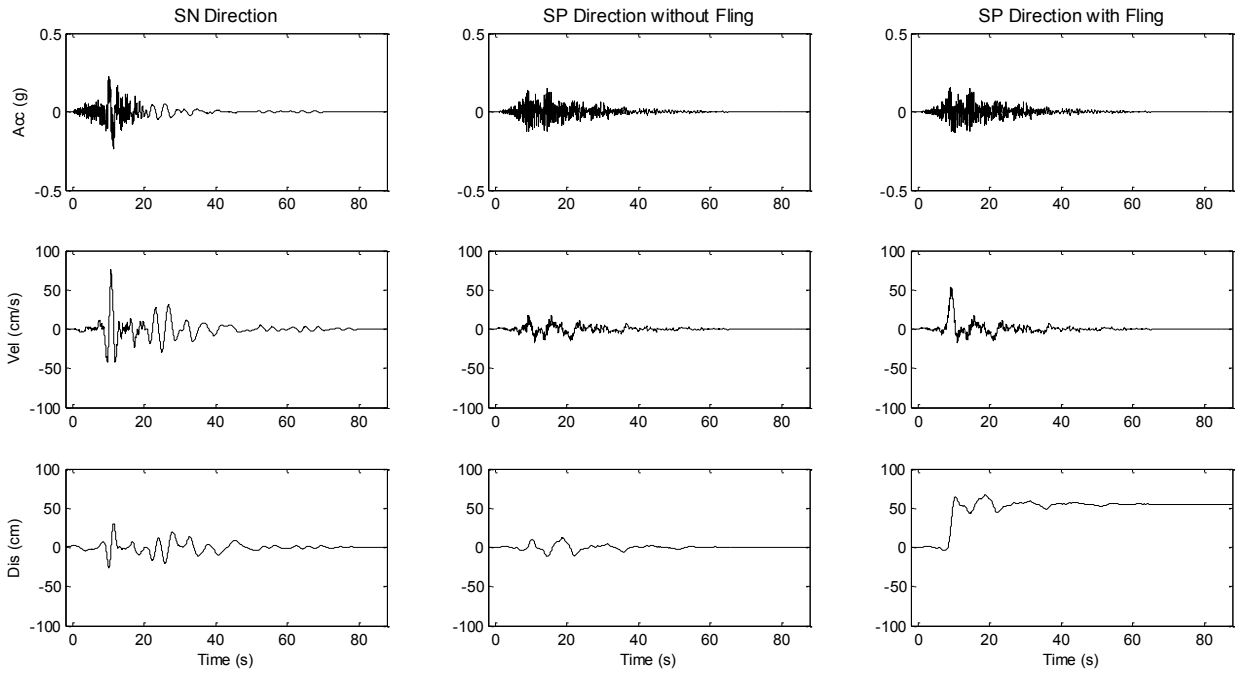

Figure 6.49 Strike-normal (left) and strike-parallel (right) components of a simulated pulselike near-fault ground motion that contains a directivity pulse and a fling step, for $F = 0$, $\mathbf{M} = 7$, $Z_{TOR} = 0$ km, $R_{RUP} = R_x = 10$ km, $V_{s30} = 525$ m/s, $s_{or}d = 30$ km and $\theta_{or}\phi = 18.4°$. The middle column shows the simulated strike-parallel component before addition of the fling step. $\alpha_P = 90°$.

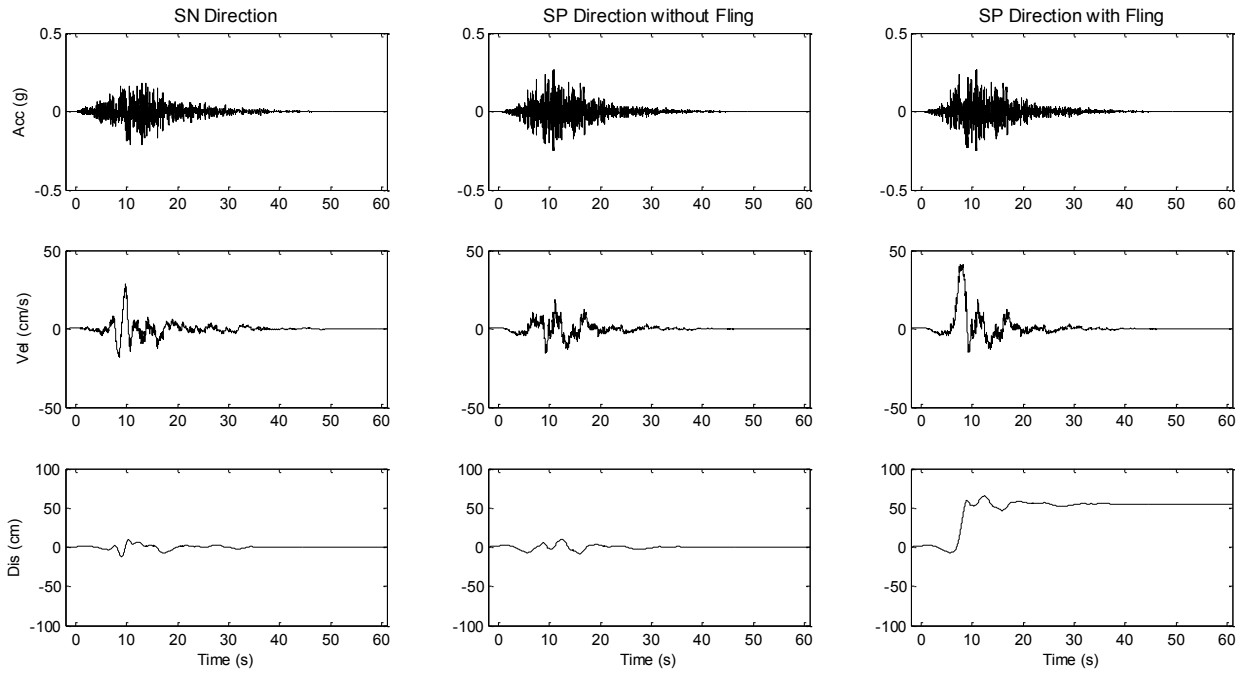

Figure 6.50 Strike-normal (left) and strike-parallel (right) components of a simulated pulselike near-fault ground motion that contains a directivity pulse and a fling step, for $F = 0$, $\mathbf{M} = 7$, $Z_{TOR} = 0$ km, $R_{RUP} = R_x = 10$ km, $V_{s30} = 525$ m/s, $s_{or}d = 30$ km and $\theta_{or}\phi = 18.4°$. The middle column shows the simulated strike-parallel component before addition of the fling step. $\alpha_P = 66.9°$.

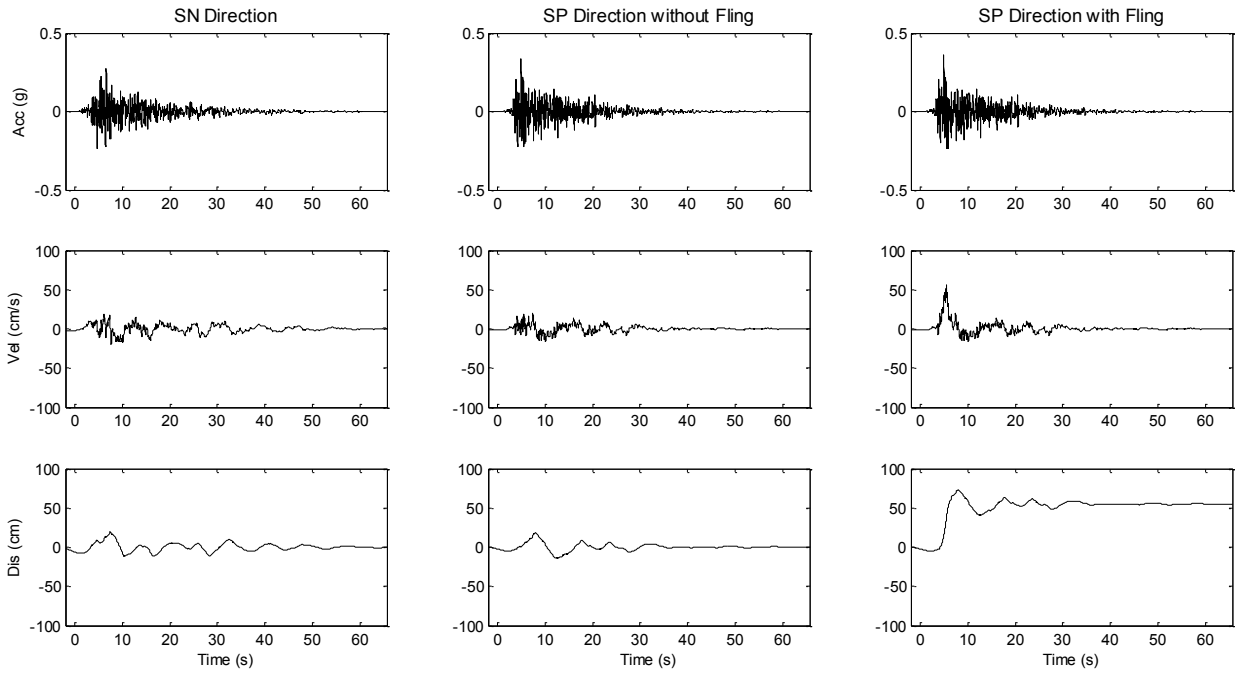

Figure 6.51 Strike-normal (left) and strike-parallel (right) components of a simulated non-pulselike near-fault ground motion that contains fling step, for $F = 0$, $\mathbf{M} = 7$, $Z_{TOR} = 0$ km, $R_{RUP} = R_x = 10$ km, $V_{s30} = 525$ m/s, $s_{or}d = 30$ km and $\theta_{or}\phi = 18.4°$. The middle column shows the simulated strike-parallel component before addition of the fling step. $\alpha_{NP1} = 21.7°$.

6.6 SUMMARY

In this chapter, we present and illustrate the procedure to simulate two horizontal orthogonal components of artificial pulselike and non-pulselike near-fault ground motions. The procedure employs the stochastic models of pulselike and non-pulselike near-fault ground motions formulated in Chapter 4 and the predictive equations developed in Chapter 5.

First, we illustrate the procedure for simulating near-fault ground motions that have the same model parameters as those identified for the pulselike and non-pulselike near-fault ground motion records NGA#171 and NGA#351. These simulations can be regarded as other realizations of the same respective events. Their variability arises only from the white-noise process underlying our model. By comparing the time series and elastic spectra of the recorded and synthetic motions, we validate the formulation of the models proposed in Chapter 4.

Next, we simulate near-fault ground motions using randomly selected values of the model parameters for specified earthquake source and site characteristics (F, $\mathbf{M}$, Z_{TOR}, R_{RUP}, V_{s30}, $s_{or}d$, $\theta_{or}\phi$). This approach is useful for design situations. In addition to the proposed stochastic ground motion models, this procedure employs the models for predicting the model parameters resulting from the regression and correlation analyses of Chapter 5, as well as the pulse probability model by Shahi and Baker (2011) and the pulselike and non-pulselike directionality models developed in Chapter 4. The variability in this type of simulation is larger

than the variability in the simulation with fitted model parameter values. It arises from the underlying white-noise process as well as from the uncertainty in the model parameter values for the given earthquake source and site characteristics. This approach produces near-fault ground motions that possess the physical and statistical characteristics of real near-fault ground motions, including the characteristics of the velocity pulse arising due to the directivity effect in pulselike motions, and that have the same natural variability that is present in a collection of recorded ground motions with the specified earthquake source and site characteristics.

One feature of our simulation procedure is that, through input parameters $s_{or}d$ and $\theta_{or}\phi$, it allows distinction between forward and backward directivity scenarios. It also generates pulselike and non-pulselike ground motions with likelihoods similar to those observed for recorded ground motions. For a given earthquake scenario, the NGA-West2 GMPEs are compared with simulations for forward and backward directivity conditions. The comparisons show that (1) at longer periods and due to the long period velocity pulse, forward directivity scenarios result in larger median spectral values than backward directivity scenarios; (2) the median spectra from backward directivity scenarios are overall in good agreement with the corresponding median spectra predicted by the NGA-West2 GMPEs, (3) the difference observed at longer periods between the simulations and the GMPEs for the average or random directivity condition indicate that the NGA-West2 GMPEs do not adequately represent the near-fault rupture directivity effect. Furthermore, our simulations exhibit variability in elastic response spectral amplitudes that is consistent at most periods of interest with that predicted by the GMPEs. These results validate the proposed ground motion models, the predictive models of the model parameters, and the simulation procedure. Hence, our proposed models and predictive equations can be used with confidence to simulate realistic near-fault ground motions for specified earthquake source and site characteristics within the boundaries of the databases we have used, in particular for $6 \leq \mathbf{M} \leq 7.5$, $5 < R_{RUP} \leq 25$ km and $400 < V_{S30} < 1000$ m/s.

The chapter concludes by introducing an additional component to our ground motion simulation methodology, a simplified model of the fling step. Despite being preliminary, the inclusion of the fling model illustrates how the formulation of our model allows a more complete bidirectional characterization of near-fault ground motion in the horizontal plane, including the two near-fault effects of rupture directivity and the fling step. To the extent of our knowledge, this feature is novel in site-based stochastic models of near-fault ground motion time series.

7 PBEE Application: Probabilistic Seismic Hazard Analysis using Simulated Near-Fault Ground Motions

7.1 INTRODUCTION

Synthetic near-fault ground motions generated by the simulation method proposed in this study can be used for a variety of engineering applications. They can be used for nonlinear dynamic analysis of tall buildings, base-isolated structures, bridges or other structures located at near-fault sites. Such structures can be particularly vulnerable to near-fault motions if they possess resonant periods that are long and close to the period of the directivity pulse. A suite of the synthetic motions can be used in PBEE applications, where estimates of expected costs of damage or downtime must be made. Finally, the synthetic motions offer a possibility for parametric analysis to understand the influences of various assumptions in the design stage. In this chapter, we illustrate the use of our parameterized stochastic model and proposed simulation procedure in a new approach to probabilistic seismic hazard analysis (PSHA), which is the first step of PBEE.

The current approach to PSHA consists of representing the hazard at a site of interest by a target response spectrum obtained using GMPEs. The spectrum is then used in modal analysis to compute structural responses. This approach is only adequate for elastic structures located far from the fault rupture. If the structure is expected to respond in its non-linear range, response history analysis is a necessary approach. This is particularly true for sites located in near-fault regions because, as demonstrated in Section 6.4.6, the GMPEs currently proposed in the literature do not adequately represent the seismic demands of near-fault ground motions, namely the forward directivity pulse. These pulses can drive structures into the inelastic range. Furthermore, the spectral ordinates at different periods of the uniform hazard spectrum often used in traditional PSHA are not necessarily associated with the same earthquake. This discrepancy results in overestimation of the structural response of a multi-degree of freedom system when modal contributions are combined.

Therefore, especially when dealing with near-fault sites, response history analyses may need to be performed to adequately compute potential structural responses. Recorded ground motions, possibly modified by scaling or spectral matching, can be used. However, since near-fault recordings that contain directivity pulses are relatively scarce, and since spectral matching cannot create a pulse in a record that does not initially contain a pulse (Somerville, 2000), simulated near-fault ground motions that include the rupture directivity effect are needed.

In this chapter, we illustrate the use of simulated ground motions to perform PSHA. The parameterized stochastic model developed in earlier chapters is employed to generate synthetic ground motions. The seismic hazard is directly characterized in terms of these simulated ground motion time series, instead of a response spectrum. We begin by outlining the Monte Carlo procedure that is used to simulate an earthquake ground motion catalog over a selected period of time. We illustrate this procedure by building a realistic but simplified catalog of rupture occurrences on a fault near a site located in Berkeley, California. Next, we simulate ground motions for each of the rupture scenarios in the simulated catalog. We finally proceed to

calculate the hazard for a simple structure located at the site and idealized as an inelastic single-degree-of-freedom (SDOF) oscillator. We emphasize the contribution of pulselike ground motions to the hazard. An earlier version of this study is reported in Dabaghi et al. (2013).

7.2 SIMULATION-BASED PSHA

To calculate the ground motion hazard at a site, PSHA requires the use of two models: a seismic source model and a ground motion model. The seismic source model consists of identifying relevant seismic sources and using probabilistic models to define source seismicity and source-site geometry. For each possible source rupture scenario, the ground motion model is then used to define the expected ground motion level and the associated uncertainty and variability. As discussed in Chapter 2, GMPEs and stochastic models both are models of ground motion, the latter more comprehensive than the former. For similar inputs (in terms of earthquake source and site characteristics), a GMPE models a single ground motion measure, most commonly the pseudo-spectral acceleration at the period of interest, and directly predicts the expected ground motion level and associated variability. On the other hand, a stochastic ground motion model typically involves more model parameters and results in a suite of synthetic ground motion time series that could potentially occur at the site. These synthetic time series can in turn be used in conjunction with response-history dynamic analysis to compute the expected spectral ground motion level and variability. As pointed out by Yamamoto and Baker (2011), the availability of ground motion time series resulting from simulation-based PSHA allows calculations that are not possible in the traditional framework.

To illustrate the use of simulated ground motions to perform PSHA of a structure at a given site, the first step is to determine the seismic sources that will affect the site, and their corresponding rates of rupture. For each rupture source, we also need to build a representative set of possible rupture scenarios and their associated probabilities. These then characterize the seismic hazard at the site. The rupture scenarios are defined in terms of the input parameters that are required for the ground motion simulation model, namely the characteristics of the earthquake source (F, $\mathbf{M}$, Z_{TOR}), the site (V_{s30}), and the position of the site relative to the fault rupture (R_{RUP}, $s_{or}d$, $\theta_{or}\phi$). For strike-slip faulting, which is the type considered in the example application, the directivity parameter $s_{or}d$ represents the length (in kilometers) of the portion of the rupture that propagates between the hypocenter and the site, and $\theta_{or}\phi$ denotes the angle in the horizontal plane (in degrees) between the rupture plane and the direction between the hypocenter and the site. This procedure also constitutes the first step of traditional PSHA. The only difference is that in the traditional framework the rupture scenarios should be defined in terms of the input parameters that are required for the selected GMPE(s). It is noted that input parameters of recent GMPEs tend to be more numerous, but they usually do not include directivity parameters.

The next step is to build a stochastic ground motion catalog over a period of Y years. The catalog is built using a Monte Carlo simulation procedure as also used by Crowley and Bommer (2006) and by Yamamoto and Baker (2011). This catalog can be regarded as one possible realization of the set of earthquakes to affect the site over the next Y years. Some underlying assumptions in the Monte Carlo simulation are that earthquake occurrences on a given rupture source are homogeneous Poisson events and that the current characterization of the seismic environment does not change (at least drastically) over the period in question. Alternatively, if a

shorter time period, say $y \ll Y$, is of interest, then the catalog can be considered as Y/y repeated realizations of the seismic events at the site during the next y years.

For each rupture source i, let λ_i be the mean annual rupture rate. Let K_i be the number of representative scenarios identified (which can possibly be reduced by clustering of similar scenarios) and $p_{k,i}$ be the probability for the kth scenario, given that source i has ruptured. One instance of the stochastic ground motion catalog over the study period is generated as follows:

1. For each source i, the number of ruptures N_i in Y years is drawn from a Poisson distribution with mean $\lambda_i Y$.
2. For each rupture event $n_i = 1 \dots N_i$, a scenario k_i is randomly selected according to the associated probability distribution.
3. For each rupture event $n_i = 1 \dots N_i$ and its associated scenario k_i, a ground motion is simulated using the stochastic ground motion simulation model. The model implicitly accounts for the variability of ground motion from event to event, including the possibility of a pulselike motion, if the site is positioned near the fault and in a forward directivity position.

The end result is a potential set of realizations of all earthquake occurrences and corresponding rupture scenarios and ground motions over the length Y of the period of study for the site of interest. Next, for each ground motion in the simulated catalog, the inelastic displacement of the SDOF oscillator is calculated using response history analysis. A hazard curve can then be computed, which consists of the mean rate of exceeding each selected response threshold per year. To compute hazard curves in the traditional framework, the probabilistic characterization of the seismic source is combined with the selected GMPE(s) in the PSHA integral.

It should be noted that hazard curves obtained by Monte Carlo procedures lose accuracy at high response thresholds due to rarity of ground motions that produce such large responses. This can be overcome by increasing the length of the study period, or by running multiple Monte Carlo simulations. (The two are equivalent under our assumption of homogenous Poisson events.) However, this requires an increased computational effort (Crowley and Bommer, 2006), which can be overcome by performing Monte Carlo simulation with importance sampling. As shown by Kiremidjian et al. (2007) and Jayaram and Baker (2010), this approach samples more of the larger than average ground motions that contribute to the hazard at high thresholds, with appropriate adjustments in the corresponding probabilities. Here, we resort to a crude form of importance sampling by ignoring more frequent and small-magnitude earthquakes and only considering large characteristic earthquakes.

A similar procedure was proposed by Yamamoto and Baker (2011), using synthetic ground motions generated from the wavelet-based stochastic ground motion model that they developed. Yamamoto and Baker (2011) illustrated the use of simulated ground motions in place of GMPEs to perform PSHA and compared the results of the two approaches. They showed that the two results are generally comparable and pointed out that it is due to the fact that the response spectra of synthetic ground motions generated from their stochastic model are consistent with the GMPEs used in traditional PSHA. In Chapter 6, we showed similar agreement in the elastic response spectra between our simulated motions and the NGA-West2 GMPEs. Thus, we expect our simulation-based PSHA results to also be consistent with those from a traditional PSHA that uses NGA-West2 GMPEs. However, since at short periods our standard deviations are smaller than those predicted by the GMPEs, our PSHA results might be

unconservative for short period structures and long return periods. Such comparisons are not pursued here but will be included in a follow-up study. In their study, Yamamoto and Baker (2011) computed hazard curves for elastic and inelastic spectral displacements at an example site. They also produced deaggregation results for magnitude, as well as for the ground motion measures of Arias intensity I_a, effective duration D_{5-95} and mean period T_m. The latter deaggregation results cannot be obtained from a traditional PSHA. As shown below, our study goes beyond the work of Yamamoto and Baker (2011) by deaggregating the hazard into contributions from pulselike and non-pulselike ground motions, and into the pulse period of pulselike motions. This is made possible by the formulation of our model of near-fault ground motion and its special feature that allows the simulation of pulselike and non-pulselike motions in appropriate proportions. Other deaggregations are possible, for example in terms of other parameters of the model or other measures that can be computed from the simulated time series, but such deaggregations results are not pursued here.

7.3 STOCHASTIC EARTHQUAKE CATALOG

7.3.1 Seismic environment

Following Luco (2002) and Luco et al. (2002), we illustrate the above procedure at a site located in Berkeley, California, 10 km away from the Hayward-Rodgers Creek fault system. For the sake of simplicity, we neglect other far-field sources, such as the San Andreas and Calaveras faults. A simplified plan view of the source and site is shown in Figure 7.1. It can be seen that the site is subject to near-fault ground motions, here taken as motions resulting within 30 km from the fault rupture. The shear-wave velocity at the site is estimated as $V_{s30} = 500$ m/s. Information available in the report by the 2003 USGS Working Group on California Earthquake Probabilities (USGS WG 2003) is used as the basis for the source characterization, but with further simplifications.

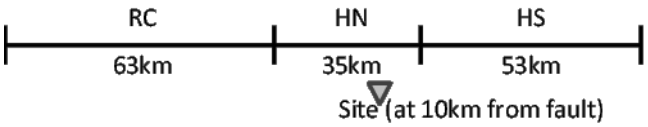

Figure 7.1 Plan view of the Hayward-Rodgers Creek fault and hypothetical site considered.

The Hayward-Rodgers Creek fault is a strike-slip fault ($F = 0$) and it consists of three segments: South Hayward (HS), North Hayward (HN) and Rodgers Creek (RC). The segment dimensions are not known with certainty, but we assume them to be 53, 35 and 63 km, respectively. In order to simplify the analysis, we consider characteristic earthquakes, i.e. large earthquakes that fully rupture a single or multiple fault segments, and neglect the more frequent but less hazardous small-magnitude events. Consequently, the considered rupture sources are three single-segment sources (HS, HN and RC), two two-segment sources (HS+HN and HN+RC), and one full-fault-rupture source (HS+HN +RC). We also consider a floating earthquake rupture source that can occur at any location along the fault (all according to the USGS WG 2003 report). The rupture widths are assumed to be 12 km. The mean moment magnitude of the characteristic events is denoted by $\bar{M}_{char}$ and several expressions relating it to the rupture area have been proposed. For strike-slip faulting, we assume that

$$\bar{M}_{char} = 1.02\log_{10} A + 3.98, \tag{7.1}$$

where A is in km^2 (Wells & Coppersmith, 1994). However, for a given rupture area, there remains variability in the actual magnitude of the resulting earthquake, because of uncertainty and variability in the details of the rupture, such as stress drop, slip distribution, etc. So, for each of the seven rupture sources considered, we assume (as per USGS WG 2003) that the magnitude of the characteristic event has a normal distribution with mean $\bar{M}_{char}$ and variance σ_m^2, and that the distribution is truncated at $\pm 2\sigma_m$. Different values of σ_m are used for the different rupture sources to reflect the uncertainty in the actual dimensions of the rupture; the larger the uncertainty in the rupture dimensions, the larger σ_m. The $\bar{M}_{char}$ and σ_m values used for each of the seven rupture sources are listed in Table 7.1. These are different from the values listed in the USGS WG 2003 report (except for the floating source). There, $\sigma_m = 0.12$ was used for all rupture sources while the uncertainty in the rupture dimensions was separately accounted for.

The mean annual rupture rate of each of the seven rupture sources is estimated following the procedure used by USGS WG 2003 to achieve seismic moment balance. We used the preferred values listed in the USGS WG 2003 report for the slip rate along the fault (9mm/yr) and for the fraction of moment rate expended in characteristic earthquakes (0.94), while also accounting for the additional simplifying assumptions that we introduced, i.e., we only considered characteristic earthquakes and ignored the uncertainty in their rupture dimensions. The estimated mean annual rupture rates are given in Table 7.1. These are slightly different from the mean values listed in the USGS WG 2003 report, but they fall within the 95% confidence bounds of their mean estimates.

7.3.2 Rupture scenarios and seismic hazard at the site

Next, we build a representative set of possible rupture scenarios and their associated probabilities for each of the rupture sources. These characterize the seismic hazard at the site and they must be defined in terms of the input parameters required for the ground motion simulation model, namely (F, $\mathbf{M}$, Z_{TOR}, R_{RUP}, V_{s30}, $s_{or}d$, $\theta_{or}\phi$). We already have that $F = 0$ and $V_{s30} = 500$ m/s. We also assume that we know the rupture geometry for each of the six characteristic rupture sources, namely that the full length of the corresponding segment(s) ruptures. We additionally assume that for such large earthquakes, the rupture reaches the surface (Abrahamson, 2013), i.e., $Z_{TOR} = 0$. Therefore, we can compute the closest distance R_{RUP} between the site and each rupture source and we obtain distances ranging from 10 km to 29 km. Next, magnitudes $\mathbf{M}$ are clustered into bins of width 0.2 (centered at magnitudes ranging from 6.2 to 7.4), and the probability of each bin is computed according to the assumed truncated normal distribution for each rupture source. Finally, given the location of the site, the directivity parameters $s_{or}d$ and $\theta_{or}\phi$ (for the vertical strike-slip fault) depend on the location of the hypocenter along the strike. For a given rupture geometry, the hypocenter is assumed to have a uniform distribution along the strike of the fault, except for buffer zones of length 0.1 times the rupture length at both ends of the fault (Abrahamson, 2013). The hypocenter locations are then clustered into five discrete locations along the rupture length, with associated probabilities, and the values of $s_{or}d$ and $\theta_{or}\phi$ are calculated for each. Note that, since the rupture geometry is assumed to be known for each rupture source, the magnitude, closest distance and hypocenter location are statistically independent. Thus the probability of each scenario can be obtained by multiplying the

corresponding probabilities. For the floating source, the rupture location is additionally assumed to be random and uniformly distributed along the fault.

The above analysis for the Berkeley site yielded 210 earthquake scenarios with corresponding probabilities, arising from the 7 rupture sources. Monte Carlo simulation is then used to randomly simulate earthquake occurrences over time and to randomly select from the set of 210 scenarios according to their respective probabilities. In turn, each selected scenario is used to generate artificial ground motions using the stochastic model, as described in Section 6.4.

Table 7.1 Rupture source characteristics: mean characteristic magnitude, standard deviation of magnitude, estimated rupture rate, number of scenarios per rupture source, and number of simulated events per rupture source in the illustrative example.

i	Rupture Source	$\bar{M}_{char}$	σ_m	Rate λ_i (/yr)	K_i	N_i
1	HS	6.78	0.22	0.0041	25	412
2	HN	6.72	0.24	0.0041	30	400
3	RC	6.92	0.14	0.0041	20	393
4	HS+HN	6.85	0.15	0.0021	20	210
5	HN+RC	7.00	0.14	0.0004	15	41
6	HS+HN+RC	7.15	0.14	0.0001	20	13
7	floating	6.90	0.12	0.0003	80	27

7.4 SIMULATED GROUND MOTIONS

As mentioned above, the considered site is subject to near-fault ground motions, here taken as those within 30 km of the fault rupture. The site may experience forward directivity, when the fault rupture propagates towards the site with a velocity almost equal to the shear-wave velocity (Somerville et al. 1997). The resulting ground motion typically exhibits a large velocity pulse in the fault-normal (and also strike-normal) direction and it may impose a large demand on the structure (Somerville et al. 1997). As discussed earlier, not all near-fault ground motions contain a forward directivity pulse, and our simulation-based PSHA procedure is developed to cater for both pulselike and non-pulselike cases. This is achieved by use of the stochastic model of pulselike and non-pulselike near-fault ground motion introduced in Chapter 4 and of the simulation procedure described in Section 6.4 to generate a realization of the stochastic ground motion catalog.

It is noted that an earlier and preliminary version of our near-fault ground motion model was used in the following example of hazard calculation. That version was developed for pulselike motions in the horizontal strike-normal direction. The parameterized stochastic model for far-field ground motions developed by Rezaeian and Der Kiureghian (2010) was used to simulate the non-pulselike ground motions. This far-field model is applicable for distances $R_{RUP} \geq 10$ km, but it is not well constrained for distances near the lower limit. Moreover, it is applicable for shear wave velocities $V_{s30} \geq 600$ m/s, while $V_{s30} = 500$ m/s at the site considered. Therefore, the results presented in the following sections should be considered as

illustrative of the methodology. The refined model will be used in a follow-up study, along with a more realistic characterization of the seismic environment.

7.5 HAZARD CALCULATION

We are interested in computing the seismic hazard for a structure located at the considered site. We assume that the structure can be idealized as an elastic-perfectly plastic SDOF oscillator and we use response history analysis to compute the response for each ground motion in the simulated catalog. The SDOF oscillator is characterized by its initial period T, viscous damping ratio ζ, here taken to be $\zeta = 5\%$, and yield displacement d_y.

7.5.1 Ground motion hazard at the site

We begin by examining the ground motion hazard at the site, as represented by the simulated stochastic catalog. For this purpose, we simulate a single realization of a stochastic earthquake catalog for a period of $Y = 100{,}000$yrs. Due to the assumption of homogeneous Poisson events, this is equivalent to 1000 simulations of a 100-year period, 2000 simulations of a 50-year period, or 100,000 simulations of a 1-year period. The simulated catalog contains $\sum_{i=1}^{7} N_i = 1496$ motions, of which 241 (16%) are pulselike and 1255 are non-pulselike. The values of N_i for each rupture source are listed in Table 7.1. Note that the numbers for sources 1 to 3 are different even though the corresponding mean rates are identical. This is due to the natural randomness in the number of events for a given mean value. The ground motion hazard is represented by the elastic displacement response spectrum as a function of the oscillator period, T for damping ratio $\zeta = 5\%$; the median hazard levels from pulselike, non-pulselike, and all ground motions are compared in Figure 7.2. The statistics of the hazard curves from pulselike, non-pulselike and all combined ground motions are shown in Figure 7.3. It can be seen that pulselike ground motions, although less frequent, make a larger contribution to the hazard than non-pulselike motions, particularly in the long-period range. The normalized frequency diagram of the pulse periods for the 241 simulated pulselike motions is shown in Figure 7.4.

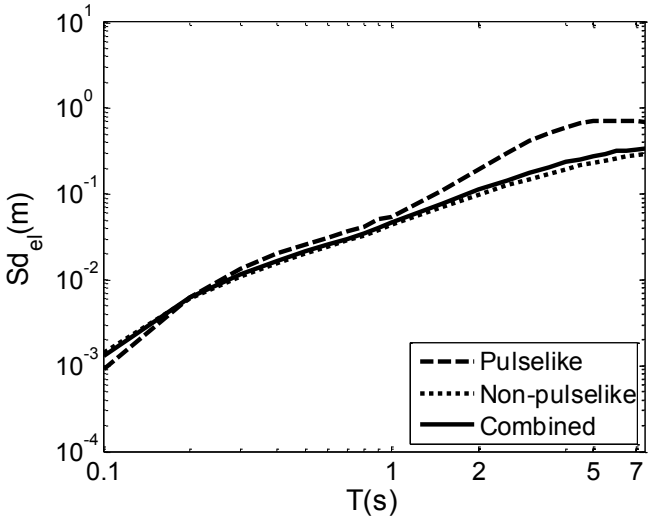

Figure 7.2 Median pulselike, non-pulselike and combined total hazard levels.

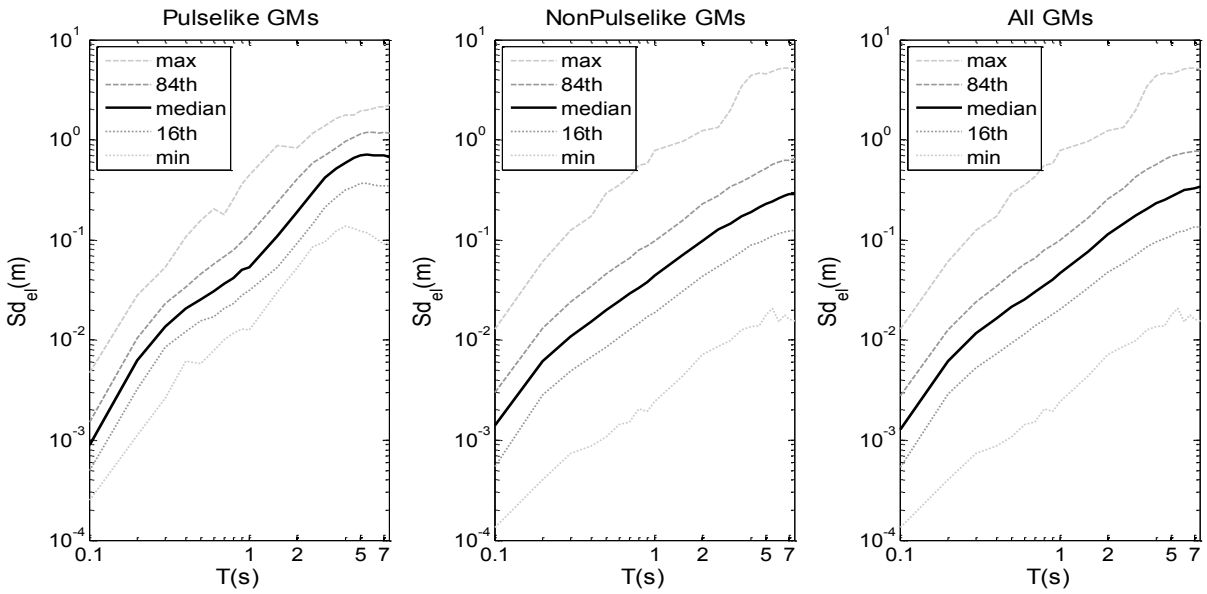

Figure 7.3 Statistics of the hazard from pulselike and non-pulselike ground motions and of the total hazard.

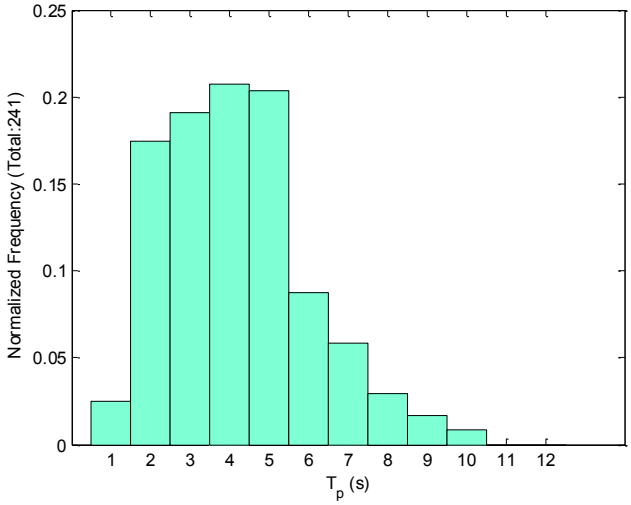

Figure 7.4 Histogram of pulse periods of simulated pulselike motions.

7.5.2 Inelastic displacement hazard for SDOF oscillator

For the simulated ground motion catalog, we first compute the displacement response of four elastic oscillators having periods $T = 0.5$ s, 1 s, 2 s and 4.5 s with a viscous damping ratio $\zeta = 5\%$. We then compute the displacement hazard curve for each oscillator, i.e. the annual rate of exceeding specified displacement thresholds. The hazard curves at the four periods are plotted in Figure 7.5 (solid lines) along with the 2% probability of exceedance (PE) in 50yrs (equivalent to an annual rate of exceedance of 4.041×10^{-4}).

For each elastic oscillator, we examine three elasto-plastic oscillators that have the same initial period, but reduced yield strengths. The yield displacements d_y of the inelastic oscillators

are determined by using the strength reduction factors $R_y = 2$, 4 and 8 relative to an oscillator that remains elastic up to the 2% in 50yrs hazard level. The inelastic displacements and hazard curves are calculated for each of the inelastic oscillators. The latter are plotted in Figure 7.5 (dashed and dotted lines), which also indicates the yield displacement for each oscillator in the legend. Hazard curves for the ductility demand μ (the ratio of maximum inelastic to elastic displacement) are plotted for each of the inelastic oscillators in Figure 7.6.

Figure 7.5 shows that the displacement demand increases with period. Furthermore, for the shorter periods ($T \leq 1$ s), the displacement demand increases as the yield displacement decreases, and the more inelastic the oscillator is, the earlier the inelastic hazard diverges from the elastic hazard. However, for $T \geq 2$ s, the elastic and inelastic displacements more or less coincide at the different hazard levels. The latter suggests that, for long period oscillators, the 'equal displacement' rule is valid in an average sense. Finally, Figure 7.6 shows that for long periods, the ductility demand μ tends towards the strength reduction factor R_y at small hazard level. As T decreases, the ductility demand increases and the effect of yielding becomes more important.

In a future study, our simulated motions will be compared with GMPEs for inelastic response spectra (e.g., Bozorgnia et al., 2010) and our hazard calculations will be compared with PSHA results obtained using such GMPEs.

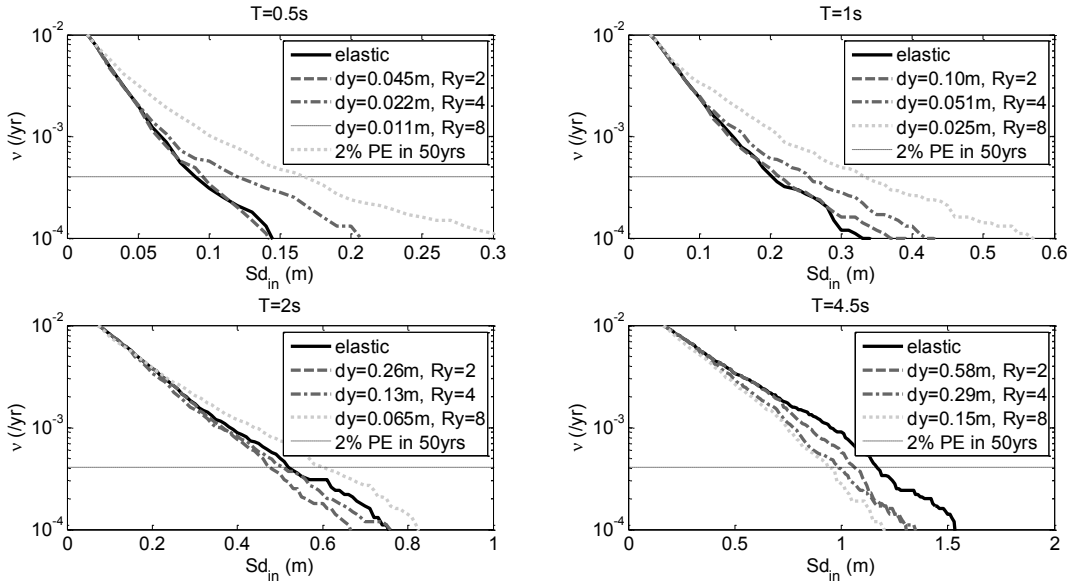

Figure 7.5 Displacement hazard curves for selected initial periods T and yield displacements d_y.

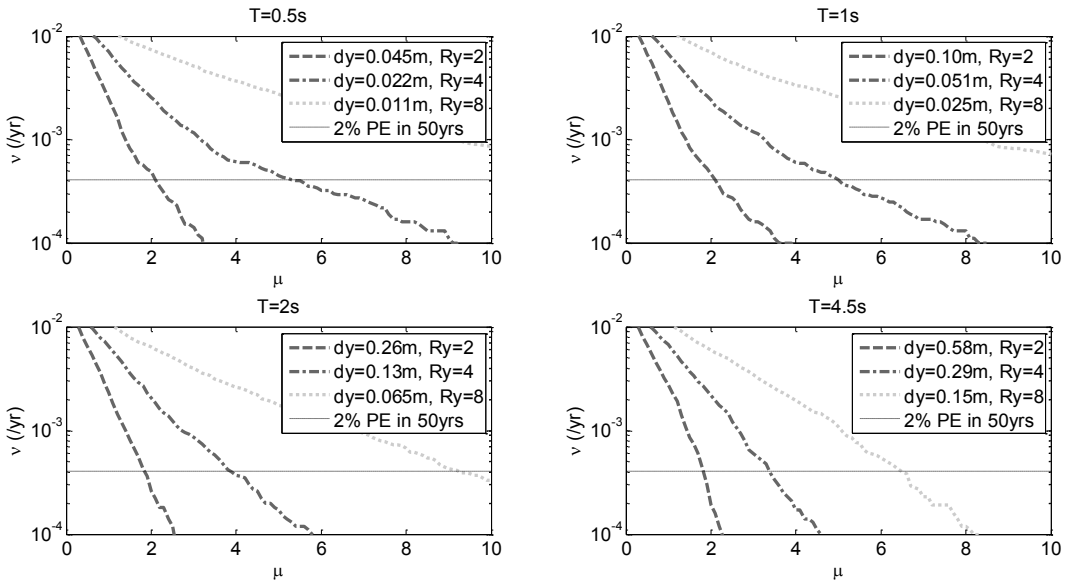

Figure 7.6 Ductility demand hazard curves for selected initial periods T and yield displacements d_y.

7.5.3 Hazard deaggregation at the site

For each of the oscillators considered (with each initial period and each value of strength reduction factor), the ground motions contributing to the 2% in 50yrs hazard level are identified. For each oscillator, the mean period of the pulses in the pulselike ground motions contributing to the 2% PE in 50yrs hazard is identified and listed in Table 7.2. Also for each oscillator, the percentage of pulselike ground motions among all the ground motions contributing to the 2% PE in 50yrs hazard is listed in Table 7.3. The histograms of the pulse periods of the pulselike ground motions contributing to the 2% probability of exceedance in 50yrs hazard level are shown in Figures 7.7-7.10. Such deaggregation results could not have been obtained from a traditional PSHA.

As can be observed in Table 7.2 and Figures 7.7-7.10, the (mean) pulse period of the pulselike motions contributing to the hazard tends to increase with the initial period of the oscillator and with the strength reduction factor. The increase with the oscillator period is consistent with the resonance effect: An oscillator experiences large demand when the predominant period of the ground motion matches its period. As a result, pulselike ground motions with periods close to the oscillator period make strong contributions to the hazard. The increase with the strength reduction factor is consistent with softening of inelastic oscillators; as the oscillator becomes softer, its effective period increases, and it becomes vulnerable to pulses that have longer periods. These arguments do not hold at short periods, as is obvious for the oscillator with $T = 0.5$ s, because pulselike ground motions make little contribution to the hazard at such periods.

Moreover, since the number of pulselike ground motions increases with pulse period for periods up to 4-5 s, then decreases with period for periods longer than 5 s (see Figure 7.4), we expect the 2% PE in 50yrs hazard to be increasingly contributed by pulselike ground motions as

the oscillator period increases from 0.5 s to 4.5 s. Based on the same argument, we also expect the hazard to be increasingly contributed by pulselike ground motions as the strength reduction increases. As the initial period of the oscillator approaches 5 s, reduction in strength and the ensuing softening result in an increase of the effective period beyond 5 s, thus a decrease in the contribution of pulselike ground motions as observed in the last two columns of Table 7.3. Consequently, for a given oscillator, the hazard depends on the periods of the directivity pulses of ground motions in the simulated catalog.

Table 7.2 Mean pulse period of pulselike ground motions contributing to the 2% PE in 50yrs hazard.

$\bar{T}_p$ (s)	$T = 0.5$ s	$T = 1$ s	$T = 2$ s	$T = 4.5$ s
Elastic	3.1	1.3	2.2	4.6
$R_y = 2$	2.4	1.9	2.3	4.4
$R_y = 4$	1.9	2.3	2.6	4.6
$R_y = 8$	1.8	2.4	3.5	5.2

Table 7.3 Percentage of pulselike ground motions among those contributing to the 2% PE in 50yrs hazard. 16% of all motions are pulselike.

%(%)	$T = 0.5$ s	$T = 1$ s	$T = 2$ s	$T = 4.5$ s
Elastic	10	19	52	63
$R_y = 2$	10	26	45	54
$R_y = 4$	22	27	38	44
$R_y = 8$	25	30	28	36

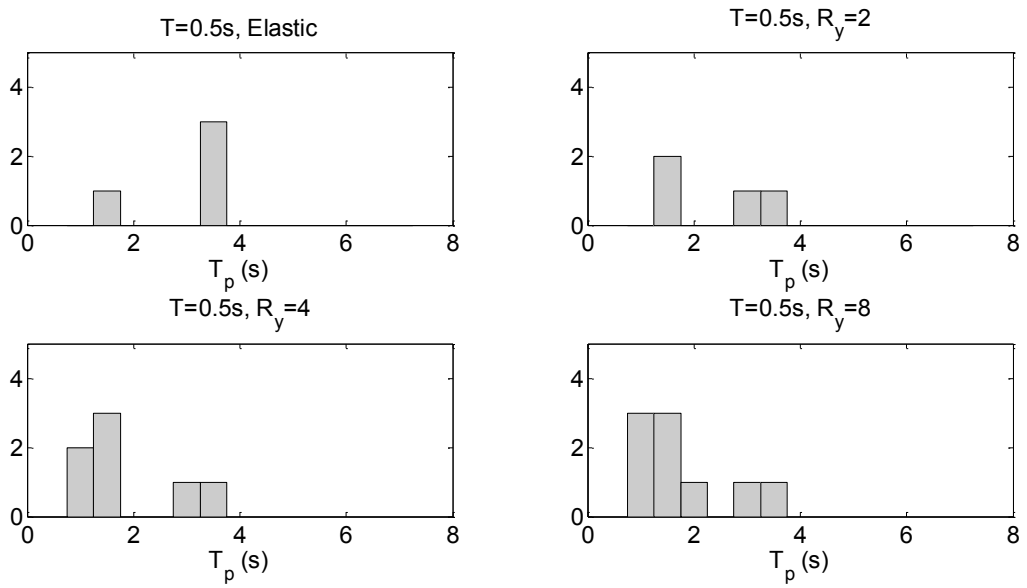

Figure 7.7 Histograms of periods of pulselike ground motions contributing to the 2% probability of exceedance in 50yrs hazard level for different elastic and inelastic oscillators with initial period $T = 0.5$ s.

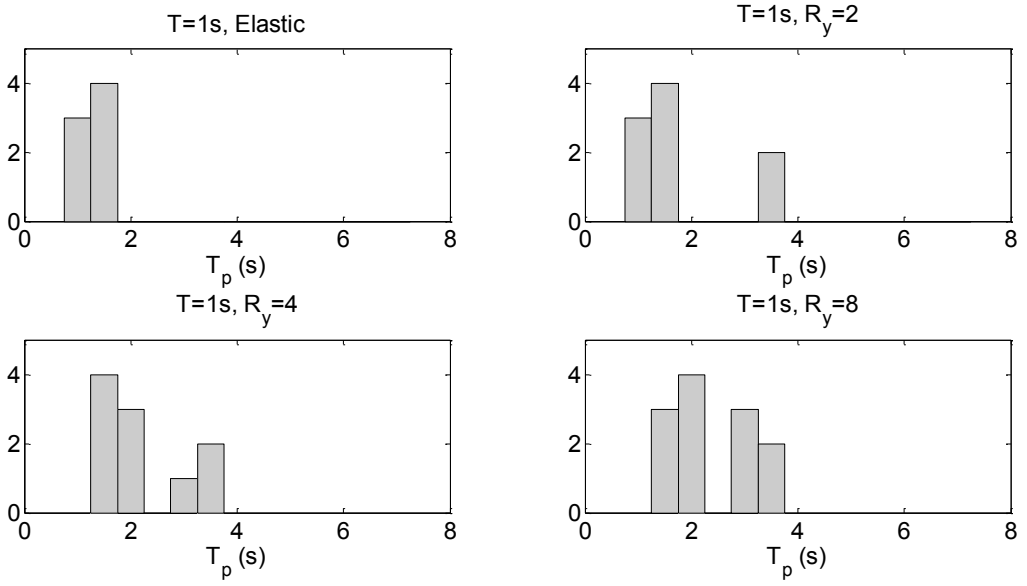

Figure 7.8 Histograms of periods of pulselike ground motions contributing to the 2% probability of exceedance in 50yrs hazard level for different elastic and inelastic oscillators with initial period $T = 1.0$ s.

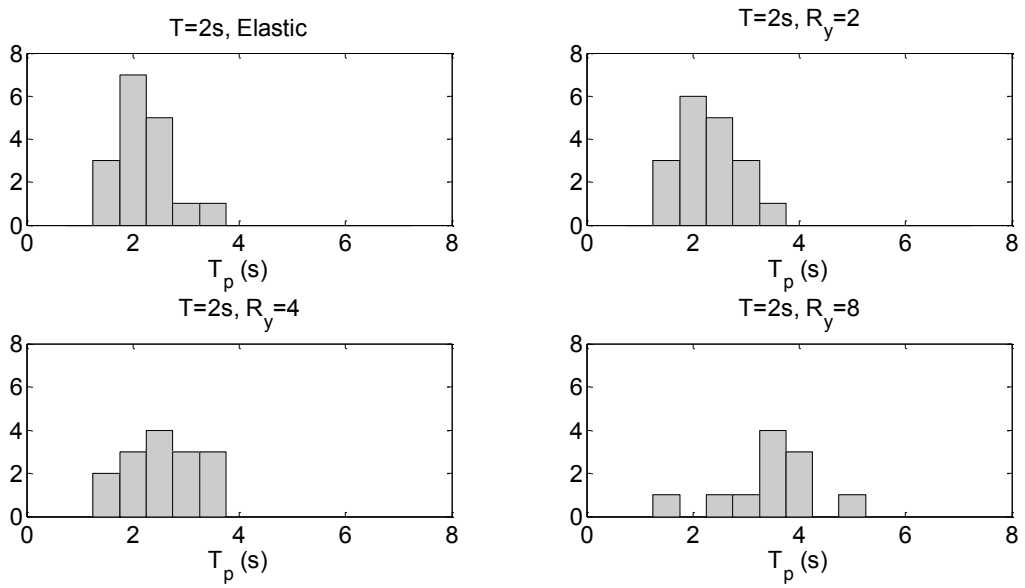

Figure 7.9 Histograms of periods of pulselike ground motions contributing to the 2% probability of exceedance in 50yrs hazard level for different elastic and inelastic oscillators with initial period $T = 2.0$ s.

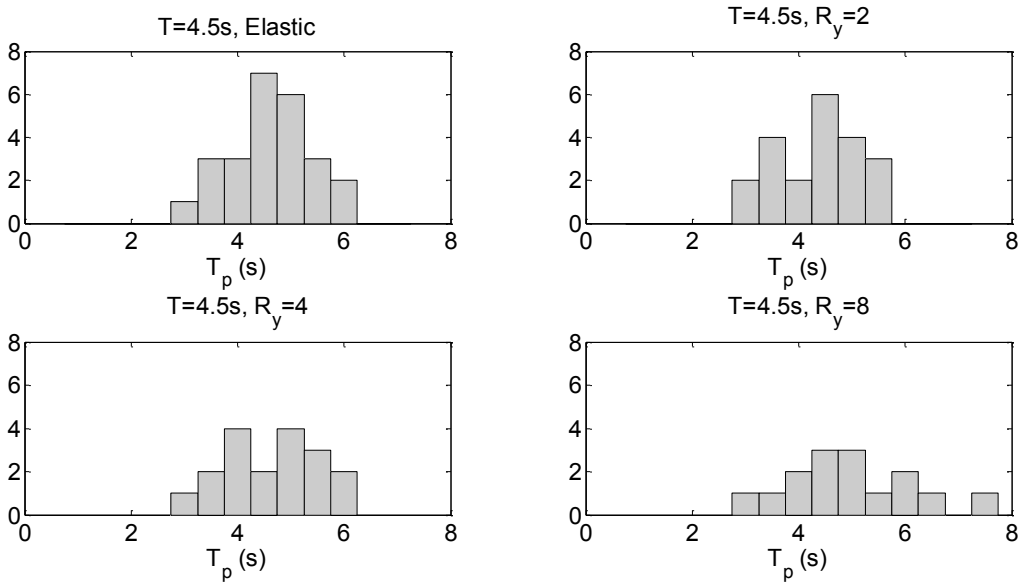

Figure 7.10 Histograms of periods of pulselike ground motions contributing to the 2% probability of exceedance in 50yrs hazard level for different elastic and inelastic oscillators with initial period $T = 4.5$ s.

7.6 SUMMARY

In this chapter, we illustrate one of the useful applications of the stochastic model of near-fault ground motions that we developed. Namely, we illustrate the use of simulated ground motions to perform PSHA. A Monte Carlo procedure is used to simulate an earthquake ground motion catalog for a site located in Berkeley over a period of 100,000yrs (equivalent to 100,000 simulations for a 1yr period) using the parameterized stochastic models for pulselike and non-pulselike near-fault ground motions. The seismic hazard is determined in terms of these simulated ground motion time series, instead of a response spectrum. Displacement and ductility demand hazard curves are computed for SDOF oscillators having different periods and yield displacements. The observed trends are consistent with expectations. Specifically, from the hazard deaggregation into pulselike and non-pulselike ground motions, we find that the period of the pulselike motions contributing to the hazard tends to increase with the initial period of the oscillator and with the strength reduction factor. Moreover, for a given oscillator, the hazard depends on velocity pulse periods of ground motions in the simulated catalog.

Our results demonstrate the importance of using a near-fault stochastic model that allows generating both pulselike and non-pulselike synthetic ground motions in a simulation-based PSHA approach. Ignoring the near-fault forward directivity effect by using an average ground motion model and/or by not accounting for the possibility of a directivity pulse would have resulted in an underestimation of the hazard.

In the next stages of this work, we plan on using the refined version of the near-fault ground motion model and a more realistic characterization of the seismic sources near the selected site. We also plan on extending the hazard calculation to multi-degree of freedom systems, for which the currently used uniform hazard spectrum approach is overly conservative.

8 Summary, Conclusions and Future Work

8.1 SUMMARY OF THE STUDY

The research presented in this study concerns the stochastic modeling and simulation of near-fault ground motion time-series. It addresses a crucial need in performance-based earthquake engineering (PBEE). Specifically, this research contributes to the first step of PBEE, namely characterization of the seismic hazard at a location of interest through ground motion modeling and probabilistic seismic hazard analysis (PSHA), with a special focus on near-fault sites, i.e., sites located within 30 km of the fault rupture. This first step is crucial for the ensuing steps in PBEE of computing structural responses for the given hazard, defining and computing relevant measures of damage to structural and non-structural components and equipment, and computing decision variables that relate to casualties, cost and downtime. These decision variables drive performance-based design of structures, rendering careful characterization of ground motions essential.

In Chapter 1, three main objectives were proposed for this dissertation: (1) to develop a parameterized stochastic model of pulselike and non-pulselike near-fault ground motions in two orthogonal horizontal directions and employ it to generate synthetic motions, (2) to validate the proposed model and simulation procedure, and (3) to demonstrate the use and importance of the proposed procedure in engineering applications. These objectives are achieved as follows:

- In Chapters 4-6, we developed a parameterized stochastic model of near-fault ground motions in two horizontal orthogonal directions and we presented a practical method of generating synthetic near-fault ground motions for specified earthquake source and site characteristics that are readily available to design engineers. These synthetic motions can be used in response history analysis and in PBEE applications, in addition to or in place of recorded motions.

- In developing our model, we focused on the features that most influence structural response. We aimed at preserving the physical characteristics dictated by seismological theory and on accounting for variability that is inherent in real earthquake ground motions. In Chapters 5 and 6, we validated the model and the simulation method by comparing our predictive relations and our simulated motions to GMPEs proposed in the literature and to recorded earthquake ground motions.

- In Chapter 7, we illustrated the use of the model and simulation procedure in a new approach to PSHA, where the ground motion hazard at a site was represented by a catalog of simulated ground motions. The example highlighted the significant contribution of pulselike ground motions to the hazard for a near-fault site.

8.2 MAJOR CONTRIBUTIONS, FINDINGS AND CONCLUSIONS

The major developments and findings of this study are summarized as follows:

- A new site-based stochastic model that describes near-fault earthquake ground motions in two orthogonal horizontal components is developed. The model is formulated in terms of a

relatively small number of physically meaningful parameters and is able to represent the characteristics of recorded ground motions, including temporal and spectral non-stationarity, and near-fault effects. The model accounts for the occurrence of forward directivity effect in the form of a two-sided velocity pulse and the occurrence of a fling step in the form of a one-sided velocity pulse. Models for both pulselike and non-pulselike ground motions are considered with likelihoods similar to those among recorded motions. To our knowledge, this study offers the first site-based stochastic ground motion model that accounts for the near-fault rupture directivity effect. This is also the first site-based model to provide a complete bidirectional characterization of the near-fault ground motion in the horizontal plane.

- The proposed model draws on several existing models, as follows:
    - To model the broadband near-fault ground motion, the non-stationary filtered white-noise model formulated by Rezaeian and Der Kiureghian (2008, 2010) is used with a modified modulating function and a total of 7 parameters. The amplitude of near-fault ground motions exhibits sharp build-up and decay segments, with no quasi-stationary phase in between. The modification is implemented to better represent this evolution.
    - To represent the directivity pulse, a modified version of the 5-parameter idealized model earlier developed by Mavroeidis and Papageorgiou (2003) is employed. The modification is implemented to achieve zero residual displacement at the end of the pulse.
    - To represent the fling step, a simple model developed by Abrahamson (2001) based on a simplified dislocation theory is employed. The fling model used is still in a preliminary state. However, it illustrates how an improved version of the model can be easily incorporated into the proposed model formulation and simulation procedure, if and when adequate observational data of the fling step become available.
    - To appropriately represent the proportion of pulselike and non-pulselike ground motions, the pulse probability model developed by Shahi and Baker (2011) is used. It predicts the probability of occurrence of a directivity pulse in at least one direction at a site.
- Additionally, directionality models are developed to describe the orientations of near-fault ground motion components relative to the fault strike.

- The framework proposed by Rezaeian and Der Kiureghian (2010) for fitting a parameterized stochastic ground motion model to recorded ground motions is adapted and extended in this study. Specific developments include:
    - Our stochastic models of pulselike and non-pulselike near-fault ground motions are fitted to recorded ground motions in two databases, one for pulselike and another for non-pulselike motions. The fitting is performed by relating the model parameters to physically meaningful ground motion characteristics. The records used in this study are taken from PEER's NGA-West2 database and have known earthquake source and site characteristics. For consistency, records with $\Delta t \neq 0.005$ s are resampled to $\Delta t = 0.005$ s using *sinc* interpolation.

- Regression and correlation analyses are performed to develop models for predicting the parameters of the pulselike and non-pulselike models in terms of a small number of earthquake source and site characteristics. The empirical predictive equations of the parameters are developed by regressing against the explanatory variables (F, $\mathbf{M}$, Z_{TOR}, R_{RUP}, V_{s30}, $s_{or}d$). A random-effects model is used to account for multiple records from certain earthquakes. To the greatest extent possible, functional forms for the predictive equations are chosen to be consistent with seismological theory. The directivity parameter $s_{or}d$ is included among the explanatory variables to describe the directivity condition.

- A new procedure to simulate two horizontal orthogonal components of synthetic pulselike and non-pulselike near-fault ground motions for specified earthquake source and site characteristics (F, $\mathbf{M}$, Z_{TOR}, R_{RUP}, V_{s30}, $s_{or}d$, $\theta_{or}\phi$) is proposed. It can be used within the boundaries of the databases we have used, in particular for $6 \leq \mathbf{M} \leq 7.5$, $5 < R_{RUP} \leq 25$ km and $400 < V_{S30} < 1000$ m/s. The procedure employs the stochastic models of pulselike and non-pulselike near-fault ground motions, the empirical equations for predicting the parameters of these models, the pulselike and non-pulselike directionality models, as well as the pulse probability model by Shahi and Baker (2011). For a prescribed set of earthquake source and site characteristics, the probability of occurrence of a directivity pulse is first computed and then pulselike and non-pulselike bi-directional horizontal ground motions are simulated according to the predicted proportions. The pulselike and non-pulselike empirical predictive models are used to simulate realizations of the parameters of the respective stochastic models. Next, each set of simulated parameter values together with a simulated white-noise process are input into the corresponding stochastic model to generate synthetic near-fault ground motions. If the site is located adjacent to the fault rupture, a fling step is added.

- The proposed models and simulation procedure are validated as follows:

  - Synthetic motions generated using model parameters obtained by fitting to a specific recorded motion in the database are compared to their recorded counterparts. The formulation of our models are validated by visually comparing the acceleration, velocity and displacement time series, and the elastic pseudo-acceleration response spectra at 5% damping of the recorded and synthetic motions. The recorded and simulated motions in this case may be considered as different realizations from the same earthquake.
  - Our empirical predictive equations are compared with several similar relations proposed in the literature. The comparison shows that our estimates are generally consistent with those provided by other GMPEs. The advantage of our relations is that they make the crucial distinction between pulselike and non-pulselike ground motions.
  - Suites of synthetic ground motions generated for given earthquake source and site characteristics are compared with the NGA-West2 GMPEs in terms of median elastic response spectra and associated variability. Backward directivity scenarios are overall in good agreement with the corresponding median spectra predicted by the NGA-West2 GMPEs. On the other hand, for forward directivity sites, median spectra

obtained for synthetic ground motions show higher amplitudes in the long period range than the GMPE spectra. This shows that spectra obtained from GMPEs do not properly account for the contribution of pulselike motions. Moreover, our simulations exhibit variability in elastic response spectral amplitudes that is consistent at most periods of interest with that predicted by the NGA-West2 GMPEs.

- Our proposed simulation procedure has several features and advantages :
    - Our procedure is of practical use for design situations, since it requires only inputting values of the earthquake source and site characteristics (F, $\mathbf{M}$, Z_{TOR}, R_{RUP}, V_{s30}, $s_{or}d$, $\theta_{or}\phi$) to simulate a representative set of acceleration time series at a site of interest. The simulated components can be rotated into any desired direction, e.g., to match the orientation relative to the fault strike of the axes of a structure of interest.
    - The simulations account for the stochasticity in the ground motion process as well as for the uncertainty in the model parameter values for the given earthquake source and site characteristics. The simulated motions have the same natural variability that is present in a collection of recorded ground motions having similar earthquake source and site characteristics.
    - Through input parameters $s_{or}d$ and $\theta_{or}\phi$, our procedure allows distinction between forward and backward directivity scenarios. It also generates pulselike and non-pulselike ground motions with likelihoods similar to those observed for recorded ground motions. In contrast with the NGA-West2 GMPEs, our simulations are able to represent the near-fault rupture directivity effect and the differences at longer periods between the response spectra at forward and backward directivity sites. Furthermore, our procedure generates ground motions with and without a fling step, depending on the position of the site relative to the fault rupture.
    - Even though our models cannot reproduce all features of recorded motions, e.g., multiple sub-events with intermittent spikes in the time series, overall they provide synthetic motions that are realistic and faithfully reproduce those features that are particularly important from the viewpoint of designing bridges and long-period structures, as well as ductile short- and medium-period structures that are expected to respond inelastically.
- Our model and simulation procedure have some limitations that result from the use of the ground motion model and simulation framework of Rezaeian and Der Kiureghian (2008, 2010). The selected idealized modulating function is only able to represent cases where energy in the recorded motion arrives in a single event, whereas in real earthquakes energy may arrive in multiple sub-events. Furthermore, the model in its current formulation can only represent a single predominant frequency in the ground motion.

- Besides using a modulating function that is more suitable for near-fault ground motions, our model improves on a number of features of the filtered white-noise model formulated by Rezaeian and Der Kiureghian (2008, 2010). We recommend that these improvements be extended to their model for far-field ground motion.

- A low-cut filter is applied to simulated acceleration time-series to force the resulting velocity and displacement time series to go to zero at the end of the shaking. The critically damped oscillator that was selected as a filter by Rezaeian and Der Kiureghian (2008, 2010) is replaced here by a 4th order acausal Butterworth filter. This filter is applied in the frequency domain. Apart from the order, it is similar to the filter used to process most of the recorded ground motions in the NGA West2 database. Moreover, the filter cutoff frequency is made magnitude dependent instead of being a constant, consistently with the theoretical scaling of the Fourier-amplitude spectra of recorded ground motions. This modification results in more realistic displacement time series.
- In the simulation procedure, for a fixed set of parameters of the modulating function, variability in the underlying white noise process generates variability in the Arias intensity related parameters. To avoid overestimating variability in the generated synthetic ground motions, these motions are uniformly scaled to the Arias intensity value targeted by the simulation.
- The predictive relations used by Rezaeian and Der Kiureghian (2008, 2010) have simplified functional forms that do not account for magnitude and distance saturation. We resolve this matter by selecting functional forms that have been used in developing recent GMPEs and are consistent with seismological theory.

- Our proposed models and simulation procedure are used in a simulation-based PSHA application to demonstrate the importance of using a near-fault stochastic model that allows generating both pulselike and non-pulselike synthetic ground motions. Ignoring the forward directivity effect by using an average ground motion model and/or by not accounting for the possibility of a directivity pulse would have resulted in an underestimation of the hazard, particularly for long-period or strongly inelastic structures.

8.3 RECOMMENDATIONS FOR FUTURE STUDIES

The research presented in this dissertation can be used as a reference point in developing new GMPEs that incorporate the effects of directivity for near-fault sites. Nevertheless, several studies are recommended to improve and expand on the various constituents presented in this study.

The validation of our model so far has mainly consisted of comparing elastic response spectra of simulated motions with those of recorded motions and those obtained from GMPEs. However, since near-fault ground motions are expected to drive structures into the inelastic range, it is important to also compare inelastic response spectra (e.g., Bozorgnia et al., 2010). A brief investigation that was performed indicated agreements similar to those of elastic spectra. This investigation will be further pursued in the next stage of the present study. Furthermore, to compute the response of multi-degree of freedom systems, it is important that correlations between various spectral periods for simulated ground motions be consistent with those for recorded ground motions. These correlations will also be investigated in the next stage of the study.

8.3.1 Improvement and extension of the stochastic model of near-fault ground motion

- The set of parameters used in this study to represent the important characteristics of near-fault ground motion is not unique. Alternate or additional parameters may improve the representation of the ground motion. This requires that the formulation of the model be updated and new predictive relations and correlation matrices be developed for improved simulations. For example, a fitting procedure that uses the cumulative absolute velocity (CAV) intensity measure in place of Arias intensity can be developed.

- The synthetic displacement time series and the long-period content of the simulated motions are strongly sensitive to the choice of the cutoff frequency of the low-cut filter. In this study, this parameter was selected following a preliminary investigation. Further study of this matter is recommended, if accurate depiction of the ground displacement is essential for the structural response.

- When sufficient numbers of recorded motions with fling step become available, predictive equations for the fling model parameters can be developed in terms of earthquake source and site characteristics. The techniques used to model, fit and simulate pulselike near-fault ground motions can be then easily extended to include the fling step.

- This study is focused on modeling the rupture directivity effect and fling step only in the horizontal components of near-fault ground motion. To provide a complete multi-component description, a continuing study will focus on characterization of the ground motion in the vertical direction. The techniques used to model, fit and simulate two horizontal components of ground motion can be easily extended to include the vertical component.

- This study is limited to the simulation of the near-fault ground motion at a single station for given earthquake source and site characteristics. It does not account for the correlation and spatial variability of ground motions from the same event but recorded at different stations. For analysis and design of bridges in near-fault regions, we wish to model and simulate synthetic arrays of near-fault ground motions at multiple sites arising from a single earthquake event. These arrays should include the effects of spatial variability that arise from wave passage and incoherence. A continuing study will focus on characterization of these spatial variability effects in both the directivity pulse and the broadband motion. It is noted that for structures subjected to differential support motions, accurate description of ground displacement is essential. Hence, alluded to above, special attention should be given to the selection of the cut-off frequency.

- The procedure presented in this study allows the simulation of ground motions at near-fault sites located within 30 km from the fault rupture, while the procedure developed by Rezaeian and Der Kiureghian applies to sites located at least 10 km from the fault rupture. Further studies are required to develop a method of combining the two simulation procedures in a manner consistent with recorded ground motions.

- The model and simulation procedure were developed for ground motions from shallow crustal earthquakes in active tectonic regions. The model can be extended to ground motions

in other seismic environments, such as stable continental regions and subduction zones. To reflect possibly different seismic-environment-specific ground motion characteristics, changes to the formulation of the model and to the functional forms of the predictive relations may be required.

8.3.2 Improvement of predictive equations for ground motion model parameters

- As more earthquakes occur and more data becomes available, a number of improvements can be made to the predictive equations: (1) the coefficients of the regression equations and the estimated correlation coefficients can be updated; (2) new functional forms can be investigated, e.g., functional forms that include additional terms to represent non-linear, basin, and hanging-wall effects; (3) non-linear regression analysis can be used. We expect these updates to reduce the error standard deviations of the predictive relations, several of which currently have only small explanatory power.

- In this study, the pulselike and non-pulselike databases include ground motions recorded on soft sites with V_{s30} lower than 760 m/s. This was done in order to retain a sufficient sample size to perform statistical analysis. However, the response of a soft site to the input bedrock motion is non-linear and strongly dependent on the details of the soil profile. These details are not sufficiently described by V_{s30} alone. The modeling of the effects of local soils can be improved by taking each recording on a non-rock site and, through back-calculation and use of detailed local site information, determining the corresponding bedrock motion. After fitting the model to bedrock motions, simulated rock motions can be used as input into a soil profile to compute surface motions at a site. These surface motions can be obtained by performing 1-dimensional equivalent visco-elastic site response analysis. If very high strain levels are expected, or if basin and topographic effects are deemed important, then 2- or 3-dimensional analyses should be performed. However, this approach requires detailed knowledge of each recording site, which is not available for many of the near-fault records in our database. We intend to continue exploring ways of better accounting for the site effects.

8.3.3 Illustration of the advantages and diversity of applications of the proposed method in PBEE

- We plan on comparing the results of a PSHA that uses our site-based simulation procedure to the results from a PSHA that uses a physics-based ground motion simulation model. For this purpose, we will update the PSHA study of Chapter 7 by using a less simplistic seismic source model and earthquake scenarios for which physics-based PSHA results are available. Our results will be compared with those from the Southern California Earthquake Center CyberShake project (Graves et al., 2011), which uses a physics-based model based on finite-fault rupture and full 3D wave propagation models.

- The proposed simulation procedure can also be used in other PBEE applications, such as seismic risk assessment and loss estimation studies. In a forthcoming study ,the collapse risk and loss estimates will be calculated for an example reinforced concrete building located in San Francisco. The results of the seismic risk assessment will be compared to those obtained through Incremental Dynamic Analysis (IDA) (Vamatsikos, 2002), which uses real ground motion records scaled gradually until the structure reaches collapse.

References

Abrahamson, N. A. (2013). Personal communication.

Abrahamson, N. A. (2001). Development of Fling Model for Diablo Canyon ISFSI. Pacific Gas and Electric Company, Geosciences Department, Calc. No. GEO.DCPP.01.12.

Abrahamson, N. A. (1998). Statistical properties of peak ground accelerations recorded by the SMART 1 array. *Bulletin of the Seismological Society of America* **78**(1): 26-41.

Abrahamson, N. A., G. Atkinson, D. Boore, Y. Bozorgnia, K. Campbell, B. Chiou, I. M. Idriss, W. Silva and R. Youngs (2008). Comparisons of the NGA Ground-Motion Relations. *Earthquake Spectra*, **24** (1):45-66.

Abrahamson, N. A., W. J. Silva and R. Kamai (2014). Summary of the Abrahamson, Silva, and Kamai (2014) NGA-West2 ground-motion relations for active crustal regions. *Earthquake Spectra*, in press.

Abrahamson, N. A., W. J. Silva and R. Kamai (2013). Update of the AS08 Ground-Motion Prediction Equations Based on the NGA-West2 Data Set. *PEER Report No. 2013/04*, Pacific Earthquake Engineering Research Center, University of California, Berkeley, CA, 143 pp.

Abrahamson, N. A., and P. G. Somerville (1996). Effects of the Hanging Wall and Footwall on Ground Motions Recorded during the Northridge. *Earthquake Bulletin of the Seismological Society of America*, **86**(1B): 93-99.6

Abrahamson N. A., and R. Youngs (1992). A stable algorithm for regression analyses using the random effects model. *Bulletin of the Seismological Society of America,* **82**: 505-510.

Aki, K., and P. G. Richard (2002). Quantitative Seismology: Theory and Method. 2nd. Ed. W.H. Freeman and Co., San Francisco.

Aki, K., and P. G. Richards (1980). Quantitative Seismology: Theory and Methods. W.H. Freeman, San Francisco.

Al Atik, L., and R. R. Youngs (2014). Epistemic uncertainty for NGA-West2 models. *Earthquake Spectra*, in press.

Al Atik, L., and R. R. Youngs (2013). Epistemic Uncertainty for NGA-West2 Models. *PEER Report No. 2013/11*, Pacific Earthquake Engineering Research Center, University of California, Berkeley, CA, 59 pp.

Alavi, B., and H. Krawinkler (2000). Consideration of near-fault ground motion effects in seismic design. *Proc. 12th World Conference on Earthquake Engineering*, New Zealand, 1-8.

Ambraseys, N. N., J. Douglas, S. K. Sarma and P. M. Smit PM (2005). Equations for the estimation of strong ground motions from shallow crustal earthquakes using data from Europe and the Middle East: horizontal peak ground acceleration and spectral acceleration. *Bulletin of Earthquake Engineering,* **3**(1): 1–53.

Ancheta, T. D., R. B. Darragh, J. P. Stewart, E. Seyhan, W. J. Silva, B. S. J. Chiou, K. E. Wooddell, R. W. Graves, A. R. Kottke, D. M. Boore, T. Kishida and J. L. Donahue (2014). PEER NGAWest2 database. *Earthquake Spectra*, in press.

Ancheta, T. D., R. B. Darragh, J. P. Stewart, E. Seyhan, W. J. Silva, B. S. J. Chiou, K. E. Wooddell, R. W. Graves, A. R. Kottke, D. M. Boore, T. Kishida and J. L. Donahue (2013). PEER NGAWest2 Database. *PEER Report No. 2013/03*, Pacific Earthquake Engineering Research Center, University of California, Berkeley, CA.

Anderson J. C. and V. V. Bertero (1987). Uncertainties in Establishing Design Earthquakes. *Journal of Structural Engineering*, **113**(8):1709-1724.

Anderson, J. G., and S. E. Hough (1984). A Model for the Shape of the Fourier Amplitude Spectrum ofAcceleration at High Frequencies. *Bulletin of the Seismological Society of America*, **74**:1969–1993.

Archuleta, R. J., and S. H. Hartzell (1981). Effects of fault finiteness on near-source ground motion. *Bulletin of the Seismological Society of America*, **71**:939-957.

Atkinson, G. M., K. Assatourians, D. M. Boore, K. Campbell and D. Motazedian (2009). A guide to differences between stochastic point-source and stochastic finite-fault simulations. *Bulletin of the Seismological Society of America*, **99**:3192-3201.

Atkinson, G. M., and W. Silva (2000). Stochastic modeling of California ground motions. *Bulletin of the Seismological Society of America*, **90**:255-274.

Atkinson, G. M., and W. Silva (1997). An empirical study of earthquake source spectra for California earthquakes. *Bulletin of the Seismological Society of America*, **87**:97–113.

Arias A. (1970). A measure of earthquake intensity. In Seismic Design for Nuclear Power Plants, Hansen RJ (ed.). MIT Press: Cambridge, MA, 1970; 438–483.

Baher, S. A., and P. M. Davis (2003). An application of seismic tomography to basin focusing of seismic waves and Northridge earthquake damage. *Journal of Geophysical Research*, **108**(B2):2122.Baker, J. (2007). Quantitative classification of near-fault ground motions using wavelet analysis. *Bulletin of the Seismological Society of America*, **97**(5):1486-1501.

Bayless, J., and P. Somerville (2013). Bayless-Somerville Directivity Model, *Chapter 3 of Pacific Earthquake Engineering Research Center Report PEER-2013/09*, P. Spudich (editor), Berkeley,CA.

Bertero V.V., R. A. Herrera and S. A. Mahin (1976). Establishment of design earthquakes - evaluation of present methods. *Proceedings of the International Symposium on Earthquake Structural Engineering*, St. Louis, Missouri, 551-580.

Bertero, V. V., S. A. Mahin and R. A. Herrera (1978). Aseismic design implications of near-fault San Fernando earthquake records. *Earthquake Engineering and Structural Dynamics*, **6**:31-42.

Boatwright, J., and G L. Choy (1992). Acceleration source spectra anticipated for large earthquakes in Northeastern North America. *Bulletin of the Seismological Society of America*, **82**(2):660-682.

Boatwright, J., L. C. Seekins, T. E. Fumal, H.-P. Liu and C. S. Mueller (1991). Ground motion amplification in the Marina district. *Bulletin of the Seismological Society of America*, **81**(5):1980-1997.

Bommer, J. J., P. J. Stafford and J. E. Alarcon (2009). Empirical equations for the prediction of the significant, bracketed, and uniform duration of earthquake ground motion. *Bulletin of the Seismological Society of America*, **99**:3217-3233.

Boore, D. M. (2010). Orientation-independent, nongeometric-mean measures of seismic intensity from two horizontal components of motion. *Bull. Seismol. Soc. Am.*, **100**:1830–1835.

Boore, D. M. (2009). Comparing stochastic point-source and finite-source ground-motion simulations: SMSIM and EXSIM. *Bulletin of the Seismological Society of America,* **99**:3202-3216.

Boore, D. M. (2005). On pads and filters: Processing strong-motion data, *Bulletin of the Seismological Society of America,* **95**:745–750.

Boore, D. M. (2003a). Analog-to-digital conversion as a source of drifts in displacements derived from digital recordings of ground acceleration. *Bulletin of the Seismological Society of America,* **93**:2017–24.

Boore, D. M. (2003b). Simulation of ground motion using the stochastic method. *Pure appl. Geophys*, **160**:635-676.

Boore, D. M. (1983). Stochastic simulation of high-frequency ground motions based on Sseismological models of the radiated spectra. *Bulletin of the Seismological Society of America,* **73**:1865–1894.

Boore, D. M., and S. Akkar (2003). Effect of causal and acausal filters on elastic and inelastic response spectra. *Earthquake Engineering & Structural Dynamics*, **32**:1729–1748.

Boore, D. M., A. Azari Sisi, and S. Akkar (2012). Using pad-stripped acausally filtered strong-motion data. *Bulletin of the Seismological Society of America*, **102**: 751–760.

Boore, D. M., and J. Bommer (2005). Processing of strong-motion accelerograms: needs, options and consequences. *Soil Dynamics and Earthquake Engineering*, **25**: 93-115.

Boore, D. M., C. A. Goulet (2014), The effect of sampling rate and anti-aliasing filters on high-frequency response spectra. *Bulletin of Earthquake Engineering*, **12**(1):203:216.

Boore, D. M., J. P. Stewart, E. Seyhan and G. A. Atkinson (2014). NGA-West2 equations for predicting response spectral accelerations for shallow crustal earthquakes. *Earthquake Spectra*, in press.

Boore, D. M., J. P. Stewart, E. Seyhan and G. A. Atkinson (2013). NGA-West2 Equations for Predicting Response Spectral Accelerations for Shallow Crustal Earthquakes. *PEER Report No. 2013/05*, Pacific Earthquake Engineering Research Center, University of California, Berkeley, CA, 134 pp.

Boore, D. M., J. Watson-Lamprey and N. A. Abrahamson (2006). Orientation-independent measures of ground motion. *Bulletin of the Seismological Society of America*, **96**(4):1502–1511.

Bozorgnia, Y., N. A. Abrahamson, L. Al Atik, T. D. Ancheta, G. M. Atkinson, J. W. Baker, A. Baltay, D. M. Boore, K. W. Campbell, B. S. J. Chiou, R. Darragh, S. Day, J. Donahue, R. W. Graves, N. Gregor, T. Hanks, I. M. Idriss, R. Kamai, T. Kishida, A. Kottke, S. A. Mahin, S. Rezaeian, B. Rowshandel, E. Seyhan, S. Shahi, T. Shantz, W. Silva, P. Spudich, J. P. Stewart, J. Watson-Lamprey, K. Wooddell, and R. Youngs (2014) NGA-West2 Research Project. *Earthquake Spectra,* in press.

Bozorgnia, Y., and K. W. Campbell (2004a). Engineering characterization of ground motion, in Earthquake Engineering: From Engineering Seismology to Performance-Based Engineering, Y. Bozorgnia and V. V. Bertero (editors), Chapter 5, pp. 1–74, CRC Press, Boca Raton, FL.

Bozorgnia, Y., and K. W. Campbell (2004b). Vertical-to-horizontal response spectra ratio and tentative procedures for developing simplified V/H and vertical design spectra. *J. Earthq. Eng.g*, **8**(2):175-207

Bozorgnia, Y., M. M. Hachem and K. W. Campbell (2010). Ground Motion Prediction Equation ("Attenuation Relationship") for Inelastic Response Spectra. *Earthquake Spectra*, **26(**1):1–23.

Bozorgnia, Y., and S. A. Mahin (1998). Ductility and strength demands of near-fault ground motions of the Northridge earthquake. *Proceedings, 6th U.S. National Conference on Earthquake Engineering*, Earthquake Engineering Research Institute, Seattle, WA.

Bray, J. D., and A. Rodriguez-Marek (2004). Characterization of forward-directivity ground motions in the near-fault region. *Soil Dynamics and Earthquake Engineering*, **24**:815-828.

Brillinger D. R., H. K. Preisler (1985). Further analysis of the Joyner-Boore attenuation data. *Bulletin of the Seismological Society of America,* **75**:611-614.

Broccardo M., and A. Der Kiureghian (2014). Simulation of near-fault ground motion using frequency-domain discretization. *Proceedings of the 10th National Conference on Earthquake Engineering*, Earthquake Engineering Research Institute, Anchorage, AK.

Building Seismic Safety Council (BSSC) (2009). NEHRP (National Earthquake Hazards Reduction Program) Recommended Seismic Provisions for New Buildings and Other Structures (FEMA P-750) 2009 Edition

Butterworth, S. (1930). On the theory of filter amplifiers. *Experimental Wireless and the Wireless Engineer* , **7**:536–541

Campbell, K. W., and Y. Bozorgnia (2014). Campbell-Bozorgnia NGA-West2 ground motion model for the average horizontal components of PGA, PGV, and 5%-damped linear Response Spectra. *Earthquake Spectra*, in press.

Campbell, K. W., and Y. Bozorgnia (2013). NGA-West2 Campbell-Bozorgnia Ground Motion Model for the Horizontal Components of PGA, PGV, and 5%-Damped Elastic Pseudo-Acceleration Response Spectra for Periods Ranging from 0.01 to 10 s. *PEER Report No. 2013/06*, Pacific Earthquake Engineering Research Center, University of California, Berkeley, CA, 238 pp.

Campbell, K. W., and Y. Bozorgnia (2010). A ground motion prediction equation for the horizontal component of cumulative absolute velocity (CAV) based on the PEER-NGA strong motion database. *Earthquake Spectra*, 26(3):635–650, August 2010; © 2010, Earthquake Engineering Research Institute

Campbell K. W., and Y. Bozorgnia (2008). NGA ground motion model for the geometric mean horizontal component of pga, pgv, pgd and 5% damped linear elastic response spectra for periods ranging from 0.01 to 10 s. *Earthquake Spectra*, **24**(1):139-171

Campbell, K. W., and Y. Bozorgnia (2007). Campbell-Bozorgnia NGA Ground motion Relations for the Geometric Mean Horizontal Component of Peak and Spectral Ground Motion Parameters. *PEER Report No. 2007/02*, Pacific Earthquake Engineering Research Center, University of California, Berkeley, CA, 238 pp.

Camstra, A. and A. Boomsma (1992). Cross-validation in regression and covariance structure analysis: An overview. *Sociological Methods & Research*, **21**(1):89-115.

Cauer, W. (1931). Siebschaltungen. VDI-Verlag G.m.b.H., Berlin, 1931.

Chebyshev, P. L. (1854). Théorie des mécanismes connus sous le nom de parallélogrammes. *Mémoires des Savants étrangers présentés à l'Académie de Saint-Pétersbourg*, **7**:539–586.

Chang, T., F. Cotton, Y. Tsai and J. Angelier (2004). Quantification of Hanging-Wall Effects on Ground Motion: Some Insights from the 1999 Chi-Chi Earthquake. *Bulletin of the Seismological Society of America*, **94**(6):2186:2197.

Chinnery, M. A. (1961). Deformation of the ground around faults. *Bull. Seismol. Soc. Am.*, **51**:355–372.

Chioccarelli, E., and I. Iervolino (2010). Near-source seismic demand and pulse-like records: A discussion for L'Aquila earthquake. *Earthquake Engineering and Structural Dynamics*, **39**(9):1039–1062.

Chiou, B. S. J., and R. R. Youngs (2014). Update of the Chiou and Youngs NGA ground motion model for average horizontal component of peak ground motion and response spectra. *Earthquake Spectra*, in press.

Chiou, B. S. J., and R. R. Youngs (2013). Update of the Chiou and Youngs NGA Ground Motion Model for Average Horizontal Component of Peak Ground Motion and Response Spectra. *PEER Report No. 2013/07*, Pacific Earthquake Engineering Research Center, University of California, Berkeley, CA, 76 pp.

Choi, Y., J. P. Stewart and R. W. Graves (2005). Empirical model for basin effects accounts for basin depth and source location. *Bulletin of the Seismological Society of America*, **95**(4):1412–1427.

Converse A. M., and A. G. Brady (1992). BAP basic strong-motion accelerogram processing software, version 1.0. *Open-File Report 92-296A*, US Geological Survey.

Crowley H. and J. J. Bommer (2006). Modelling seismic hazard in earthquake loss models with spatially distributed exposure. *Bulletin of Earthquake Engineering*, **4**(3):249–273.

Dabaghi, M., and A. Der Kiureghian (2014). Simulation of orthogonal horizontal components of near-fault ground motions for specified earthquake source and site characteristics. *Proceedings, 10th National Conference on Earthquake Engineering*, Anchorage, AK.

Dabaghi, M., A. Der Kiureghian, S. Rezaeian, and N. Luco (2013). Seismic hazard analysis using simulated ground motions. *Proceedings, 11th International Conference on Structural Safety & Reliability*, Columbia, NY.

Dabaghi M., and A. Der Kiureghian (2011). Stochastic model and simulation of near fault ground motions for specified earthquake source and site characteristics. *Report to California Department of Transportation*.

Dabaghi, M., S. Rezaeian and A. Der Kiureghian (2011). Stochastic simulation of near-fault ground motions for specified earthquake and site characteristics. *Proceedings of the International Conference on Applications of Statistics and Probability in Civil Engineering*, Zurich, Switzerland.

Darlington, S. (1939). Synthesis of reactance 4-poles which produce prescribed insertion loss characteristics. *Journal of Mathematics and Physics*, **18**:257-353.

Darragh, R. B., W.J. Silva and N. Gregor N. (2004). Strong motion record processing procedures for the PEER center. *Proceedings of COSMOS Workshop on Strong-Motion Record Processing*, Richmond, California, pp. 1–12.

Day, S., R. Graves, J. Bielak, D. Dreger, S. Larsen, K. Olsen, A. Pitarka and L. Ramizrez-Guzmanc (2008). Model for basin effects on long-period response spectra in Southern California. *Earthquake Spectra*, **24**(1):257-277.

Donahue, J. L., and N. A. Abrahamson (2014). Simulation-based hanging wall effects model. *Earthquake Spectra*, in press.

Douglas, J., and H. Aochi (2008). A survey of techniques for predicting earthquake ground motions for engineering purposes. *Surveys in Geophysics*, **29**:187-220.

Douglas, J. and D. M. Boore (2011). High-frequency filtering of strong-motion records. *Bull Earthquake Engineering*, **9**:395–409.

Dreger, D., G. Hurtado, A. Chopra and S. Larsen (2011). Near-field across-fault seismic ground motions. *Bulletin of the Seismological Society of America*, **101**(1):202-221.

Electrical Power Research Institute (EPRI), (1988). A Criterion for Determining Exceedance of the Operating Basis Earthquake. *Report No. EPRI NP-5930*, Palo Alto, California

Frankel, A., C. Mueller, T. Barnhard, D. Perkins, E. Leyendecker, N. Dickman, S. Hanson and M. Hopper (1996). National Seismic Hazard Maps: Documentation June 1996. *U.S. Geol. Surv*, Open-File Rept. 96:532, 69 pp.

Fu, Q., and C. Menun (2004). Seismic-environment-based simulation of near-fault ground motions. *Proceedings of the 13th World Conference on Earthquake Engineering*. Vancouver, Canada.

Galanis, P. H., and J. P. Moehle (2014). Development of Collapse Indicators for Risk Assessment of Older-Type Reinforced Concrete Builldings. *Earthquake Spectra*, in press.

Gao, S., H. Liu, P. M. Davis, and L. Knopoff (1996). Localized amplification of seismic waves and correlation with damage due to the Northridge earthquake: evidence for focusing in Santa Monica. *Bulletin of the Seismological Society of America,* **86**(1B):S209-S230.

Graves, R. W. (1993). Modeling three-dimensional site response effects in the marina district basin, San Francisco, California. *Bulletin of the Seismological Society of America*, **83**(4):1042-1063.

Graves, R. W., T. H. Jordan, S. Callaghan, E. Deelman, E. H. Field, G. Juve, C. Kesselman, P. Maechling, G. Mehta, D. Okaya, P. Small, and K. Vahi (2011). CyberShake: A Physics-Based Seismic Hazard Model for Southern California. *Pure and Applied Geophysics*, **168**(3-4), 367-381.

Graves, R. W., A. Pitarka, and P. Somerville (1998). Ground-motion amplification in the Santa Monica area: Effects of shallow basin-edge structure. *Bulletin of the Seismological Society of America,* **88:**1224– 1242.

Grazier, V.M. (1979). Determination of the true ground displacement by using strong motion records. Izvestiya Academy of Sciences, USSR, *Physics of the Solid Earth* **15**(12): 875-885.

Gregor, N., N. A. Abrahamson, G. M. Atkinson, D. M. Boore, Y. Bozorgnia, K. W. Campbell, B. S. J. Chiou, I. M. Idriss, R. Kamai, E. Seyhan, W. Silva, J. P. Stewart, and R. Youngs (2014). Comparison of NGA-West2 GMPEs. *Earthquake Spectra*, in press.

Gülerce, Z., and N. A. Abrahamson (2011). Site-specific design spectra for vertical ground motion. *Earthquake Spectra*, **27**:1023-1047.

Holzer ,T. L., A C. Padovani, M. J. Bennett, T. E. Noce, and J. C. Tinsley, III (2005). Mapping NEHRP VS30 Site Classes. *Earthquake Spectra*, **21**(2):1–18.

Idriss, I. M. (2014). NGA-West2 model for estimating average horizontal values of pseudo-absolute spectral accelerations generated by crustal earthquakes. *Earthquake Spectra*, in press.

Idriss, I. M. (2013). NGA-West2 Model for Estimating Average Horizontal Values of Pseudo-Absolute Spectral Accelerations Generated by Crustal Earthquakes. *PEER Report No. 2013/08*, Pacific Earthquake Engineering Research Center, University of California, Berkeley, CA, 31 pp.

Iervolino, I., and C. A. Cornell (2008). Probability of occurrence of velocity pulses in near-source ground motions. *Bulletin of the Seismological Society of America*, **98**(5):2262–2277.

Iwan, W. D., M. A. Moser, and C.-Y. Peng (1985). Some observations on strong-motion earthquake measurement using a digital accelerograph. *Bulletin of the Seismological Society of America*, **75:**1225-1246.

Jayaram, N., and J. W. Baker (2010). Efficient sampling and data reduction techniques for probabilistic seismic lifeline risk assessment. *Earthquake Engineering & Structural Dynamics*, **39**(10):1109-1131.

Jayaram, N., and J. W. Baker (2008). Statistical tests of the joint distribution of spectral accelerationvalues. *Bulletin of the Seismological Society of America*, **98**(5):2231-2243.

Joyner, W. B. (1984). A scaling law for the spectra of large earthquakes, *Bull. Seism. Soc. Am.*, **74**:1167-1188

Kamai, R., N. A. Abrahamson, and W. J. Silva (2014). Nonlinear horizontal site amplification for constraining the NGA-West2 GMPEs. *Earthquake Spectra*, in press.

Kamai, R., N. A. Abrahamson, and W. J. Silva (2013). Nonlinear Horizontal Site Response for the NGA-West2 Project. *PEER Report No. 2013/12*, Pacific Earthquake Engineering Research Center, University of California, Berkeley, CA, 69 pp.

Kanasewich, E.R. (1981). Time Sequence Analysis in Geophysics. *The University of Alberta Press*, Edmonton, Alberta, Canada, 480 pp.

Key, F.A. (1968). Some observations and analyses of signal generated noise. *Geophysical Journal of the Royal Astronomical Society*, **15**:377-392.

Kiremidjian A.S., E. Stergiou and R. Lee (2007). Issues in seismic risk assessment of transportation networks. *Earthquake Geotechnical Engineering*, Chapter 19:939–964. Berlin: Springer.

Kramer, S. L. (1996). Geotechnical Earthquake Engineering. Upper Saddle River, New Jersey: Prentice Hall.

Krawinkler, H. and B. Alavi (1998). Development of improved design procedures for near-fault ground motions. *SMIP98*, seminar on utilization of strong motion data, Oakland, CA.

Luco, N. (2002). Probabilistic seismic demand analysis, SMRF connection fractures, and near-source effects. *Ph.D. Thesis*, Dept. of Civil and Environmental Eng., Stanford University, California.

Luco N., P. M. Mai, C. A. Cornell and G. C. Beroza (2002). Probabilistic seismic demand analysis at a near-fault site using ground motion simulations based on a stochastic-kinematic earthquake source model. *Proceedings of the 7th U.S. National Conference on Earthquake Engineering*, Boston, MA.

Mavroeidis, G. P., and A. S. Papageorgiou (2003). A mathematical representation of nearfault ground motions. *Bulletin of the Seismological Society of America*, **93**(3):1099-1131.

Mavroeidis, G. P., and A. S. Papageorgiou (2002). Near-source strong ground motion: characteristics and design issues. *Proc. of the Seventh U.S. National Conf. on Earthquake Engineering (7NCEE)*, Boston, Massachusetts.

Menun, C., and Q. Fu (2002). An analytical model for near-fault ground motions and the response of SDOF systems. *Proceedings of the 7th U.S. National Conference on Earthquake Engineering*, Boston, Massachusetts.

Nakamura, M., F. Sasaki, K. Yokoyama, and T. Tamaoki (2008). Generation of artificial earthquake motion using observed earthquake motions. *Proc. of the 14th World Conference on Earthquake*, Beijing, China, 12–17 October 2008.

Pacific Earthquake Engineering Research Center (PEER), (2014). Weighted average of 2014 NGA WEST-2 GMPEs. Retrieved from http://peer.berkeley.edu/

Papageorgiou, A. S., and K. Aki (1983). A specific barrier model for the quantitative description of inhomogeneous faulting and the prediction of strong ground motion. I. Description of the model. *Bulletin of the Seismological Society of America,* **73:**693–722.

Penzien J, M. Watabe (1975). Characteristics of 3-dimensional earthquake ground motions. *Earthquake Engineering and Structural Dynamics*, **3**:365–373.

Power, M., B. Chiou, N. A. Abrahamson, Y. Bozorgnia, T. Shantz, and C. Roblee (2008). An overview of the NGA Project. *Earthquake Spectra*, **24**:3–21.

Rathje E. M., F. Faraj, S. Russell and J. D. Bray (2004). Empirical relationships for frequency content parameters of earthquake ground motions. *Earthquake Spectra*, **20**(1): 119-144.

Rezaeian, S., Y. Bozorgnia, I. M. Idriss, N. A. Abrahamson, K. W. Campbell and W. J. Silva (2014a). Damping scaling factors for elastic response spectra for shallow crustal earthquakes in active tectonic regions: Vertical component. *Earthquake Spectra*, in press.

Rezaeian, S., Y. Bozorgnia, I. M. Idriss, N. A. Abrahamson, K. W. Campbell, and W. J. Silva (2014b). Damping scaling factors for elastic response spectra for shallow crustal earthquakes in active tectonic regions: "Average" horizontal component. *Earthquake Spectra,* **30**: 939-963.

Rezaeian, S., and A. Der Kiureghian (2012). Simulation of orthogonal horizontal ground motion components for specified earthquake and site characteristics. *Earthquake Engineering & Structural Dynamics*, **41**:335-353.

Rezaeian, S., and A. Der Kiureghian (2010a). Simulation of synthetic ground motions for specified earthquake and site characteristics. *Earthquake Engineering & Structural Dynamics*, **39**:1155-1180.

Rezaeian, S., and A. Der Kiureghian (2010b). Stochastic modeling and simulation of ground motions for performance-based earthquake engineering. *PEER Report 2010/02*, Pacific Earthquake Engineering Research Center, University of California, Berkeley, CA.

Rezaeian, S., and A. Der Kiureghian (2008). A stochastic ground motion model with separable temporal and spectral nonstationarities. *Earthquake Engineering & Structural Dynamics*, **37**:1565-1584.

Rezaeian, S., M. Petersen, M. Moschetti, P. Powers, S. Harmsen, and A. Frankel (2014). Implementation of NGA-West2 Ground Motion Models in the U.S. National Seismic Hazard Maps. *Earthquake Spectra*, in press.

Roechester,M. G. (1956). The application of dislocation theory to fracture in the Earth's crust. *Master's Thesis*, University of Toronto

Sasani, M., and V. V. Bertero (2000). Importance of severe pulse-type ground motions in performance-based engineering: historical and critical review. *Proceedings, 12th World Conference on Earthquake Engineering* , (12WCEE), Auckland, New Zealand.

Seyhan, E., and J. P. Stewart (2014). Semi-empirical nonlinear site amplification and its application in NEHRP site factors. *Earthquake Spectra*, in press.

Shahi, S. K., and J. W. Baker (2014). NGA-West2 models for ground-motion directionality. *Earthquake Spectra*, in press.

Shahi, S. K., and J. W. Baker (2013a). NGA-West2 Models for Ground-Motion Directionality. *PEER Report No. 2013/10*, Pacific Earthquake Engineering Research Center, University of California, Berkeley, 45 pp.

Shahi, S. K., and J. W. Baker (2013b). Shahi-Baker Directivity Model. *Chapter 4 of Pacific Earthquake Engineering Research Center Report PEER-2013/09*, P. Spudich (editor), Berkeley, CA.

Shahi, S. K., and J. W. Baker (2011). An empirically calibrated framework for including the effects of near-fault directivity in probabilistic seismic hazard analysis. *Bulletin of the Seismological Society of America*, **101**(2):742-755.

Shinozuka, M., G. Deodatis, R. Zhang and A. Papageorgiou (1999). Modeling, synthetics and engineering applications of strong earthquake wave motion. *Soil Synamics and Earthquake Engineering*, **18**:209-228.

Somerville, P. G. (2003). Magnitude scaling of the near fault rupture directivity pulse. *Physics of the Earth and Planetary Interiors*, **137**:201-212.

Somerville, P. (2002). Characterizing Near Fault Ground Motion for the Design and Evaluation of Bridges. *The 3rd National Conference & Workshop on Bridges & Highways*, Portland, Oregon.

Somerville, P. (2000). Seismic Hazard Evaluation. *12th World Conference on Earthquake Engineering*. Auckland, N.Z.

Somerville, P. G. (1998). Development of an Improved Representation of Near-Fault Ground Motions. *SMIP 98: Seminar on Utilization of Strong Motion Data*, 1-20. Oakland, CA.

Somerville, P. G., and N. A. Abrahamson (1996). Accounting for near-fault rupture directivity effects on the development of design ground motions. *Proceedings, 11th World Conference on Earthquake Engineering*, Acapulco, ME. Paper No. 711

Somerville, P., N. Collins, N. A. Abrahamson, R. Graves, and C. Saikia (2001). Ground motion attenuation relations for the Central and Eastern United States—Final report. *Report to U.S. Geological Survey for award 99HQGR0098*, June 30, 38 p.

Somerville, P. G., and R. Graves (1993). Conditions that give rise to unusually large long period ground motions. *Structural Design of Tall Buildings*, **2**:211–232.

Somerville, P. G., N. F. Smith, R. Graves and N. A. Abrahamson (1997). Modification of Empirical Strong Ground Motion Attenuation Relations to Include the Amplitude and Duration Effects of Rupture Directivity. *Seismological Research Letters*, **68**: 94-127.

Spudich, P., J. R. Bayless, J. W. Baker, B. S. J. Chiou, B. Rowshandel, S. K. Shahi and P. Somerville (2013). Final Report of the NGA-West2 Directivity Working Group, *PEER Report No. 2013/09*, Pacific Earthquake Engineering Research Center, University of California, Berkeley, 129 pp.

Spudich, P., and B. S.-J. Chiou (2013). The Spudich and Chiou NGA-West2 directivity model. *Chapter 5 in Pacific Earthquake Engineering Research Center Report PEER-2013/09*, P. Spudich (editor), Berkeley, CA.

Spudich, P., and B.S.-J. Chiou (2008). Directivity in NGA earthquake ground motions: Analysis using isochrone theory. *Earthquake Spectra*, **24(**1):279-298.

Spudich, P., B. Rowshandel, S. Shahi, J. W. Baker and B. S. J. Chiou (2014) Comparison of NGA-West2 directivity models. *Earthquake Spectra,* in press.

Stacey, F.D., and Davis, P.M., (2008) Physics of the Earth, 4th Edition:September 2008 ISBN: 9780521873628 Cambridge University Press; UK

Stewart, J. P., N. A. Abrahamson, G. M. Atkinson, J. W. Baker, D. M. Boore, Y. Bozorgnia, K. W. Campbell, C. D. Comartin, I. M. Idriss, M. Marshall Lew, M. Mehrain, J. P. Moehle, F. Naeim and T. A. Sabol (2011). Representation of bidirectional ground motions for design spectra in building codes. *Earthquake Spectra*, **27**(3):927-937.

Stewart, J. P., and E. Seyhan (2013). Semi-Empirical Nonlinear Site Amplification and its Application in NEHRP Site Factors, *PEER Report No. 2013/13*, Pacific Earthquake Engineering Research Center, University of California, Berkeley, CA, 59 pp.

Trifunac, M.D. (1971). Zero baseline correction of strong-motion accelerograms. *Bulletin of the Seismological Society of America*, **61**:1201–1211.

Trifunac, M. D. and A. G. Brady (1975). A study on the duration of strong earthquake ground motion. *Bulletin of the Seismological Society of America*, **65**(3):581-626.

Vamvatsikos, D., A. C. Cornell (2002). Incremental Dynamic Analysis. *Earthquake Engineering and Structural Dynamics*, **31**:491-514

Walling, M., W. J. Silva and N. A. Abrahamson (2008). Non-linear site amplification factors for constraining the NGA models. *Earthquake Spectra*, **24**:243–255.

Wells, D. L., and K. J. Coppersmith (1994). New empirical relationships among magnitude, rupture length, rupture width, rupture area, and surface displacement. *Bulletin of the Seismological Society of America*, **84**(4):974-1002.

Wooddell, K. E., and N. A. Abrahamson (2014). New earthquake classification scheme for mainshocks and aftershocks in the NGA-West2 ground motion prediction equations (GMPEs). *Earthquake Spectra*, in press.

Wooddell, K. E., and N. A. Abrahamson (2012). New earthquake classification scheme for mainshocks and aftershocks in the NGA-West2 ground motion prediction equations (GMPEs). *Proceedings of 15th World Conference on Earthquake Engineering*, Paper No. 3872, Lisbon, Portugal.

Working Group on California Earthquake Probabilities 2003. Earthquake probabilities in the San Francisco bay region: 2002 to 2031. *U.S. Geological Survey Open-File Report 03-214*.

Yamamoto, Y., and J. W. Baker, (2013). Stochastic model for earthquake ground motion using wavelet packets. *Bulletin of the Seismological Society of America*, **103**(6):3044–3056.

Yamamoto, Y., and J. W. Baker, (2011). Stochastic model for earthquake ground motion using wavelet packets. *Technical Report Blume Center Report 176*, Stanford, California.

Zerva A. (1988). Seismic source mechanisms and ground motion models, review paper. *Probabilistic Engineering Mechanics*; **3**:64–74.

Zhu, L. (2003). Recovering permanent displacements from seismic records of the June 9, 1994 Bolivia deep earthquake. *Geophysical Research Letters*, 30(14):1740.

Appendix A: Pulselike and Non-pulselike Databases

This appendix provides information on the 130 recorded pulselike ground motions and 311 recorded non-pulselike ground motions that constitute the pulselike and non-pulselike databases used in this study. These databases are introduced in Chapter 5.

PULSELIKE DATABASE

Table A.1 describes the record characteristics of pulselike ground motions. For each record, it includes information about the NGA record sequence number, the name and year of the earthquake, the name of the recording station, the time step Δt_0 of the original signal and corresponding Nyquist frequency f_{N_0} (see Section 3.4), the frequencies f_{HC} and f_{LC} of the high-cut (low-pass) and low-cut (high-pass) filters, respectively, used by PEER to process the record (see Sections 3.2.4 and 3.2.5), and the longest usable period T_{max} (see Sections 3.2.6). For each record, the table also gives the cutoff frequency f_c, computed according to (3.15), of the low-cut filter applied to the time series that are simulated using the parameters fitted to the record. Furthermore, it gives the period T_p of the mMP velocity pulse fitted to the pulse extracted from the record by use of Baker's wavelet method (Baker 2007).

The frequency f_{HC} of the high-cut filter is compared to the Nyquist frequency f_{N_0} of the original signal. For most records, we find that f_{HC} is much smaller than f_{N_0}.This finding indicates that the initial signal has extremely small Fourier amplitudes near f_{N_0}. Therefore, resampling by *sinc*-interpolation (i.e., padding the FAS with zeros at frequencies above f_{N_0}) is expected to be a good approximation of the signal, were it recorded at a higher sampling rate.

The longest usable period T_{max} is the inverse of the lowest usable frequency f_{min}, which is equal to $1.25f_{LC}$, when the record is low-cut filtered using a 5th order acausal Butterworth filter. In most cases, T_p is much smaller than T_{max} and thus falls within the usable range of periods, i.e., the range of periods over which the processed signal is reliable.

Table A.2 lists the earthquake source and site characteristics used as explanatory variables in the regression analysis, namely the style of faulting, F, the moment magnitude $\mathbf{M}$, the depth to the top of the rupture, Z_{TOR}, the closest distance to the fault rupture, R_{RUP}, the shear-wave velocity in the top 30m of the soil at the site, V_{s30}, and the two directivity parameters $s_{or}d$ and $\theta_{or}\phi$.

Finally, for each recorded ground motion, the parameters of the pulselike model presented in Section 4.4 are identified according to the fitting procedure described in Section 5.3.3. The identified parameter values of the velocity pulse model in the direction of the largest pulse, and of the models of residual and orthogonal motion, are listed in Tables A.3, A.4 and A.5, respectively. Table A.3 also lists the value of the angle α_p between the largest pulse direction and the strike of the fault.

Table A. 1 Characteristics of ground motion records in the pulselike database.

NGA#	EQ Name	Year	Station Name	Δt_0 (s)	f_{N0} (Hz)	f_{HC} (Hz)	f_{LC} (Hz)	T_{max} (s)	f_c (Hz)	T_p (s)
77	San Fernando	1971	Pacoima Dam-up left ab	0.01	50	35	0.07	11.4	0.13	1.4
143	Tabas, Iran	1978	Tabas	0.02	25	15	0.10	8.0	0.07	5.1
147	Coyote Lake	1979	Gilroy Array #2	0.005	100	43	0.13	6.2	0.27	1.4
148	Coyote Lake	1979	Gilroy Array #3	0.005	100	40	0.13	6.2	0.27	1.1
149	Coyote Lake	1979	Gilroy Array #4	0.005	100	30	0.12	6.7	0.27	1.1
150	Coyote Lake	1979	Gilroy Array #6	0.005	100	33	0.10	8.0	0.27	1.1
159	Imp. Valley-06	1979	Agrarias	0.01	50	20	0.13	6.2	0.14	1.9
161	Imp. Valley-06	1979	Brawley Airport	0.005	100	40	0.04	18.6	0.14	4.2
170	Imp. Valley-06	1979	EC County Center FF	0.005	100	33	0.06	13.3	0.14	4.1
171	Imp. Valley-06	1979	El Centro-Mel.Geot.Arr.	0.005	100	50	0.08	10.0	0.14	2.8
173	Imp. Valley-06	1979	El Centro Array #10	0.005	100	40	0.06	13.3	0.14	4.2
178	Imp. Valley-06	1979	El Centro Array #3	0.005	100	40	0.05	16.0	0.14	4.0
179	Imp. Valley-06	1979	El Centro Array #4	0.005	100	40	0.05	16.0	0.14	4.5
180	Imp. Valley-06	1979	El Centro Array #5	0.005	100	40	0.04	20.0	0.14	3.8
181	Imp. Valley-06	1979	El Centro Array #6	0.005	100	40	0.05	16.0	0.14	3.7
182	Imp. Valley-06	1979	El Centro Array #7	0.005	100	40	0.06	13.3	0.14	3.5
184	Imp. Valley-06	1979	El Centro Diff. Array	0.005	100	40	0.02	34.8	0.14	5.9
185	Imp. Valley-06	1979	Holtville Post Office	0.005	100	40	0.06	13.3	0.14	4.1
316	Westmorland	1981	Parachute Test Site	0.005	100	33	0.09	8.9	0.24	3.7
451	Morgan Hill	1984	Coy.LakeDam-SW Ab.	0.005	100	45	0.10	8.0	0.19	0.8
459	Morgan Hill	1984	Gilroy Array #6	0.005	100	35	0.13	6.2	0.19	1.0
568	San Salvador	1986	Geotech Investig Center	0.005	100	30	0.10	8.0	0.26	0.7
569	San Salvador	1986	National Geo.Inst	0.005	100	30	0.10	8.0	0.26	0.9
722	Supers.Hills-02	1987	Kornbloom Road (temp)	0.01	50	30	0.20	4.0	0.14	1.8
723	Supers.Hills-02	1987	Parachute Test Site	0.01	50	30	0.12	6.7	0.14	2.0
764	Loma Prieta	1989	Gilroy - Historic Bldg.	0.005	100	40	0.18	4.4	0.10	1.6
766	Loma Prieta	1989	Gilroy Array #2	0.005	100	40	0.06	13.3	0.10	1.5
767	Loma Prieta	1989	Gilroy Array #3	0.005	100	40	0.10	8.0	0.10	2.3
802	Loma Prieta	1989	Saratoga - Aloha Ave	0.005	100	50	0.10	8.0	0.10	4.4
803	Loma Prieta	1989	Saratoga - WValleyColl.	0.005	100	49	0.10	8.0	0.10	5.0
3548	Loma Prieta	1989	Los Gatos - Lex. Dam	0.01	50	30	0.08	10.0	0.10	1.3
828	Cape Mendocino	1992	Petrolia	0.02	25	23	0.07	14.3	0.10	2.8
3744	Cape Mendocino	1992	Bunker Hill FAA	0.005	100	20	0.00		0.10	4.5
3746	Cape Mendocino	1992	Cent. Beach Nav.Fac	0.005	100	30	0.15	5.3	0.10	1.8
879	Landers	1992	Lucerne	0.005	100	60	0.00		0.08	5.3
900	Landers	1992	Yermo Fire Station	0.02	25	23	0.07	14.3	0.08	6.8
982	Northridge-01	1994	Jens. FilterPlant Ad.Bld	0.005	100	30	0.10	5.0	0.13	2.8
983	Northridge-01	1994	Jens.FilterPlantGen.Bld	0.005	100	30	0.10	7.1	0.13	2.8
1004	Northridge-01	1994	LA – Sepul. VA Hosp.	0.005	100	33	0.13	5.5	0.13	0.9
1013	Northridge-01	1994	LA Dam	0.005	100	33	0.12	6.7	0.13	1.5
1044	Northridge-01	1994	Newhall - Fire Sta	0.02	25	23	0.12	8.3	0.13	1.2
1045	Northridge-01	1994	Newhall -WPicoCan.Rd.	0.01	50	30	0.10	8.0	0.13	2.5
1050	Northridge-01	1994	Pacoima Dam (downstr)	0.02	25	23	0.16	6.3	0.13	0.5
1051	Northridge-01	1994	Pacoima Dam (up. left)	0.02	25	23	0.16	6.3	0.13	0.9
1052	Northridge-01	1994	Pacoima Kagel Canyon	0.02	25	23	0.14	7.1	0.13	0.8
1054	Northridge-01	1994	Pardee - SCE	0.005	100	20	0.40	2.0	0.13	1.1
1063	Northridge-01	1994	Rinaldi Receiving Sta	0.01	50	30	0.08	10.0	0.13	1.2
1084	Northridge-01	1994	Sylmar - Converter Sta	0.005	100	40	0.23	4.3	0.13	2.8

NGA#	EQ Name	Year	Station Name	Δt_0 (s)	f_{N0} (Hz)	f_{HC} (Hz)	f_{LC} (Hz)	T_{max} (s)	f_c (Hz)	T_p (s)
1085	Northridge-01	1994	Sylm. - Converter Sta E	0.005	100	30	0.23	4.3	0.13	2.9
1086	Northridge-01	1994	Sylm.- OliveViewMedFF	0.02	25	23	0.12	8.3	0.13	2.0
1106	Kobe, Japan	1995	KJMA	0.02	25	0	0.05	16.0	0.11	0.8
1114	Kobe, Japan	1995	Port Island (0 m)	0.01	50	0	0.10	8.0	0.11	2.5
1119	Kobe, Japan	1995	Takarazuka	0.01	50	40	0.13	6.2	0.11	1.5
1120	Kobe, Japan	1995	Takatori	0.01	50	0	0.10	8.0	0.11	1.7
3763	Kobe, Japan	1995	Port Island (83 m)	0.01	50	0	0.10	8.0	0.11	2.4
1148	Kocaeli, Turkey	1999	Arcelik	0.005	100	50	0.07	11.4	0.07	6.6
1161	Kocaeli, Turkey	1999	Gebze	0.005	100	30	0.08	10.0	0.07	5.6
1165	Kocaeli, Turkey	1999	Izmit	0.005	100	30	0.10	8.0	0.07	4.6
1176	Kocaeli, Turkey	1999	Yarimca	0.005	100	50	0.07	11.4	0.07	4.5
1193	Chi-Chi, Taiwan	1999	CHY024	0.005	100	50	0.02	40.0	0.06	5.3
1244	Chi-Chi, Taiwan	1999	CHY101	0.005	100	50	0.04	20.0	0.06	4.8
1403	Chi-Chi, Taiwan	1999	NSY	0.005	100	30	0.06	13.3	0.06	7.3
1462	Chi-Chi, Taiwan	1999	TCU	0.005	100	10	0.04	20.0	0.06	4.5
1476	Chi-Chi, Taiwan	1999	TCU029	0.005	100	50	0.04	20.0	0.06	4.7
1477	Chi-Chi, Taiwan	1999	TCU031	0.005	100	30	0.02	40.0	0.06	5.1
1480	Chi-Chi, Taiwan	1999	TCU036	0.005	100	40	0.02	40.0	0.06	4.8
1481	Chi-Chi, Taiwan	1999	TCU038	0.005	100	50	0.05	16.0	0.06	8.3
1482	Chi-Chi, Taiwan	1999	TCU039	0.005	100	50	0.02	40.0	0.06	7.8
1483	Chi-Chi, Taiwan	1999	TCU040	0.005	100	50	0.03	26.7	0.06	6.0
1485	Chi-Chi, Taiwan	1999	TCU045	0.005	100	50	0.04	20.0	0.06	7.9
1486	Chi-Chi, Taiwan	1999	TCU046	0.005	100	30	0.06	13.3	0.06	7.4
1489	Chi-Chi, Taiwan	1999	TCU049	0.005	100	50	0.02	40.0	0.06	9.6
1491	Chi-Chi, Taiwan	1999	TCU051	0.005	100	50	0.03	26.7	0.06	10.1
1492	Chi-Chi, Taiwan	1999	TCU052	0.005	100	50	0.04	20.0	0.06	10.4
1493	Chi-Chi, Taiwan	1999	TCU053	0.005	100	50	0.03	26.7	0.06	10.4
1496	Chi-Chi, Taiwan	1999	TCU056	0.005	100	50	0.04	20.0	0.06	8.9
1498	Chi-Chi, Taiwan	1999	TCU059	0.005	100	30	0.03	26.7	0.06	6.8
1501	Chi-Chi, Taiwan	1999	TCU063	0.005	100	50	0.03	26.7	0.06	5.6
1502	Chi-Chi, Taiwan	1999	TCU064	0.005	100	50	0.03	26.7	0.06	6.9
1503	Chi-Chi, Taiwan	1999	TCU065	0.005	100	50	0.06	13.3	0.06	5.0
1505	Chi-Chi, Taiwan	1999	TCU068	0.005	100	50	0.03	26.7	0.06	10.3
1510	Chi-Chi, Taiwan	1999	TCU075	0.005	100	50	0.04	20.0	0.06	5.1
1511	Chi-Chi, Taiwan	1999	TCU076	0.005	100	50	0.10	8.0	0.06	4.1
1515	Chi-Chi, Taiwan	1999	TCU082	0.005	100	50	0.04	20.0	0.06	8.4
1519	Chi-Chi, Taiwan	1999	TCU087	0.005	100	30	0.05	16.0	0.06	8.8
1528	Chi-Chi, Taiwan	1999	TCU101	0.005	100	50	0.04	20.0	0.06	8.5
1529	Chi-Chi, Taiwan	1999	TCU102	0.005	100	50	0.05	16.0	0.06	8.0
1530	Chi-Chi, Taiwan	1999	TCU103	0.005	100	50	0.05	16.0	0.06	7.2
1531	Chi-Chi, Taiwan	1999	TCU104	0.005	100	50	0.03	26.7	0.06	6.7
1548	Chi-Chi, Taiwan	1999	TCU128	0.005	100	30	0.05	16.0	0.06	8.0
1595	Chi-Chi, Taiwan	1999	WGK	0.005	100	50	0.07	11.4	0.06	4.7
1602	Duzce, Turkey	1999	Bolu	0.01	50	0	0.05	16.0	0.09	0.9
2114	Denali, Alaska	2002	TAPS Pump Station #10	0.005	100	40	0.10	7.7	0.05	2.8
3965	Tottori, Japan	2000	TTR008	0.01	50	30	0.01	66.7	0.13	1.2
4040	Bam, Iran	2003	Bam	0.005	100	80	0.05	16.0	0.14	1.7
4065	Parkfield-02, CA	2004	PARKFIELD - EADES	0.005	100	50	0.10	8.0	0.22	1.0
4097	Parkfield-02, CA	2004	Slack Canyon	0.005	100	30	0.10	8.0	0.22	0.7
4098	Parkfield-02, CA	2004	Parkfield - Cholame 1E	0.005	100	30	0.13	6.2	0.22	1.3

GA#	EQ Name	Year	Station Name	Δt_0 (s)	f_{N0} (Hz)	f_{HC} (Hz)	f_{LC} (Hz)	T_{max} (s)	f_c (Hz)	T_p (s)
4100	Parkfield-02, CA	2004	Parkf. - Cholame 2WA	0.005	100	30	0.30	2.7	0.22	1.0
4101	Parkfield-02, CA	2004	Parkfield - Cholame 3E	0.005	100	40	0.33	2.4	0.22	0.5
4102	Parkfield-02, CA	2004	Parkfield - Cholame 3W	0.005	100	33	0.20	4.0	0.22	1.0
4103	Parkfield-02, CA	2004	Parkfield - Cholame 4W	0.005	100	33	0.12	6.7	0.22	0.7
4107	Parkfield-02, CA	2004	Parkfield - Fault Zone 1	0.005	100	30	0.15	5.3	0.22	1.1
4113	Parkfield-02, CA	2004	Parkfield - Fault Zone 9	0.005	100	40	0.10	8.0	0.22	1.2
4115	Parkfield-02, CA	2004	Parkf. - Fault Zone 12	0.005	100	33	0.09	8.9	0.22	1.1
4126	Parkfield-02, CA	2004	Parkf. - Stone Corral 1E	0.005	100	30	0.30	2.7	0.22	0.6
4211	Niigata, Japan	2004	NIG021	0.01	50	30	0.07	11.4	0.13	0.3
4228	Niigata, Japan	2004	NIGH11	0.005	100	30	0.04	20.0	0.13	1.8
4451	Montenegro,Yugo	1979	Bar-Skupstina Opstine	0.01	50	30	0.20	4.0	0.09	1.3
4458	Montenegro,Yugo	1979	Ulcinj - Hotel Olimpic	0.01	50	30	0.13	6.2	0.09	1.6
4716	Wenchuan,China	2008	Deyangbaima	0.005	100	50	0.06	13.3	0.05	7.1
4816	Wenchuan,China	2008	Mianzuqingping	0.005	100	0	0.04	20.0	0.05	7.8
4847	Chuetsu-oki	2007	Joetsu Kakizakiku Ka.	0.01	50	50	0.07	11.4	0.12	1.5
8161	El Mayor-Cuc.	2010	El Centro Array #12	0.005	100	80	0.04	20.0	0.08	7.0
8606	El Mayor-Cuc.	2010	Westside Elem. School	0.01	50	36	0.04	20.0	0.08	5.7
6887	Darfield, NZ	2010	Christchurch Bot. Gardens	0.005	100	70	0.04	20.0	0.10	9.0
6897	Darfield, NZ	2010	DSLC	0.005	100	30	0.06	13.3	0.10	6.7
6906	Darfield, NZ	2010	GDLC	0.005	100	60	0.05	16.0	0.10	6.3
6911	Darfield, NZ	2010	HORC	0.005	100	60	0.10	8.0	0.10	7.4
6927	Darfield, NZ	2010	LINC	0.005	100	60	0.06	13.3	0.10	6.4
6928	Darfield, NZ	2010	LPCC	0.005	100	70	0.10	8.0	0.10	8.3
6942	Darfield, NZ	2010	NNBS North New Br.Sch.	0.005	100	60	0.04	20.0	0.10	6.5
6959	Darfield, NZ	2010	Christchurch Resthaven	0.005	100	50	0.05	16.0	0.10	8.4
6960	Darfield, NZ	2010	Riccarton High School	0.005	100	24	0.04	20.0	0.10	7.8
6962	Darfield, NZ	2010	ROLC	0.005	100	60	0.13	6.2	0.10	6.4
6966	Darfield, NZ	2010	Shirley Library	0.005	100	40	0.04	20.0	0.10	8.1
6969	Darfield, NZ	2010	Styx Mill Transf. Station	0.005	100	40	0.04	20.0	0.10	7.4
6975	Darfield, NZ	2010	TPLC	0.005	100	60	0.05	16.0	0.10	6.9
8119	Christchurch, NZ	2011	Pages Rd. Pumping St.	0.005	100	80	0.08	10.0	0.19	4.0
8123	Christchurch, NZ	2011	Christchurch Resthaven	0.005	100	40	0.08	10.0	0.19	1.4

Table A. 2 Earthquake source and site characteristics for records in the pulselike database.

NGA#	F	**M**	Z_{TOR} (km)	R_{RUP} (km)	V_{s30} (m/s)	$s_{or}d$ (km)	$\theta_{or}\phi$ (°)
77	1	6.6	0.0	1.8	2016	21.9	7.5
143	1	7.4	1.0	2.1	767	53.9	12.6
147	0	5.7	3.1	9.0	271	5.0	38.7
148	0	5.7	3.1	7.4	350	5.0	32.2
149	0	5.7	3.1	5.7	222	5.0	24.5
150	0	5.7	3.1	3.1	663	5.0	0.9
159	0	6.5	0.0	0.7	242	10.0	3.8
161	0	6.5	0.0	10.4	209	38.1	10.5
170	0	6.5	0.0	7.3	192	27.6	18.2
171	0	6.5	0.0	0.1	265	19.4	5.4
173	0	6.5	0.0	8.6	203	26.9	21.1
178	0	6.5	0.0	12.9	163	26.3	23.2
179	0	6.5	0.0	7.1	209	26.6	11.5
180	0	6.5	0.0	4.0	206	27.7	4.7
181	0	6.5	0.0	1.4	203	27.5	0.8
182	0	6.5	0.0	0.6	211	27.5	4.8
184	0	6.5	0.0	5.1	202	26.4	14.6
185	0	6.5	0.0	7.5	203	18.9	17.2
316	0	5.9	2.0	16.7	349	6.0	42.3
451	0	6.2	0.5	0.5	561	24.6	0.4
459	0	6.2	0.5	9.9	663	26.5	1.0
568	0	5.8	5.9	6.3	489	6.0	12.1
569	0	5.8	5.9	7.0	456	6.0	12.8
722	0	6.5	0.0	18.5	266	9.0	64.0
723	0	6.5	0.0	1.0	349	16.0	3.4
764	1	6.9	3.9	11.0	309	20.0	30.9
766	1	6.9	3.9	11.1	271	20.0	25.4
767	1	6.9	3.9	12.8	350	20.0	27.1
802	1	6.9	3.9	8.5	381	20.0	23.2
803	1	6.9	3.9	9.3	348	20.0	27.6
3548	1	6.9	3.9	5.0	1070	18.6	23.9
828	1	7.0	5.2	8.2	422	6.7	50.7
3744	1	7.0	5.2	12.2	566	11.1	5.3
3746	1	7.0	5.2	18.3	459	11.1	10.3
879	0	7.3	0.0	2.2	1369	47.5	20.2
900	0	7.3	0.0	23.6	354	65.8	17.2
982	1	6.7	5.0	5.4	373	19.4	13.7
983	1	6.7	5.0	5.4	526	19.4	13.7
1004	1	6.7	5.0	8.4	380	17.3	26.0
1013	1	6.7	5.0	5.9	629	19.4	16.0
1044	1	6.7	5.0	5.9	269	19.4	4.0
1045	1	6.7	5.0	5.5	286	19.4	11.0
1050	1	6.7	5.0	7.0	2016	19.4	1.5
1051	1	6.7	5.0	7.0	2016	19.4	1.5
1052	1	6.7	5.0	7.3	508	19.4	5.4
1054	1	6.7	5.0	7.5	326	19.4	0.8
1063	1	6.7	5.0	6.5	282	19.4	18.3
1084	1	6.7	5.0	5.4	251	19.4	13.3

NGA#	F	**M**	Z_{TOR} (km)	R_{RUP} (km)	V_{s30} (m/s)	$s_{or}d$ (km)	$\theta_{or}\phi$ (˚)
1085	1	6.7	5.0	5.2	371	19.4	12.2
1086	1	6.7	5.0	5.3	441	19.4	6.3
1106	0	6.9	0.2	1.0	312	18.1	7.8
1114	0	6.9	0.2	3.3	198	18.6	14.6
1119	0	6.9	0.2	0.3	312	38.6	2.0
1120	0	6.9	0.2	1.5	256	17.4	13.5
3763	0	6.9	0.2	3.3	198	18.6	14.6
1148	0	7.5	0.0	13.5	523	47.4	19.9
1161	0	7.5	0.0	10.9	792	46.5	23.9
1165	0	7.5	0.0	7.2	811	15.0	6.8
1176	0	7.5	0.0	4.8	297	18.8	13.9
1193	1	7.6	0.0	9.6	428	17.2	67.4
1244	1	7.6	0.0	9.9	259	33.6	58.7
1403	1	7.6	0.0	13.1	600	56.0	34.6
1462	1	7.6	0.0	5.2	473	29.3	42.8
1476	1	7.6	0.0	28.0	407	56.0	30.9
1477	1	7.6	0.0	30.2	489	56.0	34.4
1480	1	7.6	0.0	19.8	478	45.3	39.1
1481	1	7.6	0.0	25.4	298	45.3	39.8
1482	1	7.6	0.0	19.9	541	56.0	29.8
1483	1	7.6	0.0	22.1	362	45.3	43.3
1485	1	7.6	0.0	26.0	705	56.0	30.0
1486	1	7.6	0.0	16.7	466	56.0	24.4
1489	1	7.6	0.0	3.8	487	32.9	42.7
1491	1	7.6	0.0	7.6	350	30.8	43.7
1492	1	7.6	0.0	0.7	579	35.6	35.9
1493	1	7.6	0.0	6.0	455	34.6	43.0
1496	1	7.6	0.0	10.5	403	30.6	47.1
1498	1	7.6	0.0	17.1	273	39.2	41.9
1501	1	7.6	0.0	9.8	476	15.8	52.4
1502	1	7.6	0.0	16.6	646	44.1	46.1
1503	1	7.6	0.0	0.6	306	15.6	44.9
1505	1	7.6	0.0	0.3	487	45.7	34.5
1510	1	7.6	0.0	0.9	573	12.5	4.1
1511	1	7.6	0.0	2.7	615	10.7	0.1
1515	1	7.6	0.0	5.2	473	29.3	42.8
1519	1	7.6	0.0	7.0	539	56.0	37.2
1528	1	7.6	0.0	2.1	389	39.2	36.9
1529	1	7.6	0.0	1.5	714	40.4	34.9
1530	1	7.6	0.0	6.1	494	45.3	40.0
1531	1	7.6	0.0	12.9	410	39.2	42.8
1548	1	7.6	0.0	13.1	600	56.0	34.6
1595	1	7.6	0.0	9.9	259	33.6	58.7
1602	0	7.1	0.0	12.0	294	29.3	14.4
2114	0	7.9	0.0	2.7	329	60.7	3.8
3965	0	6.6	0.5	6.9	139	15.0	24.5
4040	0	6.6	1.4	1.7	487	12.6	2.7
4065	0	6.0	2.5	2.9	384	9.8	8.5
4097	0	6.0	2.5	3.0	648	30.0	1.0
4098	0	6.0	2.5	3.0	327	10.0	5.0

NGA#	F	**M**	Z_{TOR} (km)	R_{RUP} (km)	V_{s30} (m/s)	$s_{or}d$ (km)	$\theta_{or}\phi$ (˚)
4100	0	6.0	2.5	3.0	173	10.0	3.1
4101	0	6.0	2.5	5.6	397	10.0	24.9
4102	0	6.0	2.5	3.6	231	10.0	7.2
4103	0	6.0	2.5	4.2	410	10.0	12.4
4107	0	6.0	2.5	2.5	178	8.4	0.4
4113	0	6.0	2.5	2.9	372	9.9	7.3
4115	0	6.0	2.5	2.7	265	11.0	5.1
4126	0	6.0	2.5	3.8	261	6.5	24.3
4211	1	6.6	4.0	11.3	419	11.0	9.7
4228	1	6.6	4.0	8.9	375	11.0	3.9
4451	1	7.1	3.6	7.0	462	10.9	4.2
4458	1	7.1	3.6	5.8	319	12.2	18.9
4716	1	7.9	0.0	30.5	418	101.5	23.8
4816	1	7.9	0.0	6.6	551	89.7	1.8
4847	1	6.8	3.1	11.9	383	26.0	0.1
8161	0	7.2	0.5	11.3	197	51.0	24.8
8606	0	7.2	0.5	11.4	242	51.0	15.0
6887	0	7.0	0.0	18.1	187	29.0	6.4
6897	0	7.0	0.0	8.5	296	11.4	31.7
6906	0	7.0	0.0	1.2	344	11.0	6.2
6911	0	7.0	0.0	7.3	326	11.0	31.1
6927	0	7.0	0.0	7.1	263	29.0	6.9
6928	0	7.0	0.0	25.7	650	29.0	4.0
6942	0	7.0	0.0	26.8	211	29.0	8.5
6959	0	7.0	0.0	19.5	141	29.0	7.1
6960	0	7.0	0.0	13.6	293	29.0	6.8
6962	0	7.0	0.0	1.5	296	26.9	0.1
6966	0	7.0	0.0	22.3	207	29.0	8.7
6969	0	7.0	0.0	20.9	248	29.0	14.7
6975	0	7.0	0.0	6.1	249	29.0	6.6
8119	1	6.2	0.5	2.0	206	6.0	12.3
8123	1	6.2	0.5	5.1	141	6.0	27.8

Table A. 3 Identified parameters for velocity pulse of pulselike records.

NGA#	V_p (cm/s)	T_p (s)	γ	ν/π (rad)	$t_{max,p}{}^{\star}$ (s)	α_P (°)
77	89.4	1.4	2.4	0.1	2.6	84
143	108.0	5.1	2.4	1.1	11.5	30
147	18.2	1.4	2.1	1.6	2.9	17
148	24.0	1.1	2.1	0.7	2.7	18
149	21.2	1.1	2.5	0.3	2.1	14
150	34.4	1.1	2.1	1.8	2.1	90
159	37.9	1.9	2.4	1.2	7.0	90
161	24.2	4.2	2.2	0.6	6.7	83
170	45.6	4.1	2.1	1.8	5.4	68
171	80.3	2.8	2.4	1.0	3.7	84
173	38.2	4.2	2.0	1.7	6.3	64
178	34.1	4.0	2.1	1.9	6.4	57
179	65.8	4.5	2.1	0.7	5.5	86
180	78.9	3.8	2.1	0.7	5.0	85
181	98.9	3.7	2.1	1.6	5.1	72
182	71.7	3.5	2.5	1.3	4.9	87
184	35.0	5.9	2.2	0.6	5.1	70
185	49.3	4.1	2.3	1.1	5.5	60
316	32.8	3.7	2.3	0.1	8.9	40
451	67.9	0.8	2.6	1.3	3.3	34
459	34.4	1.0	2.4	1.2	5.5	70
568	62.7	0.7	2.1	1.9	1.3	89
569	65.8	0.9	2.5	1.4	1.8	19
722	24.9	1.8	2.4	1.2	5.2	14
723	97.2	2.0	2.4	1.1	12.0	65
764	33.7	1.6	2.1	0.7	3.0	19
766	47.9	1.5	2.3	0.9	3.3	62
767	31.3	2.3	2.2	1.7	4.2	31
802	32.6	4.4	2.1	0.7	5.0	58
803	40.9	5.0	2.2	1.8	4.7	28
3548	81.3	1.3	2.4	1.3	3.3	79
828	44.4	2.8	2.1	1.7	2.5	63
3744	42.8	4.5	2.3	2.0	4.5	75
3746	55.5	1.8	2.1	0.7	5.5	55
879	75.8	5.3	2.2	0.5	9.7	59
900	38.8	6.8	2.1	0.9	16.9	77
982	81.7	2.8	2.2	1.8	3.8	73
983	64.3	2.8	2.5	1.3	3.4	88
1004	77.1	0.9	2.1	0.7	2.4	31
1013	53.2	1.5	2.0	0.7	2.1	89
1044	71.8	1.2	2.4	0.2	4.5	79
1045	74.9	2.5	2.4	1.2	4.7	88
1050	35.0	0.5	2.5	0.3	3.4	83
1051	80.7	0.9	2.2	1.5	3.8	81
1052	45.2	0.8	2.2	1.4	3.4	89
1054	85.3	1.1	2.3	1.9	5.9	-
1063	118.6	1.2	2.2	0.6	2.3	87
1084	77.7	2.8	2.2	1.7	3.8	59

NGA#	V_p (cm/s)	T_p (s)	γ	ν/π (rad)	$t_{max,p}{}^*$ (s)	α_P (°)
1085	57.2	2.9	2.4	1.1	3.2	85
1086	73.3	2.0	2.4	1.2	3.6	78
1106	91.7	0.8	2.7	1.4	3.2	88
1114	80.4	2.5	2.2	1.0	5.6	78
1119	62.2	1.5	2.5	0.0	4.3	71
1120	139.5	1.7	2.2	1.5	4.8	88
3763	45.0	2.4	2.1	0.7	4.4	65
1148	29.9	6.6	2.3	1.1	13.9	14
1161	41.9	5.6	2.0	0.8	5.6	61
1165	20.2	4.6	2.4	0.8	3.2	5
1176	74.9	4.5	2.1	1.7	7.8	64
1193	44.2	5.3	2.6	0.2	14.4	33
1244	96.6	4.8	2.1	1.9	17.7	13
1403	41.0	7.3	2.5	0.3	24.6	53
1462	38.4	4.5	2.2	1.6	14.8	40
1476	67.2	4.7	2.2	0.9	30.8	61
1477	60.0	5.1	2.3	1.0	30.4	87
1480	66.8	4.8	2.2	2.0	24.8	56
1481	39.5	8.3	2.3	0.0	24.4	62
1482	56.5	7.8	2.4	0.1	25.6	58
1483	48.6	6.0	2.0	0.8	22.2	25
1485	28.1	7.9	2.4	1.1	23.2	39
1486	34.3	7.4	2.1	1.8	25.3	76
1489	35.3	9.6	2.1	0.7	14.9	68
1491	29.8	10.1	2.1	0.5	14.7	86
1492	131.0	10.4	2.3	1.1	13.9	46
1493	25.1	10.4	2.5	0.5	13.9	75
1496	27.2	8.9	2.2	0.6	14.0	63
1498	58.2	6.8	2.3	2.0	23.8	38
1501	61.1	5.6	2.3	1.8	20.9	43
1502	65.5	6.9	2.5	0.2	24.0	28
1503	112.7	5.0	2.2	0.9	10.0	66
1505	202.6	10.3	2.4	1.2	28.9	45
1510	67.4	5.1	2.2	0.5	8.0	69
1511	41.6	4.1	2.3	0.1	6.3	56
1515	38.0	8.4	2.2	0.5	12.8	69
1519	35.7	8.8	2.4	1.1	19.4	55
1528	46.3	8.5	2.3	0.9	15.1	62
1529	54.6	8.0	2.3	0.9	16.0	68
1530	53.4	7.2	2.4	1.2	17.5	68
1531	49.9	6.7	2.1	1.7	22.8	26
1548	62.9	8.0	2.2	1.8	23.7	48
1595	78.6	4.7	2.4	1.2	17.9	25
1602	60.3	0.9	2.2	1.5	5.5	10
2114	79.1	2.8	2.2	0.8	16.9	13
3965	51.6	1.2	2.5	0.4	7.5	54
4040	87.3	1.7	2.3	1.0	2.4	78
4065	31.3	1.0	2.4	1.2	2.3	80
4097	48.1	0.7	2.3	2.0	3.5	39
4098	35.0	1.3	2.1	0.6	2.7	83

NGA#	V_p (cm/s)	T_p (s)	γ	ν/π (rad)	$t_{max,p}{}^{\star}$ (s)	α_P (°)
4100	49.7	1.0	2.1	0.7	2.8	74
4101	29.0	0.5	2.2	0.8	2.5	75
4102	32.4	1.0	2.1	0.6	2.7	66
4103	30.1	0.7	2.1	0.5	2.6	82
4107	63.4	1.1	2.1	0.8	2.8	52
4113	25.7	1.2	2.2	1.6	2.5	78
4115	55.4	1.1	2.1	1.8	2.5	88
4126	36.9	0.6	2.1	0.7	1.9	85
4211	65.1	0.3	2.0	1.8	5.4	8
4228	31.3	1.8	2.0	1.7	5.1	11
4451	73.1	1.3	2.1	2.0	8.3	9
4458	50.6	1.6	2.4	1.1	2.6	1
4716	32.3	7.1	2.2	1.6	25.7	37
4816	68.0	7.8	2.3	0.2	11.6	67
4847	56.5	1.5	2.2	1.5	7.3	52
8161	66.7	7.0	2.5	1.3	27.5	48
8606	63.8	5.7	2.5	1.3	25.7	0
6887	25.5	9.0	3.1	0.6	16.5	81
6897	65.3	6.7	2.3	2.0	18.8	41
6906	75.1	6.3	2.2	1.6	12.6	30
6911	43.5	7.4	2.4	1.9	14.1	69
6927	64.1	6.4	2.2	0.8	17.1	86
6928	13.1	8.3	2.6	1.4	17.1	87
6942	31.5	6.5	2.4	1.2	17.0	69
6959	26.4	8.4	3.2	0.6	17.7	77
6960	43.2	7.8	2.4	0.8	16.9	90
6962	81.3	6.4	2.2	1.8	16.6	66
6966	37.1	8.1	2.1	0.6	17.0	72
6969	48.5	7.4	2.5	1.1	20.2	68
6975	77.0	6.9	2.7	1.3	22.1	89
8119	61.2	4.0	2.4	0.2	4.1	76
8123	93.9	1.4	2.1	0.8	6.1	12

Table A. 4 Identified parameters for residual motion of pulselike records.

NGA#	$I_{a,res}$ (cm/s)	$D_{5-95,res}$ (s)	$D_{0-5,res}$ (s)	$D_{0-30,res}$ (s)	$\omega_{mid,res}/\pi$ (rad/s)	ω'_{res}/π (rad/s^2)	$\zeta_{f,res}$
77	929	6.8	2.5	5.7	11.9	0.34	0.54
143	1249	17.2	4.5	9.6	9.6	0.00	0.09
147	43	5.0	2.3	2.8	7.9	-0.37	0.19
148	32	8.7	2.0	2.6	10.8	-0.58	0.11
149	37	11.8	1.7	2.3	7.8	-0.36	0.04
150	52	5.8	1.4	2.3	7.1	0.13	0.06
159	85	13.0	2.1	5.1	18.8	-0.80	0.36
161	26	15.7	4.5	5.4	13.8	-0.45	0.19
170	51	15.6	3.7	6.1	8.3	-0.31	0.16
171	77	8.6	2.6	3.8	3.1	0.21	0.27
173	45	14.3	5.1	7.8	8.5	-0.18	0.19
178	72	14.9	4.1	4.8	11.2	-0.31	0.11
179	66	12.5	3.2	4.7	10.7	-0.38	0.32
180	122	11.3	2.2	4.0	11.1	-0.51	0.20
181	113	11.5	1.0	3.6	11.2	-0.52	0.12
182	121	7.0	3.2	3.6	6.4	-0.03	0.46
184	167	7.4	3.9	5.7	12.5	-0.39	0.02
185	73	13.5	2.9	3.9	8.8	-0.17	0.19
316	60	16.4	5.8	7.9	6.7	-0.15	0.05
451	204	6.4	1.4	3.3	9.1	-0.89	0.13
459	59	8.7	0.8	1.4	7.0	-0.35	0.04
568	153	4.6	1.1	1.4	8.5	-1.38	0.13
569	80	7.2	1.3	2.2	4.0	-0.15	0.23
722	30	13.7	3.3	6.5	7.9	-0.08	0.28
723	234	11.5	5.2	9.3	7.0	-0.26	0.09
764	51	11.2	2.5	3.3	7.1	0.03	0.22
766	108	11.1	2.4	3.7	5.9	0.19	0.16
767	121	12.5	2.9	4.4	10.7	-0.18	0.13
802	113	8.4	3.5	5.7	9.3	-0.03	0.21
803	104	11.8	3.9	5.0	6.5	-0.09	0.17
3548	122	5.1	2.1	3.1	3.5	0.47	0.15
828	379	15.4	2.3	2.8	8.5	-0.02	0.23
3744	57	12.2	3.3	4.7	3.5	0.06	0.07
3746	80	12.3	4.0	5.4	8.4	0.01	0.09
879	650	13.4	6.9	10.2	30.1	0.10	0.24
900	94	17.2	11.9	15.1	8.5	-0.09	0.09
982	194	15.9	2.4	3.3	4.3	-0.16	0.10
983	210	8.6	2.4	5.1	7.7	-0.23	0.10
1004	286	10.0	2.3	4.1	8.2	-0.13	0.19
1013	133	7.2	1.7	2.4	8.6	-0.07	0.17
1044	521	5.8	3.4	4.6	4.8	-0.03	0.07
1045	85	11.5	2.8	4.6	3.7	-0.16	0.16
1050	48	5.0	3.1	3.8	15.2	-1.48	0.20
1051	832	6.3	3.4	4.3	9.2	-0.36	0.09
1052	144	10.3	3.2	4.4	6.6	-0.10	0.06
1054	132	10.5	3.3	4.7	6.4	0.42	0.80
1063	471	9.0	1.7	3.2	7.6	0.17	0.13
1084	486	16.3	2.5	3.2	5.5	-0.14	0.28

NGA#	$I_{a,res}$ (cm/s)	$D_{5-95,res}$ (s)	$D_{0-5,res}$ (s)	$D_{0-30,res}$ (s)	$\omega_{mid,res}/\pi$ (rad/s)	ω'_{res}/π (rad/s^2)	$\zeta_{f,res}$
1085	389	7.1	2.7	2.9	6.9	-0.08	0.11
1086	346	6.4	3.1	3.6	5.3	0.08	0.05
1106	610	10.6	3.0	5.5	5.2	-0.08	0.04
1114	176	8.3	3.2	3.8	4.1	-0.15	0.26
1119	288	5.2	2.9	4.1	4.2	0.32	0.05
1120	666	11.5	1.4	2.6	3.7	-0.04	0.18
3763	232	8.8	2.9	3.9	8.8	-0.22	0.29
1148	17	10.4	12.0	14.4	12.1	0.04	0.27
1161	29	8.6	4.6	7.6	6.4	0.25	0.16
1165	79	13.5	2.4	4.9	8.2	-0.08	0.11
1176	83	16.1	5.9	9.9	5.0	-0.10	0.34
1193	160	24.5	7.2	10.6	7.5	-0.01	0.10
1244	250	28.6	7.4	14.2	5.1	-0.02	0.22
1403	47	20.2	13.0	19.7	7.1	-0.20	0.09
1462	78	26.4	6.0	13.5	5.2	-0.08	0.07
1476	59	23.0	14.7	20.9	7.9	-0.23	0.16
1477	35	27.3	13.4	21.7	4.9	-0.17	0.07
1480	65	25.2	14.1	19.5	4.8	-0.13	0.10
1481	78	30.1	12.1	17.4	5.5	-0.12	0.23
1482	87	27.0	13.9	20.6	5.3	-0.18	0.30
1483	44	31.6	11.2	17.7	5.7	-0.12	0.30
1485	113	12.0	16.5	23.9	7.3	0.06	0.47
1486	43	18.7	15.1	19.4	7.0	-0.13	0.06
1489	126	21.8	9.5	14.1	10.2	-0.24	0.27
1491	125	24.5	8.8	15.5	7.4	-0.05	0.12
1492	415	14.4	11.5	12.0	2.8	0.01	0.90
1493	89	22.4	10.7	14.6	8.3	-0.12	0.27
1496	83	26.8	8.8	15.6	6.8	-0.08	0.23
1498	102	36.6	8.3	16.3	4.0	-0.06	0.05
1501	135	35.7	6.6	14.1	4.6	-0.06	0.24
1502	36	34.2	12.2	22.4	3.4	-0.10	0.22
1503	762	27.6	5.4	11.4	2.5	0.01	0.27
1505	270	14.9	24.8	27.8	3.6	0.03	0.58
1510	256	27.8	4.9	11.8	10.6	-0.07	0.16
1511	374	27.7	4.2	7.9	13.2	-0.21	0.36
1515	109	24.3	8.3	13.7	6.1	-0.15	0.38
1519	40	24.3	10.8	14.8	4.5	-0.07	0.07
1528	71	20.3	7.8	12.0	9.4	-0.07	0.20
1529	195	14.3	12.8	14.8	2.6	0.04	0.26
1530	56	24.9	10.0	15.4	5.2	-0.12	0.26
1531	34	29.3	12.9	21.3	7.0	-0.15	0.27
1548	49	20.8	13.1	19.6	6.7	-0.14	0.11
1595	258	26.9	7.5	14.5	4.9	-0.04	0.27
1602	130	14.2	4.4	5.5	9.6	-0.35	0.44
2114	126	28.2	14.3	15.9	4.4	0.14	0.14
3965	110	19.9	4.1	7.7	6.2	-0.04	0.21
4040	681	8.1	2.1	4.8	12.3	0.44	0.36
4065	71	7.4	1.8	1.9	12.1	-0.46	0.20
4097	63	6.1	2.9	5.0	3.8	-0.07	0.08
4098	50	7.8	2.1	2.5	4.6	0.06	0.16

NGA#	$I_{a,res}$ (cm/s)	$D_{5-95,res}$ (s)	$D_{0-5,res}$ (s)	$D_{0-30,res}$ (s)	$\omega_{mid,res}/\pi$ (rad/s)	ω'_{res}/π (rad/s^2)	$\zeta_{f,res}$
4100	79	9.4	2.4	3.2	5.0	0.03	0.14
4101	41	6.3	1.9	2.5	15.6	-0.74	0.13
4102	56	8.3	2.1	2.6	7.5	-0.28	0.07
4103	77	5.2	2.4	2.7	6.4	0.05	0.07
4107	111	9.7	2.1	3.1	6.2	-0.16	0.11
4113	12	9.9	1.7	3.2	7.5	0.25	0.50
4115	70	12.1	1.8	3.7	4.5	-0.06	0.42
4126	119	8.3	1.4	1.9	8.6	-0.09	0.23
4211	661	3.9	5.1	5.7	12.9	-0.13	0.05
4228	198	9.8	4.0	5.5	15.0	-0.36	0.14
4451	244	20.6	6.7	7.8	5.9	-0.02	0.26
4458	103	25.2	3.4	6.5	8.3	-0.01	0.38
4716	70	90.7	18.7	28.4	9.5	0.03	0.09
4816	1098	33.0	8.6	13.6	28.1	0.07	0.49
4847	153	16.7	6.2	7.3	9.4	-0.28	0.25
8161	309	31.5	13.4	19.6	6.2	-0.05	0.24
8606	154	23.5	17.5	20.6	5.7	-0.10	0.18
6887	82	24.7	11.3	16.2	4.5	-0.03	0.31
6897	132	20.2	9.6	14.9	8.5	-0.08	0.14
6906	422	16.0	6.2	8.8	11.4	-0.41	0.79
6911	310	7.9	10.3	11.6	7.9	-0.23	0.53
6927	237	12.4	10.6	15.8	15.5	-0.67	0.22
6928	63	11.4	11.7	17.2	21.1	0.39	0.37
6942	67	27.3	10.9	16.8	7.6	-0.05	0.60
6959	199	26.2	10.1	17.5	4.8	-0.03	0.12
6960	110	25.6	10.7	14.9	5.8	-0.03	0.06
6962	134	11.1	11.4	14.5	9.2	-0.03	0.56
6966	75	25.4	10.5	16.5	5.3	-0.07	0.14
6969	96	38.0	12.1	17.5	6.0	-0.20	0.75
6975	122	25.7	11.6	18.1	11.4	-0.39	0.72
8119	299	3.2	1.8	2.5	9.1	1.92	0.36
8123	141	11.8	2.2	5.2	3.6	-0.13	0.45

Table A. 5 Identified parameters for orthogonal motion of pulselike records.

NGA#	$I_{a,PO}$ (cm/s)	$D_{5-95,PO}$ (s)	$D_{0-5,PO}$ (s)	$D_{0-30,PO}$ (s)	$\omega_{mid,PO}/\pi$ (rad/s)	ω'_{PO}/π (rad/s^2)	$\zeta_{f,PO}$
77	586	6.9	2.2	5.5	14.2	-0.17	0.37
143	1049	16.0	5.1	9.5	9.8	0.10	0.12
147	29	7.5	2.2	2.7	11.2	-0.60	0.10
148	31	10.4	2.1	2.5	11.1	-0.70	0.13
149	62	8.3	1.8	2.2	5.8	-0.16	0.06
150	60	3.4	1.3	1.8	7.1	0.02	0.06
159	66	13.2	2.6	5.2	24.9	-1.08	0.19
161	45	14.3	5.2	5.9	11.7	-0.40	0.21
170	83	9.5	4.4	5.5	5.8	0.07	0.19
171	56	10.7	2.5	2.8	6.3	0.07	0.27
173	74	12.2	4.7	6.5	8.2	-0.16	0.25
178	104	12.6	4.8	6.9	10.0	-0.31	0.09
179	136	6.7	4.3	4.9	10.3	-0.38	0.18
180	170	8.3	2.6	3.8	9.2	-0.35	0.25
181	144	11.4	1.0	3.7	11.3	-0.66	0.16
182	94	6.6	3.4	4.7	6.5	0.09	0.31
184	213	6.5	4.0	4.9	8.9	0.12	0.05
185	85	11.6	3.8	4.8	9.0	-0.11	0.12
316	51	18.6	5.9	7.7	6.4	-0.12	0.08
451	297	3.8	1.2	3.2	9.7	-1.29	0.10
459	35	7.3	0.5	1.0	7.9	-0.28	0.11
568	111	4.3	1.0	1.8	6.0	-0.44	0.09
569	92	6.7	1.2	1.6	6.9	-0.29	0.12
722	21	14.8	3.7	8.7	11.1	-0.56	0.17
723	162	11.2	5.5	9.3	6.2	-0.03	0.08
764	50	13.4	2.3	3.3	5.8	0.07	0.22
766	97	11.2	2.7	3.3	7.1	-0.03	0.12
767	210	6.4	3.5	3.8	7.1	0.00	0.07
802	136	9.4	3.5	5.4	11.7	-0.39	0.11
803	120	11.1	4.2	5.0	6.1	-0.07	0.13
3548	80	4.8	2.8	3.1	6.0	0.37	0.07
828	322	18.0	2.3	3.2	9.6	-0.18	0.15
3744	55	13.4	3.2	3.5	3.8	0.08	0.06
3746	155	10.6	4.3	5.1	8.0	0.02	0.05
879	673	13.7	6.3	10.1	29.3	0.25	0.33
900	60	19.6	11.1	13.9	9.8	-0.11	0.10
982	519	5.9	2.3	3.2	3.5	-0.03	0.08
983	720	5.5	2.6	4.1	5.8	0.27	0.09
1004	697	8.5	2.3	4.3	8.4	-0.07	0.09
1013	127	6.2	2.3	3.4	8.0	-0.11	0.13
1044	366	6.1	3.5	4.1	5.6	0.04	0.04
1045	98	8.8	3.5	4.7	2.7	-0.09	0.09
1050	38	4.5	3.2	3.7	16.8	-1.55	0.20
1051	655	5.1	3.6	4.4	9.6	-0.23	0.10
1052	108	10.7	3.9	6.5	5.1	-0.14	0.05
1054	172	8.0	3.6	5.9	7.4	0.69	0.63
1063	350	9.7	1.5	3.0	10.8	-0.05	0.11
1084	583	6.7	2.2	4.9	4.6	-0.09	0.38

NGA#	$I_{a,PO}$ (cm/s)	$D_{5-95,PO}$ (s)	$D_{0-5,PO}$ (s)	$D_{0-30,PO}$ (s)	$\omega_{mid,PO}/\pi$ (rad/s)	ω'_{PO}/π (rad/s^2)	$\zeta_{f,PO}$
1085	295	6.9	2.6	4.6	8.3	-0.10	0.10
1086	327	6.5	3.2	3.7	4.8	0.12	0.08
1106	449	8.0	3.2	4.4	5.4	0.08	0.07
1114	42	16.1	2.8	4.1	6.6	-0.39	0.21
1119	323	4.5	3.2	3.9	2.6	0.26	0.08
1120	631	11.9	1.4	2.5	4.7	-0.17	0.10
3763	146	11.1	3.1	5.6	8.6	-0.27	0.18
1148	30	11.0	9.7	14.3	13.8	-0.06	0.15
1161	49	7.1	5.4	6.9	7.2	0.21	0.07
1165	56	15.1	2.4	4.9	8.6	-0.05	0.12
1176	142	14.8	6.5	8.8	4.4	-0.05	0.53
1193	132	27.8	7.1	12.0	5.8	0.00	0.13
1244	234	30.3	5.7	12.6	6.0	-0.07	0.18
1403	47	20.6	12.6	16.7	6.4	-0.15	0.09
1462	152	23.9	5.6	12.4	4.9	-0.06	0.06
1476	53	26.1	14.4	20.8	7.7	-0.24	0.19
1477	45	33.6	13.2	21.5	4.5	-0.15	0.13
1480	60	28.8	11.5	18.7	5.2	-0.09	0.07
1481	96	25.2	12.5	17.4	5.2	-0.09	0.09
1482	82	23.6	13.8	18.9	7.1	-0.15	0.24
1483	63	24.8	13.2	20.9	6.3	-0.10	0.24
1485	141	10.0	18.1	24.0	11.1	-0.19	0.61
1486	31	18.5	15.4	19.4	6.8	-0.10	0.08
1489	142	22.2	8.2	13.2	9.0	-0.03	0.18
1491	114	29.0	7.4	14.6	8.2	-0.08	0.11
1492	117	22.5	8.4	13.1	3.4	0.01	0.67
1493	64	27.6	6.5	13.6	6.6	-0.10	0.24
1496	87	32.0	7.4	18.4	5.8	-0.10	0.30
1498	185	28.6	10.5	18.9	4.0	-0.05	0.03
1501	103	31.2	9.2	16.3	6.4	-0.10	0.17
1502	47	25.3	11.9	20.2	4.2	-0.10	0.17
1503	659	29.1	5.0	8.9	3.5	-0.02	0.10
1505	254	12.4	26.8	27.5	4.1	-0.06	0.50
1510	138	30.2	5.0	10.1	10.3	-0.07	0.25
1511	330	29.2	5.2	9.4	11.4	-0.11	0.33
1515	135	26.4	5.9	12.8	6.2	-0.13	0.27
1519	52	24.1	11.4	16.4	3.3	-0.02	0.11
1528	120	18.9	8.6	11.7	8.1	-0.11	0.19
1529	167	20.4	10.1	16.2	3.0	0.03	0.54
1530	62	24.6	9.9	15.5	5.3	-0.15	0.27
1531	45	27.9	10.7	20.3	6.4	-0.15	0.23
1548	84	20.7	13.2	17.9	4.6	-0.14	0.12
1595	230	28.0	5.7	12.2	6.9	-0.14	0.17
1602	368	8.6	4.1	5.3	5.0	0.09	0.27
2114	103	30.0	14.5	16.6	5.6	0.08	0.14
3965	168	15.9	3.9	7.4	6.2	-0.04	0.27
4040	481	9.7	1.9	4.1	12.9	0.26	0.22
4065	40	10.8	1.9	3.2	11.7	-0.53	0.08
4097	63	6.4	2.4	3.6	3.9	-0.11	0.07
4098	43	8.2	2.3	2.6	6.9	-0.22	0.08

NGA#	$I_{a,PO}$ (cm/s)	$D_{5-95,PO}$ (s)	$D_{0-5,PO}$ (s)	$D_{0-30,PO}$ (s)	$\omega_{mid,PO}/\pi$ (rad/s)	ω'_{PO}/π (rad/s^2)	$\zeta_{f,PO}$
4100	116	7.5	2.5	2.8	4.1	0.17	0.12
4101	108	3.6	1.3	2.5	20.4	-1.13	0.05
4102	43	8.3	1.9	2.6	12.2	-0.82	0.07
4103	60	6.4	2.5	2.6	7.7	-0.09	0.11
4107	217	9.2	2.4	3.2	3.6	-0.15	0.18
4113	11	11.4	1.8	3.6	10.6	-0.48	0.30
4115	55	11.9	1.8	3.3	3.9	0.06	0.32
4126	118	8.2	1.5	1.6	14.8	-0.87	0.15
4211	490	4.7	5.1	5.7	14.4	0.04	0.06
4228	163	11.2	4.8	5.7	14.8	-0.33	0.12
4451	164	23.4	6.2	7.9	7.6	-0.13	0.37
4458	160	25.8	2.2	5.3	9.0	-0.05	0.37
4716	88	90.9	17.6	28.7	9.2	0.05	0.12
4816	1197	32.8	9.2	13.9	31.1	-0.04	0.39
4847	135	20.3	5.5	7.1	10.9	-0.35	0.23
8161	277	33.1	11.0	18.5	6.0	-0.03	0.17
8606	145	25.1	15.4	20.4	5.9	-0.08	0.17
6887	58	28.1	10.6	16.9	5.7	-0.06	0.33
6897	224	17.8	9.6	12.2	9.0	-0.13	0.09
6906	473	10.0	7.2	9.0	15.9	-0.77	0.60
6911	309	9.4	10.0	12.5	8.7	-0.19	0.41
6927	287	11.3	10.2	14.7	17.6	-0.72	0.14
6928	73	12.8	11.4	16.4	20.3	-0.01	0.44
6942	83	29.1	11.5	16.3	6.0	-0.05	0.27
6959	133	31.7	9.1	16.5	5.3	-0.04	0.19
6960	92	23.3	10.2	15.2	5.3	-0.02	0.06
6962	145	11.4	10.4	14.3	9.4	0.01	0.54
6966	99	26.8	9.0	15.8	5.9	-0.06	0.07
6969	55	28.8	9.6	16.4	8.3	-0.21	0.25
6975	87	23.3	10.6	16.8	12.4	-0.39	0.40
8119	124	5.4	1.4	2.8	15.5	-2.07	0.90
8123	268	11.5	2.1	3.6	3.8	-0.23	0.31

NON-PULSELIKE DATABASE

Table A.6 describes the record characteristics of non-pulselike ground motions. For each record, it includes information about the NGA record sequence number, the name and year of the earthquake, the name of the recording station, the time step Δt_0 of the original signal and corresponding Nyquist frequency f_{N_0} (see Section 3.4), the frequencies f_{HC} and f_{LC} of the high-cut (low-pass) and low-cut (high-pass) filters, respectively, used by PEER to process the record (see Sections 3.2.4 and 3.2.5), and the longest usable period T_{max} (see Sections 3.2.6). For each record, the table also gives the cutoff frequency f_c, computed according to (3.15), of the low-cut filter applied to the time series that are simulated using the parameters fitted to the record.

The frequency f_{HC} of the high-cut filter is compared to the Nyquist frequency f_{N_0} of the original signal. For most records, we find that f_{HC} is much smaller than f_{N_0}.This finding indicates that the initial signal has extremely small Fourier amplitudes near f_{N_0}. Therefore, resampling by *sinc*-interpolation (i.e., padding the FAS with zeros at frequencies above f_{N_0}) is expected to be a good approximation of the signal, were it recorded at a higher sampling rate.

The longest usable period T_{max} is the inverse of the lowest usable frequency f_{min}, which is equal to $1.25f_{LC}$, when the record is processed using a 5th order acausal Butterworth filter.

Table A.7 lists the earthquake source and site characteristics used as explanatory variables in the regression analysis, namely the style of faulting, F, the moment magnitude $\mathbf{M}$, the depth to the top of the rupture, Z_{TOR}, the closest distance to the fault rupture, R_{RUP}, the shear-wave velocity in the top 30m of the soil at the site, V_{s30}, and the two directivity parameters $s_{or}d$ and $\theta_{or}\phi$.

Finally, for each recorded ground motion, the parameters of the non-pulselike model presented in Section 4.5 are identified according to the fitting procedure described in Section 5.3.4. The identified parameter values of the major and intermediate ground motion components are listed in Tables A.8 and A.9, respectively. Table A.8 also lists the value of the angle α_{NP1} between the major principal direction and the strike of the fault.

Table A. 6 Characteristics of ground motion records in the non-pulselike database.

NGA#	EQ Name	Year	Station Name	Δt_0 (s)	f_{N0} (Hz)	f_{HC} (Hz)	f_{LC} (Hz)	T_{max} (s)	f_c (Hz)
1	Helena, Mont.-01	1935	Carroll College	0.010	50	15	0.13	6.2	0.22
28	Parkfield	1966	Cholame - Shandon Ar #12	0.010	50	20	0.10	8.0	0.19
33	Parkfield	1966	Temblor pre-1969	0.010	50	15	0.15	5.3	0.19
57	San Fernando	1971	Castaic - Old Ridge Route	0.010	50	35	0.30	2.7	0.13
63	San Fernando	1971	Fairmont Dam	0.010	50	35	0.15	5.3	0.13
70	San Fernando	1971	Lake Hughes #1	0.010	50	35	0.12	6.7	0.13
71	San Fernando	1971	Lake Hughes #12	0.010	50	35	0.20	4.0	0.13
72	San Fernando	1971	Lake Hughes #4	0.010	50	35	0.20	4.0	0.13
73	San Fernando	1971	Lake Hughes #9	0.010	50	35	0.50	1.6	0.13
78	San Fernando	1971	Palmdale Fire Station	0.010	50	35	0.15	5.3	0.13
79	San Fernando	1971	Pasadena - CIT Ath.	0.010	50	35	0.30	2.7	0.13
80	San Fernando	1971	Pasadena - Old Seis.Lab	0.010	50	35	0.50	1.6	0.13
87	San Fernando	1971	Santa Anita Dam	0.010	50	35	0.30	2.7	0.13
125	Friuli, Italy-01	1976	Tolmezzo	0.005	100	30	0.13	6.2	0.15
136	Santa Barbara	1978	Santa Barbara Court.	0.010	50	30	0.13	6.2	0.23
139	Tabas, Iran	1978	Dayhook	0.020	25	15	0.20	4.0	0.07
146	Coyote Lake	1979	Gilroy Array #1	0.005	100	33	0.12	6.7	0.27
152	Coyote Lake	1979	SJB Overpass, Bent 3gl	0.005	100	50	0.20	4.0	0.27
153	Coyote Lake	1979	S.J.Bautista - Hwy101/156 Ov.	0.005	100	60	0.20	4.0	0.27
164	Imp. Valley-06	1979	Cerro Prieto	0.010	50	30	0.09	8.9	0.14
190	Imp. Valley-06	1979	Superstition Mtn Camera	0.005	100	40	0.10	8.0	0.14
210	Livermore-01	1980	APEEL 3E Hayward CSUH	0.005	100	20	0.20	4.0	0.26
214	Livermore-01	1980	S.Ramon - Eastman Kod.	0.005	100	20	0.12	6.7	0.26
215	Livermore-01	1980	San Ramon Fire Station	0.005	100	15	0.20	4.0	0.26
265	Victoria, Mexico	1980	Cerro Prieto	0.010	50	63	0.30	2.7	0.17
318	Westmorland	1981	Superstition Mtn Camera	0.005	100	33	0.08	10.0	0.24
336	Coalinga-01	1983	Parkfield - Fault Zone 11	0.010	50	28	0.20	4.0	0.16
340	Coalinga-01	1983	Parkfield - Fault Zone 16	0.010	50	27	0.23	3.5	0.16
351	Coalinga-01	1983	Parkfield - Gold Hill 3E	0.010	50	27	0.20	4.0	0.16
359	Coalinga-01	1983	Parkfield - Vineyard Cany 1E	0.010	50	24	0.23	3.5	0.16
362	Coalinga-01	1983	Parkfield - Vineyard Cany 2W	0.010	50	30	0.23	3.5	0.16
369	Coalinga-01	1983	Slack Canyon	0.010	50	21	0.20	4.0	0.16
448	Morgan Hill	1984	Anderson Dam (Down.)	0.005	100	38	0.13	6.2	0.19
450	Morgan Hill	1984	Corralitos	0.005	100	26	0.10	8.0	0.19
454	Morgan Hill	1984	Gilroy - Gavilan Coll.	0.005	100	30	0.30	2.7	0.19
455	Morgan Hill	1984	Gilroy Array #1	0.005	100	40	0.16	5.0	0.19
514	N. Palm Springs	1986	Cabazon	0.005	100	40	0.13	6.2	0.21
516	N. Palm Springs	1986	Cranston Forest Station	0.005	100	50	0.30	2.7	0.21
518	N. Palm Springs	1986	Fun Valley	0.005	100	33	0.23	3.5	0.21
521	N. Palm Springs	1986	Hurkey Creek Park	0.005	100	43	0.43	1.9	0.21
524	N. Palm Springs	1986	Joshua Tree	0.005	100	30	0.30	2.7	0.21
527	N. Palm Springs	1986	Morongo Valley Fire Station	0.005	100	60	0.00	-	0.21
534	N. Palm Springs	1986	San Jacinto - Soboba	0.005	100	49	0.20	4.0	0.21
537	N. Palm Springs	1986	Silent Valley - Poppet Flat	0.005	100	49	0.50	1.6	0.21
540	N. Palm Springs	1986	Whitewater Trout Farm	0.005	100	50	0.12	6.7	0.21
543	ChalfantValley-01	1986	Benton	0.005	100	30	0.20	4.0	0.26
545	ChalfantValley-01	1986	Bishop - Paradise Lodge	0.005	100	30	0.11	7.3	0.26
546	ChalfantValley-01	1986	Lake Crowley - Shehorn Res.	0.005	100	30	0.16	5.0	0.26

NGA#	EQ Name	Year	Station Name	Δt_0 (s)	f_{N0} (Hz)	f_{HC} (Hz)	f_{LC} (Hz)	T_{max} (s)	f_c (Hz)
548	ChalfantValley-02	1986	Benton	0.005	100	40	0.10	8.0	0.19
550	ChalfantValley-02	1986	Bishop - Paradise Lodge	0.005	100	40	0.10	8.0	0.19
552	ChalfantValley-02	1986	Lake Crowley - Shehorn Res.	0.005	100	30	0.17	4.7	0.19
553	ChalfantValley-02	1986	Long Valley Dam (Downst)	0.005	100	40	0.20	4.0	0.19
585	Baja California	1987	Cerro Prieto	0.005	100	50	0.13	6.2	0.33
589	Whittier Narr.-01	1987	Alhambra - Fremont School	0.005	100	40	0.33	2.4	0.22
590	Whittier Narr.-01	1987	Altadena - Eaton Canyon	0.005	100	40	0.21	3.8	0.22
592	Whittier Narr.-01	1987	Arcadia - Campus Dr	0.005	100	30	0.20	5.0	0.22
594	Whittier Narr.-01	1987	Baldwin Park - N Holly	0.005	100	30	0.10	10.0	0.22
596	Whittier Narr.-01	1987	Beverly Hills - 12520 Mulhol	0.005	100	30	0.33	3.0	0.22
598	Whittier Narr.-01	1987	Big Tujunga, Angeles Nat F	0.005	100	30	1.00	1.0	0.22
600	Whittier Narr.-01	1987	Brea Dam (Downstream)	0.005	100	25	0.20	4.0	0.22
619	Whittier Narr.-01	1987	Garvey Res. - Control Bldg	0.005	100	25	0.30	2.7	0.22
620	Whittier Narr.-01	1987	Glendale - Las Palmas	0.005	100	30	0.40	2.5	0.22
621	Whittier Narr.-01	1987	Glendora - N Oakbank	0.005	100	30	0.50	2.0	0.22
632	Whittier Narr.-01	1987	LA - Cypress Ave	0.005	100	30	0.30	3.3	0.22
637	Whittier Narr.-01	1987	LA - N Figueroa St	0.005	100	23	0.40	2.5	0.22
643	Whittier Narr.-01	1987	LA - Wonderland Ave	0.005	100	33	0.60	1.7	0.22
648	Whittier Narr.-01	1987	La Crescenta - New York	0.005	100	20	0.50	2.0	0.22
663	Whittier Narr.-01	1987	Mt Wilson - CIT Seis Sta	0.005	100	40	0.23	3.5	0.22
669	Whittier Narr.-01	1987	Orange Co. Reservoir	0.005	100	25	0.60	1.3	0.22
675	Whittier Narr.-01	1987	Pasadena - CIT Athenaeum	0.005	100	40	0.20	4.0	0.22
680	Whittier Narr.-01	1987	Pasadena - CIT Kresge Lab	0.005	100	40	0.33	2.4	0.22
683	Whittier Narr.-01	1987	Pasadena - Old House Rd	0.005	100	30	0.13	7.7	0.22
685	Whittier Narr.-01	1987	Pomona - 4th & Locust FF	0.005	100	30	0.40	2.0	0.22
690	Whittier Narr.-01	1987	San Gabriel - E Grand Ave	0.005	100	25	0.10	10.0	0.22
691	Whittier Narr.-01	1987	San Marino - SW Academy	0.005	100	40	0.30	2.7	0.22
697	Whittier Narr.-01	1987	Sunland - Mt Gleason Ave	0.005	100	23	0.30	3.3	0.22
727	Supers. Hills-02	1987	Superstition Mtn Camera	0.010	50	23	1.00	0.8	0.14
739	Loma Prieta	1989	Anderson Dam (Down.)	0.005	100	41	0.08	10.0	0.10
741	Loma Prieta	1989	BRAN	0.005	100	0	0.10	8.0	0.10
753	Loma Prieta	1989	Corralitos	0.005	100	40	0.15	5.3	0.10
763	Loma Prieta	1989	Gilroy - Gavilan Coll.	0.005	100	45	0.10	8.0	0.10
765	Loma Prieta	1989	Gilroy Array #1	0.005	100	50	0.06	13.3	0.10
769	Loma Prieta	1989	Gilroy Array #6	0.005	100	38	0.13	6.2	0.10
775	Loma Prieta	1989	Hollister - SAGO Vault	0.005	100	32	0.10	8.0	0.10
779	Loma Prieta	1989	LGPC	0.005	100	0	0.10	8.0	0.10
787	Loma Prieta	1989	Palo Alto - SLAC Lab	0.005	100	33	0.10	8.0	0.10
801	Loma Prieta	1989	San Jose - S.Teresa Hills	0.005	100	33	0.03	26.7	0.10
809	Loma Prieta	1989	UCSC	0.005	100	50	0.10	8.0	0.10
810	Loma Prieta	1989	UCSC Lick Observatory	0.005	100	40	0.12	6.7	0.10
811	Loma Prieta	1989	WAHO	0.005	100	70	0.08	10.0	0.10
825	Cape Mendocino	1992	Cape Mendocino	0.020	25	23	0.07	14.3	0.10
827	Cape Mendocino	1992	Fortuna - Fortuna Blvd	0.020	25	23	0.07	14.3	0.10
830	Cape Mendocino	1992	Shelter Cove Airport	0.020	25	23	0.50	2.0	0.10
3748	Cape Mendocino	1992	Ferndale Fire Station	0.005	100	23	0.10	8.0	0.10
3750	Cape Mendocino	1992	Loleta Fire Station	0.005	100	30	0.05	16.0	0.10
864	Landers	1992	Joshua Tree	0.020	25	23	0.07	14.3	0.08
881	Landers	1992	Morongo Valley Fire St.	0.005	100	30	0.20	4.0	0.08
3753	Landers	1992	Fun Valley	0.005	100	30	0.05	16.0	0.08
3757	Landers	1992	N Palm Springs Fire St #36	0.005	100	30	0.09	8.9	0.08
3759	Landers	1992	Whitewater Trout Farm	0.005	100	30	0.30	2.7	0.08

NGA#	EQ Name	Year	Station Name	Δt_0 (s)	f_{N0} (Hz)	f_{HC} (Hz)	f_{LC} (Hz)	T_{max} (s)	f_c (Hz)
901	Big Bear-01	1992	Big Bear Lake - Civ Center	0.010	50	46	0.12	8.3	0.15
6057	Big Bear-01	1992	Highland Fire Station	0.005	100	60	0.10	8.0	0.15
6059	Big Bear-01	1992	Morongo Valley Fire St	0.005	100	80	0.20	4.0	0.15
952	Northridge-01	1994	Beverly Hills - 12520 Mulhol	0.010	50	30	0.15	5.3	0.13
954	Northridge-01	1994	Big Tujunga, Angeles Nat F	0.010	50	30	0.33	2.4	0.13
957	Northridge-01	1994	Burbank - Howard Rd.	0.010	50	30	0.10	8.0	0.13
963	Northridge-01	1994	Castaic - Old Ridge Route	0.020	25	23	0.12	8.3	0.13
974	Northridge-01	1994	Glendale - Las Palmas	0.010	50	30	0.30	2.7	0.13
986	Northridge-01	1994	LA - Brentwood VA Hospital	0.005	100	33	0.14	5.1	0.13
989	Northridge-01	1994	LA - Chalon Rd	0.010	50	30	0.21	3.8	0.13
991	Northridge-01	1994	LA - Cypress Ave	0.010	50	30	0.12	6.7	0.13
1006	Northridge-01	1994	LA - UCLA Grounds	0.020	25	23	0.16	6.3	0.13
1011	Northridge-01	1994	LA - Wonderland Ave	0.010	50	30	0.14	5.7	0.13
1012	Northridge-01	1994	LA 00	0.010	50	40	0.13	6.2	0.13
1016	Northridge-01	1994	La Crescenta - New York	0.010	50	30	0.30	2.7	0.13
1020	Northridge-01	1994	Lake Hughes #12A	0.010	50	46	0.12	8.3	0.13
1023	Northridge-01	1994	Lake Hughes #9	0.020	25	23	0.14	5.7	0.13
1078	Northridge-01	1994	Santa Susana Ground	0.005	100	40	0.10	7.1	0.13
1080	Northridge-01	1994	Simi Valley - Katherine Rd	0.010	50	30	0.21	3.8	0.13
1083	Northridge-01	1994	Sunland - Mt Gleason Ave	0.010	50	30	0.10	8.0	0.13
1089	Northridge-01	1994	Topanga - Fire Sta	0.005	100	40	0.12	6.0	0.13
1091	Northridge-01	1994	Vasquez Rocks Park	0.020	25	23	0.20	4.0	0.13
1099	Double Springs	1994	Woodfords	0.005	100	30	0.50	2.0	0.24
1108	Kobe, Japan	1995	Kobe University	0.010	50	30	0.10	8.0	0.11
1111	Kobe, Japan	1995	Nishi-Akashi	0.010	50	23	0.10	8.0	0.11
1166	Kocaeli, Turkey	1999	Iznik	0.005	100	25	0.10	8.0	0.07
1197	Chi-Chi, Taiwan	1999	CHY028	0.005	100	50	0.12	6.7	0.06
1198	Chi-Chi, Taiwan	1999	CHY029	0.005	100	50	0.03	26.7	0.06
1202	Chi-Chi, Taiwan	1999	CHY034	0.005	100	50	0.04	20.0	0.06
1205	Chi-Chi, Taiwan	1999	CHY041	0.005	100	50	0.04	20.0	0.06
1206	Chi-Chi, Taiwan	1999	CHY042	0.005	100	30	0.06	13.3	0.06
1208	Chi-Chi, Taiwan	1999	CHY046	0.005	100	50	0.04	20.0	0.06
1227	Chi-Chi, Taiwan	1999	CHY074	0.005	100	40	0.02	40.0	0.06
1231	Chi-Chi, Taiwan	1999	CHY080	0.005	100	50	0.10	8.0	0.06
1234	Chi-Chi, Taiwan	1999	CHY086	0.005	100	30	0.10	8.0	0.06
1235	Chi-Chi, Taiwan	1999	CHY087	0.005	100	50	0.03	26.7	0.06
1380	Chi-Chi, Taiwan	1999	KAU054	0.005	100	50	0.04	20.0	0.06
1484	Chi-Chi, Taiwan	1999	TCU042	0.005	100	50	0.05	16.0	0.06
1488	Chi-Chi, Taiwan	1999	TCU048	0.005	100	50	0.04	20.0	0.06
1490	Chi-Chi, Taiwan	1999	TCU050	0.005	100	50	0.03	26.7	0.06
1494	Chi-Chi, Taiwan	1999	TCU054	0.005	100	50	0.02	40.0	0.06
1497	Chi-Chi, Taiwan	1999	TCU057	0.005	100	50	0.03	26.7	0.06
1499	Chi-Chi, Taiwan	1999	TCU060	0.005	100	50	0.03	26.7	0.06
1500	Chi-Chi, Taiwan	1999	TCU061	0.005	100	50	0.04	20.0	0.06
1504	Chi-Chi, Taiwan	1999	TCU067	0.005	100	50	0.03	26.7	0.06
1506	Chi-Chi, Taiwan	1999	TCU070	0.005	100	50	0.03	26.7	0.06
1507	Chi-Chi, Taiwan	1999	TCU071	0.005	100	50	0.20	4.0	0.06
1508	Chi-Chi, Taiwan	1999	TCU072	0.005	100	50	0.05	16.0	0.06
1509	Chi-Chi, Taiwan	1999	TCU074	0.005	100	50	0.13	6.2	0.06
1512	Chi-Chi, Taiwan	1999	TCU078	0.005	100	50	0.15	5.3	0.06
1513	Chi-Chi, Taiwan	1999	TCU079	0.005	100	50	0.20	4.0	0.06
1517	Chi-Chi, Taiwan	1999	TCU084	0.005	100	50	0.20	4.0	0.06
1520	Chi-Chi, Taiwan	1999	TCU088	0.005	100	60	0.08	10.0	0.06

NGA#	EQ Name	Year	Station Name	Δt_0 (s)	f_{N0} (Hz)	f_{HC} (Hz)	f_{LC} (Hz)	T_{max} (s)	f_c (Hz)
1521	Chi-Chi, Taiwan	1999	TCU089	0.005	100	50	0.07	11.4	0.06
1527	Chi-Chi, Taiwan	1999	TCU100	0.005	100	50	0.03	26.7	0.06
1532	Chi-Chi, Taiwan	1999	TCU105	0.005	100	40	0.03	26.7	0.06
1533	Chi-Chi, Taiwan	1999	TCU106	0.005	100	50	0.04	20.0	0.06
1534	Chi-Chi, Taiwan	1999	TCU107	0.005	100	50	0.03	26.7	0.06
1535	Chi-Chi, Taiwan	1999	TCU109	0.005	100	50	0.05	16.0	0.06
1541	Chi-Chi, Taiwan	1999	TCU116	0.005	100	50	0.03	26.7	0.06
1545	Chi-Chi, Taiwan	1999	TCU120	0.005	100	50	0.03	26.7	0.06
1546	Chi-Chi, Taiwan	1999	TCU122	0.005	100	50	0.02	40.0	0.06
1549	Chi-Chi, Taiwan	1999	TCU129	0.005	100	50	0.03	26.7	0.06
1611	Duzce, Turkey	1999	Lamont 1058	0.010	50	0	0.06	13.3	0.09
1612	Duzce, Turkey	1999	Lamont 1059	0.010	50	0	0.06	13.3	0.09
1613	Duzce, Turkey	1999	Lamont 1060	0.010	50	0	0.06	13.3	0.09
1614	Duzce, Turkey	1999	Lamont 1061	0.010	50	0	0.07	11.4	0.09
1616	Duzce, Turkey	1999	Lamont 362	0.010	50	0	0.06	13.3	0.09
1617	Duzce, Turkey	1999	Lamont 375	0.010	50	0	0.15	5.3	0.09
1618	Duzce, Turkey	1999	Lamont 531	0.010	50	0	0.06	13.3	0.09
1631	Upland	1990	Pomona - 4th & Locust FF	0.020	25	23	0.50	2.0	0.29
1632	Upland	1990	Rancho Cucamonga	0.020	25	23	0.60	1.7	0.29
1633	Manjil, Iran	1990	Abbar	0.020	25	20	0.13	7.7	0.07
1641	Sierra Madre	1991	Altadena - Eaton Canyon	0.020	25	23	0.50	2.0	0.30
1643	Sierra Madre	1991	LA - City Terrace	0.010	50	46	0.20	5.0	0.30
1645	Sierra Madre	1991	Mt Wilson - CIT Seis Sta	0.020	25	23	0.50	2.0	0.30
1647	Sierra Madre	1991	San Marino - SW Academy	0.020	25	23	0.50	2.0	0.30
6875	Joshua Tree, CA	1992	Morongo Valley Fire St	0.005	100	60	0.10	8.0	0.20
6876	Joshua Tree, CA	1992	Whitewater Trout Farm	0.005	100	70	0.14	5.7	0.20
6878	Joshua Tree, CA	1992	N Palm Springs Fire Sta #36	0.005	100	70	0.10	8.0	0.20
1787	Hector Mine	1999	Hector	0.010	50	53	0.03	26.7	0.09
3871	Tottori, Japan	2000	HRS002	0.010	50	30	0.08	10.0	0.13
3907	Tottori, Japan	2000	OKY004	0.010	50	30	0.30	2.7	0.13
3925	Tottori, Japan	2000	OKYH07	0.005	100	30	0.01	133.3	0.13
3926	Tottori, Japan	2000	OKYH08	0.005	100	30	0.03	26.7	0.13
3927	Tottori, Japan	2000	OKYH09	0.005	100	30	0.02	38.1	0.13
3932	Tottori, Japan	2000	OKYH14	0.005	100	30	0.10	8.0	0.13
3943	Tottori, Japan	2000	SMN015	0.010	50	30	0.06	13.3	0.13
3947	Tottori, Japan	2000	SMNH01	0.005	100	30	0.05	16.0	0.13
3948	Tottori, Japan	2000	SMNH02	0.005	100	30	0.20	4.0	0.13
3954	Tottori, Japan	2000	SMNH10	0.005	100	30	0.03	26.7	0.13
3964	Tottori, Japan	2000	TTR007	0.010	50	30	0.06	13.3	0.13
3966	Tottori, Japan	2000	TTR009	0.010	50	30	0.10	8.0	0.13
3979	San Simeon, CA	2003	Cambria - Hwy 1 Cltrs Br.	0.005	100	50	0.08	10.0	0.14
4013	San Simeon, CA	2003	San Antonio Dam - Toe	0.005	100	20	0.20	4.0	0.14
4031	San Simeon, CA	2003	Templeton - 1-story Hosp	0.005	100	80	0.07	11.4	0.14
4064	Parkfield-02, CA	2004	PARKF.- DONNA LEE	0.005	100	50	0.10	8.0	0.22
4067	Parkfield-02, CA	2004	PARKF. - GOLD HILL	0.005	100	50	0.10	8.0	0.22
4068	Parkfield-02, CA	2004	PARKF. - HOG CANYON	0.010	50	40	0.11	7.3	0.22
4069	Parkfield-02, CA	2004	PARKF. - JACK CANYON	0.005	100	50	0.10	8.0	0.22
4070	Parkfield-02, CA	2004	PARKF.- JOAQUIN CAN	0.005	100	50	0.10	8.0	0.22
4071	Parkfield-02, CA	2004	PARKF. - MIDDLE MTN	0.005	100	50	0.10	8.0	0.22
4073	Parkfield-02, CA	2004	PARKF. - STOCKDALE MTN	0.005	100	50	0.30	2.7	0.22
4075	Parkfield-02, CA	2004	PARKF. - WORK RANCH	0.005	100	50	0.50	1.6	0.22
4083	Parkfield-02, CA	2004	PARKF. – TUR. FLAT #1 (0M)	0.005	100	50	0.15	5.3	0.22
4099	Parkfield-02, CA	2004	Parkfield - Cholame 2E	0.005	100	40	0.22	3.6	0.22

NGA#	EQ Name	Year	Station Name	Δt_0 (s)	f_{N0} (Hz)	f_{HC} (Hz)	f_{LC} (Hz)	T_{max} (s)	f_c (Hz)
4114	Parkfield-02, CA	2004	Parkfield - Fault Zone 11	0.005	100	40	0.40	2.0	0.22
4119	Parkfield-02, CA	2004	Parkfield - Gold Hill 2E	0.005	100	33	0.70	1.1	0.22
4121	Parkfield-02, CA	2004	Parkfield - Gold Hill 3E	0.005	100	30	0.20	4.0	0.22
4122	Parkfield-02, CA	2004	Parkfield - Gold Hill 3W	0.005	100	30	0.10	8.0	0.22
4123	Parkfield-02, CA	2004	Parkfield - Gold Hill 4W	0.005	100	33	0.30	2.7	0.22
4124	Parkfield-02, CA	2004	Parkfield - Gold Hill 5W	0.005	100	40	0.20	4.0	0.22
4127	Parkfield-02, CA	2004	Parkfield - Stone Corral 2E	0.005	100	33	0.40	2.0	0.22
4128	Parkfield-02, CA	2004	Parkfield - Stone Corral 3E	0.005	100	30	0.33	2.4	0.22
4129	Parkfield-02, CA	2004	PARKFIELD - TEMBLOR	0.005	100	30	0.30	2.7	0.22
4130	Parkfield-02, CA	2004	Parkf. - Vineyard Cany 1E	0.005	100	33	0.09	8.9	0.22
4132	Parkfield-02, CA	2004	Parkf. - Vineyard Cany 2E	0.005	100	40	0.40	2.0	0.22
4133	Parkfield-02, CA	2004	Parkf. - Vineyard Cany 2W	0.005	100	33	0.10	8.0	0.22
4135	Parkfield-02, CA	2004	Parkf. - Vineyard Cany 4W	0.005	100	40	0.23	3.5	0.22
4137	Parkfield-02, CA	2004	Parkf. - Vineyard Cany 6W	0.005	100	30	0.30	2.7	0.22
4139	Parkfield-02, CA	2004	PARKFIELD - UPSAR 02	0.005	100	70	0.07	11.4	0.22
4140	Parkfield-02, CA	2004	PARKFIELD - UPSAR 03	0.005	100	70	0.07	11.4	0.22
4141	Parkfield-02, CA	2004	PARKFIELD - UPSAR 05	0.005	100	70	0.04	20.0	0.22
4142	Parkfield-02, CA	2004	PARKFIELD - UPSAR 06	0.005	100	70	0.05	16.0	0.22
4143	Parkfield-02, CA	2004	PARKFIELD - UPSAR 07	0.005	100	70	0.10	8.0	0.22
4144	Parkfield-02, CA	2004	PARKFIELD - UPSAR 08	0.005	100	70	0.08	10.0	0.22
4145	Parkfield-02, CA	2004	PARKFIELD - UPSAR 09	0.005	100	70	0.10	8.0	0.22
4147	Parkfield-02, CA	2004	PARKFIELD - UPSAR 11	0.005	100	70	0.07	11.4	0.22
4148	Parkfield-02, CA	2004	PARKFIELD - UPSAR 12	0.005	100	70	0.08	10.0	0.22
4149	Parkfield-02, CA	2004	PARKFIELD - UPSAR 13	0.005	100	70	0.06	13.3	0.22
4150	Parkfield-02, CA	2004	COALINGA - PRIEST VALLEY	0.005	100	30	0.00	-	0.22
4169	Niigata, Japan	2004	FKSH21	0.005	100	30	0.05	16.0	0.13
4206	Niigata, Japan	2004	NIG016	0.010	50	30	0.06	13.3	0.13
4209	Niigata, Japan	2004	NIG019	0.010	50	30	0.10	8.0	0.13
4213	Niigata, Japan	2004	NIG023	0.010	50	30	0.06	13.3	0.13
4218	Niigata, Japan	2004	NIG028	0.005	100	30	0.06	13.3	0.13
4219	Niigata, Japan	2004	NIGH01	0.005	100	30	0.10	8.0	0.13
4226	Niigata, Japan	2004	NIGH09	0.005	100	30	0.06	13.3	0.13
4229	Niigata, Japan	2004	NIGH12	0.005	100	30	0.04	20.0	0.13
4231	Niigata, Japan	2004	NIGH15	0.005	100	30	0.03	26.7	0.13
4455	Montenegro,Yugo.	1979	Herceg Novi - O.S.D. Paviviv	0.010	50	30	0.50	1.6	0.09
4456	Montenegro,Yugo.	1979	Petrovac - Hotel Olivia	0.010	50	30	0.40	2.0	0.09
4457	Montenegro,Yugo.	1979	Ulcinj - Hotel Albatros	0.010	50	30	0.20	4.0	0.09
4740	Wenchuan, China	2008	Maoxiandiban	0.005	100	50	0.01	80.0	0.05
4742	Wenchuan, China	2008	Maoxiannanxin	0.005	100	70	0.03	26.7	0.05
4744	Wenchuan, China	2008	Shifangbajiao	0.005	100	70	0.09	8.9	0.05
4757	Wenchuan, China	2008	Dayiyinping	0.005	100	40	0.02	40.0	0.05
4781	Wenchuan, China	2008	Jiangyouchonghua	0.005	100	0	0.07	12.3	0.05
4787	Wenchuan, China	2008	Jiangyoudizhentai	0.005	100	70	0.03	26.7	0.05
4806	Wenchuan, China	2008	Bixianzoushishan	0.005	100	40	0.03	26.7	0.05
4820	Wenchuan, China	2008	Wenchuanwolong	0.005	100	70	0.06	14.5	0.05
4841	Chuetsu-oki	2007	Joetsu Yasuzukaku Yasuzuka	0.010	50	50	0.04	20.0	0.12
4842	Chuetsu-oki	2007	Joetsu Uraga. Kamabucchi	0.010	50	50	0.06	13.3	0.12
4843	Chuetsu-oki	2007	Matsushiro Tokamachi	0.010	50	50	0.04	20.0	0.12
4844	Chuetsu-oki	2007	Tokamachi Matsunoyama	0.010	50	50	0.04	20.0	0.12
4845	Chuetsu-oki	2007	Joetsu Oshimaku Oka	0.010	50	50	0.10	8.0	0.12
4848	Chuetsu-oki	2007	Joetsu Ogataku	0.010	50	50	0.07	11.4	0.12
4850	Chuetsu-oki	2007	Yoshikawaku Joetsu City	0.010	50	50	0.05	16.0	0.12
4858	Chuetsu-oki	2007	Tokamachi Chitosecho	0.010	50	50	0.05	16.0	0.12

NGA#	EQ Name	Year	Station Name	Δt_0 (s)	f_{N0} (Hz)	f_{HC} (Hz)	f_{LC} (Hz)	T_{max} (s)	f_c (Hz)
4863	Chuetsu-oki	2007	Nagaoka	0.010	50	50	0.12	6.7	0.12
4864	Chuetsu-oki	2007	Yoitamachi Yoita Nagaoka	0.010	50	50	0.08	10.0	0.12
4865	Chuetsu-oki	2007	Tani Kozima Nagaoka	0.010	50	50	0.09	8.9	0.12
4867	Chuetsu-oki	2007	Teradomari Ueda.Nagaoka	0.010	50	50	0.06	13.3	0.12
4868	Chuetsu-oki	2007	Yamakoshi Take. Nagaoka	0.010	50	50	0.08	10.0	0.12
4869	Chuetsu-oki	2007	Kawaguchi	0.010	50	50	0.05	16.0	0.12
4872	Chuetsu-oki	2007	Sawa Mizuguti Tokamachi	0.010	50	50	0.07	11.4	0.12
4873	Chuetsu-oki	2007	Kashiwazaki City Takayan.	0.010	50	50	0.06	13.3	0.12
4874	Chuetsu-oki	2007	Oguni Nagaoka	0.010	50	50	0.08	10.0	0.12
4876	Chuetsu-oki	2007	Kashiwazaki Nishiya. Ikeura	0.010	50	50	0.20	4.0	0.12
4882	Chuetsu-oki	2007	Ojiya City	0.010	50	40	0.08	10.0	0.12
5262	Chuetsu-oki	2007	NIG016	0.010	50	30	0.08	10.0	0.12
5265	Chuetsu-oki	2007	NIG019	0.010	50	30	0.09	8.9	0.12
5267	Chuetsu-oki	2007	NIG021	0.010	50	30	0.02	40.0	0.12
5270	Chuetsu-oki	2007	NIG024	0.010	50	30	0.02	40.0	0.12
5274	Chuetsu-oki	2007	NIG028	0.010	50	30	0.02	40.0	0.12
5275	Chuetsu-oki	2007	NIGH01	0.005	100	30	0.03	26.7	0.12
5284	Chuetsu-oki	2007	NIGH11	0.005	100	30	0.07	11.4	0.12
5474	Iwate	2008	AKT019	0.010	50	30	0.02	40.0	0.11
5478	Iwate	2008	AKT023	0.010	50	30	0.10	8.0	0.11
5482	Iwate	2008	AKTH04	0.010	50	30	0.02	40.0	0.11
5484	Iwate	2008	AKTH06	0.010	50	30	0.05	16.0	0.11
5618	Iwate	2008	IWT010	0.010	50	30	0.02	40.0	0.11
5623	Iwate	2008	IWT015	0.010	50	30	0.07	11.4	0.11
5636	Iwate	2008	IWTH04	0.010	50	30	0.02	40.0	0.11
5651	Iwate	2008	IWTH19	0.010	50	30	0.07	11.4	0.11
5654	Iwate	2008	IWTH22	0.010	50	30	0.02	40.0	0.11
5656	Iwate	2008	IWTH24	0.010	50	30	0.05	16.0	0.11
5657	Iwate	2008	IWTH25	0.010	50	30	0.06	13.3	0.11
5658	Iwate	2008	IWTH26	0.010	50	30	0.09	8.9	0.11
5663	Iwate	2008	MYG004	0.010	50	30	0.05	16.0	0.11
5664	Iwate	2008	MYG005	0.010	50	30	0.07	11.4	0.11
5678	Iwate	2008	MYGH02	0.010	50	30	0.03	26.7	0.11
5775	Iwate	2008	Tamati Ono	0.010	50	50	0.08	10.0	0.11
5776	Iwate	2008	Kami, Miyagi Miyazaki	0.010	50	50	0.06	13.3	0.11
5783	Iwate	2008	Semine Kurihara	0.010	50	50	0.04	20.0	0.11
5800	Iwate	2008	Yokote Masuda Tam. Ma.	0.010	50	50	0.12	6.7	0.11
5804	Iwate	2008	Yamauchi Tsuchi. Yok.	0.010	50	50	0.04	20.0	0.11
5806	Iwate	2008	Yuzawa Town	0.010	50	50	0.19	4.2	0.11
5807	Iwate	2008	Yuzama Yokobori	0.010	50	50	0.13	6.2	0.11
5809	Iwate	2008	Minase Yuzawa	0.010	50	50	0.19	4.2	0.11
5810	Iwate	2008	Machimukai Town	0.010	50	50	0.15	5.3	0.11
5813	Iwate	2008	Mizusawaku Int. O gan.	0.010	50	30	0.08	10.0	0.11
5815	Iwate	2008	Yuzawa	0.010	50	30	0.08	10.0	0.11
5818	Iwate	2008	Kurihara City	0.010	50	30	0.08	10.0	0.11
5819	Iwate	2008	Ichinoseki Maikawa	0.010	50	30	0.08	10.0	0.11
6915	Darfield, NZ	2010	Heathcote Valley Prim. Sch.	0.005	100	60	0.06	13.3	0.10
6948	Darfield, NZ	2010	OXZ	0.020	25	0	0.08	10.0	0.10
6971	Darfield, NZ	2010	SPFS	0.005	100	60	0.03	26.7	0.10
8110	Christchurch, NZ	2011	MQZ	0.020	25	22	0.02	40.0	0.19
8157	Christchurch, NZ	2011	Heathcote Valley Prim. Sch	0.005	100	70	0.06	13.3	0.19
8158	Christchurch, NZ	2011	LPCC	0.005	100	70	0.06	13.3	0.19

Table A. 7 Earthquake source and site characteristics for records in the non-pulselike database.

NGA#	F	**M**	Z_{TOR} (km)	R_{RUP} (km)	V_{s30} (m/s)	$s_{or}d$ (km)	$\theta_{or}\phi$ (°)
1	0	6.0	2.0	2.9	593	5.5	29.9
28	0	6.2	0.0	17.6	409	24.9	33.4
33	0	6.2	0.0	16.0	528	24.9	10.4
57	1	6.6	0.0	22.6	450	7.1	59.7
63	1	6.6	0.0	30.2	634	5.7	69.9
70	1	6.6	0.0	27.4	425	5.7	68.9
71	1	6.6	0.0	19.3	602	5.7	34.6
72	1	6.6	0.0	25.1	600	5.7	59.1
73	1	6.6	0.0	22.6	671	5.7	40.5
78	1	6.6	0.0	29.0	453	10.3	51.3
79	1	6.6	0.0	25.5	415	23.6	23.4
80	1	6.6	0.0	21.5	969	23.6	23.8
87	1	6.6	0.0	30.7	667	23.6	11.9
125	1	6.5	2.3	15.8	505	6.5	30.0
136	1	5.9	11.6	12.2	515	2.7	32.6
139	1	7.4	1.0	13.9	472	16.1	40.6
146	0	5.7	3.1	10.7	1428	5.0	43.5
152	0	5.7	3.1	20.7	367	5.0	53.9
153	0	5.7	3.1	20.7	363	5.0	53.9
164	0	6.5	0.0	15.2	472	11.9	35.7
190	0	6.5	0.0	24.6	362	38.1	17.3
210	0	5.8	7.1	30.6	517	5.0	70.2
214	0	5.8	7.1	17.2	378	5.0	51.7
215	0	5.8	7.1	17.9	384	5.0	58.0
265	0	6.3	4.0	14.4	472	20.0	3.2
318	0	5.9	2.0	19.4	362	6.0	14.1
336	1	6.4	3.4	28.5	542	9.2	54.9
340	1	6.4	3.4	27.7	384	9.2	64.1
351	1	6.4	3.4	30.1	451	9.2	46.1
359	1	6.4	3.4	26.4	381	9.2	69.6
362	1	6.4	3.4	30.4	439	9.2	70.8
369	1	6.4	3.4	27.5	648	8.7	37.8
448	0	6.2	0.5	3.3	489	16.4	11.1
450	0	6.2	0.5	23.2	462	19.1	50.6
454	0	6.2	0.5	14.8	730	26.5	15.1
455	0	6.2	0.5	14.9	1428	26.5	15.6
514	1	6.1	4.0	7.9	377	10.7	47.0
516	1	6.1	4.0	27.5	425	10.7	71.3
518	1	6.1	4.0	14.2	389	9.3	5.0
521	1	6.1	4.0	29.8	408	9.7	29.2
524	1	6.1	4.0	26.9	379	9.3	44.9
527	1	6.1	4.0	12.0	396	3.7	72.9
534	1	6.1	4.0	23.3	447	10.7	59.3
537	1	6.1	4.0	17.0	659	10.7	53.7
540	1	6.1	4.0	6.0	425	9.4	32.4
543	0	5.8	2.0	24.3	371	5.3	53.0
545	0	5.8	2.0	15.1	585	4.7	10.6
546	0	5.8	2.0	24.5	457	4.7	67.5

NGA#	F	**M**	Z_{TOR} (km)	R_{RUP} (km)	V_{s30} (m/s)	$s_{or}d$ (km)	$\theta_{or}\phi$ (˚)
548	0	6.2	4.0	21.9	371	8.7	26.8
550	0	6.2	4.0	18.3	585	2.0	82.4
552	0	6.2	4.0	24.5	457	8.7	52.5
553	0	6.2	4.0	21.1	537	8.7	44.5
585	0	5.5	2.8	4.5	472	3.2	28.6
589	1	6.0	14.5	14.7	550	5.0	9.9
590	1	6.0	14.5	19.5	375	4.6	76.7
592	1	6.0	14.5	17.4	368	2.5	75.2
594	1	6.0	14.5	16.7	545	5.0	39.8
596	1	6.0	14.5	29.9	546	5.0	6.2
598	1	6.0	14.5	28.5	550	5.8	61.7
600	1	6.0	14.5	24.0	438	5.0	41.2
619	1	6.0	14.5	14.5	468	2.8	10.7
620	1	6.0	14.5	22.8	371	5.0	40.6
621	1	6.0	14.5	22.1	362	5.0	38.2
632	1	6.0	14.5	17.0	367	5.0	8.4
637	1	6.0	14.5	16.5	365	5.0	24.6
643	1	6.0	14.5	27.6	1223	5.0	4.7
648	1	6.0	14.5	26.0	412	5.8	69.2
663	1	6.0	14.5	22.7	680	5.8	66.8
669	1	6.0	14.5	22.8	416	5.0	24.8
675	1	6.0	14.5	17.2	415	5.0	59.8
680	1	6.0	14.5	18.1	969	5.0	43.3
683	1	6.0	14.5	19.2	397	4.0	78.2
685	1	6.0	14.5	29.7	384	5.0	11.5
690	1	6.0	14.5	15.2	401	1.9	66.6
691	1	6.0	14.5	15.9	379	5.0	48.3
697	1	6.0	14.5	30.4	402	5.8	65.4
727	0	6.5	0.0	5.6	362	9.0	32.0
739	1	6.9	3.9	20.3	489	14.6	35.0
741	1	6.9	3.9	10.7	477	14.6	35.9
753	1	6.9	3.9	3.9	462	14.6	3.5
763	1	6.9	3.9	10.0	730	20.0	23.0
765	1	6.9	3.9	9.6	1428	20.0	22.8
769	1	6.9	3.9	18.3	663	20.0	35.5
775	1	6.9	3.9	30.2	621	20.0	0.2
779	1	6.9	3.9	3.9	595	17.9	14.4
787	1	6.9	3.9	30.9	425	20.0	17.6
801	1	6.9	3.9	14.7	672	14.6	27.7
809	1	6.9	3.9	18.5	714	11.9	57.2
810	1	6.9	3.9	18.4	714	11.9	57.0
811	1	6.9	3.9	17.5	388	12.2	54.8
825	1	7.0	5.2	7.0	568	11.5	30.9
827	1	7.0	5.2	20.0	457	11.1	24.6
830	1	7.0	5.2	28.8	519	8.9	12.7
3748	1	7.0	5.2	19.3	388	11.1	4.7
3750	1	7.0	5.2	25.9	516	11.1	11.7
864	0	7.3	0.0	11.0	379	7.1	59.0
881	0	7.3	0.0	17.4	396	7.1	79.0
3753	0	7.3	0.0	25.0	389	7.1	77.5
3757	0	7.3	0.0	27.0	368	7.1	80.7
3759	0	7.3	0.0	27.1	425	7.1	81.3

NGA#	F	**M**	Z_{TOR} (km)	R_{RUP} (km)	V_{s30} (m/s)	$s_{or}d$ (km)	$\theta_{or}\phi$ (˚)
901	0	6.5	3.9	8.3	430	9.0	26.9
6057	0	6.5	3.9	26.5	362	10.8	22.0
6059	0	6.5	3.9	29.1	396	9.0	70.1
952	1	6.7	5.0	18.4	546	11.0	50.5
954	1	6.7	5.0	19.7	550	19.4	3.5
957	1	6.7	5.0	16.9	582	19.4	15.2
963	1	6.7	5.0	20.7	450	19.4	9.4
974	1	6.7	5.0	22.2	371	19.4	8.9
986	1	6.7	5.0	22.5	417	4.3	77.3
989	1	6.7	5.0	20.5	740	5.3	73.8
991	1	6.7	5.0	30.7	367	15.1	33.6
1006	1	6.7	5.0	22.5	398	5.5	72.9
1011	1	6.7	5.0	20.3	1223	11.0	50.5
1012	1	6.7	5.0	19.1	706	7.7	64.5
1016	1	6.7	5.0	18.5	412	19.4	4.7
1020	1	6.7	5.0	21.4	602	19.4	12.9
1023	1	6.7	5.0	25.4	671	19.4	15.1
1078	1	6.7	5.0	16.7	715	13.7	20.4
1080	1	6.7	5.0	13.4	557	12.2	0.2
1083	1	6.7	5.0	13.4	402	19.4	3.8
1089	1	6.7	5.0	22.3	506	3.6	75.4
1091	1	6.7	5.0	23.6	996	19.4	15.3
1099	0	5.9	3.0	12.8	393	10.0	49.0
1108	0	6.9	0.2	0.9	1043	25.3	5.5
1111	0	6.9	0.2	7.1	609	17.6	25.1
1166	0	7.5	0.0	30.7	477	24.3	66.9
1197	1	7.6	0.0	3.1	543	35.0	45.0
1198	1	7.6	0.0	11.0	545	35.0	48.0
1202	1	7.6	0.0	12.7	573	35.0	30.0
1205	1	7.6	0.0	19.8	492	35.0	21.5
1206	1	7.6	0.0	28.2	665	35.0	18.6
1208	1	7.6	0.0	24.1	442	35.0	36.5
1227	1	7.6	0.0	10.8	553	35.0	18.0
1231	1	7.6	0.0	2.7	496	35.0	29.5
1234	1	7.6	0.0	28.4	665	35.0	17.6
1235	1	7.6	0.0	28.9	505	35.0	25.0
1380	1	7.6	0.0	30.9	497	35.0	14.0
1484	1	7.6	0.0	26.3	579	56.0	26.8
1488	1	7.6	0.0	13.5	551	32.9	48.2
1490	1	7.6	0.0	9.5	542	33.2	43.7
1494	1	7.6	0.0	5.3	461	30.9	43.1
1497	1	7.6	0.0	11.8	555	32.2	47.1
1499	1	7.6	0.0	8.5	375	38.1	43.1
1500	1	7.6	0.0	17.2	380	15.8	56.2
1504	1	7.6	0.0	0.6	434	23.0	40.2
1506	1	7.6	0.0	19.0	401	34.7	51.1
1507	1	7.6	0.0	5.8	625	12.8	15.8
1508	1	7.6	0.0	7.1	468	22.1	21.1
1509	1	7.6	0.0	13.5	549	22.1	60.1
1512	1	7.6	0.0	8.2	443	5.0	32.3
1513	1	7.6	0.0	11.0	364	6.6	69.8
1517	1	7.6	0.0	11.5	665	5.9	73.1
1520	1	7.6	0.0	18.2	665	56.0	44.3

NGA#	F	**M**	Z_{TOR} (km)	R_{RUP} (km)	V_{s30} (m/s)	$s_{or}d$ (km)	$\theta_{or}\phi$ (˚)
1521	1	7.6	0.0	9.0	672	4.1	31.1
1527	1	7.6	0.0	11.4	535	33.6	45.3
1532	1	7.6	0.0	17.2	576	39.2	44.7
1533	1	7.6	0.0	15.0	451	15.8	59.6
1534	1	7.6	0.0	16.0	409	15.3	60.9
1535	1	7.6	0.0	13.1	535	15.8	57.9
1541	1	7.6	0.0	12.4	493	13.1	9.3
1545	1	7.6	0.0	7.4	459	13.8	10.5
1546	1	7.6	0.0	9.3	475	11.4	4.5
1549	1	7.6	0.0	1.8	511	9.7	3.7
1611	0	7.1	0.0	0.2	529	15.4	0.7
1612	0	7.1	0.0	4.2	551	18.5	21.7
1613	0	7.1	0.0	25.9	782	18.5	6.8
1614	0	7.1	0.0	11.5	481	18.5	20.4
1616	0	7.1	0.0	23.4	517	18.5	20.9
1617	0	7.1	0.0	3.9	454	18.5	22.8
1618	0	7.1	0.0	8.0	638	18.5	30.2
1631	0	5.6	0.8	7.2	384	3.8	10.5
1632	0	5.6	0.8	11.0	390	3.8	56.1
1633	0	7.4	0.0	12.6	724	28.1	6.0
1641	1	5.6	10.0	13.2	375	3.7	18.2
1643	1	5.6	10.0	25.7	365	3.7	27.6
1645	1	5.6	10.0	10.4	680	3.7	9.2
1647	1	5.6	10.0	18.7	379	3.7	25.5
6875	0	6.1	5.0	22.3	396	7.5	47.7
6876	0	6.1	5.0	29.4	425	7.5	63.8
6878	0	6.1	5.0	22.0	368	7.4	59.9
1787	0	7.1	0.0	11.7	726	14.9	21.5
3871	0	6.6	0.5	30.7	458	19.0	38.8
3907	0	6.6	0.5	19.7	476	19.0	8.4
3925	0	6.6	0.5	15.2	940	19.0	36.2
3926	0	6.6	0.5	24.8	694	19.0	22.6
3927	0	6.6	0.5	21.2	519	19.0	40.2
3932	0	6.6	0.5	26.5	710	19.0	3.3
3943	0	6.6	0.5	9.1	617	16.4	29.1
3947	0	6.6	0.5	5.9	446	12.0	25.0
3948	0	6.6	0.5	23.6	503	12.0	62.1
3954	0	6.6	0.5	15.6	967	19.0	22.2
3964	0	6.6	0.5	11.3	470	12.0	42.1
3966	0	6.6	0.5	8.8	420	12.0	35.2
3979	1	6.5	2.0	7.3	362	8.3	16.8
4013	1	6.5	2.0	19.0	509	12.6	54.1
4031	1	6.5	2.0	6.2	411	31.5	3.3
4064	0	6.0	2.5	4.9	657	14.0	17.3
4067	0	6.0	2.5	3.4	558	5.6	15.9
4068	0	6.0	2.5	2.7	364	5.6	6.4
4069	0	6.0	2.5	9.5	576	10.0	12.7
4070	0	6.0	2.5	4.6	379	14.4	15.2
4071	0	6.0	2.5	2.6	398	19.6	2.1
4073	0	6.0	2.5	4.8	394	25.6	9.0
4075	0	6.0	2.5	10.8	447	8.1	51.9
4083	0	6.0	2.5	5.3	907	5.6	29.5
4099	0	6.0	2.5	4.1	523	10.0	13.5

NGA#	F	**M**	Z_{TOR} (km)	R_{RUP} (km)	V_{s30} (m/s)	$s_{or}d$ (km)	$\theta_{or}\phi$ (˚)
4114	0	6.0	2.5	4.0	542	8.7	20.3
4119	0	6.0	2.5	3.8	361	5.6	19.4
4121	0	6.0	2.5	6.3	451	5.6	35.0
4122	0	6.0	2.5	5.4	511	5.6	31.1
4123	0	6.0	2.5	8.3	421	5.6	44.9
4124	0	6.0	2.5	11.5	441	5.6	55.0
4127	0	6.0	2.5	5.8	566	5.6	32.4
4128	0	6.0	2.5	8.1	565	5.6	42.9
4129	0	6.0	2.5	12.5	525	10.0	15.9
4130	0	6.0	2.5	3.0	381	18.7	5.2
4132	0	6.0	2.5	4.5	468	19.3	11.1
4133	0	6.0	2.5	3.5	439	17.7	7.7
4135	0	6.0	2.5	7.3	386	18.1	20.5
4137	0	6.0	2.5	13.7	392	17.2	37.9
4139	0	6.0	2.5	10.0	417	8.5	48.5
4140	0	6.0	2.5	10.0	441	8.3	48.9
4141	0	6.0	2.5	9.6	441	8.5	47.4
4142	0	6.0	2.5	9.6	441	8.5	47.4
4143	0	6.0	2.5	9.6	441	8.5	47.4
4144	0	6.0	2.5	9.4	441	8.4	46.8
4145	0	6.0	2.5	9.3	466	8.5	46.3
4147	0	6.0	2.5	9.4	466	8.6	46.3
4148	0	6.0	2.5	9.5	466	8.8	45.9
4149	0	6.0	2.5	9.5	466	8.8	45.9
4150	0	6.0	2.5	22.0	413	30.0	2.5
4169	1	6.6	4.0	30.8	365	13.0	53.0
4206	1	6.6	4.0	30.1	370	13.0	41.6
4209	1	6.6	4.0	9.9	372	5.3	61.8
4213	1	6.6	4.0	25.8	655	11.0	5.0
4218	1	6.6	4.0	9.8	431	13.0	14.5
4219	1	6.6	4.0	9.5	480	13.0	12.7
4226	1	6.6	4.0	22.7	463	13.0	13.3
4229	1	6.6	4.0	10.7	564	9.0	13.6
4231	1	6.6	4.0	22.1	686	11.0	58.4
4455	1	7.1	3.6	25.6	585	48.0	9.9
4456	1	7.1	3.6	8.0	543	27.8	10.3
4457	1	7.1	3.6	4.4	410	12.6	18.0
4740	1	7.9	0.0	22.3	638	86.3	15.9
4742	1	7.9	0.0	21.9	430	70.3	18.7
4744	1	7.9	0.0	1.6	379	67.5	13.2
4757	1	7.9	0.0	28.6	379	15.0	67.5
4781	1	7.9	0.0	27.2	430	135.0	18.4
4787	1	7.9	0.0	22.6	476	135.0	19.7
4806	1	7.9	0.0	17.0	418	20.0	57.4
4820	1	7.9	0.0	18.2	511	9.1	62.3
4841	1	6.8	3.1	25.5	655	26.0	16.0
4842	1	6.8	3.1	22.7	655	26.0	12.5
4843	1	6.8	3.1	25.0	640	26.0	33.3
4844	1	6.8	3.1	28.8	640	26.0	33.3
4845	1	6.8	3.1	22.5	610	26.0	22.1
4848	1	6.8	3.1	17.9	414	26.0	2.1
4850	1	6.8	3.1	16.9	562	26.0	6.3
4858	1	6.8	3.1	30.7	640	26.0	49.2

NGA#	F	**M**	Z_{TOR} (km)	R_{RUP} (km)	V_{s30} (m/s)	$s_{or}d$ (km)	$\theta_{or}\phi$ (˚)
4863	1	6.8	3.1	16.3	514	7.2	66.5
4864	1	6.8	3.1	16.1	655	6.2	68.2
4865	1	6.8	3.1	13.8	562	6.0	40.5
4867	1	6.8	3.1	15.2	562	6.0	16.1
4868	1	6.8	3.1	28.1	655	13.9	51.0
4869	1	6.8	3.1	29.3	640	13.9	50.4
4872	1	6.8	3.1	27.3	640	26.0	49.9
4873	1	6.8	3.1	20.0	562	26.0	37.5
4874	1	6.8	3.1	20.0	562	17.1	51.7
4876	1	6.8	3.1	12.6	655	5.2	60.4
4882	1	6.8	3.1	23.4	430	13.9	54.3
5262	1	6.8	3.1	14.8	370	6.0	14.8
5265	1	6.8	3.1	23.4	372	13.9	54.4
5267	1	6.8	3.1	29.8	419	26.0	48.1
5270	1	6.8	3.1	25.3	375	26.0	15.4
5274	1	6.8	3.1	23.1	431	13.9	54.7
5275	1	6.8	3.1	23.4	480	13.9	54.4
5284	1	6.8	3.1	27.3	375	26.0	49.7
5474	1	6.9	0.7	28.8	640	16.7	63.1
5478	1	6.9	0.7	17.0	556	9.0	59.3
5482	1	6.9	0.7	17.9	459	9.0	58.0
5484	1	6.9	0.7	22.8	455	20.7	51.5
5618	1	6.9	0.7	16.3	826	9.0	24.3
5623	1	6.9	0.7	21.0	567	19.0	43.7
5636	1	6.9	0.7	29.5	456	19.0	40.2
5651	1	6.9	0.7	30.9	482	19.0	16.2
5654	1	6.9	0.7	29.8	532	19.0	18.3
5656	1	6.9	0.7	5.2	486	19.0	3.3
5657	1	6.9	0.7	4.8	506	4.3	47.6
5658	1	6.9	0.7	6.0	371	9.0	13.2
5663	1	6.9	0.7	20.2	479	21.0	49.6
5664	1	6.9	0.7	13.5	361	21.0	8.9
5678	1	6.9	0.7	11.1	399	21.0	16.5
5775	1	6.9	0.7	28.9	562	21.0	19.7
5776	1	6.9	0.7	25.2	478	21.0	16.7
5783	1	6.9	0.7	28.9	363	21.0	51.1
5800	1	6.9	0.7	29.9	368	9.0	50.8
5804	1	6.9	0.7	28.4	562	13.6	67.4
5806	1	6.9	0.7	25.6	655	9.0	52.5
5807	1	6.9	0.7	29.8	571	14.8	66.4
5809	1	6.9	0.7	21.3	655	9.0	55.0
5810	1	6.9	0.7	24.1	655	21.0	16.6
5813	1	6.9	0.7	7.9	413	19.0	35.0
5815	1	6.9	0.7	25.6	655	9.0	52.5
5818	1	6.9	0.7	12.9	512	15.0	52.8
5819	1	6.9	0.7	23.0	640	9.0	27.7
6915	0	7.0	0.0	24.5	422	29.0	0.9
6948	0	7.0	0.0	30.6	482	11.0	63.5
6971	0	7.0	0.0	29.9	390	11.0	63.0
8110	1	6.2	0.5	16.1	650	1.2	84.4
8157	1	6.2	0.5	3.4	422	5.1	33.4
8158	1	6.2	0.5	6.1	650	3.9	57.4

Table A. 8 Identified parameters for major component of non-pulselike records.

NGA#	$I_{a,NP1}$ (cm/s)	$D_{5-95,NP1}$ (s)	$D_{0-5,NP1}$ (s)	$D_{0-30,NP1}$ (s)	$\omega_{mid,NP1}/\pi$ (rad/s)	ω'_{NP1}/π (rad/s^2)	$\zeta_{f,NP1}$	α_{NP1} (°)
1	10	2.5	0.8	1.5	12.6	0.72	0.06	14.5
28	7	27.5	2.2	5.4	11.2	-0.38	0.12	31.9
33	53	4.3	2.2	3.2	6.7	-0.31	0.06	84.4
57	100	16.8	0.9	2.2	6.4	-0.05	0.37	8.1
63	8	12.2	0.7	1.3	19.1	-0.46	0.49	73.8
70	26	15.4	2.0	3.6	5.9	0.07	0.61	74.0
71	98	10.2	1.1	1.3	13.5	-0.01	0.26	59.6
72	32	11.9	1.7	3.0	24.1	-0.18	0.19	41.3
73	17	9.5	0.2	1.1	33.1	-1.02	0.20	70.2
78	34	18.3	1.1	3.3	8.2	-0.18	0.16	10.4
79	21	12.4	4.9	7.2	5.9	-0.12	0.17	26.9
80	34	6.9	2.7	4.9	10.0	0.17	0.08	22.6
87	40	10.8	0.6	2.2	17.5	-0.34	0.15	56.9
125	121	4.9	2.8	3.1	3.7	0.19	0.15	25.7
136	24	4.4	1.4	2.0	8.4	-0.69	0.07	56.7
139	150	11.4	3.0	4.6	12.1	0.32	0.07	85.2
146	8	5.3	1.9	2.3	22.9	-1.06	0.07	10.2
152	13	7.0	3.2	3.8	6.8	-0.24	0.23	15.9
153	10	6.8	3.2	3.7	9.2	-0.49	0.29	20.3
164	147	34.6	5.1	13.3	8.6	-0.13	0.28	50.0
190	21	6.7	5.7	7.2	12.9	-0.55	0.07	1.7
210	5	8.7	4.3	5.1	8.3	-0.08	0.04	68.8
214	22	10.5	4.1	4.9	3.9	-0.09	0.05	3.5
215	5	27.1	1.7	5.0	5.8	-0.14	0.07	3.6
265	199	8.2	3.3	5.2	11.1	-0.83	0.39	89.7
318	8	7.9	1.6	2.8	13.1	-0.60	0.08	60.3
336	12	11.3	4.0	5.0	4.4	0.00	0.07	78.8
340	37	11.6	3.8	6.2	6.6	-0.08	0.05	53.8
351	12	14.0	3.9	5.7	4.6	0.11	0.17	38.8
359	48	10.6	4.0	5.5	5.3	-0.13	0.08	81.9
362	12	13.8	2.7	7.1	8.5	0.04	0.08	1.1
369	29	13.3	4.2	6.1	4.3	-0.06	0.07	87.9
448	100	5.1	2.8	4.4	9.1	-0.59	0.20	46.8
450	11	7.8	4.0	5.6	6.3	-0.17	0.07	47.4
454	6	8.4	0.6	2.6	17.6	-0.46	0.07	71.1
455	6	8.9	0.9	3.1	16.5	-0.73	0.15	3.6
514	35	6.7	2.2	2.6	11.0	0.17	0.19	21.5
516	20	6.6	1.7	4.8	23.6	-4.90	0.27	45.6
518	17	9.8	1.1	3.2	16.5	-0.47	0.11	57.3
521	15	6.5	2.3	4.2	22.1	-0.60	0.17	63.8
524	6	16.9	3.0	5.4	6.2	-0.09	0.15	56.8
527	75	5.5	2.2	3.4	3.3	0.26	0.90	20.9
534	39	8.4	3.8	4.3	15.4	-0.31	0.25	55.2
537	12	6.9	1.9	2.3	22.1	0.47	0.16	76.7
540	216	3.6	1.2	1.9	9.6	0.88	0.25	5.1
543	5	15.8	3.8	5.1	10.5	-0.21	0.22	67.1
545	4	8.7	1.7	2.4	18.0	0.26	0.19	66.3
546	2	14.6	2.6	3.7	10.1	-0.06	0.31	45.9

NGA#	$I_{a,NP1}$ (cm/s)	$D_{5-95,NP1}$ (s)	$D_{0-5,NP1}$ (s)	$D_{0-30,NP1}$ (s)	$\omega_{mid,NP1}/\pi$ (rad/s)	ω'_{NP1}/π (rad/s^2)	$\zeta_{f,NP1}$	α_{NP1} (°)
548	37	16.7	3.4	4.2	8.9	-0.16	0.22	46.2
550	20	8.8	1.3	2.8	20.1	0.13	0.11	20.2
552	13	9.9	3.0	3.8	10.3	-0.15	0.14	24.5
553	6	10.5	2.7	3.2	10.8	-0.12	0.21	9.5
585	393	3.1	1.4	2.0	10.9	0.22	0.41	13.4
589	94	5.1	2.2	2.8	10.1	-0.35	0.10	45.4
590	41	4.4	2.2	3.0	12.2	-0.04	0.09	85.7
592	88	3.1	2.0	2.4	8.7	-0.09	0.04	81.1
594	14	8.5	2.0	3.0	11.4	-0.20	0.10	75.6
596	15	10.4	3.4	4.4	12.1	-0.08	0.08	6.8
598	16	8.1	3.6	4.2	17.6	-0.05	0.08	89.7
600	48	6.3	3.3	3.9	11.0	-0.17	0.06	54.1
619	138	4.0	2.2	2.6	14.4	-0.17	0.06	13.2
620	44	6.6	2.5	3.1	11.3	0.12	0.17	78.7
621	11	12.5	2.4	3.7	14.6	-0.16	0.14	70.0
632	18	8.7	1.9	2.5	11.0	-0.05	0.12	70.2
637	40	5.6	1.8	3.2	5.9	0.51	0.20	55.3
643	1	6.7	1.8	2.7	22.5	-0.11	0.10	10.9
648	25	3.7	3.0	3.7	7.1	0.70	0.09	87.3
663	27	8.0	1.7	3.3	19.6	0.37	0.19	6.4
669	27	8.3	3.1	4.6	13.7	-0.14	0.08	73.9
675	22	6.9	1.5	2.4	12.3	-0.26	0.31	79.7
680	9	3.5	1.6	2.5	13.3	0.92	0.30	4.4
683	43	4.8	2.1	2.8	10.8	0.11	0.05	86.9
685	4	13.4	4.0	5.2	16.8	-0.20	0.13	44.0
690	87	5.1	1.6	2.4	7.1	0.14	0.21	65.0
691	30	7.4	1.5	2.2	13.6	0.01	0.25	78.8
697	7	9.4	0.8	1.3	8.4	-0.02	0.09	71.2
727	661	12.2	3.6	9.2	8.8	-0.38	0.05	32.9
739	95	10.2	2.9	5.9	9.5	-0.14	0.10	76.8
741	677	9.5	3.4	5.6	9.0	0.07	0.31	83.6
753	327	6.7	1.5	1.8	5.5	0.01	0.09	42.6
763	95	4.8	1.9	2.4	12.2	0.35	0.10	38.3
765	178	4.4	2.0	2.9	13.0	0.20	0.29	57.3
769	48	12.1	2.6	3.7	8.1	-0.13	0.04	58.8
775	5	14.5	3.4	7.1	10.1	-0.37	0.17	18.1
779	850	10.2	4.0	6.6	3.4	0.12	0.72	70.3
787	100	11.5	6.2	8.0	6.3	-0.04	0.07	76.7
801	132	10.2	5.0	7.3	15.2	0.09	0.12	72.7
809	166	8.4	3.9	6.8	15.5	0.11	0.15	55.2
810	329	9.7	3.2	6.3	11.7	-0.09	0.06	16.7
811	640	11.0	3.6	6.5	15.6	-0.35	0.17	50.3
825	632	5.7	2.6	2.9	9.6	0.07	0.08	26.9
827	27	18.6	5.4	6.6	6.6	-0.12	0.09	42.6
830	57	16.3	6.2	9.7	13.7	0.02	0.04	37.9
3748	185	11.5	4.7	5.7	4.0	-0.13	0.12	58.2
3750	95	15.0	5.5	6.9	7.7	-0.39	0.07	48.5
864	258	25.5	5.4	9.6	6.1	-0.08	0.07	87.5
881	125	29.2	5.5	6.7	6.1	0.02	0.31	86.2
3753	172	28.0	4.9	6.9	8.5	-0.10	0.09	65.8
3757	75	35.3	6.2	14.6	9.9	-0.05	0.15	36.8
3759	61	31.4	6.1	11.9	11.1	0.01	0.08	19.0

NGA#	$I_{a,NP1}$ (cm/s)	$D_{5-95,NP1}$ (s)	$D_{0-5,NP1}$ (s)	$D_{0-30,NP1}$ (s)	$\omega_{mid,NP1}/\pi$ (rad/s)	ω'_{NP1}/π (rad/s^2)	$\zeta_{f,NP1}$	α_{NP1} (°)
901	424	9.2	2.8	3.4	9.2	0.55	0.06	74.3
6057	36	11.6	4.7	5.9	13.5	-0.03	0.08	15.3
6059	57	10.5	5.0	8.3	8.8	-0.54	0.14	28.5
952	352	7.5	2.2	3.8	10.3	-0.26	0.08	54.3
954	65	9.5	3.9	5.0	12.7	-0.13	0.08	86.4
957	34	7.9	2.5	4.2	9.8	-0.13	0.11	34.2
963	319	8.5	4.9	6.5	5.0	-0.22	0.06	43.8
974	121	9.4	3.3	4.7	13.5	-0.37	0.08	50.8
986	56	10.1	3.8	7.0	5.9	-0.19	0.13	24.4
989	65	7.3	3.2	6.7	7.8	-0.65	0.35	49.8
991	50	10.8	3.1	6.4	11.4	-0.61	0.04	69.7
1006	175	9.7	3.3	6.1	14.7	-0.28	0.15	39.2
1011	21	6.7	2.4	4.2	11.0	-0.04	0.15	41.5
1012	126	7.6	3.8	5.9	10.0	-0.30	0.09	71.9
1016	47	9.0	3.2	4.1	9.8	0.22	0.14	49.2
1020	51	9.0	3.3	6.7	15.0	-0.38	0.04	83.5
1023	33	6.5	3.8	5.9	13.7	-0.54	0.05	8.3
1078	120	6.6	2.2	3.7	10.3	-0.04	0.20	74.7
1080	413	6.7	2.8	4.2	6.9	-0.03	0.09	45.1
1083	54	12.5	3.1	4.6	6.8	-0.10	0.08	75.0
1089	105	8.7	3.0	5.2	10.9	-0.26	0.15	22.4
1091	37	8.3	4.0	5.5	10.3	0.18	0.10	59.0
1099	14	7.3	2.8	4.2	5.9	0.11	0.16	75.7
1108	124	7.1	4.7	5.9	4.4	0.06	0.15	62.5
1111	383	9.5	2.8	4.6	6.8	-0.03	0.05	79.0
1166	42	16.9	6.6	11.0	5.5	-0.17	0.15	1.4
1197	608	6.5	10.3	12.4	7.9	-0.01	0.37	45.8
1198	87	24.6	11.2	12.5	5.8	-0.05	0.53	13.8
1202	168	26.4	9.5	13.3	5.0	-0.03	0.13	41.0
1205	379	21.0	13.1	15.9	6.3	-0.02	0.07	5.3
1206	32	30.8	13.2	17.9	4.7	-0.04	0.08	72.6
1208	77	32.5	12.9	17.3	8.2	-0.10	0.19	12.6
1227	109	29.1	9.1	12.1	3.9	-0.01	0.09	78.2
1231	1253	15.1	9.9	14.8	3.5	0.03	0.19	32.7
1234	108	26.4	12.9	16.0	4.0	-0.02	0.05	2.5
1235	63	31.9	13.6	16.3	6.9	-0.03	0.06	83.2
1380	16	33.2	14.0	16.5	7.9	-0.03	0.07	26.0
1484	115	18.4	13.8	19.1	5.7	-0.09	0.11	81.4
1488	78	31.1	9.9	20.3	11.8	-0.31	0.13	49.1
1490	91	26.6	6.8	15.4	6.3	-0.03	0.17	76.8
1494	129	24.9	6.6	14.1	6.8	-0.17	0.24	51.3
1497	68	30.9	9.0	18.9	5.2	-0.09	0.23	63.5
1499	69	21.9	10.6	16.1	7.1	-0.06	0.19	85.7
1500	135	35.6	7.4	16.7	5.1	-0.07	0.34	44.1
1504	464	22.6	5.4	7.5	4.9	0.03	0.18	74.6
1506	230	26.5	12.5	21.5	3.6	-0.03	0.25	73.0
1507	1026	21.9	4.7	8.9	10.1	-0.06	0.08	22.0
1508	586	22.2	3.3	9.7	8.4	-0.03	0.36	87.8
1509	734	12.5	12.7	17.0	5.4	-0.04	0.32	84.3
1512	579	25.9	2.8	6.5	10.2	-0.15	0.07	67.4
1513	773	24.0	4.8	18.0	9.5	-0.11	0.31	74.2
1517	2040	14.7	11.6	15.0	2.6	0.00	0.10	65.7
1520	306	8.8	11.4	13.5	19.9	0.34	0.14	57.0

NGA#	$I_{a,NP1}$ (cm/s)	$D_{5-95,NP1}$ (s)	$D_{0-5,NP1}$ (s)	$D_{0-30,NP1}$ (s)	$\omega_{mid,NP1}/\pi$ (rad/s)	ω'_{NP1}/π (rad/s^2)	$\zeta_{f,NP1}$	α_{NP1} (°)
1521	301	24.1	3.0	11.2	7.9	-0.01	0.11	65.3
1527	68	27.2	9.1	17.7	4.9	-0.05	0.25	72.8
1532	67	27.1	12.9	22.3	4.3	-0.09	0.19	39.6
1533	145	32.4	9.4	17.5	5.0	-0.09	0.09	76.6
1534	146	37.3	10.4	16.1	4.0	-0.06	0.61	55.1
1535	194	30.6	8.4	16.6	4.3	-0.06	0.47	64.4
1541	167	28.2	7.8	11.5	5.1	-0.03	0.22	46.4
1545	201	32.0	7.0	13.3	7.7	-0.09	0.22	76.2
1546	157	30.3	5.7	13.2	7.4	-0.03	0.20	46.7
1549	951	27.3	3.8	7.7	9.9	-0.05	0.05	84.1
1611	12	13.0	4.9	6.8	19.0	-0.73	0.58	17.9
1612	48	14.1	3.8	6.4	12.7	-0.27	0.25	55.2
1613	4	18.4	5.7	8.5	10.7	-0.22	0.07	15.0
1614	30	14.0	5.4	6.5	10.8	-0.31	0.06	40.8
1616	4	18.8	3.9	8.6	8.7	-0.26	0.24	63.7
1617	1027	12.9	4.5	7.3	10.2	-0.15	0.15	79.1
1618	51	14.4	4.5	6.9	7.5	-0.05	0.08	51.3
1631	30	6.5	2.0	2.9	8.8	-0.11	0.21	61.6
1632	53	5.0	2.0	3.3	16.6	-0.14	0.06	7.2
1633	787	28.9	5.7	9.6	16.2	-0.05	0.07	-70.9
1641	120	1.2	2.3	2.5	7.9	2.50	0.04	50.0
1643	11	9.2	4.3	5.2	12.8	-0.22	0.20	37.5
1645	45	3.2	0.4	1.5	13.3	0.58	0.18	31.9
1647	13	5.3	2.7	3.4	7.9	-0.11	0.10	69.1
6875	18	12.8	3.7	5.6	7.6	-0.32	0.24	62.5
6876	43	7.8	2.3	5.4	15.5	0.23	0.08	70.8
6878	35	10.5	2.3	3.9	12.8	-0.70	0.13	1.2
1787	196	9.7	4.2	6.0	6.5	0.20	0.20	45.5
3871	382	13.5	7.3	8.1	27.5	0.07	0.02	21.8
3907	908	10.7	6.5	8.3	11.7	0.21	0.03	89.6
3925	29	18.2	3.7	7.1	26.4	0.10	0.04	37.5
3926	64	23.8	2.7	7.0	17.6	0.03	0.02	14.7
3927	133	24.7	3.2	6.7	16.1	0.03	0.01	48.4
3932	125	12.2	5.7	6.1	16.1	0.37	0.07	71.7
3943	40	8.7	4.7	7.5	13.4	-0.01	0.21	26.3
3947	544	11.6	2.7	6.3	13.5	0.12	0.07	7.6
3948	287	14.4	5.6	8.2	14.8	0.08	0.01	9.6
3954	48	8.7	7.1	8.1	10.1	-0.53	0.07	60.2
3964	569	8.7	4.7	5.8	15.5	0.23	0.17	55.8
3966	357	10.8	4.4	6.1	15.6	0.37	0.08	22.2
3979	47	10.2	3.1	4.0	13.1	-0.16	0.21	42.2
4013	26	15.6	2.6	4.5	7.1	-0.08	0.11	19.6
4031	206	9.9	3.8	4.5	9.7	-0.26	0.13	79.6
4064	80	4.9	2.7	3.3	12.2	0.45	0.09	15.4
4067	19	8.0	1.1	1.5	17.4	-0.34	0.08	43.3
4068	93	12.1	2.4	3.7	6.6	-0.24	0.35	38.2
4069	19	11.2	3.3	6.2	18.3	-0.65	0.05	72.9
4070	279	5.7	2.8	3.4	15.3	-0.60	0.11	1.5
4071	63	4.2	3.2	4.9	8.0	-0.37	0.10	57.2
4073	23	1.9	3.9	4.1	16.3	-1.07	0.13	41.7
4075	30	2.8	2.6	3.5	22.2	-1.73	0.06	49.3
4083	22	7.4	2.1	2.4	10.3	-0.40	0.08	0.4
4099	161	3.3	2.1	2.7	12.8	-0.21	0.02	14.4

NGA#	$I_{a,NP1}$ (cm/s)	$D_{5-95,NP1}$ (s)	$D_{0-5,NP1}$ (s)	$D_{0-30,NP1}$ (s)	$\omega_{mid,NP1}/\pi$ (rad/s)	ω'_{NP1}/π (rad/s^2)	$\zeta_{f,NP1}$	α_{NP1} (°)
4114	324	3.8	2.0	2.2	19.2	-1.64	0.08	53.0
4119	28	8.6	1.0	1.7	19.6	-1.09	0.18	36.5
4121	25	8.2	1.8	2.5	19.0	-0.91	0.08	34.1
4122	122	3.1	1.9	1.9	16.2	0.35	0.04	35.0
4123	92	6.8	1.9	2.8	22.2	-0.53	0.05	44.2
4124	38	11.0	2.0	2.9	16.1	-0.74	0.24	78.8
4127	24	8.5	1.4	2.1	18.3	-0.79	0.17	11.2
4128	31	7.9	2.0	2.4	14.1	0.09	0.06	10.0
4129	16	9.2	3.4	4.3	8.9	-0.06	0.09	71.3
4130	107	5.4	2.7	3.7	8.2	0.01	0.09	60.4
4132	75	5.8	2.8	3.9	10.9	-0.28	0.19	71.5
4133	151	4.4	2.9	3.2	13.2	-0.49	0.10	65.8
4135	10	7.3	2.7	4.3	13.4	-0.20	0.37	76.9
4137	23	8.6	4.2	6.2	13.7	-0.45	0.08	22.1
4139	100	10.0	3.5	5.8	9.5	-0.26	0.11	37.9
4140	60	13.7	2.8	5.4	11.8	-0.34	0.05	35.1
4141	134	12.7	2.8	5.2	10.6	-0.36	0.14	41.5
4142	104	14.9	3.0	5.6	7.7	-0.19	0.19	58.1
4143	147	14.5	2.7	5.8	10.9	-0.33	0.12	55.2
4144	80	14.6	3.0	5.8	7.4	-0.22	0.17	17.0
4145	133	13.7	3.7	5.4	4.4	-0.07	0.14	17.7
4147	151	12.1	2.8	5.7	8.0	-0.20	0.12	68.1
4148	76	12.7	2.9	5.3	9.0	-0.29	0.13	16.8
4149	87	14.0	3.4	5.6	6.6	-0.17	0.15	2.8
4150	2	14.8	3.0	7.8	9.8	-0.83	0.48	64.3
4169	165	9.9	5.2	6.4	15.4	0.11	0.05	39.0
4206	22	16.2	5.8	7.4	14.2	-0.25	0.07	74.1
4209	2562	5.0	3.1	5.2	5.1	0.02	0.43	89.4
4213	73	6.4	7.5	7.6	10.0	-0.16	0.15	1.9
4218	560	5.1	2.5	3.7	13.4	-0.73	0.10	54.4
4219	863	6.6	3.2	4.5	9.7	-0.14	0.09	22.3
4226	166	8.5	4.8	5.7	15.5	-0.15	0.08	54.6
4229	231	8.2	2.7	4.6	12.4	0.82	0.08	54.3
4231	44	12.3	4.1	7.1	29.3	0.28	0.15	22.2
4455	80	10.3	10.9	11.3	8.3	0.01	0.23	83.6
4456	456	12.0	5.8	7.6	4.5	0.12	0.14	61.2
4457	85	12.2	2.3	4.0	11.8	-0.14	0.41	64.6
4740	413	49.6	13.4	20.4	20.6	0.05	0.23	30.8
4742	540	65.8	9.9	18.0	21.2	-0.01	0.41	2.3
4744	1870	82.9	13.5	20.3	8.2	0.03	0.04	83.6
4757	144	90.4	10.7	31.8	10.0	0.00	0.09	38.2
4781	329	43.6	23.1	28.9	6.8	0.03	0.20	19.7
4787	1184	71.6	22.0	31.6	11.8	0.02	0.05	20.5
4806	69	49.4	11.8	20.5	5.3	0.00	0.11	80.0
4820	1621	48.6	5.7	9.3	10.9	0.04	0.16	77.5
4841	76	12.6	5.4	7.1	6.1	0.06	0.12	45.8
4842	143	6.3	6.0	7.5	11.5	-0.25	0.11	45.4
4843	73	17.2	6.8	9.7	6.7	-0.19	0.09	47.8
4844	36	22.6	7.0	10.3	5.0	-0.16	0.10	27.0
4845	297	4.2	5.2	7.3	11.5	0.52	0.09	39.1
4848	71	14.2	6.6	7.7	11.5	-0.42	0.12	22.2
4850	193	13.7	5.6	6.7	4.7	-0.05	0.19	27.5
4858	59	14.5	7.9	9.4	10.6	-0.45	0.38	70.1

NGA#	$I_{a,NP1}$ (cm/s)	$D_{5-95,NP1}$ (s)	$D_{0-5,NP1}$ (s)	$D_{0-30,NP1}$ (s)	$\omega_{mid,NP1}/\pi$ (rad/s)	ω'_{NP1}/π (rad/s^2)	$\zeta_{f,NP1}$	α_{NP1} (°)
4863	250	16.3	4.6	9.8	7.0	-0.21	0.16	71.2
4864	234	12.6	5.6	7.9	8.0	-0.18	0.16	78.6
4865	196	19.6	4.3	6.1	5.9	-0.06	0.34	86.6
4867	134	10.8	4.5	6.8	15.7	-0.07	0.04	63.7
4868	423	14.5	8.3	11.6	3.6	-0.01	0.15	83.8
4869	51	21.8	6.0	10.1	11.9	-0.46	0.29	43.3
4872	32	22.0	7.3	9.8	9.1	-0.29	0.13	48.1
4873	265	5.9	6.3	8.0	14.5	-0.68	0.48	40.3
4874	561	8.2	6.0	9.3	4.4	0.00	0.10	76.4
4876	1068	9.3	2.9	3.9	5.5	-0.16	0.61	70.8
4882	188	15.3	4.3	8.0	11.6	-0.29	0.06	72.1
5262	78	10.9	3.8	4.5	14.9	-0.09	0.07	68.8
5265	288	17.0	5.2	8.7	7.0	-0.11	0.07	65.9
5267	79	8.9	7.3	8.8	16.2	-0.59	0.06	55.7
5270	45	12.2	6.5	7.3	7.5	-0.08	0.08	13.3
5274	41	24.6	4.6	8.4	12.3	-0.26	0.13	59.0
5275	40	23.7	4.9	8.4	11.0	-0.18	0.14	29.8
5284	32	35.5	7.3	9.8	9.6	-0.22	0.29	70.5
5474	87	17.2	5.3	9.0	22.4	0.04	0.12	85.4
5478	232	9.8	3.5	5.7	14.7	-0.34	0.07	35.9
5482	2609	8.0	3.8	8.3	8.5	-0.03	0.08	69.7
5484	53	14.7	5.5	9.8	15.7	-0.12	0.12	37.4
5618	139	19.6	5.1	8.1	20.1	-0.44	0.21	89.1
5623	50	14.4	4.3	7.8	16.0	-0.12	0.13	4.4
5636	62	22.6	7.4	11.5	19.7	-0.06	0.07	82.0
5651	54	25.2	7.0	12.0	18.0	-0.08	0.08	81.8
5654	83	23.1	6.5	12.3	20.3	-0.03	0.08	4.7
5656	348	22.3	3.9	7.9	15.1	-0.39	0.14	55.0
5657	2679	11.2	1.5	4.5	14.8	0.09	0.17	39.9
5658	1573	11.1	3.7	6.4	12.5	-0.07	0.10	88.3
5663	938	13.6	4.6	6.0	14.9	-0.15	0.05	25.3
5664	425	36.5	5.2	8.7	6.3	-0.16	0.23	40.7
5678	80	9.2	4.3	5.4	7.1	0.03	0.10	24.4
5775	93	16.2	6.1	7.6	26.1	-0.57	0.08	89.5
5776	39	16.6	5.7	7.6	14.6	-0.26	0.18	88.3
5783	78	18.7	5.7	8.6	11.7	-0.05	0.19	45.8
5800	35	18.0	5.5	9.0	14.3	-0.47	0.25	36.3
5804	101	9.7	4.6	8.5	24.8	-0.77	0.16	48.8
5806	74	16.8	4.8	8.5	7.1	-0.26	0.38	14.2
5807	174	11.3	4.5	7.1	24.0	-0.42	0.12	40.1
5809	105	11.3	4.2	6.5	15.5	-0.23	0.20	64.5
5810	50	28.1	3.6	8.5	15.6	-0.51	0.34	36.0
5813	214	32.6	5.4	9.0	12.9	-0.36	0.60	42.8
5815	94	13.2	5.5	8.2	10.5	0.07	0.05	44.9
5818	787	13.0	3.3	4.7	8.3	0.15	0.08	39.2
5819	272	18.1	6.0	9.8	26.4	0.03	0.11	70.2
6915	472	13.3	10.4	16.3	12.3	-0.06	0.13	8.6
6948	58	23.2	7.6	14.7	13.9	0.03	0.14	31.0
6971	103	21.0	8.2	16.1	6.0	-0.05	0.19	41.9
8110	16	7.9	3.3	3.9	16.0	0.34	0.10	33.5
8157	1551	5.0	1.0	2.1	8.4	0.12	0.68	7.9
8158	648	3.9	2.2	3.0	20.1	0.15	0.19	54.9

Table A. 9 Identified parameters for intermediate component of non-pulselike records.

NGA#	$I_{a,NP2}$ (cm/s)	$D_{5-95,NP2}$ (s)	$D_{0-5,NP2}$ (s)	$D_{0-30,NP2}$ (s)	$\omega_{mid,NP2}/\pi$ (rad/s)	ω'_{NP2}/π (rad/s^2)	$\zeta_{f,NP2}$
1	7	2.5	0.9	1.6	11.5	1.14	0.07
28	5	28.3	1.8	5.5	12.2	-0.42	0.13
33	23	6.0	2.1	3.2	8.9	-0.57	0.06
57	70	15.4	1.2	2.4	10.3	-0.19	0.25
63	3	17.9	0.7	1.8	20.6	-0.23	0.48
70	20	19.3	1.2	4.5	9.1	-0.07	0.36
71	74	12.5	0.8	1.5	14.9	-0.16	0.26
72	15	13.7	1.3	3.4	21.3	-0.27	0.20
73	10	11.8	0.5	1.2	27.2	-0.77	0.27
78	26	18.9	0.8	2.5	10.2	-0.28	0.17
79	13	14.6	4.8	7.3	10.4	-0.40	0.29
80	11	14.0	1.5	4.1	11.4	0.03	0.14
87	18	13.0	0.6	3.4	19.7	-0.43	0.21
125	78	4.3	2.5	3.2	7.4	0.01	0.07
136	7	7.8	1.5	2.4	10.2	-1.11	0.08
139	131	10.5	3.9	6.4	13.4	0.08	0.06
146	6	6.8	1.2	2.5	20.5	-0.94	0.17
152	5	8.9	1.9	4.0	10.1	-0.57	0.13
153	5	8.6	2.8	4.5	8.8	-0.37	0.15
164	108	33.4	5.1	10.3	11.9	-0.13	0.19
190	9	11.6	2.8	7.0	12.5	-0.46	0.14
210	2	13.4	4.2	5.4	10.2	-0.17	0.06
214	7	14.0	3.4	5.8	6.5	-0.35	0.05
215	4	25.2	1.4	3.8	5.8	-0.11	0.07
265	100	7.5	3.2	4.8	13.9	-0.61	0.50
318	4	11.5	1.5	3.1	14.3	-0.63	0.08
336	7	13.8	4.1	5.7	7.3	-0.16	0.07
340	27	12.0	3.6	6.8	7.8	-0.27	0.05
351	9	15.2	3.9	5.5	5.5	-0.07	0.09
359	34	11.5	4.7	6.4	5.3	-0.13	0.05
362	10	14.6	2.6	6.1	8.5	-0.03	0.09
369	24	13.6	5.0	6.1	3.4	-0.03	0.11
448	53	7.9	2.5	4.2	11.7	-0.73	0.09
450	5	11.0	3.6	5.6	5.4	0.00	0.09
454	5	8.7	0.6	2.6	15.6	-0.45	0.11
455	5	9.5	0.9	2.8	18.7	-0.75	0.11
514	25	8.4	2.0	2.7	15.5	-0.24	0.15
516	11	7.0	1.7	4.9	29.9	-6.20	0.26
518	12	10.6	0.8	3.3	14.8	-0.28	0.13
521	13	4.9	4.1	4.3	18.2	0.47	0.19
524	4	15.9	2.9	4.6	5.1	0.14	0.21
527	52	6.7	1.8	3.2	5.0	0.24	0.71
534	31	8.6	3.3	4.4	16.1	-0.10	0.30
537	4	9.5	2.0	2.6	24.1	0.40	0.39
540	175	5.4	1.3	1.9	10.3	0.42	0.10
543	3	20.0	2.9	4.8	14.0	-0.29	0.28
545	2	16.9	1.3	2.3	25.3	-0.28	0.14
546	1	17.1	2.9	3.7	7.4	0.00	0.22

NGA#	$I_{a,NP2}$ (cm/s)	$D_{5-95,NP2}$ (s)	$D_{0-5,NP2}$ (s)	$D_{0-30,NP2}$ (s)	$\omega_{mid,NP2}/\pi$ (rad/s)	ω'_{NP2}/π (rad/s^2)	$\zeta_{f,NP2}$
548	32	12.7	3.3	4.1	9.9	-0.20	0.18
550	13	11.1	1.2	3.4	26.8	-0.51	0.06
552	9	9.6	3.2	3.9	8.2	-0.05	0.08
553	4	13.1	3.0	4.7	10.2	-0.45	0.41
585	287	4.5	1.6	2.6	10.9	-0.56	0.59
589	74	6.3	2.1	2.7	13.9	-0.59	0.10
590	17	8.7	2.2	2.9	15.4	-0.35	0.15
592	19	10.7	1.9	3.3	11.2	-0.17	0.08
594	6	12.0	2.1	3.1	10.9	-0.26	0.12
596	6	11.7	3.4	4.5	13.9	-0.19	0.08
598	12	10.5	2.5	4.2	18.1	0.01	0.07
600	14	11.4	2.9	4.0	11.9	-0.24	0.10
619	75	6.3	1.9	3.0	14.5	-0.41	0.08
620	26	7.4	2.4	2.9	13.5	0.17	0.14
621	7	12.7	2.6	3.9	12.0	-0.03	0.14
632	10	9.5	1.9	2.5	10.7	-0.41	0.07
637	15	8.7	1.9	2.6	9.6	-0.18	0.10
643	1	7.2	1.9	2.5	17.2	0.31	0.12
648	13	6.3	3.1	3.8	10.4	0.31	0.14
663	13	10.3	1.4	3.2	29.2	0.08	0.14
669	21	9.7	2.6	4.6	13.5	-0.18	0.09
675	10	11.0	1.9	2.8	10.5	-0.30	0.19
680	5	6.3	1.7	2.5	13.6	0.65	0.37
683	29	6.8	2.1	2.8	13.1	-0.31	0.10
685	3	16.4	3.6	5.2	14.9	-0.29	0.19
690	34	8.4	1.8	3.2	10.5	-0.10	0.06
691	13	11.4	1.4	2.2	14.3	-0.21	0.32
697	5	12.4	0.8	2.1	8.0	0.00	0.14
727	299	12.7	3.0	5.9	10.0	-0.18	0.06
739	66	11.2	2.8	4.8	9.1	-0.14	0.19
741	388	9.5	3.8	6.3	9.1	0.20	0.31
753	253	7.9	1.6	3.0	3.8	0.16	0.11
763	66	5.2	2.0	2.4	11.8	0.32	0.14
765	98	6.8	2.0	2.6	17.1	-0.14	0.13
769	19	13.8	2.6	4.0	10.1	-0.24	0.15
775	3	16.7	3.2	6.3	12.0	-0.40	0.14
779	251	10.6	3.3	5.1	8.5	-0.45	0.26
787	47	12.8	6.2	8.1	6.9	-0.05	0.08
801	99	9.6	4.9	6.9	15.4	-0.11	0.13
809	78	9.2	4.1	7.0	23.2	-0.75	0.12
810	143	9.1	3.2	6.4	12.0	0.17	0.16
811	358	10.5	3.1	5.6	13.2	-0.16	0.16
825	203	14.4	1.7	2.9	9.3	-0.07	0.13
827	22	18.7	5.3	7.0	6.4	-0.11	0.09
830	47	17.5	5.0	12.2	15.1	-0.02	0.07
3748	89	14.4	4.4	6.3	5.7	-0.09	0.12
3750	62	13.2	5.5	6.4	10.1	-0.53	0.08
864	141	26.9	4.7	9.0	5.2	-0.04	0.10
881	66	31.5	4.7	10.7	6.5	-0.02	0.46
3753	71	32.4	4.6	9.2	10.5	-0.10	0.11
3757	52	36.1	5.7	12.3	10.5	-0.09	0.15
3759	55	33.3	3.5	10.4	15.4	-0.01	0.12

NGA#	$I_{a,NP2}$ (cm/s)	$D_{5-95,NP2}$ (s)	$D_{0-5,NP2}$ (s)	$D_{0-30,NP2}$ (s)	$\omega_{mid,NP2}/\pi$ (rad/s)	ω'_{NP2}/π (rad/s^2)	$\zeta_{f,NP2}$
901	191	10.6	2.5	4.0	11.5	0.28	0.08
6057	16	15.2	4.0	7.0	14.2	-0.05	0.13
6059	28	12.0	5.2	9.8	8.9	-0.55	0.38
952	191	8.3	2.2	3.8	10.3	-0.19	0.06
954	34	11.1	4.1	5.8	15.5	-0.24	0.06
957	22	11.6	2.5	3.8	8.0	-0.07	0.18
963	276	9.2	4.7	6.8	6.4	-0.18	0.04
974	62	11.7	3.7	5.6	12.0	-0.25	0.13
986	36	11.6	2.6	6.9	6.8	-0.13	0.19
989	62	8.9	2.6	5.1	8.6	-0.24	0.09
991	27	9.8	3.9	7.0	10.5	-0.40	0.05
1006	77	13.0	3.0	6.3	13.9	-0.44	0.07
1011	14	8.9	2.4	4.3	16.0	-0.54	0.10
1012	78	8.4	2.8	5.3	13.3	-0.49	0.27
1016	28	11.0	3.3	4.9	10.1	-0.10	0.07
1020	29	11.2	3.3	6.5	13.9	-0.12	0.09
1023	9	12.3	1.4	5.1	15.0	-0.41	0.09
1078	53	9.7	2.2	4.2	10.7	0.09	0.26
1080	361	6.2	2.9	4.0	5.1	0.47	0.15
1083	28	15.4	3.1	6.1	7.3	-0.16	0.09
1089	49	9.5	2.1	4.4	12.7	-0.26	0.17
1091	32	7.3	4.0	5.7	11.3	-0.01	0.08
1099	5	10.2	2.3	3.9	11.2	-0.51	0.20
1108	80	6.0	4.3	5.2	7.5	-0.20	0.10
1111	179	11.4	2.7	4.6	6.9	-0.02	0.09
1166	25	19.5	7.2	11.9	5.5	-0.18	0.13
1197	517	8.0	9.9	12.9	8.0	-0.08	0.45
1198	80	32.0	8.2	12.7	7.6	-0.10	0.35
1202	120	27.4	7.4	12.9	6.0	-0.04	0.10
1205	139	32.0	11.2	14.9	7.0	-0.04	0.08
1206	15	37.3	11.3	16.9	6.4	-0.06	0.08
1208	56	32.9	12.0	16.9	9.7	-0.14	0.18
1227	99	30.6	6.4	11.7	5.5	-0.04	0.07
1231	371	26.3	8.7	11.6	4.3	-0.04	0.28
1234	32	30.9	11.6	17.6	4.1	-0.01	0.09
1235	37	31.2	14.1	17.3	7.6	0.00	0.08
1380	13	31.2	13.6	16.1	8.1	-0.07	0.09
1484	92	21.3	13.9	20.4	5.8	-0.11	0.08
1488	50	31.1	11.3	19.8	9.4	-0.22	0.20
1490	65	26.4	9.8	15.7	6.5	-0.12	0.13
1494	72	28.4	6.3	14.6	7.4	-0.14	0.18
1497	46	31.2	9.3	16.9	5.5	-0.10	0.32
1499	49	26.4	9.8	16.7	6.1	-0.09	0.27
1500	98	36.3	8.9	16.9	5.6	-0.07	0.40
1504	159	24.1	5.9	7.8	7.1	-0.07	0.23
1506	170	28.7	12.4	22.2	3.6	-0.02	0.24
1507	858	25.7	2.4	9.2	9.1	-0.04	0.09
1508	487	23.7	2.7	10.6	7.1	0.06	0.25
1509	213	21.1	9.1	15.5	8.3	-0.14	0.24
1512	366	26.1	3.2	12.2	10.1	-0.11	0.09
1513	382	27.0	4.0	16.2	9.6	-0.02	0.14
1517	377	23.1	6.1	16.0	4.1	-0.03	0.11
1520	217	10.4	10.6	13.4	24.6	0.39	0.14

NGA#	$I_{a,NP2}$ (cm/s)	$D_{5-95,NP2}$ (s)	$D_{0-5,NP2}$ (s)	$D_{0-30,NP2}$ (s)	$\omega_{mid,NP2}/\pi$ (rad/s)	ω'_{NP2}/π (rad/s^2)	$\zeta_{f,NP2}$
1521	154	24.9	3.7	15.4	9.6	-0.08	0.26
1527	52	26.9	11.0	17.1	5.0	-0.07	0.26
1532	58	29.3	11.8	20.9	4.4	-0.07	0.14
1533	117	33.3	9.0	18.7	5.8	-0.10	0.09
1534	106	33.9	10.3	20.4	4.5	-0.06	0.35
1535	115	34.3	8.2	17.0	5.0	-0.09	0.30
1541	102	34.4	7.1	14.3	6.2	-0.05	0.66
1545	133	33.0	6.4	12.6	10.3	-0.18	0.17
1546	141	31.2	5.6	12.6	8.9	-0.04	0.20
1549	530	31.1	3.7	12.4	11.7	-0.15	0.05
1611	6	14.6	5.5	7.9	13.5	-0.35	0.64
1612	19	15.1	3.7	6.3	13.9	-0.26	0.21
1613	2	18.5	6.2	10.7	9.4	-0.34	0.19
1614	17	16.5	4.8	6.4	8.9	-0.17	0.07
1616	1	21.3	3.1	8.9	12.0	-0.46	0.21
1617	173	13.9	4.2	6.2	16.9	-0.69	0.18
1618	35	14.8	4.1	6.6	9.6	-0.33	0.13
1631	21	7.1	1.9	3.3	14.3	-0.27	0.09
1632	34	5.0	2.5	3.6	21.1	-0.39	0.08
1633	429	29.1	6.0	9.5	15.0	-0.04	0.11
1641	13	6.1	2.3	3.2	10.6	-0.40	0.10
1643	7	13.8	4.2	5.0	13.0	-0.18	0.25
1645	29	3.5	0.4	1.7	20.3	-0.55	0.08
1647	9	4.3	2.9	3.3	8.4	-0.19	0.08
6875	7	16.1	3.3	4.9	10.9	-0.43	0.46
6876	34	7.2	3.8	6.6	14.1	-0.03	0.08
6878	22	9.5	2.7	4.6	12.2	-0.43	0.12
1787	73	12.6	3.8	5.7	7.1	0.13	0.12
3871	131	15.7	6.9	9.7	26.4	0.10	0.03
3907	129	22.6	3.4	7.8	17.4	-0.01	0.09
3925	25	15.9	3.2	6.5	27.6	0.08	0.05
3926	50	19.1	6.2	7.1	16.5	0.03	0.06
3927	106	22.8	3.2	7.2	15.5	0.10	0.02
3932	57	16.4	5.9	6.6	21.5	0.03	0.05
3943	32	8.6	6.0	7.4	11.6	-0.03	0.36
3947	449	18.7	2.4	5.9	11.6	0.06	0.05
3948	84	21.9	5.0	8.1	15.5	0.07	0.04
3954	20	12.1	5.6	8.3	12.1	-0.42	0.08
3964	293	13.5	4.4	6.3	18.8	-0.06	0.14
3966	175	10.4	4.3	5.9	14.5	0.28	0.08
3979	21	14.2	2.4	5.0	14.4	-0.28	0.23
4013	14	20.6	2.5	4.6	6.5	-0.03	0.11
4031	148	9.8	3.7	5.2	9.8	-0.28	0.11
4064	27	7.0	2.5	3.2	18.5	-0.92	0.08
4067	14	8.3	1.1	2.1	18.9	-0.35	0.10
4068	58	11.0	2.1	3.8	8.4	-0.22	0.17
4069	14	11.1	0.8	3.4	17.6	-0.67	0.06
4070	145	6.2	2.7	3.2	12.6	-0.35	0.22
4071	31	5.6	3.3	4.1	8.8	-0.37	0.04
4073	18	2.9	3.9	4.1	16.2	-0.34	0.03
4075	17	3.1	2.4	3.4	23.1	-2.44	0.08
4083	14	10.1	2.1	2.5	11.4	-0.33	0.12
4099	75	3.4	2.1	2.4	13.4	-0.36	0.06

NGA#	$I_{a,NP2}$ (cm/s)	$D_{5-95,NP2}$ (s)	$D_{0-5,NP2}$ (s)	$D_{0-30,NP2}$ (s)	$\omega_{mid,NP2}/\pi$ (rad/s)	ω'_{NP2}/π (rad/s^2)	$\zeta_{f,NP2}$
4114	100	4.6	1.9	2.2	16.5	-0.47	0.13
4119	25	9.1	1.2	2.1	19.3	-0.83	0.20
4121	12	11.9	1.9	2.6	15.1	-0.72	0.15
4122	38	7.2	1.7	1.9	24.3	-1.15	0.09
4123	43	8.1	1.9	2.8	24.0	-0.48	0.07
4124	22	12.1	2.2	3.0	21.3	-1.06	0.22
4127	17	8.8	1.7	2.2	16.8	-1.02	0.16
4128	15	10.0	1.9	2.8	17.2	-0.51	0.08
4129	6	9.5	3.3	4.2	9.4	-0.35	0.08
4130	66	7.0	3.0	4.1	11.7	-0.85	0.07
4132	39	5.9	3.0	3.9	9.9	-0.52	0.17
4133	74	5.9	2.4	3.4	16.6	-1.10	0.19
4135	9	6.9	3.0	4.1	14.2	0.22	0.56
4137	12	10.1	3.2	5.5	15.9	-0.68	0.08
4139	40	15.2	2.7	5.2	14.3	-0.58	0.15
4140	43	15.2	2.8	5.1	9.9	-0.25	0.08
4141	71	16.7	2.8	6.0	9.2	-0.30	0.22
4142	100	15.7	2.9	6.0	8.1	-0.27	0.17
4143	113	14.3	3.1	5.8	12.1	-0.48	0.19
4144	29	19.2	2.7	6.2	10.0	-0.33	0.16
4145	33	16.8	2.7	6.3	9.6	-0.27	0.13
4147	111	14.0	3.2	5.4	8.7	-0.25	0.12
4148	54	20.3	2.8	5.6	10.1	-0.37	0.10
4149	43	22.7	2.6	5.7	8.1	-0.21	0.17
4150	1	13.9	3.4	7.2	14.8	-1.45	0.81
4169	70	12.8	4.3	7.1	16.3	0.00	0.10
4206	16	14.1	6.2	8.1	12.9	-0.09	0.05
4209	1006	11.8	3.1	5.4	5.7	-0.05	0.15
4213	34	9.6	7.0	7.6	15.8	-0.47	0.09
4218	248	5.6	2.4	3.5	14.9	-0.60	0.19
4219	648	6.8	3.2	5.5	10.2	0.03	0.16
4226	124	11.3	5.0	6.6	14.9	-0.19	0.09
4229	117	9.6	2.2	3.6	16.0	0.27	0.13
4231	25	11.7	4.9	7.1	22.3	0.47	0.18
4455	40	13.4	10.5	11.8	10.0	-0.08	0.21
4456	200	13.3	5.6	7.2	6.2	0.11	0.16
4457	53	11.7	2.5	4.4	14.2	-0.08	0.36
4740	405	56.3	13.2	20.9	21.9	0.04	0.19
4742	474	70.9	10.3	19.4	21.1	-0.04	0.36
4744	1436	86.7	12.5	18.0	8.3	0.02	0.05
4757	115	90.9	9.6	17.7	10.4	0.00	0.09
4781	265	45.2	22.8	29.4	7.5	0.07	0.18
4787	632	72.1	20.2	31.2	13.3	0.01	0.12
4806	45	51.8	10.9	21.0	5.5	0.00	0.09
4820	755	57.6	4.8	9.3	13.8	0.04	0.24
4841	39	16.0	5.7	8.0	7.7	-0.07	0.07
4842	56	12.6	6.3	7.6	14.2	-0.36	0.11
4843	50	19.7	6.5	9.0	8.0	-0.17	0.13
4844	25	23.3	7.3	10.7	4.4	-0.11	0.11
4845	162	4.9	5.3	7.3	13.5	0.05	0.05
4848	54	17.4	6.3	8.0	10.7	-0.34	0.13
4850	84	17.9	5.2	6.5	7.0	-0.20	0.18
4858	44	16.9	7.0	8.8	13.0	-0.50	0.32

NGA#	$I_{a,NP2}$ (cm/s)	$D_{5-95,NP2}$ (s)	$D_{0-5,NP2}$ (s)	$D_{0-30,NP2}$ (s)	$\omega_{mid,NP2}/\pi$ (rad/s)	ω'_{NP2}/π (rad/s^2)	$\zeta_{f,NP2}$
4863	174	19.3	5.0	9.9	7.0	-0.23	0.16
4864	141	15.2	5.8	10.3	7.9	-0.10	0.19
4865	106	24.0	4.8	10.0	8.4	-0.28	0.20
4867	81	10.3	4.4	5.1	15.8	0.03	0.08
4868	140	16.6	6.2	12.1	4.5	-0.09	0.16
4869	33	23.2	5.6	8.4	15.8	-0.48	0.22
4872	22	24.6	6.6	8.9	7.7	-0.23	0.13
4873	110	8.3	5.6	7.1	18.8	-0.65	0.38
4874	319	13.0	4.8	6.5	5.5	-0.15	0.08
4876	490	12.1	3.0	5.5	8.6	-0.34	0.50
4882	134	23.6	4.9	7.5	11.5	-0.25	0.06
5262	47	12.2	3.7	5.6	14.8	-0.12	0.05
5265	187	15.8	4.9	6.6	7.0	-0.10	0.09
5267	48	11.7	7.5	9.3	15.1	-0.53	0.12
5270	31	15.0	6.2	7.5	9.8	-0.14	0.06
5274	35	27.4	4.7	8.5	11.3	-0.24	0.17
5275	38	26.4	4.9	8.9	11.0	-0.23	0.14
5284	19	32.2	6.4	9.2	13.8	-0.33	0.20
5474	43	18.1	5.1	8.8	21.1	0.01	0.16
5478	168	9.7	3.4	6.0	18.7	-0.44	0.09
5482	1149	7.9	4.6	7.9	10.8	-0.06	0.10
5484	46	14.9	5.8	9.7	17.2	-0.16	0.09
5618	128	24.8	5.4	9.4	15.9	-0.39	0.37
5623	41	17.2	4.3	8.3	17.1	-0.18	0.09
5636	51	25.1	7.1	12.2	19.4	-0.12	0.08
5651	36	25.8	6.4	11.0	20.0	-0.09	0.12
5654	68	21.1	6.4	10.3	20.2	-0.05	0.12
5656	286	24.8	4.0	8.8	13.3	-0.39	0.27
5657	1972	12.7	1.1	2.9	14.5	0.24	0.15
5658	770	14.1	3.6	7.0	14.1	-0.08	0.12
5663	462	16.8	4.5	5.7	13.1	-0.19	0.11
5664	267	34.2	4.4	5.8	8.8	-0.18	0.23
5678	68	9.9	4.1	5.6	14.1	-0.04	0.06
5775	81	17.0	6.1	9.2	25.1	-0.76	0.24
5776	29	19.0	5.4	8.4	13.0	-0.21	0.19
5783	58	18.8	5.3	7.7	14.0	-0.07	0.21
5800	29	19.0	5.4	9.6	12.4	-0.37	0.63
5804	68	9.4	4.8	6.9	23.2	-0.64	0.15
5806	61	17.3	5.4	8.3	10.5	-0.38	0.83
5807	98	13.7	3.2	7.2	27.0	-0.55	0.18
5809	74	11.0	3.7	7.3	21.5	-0.40	0.29
5810	43	21.6	4.6	8.1	15.5	-0.49	0.26
5813	138	40.7	4.9	8.7	13.7	-0.28	0.47
5815	78	17.9	3.9	8.0	12.5	-0.18	0.06
5818	405	15.8	3.4	5.1	10.5	0.06	0.07
5819	171	17.8	5.5	9.4	28.2	-0.07	0.18
6915	323	18.2	10.1	15.7	12.7	-0.07	0.08
6948	32	22.7	7.9	15.3	15.6	-0.11	0.18
6971	91	24.0	7.9	15.2	7.0	-0.05	0.12
8110	7	10.0	3.2	4.2	21.6	0.02	0.09
8157	826	6.1	0.7	2.0	10.9	-0.57	0.41
8158	409	4.1	2.3	3.1	18.1	0.20	0.41